Cumhuriyet Science Journal
Faculty of Science, Cumhuriyet University
58140 - Sivas - Türkiye
Phone: +90(346) 487 13 72
Fax: +90(346) 219 11 86
e-mail: csj@cumhuriyet.edu.tr
http://csj.cumhuriyet.edu.tr/en
http://dergipark.org.tr/en/pub/csj

Cumhuriyet Science Journal Vol: 45 No: 3 Year 2024

Sivas Cumhuriyet University

ISSN : 2680-2587
e-ISSN : 246-2587X
dergipark.org.tr/tr/pub/csj
e-mail: csj@cumhuriyet.edu.tr

Cumhuriyet Science Journal

Cumhuriyet Science Journal (CSJ) is an official publication of Sivas Cumhuriyet University, Science Faculty. The high quality research papers related to the natural sciences are published as online four times a year. CSJ is an open access, free of charge journal and all articles in CSJ have undergone peer review and upon acceptance are immediately and permanently free for everyone to read and download.

Volume: 45 Number: 3 Year: 2024

ISSN: 2587-2680
e-ISSN: 2587-246X
Period: Quarterly
Founded: 2002
Publisher: Sivas Cumhuriyet University

Cumhuriyet Science Journal (CSJ)

Journal Previous Name: Cumhuriyet Üniversitesi Fen-Edebiyat Fakültesi Fen Bilimleri Dergisi

Old ISSN: 1300-1949

Section Editors

Abstracted&Indexeding

ULAKBİM TR-Dizin
Index Copernicus (ICI Journals Master List)
Clarivate Analytics Zoological Record
Crossref
WorldCat
Akademik Dizin
Arastirmax Bilimsel Yayın İndeksi
Bielefeld Academic Search Engine (BASE)
Directory of Research Journal Indexing (DRJI)
Google Scholar
Research Gate
Idealonline

Editorial Board

Layout Editors:

Copyeditors:

Proofreader:

Publication Type: Peer Reviewed Journal

Cite Type: Cumhuriyet Sci. J.

Contact Information

Faculty of Science Cumhuriyet University
58140 Sivas- TURKEY
Phone: +90 (346) 487 13 72
Fax: +90 (346) 219 11 86
e-mail: csj@cumhuriyet.edu.tr
http://dergipark.gov.tr/csj

Cumhuriyet Sci. J., 45(3) (2024) 449-453
DOI: https://doi.org/10.17776/csj.1488875

Cumhuriyet Science Journal

| csj.cumhuriyet.edu.tr | Founded: 2002 ISSN: 2587-2680 e-ISSN: 2587-246X Publisher: Sivas Cumhuriyet University

In Vitro Antioxidant Assessment of Methanol and Water Extracts of *Anthemis kotschyana* Boiss. var. *kotschyana*

Gülşen Güçlü[1,a,*]

[1] *Department of Health Programs, Health Services Vocational School, Sivas Cumhuriyet University, Sivas, Türkiye.*
**Corresponding author*

Research Article

History
Received: 23/05/2024
Accepted: 14/08/2024

ABSTRACT

The genus *Anthemis*, with approximately 130 species globally, is significant within the Asteraceae family and is widely used in traditional medicine. Studies on the biological activity of *Anthemis kotschyana*, an endemic species found in Turkey, are limited. This study investigated the chemical constituents and antioxidant activity of *Anthemis kotschyana* using two different extracts, methanol and water. The major components of the plant were determined by GC–MS. According to the data obtained, the major component was found to be "2-propenoic acid, a tridecyl ester" in the water extract and "cyclododecane" in the methanol extract. When the DPPH and ABTS radical scavenging activities were analysed, the methanol extract was found to be more active than the water extract in the DPPH experiment, while the opposite was observed in the ABTS experiment. The TPC was greater than the TFC based on the acquired results. The TPC of the water extract was 83.7 ± 15.6 mg GAE/g, the TPC of the MeOH extract was 170.7 ± 17.4 mg GAE/g, and the TFC of the water extract was 24.3 ± 7.2 QE/g, while the TFC of the MeOH extract was 65.6 ± 5.3 QE/g. For both substances, the amount of methanol extract was greater than that of the water extract. In conclusion, further studies on this species, known for its antioxidant activity and potential as a source of phenolic compounds, could support its use as a therapeutic agent in the future.

Keywords: *Anthemis kotschyana*, Antioxidant, DPPH, ABTS, Medicinal plant.

[a] gulsenguclu@cumhuriyet.edu.tr https://orcid.org/0000-0002-3599-213X

Introduction

The Asteraceae family is widely distributed throughout the planet, with the exception of Antarctica. It ranks first among flowering plants in terms of diversity, having more than 20,000 species and more than 1,100 genera. This family contains both annual and perennial species. The capitulum, a flower structure, is the most distinctive feature of this family [1]. The majority of plant life is found in glades, open meadowlands, and mountain vegetation. In moist tropical forests, they are less common [2]. Within the Asteraceae family, the genus *Anthemis* includes 51 species and 81 taxa that are registered in the Turkish flora [3,4]. A total of 36.3% of these species are endemic [5].

In traditional medicine, many species of this genus—especially flower organs—are widely used as sedatives, anti-inflammatory agents, gastrointestinal spasmolytics, and digestive aids. They are also applied externally to reduce pain and irritation as well as to cure wounds and ulcers [6]. It can be proposed that this therapeutic effect of *Anthemis* is related to the secondary metabolites it produces.

Sesquiterpene lactones (tatridin A, nobilin, 1-epi-tatridin B), phenolics (caffeoylquinic acid derivatives, 3-hydroxybenzoic acids, gallic and ferulic acids), and flavonoids (salvigenin, quercetin, naringenin, apigenin, pectolinarigenin, eupatilin and rutin) are the primary secondary metabolites of *Anthemis* according to phytochemical investigations [7-9]. This genus is also known to possess antibacterial, antispasmodic, antiproliferative, anticholinesterase and antioxidant properties [10-14].

Different effects on metabolic processes may emerge from variations in the kind, density, and interaction of antioxidant chemicals [15]. Exogenous antioxidants may help the healing process when a pathological outcome arises because antioxidants functioning in the defense mechanism of cells might not be enough to stifle free radicals. To improve metabolic defense in such situations, antioxidant-rich medicinal plants can be employed [16-18].

This study investigated the chemical composition and antioxidant properties of water and methanol (MeOH) extracts from *Anthemis kotschyana* plants that were grown in Turkey. In addition, this study is the first in the literature to involve the use of methanol extracts from plants. It is thought that the acquired data will benefit phytotherapeutic research.

Materials and Methods

Plant Material and Extract Preparation

Anthemis kotschyana plants were collected from Sivas Province in May 2019 in a meadow area at an average altitude of 1100 m. The general distribution of the plants was reported to be *Pinus* and *Quercus* forests, calcareous rocks and slopes at an average altitude of 400-2745 m [3]. After being harvested, the plants were shade-dried and sized appropriately for extraction using a lab-style grinder. The Biology Department of Sivas Cumhuriyet University identified the plant.

The plants were ground in a blender (blue house) after being dried in direct sunlight until they reached a constant weight. For 24 hours, with sporadic shaking, 10 g of dried plant material was soaked in 50 mL of MeOH (Sigma) and water. Next, No. 1 Whatman filter paper was used to filter the extract. A rotary evaporator operating at 40 °C and lower pressure was used three times to concentrate the filtrate.

The components and relative percentages of the extracts that were filter-dried in a rotary evaporator were ascertained by GC–MS [19]. The carrier gas, helium gas, was used at a steady flow rate of 1.5 mL/minute. For two minutes following the run, the splitless mode injection volume of 1 µl was set at 300 °C and designed to be 5 per minute between 80 and 300. The total running time was one hour [20]. Several libraries were used to investigate the chemical composition of the extract obtained from the dried leaves (W9N11. L, NIST05a. L and wiley7n.l).

In vitro Antioxidant Activity

2,2-Diphenyl-1picrylhydrazyl (DPPH) Assay

The antioxidant activity of the extracts was quantified using the DPPH radical scavenging assay, as previously described [21]. The plant extracts (water and MeOH) were dissolved in DMSO, and 180 µL of DPPH solution (made in MeOH at 40 µg/mL) was combined with 20 µl of test solutions at different concentrations in a 96-well plate. After 15 minutes in the dark, the absorbance levels on the plates were measured with a microplate reader at 540 nm. The standard and control were butylated hydroxytoluene (BHT) and DMSO, respectively. The experiments were conducted in triplicate, and the standard deviation (SD) was computed to assess the outcomes.

2,2′-Azino-bis-(3-ethylbenzothiazoline-6-sulfonic acid) (ABTS) assay

With a few minor adjustments, the ABTS cation radical decolorization activity of the extracts was assessed using the methodology of Re et al. [22]. The preparation of the test samples followed the DPPH protocol. 15 mL of 7 mM ABTS and 264 µL of 140 mM potassium persulfate solution were allowed to react in the dark at room temperature for 16 hours before the experiment to create a stock solution of ABTS + radical. The stock solution was diluted with MeOH to an absorbance of 0.70±0.02 at 734 nm, which was the starting point for the preparation of the ABTS working solution. Fifty microliters of the sample solution and 100 µL of the ABTS working solution were combined on a 96-well plate. After ten minutes of standing at room temperature, the absorbance of the mixture at 734 nm was measured. The ABTS·+ scavenging activity was compared using BHT as the antioxidant standard. The concentrations of the extracts utilized in the antioxidant tests ranged from 0–1 mg/mL.

Total phenol content

The total amount of phenol in the extract was ascertained as a result of the reaction with Folin–Ciocalteu (F–C) reagent. Following the appropriate dilution of the extract with 10 µL of DMSO, it was mixed with 100 µL of distilled water and newly diluted F–C reagent (10-fold). Five minutes later, 100 µL of 7.5% Na_2CO_3 was added, and after sixty minutes, the absorbance at 650 nm was measured. With the proper references (gallic acid in DMSO) and blanks (DMSO), parallel runs were carried out. The total amount of phenol was calculated using the sample absorbance values [21].

Total flavonoid content

A colorimetric method with aluminum chloride was used to determine the total flavonoid content of the extracts. For calibration, serial dilutions of 0.0625 mg/mL, 0.125 mg/mL, 0.25 mg/mL, 0.5 mg/mL, and 1 mg/mL were made using a 10 mg/mL quercetin stock solution. The ethanol-based test solution (150 µL, 0.3 mg/mL) was mixed with 2% $AlCl_3$ in a 96-well plate. The absorbance at 435 nm was measured following a 15-minute incubation period at room temperature. The total flavonoid concentration was calculated by multiplying the extract's dry weight by the mg equivalent of quercetin [23].

Results and Discussion

Chemical Composition

The chemical contents of the water and MeOH extracts of *Anthemis kotschyana* were determined by GC–MS (Table 1). The chemical contents of the water and MeOH extracts of plants showed significant differences in terms of a variety of components. According to the data obtained, 2-propenoic acid, a tridecyl ester, was found to constitute 24.07% of the major component of the water extract. The content of ethyl methyl ethylphosphonate was 17.17%. When we evaluated the data obtained from the MeOH extract, “cyclododecane”, with 16.72% as the major component, was found. Octadecane was the second major component at 9.15%.

Table 1. Chemical components of the water and methanol extracts of *A. kotschyana*

R.T.	Components	Area (%)	
		Water	MeOH
15.034	o-Hydroxyanisole	4.79	
15.063	Guasol		1.21
22.616	4-vinyl-2-methoxy-phenol		1.29
28.258	Tridecanol	11.16	
28.281	Dodecanol		5.80
29.374	Phenol, 2,4-bis(1,1-dimethylethyl)	9.09	3.25
32.166	Megastigmatrienone		1.50
33.041	Ethyl methyl ethylphosphonate	17.17	
33.453	2-Propenoic acid, tridecyl ester	24.07	
33.476	Cyclododecane		16.72
35.164	(-)-Loliolide		3.34
36.354	Hexahydropseudoionone		1.56
37.722	Hexadecanoic acid, methyl ester	4.88	6.64
38.420	Palmitinic acid		1.91
39.193	1-Hexadecanol	1.60	
40.463	Methyl linoleate		7.79
40.537	Oleic acid, methyl ester	1.27	
40.549	Methyl 7-octadecenoate		6.10
40.915	Methyl stearate	2.72	1.81
44.388	Oleic acid amide	2.54	
46.059	Octadecane		9.15
Total		79.29	68.07

This study represents the first investigation of the MeOH extract of *Anthemis kotschyana*. To date, studies utilizing different extracts of this plant are very limited. In 2020, a study was conducted with water and ethanol extracts of this plant, which revealed the major components to be hamnetin and quinic acid [12].

Antioxidant Activity

When the antioxidant activity of the *Anthemis kotschyana* extracts was assessed, the two extracts displayed varying levels of antioxidant activity in different *in vitro* systems. The greater the ability of the extracts to scavenge radicals was, the lower their IC_{50} value was. Both extracts displayed comparable levels of radical scavenging activity in DPPH and ABTS. The MeOH extract outperformed the water extract in the DPPH experiment (IC_{50} value: 31.04 µg/mL for water; IC_{50} value: 28.44 µg/mL for MeOH). Conversely, in the ABTS experiment, the water extract outperformed the MeOH extract (IC_{50} values: 108.9 µg/mL for MeOH and 103.8 µg/mL for water) (Figure 1). Nevertheless, in the water and MeOH extracts for DPPH and ABTS, the radical scavenging activity was less than that of the reference substance BHT (IC_{50} value: 7,7 µg/mL).

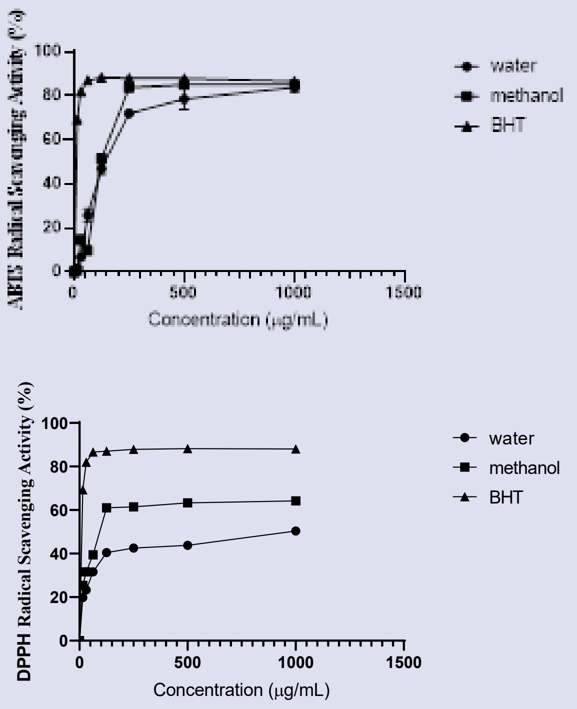

Figure 1. ABTS and DPPH radical scavenging activity of *A. kotschyana* extracts and reference BHT.

Bursal et al. (2020) reported that the DPPH radical scavenging activity of water and ethanol extracts of *A. kotschyana* was lower than that of the reference substance BHT. This result is consistent with the findings of the present study. Additionally, the water extract exhibited radical scavenging activity comparable to that of the ethanol extract, although the latter was more effective [12]. The data obtained from both studies suggest that the presence of bioactive compounds in *A. kotschyana* may play a role in its antioxidant activity.

Total Phenol and Flavonoid Content (TPC and TFC)

Phenolic compounds are important because of their antioxidant activity. The TPC and TFC of both the water and MeOH extracts of *A. kotschyana* were evaluated. The TPC was greater than the TFC, and the TFC of the MEOH extract was greater than that of the water extract (83.7 ± 15.6 mg GAE/g for the TPC of the water extract and 170.7 ± 17.4 mg GAE/g for the TPC of the MeOH extract; 24.3 ± 7.2 QE/g for the TFC of the water extract and 65.6 ± 5.3 QE/g for the TFC of the MeOH extract) (Figure 2). The observation that phenolics were present in greater quantities in the MeOH extract than in the water extract indicates that the choice of solvent has an impact on the ability to identify the phenolic compounds present in the plant.

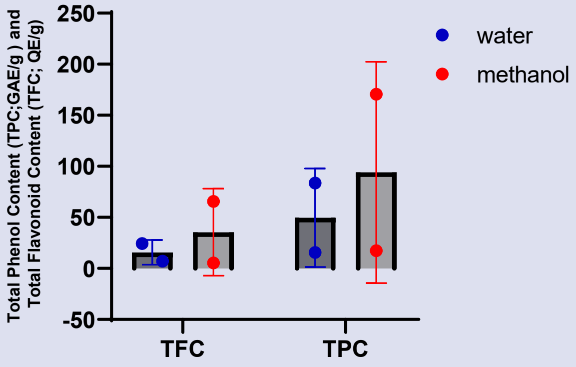

Figure 2. TPC and TFC of the A. kotschyana water and MeOH extracts

Bursal et al. (2020) employed LC–MS/MS to analyse the phenolic and flavonoid compound contents of *A. kotschyana* [12]. The results indicated that both the TFC and TPC of *A. kotschyana* were high. Two significant compounds out of twenty-seven standard compounds for *A. kotschyana* were found by LC MS/MS analysis to be quinic acid and rhamnetin. Furthermore, the *in vitro* antioxidant data indicated that *A. kotschyana* extracts possess effective antioxidant potential. However, a comparison of the water and ethanol extracts was not conducted.

Due to the limited number of studies on *A. kotschyana*, the data obtained were also compared with those of different species of this genus. In a 2020 study, the total phenolic and flavonoid contents of the MeOH extract of *Anthemis tinctoria* var. *tinctoria* were examined by LC–MS/MS, and 30 different phenolic compounds were detected [7]. In a separate study, the antioxidant activities of MeOH extracts of *A. cretica* and *A. tinctoria* were evaluated using the DPPH assay. Furthermore, in the same study, the total phenol and flavonoid contents of two species of the genus *Anthemis* were investigated with three different extracts (EA, MeOH and aqueous). The total phenol and flavonoid contents of the MeOH extract of *A. tinctoria* were greater than those of the MeOH extract of *A. cretica* [24]. A further study on *A. tinctoria* indicated that the ethanol extract exhibited high antioxidant activity, as evidenced by its ability to scavenge DPPH and ABTS radicals [13]. In a separate study investigating the antioxidant activity of various extracts of *Anthemis aciphylla* Boiss. var. *aciphylla*, it was reported that the methanol extract exhibited high DPPH, ABTS, superoxide radical, and nitric oxide scavenging activities [14]. This corroborates the notion that the antioxidant activity of different species belonging to the genus *Anthemis* is considerable.

Conclusion

The findings of this study indicate that the MeOH and water extracts of *A. kotschyana* demonstrate antioxidant properties, as evidenced by their ability to scavenge free radicals (DPPH, ABTS) and to inhibit the oxidation of phenolic and flavonoid compounds. According to the GC–MS analysis, if the major components 2-propenoic acid, tridecyl ester (water) and cyclododecane (MeOH) are obtained by fractionation, this will provide a different direction for studies on the antioxidant activity of this species.

In conclusion, the extension of the biological properties of this species, which has antioxidant activity and is a good potential source for phenolic compounds, with more comprehensive studies may allow the use of this plant as a therapeutic agent in the future.

Conflicts of interest

No conflicts of interest have been declared by the authors.

Acknowledgment

I would like to thank Prof. Dr. Hüseyin Aşkın Akpulat for identifying the plant.

Reference

[1] Yildiz B., Aktoklu, E., Bitki Sistematiği İlkin Karasal Bitkilerden bir Çeneklilere, Palme Yayıncılık, Ankara, (2010) 1-396.

[2] Kadereit J.W., Jeffrey C., (eds), Flowering Plants.Eudicots: Asterales. In Kubitzki K (ed.). The Families and Genera of Vascular Plants, Springer, Verlag Berlin Germany, 8 (2007).

[3] Davis P.H., Flora of Turkey and East Aegean Islands, Edinburgh: Edinburgh University Press (1984).

[4] Güner A., Özhatay N., Ekim T., Baser, K.H.C., Flora of Turkey and the East Aegean Islands, Edinburgh: Edinburgh University Press, 11 (2000).

[5] Güner A., Türkiye Bitkileri Listesi, Nezahat Gökyiğit Botanik Bahçesi yayını, İstanbul, (2013).

[6] Jaradat N.A., Ayesh O.I., Anderson C., Ethnopharmacological survey about medicinal plants utilized by herbalists and traditional practitioner healers for treatments of diarrhea in the West Bank/Palestine, *Journal of ethnopharmacology*, 182 (2016) 57-66.

[7] Emir A., Emir C., Anthemis tinctoria L. var. tinctoria L. Bitkisine Ait Fenolik Bileşiklerin LC-ESI-MS/MS ile Miktar Tayini ve Bitkinin Biyolojik Aktivitelerinin Belirlenmesi, *Gümüşhane Üniversitesi Fen Bilimleri Dergisi*, *10*(4) (2020), 996-1006.

[8] Sut S., Dall'Acqua S., Zengin G., Senkardes I., Bulut G., Cvetanović A., Mahomoodally F. Influence of different extraction techniques on the chemical profile and biological properties of Anthemis cotula L.: Multifunctional aspects for potential pharmaceutical applications, *Journal of Pharmaceutical and Biomedical Analysis*, 173 (2019) 75–85.

[9] Todorova M., Trendafilova A., Danova K., Dimitrov D., Phytochemical study of Anthemis rumelica (Velen) Stoj. & Acth, *Biochemical Systematics and Ecology*, 39(4–6) (2011) 868–871.

[10] Casiglia S., Bruno M., Senatore F., Rosselli S.,Chemical composition of essential oils of Anthemis secundiramea Biv. subsp. secundiramea (Asteraceae) collected wild in Sicily and their activity on microorganisms affecting historical art craft, *N Nat Prod Res*, 33 (2019) 970-979.

[11] Chemsa A.E., Zellagui A., Öztürk M., Erol E., Ceylan O., Duru M.E., Lahouel M., Chemical composition, antioxidant, anticholinesterase, antimicrobial and antibiofilm activities of essential oil and methanolic extract of Anthemis stiparum subsp. sabulicola (Pomel) Oberpr, *Microb Pathog*, 119 (2018) 233-240.

[12] Bursal E., Aras A., Kılıç Ö., Buldurun, K., Chemical constituent and radical scavenging antioxidant activity of Anthemis kotschyana Boiss, *Natural Product Research*, *35*(22) (2021) 4794-4797.

[13] Güçlü G., İnanır M., Uçar E., Eruygur N., Ataş M., Akpulat H.A., Biological activities of different plant species belonging to the Asteraceae family, *International Journal of Secondary Metabolite*, 10(1) (2023) 11-22.

[14] Tüzün B.S., Fafal T., İlhan R., Kıvçak B., Kırmızıbayrak P.B., Antioxidant, tyrosinase inhibitor, and cytotoxic effects of Anthemis aciphylla Boiss. var. aciphylla and Cota dipsacea (Bornm.) Oberpr. & Greuter, *İstanbul Journal of Pharmacy*, *53*(2) (2023) 193-198.

[15] Baroni L., Sarni A.R., Zuliani, C. Plant foods rich in antioxidants and human cognition: A systematic review, *Antioxidants*, 10(5) (2021) 714.

[16] Li A.N., Li S., Li H.B., Xu D.P., Xu X.R., Chen, F., Total phenolic contents and antioxidant capacities of 51 edible and wild flowers, *Journal of Functional Foods*, 6 (2014) 319– 330.

[17] Xu D.P., Li Y., Meng X., Zhou T., Zhou Y., Zheng J., Zhang J.J., Li, H.B., Natural antioxidants in foods and medicinal plants: Extraction, assessment and resources, *International Journal of Molecular Sciences*, 18(1) (2017) 96.

[18] Yu M., Gouvinhas I., Rocha J., Barros A.I., Phytochemical and antioxidant analysis of medicinal and food plants towards bioactive food and pharmaceutical resources, *Scientific Reports*, 11(1) (2021).

[19] Sacchetti G., Maietti S., Muzzoli M., Scaglianti M., Manfredini S., Radice M., Bruni, R., Comparative evaluation of 11 essential oils of different origin as functional antioxidants, antiradicals and antimicrobials in foods, *Food chemistry*, 91(4) (2005) 621-632.

[20] Eruygur N., Dural, E., Determination of 1-deoxynojirimycin by a developed and validated HPLC-FLD method and assessment of in-vitro antioxidant, α-amylase and α-glucosidase inhibitory activity in mulberry varieties from Turkey, *Phytomedicine*, 53 (2019) 234-242.

[21] Clarke G., Ting K.N., Wiart C., Fry J., High correlation of 2, 2-diphenyl-1-picrylhydrazyl (DPPH) radical scavenging, ferric reducing activity potential and total phenolics content indicates redundancy in use of all three assays to screen for antioxidant activity of extracts of plants from the Malaysian rainforest, *Antioxidants*, 2(1) (2013) 1-10.

[22] Re R., Pellegrini N., Proteggente A., Pannala A., Yang M., Rice-Evans, C., Antioxidant activity applying an improved ABTS radical cation decolorization assay*, Free radical biology and medicine*, 26(9-10) (1999) 1231-1237.

[23] Yang H., Dong Y., Du H., Shi H., Peng Y., Li X., Antioxidant compounds from propolis collected in Anhui, China, *Molecules*, 16(4) (2011) 3444-3455.

[24] Orlando G., Zengin G., Ferrante C., Ronci M., Recinella L. Menghini L., Comprehensive Chemical Profiling and Multidirectional Biological Investigation of Two Wild Anthemis Species (Anthemis tinctoria var. pallida and A. cretica subsp. tenuiloba): Focus on Neuroprotective Effects, *Molecules*, 24 (2019) 2582

Cumhuriyet Sci. J., 45(3) (2024) 454-464
DOI: https://doi.org/10.17776/csj.1408553

Cumhuriyet Science Journal

| csj.cumhuriyet.edu.tr | Founded: 2002 ISSN: 2587-2680 e-ISSN: 2587-246X Publisher: Sivas Cumhuriyet University

Eco-Friendly Synthesis of Silver Nanoparticles Using *Klebsormidium subtile* and Evaluation of their Antimicrobial, Anti-Quorum Sensing, and Antibiofilm Activities

İlkay Açıkgöz Erkaya[1, a], Dilek Yalçın[2, b,*], Belgin Erdem[3, c]

[1] Department of Environmental Engineering, Faculty of Architecture and Engineering, Kırşehir Ahi Evran University, Kırşehir, Türkiye
[2] Plant and Livestock Production, Organic Agriculture Program, Kahramankazan Vocational School, Başkent University, Ankara, Türkiye
[3] Medical Services and Techniques Programs, Vocational School of Health Services, Kırşehir Ahi Evran University, Kırşehir, Türkiye
**Corresponding author*

Research Article

History
Received: 22/12/2023
Accepted: 13/09/2024

ABSTRACT

In this study, both dry and fresh biomass extracts of *Klebsormidium subtile* were used for the synthesis of silver nanoparticles (AgNPs). The UV-visible spectrum showed an absorption peak at 430 nm, indicating the presence of AgNPs through surface plasmon resonance. FT-IR analysis identified bioactive functional groups, such as amines, which acted as stabilizing agents for the nanoparticles. SEM imaging revealed well-dispersed, spherical AgNPs ranging from 5 to 25 nm and 40 to 60 nm in size, accumulating on cell surfaces. EDS analysis confirmed the presence of elemental silver. The antimicrobial activity of AgNPs derived from both fresh and dry *K. subtile* extracts was similar, though AgNPs from the dry extract were more effective against *Staphylococcus aureus*, with inhibition zones of 15.8, 16.2, and 15.2 mm at 1 mM, 2 mM, and 3 mM concentrations, respectively. AgNPs also showed strong activity against *Bacillus subtilis*, *Pseudomonas aeruginosa*, and *Candida albicans*, but were less effective against *Bacillus cereus* and *Aeromonas hydrophila*. These findings suggest that *K. subtile*-derived AgNPs have significant antimicrobial potential, particularly against *S. aureus* and *C. albicans*, and may be useful in biomedical applications, particularly for treating biofilm-related infections.

Keywords: *Klebsormidium subtile*, Antimicrobial activity, Silver nanoparticles, Anti-quorum sensing, Antibiofilm.

[a] *ilkay.acikgoz@ahievran.edu.tr* *https://orcid.org/0000-0003-1730-4951*
[c] *berdem@ahievran.edu.tr* *https://orcid.org/0000-0001-9108-5561*
[b] *dyalcin10904@gmail.com* *https://orcid.org 0000-0003-2127-8186*

Introduction

Nanotechnology is a multidisciplinary research field that involves the design, fabrication, application, and characterization of structures, devices, and systems at the nanometer scale [1]. The term 'nano' is derived from ancient Greek, referring to length scales in the range of billionths of a unit, specifically encompassing structures between 0.1 and 100 nm in size. Nanotechnology has become a pivotal field, fueled by advancements in research and technology across various scientific disciplines, including physics, chemistry, biology, environmental and materials science, medicine, and pharmacy [2]. Nanoparticles (NPs), fundamental components in the field of nanotechnology, exhibit unique physicochemical and morphological properties, such as sizes smaller than 100 nm, large surface areas with extensive binding regions, distinctive electronic structures, and enhanced interface reactivity [3]. These characteristics enable NPs to be utilized in the development of products with antimicrobial, anticancer, anti-inflammatory, surfactant, drug delivery, and pharmacological applications [2]. Furthermore, metal nanoparticles have found wide-ranging applications in fields such as cosmetics, biological labelling, optoelectronics, photocatalysis, diodes, fluorescent tubes, piezoelectric devices, sensors, lasers, photonic coatings, and photography [4].

The synthesis of nanoparticles (NPs) via conventional physical and chemical methods typically involves the use of strong chemical reducing agents or complex physical processes, which are often costly and lead to the production of hazardous by-products. In contrast, the green synthesis approach offers a more cost-effective, environmentally friendly alternative, reducing the chemical burden on the ecosystem and simplifying the overall synthesis process by eliminating unnecessary steps [5, 6]. With the rise of green nanoparticle synthesis paradigms, there has been a growing preference for eco-friendly methods that avoid the use of toxic chemicals in the production of metal nanoparticles [5]. Currently, green synthesis of NPs is achieved using a wide variety of biological materials, including bacteria, fungi, yeast, viruses, algae, and plant biomass or extracts [7,8].

Noble metal-based nanoparticles, particularly those derived from metals such as gold (Au), silver (Ag), palladium (Pd), and platinum (Pt), have been utilized since ancient times, with silver being the most widely employed metal in nanoparticle production. Silver nanoparticles typically consist of 20 to 15,000 silver atoms and generally have diameters of less than 100 nm [9]. These nanoparticles are well-known for their thermal, electrical, catalytic, and magnetic properties. Scientific studies have shown that silver nanoparticles possess anti-inflammatory properties, exhibit antibacterial, antifungal, and antiviral activities, and can be safely used in treatments if their effective concentrations against microorganisms are accurately determined [5, 10]. Various silver compounds and their derivatives continue to be used as antimicrobial agents in the treatment of burns, wounds, and infections, due to their low toxicity to human cells and high thermal stability [11].

The rising prevalence of drug-resistant microorganisms, the emergence of mutant strains, and the widespread misuse of antibiotics present significant challenges in the management of infectious diseases. The ongoing challenge of developing effective therapeutics against bacterial pathogens and combating antibiotic resistance remains a major obstacle for the scientific community [10]. Similarly, microorganisms and parasites are evolving resistance to pesticides and insecticides due to their excessive and improper use in agricultural practices. To protect agricultural products, researchers are actively pursuing sustainable biological pest control solutions that pose no harm to humans [12]. In a study by Bafghi et al. (2021), selenium nanoparticles (SeNPs) and silver nanoparticles (AgNPs) were biosynthesized using extracts from *Nepeta* and *Berberine* plants [13]. The application of these nanoparticles exhibited superior efficacy compared to treatments with conventional antifungal drugs. AgNPs are particularly favoured for their low toxicity at minimal concentrations and their broad-spectrum antimicrobial properties. While the precise mechanism of action of silver nanoparticles against pathogenic microorganisms is not fully understood, it is widely accepted that the positive charge of silver ions (Ag^+) plays a critical role. This positive charge facilitates interaction with the negatively charged plasma cell membrane and nucleic acids, leading to membrane destabilization, the generation of reactive oxygen species (ROS), and eventual cellular breakdown [14]. The antimicrobial activity of silver ions is multifaceted, targeting multiple components of microorganisms. As a result, the likelihood of microorganisms developing resistance to silver is considered lower than that of antibiotics, as mutations across multiple targets simultaneously are less probable [12, 15].

Quorum sensing (QS) is a communication mechanism used by bacteria, which relies on the continuous release of signalling molecules into the environment. Quorum quenching (QQ), on the other hand, involves the use of chemicals that reduce or completely inhibit the production of virulence factors [16]. The primary function of QS is to regulate vital cellular processes, such as the production of virulence factors and the formation of biofilms. In the context of treating antibiotic-resistant bacteria, QQ is regarded as a promising alternative antimicrobial strategy, as it disrupts microbial communication. Molecules that induce QQ can decrease or entirely halt the production of virulence factors, including biofilm formation [16]. Quorum-sensing inhibitors (QSIs), which resemble acyl-homoserine lactones (AHLs), are molecules that bind to QS response regulators without activating them. These QSI compounds are believed to have potential biotechnological applications, as they can block, inhibit, or deactivate QS signals between or within bacterial species. Previous studies have shown that AHL signal molecules are essential for biofilm formation in *Pseudomonas aeruginosa*, suggesting that disrupting bacterial cell-to-cell communication could impede biofilm formation [17]. Bacteria within biofilms exhibit distinct physiology and heightened resistance to both the immune system and antibiotics compared to free-living planktonic cells, making biofilms a source of chronic and persistent infections [18]. Due to the rising prevalence of multidrug resistance among pathogens, there is a growing need to explore anti-QS and anti-biofilm compounds from natural sources to combat bacterial infections. Additionally, QS inhibitors can enhance bacterial susceptibility to antibiotics [19]. Thus, the use of QS-inhibiting agents holds promise as a strategy to control bacterial infections. It is plausible that QS inhibition represents a natural antimicrobial strategy employed by bacteria, with a significant impact on biofilm formation [20]. Numerous studies have identified antimicrobial compounds produced by microalgae and cyanobacteria species. Although research on the anti-biofilm activity of extracts or molecules produced by these microorganisms is currently limited, their importance is increasingly recognized in anti-biofilm and anti-QS research. The use of QS-inhibitory silver nanoparticles (AgNPs) synthesized from microalgae in biofilm formation is anticipated to lead to the discovery of novel QS-inhibitory agents, offering new insights into the development of more effective antibiotic drugs for medical and industrial applications.

Microalgae are organisms rich in biochemical compounds, existing in both unicellular and multicellular forms, with high growth rates and significant biomass productivity. Their cultivation and utilization have broad applications, including heavy metal detoxification, biodiesel production (due to their high lipid content), and the generation of commercially valuable metabolites across various regions worldwide [21]. In recent years, microalgae have gained attention for their role in the biosynthesis of silver nanoparticles (AgNPs), thanks to the availability of algal biomass for metallic nanoparticle synthesis. Our research group has extensively examined the antimicrobial activity of AgNPs biosynthesized by *Pseudopediastrum boryanum* against various human pathogenic microorganisms. The results showed that AgNPs at different concentrations exhibited antimicrobial effects on certain pathogens [7]. AgNPs were also biosynthesized using *Chlorella vulgaris* as a reducing agent, demonstrating antibacterial activity against several human pathogens, including *Escherichia coli*, *Pseudomonas vulgaris*, *Staphylococcus aureus*, *Pseudomonas aeruginosa*, and *Candida albicans*. Further investigations into *Chaetoceros calcitrans*, *Spirulina platensis*, *Oscillatoria willei*, and *Plectonema boryanum* highlighted their potential for AgNP synthesis, with positive results. Additionally, several seaweeds, such as *Tetraselmis gracilis*, *Chlorella salina*, *Chaetoceros* *calcitrans*, and *Isochrysis galbana*, have been documented to synthesize AgNPs [1]. The green microalga *Scenedesmus* sp. was used for both intracellular and extracellular biosynthesis of AgNPs. These synthesized AgNPs were characterized through various techniques, and their antibacterial activity against pathogenic bacteria was successfully demonstrated [22].

In this study, both fresh and dry biomass extracts of the freshwater green microalga *Klebsormidium subtile*, a species that has not previously been used for the synthesis of silver nanoparticles, were employed. The morphological structure of the synthesized silver nanoparticles (AgNPs) was characterized using UV-Vis spectroscopy, Fourier transform infrared (FT-IR) spectroscopy, scanning electron microscopy (SEM), and energy dispersive spectroscopy (EDS). Additionally, the study explored the antimicrobial activity of the AgNPs against pathogenic microorganisms. The research further investigated the antiquorum sensing activity, violacein quantitative evaluation, and biofilm inhibition assay of AgNPs derived from both dry and fresh extracts of *K. subtile*. A key objective of the study was to prioritize sustainability in the use of limited global resources. To this end, *K. subtile*, which is abundantly available in local environments, was isolated and cultivated from its natural habitats to enable the green synthesis of AgNPs. The scalability of this process was evaluated for potential industrial applications, with a focus on the efficient utilization of resources.

Materials and Methods

Microalgae Culture and Growth Conditions

In our previous research, strains of *Klebsormidium subtile* were isolated from freshwater deposits in Ankara, Türkiye. After microscopic examination of the collected water samples, *K. subtile* was isolated from the mixed culture medium using a micropipette and the single-cell growth technique. The molecular characterization of *K. subtile* was conducted using Fourier-transform infrared (FT-IR) spectroscopy and polymerase chain reaction (PCR). Following the isolation and identification processes, K. *subtile* strain was stored under optimal environmental conditions in a culture room, assigned a code number (CCA02Stc01), and included in the Kırşehir Ahi Evran University Culture Collection (AEU-CCA).

Microalgae Extracts Preparation and Biosynthesis of Silver Nanoparticles

Klebsormidium subtile strains were cultivated under controlled conditions for approximately 4-6 weeks, until they reached a steady growth phase. The microalgae intended for AgNPs synthesis were prepared using two distinct methods to identify any potential differences between fresh and dry biomass. For the dry extraction, the microalgal biomass was dried in an oven at 60°C for 24 hours and then pulverized. Approximately 2 grams of both fresh and dried algal biomass were selected and boiled at 100°C for 20 minutes. The resulting microalgal extracts from the fresh and dry biomass were then cooled and centrifuged. Subsequently, 10 ml of fresh and dry algal extracts from the cultures were mixed with 90 ml of aqueous $AgNO_3$ at concentrations of 1 mM, 2 mM, and 3 mM [23]. The resulting supernatant was stored at 4°C until further experimentation.

Characterization of AgNPs

UV–vis spectrum analysis was conducted employing a spectrophotometer (Thermo Scientific Spectrophotometer Genesys 10S) within the range of 200–800 nm. Measurements were taken at 24-hour, 48-hour, and 72-hour intervals. To validate the synthesis of nanoparticles (NPs), all measurements were carried out in triplicate. The FT-IR spectrum analyses of AgNPs synthesized from the fresh and dry biomass of *K. subtile* were conducted using the Thermo Scientific Nicolet 6700 model FT-IR spectrometer at the Central Laboratory of Kırşehir Ahi Evran University, Kırşehir, Turkey. Scanning Electron Microscopy (SEM) and Energy Dispersive Spectroscopy (EDS) analyses were performed at the Yozgat Bozok University Science and Technology Application and Research Centre, Yozgat, Türkiye.

Determination of Antimicrobial Activities by Agar Well Diffusion Method

In vitro antimicrobial assays were conducted against Gram-positive and Gram-negative bacteria, as well as yeast strains, sourced from the Culture Collection of Kırşehir Ahi Evran University. The antimicrobial effects of AgNPs synthesized from both fresh and dry biomass of *K. subtile* were evaluated using the agar well diffusion method. Pure cultures of the microorganisms were activated by sub-culturing on nutrient agar at 37°C. Pathogenic microorganisms were cultured in Trypticase Soy Broth (TSB), and each strain was subsequently cultivated on Trypticase Soy Agar (TSA). Wells (6 mm in diameter) were created in the agar plates using a sterile cork borer, and each well was filled with 75 µL of 1 mM, 2 mM, or 3 mM silver nanoparticle (AgNP) extracts obtained from both fresh and dry *K. subtile* samples. Following 48 hours of incubation at 37°C, the diameter of the clear inhibition zones (measured in mm) was assessed. Inhibitory zones with a diameter greater than 5 mm were considered positive for antimicrobial activity. $AgNO_3$ served as the positive control, while nutrient broth was used as the negative control. All procedures adhered to the NCCLS guidelines throughout the experiment [24].

Minimum Inhibitory Concentration (MIC) Assessment of Antimicrobial Activity

Minimum Inhibitory Concentration (MIC) tests for silver nanoparticles (AgNPs) at concentrations of 1 mM, 2 mM, and 3 mM, synthesized from both fresh and dry *K. subtile* extracts, were performed against bacterial and yeast strains in accordance with NCCLS guidelines [25]. Mueller-Hinton broth, along with a bacterial suspension of 0.5 McFarland standard, was used in combination with the test solutions of *K. subtile* extracts (1 mM, 2 mM, and 3 mM AgNPs). MIC values were determined spectrophotometrically using the microdilution broth method in 96-well microtiter plates. Antimicrobial activity tests were conducted using AgNP stock solutions synthesized at a concentration of 1000 µg/mL. Bacterial and yeast stock cultures, containing approximately 10^6 colony-forming units (CFU)/mL, were prepared according to the McFarland 0.5 turbidity standard. In 96-well plates, 100 µL of dilutions ranging from 500 to 7.8 µg/mL were incubated at 37°C for 24-48 hours.

Anti-quorum Sensing Activity Assay

The anti-quorum activity of the compound was assessed on Luria-Bertani (LB) agar using *Chromobacterium violaceum* (ATCC 12472). A bacterial culture of *C. violaceum* ($1x10^6$) was evenly spread on the LB agar surface. Subsequently, wells were drilled in the LB agar using a cork borer, and these wells were filled with 75 µL of 1mM, 2mM, and 3mM AgNPs extracts obtained from both fresh and dry *K. subtile*. The plates were then incubated at 30°C for 24 hours to observe the inhibition of pigment production around the wells. The presence of a clear halo around the disc and the inhibition of bacterial growth were considered positive indicators, following the criteria outlined by McClean et al. (1997) [26].

Violaceum Quantitative Evaluation

The anti-quorum sensing activity against *Chromobacterium violaceum* (ATCC 12472) was assessed. Initially, AgNPs derived from *K. subtile* extracts (both dry and fresh) were quantified on a 96-well plate, followed by testing the inhibitory effects of AgNPs on pigment production. Bacterial culture of *C. violaceum* (ATCC 12472) with a concentration of $1x10^8$ CFU/mL was suspended in LB broth. The culture, both in the absence and presence of *K. subtile* (dry and fresh) AgNPs extracts, was then diluted twofold and incubated at 30°C for 24 hours. To initiate the process, 200 µL of both treated and untreated cultures were transferred to an Eppendorf tube. Subsequently, lysing occurred by the addition of 200 µL of 10% Sodium Dodecyl Sulphate (SDS), followed by vortexing and incubation at room temperature. Additionally, 900 µL of water-saturated butanol was introduced to the cell lysate, vortexed, and then subjected to centrifugation. The absorbance of the upper (butanol) phase containing violaceum was measured using a Spectrophotometer at 580 nm (Jasco V-730-JAPAN). The evaluation of the reduction in pigment production in the presence of *K. subtile* (dry and fresh) AgNPs extracts was conducted using the following formula [27].

Percent inhibition = [(OD of control - OD of treated) / OD of control] x100

Biofilm Inhibition Assay

The anti-biofilm activity of AgNPs was assessed by inoculating clinical pathogens *S. aureus ATCC 29213, B. cereus 709 Roma, P. aeruginosa ATCC 27853*, and *E. coli ATCC 25922* into a 96-well microtiter plate. Each well contained 100 µL concentrations of the extracts. The AgNPs was individually added to all bacterial strains and incubated at 37°C for 24 hours. After incubation, the microalgal cells were removed, and the wells were washed with sterile water. Subsequently, 125 µL of crystal violet (0.1%) was introduced to all wells and incubated. After the incubation period, the residual stain was aspirated, and the wells were rinsed with sterile distilled water to remove any unbound crystal violet stain. Subsequently, the crystal violet bound to the attached biofilm was solubilized in absolute ethanol (200 µL), and the absorbance was quantified at 595 nm [28].

Percent biofilm inhibition= [(Control OD595-Treated OD595) / (Control OD595)] × 100

Results and Discussion

Structural and Morphological Characterization of AgNPs

The biosynthesis of AgNPs was visually confirmed by the distinct colour change of the $AgNO_3$ solution, shifting from yellowish-brown to ruby-red. This colour change was attributed to the active molecules in the extract, which facilitated the reduction of silver ions, leading to the formation of silver nanoparticles. The appearance of these characteristic colours is due to the excitation of surface plasmon vibrations in the metal nanoparticles and the reduction of $AgNO_3$ [7]. In the present study, both fresh and dry extracts of *K. subtile* demonstrated changes in their initial transparent colour, transitioning to yellowish-brown and ruby-red, respectively. These alterations were influenced by the concentration of the substrate and the incubation time for nanoparticle synthesis, as observed after a 72-hour reaction period.

Reaction temperature, pH, incubation time, and concentration are critical parameters for producing nanoparticles with uniform size and stable morphology [29]. Among these, the reaction duration plays a key role in controlling the size and shape of metallic nanoparticles during synthesis. The UV-Vis spectrum is a highly sensitive and convenient method for confirming the synthesis of AgNPs, with colour changes validated through UV-Vis spectrophotometer analysis. Metallic nanoparticles typically exhibit distinctive optical properties due to Surface Plasmon Resonance (SPR), which is monitored by UV-Vis spectroscopy within the 190–1100 nm range [30]. The absorption spectra vary based on the material, and for AgNPs, the spectrum typically falls within the 400-450 nm range [31]. In this study, the synthesis of AgNPs was monitored through UV-Vis absorption spectra at 24, 48, and 72-hour intervals within the 200-800 nm range. In both fresh and dry extracts of *K. subtile*, a distinct absorption band at 430 nm was observed, providing clear evidence for the formation of silver nanoparticles. This band is associated with AgNPs and confirms the synthesis of nanoparticles with a narrow size distribution. The symmetrical shape of the band further indicates a uniform distribution of spherical nanoparticles, as shown in Figure 1 and Figure 2.

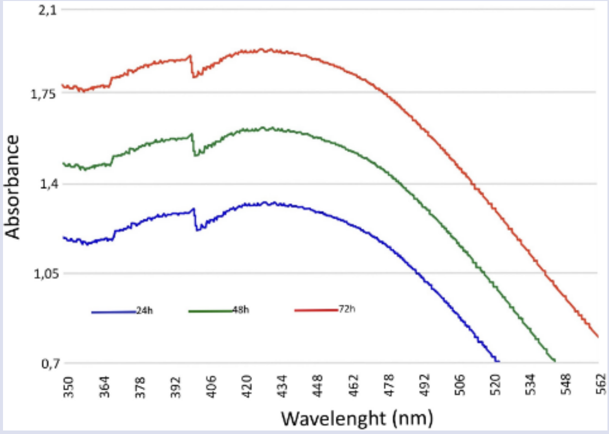

Figure 1. UV-Vis absorption spectrum of silver nanoparticles synthesized by $AgNO_3$ solution with *K. subtile* fresh extraction.

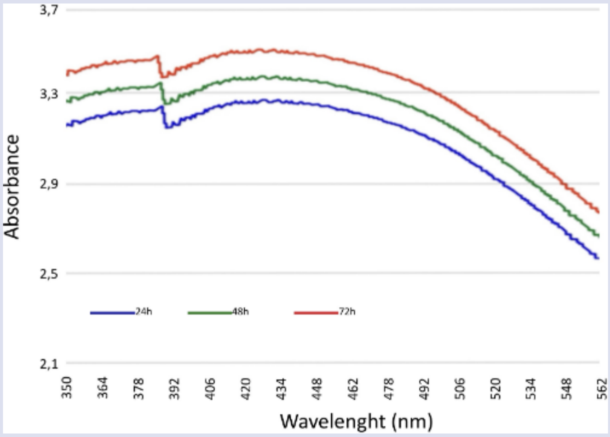

Figure 2. UV-Vis absorption spectrum of silver nanoparticles synthesized by $AgNO_3$ solution with *K. subtile* dry extraction.

FT-IR spectroscopy serves as a valuable tool for identifying the functional groups attached to nanoparticles (NPs) and investigating the mechanisms involved in their synthesis and surface chemistry. In this study, silver nanoparticles synthesized utilizing both fresh and dry extracts of *K. subtile* were subjected to FT-IR spectrum analysis. The primary objective was to ascertain whether biomolecules played a role as stabilizing and reducing agents in the synthesis process. Examination of the absorption spectrum revealed six distinct bands in the wavelength range of 4000-500 cm^{-1}. The assignment of these bands was conducted based on established standards and published FT-IR spectra [32]. In Figures (3 and 4), the FT-IR spectra of biosynthesized AgNPs exhibited distinct bands indicative of the presence of amino, carboxylic, hydroxyl, and carbonyl groups. The distribution of bands was tentatively associated with residual water (-OH; Band 1), lipid ($-CH_2$; Bands 2 and 3), amide (protein; Bands 4 and 5), nucleic acid (>P=O; Band 6), and starch (-C-O; Band 6). In a broader context, the observed bands at [3220 (Dry), 3228 (Fresh)] cm^{-1} were attributed to the stretching vibrations of amide, with the corresponding bending vibration noted at 1631 cm^{-1}. AgNPs synthesized using *K. subtile* exhibited prominent bands at 1631 cm^{-1} (aromatic ring C = C functional groups) and 1361 cm^{-1} (bi-methyls). The reduction of silver ions to AgNPs is likely facilitated by the involvement of the (-OH) group. The band at 2952 cm^{-1} corresponds to the C-N stretch of the amine. Simultaneously, a peak at [2848 (Dry) – 2825 (Fresh)] cm^{-1} can be attributed to ($-CH_2-$) groups, characteristic of lipids and proteins. Peaks within the 6th band, ranging from 1136 to 980 cm^{-1}, can be assigned to the (P = O) bond present in phospholipids, DNA, and RNA. Numerous peaks in the FT-IR spectra suggest the presence of proteins, potentially contributing to the stability of AgNPs. The FT-IR spectra indicate proteins as plausible biomolecules involved in the reduction of biosynthesized silver nanoparticles. The most prevalent functional groups attached to nanoparticles are (-C=O), ($-NH_2$), and (–SH) [22].

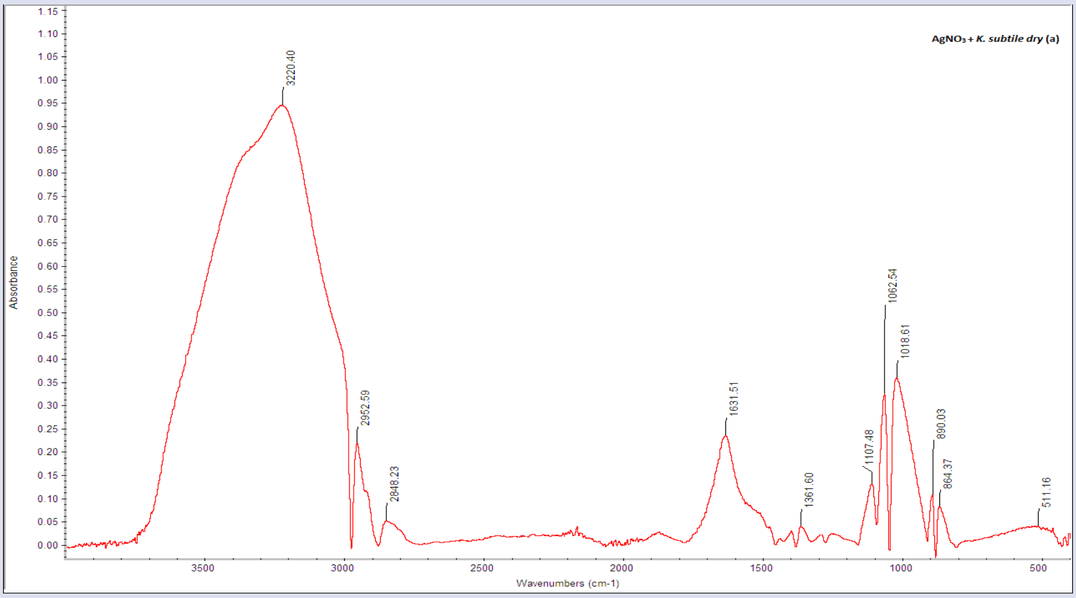

Figure 3. FT-IR spectra of AgNPs prepared by the dry (D) extracts of *K. subtile*

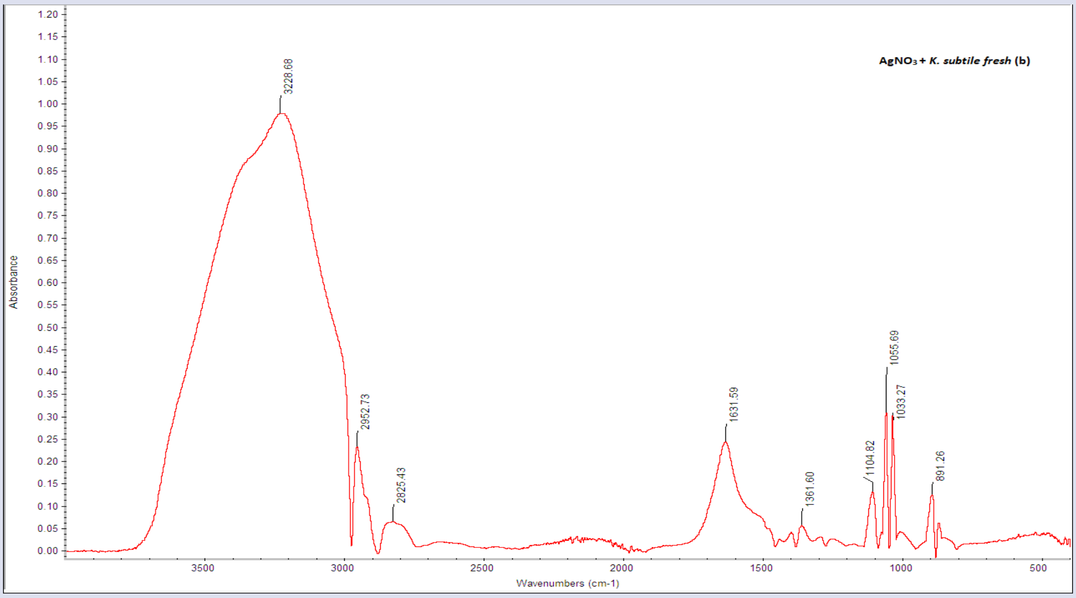

Figure 4. FT-IR spectra of AgNPs prepared by the fresh (F) supernatant of *K. subtile*

Various characterization techniques are employed to ascertain the size, shape, distribution, surface morphology, and surface area of nanoparticles (NPs). One such technique is Scanning Electron Microscopy (SEM), which offers insights into particles at the nanoscale, aiding in the determination of surface morphology and distribution of NPs within a bulk or matrix [33]. SEM analysis was conducted to elucidate the topology and size of AgNPs generated through the addition of $AgNO_3$ to both fresh and dry biomass extracts of *K. subtile*. The SEM results confirmed the presence of AgNPs, demonstrating an even distribution throughout the biomass. The deposition of AgNPs on the cell surface of *K. subtile* (both fresh and dry) was observed through SEM, as illustrated in Figure 5 and Figure 6. In the SEM micrographs of AgNPs, small spherical silver nanoparticles with average sizes ranging from 5 to 25 nm and 40 to 60 nm in diameter were observed to be well-dispersed in the solution and deposited on cell surfaces. Energy Dispersive X-ray Spectroscopy (EDS) revealed the presence of traces of nitrogen and oxygen, along with the substantial formation of silver particles. The presence of the elemental silver signal was confirmed in the EDS analysis of AgNPs obtained from *K. subtile* (both fresh and dry), as illustrated in Figure 7.

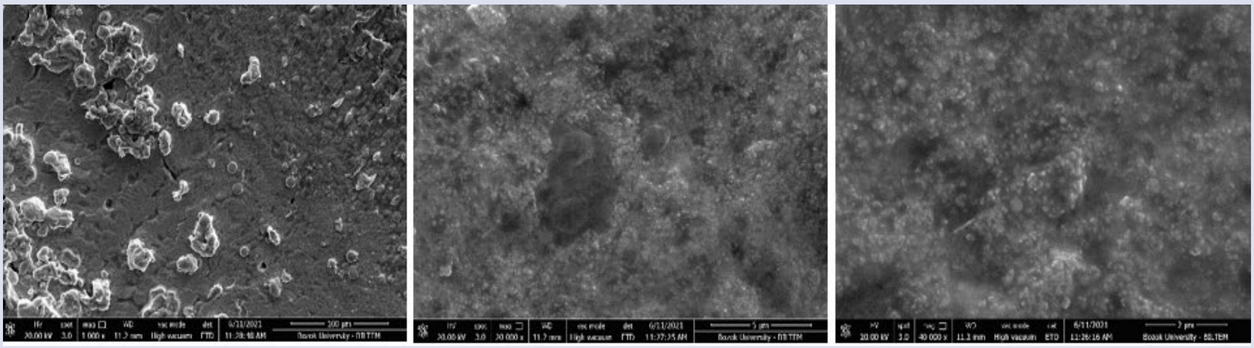

Figure 5. SEM images of synthesized AgNPs form *K. subtile* (fresh)

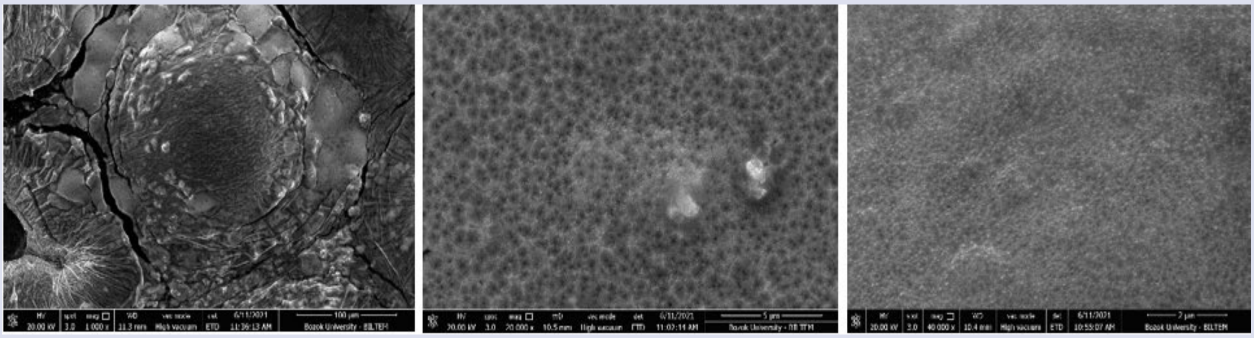

Figure 6. SEM images of synthesized AgNPs form *K. subtile* (dry

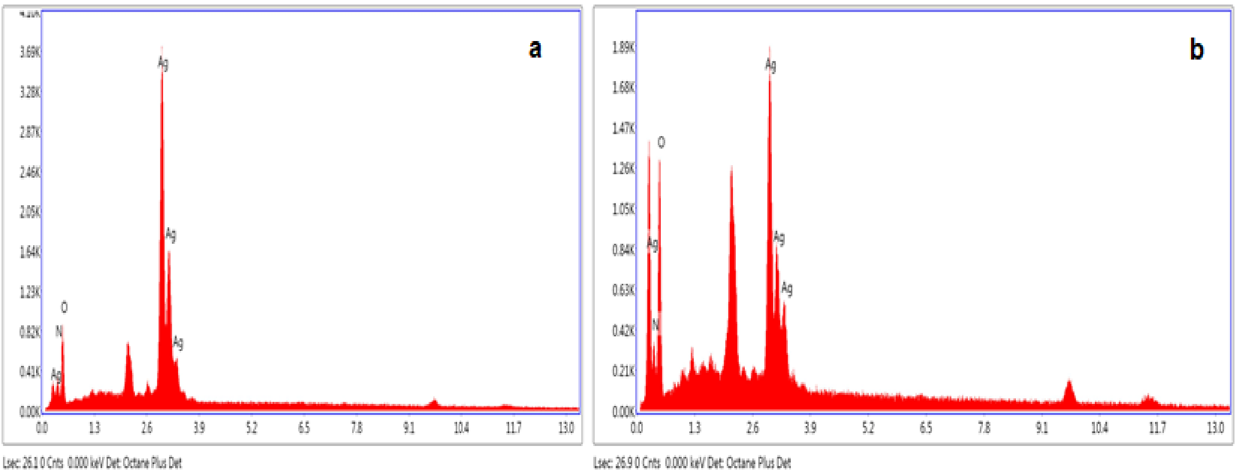

Figure 7. EDS of silver nanoparticles synthesized by $AgNO_3$ solution with *K. subtile* fresh extraction (a) and *K. subtile* dry extraction (b).

Antimicrobial Activity of AgNPs Biosynthesis from K. subtile (fresh and dry extract)

Antimicrobial activities of 1 mM, 2 mM and 3 mM AgNPs obtained from fresh and dry biomass extracts of *K. subtile* were tested by agar well diffusion method. The antimicrobial activity of AgNPs were investigated against gram-negative bacteria, gram-positive bacteria and yeast. Table 1 and 2 show the mean values of three replicates of the diameter of inhibition zones (mm) (DIZ) around each well loaded with AgNPs solution and minimal inhibitory concentration (MIC). Different concentrations of AgNPs showed several antimicrobial effects on pathogen microorganisms. The antimicrobial effects of AgNPs obtained from fresh and dry extracts of *K. subtile* were found to be close to each other. However, AgNPs obtained from the dry extract of *K. subtile* were found to be more effective against *Staphylococcus aureus*. Accordingly, the inhibition zones of *S. aureus* were measured as 15.8, 16.2 and 15.2 mm at 1mM, 2mM and 3 mM respectively. When the antimicrobial activities of all three concentrations of AgNPs obtained from the dry and fresh extracts of *K. subtile* were examined in general, it showed an effective activity against *Bacillus* subtilis and *Pseudomonas aeruginosa*. A lower antimicrobial effect was detected against *Bacillus cereus* and *Aeromonas hydrophila* compared to other microorganisms. AgNPs prepared from both dry and fresh extracts showed very strong activity against *Candida albicans*. Inhibition zones formed by pure $AgNO_3$ were detected between 12 and 18 mm. Nutrient broth was used as a negative control for both the bacterial strains and did not show any zone of inhibition around the well.

Numerous mechanisms have been proposed by researchers to elucidate how silver nanoparticles inhibit microbial cell metabolism and growth, ultimately leading to accelerated cell lysis. Silver nanoparticles release silver ions at a slower and more controlled rate compared to reactive silver salts. Silver ions are highly reactive and can react with the negatively charged cell membrane [34]. It has been suggested that AgNPs exhibit antibacterial activity by inhibiting respiratory enzymes, producing extremely reactive oxygen species that damage cell membranes and inactivate cellular enzymes [15]. Also, it has been reported that AgNPs increase membrane permeability while causing membrane damage by binding and accumulating on the cell membrane of bacteria [35].

In previous studies, the treatment of some pathogenic bacterial strains with AgNPs has detected some deep craters, indicating damage to the membrane surfaces and membrane structure of all cells, by SEM studies. It was concluded that leakage of cell contents after treatment caused the cells to appear shorter and more compact [10]. It has been determined that although some microbial cells are physiologically active and alive, there is no detectable growth and therefore microorganisms cannot be grown [36]. Raffi et al. (2008) reported that NPs have an effect on DNA polymerase enzyme, showing that treatment of *E. coli* cells with AgNPs eventually affects DNA replication [37]. Araga˜o et al. (2019) tested the AgNPs obtained by using seaweed *Gracilaria birdiae* for antimicrobial activity using *E. coli* and *S. aureus*. They reported that all samples showed antimicrobial activity against *E. coli* [5]. In another study, AgNPs prepared from *Scenedesmus abundans* were evaluated against the test pathogens *E. coli*, *K. pneumoniae* and *A. hydrophila*. The results revealed that the obtained AgNPs showed activity against these pathogens [23]. The effect of AgNPs obtained from *Pseudopediastrum boryanum* on pathogenic microorganisms was investigated. The antibacterial effect of AgNPs were effective in 6 out of 12 Gram-negative bacterial strains, 4 out of 6 Gram-positive bacterial strains and in all 6 yeasts [7]. In the study by El-Sheekh et al. (2021), silver oxide (Ag_2O|AgO-NPs) and gold nanoparticles (Au-NPs) were synthesized from cyanobacteria *Oscillatoria sp.* and *Spirulina platensis*. The efficacy of these nanoparticles as antimicrobial agents was evaluated against six human pathogenic bacteria and three fungal species. It was concluded that nanoparticles obtained from *Oscillatoria sp.* and *S. platensis* have effective antibacterial and antifungal activities [38].

In this study, antimicrobial properties of AgNPs obtained from dry and fresh extracts of *K. subtile* were tested against various pathogenic microorganisms. Although the results obtained from this study show parallelism with the literature, quite successful results were obtained. It is thought that the differences between the studies in the literature and our results are due to the microalgae species used, pathogenic microorganisms and methodologies.

Table 1. Antimicrobial activity of the inhibition zone diameters (mm) and MIC values of *K. subtile* (dry)

Bacteria	1 mM AgNO$_3$		2mM AgNO$_3$		3mM AgNO$_3$		AgN0$_3$	Nutrient Borth
	DIZ $^{a)}$ (mm)	MIC $^{b)}$ (µg/ml)	DIZ $^{a)}$ (mm)	MIC $^{b)}$ (µg/ml)	DIZ $^{a)}$ (mm)	MIC $^{b)}$ (µg/ml)		
Aeromonas hydrophila ATCC 7966	12.1	0.78	12.2	0.78	12.4	0.78	18	-
Staphylococcus aureus ATCC 29213	15.8	0.78	16.2	0.78	15.2	0.78	16	-
Klebsiella pneumoniae ATCC 13883	12.2	0.78	12.4	0.78	12.8	0.78	15	-
Bacillus subtilis ATCC 6633	13.8	0.78	13.8	0.78	14.2	0.78	12	-
Bacillus cereus 709 Roma	12.2	0.78	12.2	1.56	12.4	0.78	12	-
Vibrio anguillarum ATCC 43312	12.2	0.78	12.4	1.56	12.8	1.56	18	-
Enterococcus feacalis ATCC 29212	12.2	0.78	12.4	0.78	12.8	1.56	18	-
Pseudomonas aeruginosa ATCC 27853	13.8	0.78	13.6	0.78	14.2	1.56	16	-
Escherichia coli ATCC 25922	12.4	0.78	12.6	0.78	12.6	0.78	16	-
Candida albicans ATCC 10231	12.6	0.78	14.2	0.78	13.4	1.25	18	-

[-: No activity observed]; [a) Not active (–, inhibition zone<5mm); weak activity (5–10mm); moderate activity (10–15mm); strong activity (>15mm)]; [b) Not active (–, MIC >500 µg/mL)]

Table 2. Antimicrobial activity of the inhibition zone diameters (mm) and MIC values of *K. subtile* (fresh)

Bacteria	1 mM AgNO$_3$		2mM AgNO$_3$		3mM AgNO3		AgN0$_3$	Nutrient Borth
	DIZ $^{a)}$ (mm)	MIC $^{b)}$ (µg/ml)	DIZ $^{a)}$ (mm)	MIC $^{b)}$ (µg/ml)	DIZ $^{a)}$ (mm)	MIC b) (µg/ml)		
Aeromonas hydrophila ATCC 7966	12.1	0.78	12.2	0.78	11.8	0.78	18	-
Staphylococcus aureus ATCC 29213	15.8	0.78	12.4	0.78	10.4	1.56	16	-
Klebsiella pneumoniae ATCC 13883	12.2	0.78	13.8	0.78	12.2	0.78	15	-
Bacillus subtilis ATCC 6633	13.8	1.56	12.4	0.78	12.2	1.56	12	-
Bacillus cereus 709 Roma	12.2	1.56	12.2	0.78	11.8	1.56	12	-
Vibrio anguillarum ATCC 43312	12.2	0.78	12.2	0.78	12.2	0.78	18	-
Enterococcus feacalis ATCC 29212	12.2	1.56	12.2	0.78	11.8	1.56	18	-
Pseudomonas aeruginosa ATCC 27853	13.8	0.78	14.2	0.78	12.2	1.56	16	-
Escherichia coli ATCC 25922	12.4	0.78	12.6	0.78	13.4	1.56	16	-
Candida albicans ATCC 10231	12.6	0.78	12.4	0.78	12.2	0.78	18	-

[-: No activity observed]; [$^{a)}$ Not active (–, inhibition zone<5mm); weak activity (5–10mm); moderate activity (10–15mm); strong activity (>15mm)]; [$^{b)}$ Not active (–, MIC >500 µg/mL)]

Quantitative Analysis of Antimicrobial Activity via Microdilution

Effects of antimicrobial activity of the AgNPs' (*K. subtile* dry and fresh) (MIC) values are shown in Table 1 and 2. The MIC value was found in tested microorganisms between 0.78 and 1.56 µg/ml by microdilution method synthesized AgNPs (*K. subtile* dry and fresh). As shown in Table 1, the MIC value of 1 mM concentration of AgNPs obtained from the dry extracts of *K. subtile* was determined as 0.78 µg/ml and showed high activity against all microorganisms. While AgNPs at 2 mM concentration, the MIC value of *B. cereus* and *V. anguillarum* was determined to be the lowest with 1.56 µg/ml, other microorganisms showed MIC value of 0.78 µg/ml. At 3 mM concentration of AgNPs, the MIC value of *E. feacalis*, *V. anguillarum*, *P. aeruginosa* and *C. albicans* was found to be the lowest with 1.56 µg/ml and the highest MIC value was measured as 0.78 µg/ml in other microorganisms. As can be seen in Table 2, the highest MIC value of AgNPs obtained from the fresh extract of *K. subtile* was found to be 0.78 µg/ml at 1 mM concentration. The lowest activity at the same concentration was 1.56 µg/ml, and *B. subtilis*, *B. cereus* and *E. feacalis* showed this value. At 2 mM, the MIC value was found to be 0.78 µg/ml in all microorganisms. However, these values differed at 3 mM concentration. MIC value was found to be high with 0.78 µg/ml in *A. hydrophila, K. pneumoniae* and *V. anguillarum*.

Anti-Quorum Sensing Activity of Algal Extracts in C. violaceum (ATCC 12472)

In this study, the anti-QS properties of AgNPs algae extracts (*K. subtile* dry and fresh) were investigated using the *C. violaceum* ATCC 12472 strain. All extracts showed colourless colony formation, which is an indicator of anti-QS capacity against the *C. violaceum* strain, and zone diameters were measured in millimetres. 1 mM, 2 mM and 3 mM concentrations of AgNPs obtained from fresh biomass of *K. subtile* produced a pigment inhibition zone of 18.4 mm, 18.4 mm and 18.6 mm against *C. violaceum* ATCC 12472 strain, respectively. Inhibition of pigment production was also detected in AgNPs synthesized *K. subtile* dry algae at a concentration of 1 mM, 2 mM, and 3 mM with a pigment inhibition zone ranging from 18.4 mm, 18.6 mm and 19.2 mm against *C. violaceum* ATCC12472 (Table 3). Anti-quorum sensing activity was being investigated. *K. subtile* (dry and fresh) AgNPs were screened for anti-quorum sensing activity. At 2 mg/ml, *K. subtile* (dry) AgNPs with QSI activity inhibited violacein by 71.2%, while *K. subtile* (fresh) AgNPs inhibited violacein by 63.3%.

The emergence of multi-drug resistant bacterial pathogens worldwide has necessitated the search for alternative and new antibiotics as well as new strategies to combat the infections caused by these microorganisms. Recently, Quorum Sensing (QS) systems have been recognized as a promising anti-infective drug target in the regulation of many physiological functions of microorganisms. Quorum Sensing is a mechanism by which bacteria respond quickly and effectively to external environmental changes using their chemical language. Inhibition of QS (Anti-QS system) is a new strategy to prevent bacterial diseases and overcome its pathogenicity in the early stages of bacterial infections. Recent advances and research in Nano-biotechnology have shown that nanoparticles, such as metal nanoparticles with broad therapeutic potential and less toxicity to the host system, are promising as new anti-QS agents and formulations [39].

In various studies, silver nanoparticles were obtained by green synthesis from various algae species and used as antimicrobials against pathogens, but the use of AgNPs obtained from algae against QS-mediated bacterial infection is quite limited. In this study, both antimicrobial and anti-QS studies of the *K. subtile* strain that we tested have not been found in the literature, and there are limited studies with different algae species. According to the results of this study, AgNPs from fresh and dry extract of *K. subtile* produced a pigment inhibition zone at a concentration of 1 mM, 2 mM and 3 mM against *C. violaceum* ATCC 12472 strain. According to Tang et al. (2020) evaluated the antimicrobial and (QS) activities of phlorotannins from a seaweed, *Hizikia fusiforme*. As a result, while exhibiting antimicrobial activity against pathogenic bacteria, it also inhibited the QS activity of *C. violaceum* 12472 [39].

Table 3. Antiquorum-sensing activities of algae *K. subtile* (fresh) and (dry) against pigment-producing bacteria *C. violaceum* ATCC12472

AgNPs	Diameter of pigment inhibition (mm)[a,b] Concentrations (mM)			Violacein inhibition (%) Concentrations (mg/mL)			
	1mM $AgNO_3$	2mM $AgNO_3$	3mM $AgNO_3$	2	4	8	16
K. subtile (fresh)	18.4	18.4	18.6	63.3	50.2	23.8	17.8
K. subtile (dry)	18.4	18.6	19.2	71.2	60.0	29.7	20.3

a : QS inhibition (radius of pigment inhibition in mm) = radius of growth and pigment inhibition (r_2) – radius of bacterial growth inhibition (r_1).

b: Not active (–, inhibition zone <3mm); weak active (3–11mm); moderate active (12–15 mm); strong active (>15mm).

Assessment of Biofilm Inhibition Potential

The present study was also carried out to find the anti-biofilm activity of AgNPs extract of *K. subtile* (dry and fresh) against the pathogenic bacteria *S. aureus*, *B. cereus*, *P. aeruginosa* and *E. coli* (Table 4). The extract of AgNPs of *K. subtile* (dry and fresh) has shown the highest in biofilm inhibition activity (80.0%, and 65.0%, respectively) for *S. aureus* and (75.0% and 60.1%, respectively) for *P. aeruginosa.*

Biofilms are organized communities of dynamic and complex living microorganisms (such as bacteria, fungi, and seaweed) sheathed in extracellular polymeric substances (EPS). The biofilm formation is controlled by quorum sensing and it confers antibiotic resistance to the bacteria. Freshwater microalgae are rich sources of novel and biologically active secondary metabolites with various applications in the pharmaceutical industries. Therefore, biofilm and QS studies with freshwater microalgae have gained importance today. Biomaterials derived from silver nanoparticles synthesized from freshwater microalgae, which are non-toxic and inhibit pathogenic biofilms, have great potential. Mutungwa et al. (2015) reported only 49.36% inhibition of biofilm formation in *P. aeruginosa* when treated with *Syzygium aromaticum* at a concentration of 200 mg/ml. Whereas, methanol extract of *C. vulgaris* showed 82% inhibition even at a concentration of 1 mg/ml [40]. In this study, the extract of AgNPs of *K. subtile* (dry and fresh) has shown the highest in biofilm inhibition activity of *S. aureus* and *P. aeruginosa.* The results obtained in this study are preliminary studies to be conducted in this field and are considered promising.

Table 4. Quantification of anti-biofilm action against pathogenic bacteria

Pathogens	Activity	AgNPs activity (%)	
		K. subtile (dry)	*K. subtile* (fresh)
S. aureus ATCC 29213	Inhibition	80.0	65.0
B. cereus 709 Roma	Inhibition	50.2	23.3
P. aeruginosa ATCC 27853	Inhibition	75.0	60.1
E. coli ATCC 25922	Inhibition	42.3	36.2

Conclusion

Today, nanomaterials are produced by industries for a variety of commercial applications. The use of green synthesis in the production of nanoparticles has recently attracted the attention of many researchers and industries. Although many microorganisms are used for the intracellular, and extracellular synthesis of nanoparticles, many photo-autotrophic microorganisms such as cyanobacteria, eukaryotic algae and fungi have been reported in the biosynthesis of nanoparticles. Because algae occur naturally in various ecosystems and are grown on a large scale, they have the potential for economical and environmentally friendly production of metallic nanoparticles. In our study, silver nanoparticles were synthesized from fresh and dry extracts of *K. subtile*. Biosynthesis of AgNPs was confirmed not only by visual references but also with a UV-visible spectrophotometer, FT-IR spectroscopy analysis, Scanning Electron Microscopy (SEM) and Energy Dispersive Spectroscopic analysis (EDS). UV-vis spectra showed the characteristic Plasmon absorption peak for silver nanoparticles at 430 nm and FT-IR analyses confirmed the reduction of Ag^+ to Ag^o. In addition, the results of this study clearly reveal that AgNPs obtained from *K. subtile* extracts inhibit the growth and proliferation of the tested pathogen microorganisms. This study revealed that microalgae are able to act as a bio-control agent against pathogenic bacteria in aquaculture. Therefore, the use of QS inhibiting agents would be a promising approach to control bacterial infections. *P. aeruginosa* and *S. aureus* are responsible for nosocomial infections to severe tissue infections. In this study, the AgNPs extract of *K. subtile* (dry and fresh) significantly inhibits the biofilm formation and QS controlled virulence factors in *P. aeruginosa* and *S. aureus.* As a result, it seems that the use of algae for the synthesis of metallic NPs will be a better alternative to chemical methods. However, the production of such nanoparticles has only been carried out in the research laboratory for now. Therefore, it is necessary to reveal the reaction mechanisms, to characterize the complex compounds involved in the bio-reduction process at cellular levels, to reduce the production costs and to evaluate which algae can be preferred.

Conflicts of Interest

The authors declare no conflict of interest.

Acknowledgements

The author would like to thank the Kırşehir Ahievran University financial support (Grant No. MMF.A4.21.009).

References

[1] Hassaan M.A., Hosny S., Green Synthesis of Ag and Au Nanoparticles from Micro and Macro Algae–Review, *International Journal of Atmospheric and Oceanic Sciences*, 2(1) (2018) 10-22.

[2] Çiftçi H., Çalışkan Ç., Öztürk K., Yazici B., Bioactive Nanoparticles Synthesized by Green Method. *Black Sea Journal of Engineering and Science*, 4 (1) (2021) 1-14.

[3] Manivasagan P., Venkatesan J., Sivakumar K., Kim S.K., Actinobacteria Mediated Synthesis of Nanoparticles and their Biological Properties: A Review. *Critical Reviews in Microbiology*, 42(2) (2016) 209-221.

[4] Wiley B., Sun Y., Xia Y., Synthesis of Silver Nanostructures with Controlled Shapes and Properties, *Acc Chem Res.,* 40 (10) (2007) 1067-76.

[5] Araga˜o A.P., Oliveira T.M., Quelemes P.V., Perfeito M.L., Carvalho Arau´jo M., Santiago J.A.S., Cardoso V.S., Quaresma P., Leite J.R.S.A, Silva D.A., Green Synthesis of Silver Nanoparticles Using the Seaweed *Gracilaria birdiae* and their Antibacterial Activity, *Arabian Journal of Chemistry*, 12 (2016) 4182-4188.

[6] Kumari S., Tyagi M., Jagadevan S., Mechanistic Removal of Environmental Contaminants Using Biogenic Nano-Materials, *Int. J. Environ. Sci. Technol.,* 16 (2019) 7591–7606.

[7] Yalcin Duygu D., Acikgoz Erkaya İ., Erdem B., Yalcin B.M., Characterization of Silver Nanoparticle Produced by *Pseudopediastrum boryanum* (Turpin) E. Hegewald and its Antimicrobial Effects on Some Pathogens. *Internatıonal Journal of Envıronmental Science and Technology*, 16(11) (2019) 7093-7102.

[8] Mateia G.M., Mateia S., Cogălniceanu G., Mycosynthesis of Silver Nanoparticles by *Aspergillus flavus* : Characterization and Antifungal Activity, *Digest Journal of Nanomaterials and Biostructures*, 18(1) (2023) 411-421.

[9] Oves M., Aslam M., Rauf M.A., Qayyum S., Qari H.A., Khan M.S., Alam M.Z., Tabrez S., Pugazhendhi A., Ismail I.M.I., Antimicrobial and Anticancer Activities of Silver Nanoparticles Synthesized from the Root Hair Extract of *Phoenix dactylifera*, *Mater Sci Eng C Mater Biol Appl.*, 89 (2018) 429-443.

[10] Sayed R., Saad H., Hagagy N., Silver Nanoparticles: Characterization and Antibacterial Properties, *Rend. Lincei Sci. Fis. Nat.*, 29(1) (2018) 1-6.

[11] El-Sheekh M.M., El-Kassas H.Y., Algal Production of Nano-Silver and Gold: Their Antimicrobial and Cytotoxic Activities: A Review, *Journal of Genetic Engineering and Biotechnology*, 14(2) (2016) 299-310.

[12] Javed B., Nadhman A., Mashwani Z., Optimization, Characterization and Antimicrobial Activity of Silver Nanoparticles Against Plant Bacterial Pathogens Phyto-Synthesized by *Mentha longifolia*, *Mater. Res. Express,* 7 (2020) 085406.

[13] Bafghi M.H., Safdari H., Nazari R., Darroudi M., Sabouri Z., Zargar M., Zarrinfar H., Evaluation and Comparison of the Effects of Biosynthesized Selenium and Silver Nanoparticles Using Plant Extracts With Antifungal Drugs on the Growth Of *Aspergillus* and *Candida* Species, *Rend. Lincei Sci. Fis. Nat.,* 32 (2021) 791–803.

[14] Marchioni M., Jouneau P.H., Chevallet M., Michaud-Soret I., Deniaud A., Silver Nanoparticle Fate in Mammals: Bridging in Vitro and in Vivo Studies, *Coordination Chemistry Reviews*, 364 (2018) 118–36.

[15] Pal S., Tak Y.K., Song J.M., Does the Antibacterial Activity of Silver Nanoparticles Depend on the Shape of the Nanoparticle? A Study of the Gram-Negative Bacterium *Escherichia coli*, *Appl Environ Microbiol*., 73(6) (2007) 1712-20.

[16] Paluch E., Rewak-Soroczyńska J., Jędrusik I.E., Mazurkiewicz I.E., Jermakow K., Prevention of Biofilm Formation by Quorum Quenching, *Appl Microbiol Biotechnol.*, 104 (2020) 1871–1881

[17] Davies D.G., Parsek M.R., Pearson J.P., Iglewski B.H., Costerton J.W., Greenberg E.P., The Involvement of Cell to Cell Signals in the Development of a Bacterial Biofilm, *Science*, 280 (5361) (1998) 295-8.

[18] Roy R., Tiwari M., Donelli G., Tiwari V., Strategies for Combating Bacterial Biofilms: A Focus on Anti-Biofilm Agents and Their Mechanisms of Action, *Virulence,* 9(1) (2018) 522-554

[19] Ozcan S.S., Dieser M., Parker A.E., Balasubramanian N., Foreman C.M., Quorum Sensing Inhibition As a Promising Method to Control Biofilm Growth in Metalworking Fluids, *J. Ind. Microbiol. Biotechnol.,* 46(8) (2019) 1103-1111.

[20] Bauer W.D., Robinson J.B., Disruption of Bacterial Quorum Sensing by Other Organisms, *Curr Opin Biotechnol*., 13 (3) (2002) 234-7.

[21] Rajeshkumar S., Malarkodi C., Paulkumar K., Vanaja M., Gnanajobitha G., Annadurai G., Algae Mediated Green Fabrication of Silver Nanoparticles and Examination of Its Antifungal Activity Against Clinical Pathogens, *Int. J. Met.*, 11 (2014) 1-8

[22] Jena J., Pradhan N., Nayak R.R., Dash B.P., Sukla L.B., Panda P.K., Mishra B.K., Microalga *Scenedesmus* sp.: A Potential Low-Cost Green Machine for Silver Nanoparticle Synthesis, *J Microbiol Biotechnol*, 24(4) (2014) 522-533.

[23] Aziz N., Fatma T., Varma A., Prasad R., Biogenic Synthesis of Silver Nanoparticles Using *Scenedesmus Abundans* and Evaluation of their Antibacterial Activity, *Journal of Nanoparticles,* (2014) 1-6.

[24] NCCLS, Performance Standards for Antimicrobial Susceptibility Testing: 13th Informational Supplement (Disk Diffusion Supplemental Tables). NCCLS document M100-S13 (M2), supplement to NCCLS document M2-A8 (disk diffusion) (2003).

[25] NCCLS, Performance Standards for Antimicrobial Susceptibility Testing: 10th Informational Supplement (Aerobic Dilution, MIC Testing Supplemental Tables. NCCLS document M100-S10 (M7), supplement to NCCLS document M7-A5 (MIC testing) (2000).

[26] McClean K.H., Winson M.K., Fish L., Taylor A., Chhabra S.R., Camara M., Daykin M., Lamb J.H., Swift S., Bycroft B.W., Stewart G.S.A.B., Williams P., Quorum Sensing And *Chromobacterium violaceum*: Exploitation of Violacein Production and Inhibition for the Detection of N-acyl Homoserine Lactones, *Microbiology,* 143(12) (1997) 3703-11.

[27] Khan M.S., Zahin M., Hasan S., Husain F.M., Ahmad I., Inhibition of Quorum Sensing Regulated Bacterial Functions by Plant Essential Oils With Special Reference to Clove Oil, *Lett Appl Microbiol*., 49(3) (2009) 354-60.

[28] Schillaci D., Cusimano M.G., Cunsolo V., Saletti R., Russo D., Vazzana M., Vitale M., Arizza V., Immune Mediators of Sea-Cucumber *Holothuria tubulosa* (*Echinodermata*) as Source of Novel Antimicrobial and Anti-Staphylococcal Biofilm Agents, *AMB Express*, 3(1) (2013) 35.

[29] Kathiresan K., Manivannan S., Nabeel M.A., Dhivya B., Studies on Silver Nanoparticles Synthesised by a Marine Fungus, *Penicillium fellutanum* Isolated from Coastal Mangrove Sediment, *Colloids Surf. B*, 71 (1) (2009)133-7.

[30] Sharma A., Sharma S., Sharma K., Chetri S.P.K., Vashishtha A., Singh P., Kumar R., Rathi B., Agrawal V., Algae as Crucial Organisms in Advancing Nanotechnology: A Systematic Review, *J Appl Phycol.,* 28 (2016) 1759-1774.

[31] Aboelfetoh E.F., El-Shenody R.A., Ghobara, M.M., Eco-Friendly Synthesis of Silver Nanoparticles Using Green Algae (*Caulerpa serrulata*): Reaction Optimization, Catalytic and Antibacterial Activities, *Environ Monit Assess.*, 189 (7) (2017) 349.

[32] Sigee D.C., Dean A., Levado E., Tobin M.J., Fourier-Transform Infrared Spectroscopy of *Pediastrum duplex* Characterization of a Micro-Population Isolated From a Eutrophic Lake, *European Journal of Phycology*, 37(1) (2002) 19-26.

[33] Quester K.B., Avalos-Borja M.B., Castro-Longoria E., Biosynthesis and Microscopic Study of Metallic Nanoparticles, *Micron*, 55 (2013) 1-27.

[34] Kemp M.M., Kumar A., Clement D., Ajayan P., Mousa S., Linhardt R.J., Hyaluronan-and Heparin-Reduced Silver Nanoparticles With Antimicrobial Properties, *Nanomedicine*, 4(4) (2009) 421-9.

[35] Devi L.S., Joshi S.R., Antimicrobial and Synergistic Effects of Silver Nanoparticles Synthesized Using: Soil Fungi of High Altitudes of Eastern Himalaya, *Mycobiology*, 40(1) (2012) 27-34.

[36] Feng Q.L., Wu J., Chen G.Q., Cui F.Z., Kim T.N., Kim J.O., A Mechanistic Study of the Antibacterial Effect of Silver Ions on *Escherichia coli* and *Staphylococcus aureus*, *J Biomed Mater Res.*, 52 (4) (2000) 662-8.

[37] Raffi M., Hussain F., Bhatti T.M., Akhter J.I., Hameed A., Hasan M.M., Antibacterial Characterization of Silver Nanoparticles Against *E. coli* ATCC-15224, *J Mater Sci Technol*, 24 (2008) 192–196.

[38] El-Sheekh M.M., Hassan L.H.S., Morsi H.H., Evaluation of Antimicrobial Activities of Blue-Green Algae-Mediated Silver and Gold Nanoparticles, *Rend. Lincei Sci. Fis. Nat.*, 32 (2021) 747-759.

[39] Tang J., Wang W., Chu W., Antimicrobial and Anti-Quorum Sensing Activities of Phlorotannins from Seaweed (*Hizikia fusiforme*), *Front. Cell. Infect. Microbiol*., 10 (2020) 586750.

[40] Mutungwa M., Alluri N., Majumdar M., Anti-quorum Sensing Activity of Some Commonly Used Traditional Indian Spices, *Int J Pharm Pharm Sci.*, 7(11) (2015) 80-3.

Cumhuriyet Sci. J., 45(3) (2024) 465-470
DOI: https://doi.org/10.17776/csj.1519699

Cumhuriyet Science Journal

| csj.cumhuriyet.edu.tr | Founded: 2002 ISSN: 2587-2680 e-ISSN: 2587-246X Publisher: Sivas Cumhuriyet University

Examination of Biological Activity of *Passiflora edulis* (Çarkıfelek) Extract via Phytochemical Analysis

Tutku Tunç[1,a,*], **Zeynep Sümer**[2,b] , **Kerim Emre Öksüz**[3,4,c]

[1]*Department of Pharmaceutical Microbiology, Faculty of Pharmacy, Cumhuriyet University, Sivas, Turkey*
[2]*Department of Medical Microbiology, Faculty of Medicine, Cumhuriyet University, Sivas, Turkey*
[3]*Department of Metallurgical & Materials Engineering, Faculty of Engineering, Cumhuriyet University, Sivas, Turkey*
[4]*Institute of Science and Technology, Department of Bioengineering, Sivas Cumhuriyet University, Sivas, Turkey*
**Corresponding author*

Research Article

History
Received: 20/07/2024
Accepted: 20/09/2024

ABSTRACT

In recent years, the use of medicinal plants as sources of drugs or herbal extracts has been of great importance. *Passiflora edulis* is nowadays widely studied for its antimicrobial, anticancer, and antioxidant potential. Therefore, this study aimed to determine the phytochemical structure of ethanol extract of *P. edulis* leaves and to investigate its biological properties such as antimicrobial and anticancer activities. The ethanol extract of *P. edulis* leaves was obtained and analyzed by GC-MS. The antimicrobial activity of *P. edulis* leaf extract was determined by MIC test. XTT method was used to determine the antiproliferative activity. In the phytochemical analysis of *P. edulis* extract, dodecanoic acid, tetradecanoic acid, and n-hexadecanoic acid were found the most. The antimicrobial effect of *P. edulis* leaf extract was found against pathogenic microorganisms. In addition, *P. edulis* leaf extract was found to have high anticancer activity against OvCar and MCF-7 cell lines, while it had the highest effect on the PC-3 cell line. It is thought that the effectiveness of this antiproliferative and antimicrobial activity is related to the secondary metabolites determined by GC-MS analysis.

Keywords: *Passiflora edulis,* Dodecanoic acid, Antimicrobial effect, Secondary metabolite, Antiproliferative effect.

[a] *tutkutunc58@hotmail.com* *https://orcid.org/0000-0002-8274-9386*
[b] *drzeynepsumer@gmail.com* *https://orcid.org/0000-0002-1520-3359*
[c] *emre.oksuz@cumhuriyet.edu.tr* *https://orcid.org/0000-0001-7424-5930*

Introduction

In recent years, the use of medicinal plants as sources of drugs or herbal extracts for various chemotherapeutic purposes has been of great importance in both developing and developed countries of the world. Furthermore, the use of plant-derived natural compounds as part of herbal preparations used as alternative sources of medicines continues to play important roles in human health and the treatment of diseases all over the world [1]. Throughout history, the use of plant-derived therapies in cancer treatment has been important due to their advantages in terms of efficiency, minimal side effects, easy accessibility, and improvement in quality of life. Several studies have identified various compounds with chemopreventive and/or chemotherapeutic potential in these medicinal plants, among which the polyphenol family has received much attention [2]. Advances in the field of biomedicine have allowed significant progress in the understanding of different antitumor mechanisms, which has helped in the development of cancer prevention strategies. One of these strategies is to promote the use of food phytochemicals that have the potential to inhibit, delay or reverse the process of carcinogenesis; many of these substances have been identified in fruits, vegetables and legumes [3].

Even with current treatment modalities, cancer causes more deaths than all coronary heart disease or strokes [4]. Breast cancer is the fifth leading cause of cancer deaths worldwide, with an estimated 2.3 million new cases, representing 11.7% of all cancer cases [5]. Although ovarian cancer is the third most common gynecologic cancer worldwide, it stands out for having the highest mortality rate among these cancers. This high mortality is associated with a tendency to progress without symptoms, leading to late diagnosis and a higher chance of recurrence [6]. Approximately one in six men is likely to develop prostate cancer, with most cases occurring after the age of 50 [7]. Various treatments are used to treat prostate cancer, including hormones, surgery, radiation and chemotherapy. However, all these treatments have limitations and in the majority of cases, relapse of the disease occurs [8].

Passiflora edulis, the largest genus of the botanical family Passifloraceae, originates from tropical and subtropical regions of South America. *P. edulis* Sims (family Passifloraceae) is a strong climber. They cling to anything they can grab hold of. The leaves are evergreen and alternate, with three-lobed leaves when mature. They are fast growing and once established grow 15 - 20 feet a year. [1]. The plant is widely cultivated worldwide for the economic and medicinal value it adds to its fruits and derivatives. The sedative and tranquilizing activities of *P. edulis* are known and hence its leaves and fruits are widely used as popular compounds in the treatment of alcoholism, anxiety, migraine, nervousness and insomnia [9]. Passion fruit is a characteristic fruit of tropical regions and is particularly prominent in the pharmaceutical industry due to its various medicinal properties in its extracts, leaves and flowers, as well as the antimicrobial and antioxidant potential presented in its pulp, leaves, seeds and bark. The leaves also contain the health-valuable cyanogenic glycosides β-D-allopyranose benzyl compounds [10].

The systematic screening of antimicrobial plant extracts represents a continuous effort to find new compounds with the potential to act against multidrug-resistant resistant pathogenic bacteria and fungi. The accumulation of phytochemicals in plant cell cultures has been studied for over three decades and the knowledge generated has helped realize the use of cell cultures to produce desired phytochemicals [11]. It is possible that phytochemicals derived from medicinal plants that exhibit antimicrobial activities have different structures from microbial-derived antibiotics and may have different modes of action [12].

In many studies, biological activities and possible therapeutic applications have been demonstrated using different organs of *P. edulis* [13]. Amaral et al. conducted a study for the first time on the cytotoxic potential of leaf extracts of 14 species of the genus *Passiflora* against cancer cell lines. Of these, only *Passiflora alata* leaf extract showed relevant cytotoxic potential. Based on these data, the hypothesis that other *Passiflora* species besides the 14 species tested may also exhibit anti-cancer activity is emphasized [14].

The search for more effective and selective compounds for use in cancer treatment is a challenging task and nature provides an alternative to this problem [15]. For these reasons, new strategies for cancer treatments are needed. Due to the increase in antibiotic resistance in recent years, it has become important to investigate the antimicrobial effects of phytochemicals in plants as alternative and supportive therapy in the treatment of infectious diseases.

In this study, the phytochemical structure and biological properties of the ethanol extract obtained from *P. edulis* leaves were investigated by antioxidant, antimicrobial and antiproliferative activity assays.

Materials and Methods

Collection and Identification of Plant Material

The leaves of *P. edulis* were collected from Dim Cave, situated in the Alanya district of Antalya, Türkiye in July 2023. The plant samples were identified by Dr. Hülya Özpınar. Dim Cave, located 11 kilometers from Alanya, is situated 232 meters above sea level on the western slope of Cebeli Reis Mountain. All parts of the plant were washed ten times with sterile distilled water. They were then air-dried at 25°C for ten days in the absence of sunlight. Subsequently, the dried plant material was coarsely ground using a blender. The powdered material was weighed, placed in an airtight container, and stored in a refrigerator at 4 °C for future use.

Sample Extractions

Approximately 50 grams of the finely ground plant material were carefully transferred into an extraction thimble. This thimble was then positioned within a Soxhlet apparatus, which was connected to a reflux condenser to facilitate the continuous extraction process. The extraction was performed using a series of solvents, specifically petroleum ether, chloroform, ethyl acetate, ethanol, and distilled water, each added sequentially to the extraction flask to ensure comprehensive extraction of the plant's constituents. The Soxhlet apparatus was operated for a total of 6 hours to ensure the thorough extraction and complete exhaustion of the *P. edulis* herbal material. Following this extraction period, the resulting extracts were collected and concentrated using a rotary evaporator, which allowed for the removal of solvents under reduced pressure. The concentrated plant material was subsequently subjected to vacuum drying at a temperature of 40°C for two hours to eliminate any residual solvents and moisture. After drying, the concentrated material was transferred into sterile glass bottles to prevent contamination and was stored at 4°C until it was required for further experimental procedures [16].

Gas Chromatography-Mass Spectroscopy (GC-MS) Analysis of Passiflora Edulis Extract

GC-MS analysis of the ethanolic extract of *P. edulis* leaves was conducted using the Shimadzu QP2010 SE Ultra Version. The instrument was equipped with a DB-35 MS Capillary Standard Non-polar column, with dimensions of 30 mts x 0.25 mm ID x 0.25 µm film thickness. Helium was used as the carrier gas, flowing at a rate of 1 mL/min. The injector temperature was set to 250°C, and the oven temperature was programmed to start at 60°C for 15 minutes, then gradually increased to 280°C and held for 3 minutes. Component identification was based on comparing their mass spectra with those in the Wiley and NBS libraries, as well as their retention indices [17].

Antimicrobial Activity

The antimicrobial activity of *P. edulis* leaf extract against gram-positive and gram-negative bacteria and yeast fungi was determined using the Minimum Inhibition Concentration (MIC) test [18]. *Staphylococcus aureus* (ATCC 29213), *Enterococcus faecalis* (ATCC 29212), *Bacillus cereus* (ATCC 11778), *Pseudomonas aeruginosa* (ATCC 27853), *Escherichia coli* (ATCC 25922), *Klebsiella pneumoniae* (ATCC 13883) and *Candida albicans* (ATCC 10231) standard strains were used for this test. 10 µL of the extracts prepared by dissolving in DMSO was added to the first well and serial dilutions were made with a total of 10 concentrations. The microorganisms cultured in blood agar were then transferred to Mueller Hinton Broth (Accumix® AM1072) and Saboraud Dextrose Broth (Himedia ME033) and the concentrations were adjusted to 0.5 McFarland. 50 µL of microorganism culture was added to all wells. Microplates cultured with bacteria were incubated at 37°C and microplates cultured with yeast fungi were incubated at 35°C for 24 hours. The first well in which microorganism growth disappeared was considered as the MIC value. The analysis was performed in 3 replicates [19].

Antiproliferative Activity

Antiproliferative effects of plant extracts were tested on the human lung cancer cell line (A549, ATCC-CCL-185), human breast cancer cell line (MCF-7, ATCC-HTB-22), mouse glioma cell line (C6, ATCC-CCL-107) and human normal lung fibroblast (WI-38, ATCC-CCL-75) cell lines using XTT Assay method. Cells were first passaged and grown until they reached the appropriate density for the appropriate experiment. They were then seeded in microplates at 10.000 cells per well. The extracts were added to the cells in a total of 8 concentrations. DMSO was used as negative control and antineoplastic agents were used as positive control. Microplates were incubated for 24 hours at 37°C in an atmosphere with 5% CO_2. At the end of the incubation period, the medium was removed and 100 µL of XTT solution prepared according to the experimental procedure was added to each well. After 4 hours of incubation, optical density values were measured at 450 nm with a microplate reader (ELISA Reader) [20].

Statistical Analysis

One Way Anova test as well as Tukey test were used for statistical analysis of the findings. For this purpose, the SPSS 16.0 (SPSS, Chicago, IL, USA) statistical program was used and a $p<0.05$ value at 95% confidence interval was considered significant between groups.

Results and Discussion

Gas Chromatography-mass Spectroscopy (GC-MS) Analysis of Passiflora Edulis Extract

In the GC-MS analysis, 25 main bioactive compounds were identified in the ethanolic extract of *P. edulis* leaves extract and the results were given in Table 1. These compounds were identified based on their peak areas, molecular weights, and molecular formulas. The GC-MS spectrum indicated the presence of several long-chain hydrocarbons. As the number of carbon atoms in a molecule increases, its hydrophilicity decreases and its lipophilicity increases.

The extract of *P. edulis* extract contained 62.05 to 73.78 % of total linolenic and linoleic acids, comparable to safflower seeds. Monounsaturated fatty acids such as oleic acid and stearic acid have been shown to lower blood glucose levels when consumed as part of the diet [21]. Thus, the analysis indicates that the passiflora plant extract of *P. edulis* extract contains fatty acids with significant beneficial properties [22].

Table 1. Phytocompounds identified in the ethanolic extract of *Passiflora edulis* extract by GC-MS analysis

No	**RT (min.)**	**Compound name**	**Molecular formula**	**Molecular weight**
1	2.711	Benzhydrazide,N2-(2-methoxy-5nitrobenzylideno)-	$C_{15}H_{12}N_4O_6$	299.091
2	3.976	Styrene	$C_6H_5CH=CH_2$	104.063
3	4.356	Tetraethyl orthosilicate	$Si(OC_2H_5)_4$	208.113
4	6.543	1-Dodecene	$CH_3(CH_2)_9CH=CH_2$	168.188
5	8.146	9-Octadecene, (E)-	$C_{18}H_{36}$	252.282
6	10.153	7-Hexadecene, (Z)-	$C_{16}H_{32}$	224.25
7	12.209	cis-11-Hexadecenal	$C_{16}H_{30}O$	238.23
8	17.022	Oxacyclotetradecane-2,11-dione, 13-methyl-	$C_{14}H_{24}O_3$	240.173
9	17.622	n-Hexadecanoic acid	$C_{16}H_{32}O_2$	256.23
10	18.453	Palmitic acid	$C_{18}H_{36}O_2$	284.272
11	20.867	Linolelaidic acid	$C_{19}H_{34}O_2$	294.256
12	21.031	11-Octadecenoic acid, methyl ester, (Z)-	$C_{19}H_{36}O_2$	296.272
13	22.572	Ethyl Oleate	$C_{20}H_{38}O_2$	310.287
14	23.011	Ethyl Stearate	$C_{20}H_{40}O_2$	312.303
15	26.442	9, 12- Linoleic acid	$C_{18}H_{32}O_2$	280.24
16	27.355	Methyl nonyl acetaldehyde	$C_{12}H_{24}O$	184.183
17	27.711	Pregna-3,5-dien-20.alpha.-ol,O-trimethylsilyl	$C_{24}H_{40}Osi$	372.285
18	27.966	Heptadecane	$C_{17}H_{36}$	240.282
19	28.207	Palmitic acid β-monoglyceride	$C_{19}H_{38}O_4$	330.277
20	28.728	9,12-Tetradecadien-1-ol, (Z,E)-	$C_{14}H_{26}O$	210.198
21	30.122	4-(3,4,5,6-Tetrahydroxy-2-oxo-hexylamino)- benzonitrile	$C_{13}H_{16}N_2O_5$	280.106
22	30.439	9,17-Octadecadienal, (Z)-	$C_{18}H_{32}O$	264.245
23	30.90	15-Hydroxypentadecanoic acid	$C_{15}H_{30}O_3$	258.219
24	31.905	E-11-Hexadecenoic acid, ethyl ester	$C_{18}H_{34}O_2$	282.256
25	33.723	(R)-(-)-14-Methyl-8-hexadecyn-1-o	$C_{17}H_{32}O$	252.245

In this study, the GC-MS analysis of the ethanolic extract of *P. edulis* leaves revealed the presence of dodecanoic acid, tetradecanoic acid, n-hexadecanoic acid, 9,12-octadecadienoic acid (Z, Z), oleic acid, stearic acid, palmitic acid, and linolenic acid. Among these identified compounds, dodecanoic acid, tetradecanoic acid, and n-hexadecanoic acid possess antioxidant and antimicrobial properties. Additionally, n-hexadecanoic acid exhibits larvicidal effects, while 9,12-octadecadienoic acid (Z, Z) demonstrates anti-inflammatory and anti-arthritic activities [23].

Determination of the Antimicrobial Activity of Passiflora Edulis Extract

Antimicrobial Activity Results

In the determination of the antimicrobial activity of *P. edulis* leaf extracts, MIC values were determined by microdilution test. The results were compared with reference sources [27] and MIC values of standard antibiotics. Reference sources given as [Effective (MIC < 100 µg/mL), Moderate (100 < MIC ≤ 625 µg/mL), and Weak (MIC > 625 µg/mL)] were used. The MIC values of the extracts and antibiotics are given in the table below (Table 2).

Table 2. MIC results of *Passiflora edulis* leaf extract (µg/mL)

Microorganisms (Bacteria and Yeasts)	Leaf extract MIC (µg/mL)	Antibiotics MIC (µg/mL)	Antibiotics
E. coli	50	8	Amoxicillin
K. pneumoniae	100	16	Piperacillin/Tazobactam
P. aeruginosa	25	4	Imipenem
S. aureus	50	2	Linezolid
E. faecalis	50	2	Linezolid
B. cereus	50	1	Linezolid
C. albicans	50	0.25	Fluconazole

P. edulis leaf extract showed effective antimicrobial activity on the tested microorganisms based on reference sources. When compared with the MIC values of standard antibiotics, it was observed that the antimicrobial activity was not at the targeted level. Ripa et al. showed that *P. edulis* leaf petroleum ether and chloroform extract moderately inhibited the growth of *B. megaterium, P. aeruginosa, S. dysenteriae* and *S. boydii* microorganisms [1]. Akanbi et al. reported that the leaf hexane extract of *P. edulis* showed high antimicrobial activity in a study with *S. aureus, Salmonella paratyphi, P. aeruginosa* and *K. pneumoniae* obtained from clinical isolates [12]. Ramaiya et al. and Kannan et al. found moderate antimicrobial activity (12.0 mm / 10 ± 1.03 mm) of *P. edulis* leaf methanol extract against *Bacillus subtilis* and *S. auerus* [24, 25]. Nugraha et al. showed that *P. edulis* ethanol extract has antimicrobial activity against *S. aureus* and *E. coli* bacteria [26]. According to the results of our study, *P. edulis* leaf extract was found to have antimicrobial activity considering the reference values. These results are in agreement with the literature studies mentioned here.

Determination of the Antiproliferative Activity of Passiflora Edulis Plant Extracts

The cytotoxicity of *P. edulis* leaf extract on three different tumor cell lines (PC-3, OvCar, MCF-7) was evaluated by XTT assay. Healthy WI-38 cell line was used as a positive control. Cell viability was determined as optical density. IC_{50} values were obtained by dose-response curve and the following tables and graphs were generated (Table 3, Figure 1).

Table 3. IC_{50} values of *P. edulis* extract

P. edulis	**IC_{50}(µg/ml)**			
	PC-3	**OvCar**	**MCF-7**	**WI-38**
Leaf Ethanol	10,11±0,17	12,97±0,62	11,31±0,34	>100

Significant p≤ 0.05 level of analysis of variance (One Way Anova Tukey)

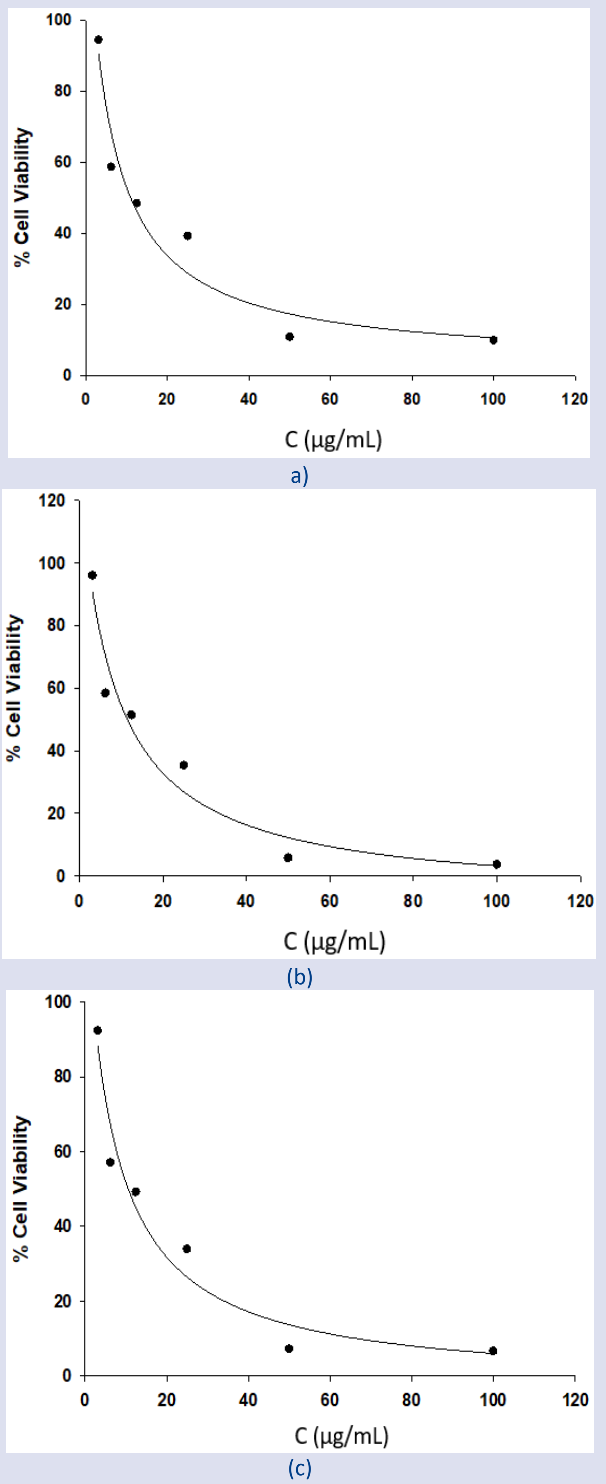

a)

(b)

(c)

Figure 1. a, b, c; Cell viability of PC-3, OvCar and MCF-7

The IC_{50} values given in Table 3 (PC-3=10.11, OvCar=12.97, MCF-7=11.31) prove that effective anticancer activity was found even at low concentrations. When the anticancer activity of the three different cell lines was compared with each other, no statistically significant difference was found ($p \geq 0.05$).

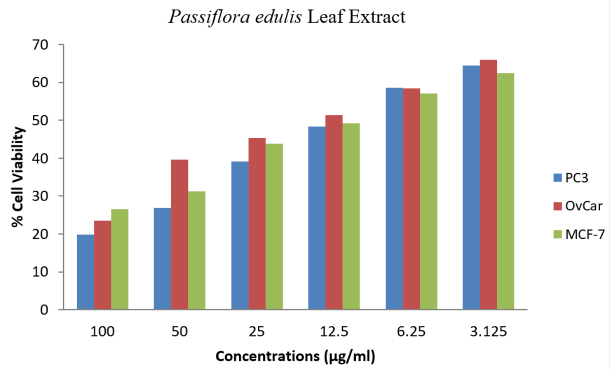

Figure 2. % Cell viability graphic of *P. edulis* extract.

P. edulis leaf extract showed high anticancer activity on cancer cells as shown in cell viability graphs (Figure 2). On healthy WI-38 cells, cell viability reached 100% even at high concentrations of the extract. This indicates that the toxic effect of *P. edulis* extract is almost negligible. Sari et al. and Kuete et al. showed antiproliferative activity on MCF-7 cells in a study with *P. edulis* extract [5, 27]. In an in vitro study conducted by Fotsing et al., *P. edulis* leaf extract showed significant inhibition in the growth of MCF-7 and MDA-MB 231 cells at 100 µg/mL [28]. An article examining the cytotoxic effect of *P. edulis* extracts on OvCar and PC-3 cells was not found in the literature. However, in a study conducted by Amaral et al. on 14 different *Passiflora* species, *P. alata* leaf extract was shown to have a high antiproliferative effect on OvCar cells [29]. In addition, da Silva et al. and Amaral et al. showed antiproliferative effects on PC-3 cells in their studies with *P. mucronate and P. alata* species [14, 30].

Conclusions

In this study, *P. edulis* leaves were extracted in ethanol and analyzed for phytochemical content. While looking at the biological activities, it was observed that antimicrobial activity and anticancer effect were high. In line with these data, more biological activities of *P. edulis* plant with high biological activity can be investigated. In addition, depending on the high antiproliferative activity, it may be recommended to investigate the apoptosis mechanisms of the cell lines examined.

Acknowledgments

The authors would like to thank Dr. Ceylan Hepokur for her aid and support and Dr. Hülya Özpınar for her aid in plant species identification.

Conflict of Interest

The authors declare that they have no conflicts of interest in the publication.

References

[1] Ripa F. A., Haque M., Nahar L., Islam M. M., Antibacterial, cytotoxic and antioxidant activity of Passiflora edulis Sims, *Eur. J. Sci. Res.*, 31(4) (2009) 592-598.

[2] Aguillón J., Arango S. S., Uribe D. F., Loango N., Cytotoxic and apoptotic activity of extracts from leaves and juice of Passiflora edulis, *J. Liver. Res. Disord. Ther.*, 4(2) (2018) 67-71.

[3] Ramírez V., Arango S. S., Uribe D., Maldonado M. E., Aguillón J., Effect of the ethanolic extract of Passiflora edulis F. Flavicarpa leaves on viability, cytotoxicity and apoptosis of colon cancer cell lines, *J. Chem. Pharm. Res.*, 9(6) (2017) 135-9.

[4] Antoni S., Soerjomataram I., Møller B., Bray F., Ferlay J., An assessment of GLOBOCAN methods for deriving national estimates of cancer incidence, *Bulletin of the World Health Organization*, 94(3) (2016) 174.

[5] Sari L. M., Sari D. K., Bustami A., Gazali A. D., Auerkari E. I., Cytotoxicity and apoptosis activities of passion fruit (Passiflora edulis Sims) seed extract on HSC-2, HSC-3, MCF-7, and HaCaT cell lines, *Journal of Pharmacy & Pharmacognosy Research*, 12(4) (2024) 659-672.

[6] Çoban H. Ş., Çil N., Önder E., Abban Mete G., Anti-cancer effects of alpha lipoic acid, cisplatin and paclitaxel combination in the OVCAR-3 ovarian adenocarcinoma cell line, *Molecular Biology Reports*, 51(1) (2024) 485.

[7] Eisermann K., Tandon S., Bazarov A., Brett A., Fraizer G., Piontkivska H., Evolutionary conservation of zinc finger transcription factor binding sites in promoters of genes co-expressed with WT1 in prostate cancer, *BMC Genomics*, 9 (2008) 1-15.

[8] Choi E. S., Kim J. S., Kwon K. H., Kim H. S., Cho N. P., Cho S. D., Methanol extract of Sanguisorba officinalis L. with cytotoxic activity against PC3 human prostate cancer cells, *Molecular Medicine Reports*, 6(3) (2012) 670-674.

[9] Li H., Zhou P., Yang Q., Shen Y., Deng J., Li L., Zhao D., Comparative studies on anxiolytic activities and flavonoid compositions of Passiflora edulis 'edulis' and Passiflora edulis 'flavicarpa', *Journal of Ethnopharmacology*, 133(3) (2011) 1085-1090.

[10] Oliveira H. M., Espinheira M. J. C. L., de Souza F. M., Duarte S. F. P., David I. R., Sousa B. R., Evaluation of the antimicrobial potential of essential oil of the leaf of Passiflora edulis, *Int. J. Adv. Eng. Res. Sci.* (IJAERS), 6(5) (2019) 390-395.

[11] Johnson M., Maridass M., Irudayaraj V., Preliminary phytochemical and anti-bacterial studies on Passiflora edulis, *Ethnobotanical Leaflets*, (1) (2008) 51.

[12] Akanbi B. O., Bodunrin O. D., Olayanju S., Phytochemical screening and antibacterial activity of Passiflora edulis, *Researcher*, 3(5) (2011) 9-12.

[13] de Sousa G. F., Santos D. K. D. D. N., da Silva R. S., Barros B. R. D. S., da Cruz-Filho I. J., Ramos B. D. A., Lagos de Melo C. M., Evaluation of cytotoxic, immunomodulatory effects, antimicrobial activities and phytochemical constituents from various extracts of Passiflora edulis F. flavicarpa (Passifloraceae), *Natural Product Research*, 35(24) (2021) 5862-5866.

[14] Amaral R. G., Gomes S. V., Andrade L. N., Dos Santos S. A., Severino P., de Albuquerque Júnior R. L., Carvalho A. A., Cytotoxic, antitumor and toxicological profile of Passiflora alata leaf extract, *Molecules*, 25(20) (2020) 4814.

[15] Dias D. A., Urban S., Roessner U., A historical overview of natural products in drug discovery, *Metabolites*, 2(2) (2012) 303-336.

[16] Bohórquez-Moreno C. D., Öksüz K. E., Dinçer E., Hepokur C., Şen L., Plant-inspired adhesive and injectable natural hydrogels: in vitro and in vivo studies, *Biotechnology Letters*, 45(9) (2023) 1209–1222.

[17] Li C., Xin M., Li L., He X., Yi P., Tang Y., Li J., Zheng F., Liu G., Sheng J., Li Z., Sun J., Characterization of the aromatic profile of purple passion fruit (Passiflora edulis Sims) during ripening by HS-SPME-GC/MS and RNA sequencing, *Food Chemistry*, 355 (2021) 129685.

[18] Rizwana H., Al Otibi F., Al-Malki N., Chemical composition, FTIR studies and antibacterial activity of Passiflora edulis f. edulis (Fruit), *J. Pure Appl. Microbiol.*, 13(4) (2019) 2489-2498.

[19] Hepokur C., Misir S., Tunç T., Tutar U., Hepokur A., Çiçek, M., In vitro antimicrobial, antioxidant, cytotoxic activities, and wound healing potential of Thymbra capitata ethanolic extract, *Turkish Journal of Biochemistry*, 45(6) (2020) 843-849.

[20] Gezegen H., Tutar U., Hepokur C., Ceylan M., Synthesis and biological evaluation of novel indenopyrazole derivatives, *Journal of Biochemical and Molecular Toxicology*, 33(5) (2019) e22285.

[21] Thomsen C., Rasmussen O., Lousen T., Holst J. J., Fenselau S., Schrezenmeir J., Hermansen K., Differential effects of saturated and monounsaturated fatty acids on postprandial lipemia and incretin responses in healthy subjects, *The American Journal of Clinical Nutrition*, 69 (6) (1999) 1135–1143.

[22] Calder P. C., Functional Roles of Fatty Acids and Their Effects on Human Health. JPEN, *Journal of Parenteral and Enteral Nutrition*, 39 (2015) (1S).

[23] Lalitharani S, Mohan VR, Regini GS., GC-MS analysis of ethanolic extract of Zanthoxylum rhetsa (roxb.) dc spines, *J. Herbal Med. Toxicol.* 4(1) (2010) 191-2.

[24] Ramaiya S. D., Bujang J. S., Zakaria M. H., Assessment of total phenolic, antioxidant, and antibacterial activities of Passiflora species, *The Scientific World Journal*, (1) (2014) 167309.

[25] Kannan S., Devi B. P., Jayakar B., Antibacterial evaluation of the methanolic extract of Passiflora edulis. *Hygeia - Journal for Drugs and Medicine*, 3(1) (2011) 46-49.

[26] Nugraha S. E., Achmad S., Sitompul E., Antibacterial activity of ethyl acetate fraction of passion fruit peel (Passiflora Edulis Sims) on Staphylococcus aureus and Escherichia coli, *Indonesian Journal of Pharmaceutical and Clinical Research*, 2(1) (2019) 07-12.

[27] Kuete V., Dzotam J. K., Voukeng I. K., Fankam A. G., Efferth T. Cytotoxicity of methanol extracts of Annona muricata, Passiflora edulis and nine other Cameroonian medicinal plants towards multi-factorial drug-resistant cancer cell lines, *Springerplus*, 5 (2016) 1-12.

[28] Fotsing S. I., Pambe J. C. N., Silihe K. K., Yembeau N. L., Choupo A., Njamen D., Zingue S., Breast cancer cell growth arrest and chemopreventive effects of Passiflora edulis Sims (Passifloraceae) ethanolic leaves extract on a rat model of mammary carcinoma, *Journal of Ethnopharmacology*, 311 (2023) 116408.

[29] Amaral R. G., Gome, S. V. F., Luciano M. C. D. S., Pessoa C. D. Ó., Andrade L. N., Severino P., Carvalho A. A., Cytotoxic potential of 14 Passiflora species against cancer cells, *Journal of Medicinal Plants Research*, 13(7) (2019) 157-166.

[30] da Silva I. C., Kaluđerović G. N., de Oliveira P. F., Guimarães D. O., Quaresma C. H., Porzel A., Leal I. C., Apoptosis caused by triterpenes and phytosterols and antioxidant activity of an enriched flavonoid extract from Passiflora mucronata, *Anti-Cancer Agents in Medicinal Chemistry*, 18(10) (2018) 1405-1416.

Cumhuriyet Sci. J., 45(3) (2024) 471-477
DOI: https://doi.org/10.17776/csj.1446224

Cumhuriyet Science Journal

| csj.cumhuriyet.edu.tr | Founded: 2002 ISSN: 2587-2680 e-ISSN: 2587-246X Publisher: Sivas Cumhuriyet University

Determination of the Short-Term Drought Stress Tolerance of Three Barley Varieties Using Physiological and Biochemical Changes

Gamze Baltacier[1,a], Okan Acar[2,b,*]

[1] *Department of Biology, School of Graduate Studies, Çanakkale Onsekiz Mart University, Türkiye*
[2] *Department of Biology, Faculty of Science, Çanakkale Onsekiz Mart University, Türkiye*
**Corresponding author*

Research Article

History
Received: 02/03/2024
Accepted: 15/09/2024

ABSTRACT

Barley (*Hordeum vulgare* L.) is an important agricultural plant that can adapt to stress conditions. Abiotic stress factors significantly reduce growth, photosynthetic efficiency and metabolic processes in barley. Drought stress increases reactive oxygen species (ROS) in plant cells, and the antioxidant defense system reduces damage caused by overproduction of ROS. The aim of this study was to determine the physiological and biochemical effects of short-term drought stress on some barley cultivars (Kalaycı-97, Harman and Yaprak) grown in Turkey. In 21-day-old seedlings, short-term drought stress decreased the total chlorophyll content. The amount of total protein reduced in the Harman variety, while it increased by 19% in Kalaycı-97 and 27% in Yaprak. The H_2O_2 content decreased in Yaprak while increasing by 76% in the Kalaycı-97 variety. It was demonstrated that TBARS levels increased by 62% in Kalaycı-97 and 26% in Yaprak. In other ways, while drought stress caused a 48% decrease in APX activity in Kalaycı-97, it caused a 42% and 20% increase in APX activity in Harman and Yaprak, respectively. However, in Kalaycı-97 and Yaprak, CAT increased by 48% and 69%, respectively. These results indicate that Yaprak genotype is tolerant, Kalaycı-97 sensitive and Harman moderately tolerant to short term drought stress.

Keywords: Barley, Drought stress, Relative water content, Catalase, Ascorbate peroxidase.

[a] *gamzebaltacier@gmail.com* *https://orcid.org/0000-0001-9299-3115*
[b] *oacar@comu.edu.tr* *https://orcid.org/0000-0002-9818-8827*

Introduction

Abiotic stress conditions that affect plants include salinity, drought, excess or shortage of ions, extremes in temperature, and inadequate or excessive light [1]. Extended periods of stress cause physiological, biochemical, and molecular alterations in plants that hinder growth and development and reduce yield [2]. The degree and duration of the stress to which a plant is subjected directly correlate with its capacity to withstand stress. ROS production is a regularly observed cellular response in plants to stressors [3]. The accumulation of ROS results in the production of potentially harmful compounds for the cell, such as superoxide (O_2*) and hydrogen peroxide (H_2O_2) [4]. ROS concentrations increase in plant cells exposed to environmental stress. Overproduction of ROS has the potential to harm cells and ultimately cause cell death. Intracellular redox balance is preserved, nevertheless, because antioxidants scavenge these radical molecules and keep them at levels that are safe for plant cells. This is crucial for optimal plant growth and yield [5]. Antioxidant enzymes like catalase (CAT) and ascorbate peroxidase (APX) or a non-enzymatic antioxidants like vitamin C and E offer protection against ROS molecules [6]. Moreover, as markers of oxidative stress, changes in malondialdehyde (MDA), H_2O_2, and protein levels are crucial for assessing stress tolerance in plants subjected to abiotic stress [6].

Barley (*Hordeum vulgare* L.), a member of *Poaceae*, is an economically important cereal crop. Between 2018 and 2019, global barley production ranked third after maize and wheat. According to the barley crop report published by the Agricultural Economics and Policy Development Institute in January 2021, in terms of the area under barley, Turkey is the second largest producer after wheat [7, 8]. It has been reported that barley has a high tolerance to dry and saline soils. This makes it one of the most adaptable cereals to different climatic conditions [9]. However, with the increasing impacts of global climate change, barley production in Turkey has become one of the crops most affected by environmental stresses such as drought and salinity. According to the Intergovernmental Panel on Climate Change (IPCC), it is predicted that the severity and frequency of abiotic stresses will increase in the near future due to global climate change [10]. Increasing population, industrialization, soil degradation, and climate change are challenging agricultural water availability [9]. In this context, evaluating and identifying drought-tolerant genotypes is crucial for the future of agriculture and food production.

This research focuses on determining for the first time the drought tolerance of three barley varieties grown in Turkey (cv. Kalaycı-97, cv. Harman and cv. Yaprak) under short-term drought stress. The determination of drought tolerance of these varieties was investigated based on physiological [relative water content (RWC), leaf water loss (LWL), total chlorophyll content (SPAD), dry weight (DW)] and biochemical [total protein content, CAT activity, APX activity, H_2O_2 level, histological localization of H_2O_2, MDA level] changes.

Materials and Methods

Plant Material and Growing Conditions

Barley (*H. vulgare*), a high-value cereal crop from the *Poaceae* family, was selected for this study. *H. vulgare* cv. Kalaycı-97 obtained from the Transitional Zone Agricultural Research Institute (Eskişehir/TÜRKİYE), while *H. vulgare* cv. Harman and *H. vulgare* cv. Yaprak were obtained from the Thrace Agricultural Research Institute (Edirne/TÜRKİYE).

The seeds were sterilized with 5% NaCl and placed in dishes with moist filter paper. Seedlings were grown in pots containing perlite and in a growth chamber (22-24°C, 65% relative humidity, 16/8h light/dark at 130-250 µmol m^{-2} s^{-1} light intensity) irrigated with Hoagland's solution (100%) [11]. The 21 days old seedlings (3 weeks old plants) were divided into two groups: Control and Drought. Each group contained 75 seedlings. In the drought group, 21 d old seedlings were subjected to drought stress through irrigation cessation. The control group continued with Hoagland (100%) irrigation. Physiological parameters such as RWC, LWL, DW, chlorophyll contents (SPAD), H_2O_2 levels, enzyme activities and histological localization of H_2O_2 were determined in leaf tissues of 31-day-old seedlings after 10 days of drought stress. Sampled leaf tissues were stored in a deep freezer (-20°C) until biochemical analyses [MDA, total protein content, CAT, APX]. The experimental design was a randomized complete block design with at least independent three replicates (each replicate is 1 pot x 20 seedlings).

Physiological Parameters

To determine LWL, the last fully developed leaf of each plant was sampled. The samples were kept in a cold chain (+4°C) to prevent water loss. After leaf fresh weight recording (0 min), leaves were left at room temperature (21°C) and leaf fresh weights were recorded at 10, 20 and 30 min. The LWL values were calculated as the percentage of weight loss from the fresh weight [12]. Five replicate samples were taken from each group.

Mature leaves of the seedlings were used to measure fresh weight. Leaves were then placed between filter papers in a plastic cuvette containing pure water for 4 hours and turgid weights recorded. Subsequently, the same leaves are dried at 70 °C for 24 h to determine their dry weight. The RWC was calculated according to the following formula (Equation 1) [13].

$$\mathrm{RWC} = \frac{\mathrm{FW} - \mathrm{DW}}{\mathrm{TW} - \mathrm{DW}} \mathrm{X100} \tag{1}$$

(FW: Fresh weight, TW: Turgida weight, DW: Dry weight)

Total chlorophyll was measured using a chlorophyll meter (Minolta, SPAD-502, Osaka, Japan). [14]. Accordingly, the measurements were carried out on the fully developed mature leaves of the seedlings, with 15 replicates being taken from three different seedlings in each group, obtained from five pots.

Leaf samples from each group were dried at 70°C for 72 h and then used to determine the leaf DW of each plant. Sampling was carried out with at least 3 replicates in each group [15].

Determination of Antioxidant Enzyme Activities

The total protein content in leaf tissues was homogenized in 3 mL of 0.05 M sodium phosphate buffer (pH 7.8) containing 1 mM EDTA (Ethylenediaminetetraacetic acid). The homogenates were then centrifuged for 30 min at +4°C and 18895×g. The supernatant was used for protein analysis. All procedures were performed at +4°C. Protein concentration was determined against a blank at 595 nm using a spectrophotometer within 5-60 min after mixing 100 µL of supernatant with 5 mL of reagent [16]. Total protein content was expressed in mg/mL using bovine serum albumin as a standard.

Catalase activity (EC 1.11.1.6) was determined as the decrease in absorbance at 240 nm due to the amount of H_2O_2 consumed. The CAT activity is expressed in terms of µmol ml^{-1} of H_2O_2 consumed per minute [17].

Ascorbate peroxidase activity (EC 1.11.1.11) was determined by homogenizing leaves in 1ml of 50mM Na-P buffer (pH 7.8) with 2mM ascorbate and 1mM EDTA. The supernatants were used for analysis of APX activity (extinction coefficient 2.8 mM^{-1} cm^{-1}). The amount of enzyme is the amount of 1 µmol ml^{-1} ascorbate oxidized per minute. [18].

For H_2O_2 determination, 0.1 g fresh sample was homogenized in a buffer containing H_2SO_4 and cold acetone (100%). The samples were subsequently centrifuged at 4000xg for 5 min. The supernatants were then mixed with e-FOX reading buffer and allowed to stand for 30 min. The results were read at 550-800 nm against a blank (water) in a polystyrene cuvette [19].

For the H_2O_2 histochemical localization leaves were incubated in a solution containing 1 mg ml^{-1} 3',3'-diaminobenzidine (DAB) at 25°C for 12 h. The incubated leaves were then immersed in 90% ethanol in a hot water bath for 15 min to remove color. Subsequently, stained leaves were photographed against a contrasting background for visualization [20].

The degree of lipid peroxidation (nmol g wet weight^{-1}) was determined by measuring the level of MDA, the product of lipid peroxidation (€=155 $mM^{-1}cm^{-1}$) [21].

Statistical Analysis

Data were subjected to multiple comparisons using one-way analysis of variance (ANOVA) followed by the Tukey test. Statistical analysis was performed using SPSS V21.0 (Statistical Package for the Social Sciences, Version 21.0) software. The significance levels are shown in the graphs, and comparisons with a significance level of $P \leq 0.05$ were considered significantly different. Table 2 presents the correlation analysis between the variables.

Results

Physiological Parameters

At the end of the experiment, the total LWL in the control group of Kalaycı-97 was 10%, while it was found to be 13% in the drought group. The best stomal conductance started after 20 min in the control group and 10 min in the drought group (Figure 1A). In the Harman variety, the total LWL within half an hour was 4% in the control group and 5% in the drought group. The best stomal conductance occurred after 10 min in the drought group (Figure 1B). At the end of the experiment, the total LWL in the Yaprak cultivar was 11% in both groups. In this variety, the best stomatal conductance started after 10 min in both groups (Figure 1C).

The relative water content decreased in all cultivars compared to the controls. However, only Kalaycı-97 showed a statistically significant decrease of 8% (Figure 1D).

Total chlorophyll content decreased by 14-28% in all varieties under short-term drought stress compared to the control (Figure 1E).

Dry weight decreased in all three cultivars due to drought stress. Indeed, Kalaycı-97 was found to have the greatest decrease in dry weight (17%) among the three varieties (Figure 1F).

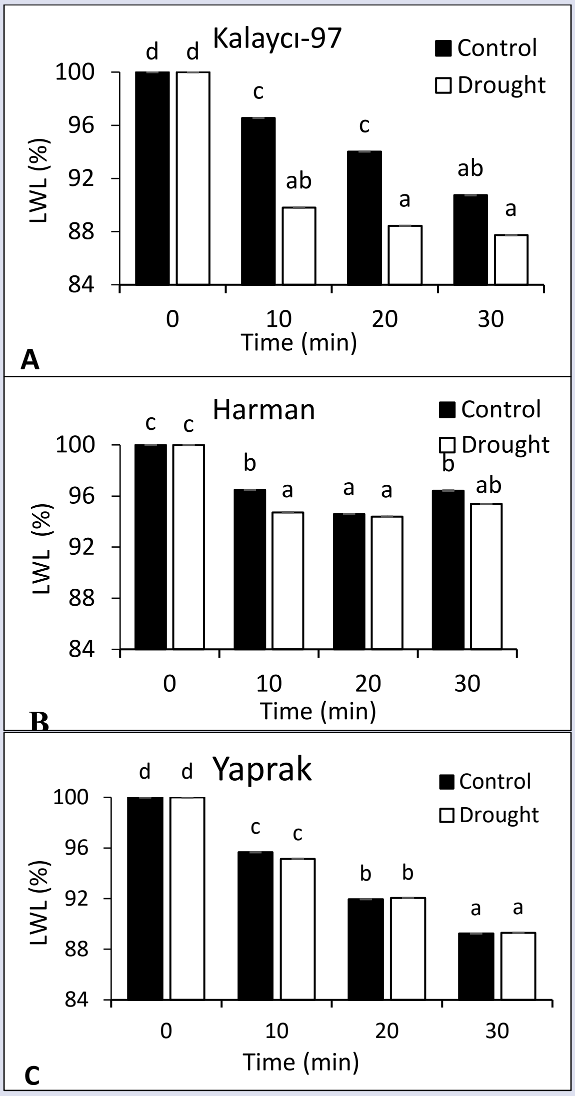

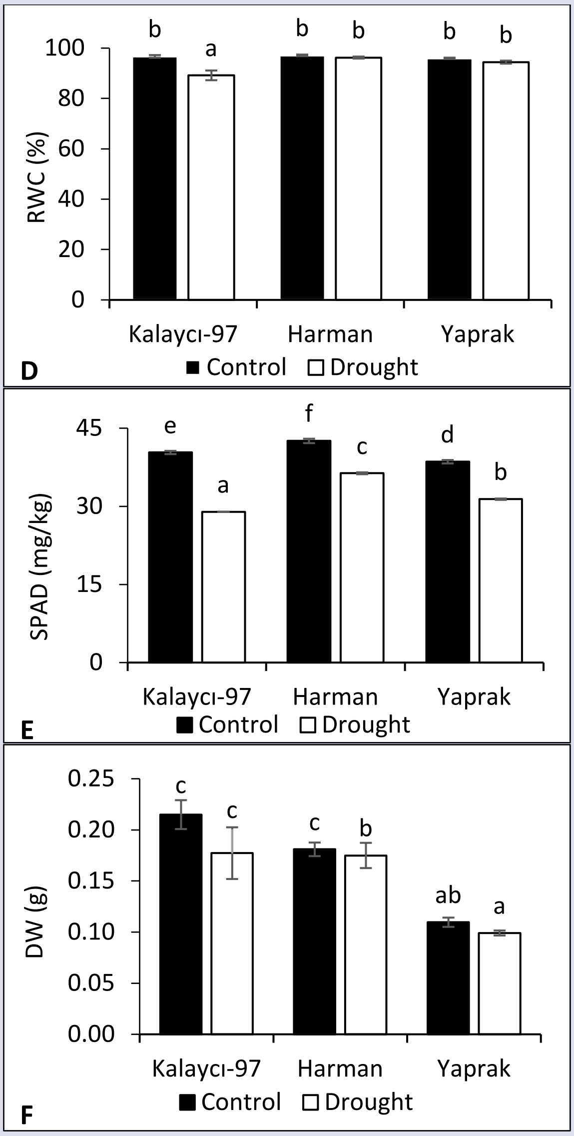

Figure 1. Changes in physiological parameters of 10-day drought stress in *H. vulgare* L. cultivars [Leaf water loss (LWL, A; Kalaycı-97, B; Harman, C; Yaprak), D; Relative water content (RWC), E; Total chlorophyll content (SPAD), F; Dry weight (DW)] (Mean values followed by different letters are significantly different at P≤0,05).

Antioxidant Enzyme Activities

Short-term drought stress decreased total protein content by 32% in Harman but increased by 19% in Kalaycı-97 and 27% in Yaprak (Figure 2A). However, catalase activity increased by 48% in Kalaycı-97 and 69% in Yaprak compared to the control but decreased by 3% in Harman (Figure 2B). On the other hand, APX activity decreased by 48% in Kalaycı-97 under drought stress compared to the control, while it increased by 42% in Harman and 20% in Yaprak (Figure 2C).

H_2O_2 levels increased by 76% in Kalaycı-97 under drought stress but decreased by 7% in Yaprak (Figure 2D,E).

Malondialdehyde levels increased by 62% in Kalaycı-97 and by 7% in Harman, while they decreased by 26% in Yaprak compared to the control (Figure 2F).

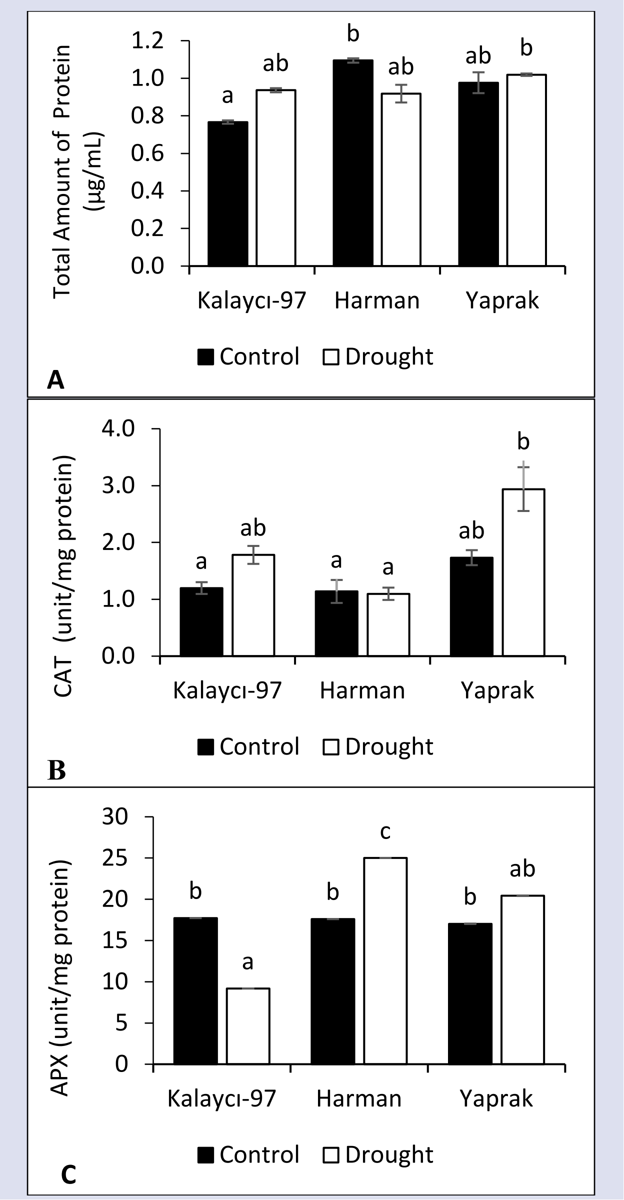

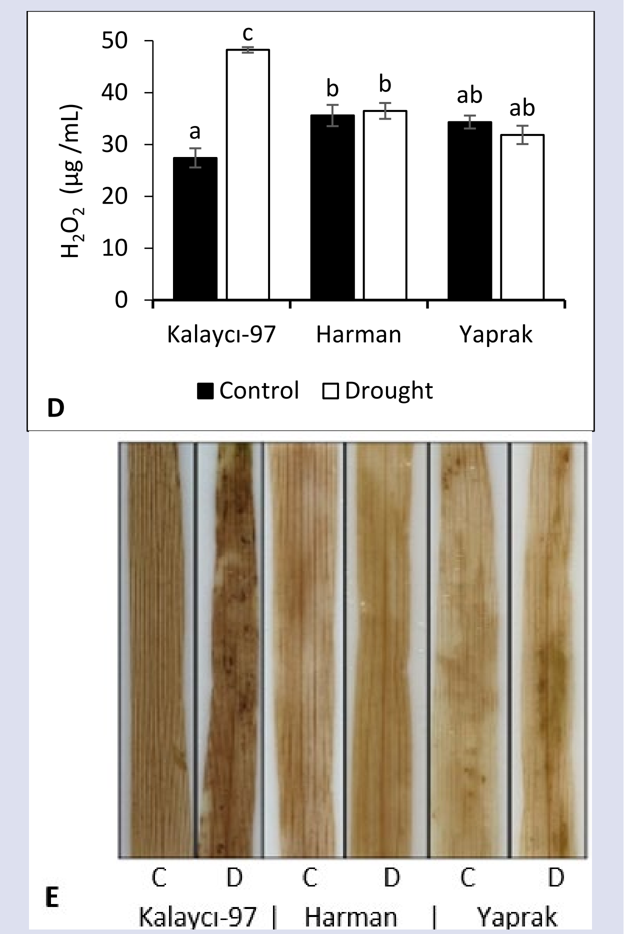

Figure 2. Changes in antioxidant enzyme activities caused by 10 days of drought stress in *H. vulgare* L. cultivars [A; Total protein amount, B; Catalase (CAT), C; Ascorbate peroxidase (APX), D; H_2O_2 amount, E; H_2O_2 Histochemical staining (C; Control, D; Drought), F; Malondialdehyde amount] (Mean values followed by different letters are significantly different at P≤0.05).

Table 1. Correlations between physiological and biochemical parameters in all varieties.

		1	2	3	4	5	6	7	8	9
1	LWL	1								
2	RWC	,545**	1							
3	SPAD	,349*	,678**	1						
4	DW	0,163	0,326	0,284	1					
5	PR	-0,001	0,07	-0,046	-0,357	1				
6	CAT	-0,251	-0,343	-,450**	-,523*	0,155	1			
7	APX	-0,122	,440*	0,164	-0,148	-0,163	-,414*	1		
8	H_2O_2	-,345*	-,683**	-,466**	-0,328	0,138	-0,034	-0,196	1	
9	MDA	-0,175	-,499**	-0,308	0,366	-0,085	-0,144	-,424*	,535**	1

Note: LWL=Leaf water loss, RWC=Relative water content, SPAD=Total chlorophyll content, DW=Dry weight, PR= Total protein amount, CAT= Catalase activity, APX=Ascorbate peroxidase, H_2O_2 amount, MDA= Malondialdehyde amount.

**: Significant correlations P<0.01, and *: P<0.05

Discussion

Drought is a limiting factor for growth and yield in barley, as in most cereal crops. There is a need to understand the effects of global climate change induced drought stress on existing varieties. This data is important for potential farmers to use these varieties. This study focuses on determining the drought tolerance of three barley cultivars (cv. Kalaycı-97, cv. Harman and cv. Yaprak) grown in Turkey based on physiological and biochemical parameters.

Relative water content reflects the water status in plant tissues [22], and drought stress negatively affects plant water content [23]. According to our results, short-term water deficit reduced RWC only in Kalaycı-97 among the three barley varieties. The LWL results indicated that Kalaycı-97 had the highest water loss of 3% compared to the control among the three varieties at the end of 30 min. On the other hand, there was no water loss in Yaprak variety, while it decreased by 1% in Harman. Accordingly, it was understood that drought stress decreased the water content most in Kalaycı-97. Similar studies have reported differences in RWC among genotypes with contrasting drought tolerance [24], and drought stress has been shown to reduce RWC in barley [22]. Furthermore, a significant relationship between RWC and drought tolerance was found in barley genotypes exposed to prolonged water shortage [25]. In addition, a positive phenotypic correlation between grain yield under water deficit conditions and RWC has been reported in barley [26]. Based on the RWC results, Kalaycı-97 seems to be less drought tolerant than other varieties.

Drought stress is known to reduce chlorophyll content in plants [3, 27, 28]. In this study, short-term drought stress resulted in reduced total chlorophyll content in all three cultivars. Similarly, severe drought stress [22, 29] and water scarcity [26] have been reported to reduce chlorophyll content in barley. Furthermore, changes in total chlorophyll contents in barley genotypes have been significantly associated with drought tolerance [30]. The decrease in the chlorophyll content of Kalaycı-97 under short-term drought stress suggests that it is much more sensitive to drought than other varieties.

Total protein content increased under drought stress in Kalaycı-97 and Yaprak, but surprisingly decreased in Harman. Drought stress has been reported to decrease protein content in barley [29]. Therefore, the increase in protein content in the cultivar Yaprak may indicate its drought tolerance.

Drought stress increases the concentration of ROS in plant cells. ROS include molecules with unpaired electrons, such as O_2^{*-}, OH^-, and H_2O_2 [31]. Increased levels of ROS can cause damage to lipids, proteins, and DNA. Therefore, the antioxidant defense system, consisting of enzymatic and non-enzymatic antioxidants, plays an important role in detoxifying ROS [32].

Drought stress decreased APX activity in Kalaycı-97 but increased it in Harman and Yaprak. In addition, CAT activities increased in Kalaycı-97 and Yaprak, but remained unchanged in Harman. High concentrations of ROS can attack lipids in cells and lead to lipid peroxidation if not detoxified. As an indicator of this, MDA levels decreased in Yaprak under short-term drought stress compared to the control but increased by 62% in Kalaycı-97 and 7% in Harman. Short-term drought stress increased H_2O_2 levels in Kalaycı-97 but decreased them in Yaprak. The localization of H_2O_2 in barley leaf tissue is visualized by histochemical staining with 3',3'-diaminobenzidine (DAB) [20]. Our histochemical staining results support the findings on H_2O_2 levels. According to our results, the high H_2O_2 levels and low APX activity in Kalaycı-97 may indicate a weaker drought tolerance compared to the other varieties.

The significant increase in H_2O_2 and MDA levels under drought stress has been associated with drought susceptibility in barley [22]. On the other hand, severe drought stress [33] or decreasing soil moisture [34] has been reported to increase CAT activity in barley. In addition, drought stress induced by 10% PEG (-0.8 MPa) was shown to increase POX, SOD and APX isoenzyme activities in barley and was confirmed to be associated with growth parameters [35]. Furthermore, different barley genotypes have been shown to exhibit different molecular and biochemical responses under the same drought conditions [36]. Interestingly, in barley leaves under water stress, there was a sharp increase in APX, CAT, POX and SOD activities during flowering and stem elongation. However, the continued increase in MDA levels suggests that the increase in these enzymes may not be sufficient [29].

According to our research results, short-term drought stress decreased RWC and pigment content, increased H_2O_2 levels and increased lipid peroxidation in Kalaycı-97. Despite the increase in CAT activity, the decrease in APX activity in this genotype suggests that increased CAT activity alone may not be sufficient to reduce lipid peroxidation. Similar results have been reported in water-stressed barley [29]. Furthermore, the results for Kalaycı-97 suggest that this cultivar has a lower drought tolerance compared to other cultivars. On the other hand, in Yaprak genotype under short-term drought stress, RWC was preserved, less chlorosis was detected, the amount of H2O2 was lower, and lipid peroxidation was found in accordance with increased APX, and CAT activities compared to other genotypes. Moreover, high RWC, pigment and antioxidant activities have been shown to be associated with high drought tolerance [22, 35, 36]. This suggests that the Yaprak genotype is more tolerant to short-term drought stress compared to other genotypes. According to our results, the Harman genotype was found to have moderate tolerance to short-term drought stress compared to the Kalaycı-97 and Yaprak genotypes. The fact that increased APX and CAT activities in this genotype could not prevent the increase in lipid peroxidation is consistent with previously reported results in barley [29].

It has been reported that a 15% differential water deficit in barley leaves is associated with signaling and ABA metabolism, leading to appropriate defense activation [37]. Furthermore, it has been reported that high temperature stress, which is prominent in global climate change, in combination with drought, causes more severe damage to barley [4]. Our results indicate that the three barley genotypes used in this study, grown in Turkey and exposed to short-term drought stress, have different drought tolerances. Accordingly, it can be said that Yaprak is tolerant, Kalaycı-97 is sensitive, and Harman is moderately tolerant to short-term drought stress.

Conclusions

In this study, tolerance to short-term drought stress has been demonstrated physiologically and biochemically in three barley cultivars grown in Turkey. However, further research is needed to understand the effects of long-term drought tolerance and the tolerance mechanisms in these genotypes. In addition, studying the interactions of drought effects with major stressors such as temperature can provide valuable insights into potential scenarios related to global climate change.

Acknowledgments

This research is part of Gamze Baltacıer's doctoral research. Gamze Baltacıer's doctoral studies are supported by the Council of Higher Education 100/2000 (CoHE 100/2000) Doctoral Scholarship Programme. The authors are therefore grateful to CoHE for this scholarship programme.

Conflict of interest

There are no conflicts of interest between the authors of the articles.

References

[1] Hussain H.A., Men S., Hussain S., Chen Y., Ali S., Zhang S., Wang L., Interactive effects of drought and heat stresses on morpho-physiological attributes, yield, nutrient uptake and oxidative status in maize hybrids. *Scientific Reports*., 9(1) (2019) 1-12.

[2] Bhuyan M.B., Hasanuzzaman M., Parvin K., Mohsin S.M., Al Mahmud J., Nahar K., Fujita M., Nitric oxide and hydrogen sulfide: two intimate collaborators regulating plant defense against abiotic stress. *Plant Growth Regulation*. 90(3) (2020) 409-424.

[3] Toraman P.Ş., Ergün N., Çalıcı B., Some abiotic stress on growth and lipid peroxidation on wheat seedlings. *Natural and Engineering Sciences*. *5*(3) (2020) 144-154.

[4] Zhanassova K., Kurmanbayeva A., Gadilgereyeva B., Yermukhambetova R., Iksat N., Amanbayeva U., Bekturova A., Tleukulova Z., Omarov R., Masalimov Z., ROS status and antioxidant enzyme activities in response to combined temperature and drought stresses in barley. *Acta Physiologiae Plan*tarum. 43(8) (2021) 1-12.

[5] Choudhury F.K., Rivero R.M., Blumwald E., Mittler R., Reactive oxygen species, abiotic stress and stress combination. *The Plant Journal*. 90(5) (2017) 856-867.

[6] Ding H., Ma D., Huang X., Hou J., Wang C., Xie Y., Wang Y., Qin H., Guo T., Exogenous hydrogen sulfide alleviates salt stress by improving antioxidant defenses and the salt overly sensitive pathway in wheat seedlings. *Acta Physiologiae Plantarum*. 41(7) (2019) 1-11.

[7] Turkish Grain Board, Cereals Industry Report for 2019 (TGB 2019). Available at: https://lk.tc/ka9by. Retrieved March 31, 2021.

[8] Agricultural Economic and Policy Development Institute, Ocak 2021 Agricultural Products Market, Barley Report Date of Access (AEPDI, 2021). Available at: https://lk.tc/nyR8w. Retrieved March 31, 2021.

[9] Torun H., Ayaz F.A., Tuz stresi koşullarında salisilik asidin zamana bağlı uygulanmasının arpa (*Hordeum vulgare* L.) köklerinin antioksidan savunma sistemi üzerine etkileri. *Anadolu Üniversitesi Bilim ve Teknoloji Dergisi-C Yaşam Bilimleri ve Biyoteknoloji.* 8(1) (2019) 69-84.

[10] Sekmen A.H., Özgür R., Uzilday B., Türkan I., Reactive oxygen species scavenging capacities of cotton (*Gossypium hirsutum*) cultivars under combined drought and heat induced oxidative stress. *Environmental and Experimental Botany*. 99 (2014) 141-149.

[11] Hoagland D.R., Arnon D.I., The Water-Culture Method for Growing Plants Without Soil. In Circular. *California Agricultural Experiment Station*. 347 (1950) 32.

[12] Li C., Liu C., Ma X., Wang A., Duan R., Nawrath C., Chen G., Characterization and genetic mapping of eceriferum-ym (cer-ym), a cutin deficient barley mutant with impaired leaf water retention capacity. *Breeding Science*. 65(4) (2015) 327-332.

[13] Smart R.E., Bingham G.E., Rapid estimates of relative water content. *Plant Physiology*. 53(2) (1974) 258-260.

[14] Peryea F.J., Kammereck R., Use of Minolta Spad-502 chlorophyll meter to quantify the effectiveness of mid-summer trunk injection of iron on chlorotic pear trees. *Journal of plant Nutrition*. 20(11) (1997) 1457-1463.

[15] Sekmen Çetinel A.H., Gökçe A., Erdik E., Çetinel B., Çetinkaya N., The Effect of *Trichoderma citrinoviride* Treatment under Salinity Combined to *Rhizoctonia solani* Infection in Strawberry (*Fragaria x ananassa* Duch.). *Agronomy*. 11(8) (2021) 1589.

[16] Bradford M. M., A rapid and sensitive method for the quantitation of microgram quantities of protein utilizing the principle of protein-dye binding. *Analytical Biochemistry*. 72(1-2) (1976) 248-254.

[17] Bergmeyer N., Methoden der enzymatischen analyse. *Akademia Verlag*, Berlin. 1 (1970) 636-647.

[18] Nakano Y., Asada K., Hydrogen Peroxide is Scavenged by Ascorbate-Specific Peroxidase in Spinach Chloroplasts Plant. *Cell Physiology*. 22(3) (1981) 867-880.

[19] Cheeseman J.M., Hydrogen peroxide concentrations in leaves under natural conditions. *Journal of Experimental Botany*. 57 (2006) 2435–44 pp.

[20] Kumar D., Yusuf M.A., Singh P., Sardar M., Sarin N.B., Histochemical detection of superoxide and H_2O_2 accumulation in *Brassica juncea* seedlings. *Bio-protocol*. 4(8) (2014) 1108.

[21] Madhava R.K.V., Sresty T.V.S., Antioxidative Parameters in the Seedlings of Pigeonpea (*Cajanus cajan* L. Millspaugh) in Response to Zn and Ni Stresses. *Plant Science*. 157 (2000) 113-128.

[22] Ferioun M., Srhiouar N., Bouhraoua S., El Ghachtouli N., Louahlia S., Physiological and biochemical changes in Moroccan barley (*Hordeum vulgar*e L.) cultivars submitted to drought stress. *Heliyon*. 9(2) (2023)

[23] Farooq T.H., Bukhari M.A., Irfan M.S., Rafay M., Shakoor A., Rashid M.H.U., Lin Y., Saqib M., Malik Z., Khurshid, N., Effect of Exogenous Application of Nicotinic Acid on Morpho-Physiological Characteristics of *Hordeum vulgare* L. under Water Stress. *Plants*. 11(18) (2022) 2443.

[24] Cai K., Chen X., Han Z., Wu X., Zhang S., Li Q., Nazir M.M., Zhang G., Zeng F., Screening of worldwide barley collection for drought tolerance: The assessment of various physiological measures as the selection criteria. *Frontiers in Plant Science*. 11 (2020) 1159.

[25] Hasanuzzaman M., Shabala L., Brodribb T.J., Zhou M., Shabala S., Understanding physiological and morphological

traits contributing to drought tolerance in barley. *Journal of Agronomy and Crop Science.* 205(2) (2019) 129-140.

[26] Fatemi R., Yarnia M., Mohammadi S., Vand E.K., Mirashkari B., Screening barley genotypes in terms of some quantitative and qualitative characteristics under normal and water deficit stress conditions. *AJAB Asian J Agric & Biol* (2) (2023).

[27] Acar O., Türkan I., Özdemir F., Superoxide dismutase and peroxidase activities in drought sensitive and resistant barley (*Hordeum vulgare* L.) varieties. *Acta Physiologiae Plantarum*. 23 (2001) 351-356.

[28] Seçkin B., Türkan I., Sekmen A.H., Özfidan C., The role of antioxidant defense systems at differential salt tolerance of *Hordeum marinum* Huds. (sea barleygrass) and *Hordeum vulgare* L. (cultivated barley). *Environmental and Experimental Botany*. 69(1) (2010) 76-85.

[29] Haddad H., Jafari B., Analysis of antioxidant enzyme activity during reproductive stages of barley under drought stress. *Journal of Ecobiotechnology*. 3(10) (2011) 40-47.

[30] Hasanuzzaman M., Shabala L., Brodribb T.J., Zhou M., Shabala S., Understanding the role of physiological and agronomical traits during drought recovery as a determinant of differential drought stress tolerance in Barley. *Agronomy*. 12(9) (2022) 2136.

[31] Patel M., Parida A.K., Role of hydrogen sulfide in alleviating oxidative stress in plants through induction of antioxidative defense mechanism, and modulations of physiological and biochemical components. *In Hydrogen Sulfide in Plant Biology: Academic Press*. (2021) 55-85.

[32] Dar O.I., Singh K., Sharma S., Aslam J., Kaur A., Bhardwaj R., Sharma A., Regulation of drought stress by hydrogen sulfide in plants. *In Hydrogen Sulfide in Plant Biology: Academic Press*. (2021). 229-242.

[33] Islam M.Z., Park B.J., Jeong S.Y., Kang, S.W., Shin B.K., Lee Y.T., Assessment of biochemical compounds and antioxidant enzyme activity in barley and wheatgrass under water-deficit condition. *Journal of the Science of Food and Agriculture*. 102(5) (2021) 1995-2002.

[34] Rohman M.M., Alam S.S., Akhi A.H., Begum F., Amiruzzaman M., Response of catalase to drought in barley (*Hordeum vulgare* L.) seedlings and its purification. *African Journal of Biotechnology.* 19(7) (2020) 478-486.

[35] Hellal F.A., El-Shabrawi H.M., Abd El-Hady M., Khatab I.A., El-Sayed S.A.A., Abdelly C., Influence of PEG induced drought stress on molecular and biochemical constituents and seedling growth of Egyptian barley cultivars. *Journal of Genetic Engineering and Biotechnology*. 16(1) (2018) 203-212.

[36] Harb A., Awad D., Samarah N., Gene expression and activity of antioxidant enzymes in barley (*Hordeum vulgare* L.) under controlled severe drought. *Journal of Plant Interactions*. 10(1) 2015) 109-116.

[37] Nykiel M., Gietler M., Fidler J., Graska J., Rybarczyk-Płońska A., Prabucka B., Muszyńska E., Bocianowski J., Labudda, M., Differential Water Deficit in Leaves Is a Principal Factor Modifying Barley Response to Drought Stress. *International Journal of Molecular Sciences.* 23(23) (2022) 15240.

Cumhuriyet Sci. J., 45(3) (2024) 478-485
DOI: https://doi.org/10.17776/csj.1424202

Cumhuriyet Science Journal

| csj.cumhuriyet.edu.tr | Founded: 2002 ISSN: 2587-2680 e-ISSN: 2587-246X Publisher: Sivas Cumhuriyet University

Investigation of Biological Activity of *Squamarina cartilaginea* (With.) P. James Species Distributed in Türkiye

Banu Ceren Değirmenci[1,a], Mustafa Kocakaya[2,b], Selen İlgün[3,c], Gökçe Şeker Karatoprak[4,d], Zekiye Kocakaya[5,e,*], Ahmet Ceylan [6,f]

[1] *Yozgat Bozok University, Institute of Science, 66900, Yozgat, Türkiye*
[2] *Yozgat Bozok University, Boğazlıyan Vocational School, Department of Organic Agriculture, 66900, Yozgat, Türkiye.*
[3] *Erciyes University, Faculty of Pharmacy, Department of Pharmaceutical Botany, 38039, Kayseri, Türkiye*
[4] *Erciyes University, Faculty of Pharmacy, Department of Pharmacognosy, 38039, Kayseri, Türkiye*
[5] *Kayseri University, Safiye Cikrikcioglu Vocational College, Department of Crop and Animal Production, 38280, Kayseri, Türkiye*
[6] *Erciyes University, Faculty of Pharmacy, Department of Pharmaceutical Biotechnology, 38039, Kayseri, Türkiye*
**Corresponding author*

Research Article

History
Received: 23/01/2024
Accepted: 19/08/2024

ABSTRACT

In this study, the methanol extract of *Squamarina cartilaginea*, a species distributed in Türkiye, was investigated for its antimicrobial, antioxidant, cytotoxic, and DNA protective effects. The chemical composition of the extract was elucidated through spectroscopic determination of total phenols, total flavonoids, and chromatographic quantification of usnic acid. Antimicrobial activity was assessed using the disk diffusion method, revealing a significant zone of inhibition with a diameter of 17.5 mm against *M. luteus* and *S. aureus*. The antioxidant activity was evaluated through scavenging activities against DPPH and ABTS radicals, demonstrating a concentration-dependent potent scavenging activity against ABTS radicals. Cytotoxic activity was determined using the MTT method on DU-145 (Human Prostate Cancer Cell Line) and Colo 205 (Human Colon Cancer Cell Line) cell lines. The extract exhibited strong cytotoxic activity against the Colo 205 cell line, with a viability percentage of 33.16±2.01 at a concentration of 3.906 µg/mL. Furthermore, the *S. cartilaginea* extract demonstrated DNA protective activity on pBR322 plasmid DNA against UV and H_2O_2 exposure.

Keywords: Cytotoxicity, Lichen, pBR322, *Squamarina,* Usni acid.

[a] *bckkocaman@gmail.com* *https://orcid.org/0009-0000-6777-5415*
[c] *erturkselen@gmail.com* *https://orcid.org/0000-0002-8544-0683*
[e] *zekiyekocakaya@kayseri.edu.tr* *https://orcid.org/0000-0001-5248-0462*
[b] *mustafa.kocakaya@yobu.edu.tr* *https://orcid.org/0000-0003-2306-8094*
[d] *gskaratoprak@gmail.com* *https://orcid.org/0000-0001-5829-6914*
[f] *ahmtcyln7@gmail.com* *https://orcid.org/0000-0002-3087-066x*

Introduction

Lichens are symbiotic associations that generally consist of two partners: a mycobiont (fungus) and a photobiont (algae or cyanobacteria). The organism takes on a thallus-shaped structure and can engage in photosynthesis due to the fungal tissue possessed by algal cells [1]. Lichens, along with phytochemicals, constitute a crucial framework for drug development in modern medicine, especially in developing countries. Presently, numerous scientific studies are underway to identify active compounds derived from plants and other organisms. Lichens, being symbiotic organisms, also produce a variety of secondary metabolites. The chemical diversity of lichen secondary metabolites positions them as potent natural resources for potential applications in medical fields [2]. Additionally, lichens are of interest due to their potent secretions that exhibit therapeutic effects against certain diseases [3].

Lichens have been employed in traditional medicine across diverse civilizations for centuries, owing to their intrinsic biological properties [4]. Utilized both as a source of sustenance and dyes during periods of scarcity, lichens have played a multifaceted role in historical contexts [5]. Throughout history, lichens have found applications across various domains, particularly in medicine, pharmacy, and the chemical industry. In the realm of medicine, their therapeutic properties have been to address ailments such as ringworm, arthritis, constipation, infections, kidney diseases, leprosy, pharyngitis, and rabies [6]. In the context of Turkish folk medicine, albeit less common than the recognized healing properties of plants, lichens are reported to be utilized in treatments [7].

In addition to the traditional applications of lichens in folk medicine, the discovery that certain lichen compounds contribute to UV-B protection, the bioplastic degradation capacity in frozen foods, and the presence of antifreeze proteins with potential implications for preventing desertification are noteworthy findings that further enhance the distinctive biological profile of lichens [8]. Numerous secondary metabolites produced by lichens exhibit potential antioxidant properties owing to their aromatic structures [9,10]. It is well-established that algae, bacteria, fungi, plants, and lichen species synthesize compounds with antimicrobial effects as a defense mechanism in nature [11].

The genus *Squamarina*, inclusive of the species *Squamarina cartilaginea*, manifests itself in calcareous soil and rocks through the formation of spreading lobes or overlapping scales, lacking a well-developed upper and lower cortex [12]. Widely distributed, this genus encompasses 28 species [13]. Although chemical studies on the *Squamarina* genus are limited, one identified compound is the naphthoquinone squamaron [14]. Several investigations into the *Squamarina* genus reveal the inhibitory effects of usnic acid extract from *Squamarina lentigera* against bacteria such as *Bacillus megaterium* and *Bacillus subtilis* [15]. Notably, psoromic acid derived from *Squamarina cartilaginea* exhibits robust antibacterial activity against oral pathogens, including *Streptococcus gordonii* and *Porphyromonas gingivalis* [16].

To further explore the therapeutic attributes of lichens, considering the information presented above, this study conducted a comprehensive examination of the antioxidant, antimicrobial, cytotoxic activities, and DNA protective effects associated with the extract derived from *Squamarina cartilaginea*. The chemical composition of the extract, as well as the presence and quantification of usnic acid, were determined through High-Performance Liquid Chromatography (HPLC). This research contributes a thorough investigation into the biological activity potential of *Squamarina cartilaginea*, providing initial data for this species, many of which lack precedent in the existing literature regarding biological activities.

Material and Method

Lichen Species Used in the Study

The species used in this study was collected in Üzümdere Village of Antalya Ibradı, along the road in a mixed woodland of *Quercus* sp. and *Pinus brutia*, located in an area characterized by predominantly limestone bedrock, with coordinates 37° 05' 07.6" N, 31° 39'43.0" E and an altitude of 550 m. This lichen was collected from limestone bedrock in the area because it is commonly found on calcium carbonate-containing substrates, especially limestone and other basic rocks [12]. Floral references such as 'Flechten Flora' [17] and 'The Lichen Flora of Great Britain and Ireland' [18] were consulted in the taxonomic identification of the collected lichen sample. External morphological characters were examined using a stereomicroscope (Olympus SZX16), while anatomical features were investigated with a light microscope (Olympus BX53 Light microscope). Additionally, macroscopic and microscopic digital photographs were meticulously taken using the Olympus DP25 digital camera connected to the Stereomicroscope Olympus SZX16 and Olympus BX53.

Critical parameters such as spore sizes, ascus sizes, hymenium heights, and paraphysis widths played a decisive role in the meticulous categorization of species and subspecies. These morphological features were precisely measured utilizing a micrometer, and chemical reagents were judiciously applied for diagnostic purposes. The specimens were systematically recorded and systematically stored in envelopes, thus constituting herbarium materials housed at Yozgat Bozok University, Boğazlıyan Vocational School, Lichen Herbarium [Leg. and Det.: Mustafa Kocakaya, herbarium number: MK0365].

Preparation of Extracts

Fifteen grams of lichen sample were subjected to extraction using 80% methanol in a water bath at 37 ºC for 8 hours, with intermittent shaking during three cycles. Methanol solution is a widely used and effective solvent for the extraction of natural antioxidants, especially phenolic compounds, from plant materials. Therefore, the extraction was performed with methanol [19]. The filtrates obtained after each methanol treatment were consolidated and concentrated under vacuum using a rotavapor (maintained at 37-38 ºC). Subsequently, all obtained extracts underwent lyophilization and were dried, then preserved at -20 ºC until analysis [20].

Chemical Composition

Determination of total phenol amount

The total phenolic content of the extract was determined as gallic acid equivalent using the Folin-Ciocalteu method [21]. For this, a sample solution (100 µL) was mixed with Folin-Ciocalteu reagent (500 µL) in the presence of 6 mL of distilled water within a 10 mL container. After one minute, 1.5 mL of 20% aqueous Na_2CO_3 was added, and the volume was adjusted to 10 mL. The control group used a reagent mixture without the extract. Following a 2-hour incubation at 25 ºC, absorbance values at a wavelength of 760 nm were measured, and these values were compared with the gallic acid calibration curve. Each experiment was replicated three times, and the results are presented as mean values.

Determination of total flavonoid amount

The total flavonoid content in the extract was determined following the method proposed by [22]. In this procedure, 1 mL of extract was mixed with 0.3 mL of 5% $NaNO_2$ solution at the initial moment (t=0). After five minutes (t=5) 0.3 mL of 10% $AlCl_3.6H_2O$ solution was added, and after six minutes (t=6) 2 mL of 1 M NaOH solution was added. The mixture was then prepared by adding 2.4 mL of water. Absorbance measurements at 510 nm wavelength were conducted, and the total flavonoid content in the extract was quantified as mg $_{CA}$ /g $_{ekstre}$, equivalent to catechin (CA). The catechin calibration curve was established using ethanol. All measurements were conducted in triplicate, and the results were reported as average values.

Quantification of usnic acid by high pressure liquid chromatography (HPLC)

The lichen extract was dissolved in 80% methanol and analyzed using Shimadzu LC-20AT HPLC system. PDA spectrophotometric detector was employed in the analyses, and the solvent of choice was methanol-water-phosphoric acid (75:25:0.9, v/v/v). The flow rate was set at 1 mL/min, and the usnic acid standard was dissolved in 0.5% DMSO (Dimethylsulfoxide).

Determination of Antimicrobial Activity

In this study, the antimicrobial activity of the *Squamarina cartilaginea* extract was investigated against Gram-negative bacteria, including *Proteus mirabilis* (ATCC 25933), *Escherichia coli* (ATCC 25922), *Enterobacter aerogenes* (ATCC 13048), and Gram-positive bacteria, such as *Bacillus subtilis* (ATCC 6633), *Micrococcus luteus* (ATCC 10240), and *Staphylococcus aureus* (ATCC 25923), using the disk diffusion method. The *S. cartilaginea* extract, prepared at a concentration of 20 mg/mL in DMSO, was filtered through sterile filters with a diameter of 0.45 µm. The resulting extract was impregnated onto sterile discs (Oxoid, blank disc) in a volume of 20 µL.

Bacterial strains were cultured by incubating at 37 °C for 24 hours in Mueller-Hinton Broth (MHB) medium, and their concentrations were adjusted to $1.5x10^8$ cfu/mL using a UV-VIS Spectrophotometer according to the 0.5 McFarland standard. Bacterial cultures were spread on Mueller-Hinton Agar (MHA) medium in volumes of 100 µL. Discs containing the lichen extract and control groups were placed onto the medium with bacteria and then incubated at 37 °C for 24 hours. Ampicillin (amp) standard antibiotic discs (10 µg/disc) were used as a positive control, and discs impregnated with sterile DMSO served as the negative control. The diameters of the inhibition zones resulting from incubation were measured using a millimetric ruler. The experiment was conducted in triplicate, and the arithmetic averages were calculated to assess the obtained results.

Determination of DNA protective activity

To assess the efficacy of the *S. cartilaginea* extract in safeguarding DNA from UV and oxidative-induced damage, pBR322 plasmid DNA (Thermo Fisher Scientific) was employed. Plasmid DNA was subjected to damage induced by H_2O_2 and UV exposure in the presence of the lichen extract. Sample preparations consisted of 5 µL of lichen extract at a concentration of 20 mg/mL, diluted by 5%, plasmid 3 µL, dH_2O 6 µL, and H_2O_2 1 µL. The samples were organized as follows:

I. In Tube: pBR322
II. In Tube: pBR322 + UV
III. In Tube: pBR322 + H_2O_2
IV. In Tube: pBR322 + UV + H_2O_2
V. In Tube: pBR322 + *S. cartilaginea* extract + UV + H_2O_2.

After exposing the tubes containing the lichen extract to UV light for 5 minutes, incubation was carried out for 3 hours. Subsequently, 3 µL of loading dye was added, and the mixture was run on a 1% agarose gel at 80 V for 3 hours. The gel was then photographed using a gel imaging system (Bio-Rad ChemiDoc™ XRS+), as described by [23].

Evaluation of cytotoxic effects of extracts by MTT (3-(4,5-dimethylthiazol–2-yl)-diphenyl tetrazolium bromide) method

In this study, DU-145 (Human Prostate Cancer Cell Line) and Colo 205 (Human Colon Cancer Cell Line) cell lines were employed to assess the cytotoxic effects of the extract on cancerous cell lines. Throughout the experiment, the cells were maintained in cell culture dishes with ventilated lids in a CO_2 incubator at +37 °C. Regular observations were conducted, the medium was refreshed every two days, and the culture was sustained.

The cytotoxic effects on DU-145 and Colo 285 cell lines were determined using the MTT colorimetric method with an 80% methanol extract. Twenty-four hours prior to the experiment, the cells in the flask were counted, and 10000 cells in 100 µL were seeded into each well. After 24 hours of incubation, the supernatant above the adhered cells was removed, and the extract, prepared by diluting in the medium, was added to the plate in volumes ranging from 3.906 to 1000 µg/mL. Subsequently, the plate was placed in a carbon dioxide incubator at 37 °C for 48 hours. An MTT working solution was prepared at a concentration of 0.5 mg/mL from the stock MTT solution, dissolved in sterile PBS, and added to the 96-well microplates. After the incubation period, the medium in the plate was aspirated, and 100 µL DMSO was added. Following shaking for 5 minutes, the optical densities of the cells in the plates were measured at a wavelength of 540 nm using an ELISA device (Bio-Rad, USA). The average absorbance values from the control wells were taken, considering this value as 100% live cells. The absorbance values obtained from the wells treated with the solvent and extract were calculated as percent viability by proportioning to the control absorbance value.

The percentage of cell viability was calculated using the formula: (Concentration O.D. / Control O.D.) × 100.

Determination of Antioxidant Activity

1,1-diphenyl-2-picrylhydrazyl ($DPPH^•$) radical scavenging capacity evaluation

A 50 nM pH 7.4 Tris-HCl buffer was mixed with 1 mL of 1,1-diphenyl-2-picrylhydrazyl solution prepared in 0.1 mM methanol. A reagent mixture without the extract was used as a control, and butyl hydroxytoluene (BHT) was included as a positive control. Following a 30-minute incubation at room temperature and in darkness, absorbances were measured at a wavelength of 517 nm.

The percentage of inhibition was calculated using the following formula. Analyses were conducted in four independent replicates, and the results were averaged [24].

% inhibition = [(Abs Control - Abs sample) / Abs control] x 100

2,2'-Azino-bis(3-ethylbenzothiazoline-6-sulfonic acid) ($ABTS^{•+}$) radical scavenging capacity evaluation

The $ABTS^{•+}$ radical, with a concentration of 7 mM, was generated by incubating it in dark conditions for 12-16 hours in its aqueous solution and $K_2S_2O_8$ (2.45 mM, final concentration). The absorbance of the resulting solution was adjusted to 0.700 (± 0.030) at 734 nm at room temperature. Subsequently, this radical solution (990 µL) and extract solutions (10 µL) were meticulously mixed, and the reaction kinetics were measured at 734 nm wavelength for 30 minutes with 1-minute intervals. Concentration-dependent inhibition percentages were calculated as Trolox equivalent (TEAC) using the acquired data. The experiments were conducted three times in parallel, and the results were averaged [21].

Results and Discussion

Squamarina cartilaginea, a widely distributed species belonging to the genus *Squamarina*, has been the subject of limited studies investigating its biological activities. In this study, the total phenol, total flavonoid content, and usnic acid—a common lichen acid—in the methanol extract obtained from *Squamarina cartilaginea* were determined using high-pressure liquid chromatography. Furthermore, the study elucidated the antimicrobial, DNA protective, cytotoxic, and antioxidant activities of the extract.

The total phenol and total flavonoid content of the extract were determined using spectrophotometric methods. The total phenol amounts are expressed in gallic acid equivalents, and the total flavonoid amounts are expressed in catechin equivalents. The total phenol content of the lichen extract was measured as 44.72±4.67 $mg_{GAE}/g_{extract}$, while the total flavonoid content was determined as 30.10±3.28 $mg_{CA}/g_{extract}$ (Table 1). When examining studies that investigated the phenolic substance content in various lichen samples, variations were observed among different species [25,26].

Table 1. Total phenol, total flavonoid and usnic acid amounts in *S. cartilaginea* extract

Extract	**Total phenol [mg_{GAE}/g_{exract}]**	**Total flavonoid [mg_{CA}/g_{exract}]**	**Usnic acid (mg/g_{exract})**
S. cartilaginea	44.72±4.67*	30.10±3.28*	451.637±0.00

*Data are expressed as mean ± standard error (n=3)

Since its first isolation in 1844, usnic acid has been a frequently studied secondary metabolite in lichens. A variety of interesting biological and physiological activities have been determined in pharmacology and clinical studies [27,28].The usnic acid content of the *Squamarina cartilaginea* extract was calculated as 451,637 mg/g_{exract} (Table 1). In the literature, the amount of usnic acid in the acetone extract of *Squamarina lentigera*, another species of the genus, was determined to be 2.47±0.01% [15]. The amount of usnic acid in the extract prepared with a mixture of dichloromethane and methanol (1:1) was determined as 345.098 m/z [29]. The calibration equation and correlation coefficient in the method using usnic acid as a standard are provided in Table 2. The chromatogram of the lichen extract is presented in Figure 1.

Table 2. Calibration equation and correlation coefficient of the usnic acid standard

Material	**Calibration Equation [y=ax+b]**	**Correlation Coefficient [r^2]**
Usnic acid	y=23.68971x+94.49502	0.99970

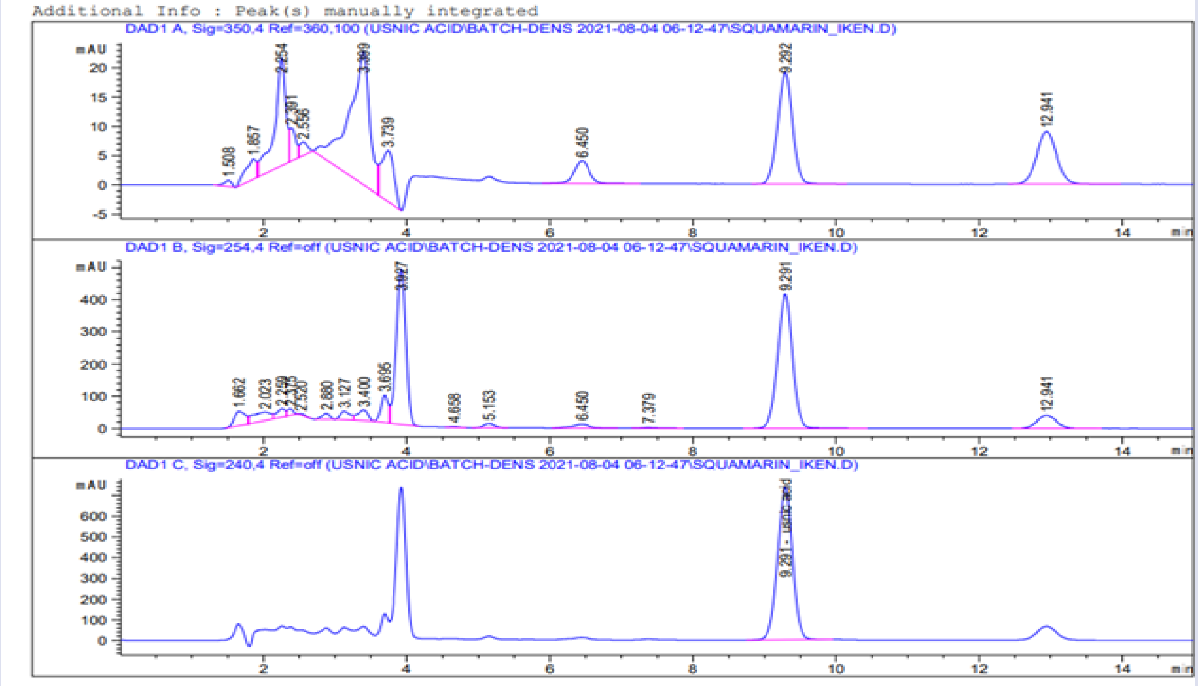

Figure 1. Chromatogram of *S. cartilaginea* extract

The antimicrobial effects of the *S. cartilaginea* extract against six bacterial strains were tested, and the resulting inhibition zones are presented in Table 3. Ampicillin, used as a positive control, exhibited higher activity than the lichen extracts, while no activity was observed in DMSO, used as a negative control.

Table 3. Antimicrobial activity of *S. cartilaginea* extract

Microorganism	***Squamarina cartilaginea***	**(-) Control empty disk**	**(+) Control (Ampicillin)**
E. coli	10.0 mm	-	16.0 mm
P. mirabilis	9.0 mm	-	24.0 mm
M. luteus	17.5 mm	-	30.0 mm
E. aerogenes	9.0 mm	-	12.0 mm
S. aureus	17.5 mm	-	20.0 mm
B. subtilis	9.5 mm	-	14.0 mm

Photographs of the inhibition zones created by the extract are presented in Figure 2. The *S. cartilaginea* extract exhibited the highest antimicrobial activity with a value of 17.5 mm against *M. luteus* and *S. aureus* strains, and the lowest activity with a value of 9.0 mm against *P. mirabilis* and *E. aerogenes* strains. In a study, it was determined that the *S. cartilaginea* methanol extract was active against *Enterobacter cloacae* up to 2000 µg/mL and affected fungal hyphae morphologically and lysosome activity against *Staphylococcus aureus*. Thus, this species has been shown to be a potentially bioactive source of compounds with antibacterial properties. In various studies, findings have indicated a correlation between the amount of usnic acid and antimicrobial activity, emphasizing that antimicrobial activity increases with the concentration of usnic acid. This highlights the importance of investigating lichens in detail as species of medical significance [15,30].

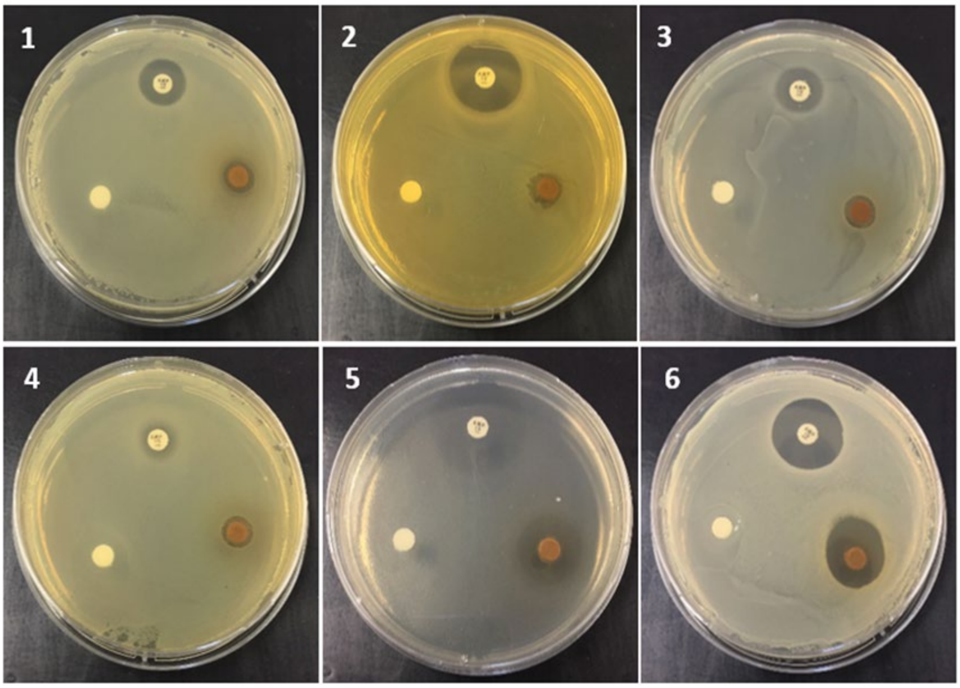

Figure 2. Antimicrobial activities of S. cartilaginea extract 1. E. coli, 2. P. mirabilis, 3. B. subtilis, 4. E. aerogenes, 5. M. luteus, 6. S. aureus

The DNA protective activity of the *S. cartilaginea* extract was assessed using pBR322 plasmid DNA, which exists in Form I (supercoil structure) and Form II (open ring structure). Form III refers to plasmid DNA in a linear structure resulting from the double-strand break in plasmid DNA. Standard pBR322 was loaded in well 1 and used as a marker. When the PBR322 plasmid DNA was exposed to UV and H_2O_2, damage occurred, alterations in Form I and Form II structures were observed, and the emergence of Form III structure was noted, as seen in the 4th well. When tested against UV or H_2O_2 individually, a decrease in the intensity of bands in Form I structure and an increase in the intensity of bands in Form II structure were observed.

In the 5th well, where the *S. cartilaginea* extract was added to the reaction mixture, it was observed that linear DNA formation was suppressed, and the structure of supercoiled DNA was preserved. Based on the obtained results, the lichen extract exhibited DNA protective activity against UV and H_2O_2 (Figure 3). The evaluation of the DNA protective effect of the *S. cartilaginea* species extract was conducted for the first time in this study, and no relevant data were found in the literature.

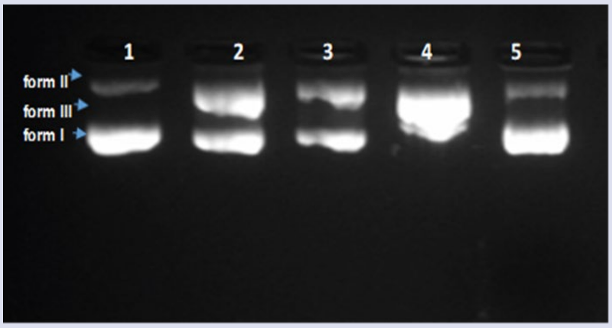

Figure 3. PBR322 DNA Cleavage agarose gel electrophoresis image. 1. pBR322, 2. pBR322 + UV, 3. pBR322 + H_2O_2, 4. pBR322 + UV + H_2O_2, 5. pBR322 + *S. cartilaginea* extract + UV + H_2O_2

As a result of the studies conducted to determine the cytotoxic effects of the *S. cartilaginea* species on DU-145 and Colo 205 cell lines, it was observed that the extract exhibited a high cytotoxic effect on both cell lines. The cytotoxic effect on DU-145 and Colo 205 cell lines for this lichen species was elucidated for the first time in this research. In the DU-145 cancer cell line, the extract reduced the viability of the cancer cell line to less than 50% in the concentration range of 31.25-1000 µg/mL compared to the control (Figure 4) and was observed to be quite toxic. The highest activity was observed at a concentration of 1000 µg/mL with a viability rate of 12.837±0.71%. The cytotoxic effects of the extract were also evaluated on the Colo-205 cell line, and it was found to be more toxic in this cell line compared to Du-145. It was determined that the extract showed high toxicity even at the lowest concentration. While 16.97±0.48% viability was observed at a concentration of 1000 µg/mL, 33.16±2.01% viability was measured at a concentration of 3.906 µg/mL (Figure 5).

When evaluating the cytotoxic effect on cancerous cell lines within the scope of this study, it can be hypothesized that the high cytotoxic activity is related to the usnic acid content in the lichen. However, it is also possible that other compounds are responsible for this effect or that multiple compounds act synergistically to produce this effect. Studies have shown that especially usnic acid, a dibenzofuran derivative, exhibits important pharmacological activities [31]. Regarding antiproliferative activity, it has been reported that both (-) and (+) isomers of usnic acid demonstrate moderate to strong cytotoxicity in vitro against a wide range of murine and human cancer cell lines [31,32,33,34,35,36,37].

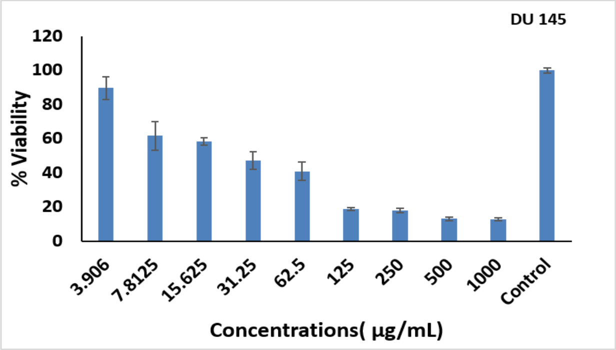

Figure 4. Cytotoxic effects of *S. cartilaginea* extract on DU-145 cells

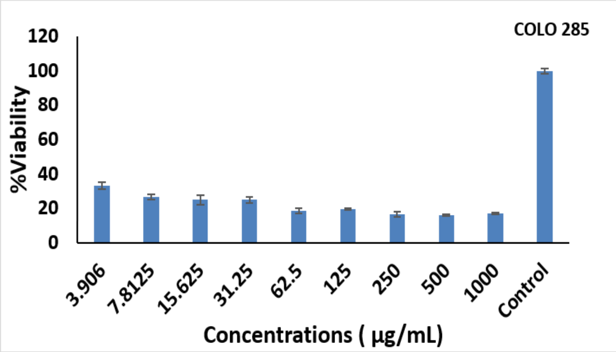

Figure 5. Cytotoxic effects of *S. cartilaginea* extract on Colo 205 cells

It has been observed that the *S. cartilaginea* extract effectively scavenges the DPPH radical in a concentration-dependent manner at physiological pH values. % Inhibition values are provided in Table 5. The extract was not as effective as BHT at the investigated concentrations. It was determined that the *S. cartilaginea* extract has moderate antioxidant capacity. In a study investigating the antioxidant capacity of *S. cartilaginea* and different lichen extracts, it was reported that the methanol extract of *S. cartilaginea* had a higher DPPH radical scavenging potential than other lichen species, and its IC_{50} value was 0.9 µg/mL [38]. When the ABTS radical scavenging effect of the *S. cartilaginea* extract was evaluated, high activity was determined, especially at 4 and 2 mg/mL concentrations (Table 4). However, it was not as effective as standard BHT at low concentrations (0.5 mg/mL and 1 mg/mL).

Table 4. DPPH$^{\bullet}$ and ABTS$^{\bullet+}$ radical scavenging effects

	DPPH• % inhibition			
	0,5 mg/mL	**1 mg/mL**	**2 mg/mL**	**4mg/mL**
S. cartilaginea	8.42±0.68	12.46±0.55	22.27±1.01	44.99±0.98
BHT	73.69±0.2	79.17±0.1	81.0±0.3	86.9±0.1
	TEAC (mmol/L/Trolox)			
S. cartilaginea	0.79±0.16	1.18±0.25	2.10±0.28	2.54±0.25
BHT	2.50±0.1	2.51±0.8	2.54±0.9	2.55±0.9

Conclusion

In conclusion, this study investigated the biological activities of *Squamarina cartilaginea*, a lichen species distributed in Türkiye. Despite its wide distribution, there has been limited research on the biological activities of *S. cartilaginea*. The methanol extract of *S. cartilaginea* exhibited antimicrobial, antioxidant, cytotoxic, and DNA protective activities. In the chemical composition of the extract, the amount of usnic acid was analyzed and the amounts of total phenols and total flavonoids were determined. Compared to a study on *Squamarina lentigera,* a high concentration of usnic acid was found. The amount of usnic acid determined shows the potential to investigate the effects of this compound on biological activities.

Antimicrobial assays demonstrated notable inhibition zones against both Gram-negative (*Escherichia coli*, *Proteus mirabilis*, *Enterobacter aerogenes*) and Gram-positive (*Bacillus subtilis*, *Micrococcus luteus*, *Staphylococcus aureus*) bacteria. The extract's efficacy in protecting plasmid DNA from UV and H_2O_2-induced damage further highlights its potential applications.

Cytotoxicity assessments on DU-145 (Human Prostate Cancer Cell Line) and Colo 205 (Human Colon Cancer Cell Line) revealed strong cytotoxic effects, particularly on the Colo 205 cell line. The extract demonstrated concentration-dependent scavenging activity against DPPH and ABTS radicals, indicating its moderate antioxidant capacity.

These findings contribute to the understanding of the biological potential of *Squamarina cartilaginea* and underscore its significance as a source of bioactive compounds. Lichens have garnered considerable attention due to their distinctive secondary metabolites. Consequently, the isolation and large-scale cultivation of lichen mycobionts hold the potential for extracting bioactive compounds, paving the way for the commercial utilization of lichens in the pharmaceutical sciences. This approach not only facilitates the exploration of unique and valuable compounds but also contributes to unlocking the commercial value inherent in lichen-derived products. The endeavor to harness the pharmaceutical potential of lichen secondary metabolites through isolation and mass culture represents a promising avenue for future research and industrial applications.

Conflict of Interest

The authors declare that there is no conflict of interest.

Acknowledgment

This study was financially supported by the Yozgat Bozok University project with project number 6601a-FBE/20-433.

Author’s Contributions

MK, ZK and BCD designed the current research experiments. BCD, MK, Sİ, ZK, GŞK, and AC performed the experiments. ZK and GŞK wrote and edited the manuscript.

References

[1] Miao V., Coëffet-LeGal M. F., Brown D., Sinnemann S., Donaldson G., Davies J., Genetic approaches to harvesting lichen products, *Trends in Biotechnology*, 19(9) (2001) 349-355.

[2] Stanojković T., Investigations of lichen secondary metabolites with potential anticancer activity. Lichen secondary metabolites: bioactive properties and pharmaceutical potential, 9 (2019) 155-174.

[3] Shukla V., Joshi G. P., Rawat M. S. M., Lichens as a potential natural source of bioactive compounds: a review, *Phytochemistry reviews*, 9 (2010) 303-314.

[4] Illana-Esteban C. Lichens used in traditional medicine, *Boletin de La Sociedad Micologica de Madrid*, 36, (2012), 163-174.

[5] Crawford S. D., Lichens used in traditional medicine, Lichen secondary metabolites: bioactive properties and pharmaceutical potential, 9 (2019) 31-97.

[6] Richardson D. H. S., Lichens and man, *Frontiers in mycology*, 1 (1991) 187-210.

[7] Çobanoğlu G. ve Yavuz M., Tıp Tarihinde Likenlerle Tedavi, *Yeni Tıp Tarihi Araştırmaları*, 9, (2003) 37-90.

[8] Oksanen I., Ecological and biotechnological aspects of lichens, *Applied microbiology and biotechnology*, 73 (2006) 723-734.

[9] Paudel B., Bhattarai H. D., Lee J. S., Hong S. G., Shin H. W., Yim J. H., Antioxidant activity of polar lichens from King George Island (Antarctica), *Polar Biology*, 31 (2008) 605-608.

[10] Behera B. C., Verma N., Sonone A., Makhija U., Antioxidant and antibacterial activities of lichen Usnea ghattensis in vitro, *Biotechnology letters*, 27 (2005) 991-995.

[11] Gyawali R., Ibrahim S. A., Natural products as antimicrobial agents, Food control, 46 (2014) 412-429.

[12] Sharnoff S., A field guide to California lichens, Yale University Press, (2014).

[13] Kirk P. M., Cannon P. F., Minter D. W., & Stalpers J. A. Dictionary of the fungi Wallingford, UK: CABI, (2008), 335.

[14] Himmelreich U., Huneck S., Feige G. B., Lumbsch H. T., Squamaron, ein Naphthochinon aus der Flechte Squamarina cartilaginea/Squamarone, a Naphthoquinone from the Lichen Squamarina cartilaginea, *Zeitschrift für Naturforschung B*, 49(9) (1994) 1289-1291.

[15] Cansaran Duman D., Halıcı M. G., Antimicrobial activity of usnic acid on Squamarina lentigera lichen species, *Turkish Bulletin of Hygiene and Experimental Biology*, 69(3) (2012) 127-134.

[16] Sweidan A., Chollet-Krugler M., Sauvager A., Van De Weghe P., Chokr A., Bonnaure-Mallet M., Tomasi S., Bousarghin L., Antibacterial activities of natural lichen compounds against Streptococcus gordonii and Porphyromonas gingivalis, *Fitoterapia*, 121 (2017) 164-169.

[17] Reiter R. J., Acuña-Castrovıejo D., Tan D. X., Burkhardt S., Free radical-mediated molecular damage: mechanisms

for the protective actions of melatonin in the central nervous system, *Annals of the New York Academy of Sciences*, 939(1) (2001) 200-215.

[18] Purvis O. W., Coppins B. J., Hawksworth D.L., James P. W., and Moore D. M., The Lichen Flora of Great Britain and Ireland. London: Natural History Museum Publications in association with the British Lichen Society (1992).

[19] Siddiq A., Anwar F., Manzoor M., Fatima M., Antioxidant activity of different solvent extracts of Moringa oleifera leaves under accelerated storage conditions of sunflower oil, *Asian J. Plant Sci.,* 4 (2005) 630- 635.

[20] Karatoprak G. Ş., Göger F., Çelik İ., Budak Ü., Akkol E. K., Aschner M., Phytochemical profile, antioxidant, antiproliferative, and enzyme inhibition-docking analyses of Salvia ekimiana Celep & Doğan, *South African Journal of Botany,* 146 (2022) 36-47.

[21] Re R., Pellegrini N., Proteggente A., Pannala A., Yang M., Rice-Evans C., Antioxidant activity applying an improved ABTS radical cation decolorization assay, *Free radical biology and medicine*, 26 (9-10) (1999) 1231-1237.

[22] Zhishen J., Mengcheng T., Jianming W., The determination of flavonoid contents in mulberry and their scavenging effects on superoxide radicals, *Food chemistry*, 64(4) (1999) 555-559.

[23] Adinortey M. B., Ansah C., Weremfo A., Adinortey C. A., Adukpo G. E., Ameyaw E. O., Nyarko A. K., DNA damage protecting activity and antioxidant potential of Launaea taraxacifolia leaves extract, *Journal of Natural Science, Biology, and Medicine*, 9(1) (2018) 6.

[24] Gyamfi M. A., Yonamine M., Aniya Y., Free-radical scavenging action of medicinal herbs from Ghana: Thonningia sanguinea on experimentally-induced liver injuries, *General Pharmacology: The Vascular System*, 32(6) (1999) 661-667.

[25] Popovici V., Bucur L., Gîrd C. E., Popescu A., Matei E., Cozaru G. C., ... & Badea V. Phenolic Secondary Metabolites and Antiradical and Antibacterial Activities of Different Extracts of Usnea barbata (L.) Weber ex FH Wigg from Călimani Mountains, Romania, *Pharmaceuticals*, 15(7) (2022) 829.

[26] Kocovic A., Jeremic J., Bradic J., Sovrlic M., Tomovic J., Vasiljevic P., Manojlovic N., Phytochemical analysis, antioxidant, antimicrobial, and cytotoxic activity of different extracts of Xanthoparmelia stenophylla lichen from Stara Planina, Serbia, *Plants*, 11(13) (2022) 1624.

[27] Manojlovic N. T., Vasiljevic P. J., Maskovic P. Z., Juskovic M., Bogdanovic-Dusanovic G., Chemical composition, antioxidant, and antimicrobial activities of lichen Umbilicaria cylindrica (L.) Delise (Umbilicariaceae) Evidence-based complementary and alternative medicine, (2012).

[28] Campanella L., Delfini M., Ercole P., Iacoangeli A., & Risuleo G., Molecular characterization and action of usnic acid: a drug that inhibits proliferation of mouse polyomavirus in vitro and whose main target is RNA transcription, *Biochimie*, 84(4) (2002) 329-334.

[29] Fernández-Pastor I., González-Menéndez V., Martínez Andrade K., Serrano R., Mackenzie T. A., Benítez G., ... & Reyes F., Xerophytic Lichens from Gypsiferous Outcrops of Arid Areas of Andalusia as a Source of Anti-Phytopathogenic Depsides, *Journal of Fungi*, 9(9) (2023) 887.

[30] Ivanova V., Bačkor M., Dahse H. M., Graefe U., Molecular structural studies of lichen substances with antimicrobial, antiproliferative, and cytotoxic effects from Parmelia subrudecta, *Preparative biochemistry biotechnology*, 40(4) (2010) 377-388.

[31] Ingolfsdottir K., Usnic acid, *Phytochemistry*, 61(7) (2002) 729-736.

[32] Takai M., Uehara Y., Beisler J. A., Usnic acid derivatives as potential antineoplastic agents, *Journal of medicinal chemistry*, 22(11) (1979) 1380-1384.

[33] Bézivin C., Tomasi S., Rouaud I., Delcros J. G., Boustie J., Cytotoxic activity of compounds from the lichen: Cladonia convoluta, *Planta medica*, 70(9) (2004) 874-877.

[34] Morris Kupchan S., Kopperman H. L., L-Usnic acid: tumor inhibitor isolated from lichens, *Experientia*, 31 (1975) 625-625.

[35] Cardarelli M., Serino G., Campanella L., Ercole P., De Cicco Nardone F., Alesiani O., Rossiello F., Antimitotic effects of usnic acid on different biological systems, *Cellular and Molecular Life Sciences CMLS*, 53 (1997) 667-672.

[36] Kumar S. P., Müller K., Lichen metabolites. 2. Antiproliferative and cytotoxic activity of gyrophoric, usnic, and diffractaic acid on human keratinocyte growth, *Journal of natural products*, 62(6) (1999) 821-823.

[37] Kumar S. P., Kekuda T. P., Vinayaka K. S., Sudharshan S. J., Anthelmintic and antioxidant efficacy of two macrolichens of Ramalinaceae, *Pharmacognosy Journal*, 1(4) (2009) 238-242.

[38] Mendili M., Bannour M., Araújo M. E. M., Seaward M. R., Khadhri A., Lichenochemical screening and antioxidant capacity of four Tunisian lichen species, *Chemistry biodiversity*, 18(2) (2021) e2000735.

Cumhuriyet Sci. J., 45(3) (2024) 486-489
DOI: https://doi.org/10.17776/csj.1478560

Cumhuriyet Science Journal

| csj.cumhuriyet.edu.tr | Founded: 2002 ISSN: 2587-2680 e-ISSN: 2587-246X Publisher: Sivas Cumhuriyet University

Brunnipila calyculiformis (Schumach.) Baral: A Novel Record for Türkiye

İsmail Acar[1,a,*], Halide Karabiyik[2,b]

[1] *Department of Organic Agriculture, Başkale Vocational High School, Van Yüzüncü Yıl University, Van, Türkiye*
[2] *Food Processing Department, Arda Vocational School, Trakya University, Edirne, Türkiye*
**Corresponding author*

Research Article

History
Received: 04/05/2024
Accepted: 15/09/2024

ABSTRACT

The research subject of this study is a specimen of *Brunnipila* collected from the Biga (Çanakkale) district in 2024. The specimen, which is characterised by outward facing brown hairs and densely septate hairs with crystals on top, was identified as *B. calyculiformis* (Schumach.) Baral, as a new record for members of the Ascomycota in Türkiye, based on morphological characters in accordance with the data obtained from field studies and laboratory analyses. In this manuscript the macro- and micromorphological characteristics of the new record were described and illustrated. This new record will contribute to the macrofungal diversity of Türkiye and the distribution of the genus *Brunnipila*.

Keywords: Ascomycota, Mycobiota, Novel record, Türkiye.

[a] *ismailacar@yyu.edu.tr* *https://orcid.org/0000-0002-6049-4896* [b] *halidekarabiyik@trakya.edu.tr* *0000-0002-1778-2200*

Introduction

The order *Helotiales* within the class *Leotiomycetes* is the most diverse order containing non-stromatic discomycetes with inoperculate asci [1-3]. Most members of *Helotiales* have very small apothecia, usually less than 2 mm in diameter. Apothecia may be sessile or stipitate, dark or brightly coloured, and superficial or erumpent along the plant host. The general shape of the apothecia is cupulate-discoid, concha funnel-shaped or clavate [4]. Most are known to be saprophytic, living on fallen leaves and decaying wood, but some are pathogenic or symbiotic parasites with other organisms. This order is reported to include 11 families, about 500 genera and about 4000 species [1-2]. With the advent of molecular phylogeny, some families in the order *Helotiales* have been revised, such as members with stromata (*Sclerotiniaceae* and *Rutstroemiaceae*) or hairs (*Hyaloscyphaceae* and *Lachnaceae*) [5].

The *Lachnaceae* Raitv are a family of inoperculate discomycetes characterised by small, often stalked, hairy apothecia, usually brightly coloured, bowl-shaped. Most family members have been described as saprophytes on dead plant tissues. However, there are also species isolated as endophytes from living leaves and roots [6,7]. Some species within the family that are not known to pass to the sexual stage and remain only in the asexual stage have also been reported. Although these species show morphological similarities, they are phylogenetically positioned in different genera [7]. The most distinctive feature of *Lachnaceae* is that the ascocarp is hairy and the excipular cells are thin-walled. In 2004, *Lachnaceae* was separated from *Hyaloscyphaceae* sensu Nannf. and became a new family, supported by phylogenetic data [8-9]. Various researchers have placed totally ten genera (*Albotricha*, *Brunnipila*, *Capitotricha*, *Dasyscyphella*, *Erioscyphella*, *Incrucipulum*, *Lachnellula*, *Lachnopsis*, *Proliferodiscus* and *Velebitea*) in the family *Lachnaceae* [10-13].

The genus *Brunnipila* Baral (*Lachnaceae*, *Helotiales*), which has unique characters that have long been overlooked, was introduced by Baral [14]. It was characterised by brown, moderately thick-walled, densely granulated hairs with a denser septation towards slightly capitate apex and firmly attached, flat or octahedral crystals on top. The lanceolate, strongly protruding paraphyses consistently lack refractive vacuolar bodies (Baral, pers. comm.). Octahedral crystals are less sharp than the crystals known from the genus *Incrucipulum* Baral, where they are more regular and sharper [15].

In recent years, valuable studies on Ascomycota have been carried out in Türkiye [3, 16-22]. In addition to these studies, [23] and [24] found that there is only one species (*Brunnipila clandestina* (Bull.) Baral) belonging to the genus *Brunnipila* in Türkiye. The aim of this study is to contribute to the Ascomycota of Türkiye and to determine the distribution of the genus *Brunnipila*.

Materials and Method

Fresh *Brunnipila* apothecia constituting the study materials were collected in Biga (Çanakkale) district on 23.03.2024. The external characteristics of the specimen were noted in the field notebook. It was subjected to photographic documentation in its natural environment. At the end of the day, they were transferred to Çanakkale Onsekiz Mart University Mycology Laboratory. The samples were dried in a non-illuminated environment and were converted into fungarium material by the author for further use. For the determination of microscopic data, preparations from the dried sample were made in water, IKI or what and examined under a Leica DM500 (Germany) research microscope, first under a 4 × 10 objective and then under 10 × 10 and 40 × 10 objectives, respectively. Finally, immersion oil was dropped onto the preparation, it was analysed and photographed under a 100 × 10 objective. Microscopic characters (asci [IKI were used for the ascus reaction], ascospores, hairs and paraphyses) in the photographs were measured at least 20 times using Leica Application Suite (version 3.4.0). Macro- and micromorphological analyses were performed following the methods described by [14-15,25]. Microscopic drawings were prepared using CorelDRAW (64-bit) (Canada). This ensured accuracy and clarity in depicting the observed features of *Brunnipila*.

Result

Ascomycota Caval.-Sm.
Leotiomycetes O.E. Erikss. & Winka
Helotiales Nannf.
Lachnaceae Raitv.
Brunnipila Baral

Brunnipila calyculiformis (Schumach.) Baral (Figure 1,2)

Syn: *Atractobolus calyculiformis* (Schumach.) Kuntze, Revis. gen. pl. (Leipzig) 3(3): 445 (1898); *Cyathicula calyculiformis* (Schumach.) P. Karst. [as 'calyculaeformis'], Not. Sällsk. Fauna et Fl. Fenn. Förh. 8: 207 (1866); *Dasyscyphus calyculiformis* (Schumach.) Rehm [as 'Dasyscypha'], Ascomyceten: no. 111b (1872); *Erinella calyculiformis* (Schumach.) Quél., Enchir. fung. (Paris): 301 (1886); *Lachnea calyculiformis* (Schumach.) Gillet [as 'calyculaeformis'], Champignons de France, Discom. (3): 69 (1880) [1879]; *Lachnella calyculiformis* (Schumach.) W. Phillips, *Man. Brit. Discomyc.* (London): 237 (1887); *Lachnum calyculiforme* (Schumach.) P. Karst., Bidr. Känn. Finl. Nat. Folk 19: 178 (1871); *Lachnum calyculiforme* var. *cyphelliforme* Rehm, in Strasser, Verh. Kaiserl.-Königl. zool.-bot. Ges. Wien 57(1): 338 (1907); *Peziza calyculiformis* Schumach. [as 'calyculaeformis'], Enum. pl. (Kjbenhavn) 2: 425 (1803); *Peziza calyculiformis* var. *gregaria* Berk. & Broome, Ann. Mag. nat. Hist., Ser. 3 7: 450 (1861); *Trichopeziza calyculiformis* (Schumach.) Rehm, Ber. naturhist. Augsburg 26: 53 (1881).

Apothecia 0.5 – 2 mm across, stipitate, outer surface brown; brown, beige-brown or olive-brown covered with hairs, often with pale (almost white) crystals at the tips of the hairs and hymenium whitish-gray. Discs pale yellowish brown. Hairs 130 – 175 × 3.5 – 11 µm, warty, 5 – 12 septate, septa often denser towards apex, lateral walls 0.5–1 µm thick; cylindrical, brown, overall covered with minute, hyaline granules, at their tips with refractive matter or octahedral-shaped crystals, in their upper part the young hairs are paler. Stipe 0.3 – 0.7 mm long. Asci 45 – 60 × 4 – 8 µm diam., hyaline, cylindrical, at apex tapering, arising from croziers, 8-spored, apex turning blue in IKI. Ascospores 7 – 11.5 × 1.5 – 2 µm diam., usually irregularly biseriate, hyaline, without septa, narrowly fusiform. Paraphyses 3 – 5.8 µm wide, lanceolate, exceeding the asci for 11–17 µm, septate towards the base. Ectal excipulum of textura prismatica - textura angularis, cells up to 15 µm diam.

Specimen examined: Biga (Çanakkale), near Kaldırımbaşı village, roadside on corticated branch fragments of *Corylus* sp. 40° 14′31"N, 27° 12′45"E, 73 m, 23.03.2024, Acar 1861.

Figure 1. *Brunnipila calyculiformis* a. Apothecia on bark of *Corylus* sp. b. Ascospores (in water). c. Asci (in IKI) d. Asci and paraphyses (in water). e. Fragments of hair (in IKI) f. Hairs lacking crystals. g. Hairs with crystals (in water). Scale bar: 10 µm

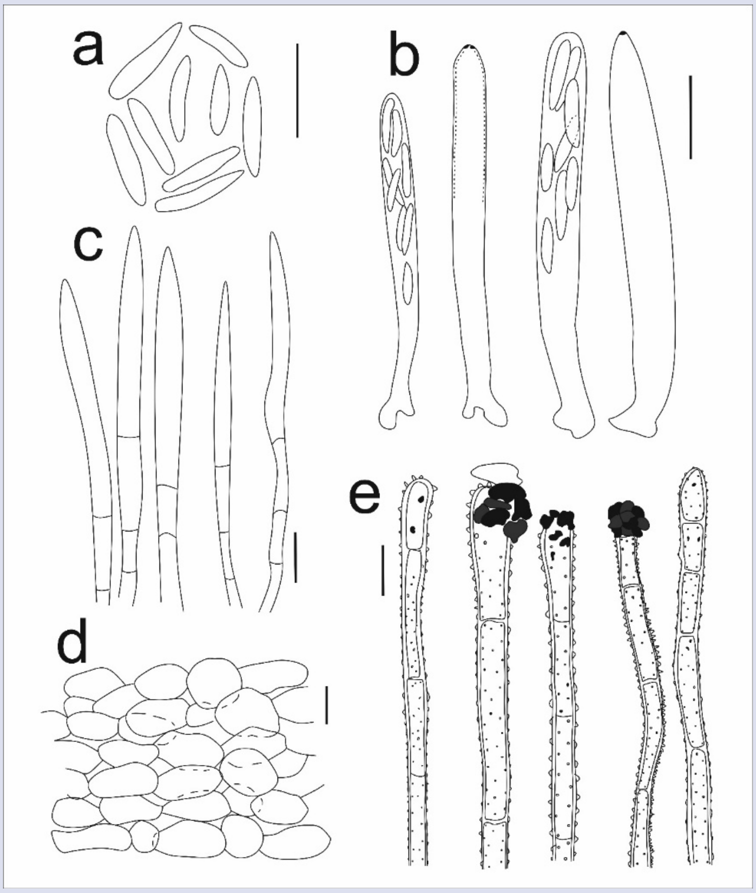

Figure 2. *Brunnipila calyculiformis* a. Ascospores b. Asci, c. Paraphyses, d. Ectal excipulum, e. Hair Scale bar: 10 µm

Discussion

Lachnum latebricola (Rehm) R. Galán & Raitv. (= *Lachnella calyculiformis* (Schum. ex Fr.) Phill. var. *latebricola* (Rehm) Phill.), previously recognised as a synonym of *Brunnipila calyculiformis*, was first discussed by [26] as a different species. Later this variety was elevated to the species level (separate due to smaller spores and partly specific substrates (*Ericaceae*) by [25,27]. *Brunnipila clandestina* (Bull.) Baral is among the species with similarities to *B. calyculiformis* in Baral. Both species have small, whitish or light-coloured apothecia. *Brunnipila calyculiformis* usually has flatter, disc-like apothecia, while the apothecia of *B. clandestina* are more hairy and prominent. Differences in substrate (*Rubus* L. and woody herbaceous stems of other dicots), larger paraphyses, smaller asci without croziers and ascospores are the distinguishing properties of *B. clandestine*. In addition, the paraphyses of *B. clandestina* are sometimes slightly yellowish in colour, whereas those of *B. calyculiformis* are hyaline [25]; [28] – here you find the statement “sans crochet”, Huhtinen apparently overlooked the value of croziers here.

The genus *Brunnipila*, which is represented by 11 species in the world [29], was previously now known with only one species in our country, *B. clandestina*. As a result of this study, the number of species belonging to the genus *Brunnipila* was increased to two and thus contributed to the mycobiota of the country.

Conflicts of interest

There are no conflicts of interest in this work.

Acknowledgment

We would like to thank Hans Otto BARAL, the author of *Brunnipila calyculiformis*, for his help in writing the manuscript.

References

[1] Kirk P.M., Cannon P.F., Minter D.W., Stalpers J.A., Dictionary of the fungi. 10th ed. Wallingford: CAB International, (2008)

[2] Baral H.O., Inoperculate discomycetes. In: Jaklitsch W., Baral H.O., Lücking R., Lumbsch T., (Eds.), Syllabus of plant families: adolf engler’s syllabus der pflanzenfamilien part 1/2 Ascomycota. 13th ed. Stuttgart: Borntraeger, (2016) 157–205.

[3] Akçay M.E., Acar İ., Uzun Y., Three New Records of Helotiales for the Mycobiota of Türkiye, *Anatolian Journal of Botany,* 7(2) (2023) 117-121.

[4] Korf R.P., Discomycetes and Tuberales. In: Ainsworth G.C., Sparrow F.K., Sussman A.S., (Eds.), The fungi: an advanced treatise. IVB New York: Academic Press., (1973) 249–319.

[5] Hosoya T., Systematics, Ecology, and Application of Helotiales: Recent Progress and Future Perspectives for Research with Special Emphasis on Activities within Japan, *Mycoscience*, 62(1) (2021) 1-9.

[6] Johnston P.R., Johansen R.B., Williams A.F.R., Wilkie P., Park D., Patterns of Fungal Diversity in New Zealand Nothofagus Forests, *Fungal Biology*, 116 (2012) 401–412.

[7] Johnston P.R., *Lachnaceae* in New Zealand – Aotearoa, Manaaki Whenua – *Landcare Research Datastore*, (2023)

[8] Johnston P.R., Quijada L., Smith C.A., Baral H.O., Hosoya T., Baschien C., Pärtel K., Zhuang W.Y., Haelewaters D., Park D., Carl S., López-Giráldez F., Wang Z., Townsend J.P., A Multigene Phylogeny Toward a New Phylogenetic Classification for the Leotiomycetes, *IMA-Fungus* 7(10) (2019) 1.

[9] Johnston P.R., Baschien C., *Tricladiaceae* fam. nov. (Helotiales, Leotiomycetes), *Fungal Systematics and Evolution,* 6 (2020) 233–242.

[10] Hosoya T., Sasagawa R., Hosoya K., GieHo S., Hirayama Y., Yamaguchi K., Toyama K., Kakishima M., Molecular Phylogenetic Studies of *Lachnum* and its Allies Based on the Japanese Material, *Mycoscience,* 51 (2010) 170–181.

[11] Perić B., Baral H.O., *Erioscyphella curvispora* spec. nov. from Montenegro, *Mycologia Montenegrina,* 17 (2014) 89–104.

[12] Guatimosum E., Schwartsburd P.B., Crous P.W., Barreto R.W., Novel Fungi from an Ancient Niche: Lachnoid and Chalara-Like Fungi on Ferns, *Mycological Progress,* 15 (2016) 1239–1267.

[13] Phookamsak R., Hyde K.D., Jeewon R. et al., Fungal Diversity Notes 929–1035: Taxonomic and Phylogenetic Contributions on Genera and Species of Fungi, *Fungal Diversity,* 95 (2019) 1–273.

[14] Baral H.O., Krieglsteiner G.J., Bausteine zu einer Askomyzeten–Flora der BR Deutschland: In Süddeutschland Gefundene Inoperculate Discomyzeten mit Taxonomischen, Ökologischen und Chorologischen Hinweisen, *Beih. Z. Mykol*., 6 (1985) 1–160.

[15] Sukova M., A Revision of Selected Material of Lignicolous species of *Brunnipila*, *Capitotricha*, *Dasyscyphella* and *Neodasyscypha* from the Czech Republic, *Czech Mycol*., 57 (2005) 139–172.

[16] Acar İ., Quijada L.., A New Species Record from the Order of Pezizales; *Coprotus disculus*, *Mantar Dergisi*, 13 (2) (2022) 120-123.

[17] Acar İ., Uzun Y., *Stictis bengalensis (Stictidaceae, Ostropales)* – A New Addition to Fungal Genera and Species for Turkey, *Österr. Z. Pilzk*, 30 (2022) 7–10.

[18] Allı H., Muğla Sıtkı Koçman Üniversitesi Kampüsünde Yetişen Makromantarlar, *Mantar Dergisi*, 13(2) (2022) 96-104.

[19] Dizkirici A., Acar İ., *Hymenoscyphus conscriptus* & *H. fucatus*, Newly Recorded from Turkey, *Mycotaxon*, 137 (3) (2022) 555-567.

[20] Şahin A., Uzun Y., Kaya A., Contribution to the Macrofungal Biodiversity of Yahyalı District, *Mantar Dergisi*, 14(2) (2023) 60-68.

[21] Uzun Y., Kaya A., First Record of *Arpinia luteola* J.Geesink from Türkiye, *Anatolian Journal of Botany,* 7(2) (2023a) 131-134.

[22] Uzun Y., Kaya A., *Leucoglossum leucosporum*, A New Record for Turkish Mycobiota, *Mantar Dergisi*, 14(2) (2023b) 92-95.

[23] Sesli E., Asan A., Selçuk F., (Eds.), Abacı Günyar Ö., Akata I., Akgül H., Aktaş S., Alkan S., Allı H., Aydoğdu H., Berikten D., Demirel K., Demirel R., Doğan HH., Erdoğdu M., Ergül C., Eroğlu G., Giray G., Halikî Uztan A., Kabaktepe Ş., Kadaifçiler D., Kalyoncu F., Karaltı .İ, Kaşık G., Kaya A., Keleş A., Kırbağ S., Kıvanç M., Ocak İ., Ökten S., Özkale E., Öztürk C., Sevindik M., Şen B., Şen İ., Türkekul İ., Ulukapı M., Uzun Ya., Uzun Yu., Yoltaş A., The checklist of fungi of Turkey. Ali Nihat Gökyiğit Vakfı Yayını, (2020) İstanbul.

[24] Solak M.H., Türkoğlu A., Macrofungi of Turkey, checklist, Volume-III, Kanyılmaz Matbaacılık, (2022) Bornova-İzmir.

[25] Huhtinen S., Additions to the Ascomycetous Flora of the Canadian North, *Karstenia*, 24(1) (1984) 1-11.

[26] Dennis R.W.G., A Redisposition of Some Fungi Ascribed to the Hyaloscyphaceae, *Kew Bulletin*, 17(2) (1963) 319-379.

[27] Raitviir, A., Synopsis of the *Hyaloscyphaceae*, *Scripta Mycol*., 1 (1970) 1-115..

[28] Répertoire des champignons du Québec,Available at https://www.mycoquebec.org/bas.php?l=r&nom=Brunnipila%20clandestina%20/%20P%C3%A9zize%20clandestine*&post=Brunnipila&gro=214&tag=Brunnipila%20clandestina. Retrieved May 2, 2024.

[29] Index Fungorum, https://www.indexfungorum.org/names/Names.asp (2024b). Retrieved May 2, 2024.

Cumhuriyet Sci. J., 45(3) (2024) 490-495
DOI: https://doi.org/10.17776/csj.1455893

Cumhuriyet Science Journal

| csj.cumhuriyet.edu.tr | Founded: 2002 ISSN: 2587-2680 e-ISSN: 2587-246X Publisher: Sivas Cumhuriyet University

Supramolecular Solvent Liquid Phase Microextraction of Voriconazole İn Pharmaceutical and Environmental Samples With High Performance Liquid Chromatography Detection

Erkan Yilmaz[1,2,3,4,a*], **Gülnihal Yildiz**[1,b]

[1]Erciyes University, Faculty of Pharmacy, Department of Analytical Chemistry, Kayseri, Türkiye
[2]Erciyes University, Nanotechnology Research Center (ERNAM), 38039 Kayseri, Türkiye
[3]Technology Research and Application Center (ERU-TAUM), Erciyes University, 38039 Kayseri, Türkiye
[4]Erciyes Teknopark A.Ş-ChemicaMed Chemical Inc., Erciyes University Technology Development Zone, Kayseri 38039, Türkiye
**Corresponding author*

Research Article

History
Received: 20/03/2024
Accepted: 14/08/2024

ABSTRACT

In this study, a new analytical method based on the supramolecular solvent liquid phase microextraction (Ss-LPME) and HPLC was developed for the analysis of voriconazole as an active drug in the class of antifungals with a wide spectrum of action at trace levels. Nano/micro sized supramolecular phase formed in 1-decanol, tetrahydrofuran and aqueous environment was used as extraction agent for separation and preconcentration of trace level of voriconazole. For the optimization of the Ss-LPME method, important analytical parameters such as the effect of sample solution pH, volume of 1-decanol, amount of THF, ultrasounic irridation time, centrifugation time and sample solution volume on the extraction efficiency were evaluated. Optimal conditions of the Ss-LPME; pH: 8, 1-decanol volume: 200 µL, THF volume: 300 µL, ultrasounic irridation time:10 min and centrifugation time: 8 min. For the developed Ss-LPME/HPLC procedure, the limit of detection (LOD), limit of quantification (LOQ) and enhancement factor (EF) were found 2.7 µg·L^{-1}, 8.8 µg·L^{-1} and 36, respectively. The Ss-LPME/HPLC procedure was applied to waste water, lake water and drug samples. The fact that recovery values ranging from 100% to 108.5% were obtained for these real samples proved that this method can be used successfully in the matrix environments studied.

Keywords: Voriconazole, anaylsis, Supramolecular solvent liquid phase microextraction, Preconcentration, High performance liquid chromatography.

[a] *erkanyilmaz@erciyes.edu.tr* *https://orcid.org/0000-0001-8962-3199* [b] *yldzglnhl84@gmail.com* *https://orcid.org/0009-0002-8418-3846*

Introduction

Voriconazole is a triazole in the antifungal class. Voriconazole prevents invasive aspergillosis and Scedosporium apiospermum and Fusarium spp. FDA approval was given in 2002 for patients who did not respond to or were resistant to other treatments. Voriconazole, a new generation triazole antifungal, is used for the treatment of life-threatening fungal infections in immunocompromised patients. Use of voriconazole has increased since the drug was launched in 2002 [1-3]. Due to excessive use of voriconazole is increasing day by day, It is important to determine the correct concentration of the voriconazole active ingredient in drug formulations and environmental samples due to its negative effects on humans and especially ecosystems as a result of its spread into the environment [4,5].

There are several analytical instruments to analyze voriconazole and other pharmaceuticals in different matrix mediums. They are mainly high performance liquid chromatography (HPLC), liquid chromatography–mass spectrometry (LC–MS/MS), high resolution mass spectrometry including time of flight (TOF), raman spectroscopy and electrochemical sensors. However, the disruptive effects of foreign species on the analysis in the matrix environment where the voriconazole drug active ingredient is located and the fact that the voriconazole concentration that may be present at ultra-trace levels is below the detection limit of these devices are the main problems that limit accurate and sensitive analysis [6-8]. Selective extraction and enrichment of trace levels of voriconazole molecules from the matrix medium into a purer analysis medium before analysis is the most effective way to solve this problem [9,10].

Liquid phase microextraction techniques (LPME), in which solvent and chemical consumption is minimal during the sample preparation process, the sample preparation process is very fast, and basic laboratory equipment is used, meet most of the requirements of green analytical methods developed in recent years [11,12]. By using deep eutectic solvents, ionic liquids, supramolecular solvents and switchable solvents, which are in the green solvent class, as extraction agents in LPME methods, these methods are closer to the classification of green analytical methods [13, 14]. Supramolecular solvents, which belong to the class of green solvents, are nano/micro structured liquids formed as a result of mixing compounds with long carbon chains containing hydroxyl (OH) and carboxylic acid (COOH) groups in an aqueous environment with compounds such as tetrahydrofuran and tetrabutyl ammonium [16, 17]. Supramolecular solvents, which consist of amphiphiles dispersed in a phase, interact strongly with analytes because they both have polar-nonpolar functional groups and contain hydrogen bonds in their structures [16, 17].

In this study, a new liquid phase microextraction technique based on the formation of supramolecular solvent was developed by combining the advantages of LPME and supramolecular solvents to separate and enrich the trace level of voriconazole drug substance from the matrix medium before its determination by HPLC. The Ss-LPME/HPLC procedure was applied to waste water, lake water and drug samples with high recovery values ranging from 100% to 108,5%.

Experimental

Instruments and Chemicals

The determination of the analyte in the samples, which were pre-separated and enriched by the liquid-liquid microextraction method, was carried out with an Agilent brand HPLC device. Optimum working conditions for HPLC analysis of voriconazole: Mobile phase: 40 mM pH 6 phosphate buffer and acetonitrile mixture at (70:30) flow rate of mobile phase: 0.7 mL·min^{-1}, retention time: 4.0 min, column: ACE S C8, Detector: DAD, 254 nm wavelength. Bandelin brand DT-255 model ultrasonic bath was used during the preparation of the mobile phase and microextraction. Sartorius brand PT-10 model pH meter was used to measure the pH of the solutions. In the study, Hettich Rotofix 32 brand centrifuge device was used to separate the aqueous phase and organic extraction phase after microextraction. VWR international brand vortex device was used in vortex mixing processes. All of these chemicals were used in analytical purity. Stock and intermediate stock solutions used for the determination of voriconazole by the liquid phase microextraction method were prepared at appropriate concentrations using deionized water. Voriconazole stock solution at 100 mg·L^{-1} concentration was prepared by weighing 100 mg of pure voriconazole and completing the volume to 1000 mL with pure water. Acetone, 1-propanol and acetonitrile were obtained from Merck. 1-decanol, ethanol and THF were obtained from Sigma-Aldrich.

Liquid Phase Microextraction-HPLC Procedure

An appropriate volume of the stock solution containing 100 mg·L^{-1} of voriconazole was taken into a 50 mL centrifuge tube and the volume was completed to 10 mL with pure water. By adding 2.0 mL of pH 8 buffer to this solution, the pH was fixed at 8. Then, 200 µL 1-decanol and 300 µL of THF were added into the solution. The resulting mixture was kept in an ultrasonic bath for 10 minutes. In this way, nano and micro sized supramolecular extraction solvent drops were formed [16, 17]. The mixture was centrifuged for 8 minutes for extraction and separation of the aqueous phase. The resulting analyte phase was taken with a syringe and methanol was added and the final volume was completed to 1.0 mL. The obtained sample was vialed with appropriate process and measured on the HPLC device. The same procedures were applied to blank samples.

Real Sample Applications

The developed method was applied to industrial wastewater sample, lake water sample and solid form pharmaceutical sample. The water samples taken were filtered through filters with a pore diameter of 0.22 microns before use. 100 mg of drug sample was dissolved in 100 mL of pure water and the developed method was applied to certain volumes taken from the resulting aqueous phase [18]. In addition, the accuracy of the method was checked by applying the developed method by adding voriconazole, whose concentration is precisely known, to these samples.

Results and Discussion

In order to separate and enrich voriconazole with the liquid phase microextraction method, optimum conditions were determined by examining the important analytical parameters on the extraction efficiency including sample solution pH, volume of 1-decanol, volume complementary solvent type, effect of ultrasonication time, model solution volume and centrifuge time. Real sample analyzes and the accuracy of the method were tested under the optimal experimental conditions.

Effect of Sample Solution pH on Extraction Efficiency of Ss-LPME

To determine the optimum sample solution pH for the separation/enrichment of voriconazole by the Ss-LPME, model solutions with pH ranging from 2-10 were prepared. Each stage was run in 3 repetitions in 10 mL model solutions. It was observed that the extraction efficiency increased from pH 2 to higher pH values, reaching a maximum at pH 8, but after pH 8, the extraction efficiency was decreased. The reason for this could be that voriconazole would be in more molecular forms when the pH was increased from 2 to 8, and yet they would be easily degraded in acidic conditions. However, the extraction efficiency slightly go down when the pH of solution was increased from 8 to 10, indicating that the liquid phase microextraction system reached saturation at pH 8. For this reason, the optimum working pH was determined as 8.0 (Figure 1).

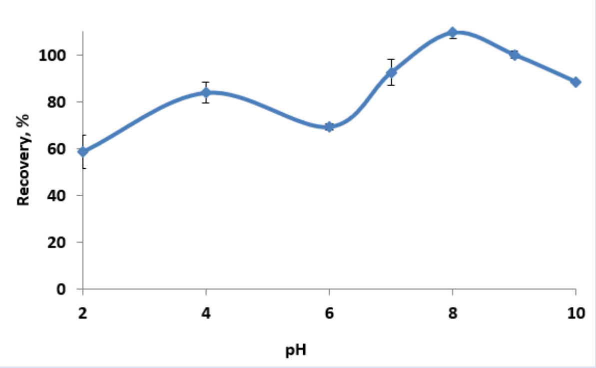

Figure 1. Effect of sample solution pH on the extraction efficiency of voriconazole (N=3).

Effect of 1-Decanol Volume on Extraction Efficiency of Ss-LPME

1-Decanol volumes varying between 50, 100, 150, 200 and 250 µL were added to the model solutions prepared at pH 8.0, and the effect of 1-Decanol volume on extraction efficiency was screened. In the method developed for the determination of voriconazole by liquid phase microextraction, as the volume of 1-decanol added to the mixture increased, the amount of analyte passing into the solvent phase increased. As seen in Figure 2, the maximum recovery values were obtained at maximum 200 µL and 250 µL of 1-Decanol volumes. When 200 µL 1-Decanol was used, the maximum analyte passed into the solvent phase and remained constant after this value. Therefore, 200 µL of 1-Decanol was recorded as the optimum value for the separation and preconcentration of voriconazole by Ss-LPME.

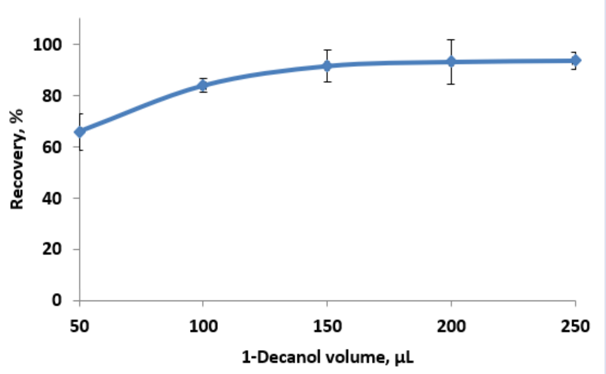

Figure 2. Effect of 1-Decanol volume on the extraction efficiency of voriconazole (N=3).

Effect of THF Volume on Extraction Efficiency of Ss-LPME

In order to determine the THF volume on extraction efficiency, 100, 200, 300, 400 and 500 µL THF volumes were added to test tubes containing voriconazole model solution with pH 8.0 and 200 µL 1-decanol. Then, the samples were centrifuged after being kept in an ultrasonic bath. The resulting analyte phase was taken, its volume was measured, and methanol was added to make up to 1.0 mL, and analyzes were carried out by HPLC. The optimum THF volume for the determination of voriconazole by liquid phase microextraction was determined as 300 µL.

Effect of Volume Complementary Solvent Type

After liquid phase microextraction of voriconazole, the extractant phase was completed to 1.0 milliliter with various organic solvents to obtain a homogeneous phase that could be injected into HPLC. For this purpose, experimental studies were carried out with HPLC grade solvents including isopropanol, ethanol, acetonitrile, methanol and 50% methanol-50% ethanol mixtures. As shown in Figure 3, the highest peak area was obtained when methanol was used as the solvent. Methanol was observed as the ideal solution for the injection of extraction phase for the determination of voriconazole by Ss-LPME. To determine the optimum methanol volume, final volumes ranging from 0.5 to 3.5 mL were injected into HPLC. The highest peak area was obtained when the extractant phase was completed to 1.0 mL with methanol after extraction. In the determination of voriconazole by Ss-LPME, the ideal volume complementary solvent was selected as 1.0 mL methanol.

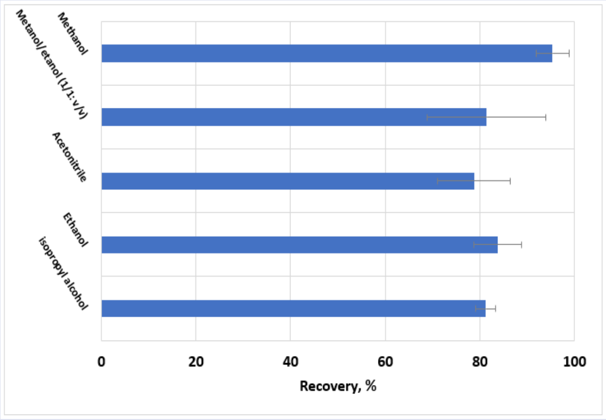

Figure 3. Effect of complementary solvent type on the recovery of voriconazole (N=3).

Effect of ultrasonic irridation time on extraction efficiency of Ss-LPME

Ultrasonic irridation effect was used to obtain nano and micro-sized supramolecular extraction droplets [16, 17]. To determine the optimum ultrasonic vibration time, the tubes prepared by adding 2..0 mL pH 8 buffer, 200 µL decanol and 300 µL THF were exposed to ultrasonic vibration for 2, 4, 6, 8 and 10 minutes, respectively. At each stage, each sample was kept in an ultrasonic bath for the specified periods of time and centrifuged for 8 minutes. The resulting analyte phase was taken, its volume was measured, and methanol was added to make it up to 1.0 mL, and then it was given to the HPLC. As seen in Figure 4, the highest recovery value was obtained at 10 minutes of ultrasonic irridation time. The optimum ultrasonic bath time for the determination of voriconazole by the liquid phase microextraction method was recorded as 10 minutes.

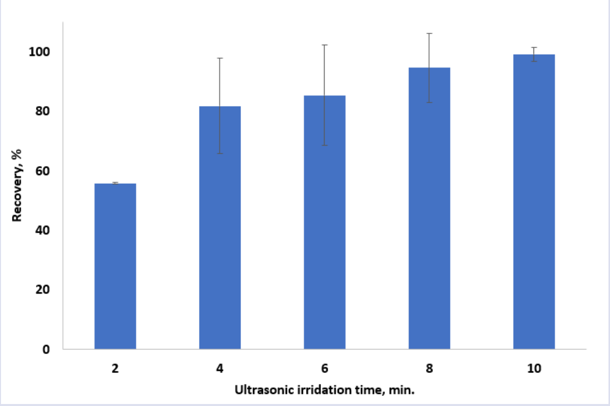

Figure 4. Effect of ultrasonic irridation time on the extraction efficiency of voriconazole (N=3).

Effect of Centrifugation Time on Extraction Efficiency of Ss-LPME

After the extraction process, centrifuge was used to separate the extraction phase and the aqueous phase. Three replicate experiments were carried out with centrifuge times varying between 2 and 10 minutes. At each stage, 2.0 mL pH 8 buffer, 200 µL decanol and 300 µL THF were added to the prepared sample solutions and the developed Ss-LPME method was applied. The highest recovery value for liquid phase microextraction of voriconazole was obtained with 8 minutes of centrifugation. It was observed that the amount of analyte passing into the supramolecular microphase was less in centrifugation processes performed for less than 8 min. Therefore, the optimum centrifuge time was determined as 8 min.

Effect of sample solution volume on extraction efficiency of Ss-LPME

For the determination of analytes with low detection limits by obtaining a high preconcentration factor, the sample volume to which a developed analytical method can be applied should be as high as possible. To determine the highest sample volume to which the developed Ss-LPME method could be applied, model solutions ranging from 15, 20, 30, 40 and 50 mL were prepared and the microextraction method was applied under optimum conditions. As shown in Figure 5, quantitative extraction efficiencies were obtained with sample solution volumes ranging from 10-40 mL. Quantitative recovery values could not be obtained in sample volumes above 40 mL. The results obtained showed that the developed method can be applied up to 40 mL sample volume. Since the final volume was 1.0 mL, a 40-fold preconcentration factor was achieved with the developed method.

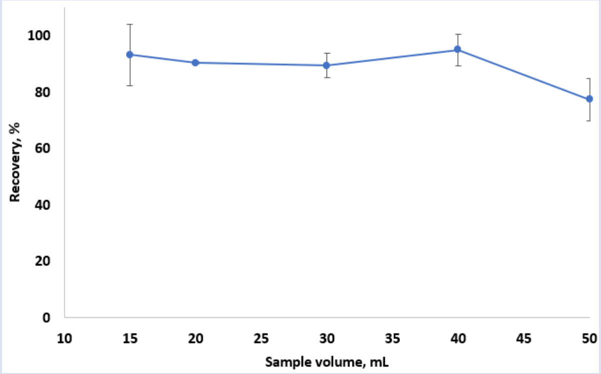

Figure 5. Effect of sample solution volume on the extraction efficiency of voriconazole (N=3).

Real Sample Analysis

The Ss-LPME method was applied to industrial wastewater and lake water samples collected from the Kayseri City region and to drug samples sold in pharmacies. Method accuracy studies were carried out with standard addition-recovery studies on these samples. The analyte concentrations specified in Table 1 were added to these samples and the developed microextraction method was applied. For this purpose, 2.0 mL of pH 8.0 buffer solution, 200 µL of 1-Decanol and 300 µL of THF were added to the analyte-added samples in 3 replicates. The samples were kept in an ultrasonic bath for 10 minutes and then centrifuged for 8 minutes. The resulting analyte phase was taken and final volume was completed to 1.0 mL with methanol. The obtained sample was vialized with appropriate procedures and measured on the HPLC. Analyzes were carried out using standard solutions prepared under the same conditions to obtain calibration curve. When the results obtained were examined, it was seen that recovery values between 100% and 108.5%. These results showed that the method we developed was applicable for these matrices.

Table 1. Standard addition-recovery and accuracy experiments for the Ss-LPME/HPLC procedure (N=3).

	Added, mg·L^{-1}	Found, mg·L^{-1}	Recovery, %
Waste water	0.0	ULOD^{a}	-
	2.0	2.17±0.03	108.5
	4.0	4.20±0.06	105.5
Lake water	0.0	ULOD	-
	1.5	1.62±0.05	108
	3.0	3.06±0.045	102
Drug sample	0.0	2.84±0.03	-
	2.0	4.90±0.03	101
	4.0	6.82±0.03	100

ULODa: Under of the limit of detection.

Analytical Performance of Ss-LPME/HPLC Procedure

Chromatograms of voriconazole before and after the Ss-LPME method are shown in Figure 6. Calibration graph, preconcentration factor, enhancement factor, limit of detection and limit of quantification were carried out to determine the analytical performances of the Ss-LPME/HPLC procedure by using The ICH analytical method validation guidelines [19]. The developed Ss-LPME/HPLC procedure was applied to 40 mL model solutions containing increasing concentrations of voriconazole and the calibration line graph was obtained. Calibration line equation was: S=156.05C-0.2449 (S: Peak area, C: Concentration of voriconazole as mg·L^{-1}). The enhancement factor was obtained by dividing the slope of the calibration graph obtained after applying the method by the slope of the calibration graph obtained before the method. The enhancement factor was found to be 36. The correlation coefficient (R^2) of the calibration line is 0.994. The limit of detection and limit of quantification values for the method were found to be 2.7 µg·L^{-1} and 8.8 µg·L^{-1}, respectively.

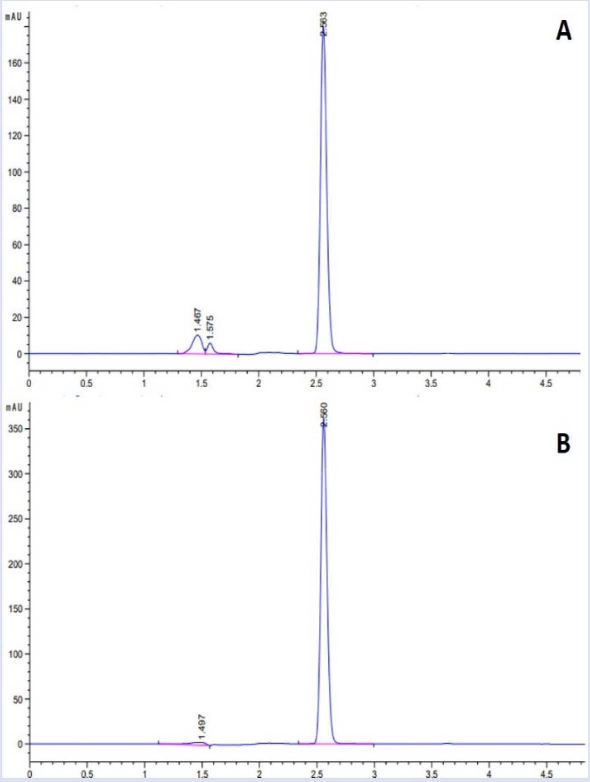

Figure 6. Chromatograms of voriconazole before (A) and after (B) the Ss-LPME method.

Conclusion

In this study, a new sample preparation method was developed to separate and enrich voriconazole in different samples by LPME based on supramolecular solvent formation. This study is the first literature study in which supramolecular solvents are used in the separation and enrichment of the active drug substance voriconazole. By combining supramolecular solvents, which are in the green solvent class, with liquid phase microextraction, which is a green analytical method, a greener analytical method has been developed compared to traditional methods. The Ss-LPME/HPLC procedure was applied to environmental water and drug samples with quantitative recoveries (>98%). Considering the above-mentioned advantages of using supramolecular solvents and liquid phase microextraction techniques, the developed Ss-LPME/HPLC procedure can be used in environmental samples and drug preparations, especially voriconazole. It has the potential to be used as a routine method in the sensitive and accurate analysis of active pharmaceutical ingredients.

Conflicts of interest

The authors declare that there are no conflicts of interest.

References

[1] Alarfaj N.A., Maha F. E., Electrochemical Sensors For Direct Potentiometric Determination of Voriconazole in Pharmaceutical Dosage Forms and Biological Fluids., *International Journal of Physical Sciences*, 7(9) (2012) 1403-1411.

[2] Liu J., Fan W., Lv X., Wang C., Rapid Quantitative Detection of Voriconazole in Human Plasma Using Surface-Enhanced Raman Scattering, *ACS omega*, 7 (51) (2022) 47634-47641.

[3] Gunawan U., Ibrahim S., Ivansyah A. L., Damayanti S., Insights Into the Selective Imprinted Polymer of Voriconazole from Host-Guest Interaction Perspective., *Journal of Molecular Liquids*, 383 (2023) 122130.

[4] Zhao Y. M., Tang G. M., Wang Y. T., Cui Y. Z., Synthesis, Spectroscopic Studies, Antimicrobial Activity, and Crystal Structure of a Zn (II) Complex Based on Voriconazole, *Journal of Coordination Chemistry*, 70 (2) (2017) 189-200.

[5] Bashir K., Chen G., Han J., Shu H., Cui X., Wang L., Fu Q., Preparation of Magnetic Metal Organic Framework and Development of Solid Phase Extraction Method for Simultaneous Determination of Fluconazole and Voriconazole in Rat Plasma Samples by HPLC, *Journal of Chromatography B*, 1152 (2020) 122201.

[6] Chawla P. K., Dherai A. J., Ashavaid T. F., Plasma Voriconazole Estimation by HPLC, *Indian Journal of Clinical Biochemistry*, 31 (2016) 209-214.

[7] Srinubabu G., Raju C. A., Sarath N., Kumar P. K., Rao J. S., Development and Validation of a HPLC Method for the Determination of Voriconazole in Pharmaceutical Formulation Using an Experimental Design, *Talanta*, 71(3) (2007) 1424-1429.

[8] Liu J., Fan W., Lv X., Wang C., Rapid Quantitative Detection of Voriconazole in Human Plasma Using Surface-Enhanced Raman Scattering, *ACS omega*, 7(51) (2022) 47634-47641.

[9] Bashir K., Chen G., Han J., Shu H., Cui X., Wang L.,Fu Q., Preparation of Magnetic Metal Organic Framework and Development of Solid Phase Extraction Method for Simultaneous Determination of Fluconazole and Voriconazole in Rat Plasma Samples by HPLC, *Journal of Chromatography B*, 1152 (2020) 122201.

[10] Michael C., Teichert J., Preiss R., Determination of Voriconazole in Human Plasma and Saliva Using High-Performance Liquid Chromatography with Fluorescence Detection, *Journal of Chromatography B*, 865(1-2) (2008) 74-80.

[11] Sarafraz-Yazdi A., AmiriA., Liquid-Phase Microextraction, *TrAC Trends in Analytical Chemistry*, 29(1) (2010) 1-14.

[12] Psillakis E., Kalogerakis N., Developments in Liquid-Phase Microextraction, *TrAC Trends in Analytical Chemistry*, 22(9) (2003) 565-574.

[13] Santos L. B., Assis R. S., Barreto J. A., Bezerra M. A., Novaes C. G., Lemos V.A., Deep Eutectic Solvents in Liquid-Phase Microextraction: Contribution to Green Chemistry, *TrAC Trends in Analytical Chemistry*, 146 (2022) 116478.

[14] Arain M. B., Yilmaz E., Soylak M., Deep Eutectic Solvent Based Ultrasonic Assisted Liquid Phase Microextraction for the FAAS Determination of Cobalt, *Journal of Molecular Liquids*, 224 (2016) 538-543.

[15] Rezaei F., Yamini Y., Moradi M., Daraei B., Supramolecular Solvent-Based Hollow Fiber Liquid Phase Microextraction of Benzodiazepines, *Analytica Chimica Acta*, 804 (2013) 135-142.

[16] Moradi M., Yamini Y., Feizi N., Development and Challenges of Supramolecular Solvents in Liquid-Based

Microextraction Methods, *TrAC Trends in Analytical Chemistry*, 138 (2021) 116231

[17] Zohrabi P., Shamsipur M., Hashemi M., Hashemi B., Liquid-Phase Microextraction of Organophosphorus Pesticides Using Supramolecular Solvent as a Carrier for Ferrofluid, *Talanta*, 160 (2016) 340-346.

[18] Mirzajani R., Kardani F., Ramezani Z., Preparation and characterization of magnetic metal–organic framework nanocomposite as solid-phase microextraction fibers coupled with high-performance liquid chromatography for determination of non-steroidal anti-inflammatory drugs in biological fluids and tablet formulation samples. *Microchemical Journal*, *144* (2019) 270-284.

[19] Valıdatıon of Analytıcal Procedures: Text And Methodology Q2(R1), Available at: https://database.ich.org/sites/default/files/Q2%28R1%29%20Guideline.pdf. Retrieved March, 2024.

Cumhuriyet Sci. J., 45(3) (2024) 496-502
DOI: https://doi.org/10.17776/csj.1501849

Cumhuriyet Science Journal

| csj.cumhuriyet.edu.tr | Founded: 2002 ISSN: 2587-2680 e-ISSN: 2587-246X Publisher: Sivas Cumhuriyet University

Isolation and Characterization of Heat Shock Protein 70-Ipek 1 from *Toxoplasma gondii*

Kübra Açıkalın Coşkun [1,a,*], **Lütfi Tutar**[2, b]

[1] *Department of Medical Biology, Faculty of Medicine, İstanbul Aydın University, İstanbul, Türkiye.*
[2] *Department of Molecular Biology and Genetics, Faculty of Science and Letters, Kırşehir Ahi Evran University, Kırşehir, Türkiye.*
**Corresponding author*

Research Article

History
Received: 15/06/2024
Accepted: 15/09/2024

ABSTRACT

Toxoplasma gondii is a common intracellular parasite that causes the toxoplasmosis. Heat shock proteins (Hsps) have a critical role in pathogenesis of toxoplasmosis. Hsps are highly conserved proteins in evolution among living organisms. This protein family responsible for a wide range of biological processes such as protein folding, protein translocation, protein aggregation. In the present study, Hsp70, a member of the Hsp family, was isolated from *T. gondii* and its sequence and motifs were determined by PCR, cloning, sequencing and homology modelling analysis. ATP hydrolysis, luciferase folding, and luciferase aggregation experiments were performed for determination of its chaperone activity while the stability and secondary structure of the Hsp70 were discovered by using biophysical experiments (FTIR, florescence and quenching experiment). In addition, *in silico* analysis were used to determine the physicochemical characteristics of Hsp70. The results revealed that Hsp70 protein obtained from *T. gondii* (Hsp70-IPEK1) is similar to Hsp70s from other organisms. Also, the chaperone activity, stability and secondary structure of Hsp70-IPEK1 were determined. Hsp70-IPEK1 together with other chaperones in the presence of nucleotide were dramatically increased protein folding and aggregation. According to these results, it is thought that Hsp70 has a potential to contribute many research areas such as pharmaceutical analysis.

Keywords: *Toxoplasma gondii*, Heat Shock Protein 70, Stress.

[a] *kubraacikalincoskun@aydin.edu.tr* *https://orcid.org/0000-0002-0047-8368* [b] *lutfitutar@gmail.com* *https://orcid.org/0000-0002-6260-3136*

Introduction

T. gondii is a highly prevalent intracellular parasite that causes toxoplasmosis. This obligate intracellular parasite leads to infection of one out of three people in the world. Toxoplasmosis is a significant health problem in humans and animals and especially it poses a potential risk for pregnant women and immuno-compromised patients in human [1,2]. Moreover, Toxoplasmosis can lead to severe diseases in high-risk group individuals (e.g., still birth, hydrocephalus, cerebral calcification retinochoroiditis and pneumonia) [3,4].

T. gondii has two distinct forms: definitive host cat and intermediate warm-blooded host. It is generally transmitted to humans through contaminated water and food, especially by ingestion of undercooked meat. Also, humans may be infected by blood transfusion and organ transplantation [3]. The life cycle of this parasite consists of three forms: oocysts, tachyzoites and bradyzoites. The rapidly replicating tachyzoites and the slow-replicating bradyzoites have asexual replication stages within intermediate hosts while the sporozoite-containing oocysts has sexual replication stages in the definitive hosts such as cat and other felids. The life cycle between the tachyzoite and bradyzoite forms is important for pathogenesis and survival of *T. gondii* within intermediate hosts [2]. *In vitro* studies indicate that Heat Shock Proteins (Hsps) can induce differentiation between tachyzoite and bradyzoite forms [3]. For example, Hsp100 participate pathogen intracellular survival and pathogen infectivity in pathogenic bacteria. Also, inhibition of Hsps lead to suppression of bradyzoite development in host cell. Therefore, Hsps can play a significant role in pathogenesis of toxoplasmosis [1,5].

Hsps are evolutionary conserved proteins among living organisms and structurally related but functionally distinct in many organisms. Hsps are localized at different parts of the cell compartments such as endoplasmic reticulum, mitochondria and cytosol. Hsps as molecular chaperones are divided into six main groups based on their molecular weight (Hsp40, Hsp60, Hsp70, Hsp90, Hsp100 and small Hsps (<40 kDa)). Hsps function to fold nascent chains properly, translocate proteins across membranes, disaggregate proteins and target damaged proteins for degradation. Hsp expressions are affected by many factors such as heat, infections, inflammation, oxidative stresses and growth factors. Therefore, many metabolic diseases are associated with expression levels of Hsps [6].

Hsp70s are a highly conserved Hsp family found in all organisms. Hsp70s are responsible for many biological processes including protein assembly, protein folding and protein denaturation [7,8]. Hsp70s have an N-terminal nucleotide binding domain (NBD) and a C-terminal substrate binding domain (SBD). N-terminal nucleotide binding domain, also known as ATPase domain, hydrolyses the nucleotide and sends a signal to the SBD [6]. While the NBD domain is a highly conserved region, the SBD domain is a variable region [7]. The NBD contains a lid-like structure and peptide-binding groove. Substrate binds a hydrophobic region in the SBD. Unlike ADP bound state, Hsp70s have lower binding affinity but faster exchange ratio for substrate at ATP bound state. Hsp70 functions usually occur via repeated cycles including substrate binding, ATP binding and ATP hydrolysis [9].

The aim of this study is to isolate and characterize Hsp70 obtained from *T. gondii* RH strain (Hsp70-IPEK1). Putative Hsp70-IPEK1 sequence was estimated by in silico analysis. Cloning, sequencing and modeling experiments were performed to determine Hsp70-IPEK1 sequence and motif. After purification and expression processes of recombination protein, chaperone activity of Hsp70-IPEK1 was investigated by ATP hydrolysis, luciferase folding and luciferase aggregation experiments. The stability and secondary structure content of the Hsp70-IPEK1 were determined by using biophysical experiments including FTIR, fluorescence and quenching methods.

Materials and Methods

In Silico Analysis

Putative Hsp70-IPEK1 sequence was predicted from *T. gondii* database (www.toxodb.org) and NCBI Conserved Domain Search (http://www.ncbi.nlm.nih.gov). *T. gondii* ME49 strain was used as template (AAC72002.1) due to this strain shows high sequence similarity to RH strain.

Expasy's ProtParam prediction server and SOSUI server were used to predict Hsp70-IPEK1 physicochemical properties such as molecular weight, amino acid composition and theoretical isoelectric point (pI) and whether it is a soluble or a transmembrane protein. Homology modelling of Hsp70-IPEK1 was performed by using I-TASSER and SWISS-MODEL tools. The model of Hsp70-IPEK1 was shown in (Figure 1).

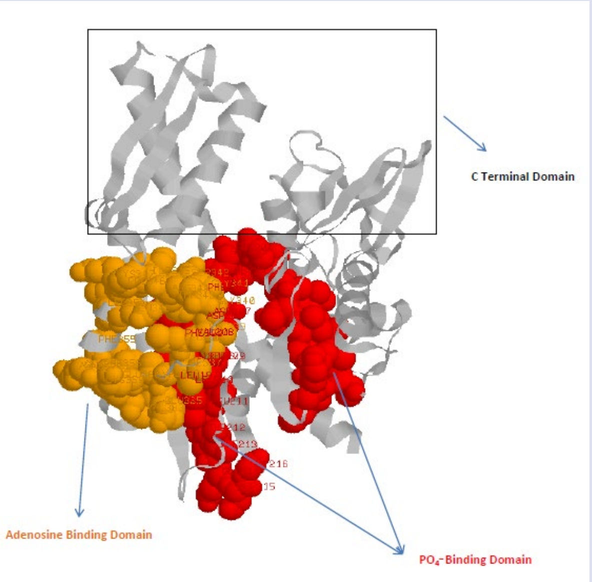

Figure 1. The tertiary structure of the Hsp70-IPEK1 and ATP and peptide binding sites

PCR Amplification, Sequencing and Sequence Analysis

T. gondii RH strain was obtained from the Saydam Public Health Centre, Ankara, Turkey. Total RNA of *T. gondii* was isolated and cDNA synthesis was performed with a commercial kit (Roche Diagnostic) according to the manufacturer's instruction. Hsp70 gene fragment of *T. gondii* was amplified by designed primers (forward primer: 5'-CACCATGGCGGACTCTCCTGCTGTG-3' and reverse primer: 5'- ATCAACTTCCTCCACGGT-3'). PCR reaction was carried out in 50 µL volume containing 1 µg cDNA, 4 µL forward and reverse primer (10 mM of each primer), 5 µL dNTP mix (2 mM), 5 µL 10×Pfu buffer with Mg_2SO_4 and 2 µL Pfu DNA polymerase (2.5 u/µL, Fermentas).

The PCR amplifications were performed in a gradient thermal cycler instrument (Thermo Scientific) with the following thermal cycling program: initial cycle, 30 s at 95 °C; next 35 cycles, denaturation for 30 s at 95 °C; 30 s at 64.2 °C temperature; and polymerization at 72 °C for 1 min; and a final cycle of 7 min at 72 °C. Amplified PCR products were run on a 1% agarose gel stained with ethidium bromide. The PCR product was sequenced and nucleotide sequence of Hsp70-IPEK1 was given in the Figure 2. Comparison of *T. gondii* Hsp70 with other organism was shown and same domains marked in (Figure 3a, Figure 3b).

```
ATGGCGGACTCTCCTGCTGTGGGTATTGACCTTGGCACCACCTATTCTTGCGTA
GGTGTGTGGAAGAACGATGCTGTGGAAATCATCGCGAACGACCAGGTCCACA
GGACGACCCCGTCCTACGTCGCGTTCACCGACACGGAGAGACTTGTCGGTGAT
GCTGCGAAGAACCAAGTCGCACGCAACCCGGAAAACACCATTTTCGATGCCAA
GCGCCTAATCGGTCGCAAGTTTGATGATCCCTCGGTCCAGTCGGACATGAAGC
ATTGGCCATTCAAGGTCATTGCTGGTCCGGGAGACAAGCCCCTCATTGAAGTC
ACGTACCAGGGAGAGAAGAAGACGTTCCACCCTGAAGAGGTTTCCGCCATGG
TTTTGGGCAAAATGAAGGAAATCGCGGAGGCTTACCTCGGCAAGGAAGTGAA
GGAGGCCGTCATTACCGTTCCTGCGTACTTCAACGATTCGCAGCGTCAGGCTA
CCAAGGATGCTGGTACTATTGCCGGCCTCAGCGTCCTCCGCATTATCAACGAG
CCCACAGCGGCTGCCATTGCTTATGGTCTGGACAAGAAGGGCTGCGGTGAGA
TGAACGTCCTCATCTTCGACATGGGTGGCGGTACGTTCGATGTGTCGCTGCTT
ACAATCGAAGACGGTATCTTTGAAGTCAAGGCCACCGCTGGTGACACCCATCT
TGGTGGTGAAGATTTCGACAACCGTTTGGTGGACTTCTGCGTCCAGGACTTCA
AGCGCAAGAACCGCGGAAAGGACATCAGCACCAACAGCCGTGCCCTTCGTCG
CCTGCGTACTCAGTGCTGGCGCACCAAGAGAACTCTCTCTAGCAGCACTCAGG
CAACCATCGAAATTGACTCTCTTTTTGAGGGCATTGACTACTCTGTGTCTATCTC
TCGTGCGCGCTTTGAGGAGCTTTGCATGGACTACTTCCGCAACTCCCTGTTGCC
CGTCGAGAAGGTCCTCAAGGACTCTGGTATTGACAAGCGCTCGGTCAGCGAA
GTTGTGTTGGTTGGTGGATCTACCCGTATCCCCAAGATTCAGCAGCTCATCACT
GACTTCTTCAACGGAAAGGAGCCGTGCAGGTCGATCAACCCCGATGAGGCCG
TTGCGTACGGTGCTGCTGTCCAGGCACCGATCTTGAAGGGAGTTACCAGCTCT
CAGGTGCAGGATTTGCTTCTTCTGGATGTTGCGCCTCTCTCTCTCGGTCTGGAG
ACAGCTGGTGGTGTCATGACCAAGCTGATTGAAAGAAACACAACGATCCCGA
CCAAGAAGTCTCAGACCTTCACCACGTACGCGGACAACCAGCCAGGAGTGCT
GATTCAGGTGTACGAAGGTGAGCGTGCGATGACCAAAGACAACAACCTCCTG
GGCAAATTCCACCTGGATGGTATCCCCCCCGCCCCCCGTGGTGTCCCCCAAATC
GAAGTCACTTTCGATATCGACGCTAACGGTATCATGAACGTCACAGCGCAAGA
CAAGTCCACCGGAAAGAGCAACCAAATCACCATCACGTACGACAAGGGCCGC
CTCAGTGCGTCCGAAATCGACCGCATGGTGCAAGAGGCAGAGAAGTACAAAG
CCGAAGACGAACAGAACAAGCACCGTGTGGAGGCGAAGAATGGCCTGCTAA
ACTACTGCTACCACATGAGACAGACCTTGGATGACGAGAAGCTTAAGGACAA
GATCTCCTCTGAGGACAGAGACACTGCCAACAAGGCCATCCAGGAGGCCCTT
GACTGGCTGGACAAGAACCAACTAGCAGAGAAGGAGGAATTCGAGGCGAAG
CAGAAGGAAGTTGAGTCCGTCTGCACACCAATCATCACCAAGCTGTACCAGGC
AGGTGCGGCTGCAGGTGGCATGCCTGCCGGTATGGGCGGTATGCCTGGTGGT
ATGGGCGGTATGCCTGGTGGTATGGGCGGTATGCCCGGCGGGATGGGCGGT
ATGCTCGGTGCAGGCATGGGAGGCTCTGGCGGCCCCACCGTGGAGGAAGTTG
ATTAA
```

Figure 2. Nucleotide sequence of Hsp70

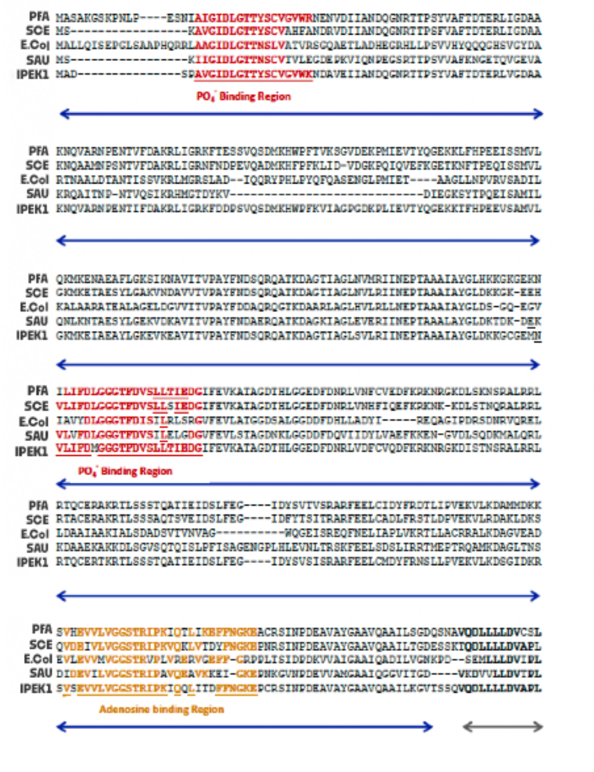

Figure 3a. Comparison of Hsp70-IPEK1 sequence with Hsp70s in different organisms and common motifs. N terminal domain

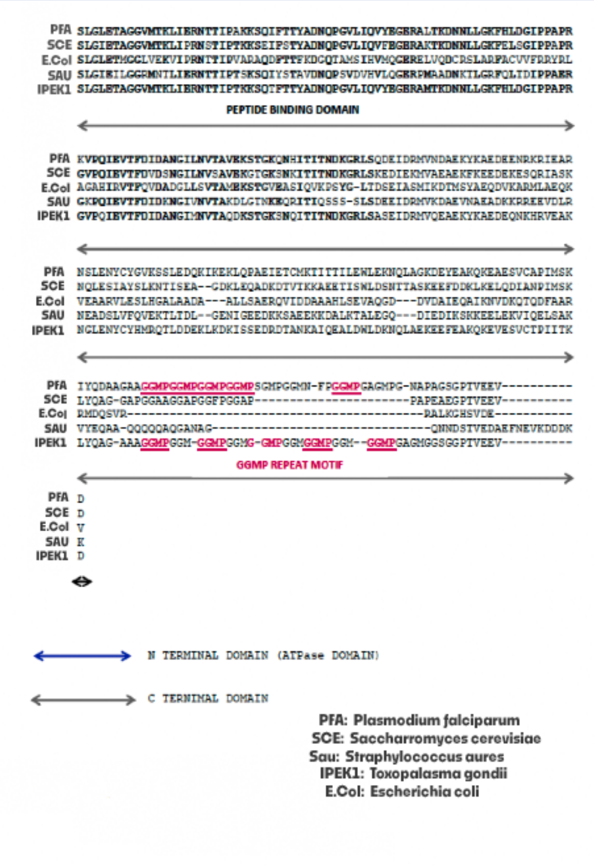

Figure 3b. Comparison of Hsp70-IPEK1 sequence with Hsp70s in different organisms and common motifs. C terminal domain.

Cloning and Purification of Recombinant Hsp70-IPEK1 Protein

The PCR product was cloned into the Champion pET Gateway Expression Kit Pet-161 (Invitrogen). Recombinant Hsp70-IPEK1 protein was produced by using topoisomerase experiments without a sub-cloning process. Firstly, topoisomerase recognition site (underlined sequence in materials and methods 2.2) was added before the forward primer. The PCR product was cloned into Pet-161 vector and then isolated plasmid DNA was transformed into BL21 Star™ (DE3) cells. Transformed cells were grown into 10 mL of LB agar plates containing 100 µg/mL ampicillin. A single colony was inoculated into 10 mL LB media (containing 100 g/mL ampicillin) and incubated overnight at 37 °C with shaking at 200 rpm. The growing cells were inoculated into 1 L of LB (containing 100 g/mL ampicillin) until OD550 was reached 0.4 and then these cells were induced with 1 mM isopropyl β-D-thiogalactopyranoside (IPTG) for 3-4 hours. At the end of the induction process, the growing cells were centrifuged and the pellet was lysed by bead beater using glass beats in the binding buffer (pH 7.4, 20 mM sodium phosphate, 0.5 M NaCl, 5 mM imidazole).

After centrifugation process, purification of recombination Hsp70-IPEK1 protein was carried out by 5 mL HisTrap™ FF column (GE Healthcare) and was eluted with imidazole gradient (20 mM–500 mM) with using Fast Protein Liquid Chromatography (FPLC, AKTA-Purifier). The collected fragments were analyzed by SDS–polyacrylamide gel electrophoresis on a 10% gel and transferred to nitrocellulose membrane via semi-dry blotter. The target protein was detected with western blot analysis by using primary and secondary antibody (anti-mouse IgG). Bands were determined with NBT (Nitro blue tetrazolium chloride) and BCIP (5-Bromo-4-chloro-3-indolyl phosphate, toluidine salt) (data not shown).

Fluorescence Experiments

Fluorescence experiments of Hsp70-IPEK1 were performed according to the method given in the reference [1]. Briefly, emission spectrums of Hsp70-IPEK1 were measured at 290 nm with 5 nm excitation and between 300 and 500 nm (Shimadzu RF 5301). The experiments were carried out in different protein concentrations at 25 °C with 20 mM Hepes, pH: 7.4, 100 mM NaCl titrations.

Quenching experiments were performed in the presence or absence nucleotides and different acrylamide. Data were analyzed according to the Stern–Volmer equation.

ATP Hydrolysis Experiments

ATPase activity screened with previously established method in our lab [8]. The enzymes used for ATP hydrolysis experiments are obtained from Roche and the reaction mixture contains 2 mM phosphoenolpyruvate, 0.2 mM NADH, 2 units/ml pyruvate kinase and 10 units/mL L-lactate dehydrogenase (both from rabbit muscle). Each analysis was performed with two replicates and the averages of them were used in the data analysis.

FTIR Experiments

FTIR experiments were carried out by Perkin–Elmer FTIR spectroscopy device at 1 cm−1 resolution. FTIR spectrum of protein solution was detected at amid-1 region and secondary structure of Hsp70-IPEK1 was determined in the absence and presence of nucleotides. Proteins were dialyzed in D2O to eliminate any interference caused by water band spectrum. Hemoglobin (76 % α-helix, 13 % ß-sheet, 11 % random, 0 % ß-turn), conconavalin A (3 % α-helix, 44 % ß-sheet, 28 % random, 25 % ß-turn), lysozyme (36 % α-helix, 10 % ß-sheet, 19 % random, 36 % ß-turn), chymotrypsin (11 % α-helix, 35 % ß-sheet, 30 % random, 25 % ß-turn) were used as standard to determine in secondary structure of Hsp-IPEK1. In the experiments, ATP and ADP concentrations were adjusted to 2 mM and Hsp70-IPEK1 protein was dialyzed against 30 mM sodium phosphate buffer solution, pH 7.4.

Luciferase Folding Experiments

The luciferase folding experiments were measured with Biofix lumi-10 Macherey–Nagel luminometer. Luciferase was used as substrate protein and denatured with urea. Denatured luciferase was diluted in prepared solution (pH 7.4, 25 mM Hepes, 50 mM KCl, 5 mM MgCl2, 2 mM ATP, and 5 mM dithiothreitol). This mixture was incubated with different amounts of IPEK1. In addition, IPEK1 protein was treated with different combinations of Hsps (Hsp40 and Hsp100) in the presence of ATP. The level of luciferase refolding with IPEK1 was measured at 320 nm as described previously [10].

Luciferase Aggregation Experiments

The luciferase aggregation experiments were measured with Shimadzu RF5301 at excitation and emission wavelengths of 341 nm. Luciferase was diluted 10-fold with the reaction mixture (pH 7.4, 25 mM Hepes, 50 mM KCl, 5 mM MgCl2, 2 mM ATP, and 5 mM dithiothreitol). The degree of aggregation was determined by light scattering by substituting different Hsps (Hsp40 and Hsp100).

Results

In Silico Analysis of Hsp70-IPEK1

A 2004 bp PCR product was obtained for Hsp70-IPEK1. Nucleotide sequence of IPEK1 was shown in Fıgure 2. Theoretically, molecular mass of IPEK1 is approximately 70 kDa. Nucleotide sequence of Hsp70-IPEK1 was analyzed by Expasy's ProtParam prediction tool to determinate physicochemical characteristics. In the amino acid composition of Hsp70-IPEK1, alanine (24.2%), cysteine (26.9 %), glycine (28.4 %) and threonine (20.5 %) were found as the most abundant amino acids.

Length (2004 amino acids), molecular weight (164131.83 Da), theoretical pI : 4.89, extinction coefficient, instability index, aliphatic index and grand average hydropathy (GRAVY) of the Hsp70-IPEK1 protein were analyzed using this tool. According to the computed isoelectric point (pI), Hsp70-IPEK1 is an acidic protein (pI lower than 7).

The computed extinction coefficient of IPEK1 protein was 33750 $M^{-1}cm^{-1}$ at 280 nm. Additionally, the experience showed that Hsp70-IPEK1 does not contain any Trp residues. The instability index value (II) was found to be 49.11 and hence this protein is predicted as unstable (Instability index >40) [10]. The aliphatic index (AI) for IPEK1 was 24.15. The low AI of a protein indicates the it is thermally unstable and more flexible [11]. The grand average hydropathicity (GRAVY) of Hsp70-IPEK1 was found to be 0.851. This protein was identified as a transmembrane protein when analyzed by SOSUI tool.

Toxoplasma Hsp70-IPEK1 sequence was also compared to homologs (*Plasmodium falciparum*, *Saccharomyces cerevisiae*, *Escherichia coli* and *Staphylococcus aureus*). It was showed that motifs and domains of Hsp70-IPEK1 were conserved in both sequence and modelling platform. The Hsp70-IPEK1 sequence contains PO^{-4} binding region, adenosine binding region and GGMP repeat motif (Figure 3).

Fluorescence Experiments of Hsp70-IPEK1

Conformational changes of Hsp70-IPEK1 protein by using fluorescence spectroscopy were investigated in the presence and absence of nucleotides. Fluorescence spectrum was blue shifted 10–15 nm when ATP and ADP are added. Experimental results are indicated that ATP binding causes conformational change in Hsp70-IPEK1 (Figure 4).

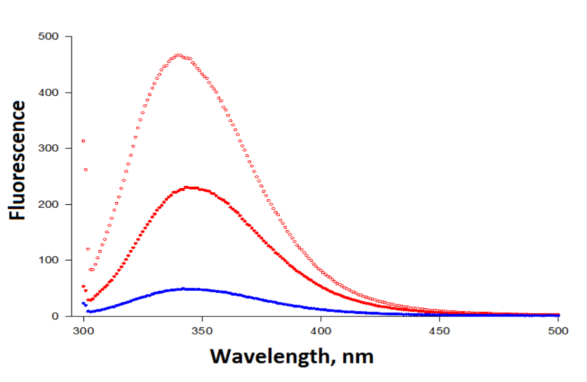

Figure 4. Intrinsic fluorescence spectra of the Hsp70-IPEK1 in the presence of ADP and ATP

ATP Hydrolysis Experiments of Hsp70-IPEK1

Hsp40 and peptide increase the activity of Hsp70. Therefore, ATP hydrolysis is an indirect indicator measure in substrate protein folding of Hsp70 and was measured by ATP regenerative system. The experiment results are shown in Figure 4. Hsp40 provides substrate proteins by binding to J domain of Hsp70 and thus, the activity of Hsp70 increases with presence of Hsp40. According to our results, the increase in the amount of Hsp40 and peptide increased the Hsp70 function. When Hsp40 was 5 µM ATP hydrolysis of Hsp70 was the highest (Figure 5).

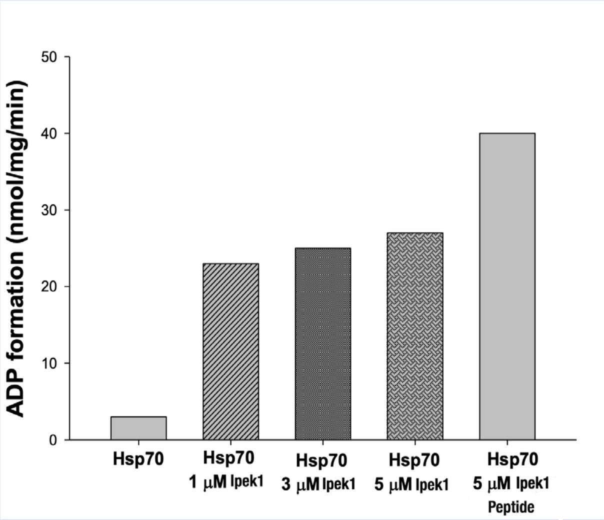

Figure 5. ATP hydrolysis under different conditions

FTIR Experiments of Hsp70-IPEK1

FTIR experiments were used to estimate the secondary structure of Hsp70-IPEK1 at Amid I region. FTIR spectra were determined by measuring different protein concentrations in the presence and absence of nucleotide. Similar to results of fluorescence experiments, FTIR results showed that conformational changes were observed in secondary structures of Hsp70-IPEK1 when it binds to nucleotides (Figure 6).

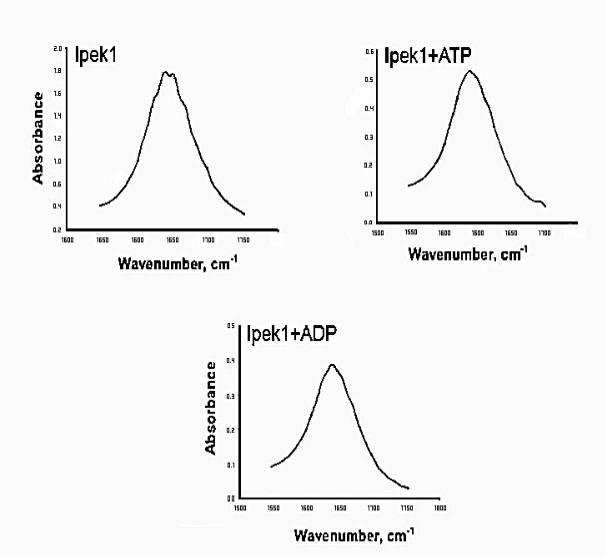

Figure 6. FTIR spectra of the Hsp70-IPEK1 in the presence of ADP and ATP

Quenching Spectra of Hsp70-IPEK1

Quenching method is an alternative method to determine the conformational changes of Hsp70-IPEK1 based on presence and/or absence of ADP. Changes affecting temperature-ligand in the protein surface chromophore were monitored with fluorescence quenching spectrum (Figure 7). In the presence and the absence of ADP form, K_{sv} values were measured 0.250 and 0.375 M^{-1} respectively.

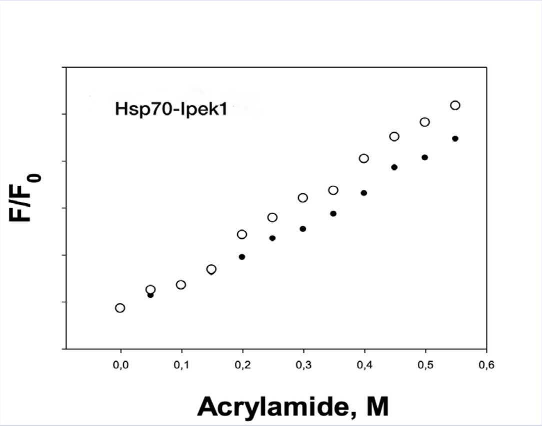

Figure 7. Fluorescent quenching results of Hsp70-IPEK1 in the presence and absence ADP

Luciferase Folding Experiments

In this experiment, the luminescence of the denatured luciferase and luciferase was accepted as '0' and '100', respectively. Addition of Hsp-IPEK1 to experiment helped luciferase folding. Moreover, the light scattering degree increased dramatically in the presence of Hsp40-Hsp70-IPEK1 complex with ATP. Thus, it is thought that Hsp70-IPEK1 can help to find the correct conformation of substrate proteins, especially when coordinated with Hsp40 and ATP.

Luciferase Aggregation Experiments

Luciferase aggregation experiment was performed in the absence and presence of different Hsps (Hsp40 and Hsp100) and ATP presence/absence. The luciferase aggregation was measured with light scattering. The aggregation degree is proportional to intensity of the scattered light. Denatured luciferase formed aggregates however these aggregates dissolved in different combinations of Hsps and ATP (Figure 8). According to the results of luciferase aggregation experiments, Hsp70-IPEK1 protein with ATP and without ATP dissolved aggregate to a certain degree. When Hsp40 and Hsp100 were added to reaction mixture in the presence of ATP, it was observed that dissolution of the aggregates was suddenly increased.

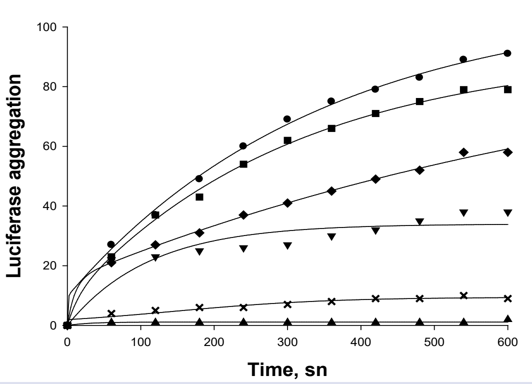

Figure 8. Luciferase aggregation prevention by Hsp complexes in the presence of ATP. Hsp70 alone (●), Hsp70IPEK1 + Hsp40 (■), Hsp70 + Hsp40 + Hsp100 (◊). Addition of Hsp40 and Hsp100 help Hsp70 to solubilize more aggregates and increase the stability by 10 °C

Discussion

Hsp70s are an important family of chaperones and are expressed in response to stress conditions. Hsp70s are involved in major cellular processes. They bind to their protein substrates to prevent non-productive interactions caused by aggregation and protein folding [9]. Also, Hsp70s help the folding of newly synthesized proteins, the subcellular transport of proteins, the degradation of misfolded proteins, assembly and disassembly of macromolecular complexes and in gene induction and apoptosis [9,13]. In folding mechanism of the proteins, Hsp70s interact with other chaperones such as Hsp40s, Hsp100s and nucleotide exchange factors. Many studies have been carried out on structural, biochemical and molecular functions of Hsp70s. However, knowledge about chaperone activity of Hsp70s is still unclear, especially the interaction between Hsp70s and their cofactors [8]. Recent studies revealed that misfolded and aggregate proteins lead to a range of diseases including cancer and neurodegeneration diseases [4,13,14]. Understanding of molecular mechanism in Hsp70s may contributed to the prevention and treatment of various diseases.

Hsps have been characterized in protozoan parasites such as Leishmania, Toxoplasma and Plasmodium [2,14]. These parasites can infect humans and cause serious diseases. Hsps have a critical role in these pathogenic protozoa. Also, *T. gondii* has improved a stress response mechanism by using Hsps to protect itself when exposed to stress. For example, *T. gondii* Hsp90 gene has been described in invasion and growth of the parasite in vitro. Moreover, it has demonstrated that this gene associates with virulence in BALB/c mice *in vivo* [2].

T. gondii leads to toxoplasmosis that is a parasitic disease. During toxoplasmosis, Hsp70s are an important control mechanism in the host immune system. Hsp70s obtained from infected cells by *T. gondii* cause a serious decrease of parasite burden [16]. Nucleotide sequences of Hsp70-IPEK1 isolated from *T. gondii* were transformed to three-dimensional protein structures by simulation. Both these structures and nucleotide sequences exhibited similar with homologous Hsps. Characteristic Hsp70 motifs indicate that this protein family are conserved among species as mentioned in the literature [3,12,17].

In this study, some physicochemical properties of Hsp70-IPEK1 were investigated by using *in silico* analysis and thus some structural characteristics of IPEK1 protein was identified such as solubility and stability. On the other hand, the roles of IPEK1 in folding and aggregation of protein were determined. Hsp70s help the proper folding of protein by ATP regulated cycles of substrate binding and release in cells [18]. This protein functions together with other co-chaperones to prevent the protein aggregation and to provide optimum protein folding [9,18]. Similarly, Hsp70-IPEK1 protein isolated from *T. gondii* assisted to protein folding and increased the solubility of the aggregates with Hsp40 and Hsp100 in the presence of ATP.

FTIR experiments, fluorescence experiments and quenching analysis were performed in the presence and absence of nucleotide to determine the conformational changes in secondary structures of *T. gondii* Hsp70. According to results of these experiments, Hsp70-IPEK1 protein exhibited conformational changes in the presence of nucleotide. Understanding of biochemical properties of Hsps is crucial to use it as a potential therapeutic target. It is thought that Hsp70 upregulated in most cancers is interacted with constituents of the apoptotic and the pro-survival pathway and thus conferring a survival advantage [18]. Hsp70s have some superior biochemical properties such as increased ATP hydrolysis [12]. However, most biochemical properties of Hsp70s are not fully known due to the crystal structure of Hsp70s is yet unavailable.

Conclusions

Hsp70-IPEK1 protein obtained from *T. gondii* were isolated and characterized for better understanding of Hsp70 mechanism. Hsp70-IPEK1 exhibited similar function with homologous Hsp70 proteins found in other organisms. Hsp70 proteins assist cellular proteostasis such as protein folding and protein aggregation. Therefore, characterization of Hsp70s, major players in cells, is essential for future studies (e.g. biotechnology and pharmaceutical areas) and results of the present work have the potential to contribute to the current literature.

Conflicts of interest

There is no conflict of interest in this study.

Acknowledgements

I would like to thank Professor Yusuf Tutar for his expert advice and for the laboratory equipment he provided for our experiments.

References

[1] Coşkun K.A., Tutar Y., Isolation and characterization of Heat Shock Protein 100-Batu1 from *Toxoplasma gondii* RH strain, *Exp. Parasitol*, 153 (2015) 91–97.

[2] Sun H., Zhuo X., Zhao X., et al., The heat shock protein 90 of *Toxoplasma gondii* is essential for invasion of host cells and tachyzoite growth, *Parasite*, 24 (2017) 1–11.

[3] Ashwinder K., Kho M.T., Chee P.M., et al., Targeting Heat Shock Proteins 60 and 70 of *Toxoplasma gondii* as a Potential Drug Target: In Silico Approach, *Interdiscip. Sci. Comput. Life Sci.*, 8 (2015) 374–387.

[4] de Barros, R. A. M., Torrecilhas, A. C., Marciano, M. A. M., Mazuz, M. L., Pereira-Chioccola, V. L., & Fux, B. Toxoplasmosis in human and animals around the world. Diagnosis and perspectives in the one health approach. *Acta tropica*, (2022) 231, 106432.

[5] Angel, S. O., Vanagas, L., & Alonso, A. M. (2024). Mechanisms of adaptation and evolution in Toxoplasma gondii, *Molecular and Biochemical Parasitology*, (2024), 258, 111615.

[6] Tutar L., Tutar Y., Heat Shock Proteins; An Overview, *Curr. Pharm. Biotechnol.*, 11 (2010) 216–222.

[7] Sherman M.Y., Gabai V.L., Hsp70 in cancer: Back to the future, *Oncogene*, (2014) 1–9.

[8] Tran N.T., Jakovlic I., Wang W.M., In silico characterisation, homology modelling and structure-based functional annotation of blunt snout bream (Megalobrama amblycephala) Hsp70 and Hsc70 proteins, *J. Anim. Sci. Technol.*, 57 (2015) 1–9.

[9] Sharma D., Masison D.C., Hsp70 structure, function, regulation and influence on yeast prions, *Protein Pept. Lett.*, 16 (2009) 571–81.

[10] Tutar Y., Okan Ş., Heat shock protein 70 purification and characterization from *Cyprinion macrastomus* and *Garra rufa* obtusa, *J. Therm. Biol.*, 37 (2012) 95–99.

[11] Guruprasad K., Reddy B.V.B., Pandit M.W., Correlation between stability of a protein and its dipeptide composition: a novel approach for predicting in vivo stability of a protein from its primary sequence, *Protein Eng. Des. Sel.*, 4 (1990) 155–161.

[12] Islam M.S., Shahik S.M., Sohel M., et al., In Silico Structural and Functional Annotation of Hypothetical Proteins of Vibrio cholerae O139, *Genomics Inform.*, 13 (2015) 53–59.

[13] Evans C.G., Chang L., Gestwick J.E., Heat Shock Protein 70 (Hsp70) as an Emerging Drug Target, *J. Med. Chem*., 53 (2010) 4585–4602.

[14] Tutar L., Is Hsp70 a folder or a modulator protein?, *Basic Clin. Sci.*, (2010) 18–24.

[15] Pallavi R., Roy N., Nageshan R.K., et al., Heat Shock Protein 90 as a Drug Target against Protozoan Infections, *J. Biol. Chem.*, 285 (2010) 37964–37975.

[16] Mammari N., Halabi, Mohamad Adnan Yaacoub S., Chlala H., Dardé, Marie-Laure Courtioux B., *Toxoplasma gondii* Modulates the Host Cell Responses: An Overview of Apoptosis Pathways, *Biomed. Res. Int.*, (2019) 1–10.

[17] Metzger D.C.H., Hemmer-Hansen J., Schulte P.M., Conserved structure and expression of Hsp70 paralogs in teleost fishes, *Comp. Biochem. Physiol. Part D Genomics Proteomics*, 18 (2016) 10–20.

[18] Luengo T.M., Mayer M.P., Rüdiger S.G.D., The Hsp70 – Hsp90 Chaperone Cascade in Protein Folding, *Trends Cell Biol.*, (2018) 1–14.

[19] Mayer M.P., Bukau B., Hsp70 chaperones : Cellular functions and molecular mechanism, *Cell Mol. Life Sci*., 62 (2005) 670–684.

Cumhuriyet Sci. J., 45(3) (2024) 503-509
DOI: https://doi.org/10.17776/csj.1449622

Cumhuriyet Science Journal

| csj.cumhuriyet.edu.tr | Founded: 2002 ISSN: 2587-2680 e-ISSN: 2587-246X Publisher: Sivas Cumhuriyet University

Design, Synthesis and Cholinesterase Inhibitory Activity of Novel 1,3,4-Thiadiazole Derivatives

Betül Kaya[1,a,*]**,Ulviye Acar Çevik**[2,b]**,Bilge Çiftçi**[3,c]**,Mesut Işık**[4,d]**, Zafer Asım Kaplancikli**[2,5,e]**, Namık Kılınç**[6,f]**, Şükrü Beydemir**[7,g]

[1] *Department of Pharmaceutical Chemistry, Faculty of Pharmacy, Zonguldak Bulent Ecevit University, 67600 Zonguldak, Türkiye*
[2] *Department of Pharmaceutical Chemistry, Faculty of Pharmacy, Anadolu University, 26470 Eskişehir, Türkiye*
[3] *Vocational School of Health Services, Bilecik Şeyh Edebali University, 11230, Bilecik, Türkiye*
[4] *Department of Bioengineering, Faculty of Engineering, Bilecik Şeyh Edebali University, 11230, Bilecik, Türkiye*
[5] *The Rectorate of Bilecik Şeyh Edebali University, 11230, Bilecik, Türkiye*
[6] *Department of Medical Services and Techniques, Vocational School of Health Services, Igdir University, Igdir, Türkiye*
[7] *Department of Biochemistry, Faculty of Pharmacy, Anadolu University, 26470 Eskişehir, Türkiye*
**Corresponding author*

Research Article

History
Received: 11/03/2024
Accepted: 22/07/2024

ABSTRACT

Inhibition of the cholinesterases (AChE and BChE) plays a pivotal role in the symptomatic treatment of Alzheimer's disease. The present study reports the synthesis and anticholinesterase activity of five novel thiadiazole analogs in search of anti-Alzheimer agents. The structures of the newly synthesized compounds were characterized using ^{1}H NMR, ^{13}C NMR and HRMS. Tested compounds inhibited acetylcholinesterase (AChE) and butyrylcholinesterase (BChE) enzymes with IC_{50} values in the range of 8.250-20.382 µM and 14.143-0.986 µM, respectively. *N*-(4-Chlorophenyl)-2-[(5-(allylamino)-1,3,4-thiadiazol-2-yl)thio]-*N*-(3-nitrobenzyl)acetamide (6e) was determined as the most potent inhibitor against both tested enzymes when compared with standard drug tacrine. Molecular docking study was carried out to reveal the binding interactions between compound 6e and the active site of AChE.

Keywords: Acetylcholinesterase, Butyrylcholinesterase, Cholinesterase inhibitors, 1,3,4-thiadiazole, Alzheimer's disease.

[a] *betul.kaya@beun.edu.tr* *https://orcid.org/0000-0002-1713-9485*
[c] *bilge.ciftci@bilecik.edu.tr* *https://orcid.org/0000-0002-4153-1209*
[e] *zakaplan@anadolu.edu.tr* *https://orcid.org/0000-0003-2252-0923*
[g] *sukrubeydemir@anadolu.edu.tr* *https://orcid.org/0000-0003-3667-6902*
[b] *uacar@anadolu.edu.tr* *https://orcid.org/0000-0003-1879-1034*
[d] *mesut.isik@bilecik.edu.tr* *https://orcid.org/0000-0002-4677-8104*
[f] *namik.kilinc@igdir.edu.tr* *https://orcid.org/0000-0002-9102-1370*

Introduction

Alzheimer's disease (AD) is a common type of neurodegenerative brain disease that affects over 55 million people globally and people with AD is estimated to increase to 78 million by 2030 [1]. Acetylcholine (ACh) is critical for cognitive processes and, in the brain of people suffering from AD, ACh is decreased, cholinergic pathway is noticed to be irreversibly impaired, resulting in cognitive dysfunction. The therapeutic strategies in the treatment of AD are mainly focused on reduced cholinergic neurotransmission and β-amyloid protein aggregation that leads to progressive loss of structure and/or function of neurons [2,3]. Cholinesterase inhibitors exert their activity by inhibiting acetylcholinesterase (AChE) and butyrylcholinesterase (BChE) which are both types of cholinesterase enzymes, eventually increase the concentration of the ACh in the brain of AD patients. Currently licensed drugs used for AD are tacrine, donepezil, rivastigmine and galantamine. However, their effectiveness is often limited by the appearance of central and peripheral side effects. For instance, tacrine has been withdrawn from the market due to hepatotoxicity [4,5].

Thiadiazole nucleus is a well-known five-membered heterocyclic scaffold in medicinal chemistry. The thiadiazole moiety functions as a "two-electron donor system" and "hydrogen-binding domain, which provide the thiadiazole ring its biological activity [6]. The sulfur atom also contributes lipo-solubility, resulting in more lipophilic analogues with enhanced blood–brain barrier (BBB) permeability. Thiadiazole ring has four isomers, 1,2,3-thiadiazole, 1,2,4-thiadiazole, 1,2,5-thiadiazole, and 1,3,4-thiadiazole, depending on the positions of heteroatoms. 1,3,4-Thiadiazole is the main isomer that has a wide range of pharmacological effects [7]. There are currently numerous marketed pharmaceutical products containing thiadiazole scaffold including acetazolamide, methazolamide (carbonic anhydrase inhibitors), megazole (antitrypanosomal), sulfamethizole (anti-microbial), cefazolin, cefazedone (antibiotics) and timolol (antihypertensive) [8,9].

Among above-mentioned thiadiazoles, 2-amino-1,3,4-thiadiazole derivatives were studied for their antibacterial, antifungal, antitubercular, antiparasitic activities, antidepressant, anticancer and cholinesterase inhibitory activities [10-15]. The activity of 1,3,4-thiadiazoles is probably due to the presence of =N–C–S moiety [16]. In view of these facts, in this paper, we synthesized new series of 2-subsitutedamino-1,3,4-

thiadiazole derivatives and evaluated their *in vitro* cholinesterase inhibitory activity.

Materials and Methods

Chemistry

All Chemicals used in the synthesis pathway of the compounds were purchased from Sigma-Aldrich (Sigma-Aldrich Corp., St. Louis, MO, USA) or Merck (Merck KGaA, Darmstadt, Germany) chemical companies and were used without further chemical purifications. Melting points (MP) were determined by an automatic melting point apparatus (MP90, Mettler-Toledo, OH, USA). The NMR spectra (^{1}H and ^{13}C) were recorded in DMSO-d_6 by a Bruker digital FT-NMR spectrometer (Bruker Bioscience, MA, USA) at 300 MHz and 75 MHz, respectively. HRMS studies were performed on an LCMS-IT-TOF system (Shimadzu, Tokyo, Japan). Chemical purities of the compounds were checked by classical TLC applications performed on silica gel 60 F254 (Merck KGaA, Darmstadt, Germany).

Synthesis of 4-chloro-*N*-(3-nitrobenzylidene)aniline (1) [17]

Yield 69%. 4-Chloroaniline (33 mmol, 4.22 g), 3-nitrobenzaldehyde (33 mmol, 5 g) and catalytic amount of glacial acetic acid (0.5 ml) were dissolved in ethanol (100 ml) and refluxed for 9 h. After TLC screening, the mixture was cooled, the product was filtered and the crude product was recrystallized from ethanol.

Synthesis of 4-chloro-*N*-(3-nitrobenzyl)aniline (2) [17]

Yield 70%. Compound 1 (27 mmol, 7.1 g) was dissolved in methanol (150 mL) and sodium borohydride was added in four portions (4×0.5 g) 15 min intervals. After addition, reaction mixture was allowed to stir for 1 h at room temperature. The solvent was evaporated and the crude product was washed with water, dried and recrystallized from ethanol.

Synthesis of 2-chloro-*N*-(4-chlorophenyl)-N-(3-nitrobenzyl)acetamide (3) [17]

Yield 67%. To a mixture of compound 2 (24 mmol, 6.2 g) and triethylamine (29 mmol, 4.04 mL) in tetrahydrofuran (100 mL), chloroacetyl chloride (29 mmol, 2.31 mL) was added dropwise with stirring at 0–5 °C. The reaction was mixed for one hour at room temperature, after dripping of $ClCH_2COCl$. To gain product, tetrahydrofuran was evaporated. The product was recrystallized from ethanol, after washing with water.

Synthesis of 4-substituted thiosemicarbazides (4a-4e) [18]

Yield 72%. Various substituted isothiocyanates (20 mmol) and hydrazine hydrate (40 mmol) were dissolved in ethanol (50 mL) and stirred at room temperature for 4 h. The precipitated compound filtered and crystallized from ethanol.

Synthesis of 5-substituted amino-1,3,4-thiadiazole-2(3*H*)-thiones (5a-5e) [18]

Yield 65%. To a solution of 4-substitutedthiosemicarbazide derivative (4a-4e) (23 mmol) in ethanol (80 mL), carbon disulfide (27 mmol, 1.6 mL) and potassium hydroxide (27 mmol) were added and the mixture was refluxed for 12 h. The solution was cooled and acidified to pH 4–5 with a hydrochloric acid solution and crystallized from ethanol.

Synthesis of *N*-(4-chlorophenyl)-2-[(5-substitutedamino-1,3,4-thiadiazol-2-yl)thio]-*N*-(3-nitrobenzyl)acetamide derivatives (6a-6e) [18]

Yield 77%. A mixture of appropriate 5-substitutedamino-1,3,4-thiadiazole-2(3*H*)-thione derivative (5a-5e) (4 mmol), compound 3 (4 mmol) and potassium carbonate (5 mmol, 0.66 g) were stirred was stirred at room temperature for 9 h in acetone (40 mL). After that, acetone was evaporated, the residue was washed and crystallized from ethanol.

N-(4-Chlororophenyl)-2-[(5-(methylamino)-1,3,4-thiadiazol-2-yl)thio]-N-(3-nitrobenzyl) acetamide (6a): Yield 77%. M.P.= 145.9 °C. ^{1}H NMR (300 MHz, DMSO-d_6, ppm) δ 2.83 (3H, s, CH_3), 3.91 (2H, s, CO-CH_2), 5.01 (2H, s, N-CH_2), 7.33 (2H, d, *J*= 8.6 Hz, Ar-H), 7.46 (2H, d, *J*= 8.6 Hz, Ar-H), 7.46 (1H, t, *J*= 7.8 Hz, Ar-H), 7.67-7.74 (2H, m, Ar-H), 8.08-8.13 (2H, m, Ar-H and NH). ^{13}C NMR (75 MHz, DMSO-d_6, ppm) δ 31.53, 38.33, 52.17, 122.81, 123.22, 130.19, 130.38, 130.53, 133.36, 135.13, 139.68, 140.31, 148.24, 149.27, 167.47, 170.77. HRMS (*m/z*): [M+H]$^+$ calcd for $C_{18}H_{16}ClN_5O_3S_2$: 450.0456; found 450.0434.

N-(4-Chlororophenyl)-2-[(5-(ethylamino)-1,3,4-thiadiazol-2-yl)thio]-N-(3-nitrobenzyl) acetamide (6b): Yield 67%. M.P.= 161.5 °C. ^{1}H NMR (300 MHz, DMSO-d_6, ppm) δ 1.14 (3H, t, *J*= 7.2 Hz, CH_2-$C\underline{H}_3$), 3.19-3.28 (2H, m, $C\underline{H}_2$-CH_3), 3.91 (2H, s, CO-CH_2), 5.01 (2H, s, N-CH_2), 7.33 (2H, d, *J*= 8.6 Hz, Ar-H), 7.47 (2H, d, *J*= 8.6 Hz, Ar-H), 7.59 (1H, t, *J*= 7.8 Hz, Ar-H), 7.69 (1H, d, *J*= 7.6 Hz, Ar-H), 7.76 (1H, t, *J*= 5.2 Hz, Ar-H), 8.08-8.13 (2H, m, Ar-H and NH). ^{13}C NMR (75 MHz, DMSO-d_6, ppm) δ 14.66, 38.32, 39.86, 52.17, 122.81, 123.21, 130.19 (2C), 130.38, 130.53 (2C), 133.36, 135.13, 139.68, 140.31, 148.24, 149.12, 167.48, 169.83. HRMS (*m/z*): [M+H]$^+$ calcd for $C_{19}H_{18}ClN_5O_3S_2$: 464.0612; found 464.0606.

N-(4-Chlorophenyl)-2-[(5-(propylamino)-1,3,4-thiadiazol-2-yl)thio]-N-(3-nitrobenzyl) acetamide (6c): Yield 72%. M.P.= 144.0 °C. ^{1}H NMR (300 MHz, DMSO-d_6, ppm) δ 0.88 (3H, t, *J*= 7.4 Hz, CH_3), 1.48-1.60 (2H, m, CH_3-$C\underline{H}_2$-CH_2-), 3.14-3.21 (2H, m, CH_3-CH_2-$C\underline{H}_2$-), 3.91 (2H, s, CO-CH_2), 5.01 (2H, s, N-CH_2), 7.33 (2H, d, *J*= 8.6 Hz, Ar-H), 7.46 (2H, d, *J*= 8.6 Hz, Ar-H), 7.59 (1H, t, *J*= 7.8 Hz, Ar-H), 7.69 (1H, d, *J*= 7.7 Hz, Ar-H), 7.79 (1H, t, *J*= 5.5 Hz, Ar-H), 8.08-8.13 (2H, m, Ar-H and NH). ^{13}C NMR (75 MHz, DMSO-d_6, ppm) δ 11.82, 22.22, 38.32, 46.84, 52.18, 122.80, 123.21, 130.18 (2C), 130.37, 130.52 (2C), 133.36, 135.13, 139.69, 140.31, 148.24, 148.99, 167.49, 170.06. HRMS (*m/z*): $[M+H]^+$ calcd for $C_{20}H_{20}ClN_5O_3S_2$: 478.0769; found 478.0749.

N-(4-Chlorophenyl)-2-[(5-(isopropylamino)-1,3,4-thiadiazol-2-yl)thio]-N-(3-nitro benzyl)acetamide (6d): Yield 69%. M.P.= 118.9 °C. ^{1}H NMR (300 MHz, DMSO-*d*$_6$, ppm) δ 1.15 (6H, d, *J*= 6.5 Hz, $2CH_3$), 3.68-3.79 (1H, m, CH), 3.91 (2H, s, CO-CH_2), 5.01 (2H, s, N-CH_2), 7.33 (2H, d, *J*= 8.6 Hz, Ar-H), 7.46 (2H, d, *J*= 8.6 Hz, Ar-H), 7.59 (1H, t, *J*= 7.9 Hz, Ar-H), 7.70 (2H, t, *J*= 5.0 Hz, Ar-H), 8.08-8.13 (2H, m, Ar-H and NH). ^{13}C NMR (75 MHz, DMSO-*d*$_6$, ppm) δ 22.57 (2C), 38.32, 46.98, 52.17, 122.81, 123.21, 130.18 (2C), 130.38, 130.53 (2C), 133.36, 135.13, 139.68, 140.30, 148.24, 148.97, 167.49, 169.01. HRMS (*m/z*): $[M+H]^+$ calcd for $C_{20}H_{20}ClN_5O_3S_2$: 478.0769; found 478.0749.

N-(4-Chlorophenyl)-2-[(5-(allylamino)-1,3,4-thiadiazol-2-yl)thio]-N-(3-nitrobenzyl) acetamide (6e): Yield 75%. M.P.= 130.2 °C. ^{1}H NMR (300 MHz, DMSO-*d*$_6$, ppm) δ 3.86-3.92 (4H, m, CH_2=CH-C$\underline{H_2}$ and CO-CH_2), 5.01 (2H, s, N-CH_2), 5.10-5.25 (2H, m, C$\underline{H}_2$=CH-CH_2), 5.82-5.95 (1H, m, CH_2=C$\underline{H}$-CH_2), 7.33 (2H, d, *J*= 8.7 Hz, Ar-H), 7.46 (2H, d, *J*= 8.6 Hz, Ar-H), 7.59 (1H, t, *J*= 7.7 Hz, Ar-H), 7.69 (1H, d, *J*= 7.5 Hz, Ar-H), 7.95 (1H, t, *J*= 5.6 Hz, Ar-H), 8.08-8.12 (2H, m, Ar-H and NH). ^{13}C NMR (75 MHz, DMSO-*d*$_6$, ppm) δ 38.28, 47.12, 52.19, 116.65, 122.80, 123.21, 130.19 (2C), 130.38, 130.52 (2C), 133.37, 134.75, 135.13, 139.67, 140.31, 148.24, 149.71, 167.46, 169.82. HRMS (*m/z*): $[M+H]^+$ calcd for $C_{20}H_{18}ClN_5O_3S_2$: 476.0612; found 476.0604.

Cholinesterase Inhibitory Activity

The anticholinesterase (AChE and BChE) activities were assayed by a modified version of the Ellman method.The inhibitory effect of novel 2-subsitutedamino-1,3,4-thiadiazole derivatives (6a-6e) on AChE (from electric eel; Sigma) and BChE (from equine serum) was investigated using acetylthiocholine iodide (ATChI) and butrylcholine iodide (BChI) as substrates at 37°C. Stock solutions of the compounds synthesized as inhibitors were prepared in 20 % DMSO. The inhibition effects of novel 2-subsitutedamino-1,3,4-thiadiazole derivatives (6a-6e) was determined in the presence of at least five different inhibitor concentrations, usually in the 10^{-2}-10^2 µM range, to obtain between 0% and 100% inhibition of cholinesterase activity. Enzyme solution (5.32×10^{-3} U, 50 µL) and inhibitor solution (20 µL) were added to a cuvette containing Tris–HCl (100 µL, 1 M; pH= 8.0). After 5 min incubation, DTNB solution (0.01 M, 100 µL) and ATChI/BChI (0.050 M, 50 µL) were added. Immediately after brief stirring, 3 replicate measurements were monitored spectrophotometrically at 412 nm [19-22]. The IC_{50} values of the derivatives were calculated from Activity (%)-[Ligand] graphs for derivatives according to our previous studies [23,24].

Molecular Docking

In silico investigations were conducted to study the interactions between the compound 6e and the AChE and BChE enzymes using molecular docking simulations, as described in our earlier research [25-27]. These simulations utilized Maestro 13.9 from the Schrödinger Molecular Modeling Suite [28]. The crystal structures of AChE and BChE, with PDB IDs 4TVK and 5NN0 respectively, were sourced from the RCSB Protein Data Bank. The receptors were prepared at physiological pH using the Protein Preparation Wizard [29], followed by optimization and minimization with the OPLS4 force field. A receptor grid was established around the natural ligands within the protein structures. Ligands were prepared and protonated at pH 7.0 ± 2.0 using the LigPrep module.

Results and Discussions

Chemistry

The target compounds were prepared as illustrated in Scheme 1. Firstly, 3-nitrobenzaldehyde and 4-chloroaniline was reacted in the presence of glacial acetic acid as a catalyst to afford compound 1, which further reacted with sodium borohydride for the reduction of imine bond to synthesize compound 2. Subsequently, compound 3 was obtained via the reaction between compound 2 and chloroacetyl chloride in the presence of triethylamine. Various substituted isothiocyanates were reacted with hydrazine hydrate to prepare compounds 4a-4e. In the next step, intermediate compounds 4a-4e were subjected to the ring closure reaction with carbon disulfide to give 5-substitutedamino-1,3,4-thiadiazole-2(3*H*)-thione derivatives (5a-5e). In the final step, compounds 5a-5e were treated with compound 3 in acetone in the presence of potassium carbonate to yield target compounds 6a-6e.

The structures of the synthesized analogues were confirmed using NMR and MS spectral analysis. In the ^{1}H NMR spectra, CH_2 protons bound to nitrogen and carbonyl group were observed at 5.01 ppm and at between 3.91-3.92 ppm, respectively. The rest aliphatic protons and all the aromatic protons were assigned at their expected area. In the ^{13}C NMR spectra, a peak at between 38.28-38.33 ppm was detected due to the signal of CH_2 carbon bound to carbonyl group. The signal belonging to the N-CH_2 carbon was determined at between 52.17-52.19 ppm. The rest aliphatic and aromatic carbons were assigned at their expected regions. In the HRMS spectra of final compounds (6a-6e), the M+1 peaks were observed in accordance with their molecular formula.

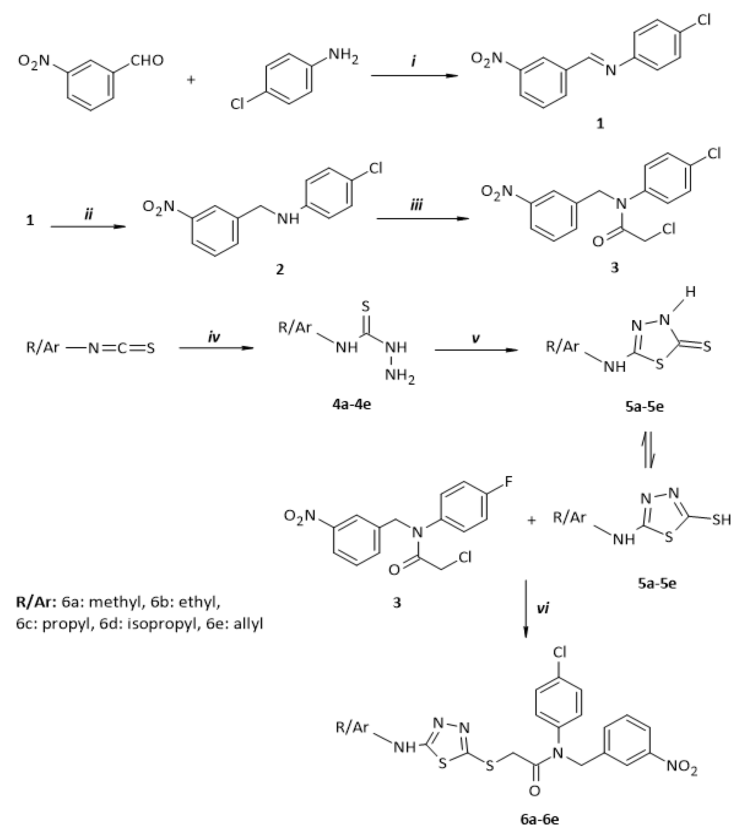

Scheme 1. The synthetic pathway of the compounds (6a-6e). Reagents and conditions; i: acetic acid, ethanol, reflux, 9 h; ii: sodium borohydride, methanol, r.t, 11 h; iii: Chloroacetyl chloride, triethylamine, tetrahydrofuran, ice-bath, 5 h; iv: hydrazine hydrate, ethanol, r.t., 4 h; v: (1) carbon disulfide/potassium hydroxide, ethanol, reflux, 12 h; (2) hydrochloric acid, pH 4–5; vi: potassium carbonate, acetone, r.t., 9 h

Biological Activity

The aim of this study was to investigate the *in vitro* effects of newly synthesized derivatives (referred to as 6a-6e) on cholinesterase enzymes. The inhibitory activities of the derivatives against key metabolic enzymes such as AChE and BChE were determined and analyzed in comparison with the known inhibitory effect of tacrine. The IC_{50} values of the derivatives were determined from Activity (%)-[Ligand] graphs for derivatives (Figure S1 and Figure S2). The inhibition data of IC_{50} values found to evaluate the potential inhibitory effects of all series of the new derivatives are presented in Table 1. The synthesized derivatives exhibited inhibitor activity in micromolar levels against AChE and BChE with the IC_{50} values in the range of 8.250-20.382 µM and 14.143-0.986 µM, respectively. The AChE inhibitory activities for the novel compounds reduced in the order of 6e (allyl-substituted) > 6d (isopropyl-substituted) > 6c (propyl-substituted) > 6b (ethyl-substituted) > 6a (methyl-substituted), as well as for BChE; 6e (allyl-substituted) > 6c (propyl-substituted) > 6d (isopropyl-substituted) > 6a (methyl-substituted) > 6b (ethyl-substituted). The 6e derivative shows a more selective inhibition potential for both cholinesterase enzymes, while the effect of compounds 6a and 6b is lower than the others. The allyl-substituted derivative 6e (IC_{50} for AChE and BChE; 8.250 µM and 0.986 µM, respectively) was identified as the most potent cholinesterase inhibitor in the series (6a-6e).

Although the inhibitory potential of the series was lower than the inhibitory potential of the standard tacrine (IC50 for AChE and BChE; 0.145 µM and 0.208 nM), they showed a more effective inhibitory effect than many compounds with similar structures given in the literature [30]. In a study, indole-based thiadiazole derivatives (1-18) were synthesized and their inhibition effects against AChE and BChE were evaluated. The IC_{50} values of the synthesized analogues against these enzymes ranging between 0.17 ± 0.05 to 33.10 ± 0.6 µM against AChE and 0.30 ± 0.1 to 37.60 ± 0.6 µM against BChE [31]. In a separate investigation, a novel set of benzimidazole-based thiadiazole hybrid analogues was synthesized, demonstrating diverse inhibitory capabilities against targeted enzymes AChE and BChE. The IC_{50} values ranged from 1.32 ± 0.10 µM to 19.26 ± 0.60 µM for AChE and from 1.94 ± 0.10 µM to 21.33 ± 0.70 µM for BChE [32]. The allyl-substituted derivative 6e has much more effective inhibitory potential than many thiadiazoles synthesized in many series in the literature and shown to have inhibitory effect on cholinesterase.

Table 1. IC_{50} values of novel 2-subsitutedamino-1,3,4-thiadiazole derivatives (6a-6e) against AChE and BChE enzymes.

Compound	AChE		BChE	
	IC_{50} (µM)	R^2	IC_{50} (µM)	R^2
6a	20.382	0.968	10.520	0.979
6b	17.769	0.974	14.143	0.987
6c	16.902	0.973	4.846	0.939
6d	13.075	0.963	5.331	0.983
6e	8.250	0.963	0.986	0.944
Tacrine	0.145	0.962	0.208	0.966

Molecular Docking

We employed the Extra Precision (XP) molecular docking method to perform detailed molecular docking studies with the 6e compound to understand the protein-ligand interactions. The 6e compound, recognized for its strong inhibitory effects on AChE and BChE enzymes, was analyzed using the XP docking protocol. Table 2 summarizes the docking scores of 6e compound against the AChE and BChE enzymes.

Table 2. The docking scores of 6e compound against the AChE and BChE enzymes.

Compound	Docking Score (Kcal/mol)	
	AChE	BChE
6e	-8.301	-5.008

Molecular docking studies of the 6e compound, which demonstrated significant inhibitory effects against AChE and BChE enzymes in *in vitro* assays, revealed high docking scores for both enzymes. Specifically, the docking simulations showed scores of -8.301 kcal/mol for AChE and -5.008 kcal/mol for BChE (Table 2), indicating a strong binding affinity between the 6e compound and the enzymes. Within the active site of the AChE enzyme, compound 6e established a hydrogen bond with TYR121. Additionally, it participated in pi-pi interactions with TRP279 and TRP84, key components of the enzyme's active site. In the BChE enzyme's active site, compound 6e formed hydrogen bonds with THR120 and SER287 residues and engaged in a halogen bond interaction with TRP82 (Figure 1).

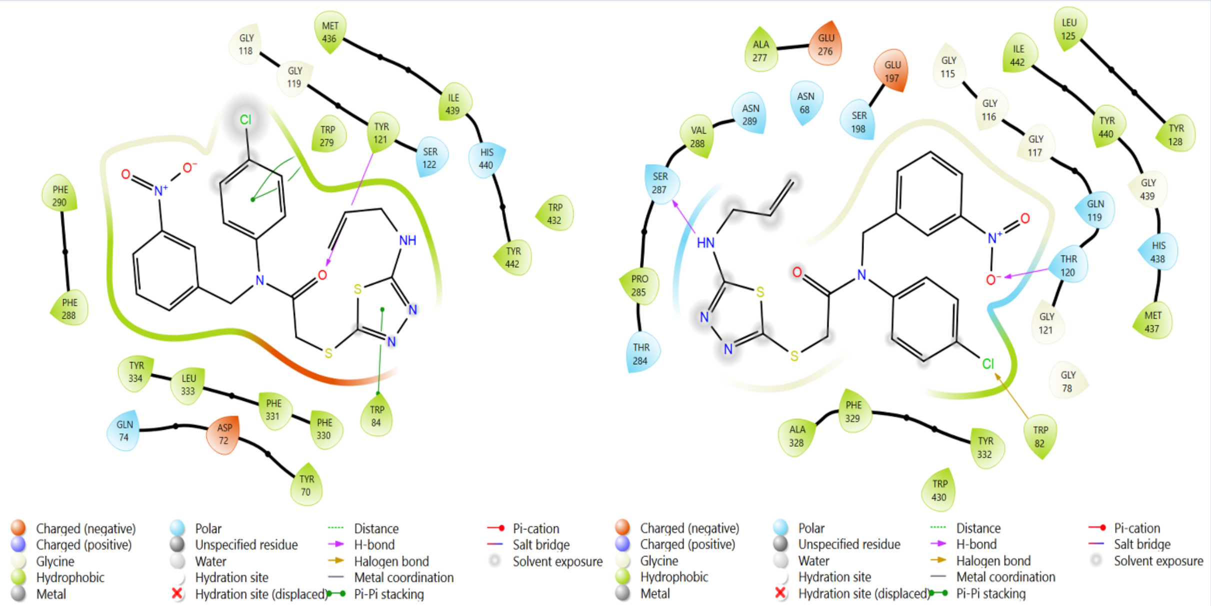

Figure 1. Ligand-enzyme interaction diagram of compound 6e with AChE (left) and BChE (right) enzymes.

Conclusions

In this study, a novel series of 2-subsitutedamino-1,3,4-thiadiazole derivatives (6a-6e) were synthesized as potential targets for treatment of AD. The structures were clarified by modern spectral techniques consisting of ^{1}H NMR, ^{13}CNMR and HRMS. Cholinesterase assay displayed that *N*-(4-chlorophenyl)-2-[(5-(allylamino)-1,3,4-thiadiazol-2-yl)thio]-*N*-(3-nitrobenzyl) acetamide (6e) was the most potent compounds against both AChE and BChE with the IC_{50} values of 8.250 µM and 0.986 µM, respectively. According to activity results, allyl group enhanced both acetylcholinesterase and butyrylcholinesterase inhibition. This might be due to the binding interactions between compound 6e and the active site of the cholinesterase enzymes.

Conflicts of interest

The authors declare that there are no conflicts of interest.

Acknowledgment

The authors thank the Anadolu University Faculty of Pharmacy Central Research Laboratory (MERLAB) for their support and contributions.

References

[1] Gauthier S., José P.R.-N., Morais A., Webster C., World Alzheimer Report 2021: Journey Through the Diagnosis of Dementia, (2021).

[2] Giacobini E., Cholinesterases: New Roles in Brain Function and in Alzheimer's Disease, *Neurochem. Res.*, 28 (2003) 515–522.

[3] Bala M., Ankalgi, A., Piplani P., Design, Synthesis and Pharmacological Evaluation of Disubstituted 1, 3, 4 Thiadiazoles Derivatives for The Treatment of Cognitive Dysfunction, *J. Mol. Struct*., 1291 (2023) 135951.

[4] Sharma D., Bansal K.K., Sharma A., Pathak M., Sharma P.C., A Brief Literature and Review of Patents on Thiazole-Related Derivatives, *Curr. Bioact. Compd*., 15 (2019) 304–315.

[5] Skrzypek A., Matysiak J., Niewiadomy A., Bajda M., Szymański, P., Synthesis and Biological Evaluation of 1, 3, 4-Thiadiazole Analogues as Novel AChE and BChE Inhibitors, *Eur. J. Med. Chem*., 62 (2013) 311-319.

[6] Atmaram U.A., Roopan S.M., Biological Activity of Oxadiazole and Thiadiazole Derivatives, *Appl. Microbiol.*, 106 (2022) 3489-3505.

[7] Sharma B., Verma A., Prajapati S., Sharma U.K., Synthetic Methods, Chemistry, and the Anticonvulsant Activity of Thiadiazoles, *Int. J. Med. Chem*., 2013 (2013) 348948.

[8] Hatami M., Basri Z., Sakhvidi B.K., Mortazavi M., Thiadiazole–A Promising Structure in Design and Development of Anti-Alzheimer Agents, *Int. Immunopharmacol*., 118 (2023) 110027.

[9] Serban, G., Future Prospects in The Treatment of Parasitic Diseases: 2-Amino-1, 3, 4-Thiadiazoles in Leishmaniasis, *Molecules*, 24 (2019) 1557.

[10] Serban G., Stanasel O., Serban E., Bota S., 2-Amino-1, 3, 4-Thiadiazole as A Potential Scaffold for Promising Antimicrobial Agents, *Drug Des. Devel. Ther*., 12 (2018) 1545-1566.

[11] Talath S, Gadad AK., Synthesis, Antibacterial and Antitubercular Activities of Some 7-[4-(5-Amino-[1,3,4]thiadiazole-2-sulfonyl)-piperazin-1-yl]fluoroquinolonic Derivatives, *Eur. J. Med. Chem*., 41 (2006) 918–924.

[12] Serban G., 2-Amino-1,3,4-thiadiazoles as Prospective Agents in Trypanosomiasis and Other Parasitoses, *Acta Pharm*., 70 (2020) 259–290.

[13] Clerici F., Pocar D., Guido M., Loche A., Perlini V., Brufani M., Synthesis of 2-Amino-5-sulfanyl-1,3,4-thiadiazole Derivatives and Evaluation of Their Antidepressant and Anxiolytic Activity, *J. Med. Chem*., 44 (2001) 931–936.

[14] Çevik U.A., Osmaniye D., Levent S., Sağlik B. N., Çavuşoğlu B. K., Özkay Y., Kaplanciklı Z.A., Synthesis and Characterization of A New Series of Thiadiazole Derivatives as Potential Anticancer Agents, *Heterocycl. Commun*., 26 (2020) 6-13.

[15] Al-Sharabi A.A., Evren A.E., Sağlık B.N., Yurttaş L., Synthesis, Characterization, Molecular Docking and Molecular Dynamics Simulations of Novel 2, 5-Disubstituted-1, 3, 4-Thiadiazole Derivatives as Potential Cholinesterase/Monoamine Oxidase Dual Inhibitors for Alzheimer's Disease, *J. Biomol. Struct. Dyn*, (2023) 1-19.

[16] Obakachi V.A., Kushwaha B., Kushwaha N.D., Mokoena S., Ganai A.M., Pathan T.K., Karpoormath R., Synthetic and Anticancer Activity Aspects of 1, 3, 4-Thiadiazole Containing Bioactive Molecules: A Concise Review, *J. Sulphur Chem*., 42 (2021) 670-691.

[17] Kaya B., Sağlık B.N., Levent S., Özkay Y., Kaplancıklı, Z.A., Synthesis of Some Novel 2-Substituted Benzothiazole Derivatives Containing Benzylamine Moiety as Monoamine Oxidase Inhibitory Agents, *J. Enzyme Inhib. Med. Chem.*, 31 (2016), 1654-1661.

[18] Sağlık B.N., Çavuşoğlu B.K., Çevik U.A., Osmaniye D., Levent S., Özkay Y., Kaplancıklı Z.A. Novel 1, 3, 4-thiadiazole compounds as potential MAO-A inhibitors–design, synthesis, biological evaluation and molecular modelling, *RSC Med. Chem*., 11 (2020) 1063-1074.

[19] Ellman G. L., Courtney K. D., Andres Jr V., Featherstone, R. M., A New and Rapid Colorimetric Determination of Acetylcholinesterase Activity, *Biochem. Pharmacol*., 7(2) (1961) 88-95.

[20] Mughal E. U., Sadiq A., Murtaza S., Rafique H., Zafar M. N., Riaz T., Khan B.A., Hameed A., Khan K. M., Synthesis, Structure–Activity Relationship and Molecular Docking Of 3-Oxoaurones And 3-Thioaurones As Acetylcholinesterase And Butyrylcholinesterase Inhibitors, *Bioorg. Med. Chem*., 25(1) (2017) 100-106.

[21] Işık M., Akocak S., Lolak N., Taslimi P., Türkeş C., Gülçin İ., Durgun M., Beydemir Ş., Synthesis, Characterization, Biological Evaluation, And in Silico Studies of Novel 1, 3-Diaryltriazene-Substituted Sulfathiazole Derivatives, *Arch. Pharm*., 353 (9) (2020) 2000102.

[22] Tarikoğulları A., Çizmecioğlu M., Saylam M., Parlar S., Alptüzün V., Soyer Z., Synthesis and Cholinesterase Inhibitory Activity of Some Phenylacetamide Derivatives Bearing 1H-Pyrazole or 1H-1, 2, 4-Triazole, *Marmara Pharm. J*., 20 (1) (2016) 21-27.

[23] Akocak S., Taslimi P., Lolak N., Işık M., Durgun M., Budak Y., Türkeş C., Gülçin İ., Beydemir Ş., Synthesis, Characterization, And Inhibition Study of Novel Substituted Phenylureido Sulfaguanidine Derivatives As α-Glycosidase and Cholinesterase Inhibitors, *Chem. Biodivers*., 18 (4) (2021) e2000958.

[24] Durgun M., Türkeş C., Işık M., Demir Y., Saklı A., Kuru A., Güzel A., Beydemir Ş., Akocak S., Osman S.M., AlOthman Z., Supuran C. T., Synthesis, Characterisation, Biological Evaluation and In Silico Studies of Sulphonamide Schiff Bases, *J. Enzyme Inhib. Med. Chem*., 35 (1) (2020) 950-962.

[25] Akıncıoğlu A., Göksu S., Naderi A., Akıncıoğlu H., Kılınç N., Gülçin İ., Cholinesterases, Carbonic Anhydrase Inhibitory Properties and in Silico Studies of Novel Substituted Benzylamines Derived from Dihydrochalcones, *Comput. Biol. Chem*., 94 (2021) 107565.

[26] Alım Z., Şirinzade H., Kılınç N., Dilek E., Süzen S., Assessing Indole Derivative Molecules as Dual Acetylcholinesterase and Butyrylcholinesterase Inhibitors through in vitro Inhibition and Molecular Modelling Studies, *J. Mol. Struct*., 1311 (2024) 138276.

[27] Gök N., Akıncıoğlu A., Erümit Binici E., Akıncıoğlu H., Kılınç N., Göksu S. Synthesis of Novel Sulfonamides with Anti-Alzheimer and Antioxidant Capacities, *Arch. Pharm*., 354(7) (2021) 2000496.

[28] Schrödinger Release 2024-1: Maestro, Schrödinger, 2024 LLC, New York, NY.

[29] Sastry G.M., Adzhigirey M., Day T., Annabhimoju R., Sherman W., Protein and Ligand Preparation: Parameters, Protocols, and Influence on Virtual Screening Enrichments, *J. Comput. Aided Mol. Des*., 27 (3) (2013) 221-234.

[30] Shah S. A. A., Ashraf M., Rehman J., Saleem R. S. Z., Synthesis, in Vitro And in Silico Studies Of S-Alkylated 5-(4-

Methoxyphenyl)-4-Phenyl-4H-1, 2, 4-Triazole-3-Thiols as Cholinesterase Inhibitors, *Pak. J. Pharm. Sci.*, 31(6) (2018) 2697-2708.

[31] Taha M., Rahim F., Uddin N., Khan I. U., Iqbal N., Salahuddin M., Farooq R.K., Gollapalli M., Khan K.M., Zafar A., Exploring Indole-Based-Thiadiazole Derivatives as Potent Acetylcholinesterase and Butyrylcholinesterase Enzyme Inhibitors, *Int. J. Biol. Macromol*., 188 (2021) 1025-1036.

[32] Hussain R., Ashraf M., Khan S., Rahim F., Rehman W., Taha M., Sardar A., Khan Y., Khan I., Shah S. A.A., Molecular Modeling, Synthesis, and in vitro Acetylcholinesterase and Butyrylcholinesterase Inhibitory Activities of Novel Benzimidazole-Bearing Thiadiazole Derivatives, *J. Mol. Struct*., 1295 (2024) 136582.

Cumhuriyet Sci. J., 45(3) (2024) 510-518
DOI: https://doi.org/10.17776/csj.1234262

Cumhuriyet Science Journal

| csj.cumhuriyet.edu.tr | Founded: 2002 ISSN: 2587-2680 e-ISSN: 2587-246X Publisher: Sivas Cumhuriyet University

Engineering Zinc Ion Hybrid Supercapacitor Performance of Graphitic Carbon Nitride Embedded Iron Oxide (Hematite)

Sevda Yetiman[1,a], Fatma Kılıç Dokan[2,b,*], Dilek Aker[1,3,c], Ahmet Turan Ozdemir [4,d], Mustafa Serdar Onses [1,5,e], Erkan Yılmaz [1,6,f], Ertugrul Sahmetlioglu[1,7,g]

[1] ERNAM-Erciyes University Nanotechnology Application and Research Center, Kayseri, 38039, Türkiye
[2] Department of Chemistry and Chemical Processing Technologies, Mustafa Çıkrıkcıoglu Vocational School, Kayseri University, Kayseri, Türkiye
[3] Department of Nuclear Technology and Radiation Safety, School of Health Services, Uskudar University, İstanbul, Türkiye
[4] Department of Electrical and Electronics Engineering, Erciyes University, 38039, Kayseri, Türkiye
[5] Department of Materials Science and Engineering, Faculty of Engineering, Erciyes University, 38039, Kayseri, Türkiye
[6] Technology Research & Application Center (TAUM), Erciyes University, Kayseri, 38039, Türkiye
[7] Department of Basic Sciences of Engineering, Kayseri University, 38039, Kayseri,Türkiye
**Corresponding author*

Research Article

History
Received: 02/12/2022
Accepted: 20/08/2024

ABSTRACT

Zinc-ion hybrid supercapacitors (ZHSC) gain high traction due to the prosperous unification of batteries and supercapacitors. Especially with graphene discovery nano carbonaceous materials have been the most investigated types in energy storage (ES) utilization including ZHSC. Among carbonaceous materials, graphitic carbon nitride (g-C_3N_4) possessing polymeric layers, quasi graphene arouses extreme interest due to its low-impact structure with economical yet chemical and mechanical stability inflicted by high nitrogen contents. Herein, we aim to examine the g-C_3N_4 doping effect on the electrochemical performance of hematite (α-Fe_2O_3) for ZHSC application. The assembled ZHSC device managed to reach the potential window of 2.0 volts with an efficient specific capacitance (Sc) of 280 F g^{-1} at a current density of 1 A g^{-1}. Moreover, the highest energy and power densities were 38.8 Wh kg^{-1} and 20 kW kg^{-1} respectively. With this remarkable efficiency, the α-Fe_2O_3/g-C_3N_4 composite material can be considered a promising cathode material for ZHSC.

Keywords: Graphitic carbon nitride, Iron (III) oxide, Zinc-ion hybrid supercapacitor.

[a] ytmnsevda@gmail.com https://orcid.org/0000-0002-8558-8688
[c] dilek.aker@uskudar.edu.tr https://orcid.org/0000-0003-3407-2750
[e] onses@erciyes.edu.tr https://orcid.org/0000-0001-6898-7700
[g] sahmetlioglu@kayseri.edu.tr https://orcid.org/0000-0002-7324-0385
[b] fatmakilic@kayseri.edu.tr https://orcid.org/0000-0002-5355-2904
[d] aturan@erciyes.edu.tr https://orcid.org/0000-0002-2796-1384
[f] erkanyilmaz@erciyes.edu.tr https://orcid.org/0000-0001-8962-3199

Introduction

Regarding the ongoing increase in energy consumption, it is crucial to diversify energy resources that are susceptible to depletion and to create efficient ES systems for future utilization. Supercapacitors (SCs) are among the most imminent electrochemical ES devices for future energy systems due to their almost unlimited lifespan,charge-discharge capability, and excellent power density. However, the low energy density (ED) of SCs is the main disadvantage limiting their utilization [1-14]. The specific capacity can be boosted by battery-like redox reactions, although, the aqueous electrolyte's voltage window is restricted by water decomposition. Therefore, improving the voltage window of aqueous SCs is crucial to obtaining high-performance SCs.

Recently, there has been a growing interest in metal ion hybrid devices, such as those containing lithium (Li), aluminium (Al), potassium (K), magnesium (Mg), and zinc (Zn) metals [3, 15, 16]. These devices combine a battery-like anode with a cathode that exhibits pseudocapacitive properties, such as metal oxides, sulfides, or conductive polymers. Zinc-ion hybrid batteries (ZIHB) and zinc-ion hybrid supercapacitors (ZHSC) are prominent ion hybrid systems that excel in terms of their high capacity (819 mAh g^{-1}) and low redox potential (Zn/Zn^{2+}) (0.78 V against Standard Hydrogen Electrode, SHE). These characteristics are crucial for improving the ED of ES devices. In addition, Zn is a more affordable and abundant metal (about 300 times greater than Li) that is also more reliable for usage in aqueous-based electrochemical systems compared to Li, Na, and K[11, 17].

Up to date, various materials have been utilized as cathode material for SCs and ZHSCs applications including especially carbon-based materials. Among carbonaceous materials, graphitic carbon nitride (g-C_3N_4) with polymeric layers, also known as quasi graphene, has piqued the interest of researchers due to its low-impact structure with no cost effect, as well as the chemical and mechanical durability conferred by high nitrogen content [18, 19].

For instance, Zhou et al. formed flower-shaped PANI/g-C_3N_4 hybrid material given the maximal Sc of 584.3 F g^{-1}, and the Sc degradation was just ~ 8 % after 1000 cycles [20]. Ragupathi et al. analyzed MnS electrochemical features with the g-C_3N_4 effect and reported the highest

Sc of 463.32 F g^{-1} at the scan rate of 10 mV s^{-1} with 98.6 % retention after 2000 cycles [21] .

Herein, we aim to utilize the synergic effect of α-Fe_2O_3 and g-C_3N_4 for high-performance ZHSC. In the first step, the electrochemical features of α-Fe_2O_3 and g-C_3N_4 were scrutinized in three electrode system. When the Sc of pure α-Fe_2O_3 at a current density of 1 A g^{-1} was 184 F g^{-1}, hybrid material achieved 438 F g^{-1} capable of operating at high rates even at 20 A g^{-1}. Moreover, the hybrid material's cyclic stability was also better than pristine α-Fe_2O_3, the degradation was 25 % while the degradation of the Sc of α-Fe_2O_3/g-C_3N_4 was 15 % after 5000 continuous cycles. Afterward, the best-yielded composite electrode was formed as the cathode electrode for ZHSC. The maximal Sc was 280 F g^{-1} at the current density of 2.5 A g^{-1} when the highest ED and PD were 38.8 Wh kg^{-1}, and 20 kW kg^{-1}, respectively. Considering these excellent findings, the resulting hybrid material is a viable cathode material for aqueous ZHSCs.

Materials and Methods

Materials

Iron (III) chloride ($FeCl_3$, 99.0 %), sodium sulfate (Na_2SO_4, ≥ 99.0 %), urea ($CO[NH_2]_2$, 98.0 %),potassium hydroxide (KOH, ≥ 85.0 %) nitric acid (HNO_3, 65.0%) were purchased from Merck (GERMANY). Sigma-Aldrich (USA) was the supplier company for polyvinylidene fluoride (PVDF, 99.9 %) and n-methyl-2-pyrrolidone (NMP, 99.0 %). All chemical reagents and solvents for synthesis and analysis were utilized without further purification and the used deionized water (DI) was 18.2 MΩ cm resistivity.

Synthesis of α-Fe_2O_3

In particular, 3 mmol $FeCl_3$ was dissolved DI. After adding 1.6 mmol of Na_2SO, this mixture was ultrasonically sonicated for 1.5 hours. The resulting dark brown solution underwent a six-hour hydrothermal treatment at 120 °C. To get pure α-Fe_2O_3, the particles were centrifuged, washed with DI and ethanol, vacuum dried at 90°C for 15 hours, then calcined at 450°C for 2.5 hours at a rate of 1°C min^{-1} in flowing air[22].

Synthesis of g-C_3N_4

In a typical method, bulk g-C_3N_4 powders were obtained after calcining 10 g urea for 4 h at 550°C at 30°C min^{-1} heating rate in air in an enclosed muffle furnace. The obtained bulk g-C_3N_4 particles were then mixed magnetically in 50 mL of HNO_3 (pH-1) aqueous solution and heated to 90 °C for 8 hours. The sample was cleaned with DI and ethanol to eliminate contaminants and bring the pH level to 7, then vacuum dried for 15 hours at 85°C. The acquired yellowish product was stored in a desiccator pending use[23] .

Structural Characterization

The crystallographic conformation of the materials was investigated using a Bruker AXS D8 X-ray powder diffractometer with a simple cubic lattice and CU K radiation (λ = 0.15 nm), with the scan range (2θ) varying from 5° to 90°. Fourier Transform Infrared Spectroscopy (FTIR, Spectrum Two, Perkin-Elmer, USA) was applied to screen the chemical bonds of the molecules. The materials' morphology was examined using a Field Emission Scanning Electron Microscope (FE-SEM, Gemini 550) and a Scanning Transmission Electron Microscope (STEM, Gemini 550). Brunauer-Emmett-Teller (BET), and (Barrett-Joyner-Halenda) BJH methods (Micromeritics, Gemini Vii) were performed to obtain the pore size distribution, total pore volume (TPV), and the specific surface area (SSA) of the materials.

Electrochemical Characterization

Electrode fabrication and Tests

The electroactive materials (α-Fe_2O_3, α-Fe_2O_3/g-C_3N_4: 85 wt %, acetylene black: 10 wt %, and PDVF:5 wt % were ultrasonicated in few drops of NMP solvent. Nickel foam (NF) (1cm × 1cm) was chosen as the current collector. The electroactive materials' slurry was dropped onto the NF and vacuum dried at 95 °C for 12 h.When the active components were obtained, they weighed around 1.5 mg.

Gamry Referance, 3000 Electrochemical Workstation was utilized to check the cyclic voltammetry (CV), galvanostatic charge-discharge (GCD), and electrochemical impedance spectroscopy (EIS) measurements. All three electrode analyses were managed in 2M KOH aqueous electrolytes by using the obtained materials as working electrodes, when silver /silver chloride (Ag/AgCl), and platinum (Pt) foil (1x1cm) were the reference, counter electrodes, respectively.

The following equations were used to measure the Sc values of the electrodes at different scan rates, and current densities

$$Sc = \frac{\int \mathrm{I(V)\,dV}}{\mathrm{v\ x\ m\ x\ \Delta V}} \tag{1}$$

$$Sc = \frac{\mathrm{I\ x\ \Delta t}}{\mathrm{m\ x\ \Delta V}} \tag{2}$$

Where Sc (F g^{-1}), $\int$ I(V) dV,v(mV s^{-1}), m(g), ΔV (V), I (A), Δt (s) indicate the specific capacitance, the area under the CV curve, scan rate, mass of the active material, potential window, discharge current and, the average discharge time, respectively.

The energy density (E,Wh kg^{-1}), and the power density (P, W kg^{-1}) were measured according to the following formulas:

$$E = \frac{\mathrm{Ccell\ x\ \Delta V}^{2}}{2\ \mathrm{x}\ 3.6} \tag{3}$$

$$P = \frac{3600\ \mathrm{x\ E}}{\Delta \mathrm{t}} \tag{4}$$

Fabrication of ZHSC device

ZHSC was formed by using α-Fe_2O_3@g-C_3N_4 as cathode, Zn foil as both the anode and current collector in 2M KOH + 0.05 M $ZnSO_4$ electrolyte at a potential range of 1.0-2.0 V. Equations (2), (3), and (4) were used to measure the Sc (F g^{-1}), the Ed (E, Wh kg^{-1}), and the Pd (P, W kg^{-1}) of the ZHSC device.

Results and Discussion

Structural and Morphological Studies

X-ray diffraction (XRD) analysis was performed to check the formation and phase character of the patterns. In Figure 2a the peaks detected at 25.50°(012),34.56°(104), 37.04°(110),41.61°(113), 49.91°(024), 55.24°(116),58.14°(018), 65.2°(214) and, 68.4°(300) are the characteristic peaks of α-Fe_2O_3 (JPCDS card no. 33-0664) [11, 15, 24]. In Figure 1a the peaks at 2Ɵ values of 13.24° and 27.71° are diacritical peaks of the (100) and (002) planes of g-C_3N_4 and observed all idiosyncratic peaks of α-Fe_2O_3 indicate α-Fe_2O_3/g-C_3N_4 composite was formed successfully [20, 21].

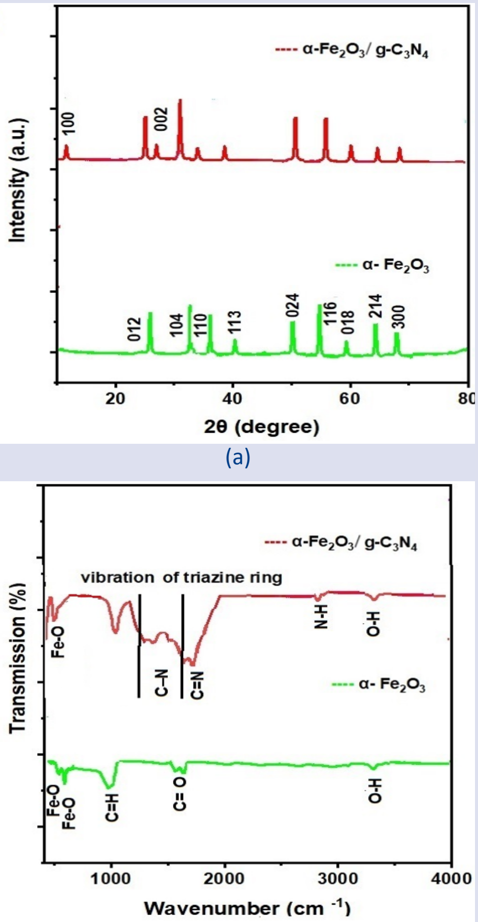

(a)

(b)

Figure 1. Structural characterization. (a) XRD patterns, and (b) FTIR spectra of α-Fe_2O_3, α-Fe_2O_3/g-C_3N_4.

FTIR screening was carried out to investigate the chemical production and chemical bonding of the components. In Figure 1b (green line). the broad band at 3450 cm^{-1} is considered to be the O-H stretching vibration. The peaks depicted at 1640 cm^{-1} and 1520 cm^{-1} own symmetric and asymmetric bending vibration of C=O. The peak at 895 cm $^{-1}$ belongs to C-H stretching vibration, and Fe-O stretching peaks were monitored at 480 and 562 cm^{-1} [25]. The presence of carbon peaks observed in the FTIR analysis, despite the absence of carbon-containing compounds in the structure, can be attributed to impurities introduced during the measurement or the carbon content present in the environment during the calcining process. In Figure 1b (red line) vibrational peaks of s-triazine units were observed at 821 cm^{-1}. The large peaks in the area of 1250-1620 cm^{-1} belong to C-N stretching vibration of the heterocyclic ring. The peak at 1648 cm^{-1} is associated with the C=N stretching vibration mode, whereas the wide peaks oriented at 2980 cm^{-1} and 3467 cm^{-1} might be related to the N-H and O-H vibrations [23, 26-28]. The screened distinct peaks of α-Fe_2O_3 demonstrate that the α-Fe_2O_3/g-C_3N_4 combination prosperously formed.

The pore chemistry of the patterns was determined by N_2 adsorption-desorption isotherms (Figure 2). The specific surface areas (SSA) and total pore volume (TPV) of α-Fe_2O_3, α-Fe_2O_3/g-C_3N_4, are 5.66m² g^{-1} ; 0.031 cm³ g^{-1}, 11.92 m² g^{-1}; 0.076 cm³/g respectively. The SSA of α-Fe_2O_3 was enhanced and nearly doubled, thanks to the high porosity structure of g-C_3N_4, α-Fe_2O_3/g-C_3N_4 composite has the highest pore volume (2~ wider than pristine α-Fe_2O_3).

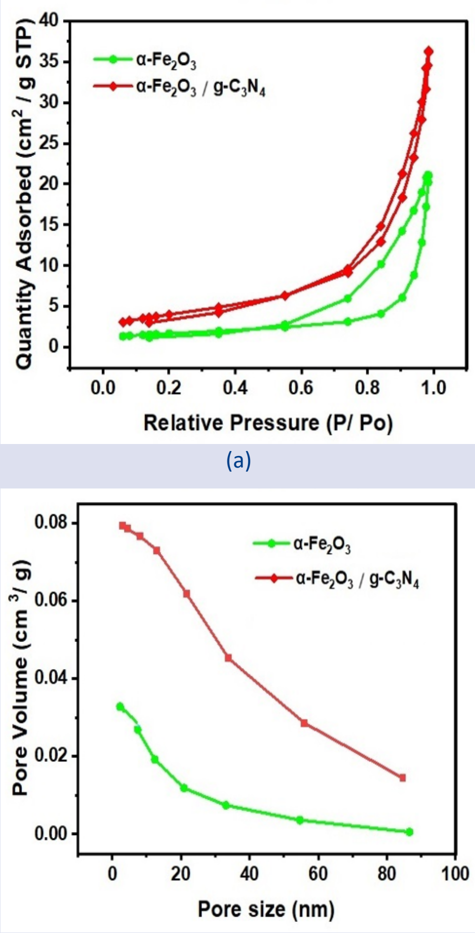

(a)

(b)

Figure 2. (a) Nitrogen adsorption-desorption isotherms of α-Fe_2O_3, α-Fe_2O_3/g-C_3N_4, and (b) BJH size distribution plots of the patterns.

In Figure 3 the surface morphology of the samples examined by FESEM and STEM are presented. In Figure 3 [20] FESEM and STEM images of nanowire α-Fe_2O_3 are shown which are dismantled with the addition of g-C_3N_4 as seen in Figure 4 (c- d). Agglomerated and interwoven particles also confirm the successful combination of the materials.

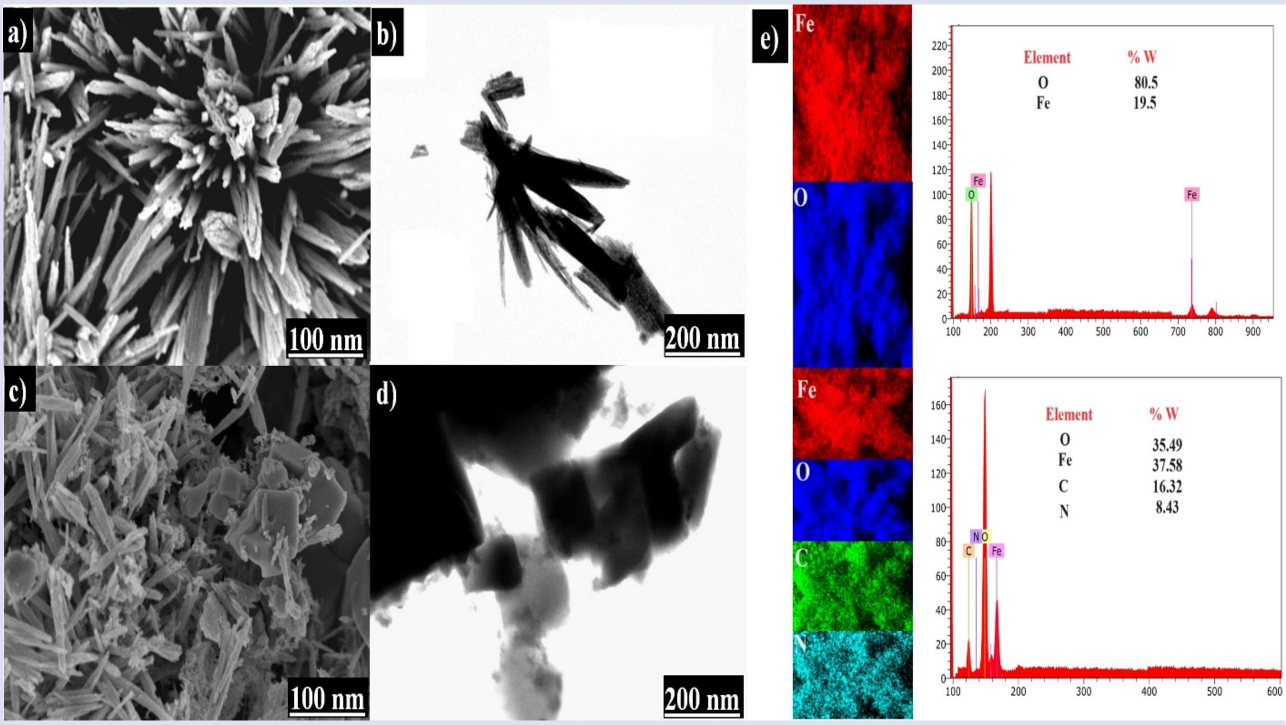

Figure 3. FESEM and STEM images of the samples. [20] α-Fe_2O_3 and, (c-d) α-Fe_2O_3/g-C_3N_4. (e) Individual elemental mapping images of Fe, O, C, N,and spectra of EDX, respectively.

Electrochemical Studies

Cyclic voltammetry studies

The electrochemical characterization findings are displayed in Figure 4. Figure4 (a-b) displays the individual CV curves for each material at various scan rates (20-50-100 mV s^{-1}).

The area under the CV curves expands with the increase in scan rates yet all samples still exhibit obvious redox peaks. The Sc of the electrodes with discrete scan rates was reckoned according to the equation (1). It can be syllogized that the oxidation and reduction peaks of α-Fe_2O_3/g-C_3N_4 are more distinct and the area under the CV curve is wider (Figure 4a) [29-31]. The obtained highest Sc of α-Fe_2O_3 and α-Fe_2O_3/g-C_3N_4 are 177 $g^{-1}$and 326 F g^{-1} in 2 M KOH at a scan rate of 5 mV s^{-1}. The other Sc variations with different scan rates are exhibited in Figure 5a.

Chronopotentiometry

Charge-discharge performance and stability after long cycles of the electrodes after extended cycles at various current densities at different current densities (1 Ag^{-1}-20 Ag^{-1}) were checked by implementing GCD measurements.

The proper potential window for the electrodes was -0.1 to 0.40 V (vs. Ag/AgCl) in 2M KOH aqueous electrolyte. On one hand, at low current densities more electroactive interference between the electrode surface and OH^{-1} ions causes an increment on specific capacitance. On the other hand, at high current density low interaction causes a decrease on the specific capacitances.

Individual GCD curves and Sc variation with different current densities are shown in Figure 4(c-d), and Figure 5(b). The highest Sc, calculated via equation (2), for all electrodes are obtained at a current density of 1 A g^{-1}. We can declare that with the addition of g-C_3N_4 charge-discharge time of α-Fe_2O_3 increased significantly. Therefore, the composite α-Fe_2O_3/g-C_3N_4 has higher Sc at the same current densities as shown in Figure (5b).

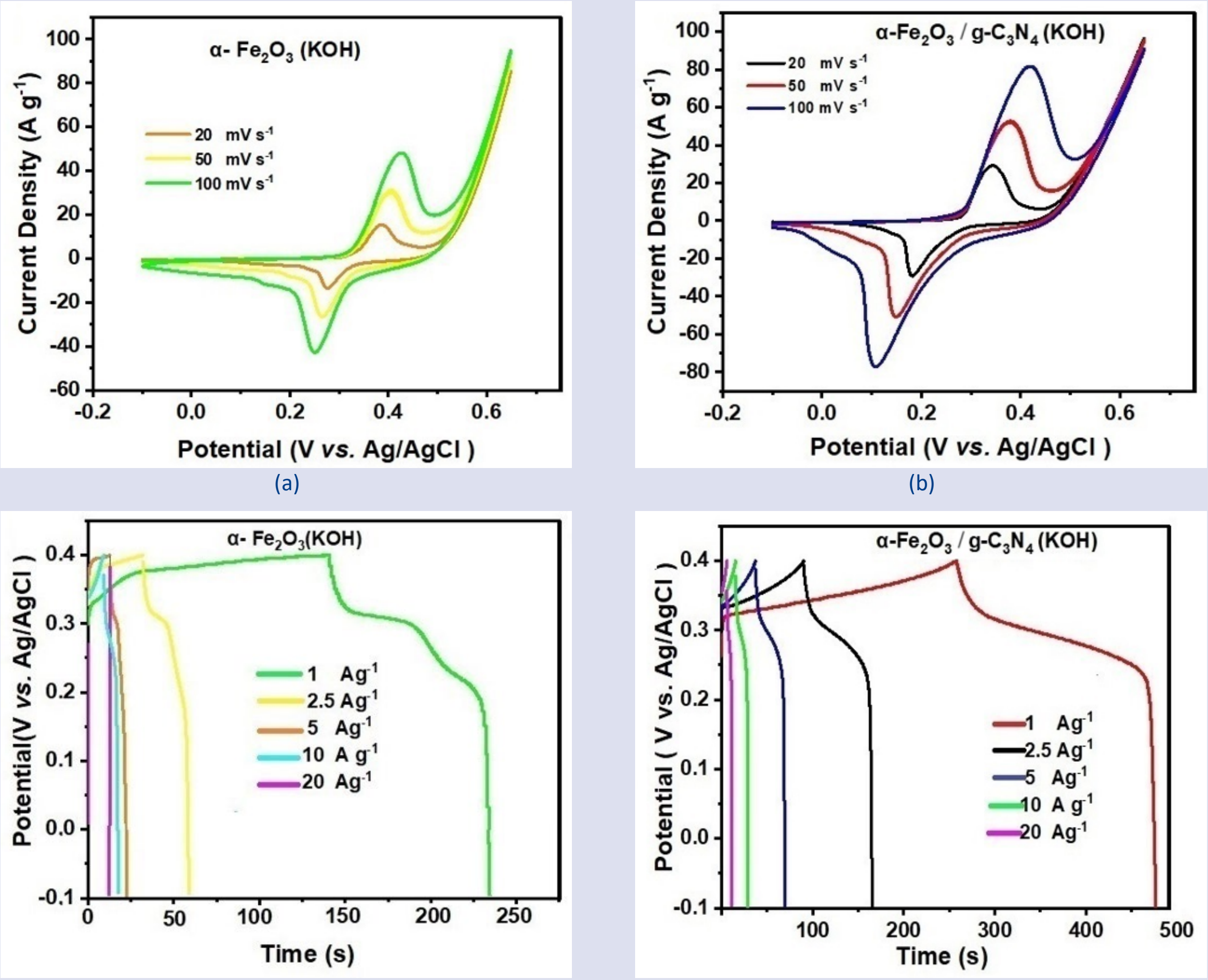

(a) (b)

(c) (d)

Figure 4. Electrochemical measurement results of the α-Fe_2O_3, and α-Fe_2O_3/g-C_3N_4. [20] CV curves, (c-d) GCD curves.

As shown in Figure 5(c) a long-term chronopotentiometry experiment at a current density of 20 Ag^{-1} for up to 5000 cycles was undertaken to further investigate the electrodes' long-term cyclic stability. When the retention of α-Fe_2O_3 were 75 % ,the retention of α-Fe_2O_3/g-C_3N_4 were 85% in 2M KOH electrolyte indicating g-C_3N_4 addition improve the cyclic stability of α-Fe_2O_3.

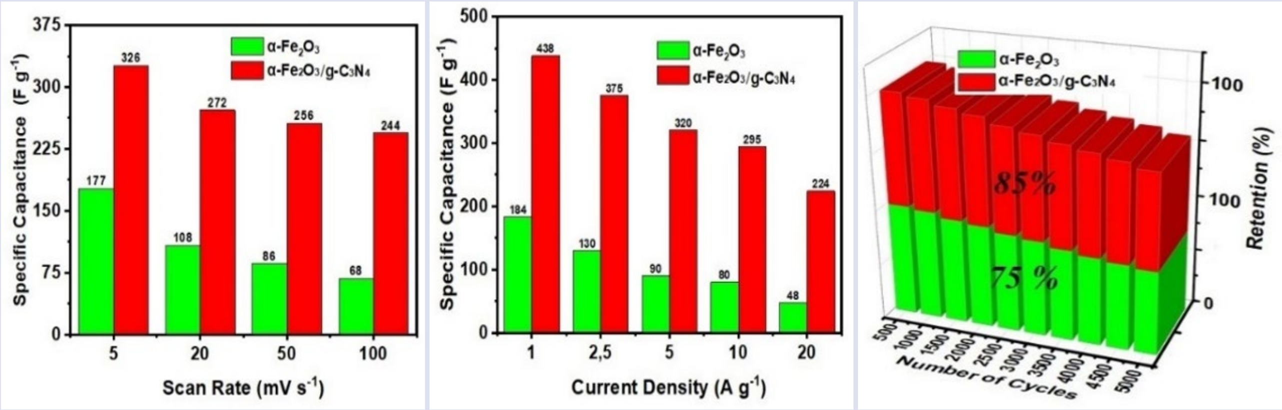

(a) (b) (c)

Figure 5. (a) Sc variation with different scan rates, (b) GCD curves, (c) Long term cyclic stabilities after 5000 cycles.

Electrochemical impedance spectroscopy (EIS)

The electrochemical impedance spectroscopy (EIS) was used to examine the kinetics of ion and charge transmission behavior of the electrodes at high and low frequencies ranging from 0.01 to 100 kHz. The low-frequency area controls the barrier to ion diffusion while the high-frequency region specifies the charge transmission [32, 33].

Ion diffusion between the electro-active area of the electrode and electrolyte intersection generates an extra line entitled the Warburg line. In Figure 6 the Nyquist plots of α-Fe_2O_3 and, α-Fe_2O_3/g-C_3N_4 are illustrated. It is possible to deduce that α-Fe_2O_3 has the lowest charge transport resistance (Rct) and equivalent series resistance (Rs), which rose with the addition of g-C_3N_4, showing that N-inclusive functional groups aroused extra resists.

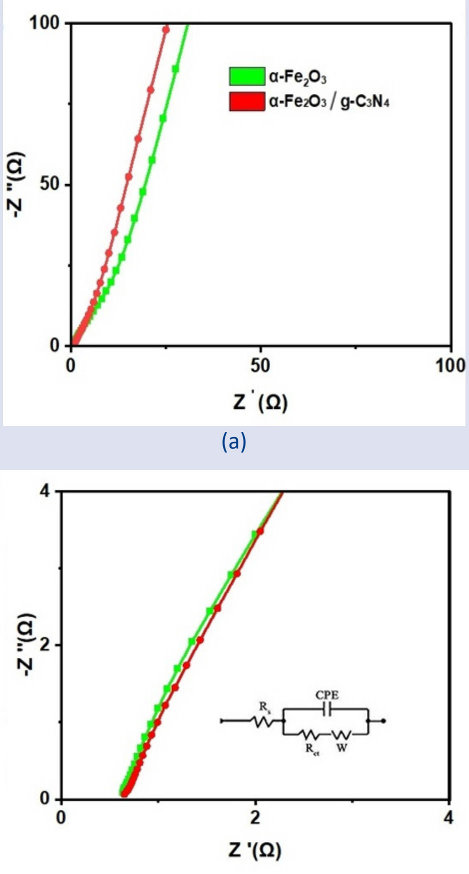

(a)

(b)

Figure 6. Nyquist plots at low (a) and high (b) frequency (The inset shows the zoom-in of Nyquist plots and, equivalent circuit model).

Electrochemical performances of the Zinc-ion hybrid supercapacitor

The formation of a highly efficient ZHSC device was achieved through the consolidation of a battery-type zinc anode and an α-Fe_2O_3/g-C_3N_4 cathode in a 2M KOH + 0.05 M $ZnSO_4$ electrolyte within the potential range of 1.0-2.0V. Figure 7 (a) shows the symbolic representation of the ZHSC device. Figure 7 (b) displays the CV curves of the device at various scan rates. The obvious redox peaks confirm the device has a high pseudocapacitive nature. The Scs of the device were measured by Equation (2). When the recorded highest Sc was 280 F g^{-1} at the current density of 2.5 A g^{-1}, the minimum Sc was 80 F g^{-1} at the current density of 40 A g^{-1}. In Figure 7 (c) GCD curves with various current densities are shown. After 10000 continuous cycles, the retention was 74%.

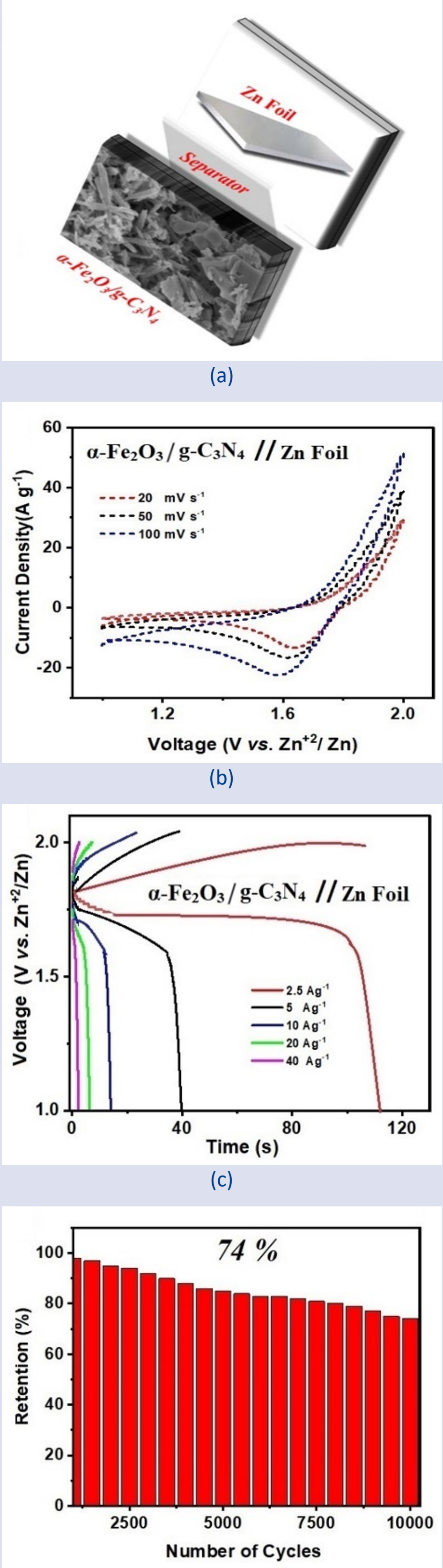

(a)

(b)

(c)

(d)

Figure 7. Electrochemical performance of the ZHSC device. (a) schematic representation of the ZHSC device, (b) CV curves at various scan rates of the ZHSC device, (c) GCD curves at various current densities of the ZHSC, (d) Long term cyclic stability after 10000 cycles.

The Nyquist plot in Figure 8 (a) notes that the device owns a low Rs of 3.2 Ω, and Rct of 3.8 Ω. The Ragon plot indicates the ED and PD of the ZHSC are in the region of the ionic supercapacitor, as seen in Figure 9 (b). In Table 1 the ED (E, Wh kg^{-1}), and the PD (P, W kg^{-1}) of the ZHSC device is recorded. The obtained results are comparable or better than the previously documented outcomes for α-Fe_2O_3 symmetric and asymmetric supercapacitor (SSC , ASC) devices. These results are summarized in Table 2, which includes information on the SC (device), electrolyte, potential range (V), ED (Wh kg^{-1}), PD (W kg^{-1}), and cyclic stability.

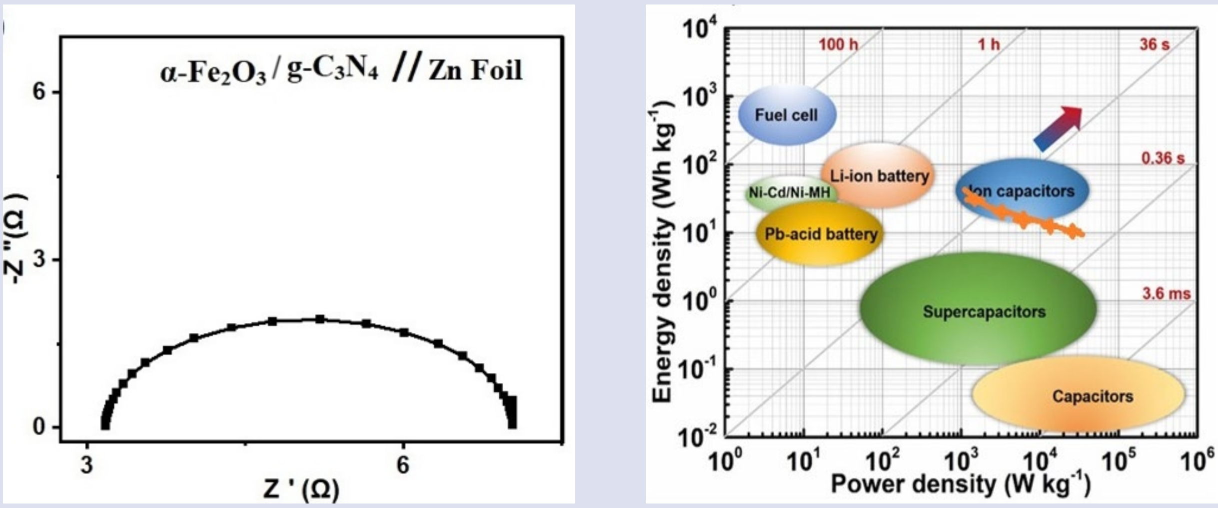

(a) (b)

Figure 8. (a) Nyquist plots at low frequency, (b) Ragone plot of the ZHSC

Table 1. Energy and power densities of the zinc ion hybrid supercapacitor at different current densities

Energy density/Power density (ED/PD) (Wh kg^{-1}/ W kg^{-1})					
Current density	2.5 Ag^{-1}	5 Ag^{-1}	10 Ag^{-1}	20 Ag^{-1}	40 Ag^{-1}
Energy density	38.8	27.7	19.4	16.6	11.1
Power density	1250	2500	5000	10.000	20.000

Table 2. Comparative Device Performance of Previously Reported α-Fe_2O_3 Energy Storage Devices

#	Device configuration	SC (Device)	Electrolyte	Potential range (V)	ED (Wh kg^{-1})	PD (W kg^{-1})	Stabilty (%) /cycles	Ref.
1	α-Fe_2O_3@CDs // 2 M KOH // BiOCl (ASC)	251 F g^{-1} at 1 Ag^{-1}	2M KOH	0-1.8 V	28	383	83/ 10.000	[15]
2	MoO_3-Fe_2O_3//AC [2]	216.7 F g^{-1} at 1 A g^{-1}	3M KOH	0-1.2	43.3	600	81.17/ 2.000	[34]
3	RGO // α-Fe_2O_3@CeO_2 (ASC)	50 F g^{-1} at 0.5Ag^{-1}	2M Na_2SO_4	0-1.5	15.62	781	87.5/ 2.000	[35]
4	α-Fe_2O_3/MnO_2/rGO//rGO (ASC)	97 F g^{-1} at 1 A g^{-1}	PVA/KOH gel-electrolyte	0-1.4	26.4	2099	91/ 5.000	[36]
6	Fe_2O_3@Ni1Co1-S//AC (ASC)	123.1 F g^{-1} at 1 Ag^{-1}	3 M KOH	0-1.6	43.8	810	92.4/ 10.000	[37]
7	α-Fe_2O_3/NiO/rGO // AC [2]	130 F g^{-1} at 1 A g^{-1}	6 M KOH	0-1.4	35.38	558	94.52/ 5.000	[38]
8	α-Fe_2O_3// NiO (ASC)	228.8 mF cm^{-2} at mA cm^{-2}	PVA/KOH gel-electrolyte	0-1.25	12.4	312	85 / 10.000	[39]
9	Fe_2O_3-P//MnO_2 (ASC)	-----	1M Na_2SO_4	0-1.6	57.3	1404	88/ 9.000	[40]
10	α-Fe_2O_3/g-C_3N_4 // Zn Foil	280 F g^{-1} at 2.5 A g^{-1}	2M KOH + 0.05 M $ZnSO_4$	1.0-2.0	38.8	1250	74/ 10.000	This work

Conclusions

To summarize, the purpose of this research was to investigate the electrochemical characteristics of g-C_3N_4 doped α-Fe_2O_3 for ZHSC applications. In the first step the composite material analyzed was done in three-electrode set up after the maximum conditions were optimized. Thereafter, the best yielded α-Fe_2O_3/g-C_3N_4 material was formed as cathode for ZHSC device when zinc foil was the both anode, and current collector. The performed ZHSC device ably reached the potential window of 2.0 volts with a high Sc of 280 F g^{-1} at a current density of 2.5 A g^{-1}. Additionally, the obtained maximum Ed and Pd were 38.8 Wh kg^{-1} and 20 kW kg^{-1}, respectively. This enhanced cell shows promise when compared to previous studies in the literature, as it exhibits a better power density with a wider working potential than asymmetric supercapacitors. Moreover, owing to these remarkable results, α-Fe_2O_3/g-C_3N_4 might be considered an appealing option for the cathode material in ZHSC.

Acknowledgements

This work was supported by the Research Fund of the Erciyes University (Project Number: 11978).

Conflicts of interest

There are no conflicts of interest in this work.

References

[1] Sharifi S., Rahimi K., Yazdani A., Highly Improved Supercapacitance Properties Of Mnfe$_2$o$_4$ Nanoparticles By Mos$_2$ Nanosheets, *Sci. Rep.,* 11 (1) (2020) 8378.

[2] Lazarte J.P.L., Dipasupil R.C., Pasco G.Y.S., Eusebio R.C.P., Orbecido A.H., Doong R.-A., Bautista-Patacsil L., Synthesis Of Reduced Graphene Oxide/Titanium Dioxide Nanotubes (Rgo/Tnt) Composites As An Electrical Double Layer Capacitor, *Nanomater,* 8(11) (2018) 934.

[3] Yetiman S., Pecenek H., Dokan F.K., Onses M.S., Yılmaz E., Sahmetlioglu E., Microwave-Assisted Fabrication Of High-Performance Supercapacitors Based On Electrodes Composed Of Cobalt Oxide Decorated With Reduced Graphene Oxide And Carbon Dot, *J. Energy Storage* , 49 (2022) 104103.

[4] El Ghazaly A., Zheng W., Halim J., Tseng E.N., Persson P.O., Ahmed B., Rosen J., Enhanced Supercapacitive Performance Of Mo1. 33c Mxene Based Asymmetric Supercapacitors In Lithium Chloride Electrolyte, *J. Energy Storage,* 41 (2021) 203-208.

[5] Yetiman S., Karagoz S., Kilic Dokan F., Onses M.S., Yilmaz E., Sahmetlioglu E., Rational Integration Of Zif-8 And Bipo(4) For Energy Storage And Environmental Applications, *Acs. Omega*, 7(49) (2022) 44878-44891.

[6] Şahan H., Ateş M.N., Dokan F.K., Ülgen A., Patat Ş., Synergetic Action Of Doping And Coating On Electrochemical Performance Of Lithium Manganese Spinel As An Electrode Material For Lithium-Ion Batteries, *B. Mater Sci.* , 38 (2015) 141-149.

[7] Mateen, A., Ansari, M.Z., Abbas, Q., Muneeb, A., Hussain, A., Eldin E.T., Alzahrani F.M., Alsaiari N.S., Ali S., Javed M.S., In Situ Nitrogen Functionalization Of 2d-Ti$_3$c$_2$t X-Mxenes For High-Performance Zn-Ion Supercapacitor**,** *Molecules*, 27 (21) (2022) 7446.

[8] Mateen A., Javed M.S., Khan S., Saleem A., Majeed M.K., Khan A.J., Tahir M.F., Ahmad M.A., Assiri M.A., Peng K.-Q., Metal-Organic Framework-Derived Walnut-Like Hierarchical Co-O-Nanosheets As An Advanced Binder-Free Electrode Material For Flexible Supercapacitor, *J. Energy Storage* , 49 (2022) 104150.

[9] Mateen A., Zubair M., Saleem M., Golubenkova A., Voskressensky L., Alothman A.A., Ouladsmane M., Ahmad A., Javed M.S., A Novel High-Performance Anode Material With An Enlarged Potential Window For A Hybrid Energy Storage System*, Energies*, 15 (24) (2022) 9577.

[10] Hussain S.K., Dudem B., Yu J.S., Enhanced Electrochemical Performance Via Ppy Encapsulated 3d Flower-Like Bismuth Molybdate Nanoplates For High-Performance Supercapacitors *, Appl. Surf. Sci.* , 478 (2019) 846-856.

[11] Yetiman S., Dokan F.K., Onses M.S., Yılmaz E., Sahmetlioglu E., Hybrid Electrodes Composed Of Graphitic Carbon Nitride And Zeolitic Imidazolate Framework-67 For Supercapacitor Applications*, Int. J. Energy Res.,* 46 (15) (2022) 22730-22743.

[12] Kiliç Dokan F., Şahan H., Özdemır B. Özdemır, N. Patat, Ş. Synthesis And Characterization Of Spinel Li$_4$ti$_5$o$_{12}$ Anode Material By Ctab Assisted Sol-Gel Method*, Acta Phys. Pol. A*, 125 (2) (2014) 648-649.

[13] Şahan H., Dokan F.K., Ülgen A., Patat Ş., Improvement Of Cycling Stability Of Limn$_2$o$_4$ Cathode By Fe$_2$o$_3$ Surface Modification For Li-Ion Battery ,*Ionics,* 20 (2014) 323-333.

[14] Patat S., Rahman S., Dokan F.K., The Effect Of Sodium And Niobium Co-Doping On Electrochemical Performance Of Li$_4$ti$_5$o$_{12}$ As Anode Material For Lithium-Ion Batteries, *Ionics,* 28 (7) (2022) 3177-3185.

[15] Yetiman S., Dokan F.K., Onses M.S., Huang, X., Yılmaz, E., Sahmetlioglu, E., Asymmetric And Zinc-Ion Hybrid Supercapacitors Based On Iron Oxide And Carbon Dots*, J. Energy Storage,* 68 (2023) 107608.

[16] Abbas Q., Mateen A., Khan A.J., Eldesoky G.E., Idrees A., Ahmad A., Eldin E.T., Das H.T., Sajjad M., Javed M.S., Binder-Free Zinc–Iron Oxide As A High-Performance Negative Electrode Material For Pseudocapacitors, *Nanomaterials*, 12 (18) (2022) 3154.

[17] Liu P., Fan X., Ouyang B., Huang Y., Hao R., Gao S., Liu W., Liu K., A Zn Ion Hybrid Capacitor With Enhanced Energy Density For Anode-Free*, J. Power Sources,* 518 (2022) 230740.

[18] Ji H., Jing X., Xu Y., Yan J., Li H., Li Y., Huang L., Zhang Q., Xu, H., Li, H., Magnetic Gc$_3$n$_4$/Nife$_2$o$_4$ Hybrids With Enhanced Photocatalytic Activity*, Rsc Advances,* 5 (71) (2015) 57960-57967.

[19] Xu M., Han L., Dong S., Facile Fabrication Of Highly Efficient G-C$_3$n$_4$/Ag$_2$o Heterostructured Photocatalysts With Enhanced Visible-Light Photocatalytic Activity*, Acs Appl. Mater. Interfaces,* 5 (23) (2013) 12533-12540.

[20] Zhou S.-X., Tao X.-Y., Ma J., Guo L.-T., Zhu Y.-B., Fan H.-L., Liu, Z.-S., Wei, X.-Y., Synthesis Of Flower-Like Pani/G-C$_3$n$_4$ Nanocomposite As Supercapacitor Electrode*, Vacuum*, 149 (2018) 175-179.

[21] Ragupathi, V., Panigrahi P., Subramaniam N.G., G-C$_3$n$_4$ Doped Mns As High Performance Electrode Material For Supercapacitor Application ,*Mater. Lett,* 246 (2019) 88-91.

[22] Li J., Chen D., Wu Q., A-Fe2o3 Based Carbon Composite As Pure Negative Electrode For Application As Supercapacitor*, Eur. J. Inorg. Chem.,* 2019 (10) (2019) 1301-1312.

[23] Song G., Chu Z., Jin W., Sun H., Enhanced Performance Of G-C_3n_4/Tio_2 Photocatalysts For Degradation Of Organic Pollutants Under Visible Light*, Chin. J. Chem. Eng,* 23(8) (2015) 1326-1334.

[24] Jiang H., Ma H., Jin Y., Wang L., Gao F., Lu Q., Hybrid A-Fe_2o_3@ Ni (Oh) $_2$ Nanosheet Composite For High-Rate-Performance Supercapacitor Electrode*, Sci. Rep ,* 6 (1) (2016) 31751.

[25] Zheng Y., Zhang X., Zhao J., Yang P., Assembled Fabrication Of A-Fe_2o_3/Biocl Heterojunctions With Enhanced Photocatalytic Performance*, Appl. Surf. Sci,* 430 (2018) 585-594.

[26] Nabi G., Riaz K.N., Nazir M., Raza W., Tahir M.B., Rafique M., Malik N., Siddiqa A., Gillani S.S.A., Rizwan M., Cogent Synergic Effect Of Tis_2/G-C_3n_4 Composite With Enhanced Electrochemical Performance For Supercapacitor*, Ceram. Int. Ceramics* , 46 (17) (2020) 27601-27607.

[27] Palanivel B., Hossain M.S., Macadangdang Jr, R.R., Ayappan C., Krishnan V., Marnadu R., Kalaivani T., Alharthi, F.A., Sreedevi G., Activation Of Persulfate For Improved Naproxen Degradation Using $Feco_2o_4$@ G-C_3n_4 Heterojunction Photocatalysts*, Acs Omega,* 6(50) (2021) 34563-34571.

[28] Chen X., Kuo D.-H., Lu D., Nanonization Of Gc_3n_4 With The Assistance Of Activated Carbon For Improved Visible Light Photocatalysis, *Rsc Adv.,* 6 (71) (2016) 66814-66821.

[29] Kumbul A., Gokturk E., Sahmetlioglu E.,Synthesis, Characterization, Thermal Stability And Electrochemical Properties Of Ortho-Imine-Functionalized Oligophenol Via Enzymatic Oxidative Polycondensation*, J. Polym. Res*., 23 (2016) 1-11.

[30] Turac E., Sahmetlioglu E., Toppare L., Yuruk H., Synthesis, Characterization And Optoelectrochemical Properties Of Poly (2, 5-Di (Thiophen-2-Yl-) 1-(4-(Thiophen-3-Yl) Phenyl)-1h-Pyrrole-Co-Edot)*, Des. Monomers Polym. ,* 13(3) (2010) 261-275.

[31] Turac E., Sahmetlioglu E., Demircan A., Toppare L., Synthesis And Characterization Of Conducting Copolymer Of Trans-1-(4-Methyl-3'-Thienyl)-2-(Ferrocenyl) Ethene With Edot*, J. Appl. Polym. Sci.,* 126 (3) (2012) 808-814.

[32] Zhu Q., Zhao D., Cheng M., Zhou J., Owusu K.A., Mai L., Yu Y., A New View Of Supercapacitors: Integrated Supercapacitors, *Adv. Energy Mater.,* 9(36) (2019) 1901081.

[33] Zhang L., Wu D., Wang G., Xu Y., Li H., Yan X., An Aqueous Zinc-Ion Hybrid Super-Capacitor For Achieving Ultrahigh-Volumetric Energy Density*, Chin. J. Chem.,* 32(2) (2021) 926-931.

[34] Sundaresan S., Subramanian D., Raju G., Exploration Of Two Dimensional Moo_3-Fe_2o_3 Nanocomposite For The Fabrication Of High Energy Density Supercapacitor Applications *, Inorg. Chem. Commun.,*148 (2023) 110360.

[35] Mazloum-Ardakani M., Sabaghian F., Yavari M., Ebady A., Sahraie N., Enhance The Performance Of Iron Oxide Nanoparticles In Supercapacitor Applications Through Internal Contact Of A-Fe_2o_3@Ceo_2 Core-Shell*, J. Alloys Compd.*, 819 (2020) 152949.

[36] Geerthana M., Prabhu S., Ramesh R., Hierarchical A-Fe_2o_3/Mno_2/Rgo Ternary Composites As An Electrode Material For High Performance Supercapacitors Application*, J. Energy Storage*, 47 (2022) 103529.

[37] Guo M., Sun J., Liu Y., Huangfu C., Wang R., Han C., Qu Z., Wang N., Zhao L., Zheng Q., Optimizing Fe_2o_3-Based Supercapacitor Cathode With Tunable Surface Pseudocapacitance Via Facile In Situ Vulcanization Process*, J. Electroanal. Chem.,* 901 (2021) 115785.

[38] Mummoorthi G., Shajahan S., Abu Haija M., Mahalingam U., Rajendran R., Synthesis And Characterization Of Ternary A-Fe_2o_3/Nio/Rgo Composite For High-Performance Supercapacitors*, Acs Omega*, 7(31) (2022) 27390-27399.

[39] Zhang S., Yin B., Wang Z., Peter F., Super Long-Life All Solid-State Asymmetric Supercapacitor Based On Nio Nanosheets And A-Fe_2o_3 Nanorods*, J. Chem. Eng.*, 306 (2016) 193-203.

[40] Liang H., Xia C., Emwas A.-H., Anjum D.H., Miao X., Alshareef H.N., Phosphine Plasma Activation Of A-Fe_2o_3 For High Energy Asymmetric Supercapacitors*, Nano Energy,* 49 (2018) 155-162.

Cumhuriyet Sci. J., 45(3) (2024) 519-523
DOI: https://doi.org/10.17776/csj.1438171

Cumhuriyet Science Journal

| csj.cumhuriyet.edu.tr | Founded: 2002 ISSN: 2587-2680 e-ISSN: 2587-246X Publisher: Sivas Cumhuriyet University

Synthesis, Anticholinesterase and Antioxidant Activity of Thiosemicarbazone Derivatives

Betül Kaya[1,a,*], Ulviye Acar Çevik[2,b], Abdüllatif Karakaya[1,c], Tuğba Erçetin[3,d]

[1]*Department of Pharmaceutical Chemistry, Faculty of Pharmacy, Zonguldak Bulent Ecevit University, 67600 Zonguldak, Türkiye*
[2]*Department of Pharmaceutical Chemistry, Faculty of Pharmacy, Anadolu University, 26470 Eskişehir, Türkiye*
[3]*Department of Pharmacognosy, Faculty of Pharmacy, Eastern Mediterranean University via Mersin 10, TR-99628 Famagusta, North Cyprus, Türkiye*
**Corresponding author*

Research Article

History
Received: 17/02/2024
Accepted: 22/07/2024

ABSTRACT

In this research, we report the synthesis and evaluation of novel thiosemicarbazones as anti-Alzheimer's agents. The structural clarification of the newly synthesized compounds was carried out by ^{1}H NMR, ^{13}C NMR, and MS analyses. According to the *in vitro* cholinesterase inhibition assay, compounds showed more inhibitory potential against AChE than BuChE. The *in vitro* antioxidant activity of the synthesized compounds was measured via two different methods. According to ferrous ion-chelating assay compound 2b demonstrated 5.26% activity when compared to BHT (2.57%). DPPH radical scavenging activity assay revealed that compound 2b showed the most potent antioxidant activity with an IC_{50} value of 43.91 ± 0.021µM. Among the synthesized compounds, compound 2b was found as the most potent antioxidant agent.

Keywords: Thiosemicarbazone, AChE, BuChE, Antioxidant.

[a] *betul.kaya@beun.edu.tr* *https://orcid.org/0000-0002-1713-9485*
[b] *uacar@anadolu.edu.tr* *https://orcid.org/0000-0003-1879-1034*
[c] *a.karakaya@beun.edu.tr* *https://orcid.org/0009-0003-9619-6705*
[d] *tugba.ercetin@emu.edu.tr* *https://orcid.org/0000-0001-7774-7266*

Introduction

Free radicals are highly very and unstable molecules with one or more unpaired electron in valency shell. They attack to other compounds to abstract electrons due to their electron deficiency [1,2]. Targets of free radicals are important macromolecules including lipids, nucleic acids and proteins. The attacked molecule loses its electron and becomes a free radical itself, initiating a chain reaction cascade therefore damaging cells and tissues in the body [3-5].

There are other reactive species that can oxidize compounds including reactive oxygen species (ROS) and reactive nitrogen species (RNS). Antioxidant defense system is capable of reduce the amount of these free radicals in the body, otherwise, excessive generation of these reactive species leads to a condition known as oxidative stress [6,7]. Oxidative stress is a common denominator in several chronic and degenerative diseases such as atherosclerosis, cancer, rheumatoid arthritis, chronic fatigue syndrome, Alzheimer's, Parkinson's, Huntington's, amyotrophic lateral sclerosis, and multiple sclerosis [8-16].

There are several hypotheses for the neurodegeneration process of Alzheimer's Disease (AD). According to the amyloid hypothesis, the accumulation of Aβ in the brain initiates the onset and progression of AD. In the brain of patients with AD, there is often a significant extent of oxidative damage related to the deposition of extracellular amyloid-β (Aβ) plaques and intracellular tau neurofibrillary tangles. Thus, Aβ is a major target in the therapy of AD. However, the etiology mechanisms underlying factors initiate Aβ aggregation are not clear yet [17,18]. Cholinergic hypothesis, the oldest known hypothesis for the neurodegeneration process in AD, suggests that there is a reduced rate of production and transportation of the neurotransmitter acetylcholine in the brains of individuals suffering from AD. Cholinesterase inhibitors such as donepezil, galantamine and rivastigmine increase the quantity of acetylcholine at cholinergic synapses by counteracting the effects of these acetylcholinesterase (AChE) and butyrylcholinesterase (BuChE) [19, 20].

Thiosemicarbazones are sulfur and nitrogen-containing compounds with potential pharmacological activities, resulting in significant attention in the field of medicinal chemistry. Thiosemicarbazone derivatives have been reported to be potent metal chelators both *in vitro* and *in vivo*. Metal ions such as Cu, Zn and Fe are associated with metal-induced Aβ fibrils aggregation in the pathogenesis of AD, thus metal ion chelators may serve as therapeutic agents [21-23]. Thiosemicarbazones have been also reported as antioxidant and cholinesterase inhibitors [24-28]. Due to the multifactorial nature of AD, here, we report the synthesis of potential multi-targeted compounds with cholinesterase inhibitory and antioxidant effects.

Materials and Methods

Chemistry

Synthesis of 2-[(3-methylthiophen-2-yl) methylidene] hydrazine-1-carbothioamide (1)

2-Methylthiophene-2-carbaldehyde and thiosemicarbazide were dissolved in ethanol. The mixture was refluxed for three hours. After this time, the mixture was set in an ice bath and the precipitated product was filtered.

General synthesis of target 2a-2f compounds

Compound 1 and appropriate aldehyde derivative were dissolved in ethanol. Following that, the mixture was refluxed for five hours. After this time, the mixture was set in an ice bath and the precipitated product was filtered.

2-((3-Methylthiophen-2-yl)methylene)-N-(5-methylfuran-2-yl)methylene)hydrazine-1-carbothioamide (2a): Yield: 74 %, M.p.= 194.1 °C. ^{1}H-NMR (300 MHz, DMSO-d_6): δ: 2.26 (6H, s, CH$_3$), 6.93-6.95 (2H, m, Aromatic CH), 7.42-7.44 (1H, m, Aromatic CH), 7.53-7.55 (1H, m, Aromatik CH), 8.17 (1H, br.s., Aromatik CH), 8.35 (1H, s, Aromatik CH), 11.29 (1H, s, NH). ^{13}C-NMR (75 MHz, DMSO-d_6): δ= 13.27, 14.94, 127.10, 127.20, 129.59, 129.68, 130.26, 132.48, 132.54, 136.56, 138.72, 140.54, 177.68.

2-((3-Methylthiophen-2-yl)methylene)-N-(5-nitrofuran-2-yl)methylene)hydrazine-1-carbothioamide (2b): Yield: 78 %, M.P.= 150.1 °C. ^{1}H-NMR (300 MHz, DMSO-d_6): δ: 2.28 (3H, s, CH$_3$), 6.95 (2H, s, Aromatic CH), 7.44-7.55 (2H, m, Aromatic CH), 8.17-8.36 (2H, m, Aromatik CH), 11.30 (1H, s, NH). ^{13}C-NMR (75 MHz, DMSO-d_6): δ= 14.11, 116.65, 120.53, 123.65, 126.03, 128.40, 131.38, 134.28, 137.65, 140.91, 166.41, 188.04. HRMS (m/z): [M+H]$^+$ calcd for $C_{12}H_{10}N_4O_3S_2$: 323.0267; found: 323.0270.

2-((3-Methylthiophen-2-yl)methylene)-N-(5-hydroxymethylfuran-2-yl)methylene) hydrazine-1-carbothioamide (2c): Yield: 79 %, M.P.= 98.6 °C. ^{1}H-NMR (300 MHz, DMSO-d_6): δ: 2.27 (3H, s, CH$_3$), 4.50 (2H, s, CH$_2$), 6.60-6.61 (1H, m, Aromatic CH), 6.93-6.95 (1H, m, Aromatic CH), 7.42-7.44 (1H, m, Aromatik CH), 7.54-7.55 (2H, m, Aromatik CH), 8.16-8.19 (1H, m, Aromatik CH), 8.35 (1H, s, Aromatik CH), 11.30 (1H, s, NH). ^{13}C-NMR (75 MHz, DMSO-d_6): δ= 14.88, 56.39, 125.40, 127.10, 127.20, 129.58, 129.68, 130.26, 132.48, 136.55, 138.77, 140.53, 177.68. HRMS (m/z): [M+H]$^+$ calcd for $C_{13}H_{13}N_3O_2S_2$: 308.0522; found: 308.0517.

2-((3-Methylthiophen-2-yl)methylene)-N-((thiophen-2-yl)methylene)hydrazine-1-carbothioamide (2d): Yield: 69 %, M.P.= 201.1 °C. ^{1}H-NMR (300 MHz, DMSO-d_6): δ: 2.26 (2H, s, CH$_3$), 6.93-6.95 (1H, m, Aromatic CH), 7.41-7.44 (1H, m, Aromatic CH), 7.53-7.55 (1H, m, Aromatik CH), 7.81 (2H, s, Aromatik CH), 8.15-8.17 (1H, m, Aromatik CH), 8.35 (1H, s, Aromatic CH), 11.30 (1H, s, NH). ^{13}C-NMR (75 MHz, DMSO-d_6): δ= 15.13, 127.15, 129.58, 130.14, 130.34, 132.40, 132.67, 136.59, 138.79, 140.32, 140.65, 177.66.

2-((3-Methylthiophen-2-yl)methylene)-N-(5-methylthiophen-2-yl)methylene)hydrazine-1-carbothioamide (2e): Yield: 70 %, M.P.= 190.0 °C. ^{1}H-NMR (300 MHz, DMSO-d_6): δ: 2.26 (6H, s, CH$_3$), 6.93-6.95 (1H, m, Aromatic CH), 7.43-7.46 (1H, m, Aromatic CH), 7.54-7.55 (1H, m, Aromatik CH), 8.17-8.19 (1H, m, Aromatik CH), 8.35 (2H, s, Aromatik CH), 11.30 (1H, s, NH). ^{13}C-NMR (75 MHz, DMSO-d_6): δ= 13.26, 14.97, 126.42, 127.10, 127.20, 129.58, 129.68, 130.26, 132.48, 132.54, 136.52, 138.75, 177.68. HRMS (m/z): [M+H]$^+$ calcd for $C_{13}H_{13}N_3S_3$: 308.0344; found: 308.0359.

2-((3-Methylthiophen-2-yl)methylene)-N-(3-methylthiophen-2-yl)methylene)hydrazine-1-carbothioamide (2f): Yield: 71 %, M.P.= 185.6 °C. ^{1}H-NMR (300 MHz, DMSO-d_6): δ: 2.27 (6H, s, CH$_3$), 6.94-7.02 (2H, m, Aromatic CH), 7.43-7.67 (2H, m, Aromatic CH), 8.17-8.35 (2H, m, Aromatik CH), 11.30 (1H, s, NH). ^{13}C-NMR (75 MHz, DMSO-d_6): δ= 14.94, 16.51, 127.11, 128.40, 129.59, 130.26, 131.37, 132.48, 136.55, 137.65, 138.76, 140.52, 177.72. HRMS (m/z): [M+H]$^+$ calcd for $C_{13}H_{13}N_3S_3$: 308.0344; found: 308.0349.

Cholinesterase Inhibition Assay

Inhibition potential of acetylcholinesterase and butyrylcholinesterase was determined by Ellman's modified spectrophotometric technique [29]. "Equine serum BuChE" (EC 3.1.1.8, Sigma) and electric eel AChE (Type-VI-S, EC 3.1.1.7, Sigma) enzymes were employed. The reaction's substrates were butyrylthiocholine chloride and acetylthiocholine iodide obtained from Sigma Aldrich at Saint Louis, USA. 5,5′-Dithiobis(2-nitrobenzoic acid) (DTNB, Sigma Aldrich at Saint Louis, United States America) was also used as a coloring reagent. The reaction mixture contained 50 mM Tris HCl buffer (pH 8.0), 6.8 mM DTNB, 10 µl of BuChE/AChE solution, and 2 µl of sample solutions in a 96-well microplate. Following that, acetythiocholine chloride or butyrylthiocholine chloride was added in 10 µl amount to the respective AChE or BuChE enzyme solution to start the enzymatic reactions. The hydrolysis of acetylthiocholine iodide/butyrylthiocholine chloride was monitored by the formation of yellow 5-thio-2-nitrobenzoate anion from the reaction of DTNB with thiocholine. This reaction catalyzed by enzymes and recorded at 412 nm, utilizing a 96-well microplate reader (Varioskan Flash, Thermo Scientific, USA). The reaction mixture was incubated for 15 min at 27 °C. Periodic test lasting 75 seconds was obtained. The Varioskan Flash software's SkanIt Software 2.4.5 RE was used to assess the measurements and computations. By comparing the sample reaction rates to those of the blank sample (DMSO and methanol) and applying the formula (E-S)/E x 100 (E: the activity of the enzyme without the test sample, S: the activity of the enzyme with the test sample) the percentage of AChE and BuChE inhibition was calculated. Three replicates of each experiment were conducted. Galantamine hydrochloride obtained from the Sigma-Al, USA has been utilized as a reference material.

Antioxidant Activity Assay

Ferrous ion-chelating effect

The ferrous ion-chelating effect of all the synthesized compounds 2a-2f and reference galantamine was measured through the method of Chua [30]. In brief, various dilutions of compounds were dissolved in ethanol (80%). After that 2 mM $FeCl_2$ solution (200 µL) was added and the mixture was incubated. 800 µL of 5 mM ferrozine (Sigma, St. Louis, MO, USA) was added into the mixture to start the reaction. The mixture was left standing at ambient temperature for 10 min. The absorbance of the reaction mixture was evaluated at 562 nm using a Unico 4802 UV–visible double beam spectrophotometer (USA) against ethanol (80%) as blank. The inhibition ratio of ferrozine-Fe^{2+} complex formation was calculated according to following equation:

$$I\% = [(A_{blank} - A_{sample})/A_{blank}] \times 100$$

A_{blank}: the absorbance of the control reaction (containing only $FeCl_2$ and ferrozine)

A_{sample}: the absorbance of the compounds/reference

Rutin and butylated hydroxytoluene (BHT) were used as references and they were obtained from Sigma Aldrich (USA) in this assay. Analyses were run in triplicates and the results were expressed as average values with S.E.M. [31,32].

DPPH Radical Scavenging Activity Assay

Blois's UV method [33] was utilized to measure the 2,2-diphenyl-1- picrylhydrazyl (DPPH) radical scavenging activity of the compounds. 40 µM and 100 µM concentrations of the tested compounds and gallic acid (reference) were prepared in 20 µL methanol. 180 µL of 0.15 mM DPPH solution in methanol was added to each solution. The rest amount of DPPH was measured at 520 nm using a Unico 4802 UV–visible double beam spectrophotometer against ethanol (80%) as blank. The percent DPPH radical scavenging activity was calculated as given below:

$I\% = [(A_{control} - A_{sample})/A_{control}] \times 100$

$A_{control}$: the absorbance of the control reaction

A_{sample}: the absorbance of the compounds/reference

Experiments were run in triplicate and the results were expressed as average values with S.E.M. (standard error mean).

Results and Discussion

Chemistry

Herein, a novel series of thiosemicarbazones (2a-2f) were synthesized according to the two-steps synthetic procedure as illustrated in Scheme 1. Firstly, intermediate thiosemicarbazone compound 1 was afforded via the reaction of starting material 3-methylthiophene-2-carbaldehyde with thiosemicarbazide. In the second step, target thiosemicarbazone compounds 2a-2f were synthesized in good yields through the reaction between compound 1 and various commercially available heterocyclic aldehydes.

In the ^1H NMR spectra of the compounds (2a-2f), the protons belonging to CH_3 group attached to thiophen ring, were observed at between 2.26-2.28 ppm. NH protons of thioamide structure were detected at between 11.29-11.30 ppm. The other aromatic and aliphatic protons were observed at the expected regions. In ^{13}C NMR spectra of the compounds, peaks due to all aliphatic and aromatic carbons were in accordance with the chemical structures of the compounds. In our previous study [34], In the ^1H NMR spectra of the compounds, the protons belonging to N=CH, and CO-NH were detected as paired peaks with respect to the presence of the E and Z forms of the compounds. Also, In the ^{13}C NMR spectra of the compounds, the carbons belonging to -N=CH- were observed as paired peaks due to E and Z isomer forms. Accordingly, it can be claimed that title compounds (2a-2f) were obtained as a single isomer.

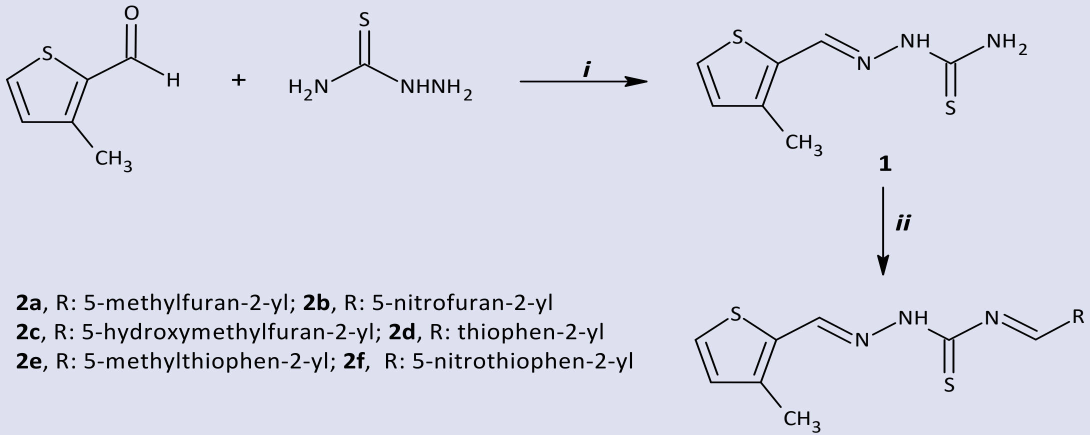

2a, R: 5-methylfuran-2-yl; **2b**, R: 5-nitrofuran-2-yl
2c, R: 5-hydroxymethylfuran-2-yl; **2d**, R: thiophen-2-yl
2e, R: 5-methylthiophen-2-yl; **2f**, R: 5-nitrothiophen-2-yl

Scheme 1. Synthesis of thiosemicarbazide 1 and thiosemicarbazones 2a-2f. (*i*) Ethanol, reflux; (*ii*) aldehyde derivatives, ethanol, reflux

Anticholinesterase Activity

The newly prepared thiosemicarbazones 2a-2f were screened *in vitro* for their ability to inhibit cholinesterase enzymes (AChE and BuChE) using Ellman's method with minor modifications [31]. The inhibition potencies of the compounds were compared to the well-known AChE inhibitor galantamine. The results were presented in Table 1. At the concentration of 50 µM, Galantamine showed anti-AChE and anti-BuChE activity with 97.89% and 62.48%, respectively. In the series, compound **2c** demonstrated the most inhibitory activity against AChE with 18.29%. Tested compounds showed weak inhibitory activity against cholinesterase enzymes.

Table 1. % Cholinesterase inhibitory activities of the synthesized compounds 2a-2f at 50 µM reaction concentrations.

Compound	AChE	BuChE
2a	3.68 ± 0.009	NA*
2b	11.86 ± 0.002	NA
2c	18.29 ± 0.013	4.86 ± 0.006
2d	16.96 ± 0.009	7.18 ± 0.002
2e	14.80 ± 0.005	NA
2f	7.27 ± 0.006	NA
Gal HBr	97.89 ± 0.01	62.48 ± 0.01

*NA: non-active

Antioxidant Activity

Ferrous ion-chelating effects

The ferrous ion chelating activities of the compounds 2a-2f, rutin and BHT are shown in Table 2. The results showed that the compounds 2a, 2b and 2e demonstrate a marked capacity for iron binding. The ferrous ion-chelating activity of the most active compounds and references decreased in the order of rutin > 2b > 2a > 2e > BHT, which were 13.21, 5.26, 4.13, 2.59 and 2.57 (%), at 50 µM concentration, respectively.

DPPH radical scavenging activity

The DPPH radical-scavenging activity of the newly synthesized compounds 2a-2f was determined using gallic acid as a reference and IC_{50} of the most active compounds were calculated (Table 2). According to the results, compounds 2b, 2c and 2f indicated free radical-scavenging effects of 59.25%, 41.28% and 43.95%, respectively, compared with that of gallic acid of 70.29% at a concentration of 50 µM IC_{50} values of the most potent compounds 2b, 2c and 2f were found 43.91, 59.26, 58.01 µM, respectively, while that of gallic acid was found 29.48 µM It can be claimed that 5-nitrofuran (2b), 5-hydroxymethylfuran (2c) and 5-nitrothiophene (2f) groups have a positive contribution on the DPPH radical-scavenging activity.

The -NH group of thiosemicarbazone scaffold in the structure of 2a-2f compounds, is thought to react with DPPH free radicals by giving hydrogen atom according to the (DPPH• + R-NH → DPPH-H + R-N•) reaction. It can be stated that weaker hydrogen bonds are necessary for higher antioxidant activity. In the light of this, nitro ($-NO_2$) group bearing compounds 2b and 2f and hydroxymethyl ($-CH_2OH$) possessing compound 2c showed the strongest DPPH radical-scavenging activity of all the tested compounds. Because the bond strength between nitrogen and hydrogen atoms weakens in the presence of electron-withdrawing groups near the donor atom, which causes easier loss of the hydrogen atom. [35]

Table 2. DPPH free radical-scavenging activity and ferric ion chelating effect (inhibition % ± S.E.M) of synthesized compounds at 50 µM and IC_{50} values (µM)

Compound	DPPH	ION CHELATING	IC_{50} (DPPH) µM
2a	26.65 ± 0.014	4.13 ± 0.003	> 60
2b	59.25 ± 0.021	5.26 ± 0.001	43.91 ± 0.021
2c	41.28 ± 0.005	NA*	59.26 ± 0.005
2d	26.43 ± 0.004	0.62 ± 0.001	> 200
2e	39.87 ± 0.023	2.59 ± 0.002	> 200
2f	43.95 ± 0.032	0.54 ± 0.001	58.01 ± 0.032
Gallic Acid	70.29 ± 0.005	4.13 ± 0.003	29.48 ± 0.014
RUTIN	-	13.21 ± 0.007	-
BHT	-	2.57 ± 0.004	-

*NA: non-active

Conclusions

In this study, six thiosemicarbazone derivative were synthesized and examined in terms of anti-cholinesterase and antioxidant activities. All tested compounds showed weak inhibitory activity against cholinesterase enzymes. The ferrous ion-chelating activity of the compounds 2a, 2b and 2e were higher than reference BHT at 50 µM concentration. In addition, compounds 2b, 2c and 2f containing electron-withdrawing groups showed more effective antioxidant activity than the reference drug according to the DPPH method.

Conflicts of interest

There are no conflicts of interest in this work.

References

[1] Sens L., Oliveira A.S.D., Mascarello A., Brighente I., Yunes R. A., Nunes R. J., Synthesis, Antioxidant Activity, Acetylcholinesterase Inhibition and Quantum Studies of Thiosemicarbazones, *J. Braz. Chem. Soc*., 29 (2018) 343-352.

[2] Phaniendra A., Jestadi D. B., Periyasamy L., Free radicals: Properties, Sources, Targets, and Their Implication in Various Diseases, *Indian J. Clin. Biochem*., 30 (2015) 11-26.

[3] Mukherji S.M., Singh S.P., Reaction Mechanism in Organic Chemistry (Revised Edition), Revised by: Singh S.P., Prakash Om, India, Laxmi Publications (2008).

[4] Lobo V., Patil A., Phatak A., Chandra N., Free Radicals, Antioxidants and Functional Foods: Impact on Human Health, *Pharmacogn. Rev*., 4 (2010) 118-126.

[5] Mostafa Abd El-Aal H.A.H., Lipid Peroxidation, In: Angel C., (Eds). Lipid Peroxidation End-Products as a Key of Oxidative Stress: Effect of Antioxidant on Their Production and Transfer of Free Radicals, IntechOpen, (2012).

[6] Engwa G.A., Phytochemicals - Source of Antioxidants and Role in Disease Prevention, In: Asao T., Asaduzzaman Md, Free Radicals and The Role of Plant Phytochemicals as Antioxidants Against Oxidative Stress-Related Diseases. Phytochemicals: Source of Antioxidants and Role in Disease Prevention, BoD–Books on Demand, (2018) 49-74.

[7] Chaudhary P., Janmeda P., Docea A.O., Yeskaliyeva B., Abdull Razis A.F., Modu B., Calina D., Sharifi-Rad, J., Oxidative Stress, Free Radicals and Antioxidants: Potential Crosstalk in the Pathophysiology of Human Diseases, *Front. Chem*., 11, (2023) 1158198.

[8] Batty M., Bennett M. R., Yu E., The Role of Oxidative Stress in Atherosclerosis, *Cells*, 11 (2022), 3843-3863.

[9] Sosa V., Moliné T., Somoza R., Paciucci R., Kondoh H., LLeonart M.E., Oxidative Stress and Cancer: An Overview, *Ageing Res. Rev*., 12 (2013) 376-390.

[10] Quiñonez-Flores C.M., González-Chávez S.A., Del Río Nájera D., Pacheco-Tena C., Oxidative Stress Relevance in The Pathogenesis of The Rheumatoid Arthritis: A Systematic Review, *Biomed Res. Int*., 2016 (2016) Article ID 6097417-6097431.

[11] Lee J.S., Kim H.G., Lee D.S., Son C.G., Oxidative Stress Is a Convincing Contributor to Idiopathic Chronic Fatigue, *Sci. Rep*., 8 (2018) 12890-12897.

[12] Huang W.J., Zhang X.I.A., Chen W.W., Role of Oxidative Stress in Alzheimer's Disease, *Biomed. Rep*., 4 (2016) 519-522.

[13] Dias V., Junn E., Mouradian M.M., The Role of Oxidative Stress in Parkinson's Disease, *J. Parkinsons Dis.*, 3 (2013) 461-491.

[14] Kumar A., Ratan R.R., Oxidative Stress and Huntington's disease: The good, the bad, and the ugly, *J. Huntington's Dis*., 5 (2016) 217-237.

[15] Hemerková P., Vališ M., Role of Oxidative Stress in the Pathogenesis of Amyotrophic Lateral Sclerosis: Antioxidant Metalloenzymes and Therapeutic Strategies, *Biomolecules*, 11 (2021) 437-460.

[16] Adamczyk B., Adamczyk-Sowa M., New Insights into The Role of Oxidative Stress Mechanisms in The Pathophysiology And Treatment of Multiple Sclerosis, *Oxid. Med. Cell. Longev*., 2016 (2016) Article ID 1973834.

[17] Zhang X., Fu Z., Meng L., He M., Zhang Z., The Early Events That Initiate β-amyloid Aggregation in Alzheimer's Disease. *Front. Aging Neurosci*., 10 (2018) 359-369.

[18] Liu P.P., Xie Y., Meng X.Y., Kang J.S., History and Progress of Hypotheses and Clinical Trials for Alzheimer's Disease, *Signal Transduct. Target Ther*., 4 (2019) 29-51.

[19] Agarwal M., Alam M.R., Haider M.K., Malik M.Z., Kim D.K., Alzheimer's Disease: An Overview of Major Hypotheses and Therapeutic Options in Nanotechnology, *Nanomaterials*, 11 (2021) 59-77.

[20] Karakaya A., Maryam Z., Erçetin T., Çevik U.A., Synthesis of Thiazole Derivatives as Cholinesterase Inhibitors with Antioxidant Activity, *Eur. J. Life Sci*., 2 (2023) 118-124.

[21] Kovacevic Z., Kalinowski D.S., Lovejoy D.B., Yu Y., Suryo Rahmanto Y., Sharpe P.C., Bernhardt P.V., Richardson D.R., The medicinal Chemistry of Novel Iron Chelators for The Treatment of Cancer. *Curr. Top. Med. Chem*., 11 (2011) 483-499.

[22] Yu Y., Kalinowski D.S., Kovacevic Z., Siafakas A.R., Jansson P.J., Stefani C., Lovejoy D.B., Sharpe P.C., Bernhardt P.V., Richardson D.R., Thiosemicarbazones from The Old to New: Iron Chelators That Are More Than Just Ribonucleotide Reductase Inhibitors., *J. Med. Chem*., 52 (2009) 5271- 5294.

[23] Fasae K.D., Abolaji A. O., Faloye T.R., Odunsi A.Y., Oyetayo B.O., Enya J.I., Rotimi J.A., Akinyemi R.O., Whitworth A.J., Aschner, M., Metallobiology and Therapeutic Chelation of Biometals (Copper, Zinc and Iron) In Alzheimer's Disease: Limitations, And Current and Future Perspectives, *J. Trace Elem. Med. Biol*., 67 (2021) 126779-126800.

[24] Koçyiğit Ü.M., Doğan M., Muğlu H., Taslimi P., Tüzün B., Yakan H., Bal H., Güzel E., Gülçin, İ., Determination of Biological Studies and Molecular Docking Calculations of Isatin-Thiosemicarbazone Hybrid Compounds, *J. Mol. Struct*., 1264 (2022) 133249.

[25] Palanimuthu D., Poon R., Sahni S., Anjum R., Hibbs D., Lin H. Y., Bernhardt P.V., Kalinowski D.S., Richardson, D.R., A Novel Class of Thiosemicarbazones Show Multi-Functional Activity for The Treatment of Alzheimer's Disease, *Eur. J. Med. Chem*., 139 (2017) 612-632.

[26] Yakan, H., Preparation, Structure Elucidation, And Antioxidant Activity of New Bis (Thiosemicarbazone) Derivatives, *Turk. J. Chem*., 44 (2020) 1085-1099.

[27] Zaib S., Munir R., Younas M.T., Kausar N., Ibrar A., Aqsa S., Shahid N., Asif T.T., Alsaab H.O., Khan, I., Hybrid Quinoline-Thiosemicarbazone Therapeutics as A New Treatment Opportunity for Alzheimer's Disease–Synthesis, In Vitro Cholinesterase Inhibitory Potential and Computational Modeling Analysis, *Molecules*, 26 (2021) 6573-6596.

[28] Nguyen D.T., Le TH., Bui T.T.T., Antioxidant Activities of Thiosemicarbazones from Substituted Benzaldehydes And N-(Tetra-O-Acetyl-Β-D-Galactopyranosyl) Thiosemicarbazide, *Eur. J. Med. Chem*., 60 (2013) 199-207.

[29] Ellman G.L., Courtney K.D., Andres Jr V., Featherstone R.M., A New and Rapid Colorimetric Determination of Acetylcholinesterase Activity, *Biochem. Pharmacol*., 7 (1961) 88-95.

[30] Chua M.T., Tung YT., Chang S.T., Antioxidant Activities of Ethanolic Extracts from The Twigs of Cinnamomum Osmophloeum, *Bioresour. Technol*., 99 (2008) 1918-1925.

[31] Dinis, T.C.P., Madeira, V.M.C., Almeida, L.M., Action of Phenolic Derivatives (Acetaminophen, Salicylate, And 5-Aminosalicylate) As Inhibitors of Membrane Lipid Peroxidation and Peroxyl Radical Scavengers, *Arch. Biochem. Biophys.*, 315 (1994) 161–169.

[32] Ercetin T., Senol F.S., Orhan I.E. Toker G., Comparative Assessment of Antioxidant and Cholinesterase Inhibitory Properties of The Marigold Extracts from *Calendula arvensis* L. and *Calendula officinalis* L, *Ind. Crops Prod.*, 36 (2012) 203-208.

[33] Blois M.S., Antioxidant Determinations by the Use of a Stable Free Radical, *Nature*, 181 (1958) 1199–1200.

[34] Kaya B., Özkay Y., Temel H.E., Kaplancıklı Z.A. Synthesis and Biological Evaluation of Novel Piperazine Containing Hydrazone Derivatives, *J. Chem*., 2016 (2016) 1-7, 5878410.

[35] Yakan H., Preparation, structure elucidation, and antioxidant activity of new bis (thiosemicarbazone) derivatives, *Turk. J. Chem*., 44 (2020) 1085-1099.

Cumhuriyet Sci. J., 45(3) (2024) 524-529
DOI: https://doi.org/10.17776/csj.1455751

Cumhuriyet Science Journal

| csj.cumhuriyet.edu.tr | Founded: 2002 ISSN: 2587-2680 e-ISSN: 2587-246X Publisher: Sivas Cumhuriyet University

Characterization of ZnSe Thin Film Electrodeposited at Room Temperature in Aqueous Medium without Complexing Agents

Sevda Ildan Ozmen[1,a,*]

[1] *Advanced Technology Education Research and Application Center, Mersin University, Mersin, Türkiye*
**Corresponding author*

Research Article

History
Received: 20/03/2024
Accepted: 23/09/2024

ABSTRACT

This study includes a simple electrodeposition technique for the fabrication of ZnSe thin film at room temperature and in an aqueous medium without additional complexing agents. Comprehensive analysis of the optical, structural, and morphological characteristics of the ZnSe thin film electrodeposited onto an ITO substrate was conducted using UV-Vis spectrometry, X-ray diffraction (XRD), Raman spectroscopy, Fourier transform infrared spectroscopy (FT-IR), and field emission–scanning electron microscopy (FE–SEM). Furthermore, the photoelectrochemical properties were evaluated through current-time (I-t) measurements and electrochemical impedance spectroscopy (EIS) under light on/off conditions. Mott-Schottky analysis was also performed to determine the conductivity type, carrier concentration, and flat band potential of the ZnSe thin film. Structural investigations revealed that the ZnSe thin film has a hexagonal structure, the longitudinal optical (LO) phonon mode, stretching and bending vibration modes of Zn-Se. The carrier type of the ZnSe thin film was identified as n- type semiconductor and photoelectrochemical measurements exhibited a photoresponse under the light illumination.

Keywords: Electrodeposition, ZnSe, Characterization, Mott–Schottky, Photoelectrochemical measurements.

[a] *sevdaildan@mersin.edu.tr* *https://orcid.org/0000-0002-4222-0330*

Introduction

Metal chalcogenides represent a crucial class of semiconductor materials, drawing substantial interest owing to their diverse applications in optics and electronics. Modern electronic devices, such as transistors, diodes, integrated circuits, photovoltaic cells, and other solid-state components, rely on thin-film materials. These materials are often made from metal chalcogenides. Zinc Selenide (ZnSe) that belongs to the II-VI metal chalcogenide family is a significant material in many technological applications because of its broad optical transmission range from the visible to the far infrared region (0.5–22 µm), high transparency, semiconductor properties, and mechanical durability. ZnSe is used for CO_2 lasers, and infrared (IR) optical systems such as lenses, mirrors, and windows [1,2]. Due to its direct and wide energy band gap of 2.7 eV and its semiconductor properties, ZnSe thin films are also important materials for use in optoelectronic devices, light-emitting technologies, and as a buffer or window layer in thin film solar cells [2–5].

Many deposition techniques have been explored to fabricate ZnSe thin films such as chemical bath deposition (CBD) [6,7], closed space sublimation [8,9], pulsed laser ablation deposition (PLAD) [10], and electrochemical deposition (ECD) [11–14]. Among these, ECD has emerged as a particularly noteworthy technique for growing semiconductor films, offering advantages such as cost-effectiveness, controllability of film properties (such as thickness, morphology, and structure), and the ability to produce large-area devices at low temperatures [3,4,15]. In the ECD method, the properties of the films can be controlled by adjusting various parameters such as applied potential, electrolyte composition and concentration, pH, temperature and deposition time [2,3,15]. The ZnSe thin films were synthesized by ECD method conducted within a temperature range of 50 to 75 °C successfully in earlier studies [3–5,13,15,16].

The ZnSe thin films were deposited on ITO substrates at room temperature by ECD and without additional complexing agents in this study. The comprehensive characterization of ZnSe thin films were carried out with optical, structural, morphological, and photoelectrochemical analysis. Additionally, the determination of the carrier type in the ZnSe semiconductor thin film was achieved through Mott-Schottky analysis.

Materials and Methods

The electrochemical deposition of the ZnSe film onto an ITO substrate was achieved in aqueous solution including 0.1 M $ZnCl_2$ and 0.1 mM SeO_2 employing the chronopotentiometry technique cathodically. The pH of the solution adjusted to ~2 using 1 M HCl and the ECD was carried out at a constant cathodic current of 0.1 mA with two 30-minute electrodeposition cycles (near -0.65 V) at room temperature. Before coating the ITO substrate and after each deposition cycle, the electrodeposited ZnSe films on the ITO substrates were rinsed with ethanol and ultrapure water, and then dried with an air drier.

To determine the energy band gap value of the ZnSe film, a Shimadzu UV–1100 spectrometer was used. The structural analysis of the ZnSe film was performed using a Rigaku Smart Lab X–ray diffractometer (XRD) with CuKα radiation (λ = 1.54 Å), an In Via Qontor Raman spectrometer, and a Perkin Elmer UATR Two Fourier transform-infrared (FT-IR) spectrophotometer. Morphological analysis was conducted using a FEI Quanta 650 field emission scanning electron microscopy (SEM) instrument.

The electrochemical (EC) measurements such as current-time (I-t) curves and electrochemical impedance spectroscopy (EIS) were carried out in a 0.1 M KCl solution with a three-electrode system using the CHI-660 D electrochemical workstation. The platinum foil as the counter electrode, the Ag/AgCl (3 M KCl) as the reference electrode, and the ZnSe-coated ITO substrate were employed as the working electrode. Illumination during EC measurements was provided by a Kessil H150 model 150 W Blue LED light source (390 nm). The electrochemical impedance spectroscopy (EIS) measurements were performed within a frequency range from 100 kHz to 1 Hz at the cathodic potential of 0.05 V with an amplitude of 5 mV.

Results and Discussion

Optical Properties

The UV-Vis spectrometer was used to determine the optical properties of the ZnSe semiconductor thin film. The energy band gap of the ZnSe thin film was determined using the relationship between the absorption coefficient and photon energy as given below:

$$\alpha = A\frac{\left(h\nu - E_g\right)^n}{h\nu} \tag{1}$$

Here, α represents the absorption coefficient, A denotes a constant, $h\nu$ stands for the photon energy, E_g represents the energy band gap, and n equals 1/2 because of the direct transition. The plot of α^2 versus $h\nu$ is given in Figure 1. The E_g value of the film was determined by extrapolating the linear portion of the graph onto the energy axis (where α^2= 0). The E_g value of the ZnSe thin film was found as 2.39 eV which below the bulk energy band gap value of ZnSe (2.7 eV) [2–4,11]. There are also studies in the literature where the E_g value is below 2.7 eV [2,4,5,15,17].

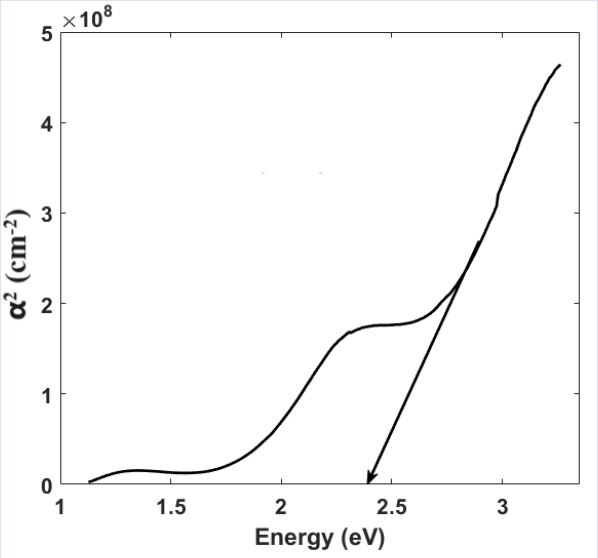

Figure 1. The α^2 - $h\nu$ graphs of the ZnSe thin film on ITO substrate.

Structural Properties

To conduct structural analysis of the ZnSe thin film, XRD measurements were performed scan range from 20° to 80°. The XRD pattern depicting the ZnSe film is presented in Figure 2. The crystal structure and miller indices of the ZnSe film was determined using Joint Committee on Powder Diffraction Standards cards. The diffraction peak at 2θ ≈ 21° is related to the ITO (PDF Card No.: 01-089-4598). The diffraction peaks at about 30°, 37°, 50°, and 60° were matched with PDF Card No.: 015-0105 which is expressed to the hexagonal crystal structure of ZnSe. The diffraction peak at about 35° is indicated the hexagonal crystal structure of the ZnSe which matched the 01-073-6558 card number. The peak at ~32° was determined to belong to the cubic crystal structure of the ZnSe (PDF Card No.: 01-070-0777). The data obtained indicates that the ZnSe film mostly possesses a hexagonal crystal structure. There are many studies made in aqueous solution by electrodeposition using temperature ≥ 50 °C. Though most of them has cubic crystal structures [4,5,11,12,15], there are some studies with hexagonal structures [16,17].

The average grain size (D), dislocation density (δ), and strain value (ε) of the ZnSe thin film were calculated by the following equations.

$$D_{hkl} = \frac{K\lambda}{\beta cos\theta} \tag{2}$$

$$\delta = \frac{1}{D_{hkl}^2} \tag{3}$$

$$\varepsilon = \frac{\beta cos\theta}{4} \tag{4}$$

K denotes a constant, with a specific value set at 0.9. The parameter β represents the Full Width at Half Maximum (FWHM) measured in radians. The symbol λ signifies the wavelength of the utilized X-ray, while θ denotes the Bragg angle [18–21]. All parameters were calculated for the diffraction peaks observed in the ZnSe thin film and given in Table 1.

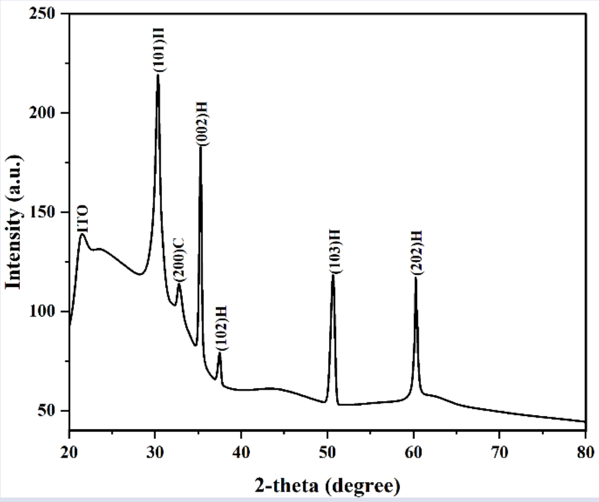

Figure 2. The XRD pattern of the ZnSe thin film on ITO substrate.

Table 1. The average grain size (D), dislocation density (δ), and strain value (ε) of the ZnSe thin film on ITO substrate.

(hkl)	Crystal System	D (nm)	δ (10^{15} lines/m^2)	ε (10^{-3})
(101)	Hexagonal	11.76	7.228	2.9
(200)	Cubic	7.67	16.99	4.5
(002)	Hexagonal	27.79	1.295	1.25
(102)	Hexagonal	22.68	1.945	1.53
(103)	Hexagonal	16.28	3.775	2.13
(202)	Hexagonal	45.70	0.479	0.76

The vibrational and electronic states of the ZnSe film were investigated by Raman spectroscopy which is providing to characterize the materials with a non-destructive technique. The Raman spectrum of the electrodeposited ZnSe film was given in Figure 3 within the Raman shift range from 150 cm^{-1} to 600 cm^{-1}. There is a peak seen at 249 cm^{-1} attributed to the longitudinal optical (LO) phonon mode of the ZnSe. The LO phonon mode within the range of 238 cm^{-1} – 252 cm^{-1} was reported in earlier studies on electrodeposited ZnSe [3,12,16,17].

Additionally, FT-IR analysis was carried out to further structural analysis. Figure 4 illustrates the FT-IR transmission spectrum of the ZnSe thin film in the wavenumber range of 400 cm^{-1} to 2000 cm^{-1}. The researchers reported that characteristic Zn-Se vibrational modes were observed between 450 cm^{-1} and 1170 cm^{-1} [7–9,22,23]. The peaks observed in the FT-IR spectrum of the ZnSe thin film at 460, 603, and 744 cm^{-1} correspond to the characteristic Zn-Se vibration modes.

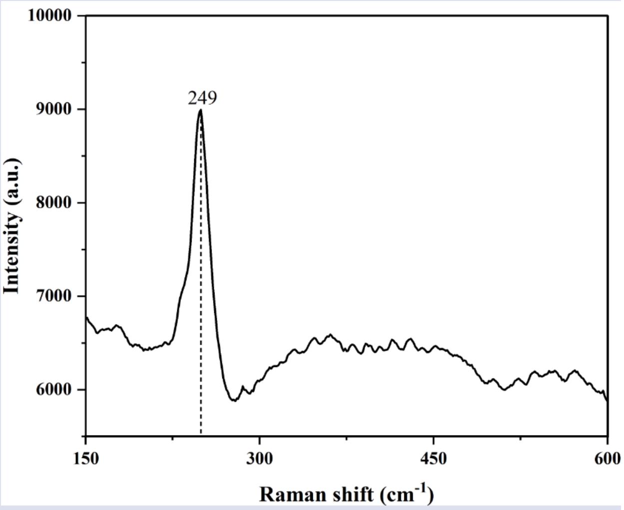

Figure 3. The Raman spectrum of the ZnSe thin film on ITO substrate.

The modes at 460 cm^{-1} and 603 cm^{-1} are attributed to the stretching vibration mode of Zn-Se, and the mode at 744 cm^{-1} represents the bending vibration mode of Zn-Se as given in the earlier studies [2,9,22].

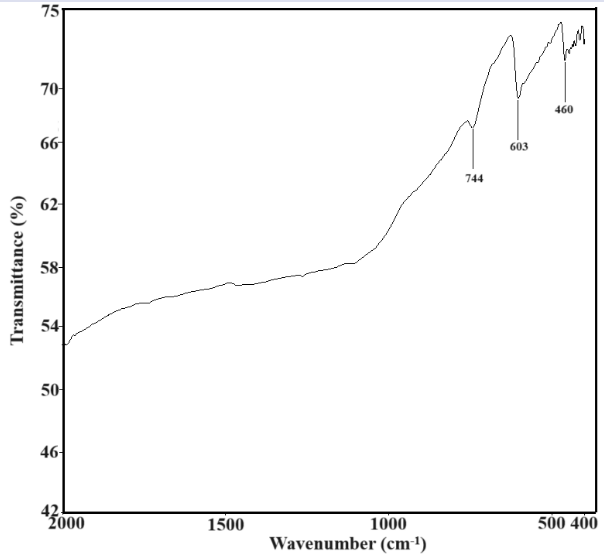

Figure 4. The FT-IR spectrum of the ZnSe thin film on ITO substrate.

Morphological Properties

The morphological properties of the ZnSe film on ITO substrate was investigated by the SEM analysis. Figure 5 presents SEM images of the ZnSe film at magnifications (a) 100.000x and (b) 5.000x. ZnSe film is made up of clusters that contain nanoparticles that range in size from 12 to 32 nm and the image taken at 100.000x magnification in Figure 5 (a) show these clusters. It can be clearly seen from Figure 5 (b) that the ZnSe thin film was deposited on the ITO substrate smoothly and homogeneously.

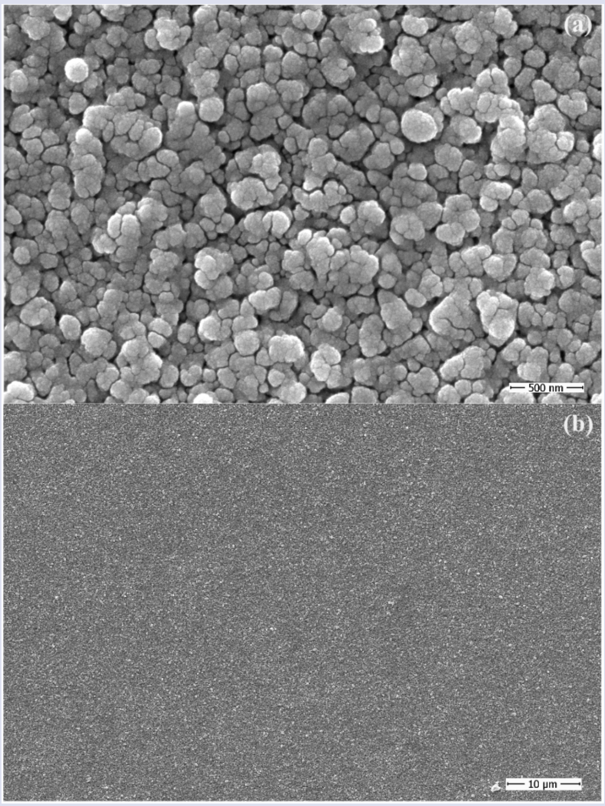

Figure 5. The SEM images of the ZnSe thin film at the (a) 100.000x and (b) 5.000x magnifications.

Electrochemical Measurements

The amperometric measurement was carried out for investigating the photoelectrochemical performance of the ZnSe thin film using the blue LED light (390 nm). Figure 6 shows the photocurrent-time graph obtained from the ZnSe thin film electrodeposited on the ITO substrate in a 0.1 M KCl solution, with the light source being switched on and off. As seen in Figure 6, the ZnSe film exhibited a photoresponse with light illumination and there was a significant increase in photocurrent.

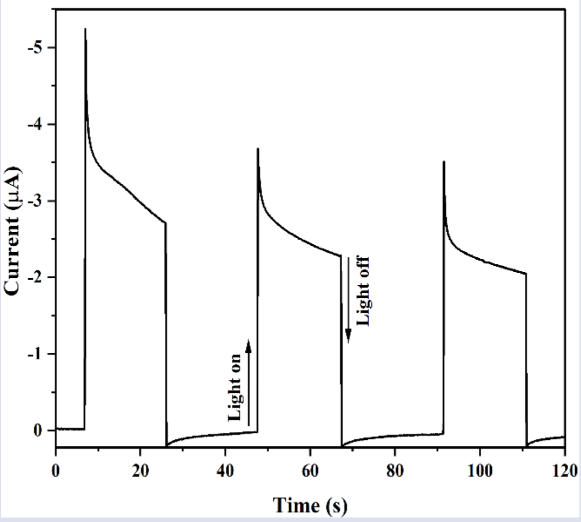

Figure 6. The current-time (I-t) plot of the ZnSe film at light on/off conditions.

Electrochemical impedance spectroscopy (EIS) measurement is a useful technique for investigating charge transfer at the interface between semiconductor and electrolyte. The EIS measurement was performed at open circuit potential (OCP) to determine the charge transport capability under dark and light illumination conditions. The Nyquist plots of the ZnSe thin film both with and without light illumination are shown in Figure 7. The plots of ZnSe have two regions of high- frequency and low-frequency and these plots were fitted with an equivalent circuit as shown in Figure 8. The Zview 2.1b software was used for simulating the Nyquist plots of the ZnSe thin films. The high-frequency region includes an electrolytic resistance (R_e), a charge transfer resistance (R_2) of the ZnSe film, and a doubled layer capacitance (C_1) which occurred interface between the ZnSe thin film/electrolyte. The Warburg (W) impedance which about the diffusion is seen at the low-frequency region. According to the fitting results, R_e decreased from 10.64 Ω to 9.87 Ω, R_2 decreased from 70.76 Ω to 67.27 Ω, and W-R decreased from 989.6 Ω to 586.4 Ω under light illumination.

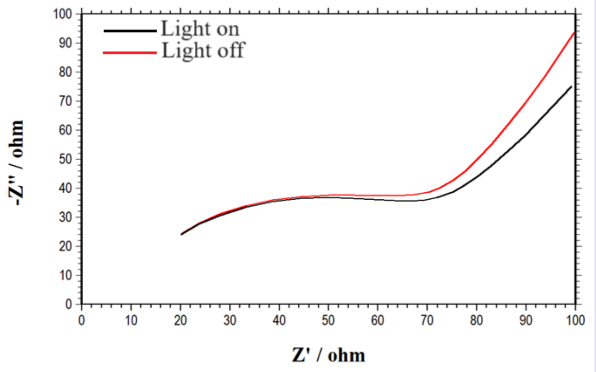

Figure 7. The Nyquist plots of the ZnSe film under light on/off conditions at OCP in 0.1 M KCl.

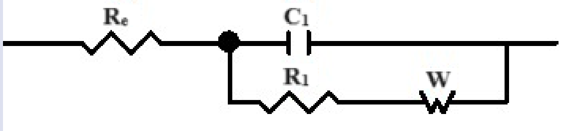

Figure 8. The equivalent circuit for the ZnSe film under light on and off conditions.

To reveal the conductivity type of the ZnSe thin film, Mott-Schottky (MS) analysis was performed with the impedance measurement in the potential range of -0.6 V to 0.1 V. The impedance measurement data was used to plot the potential versus $1/C^2$ graph that is given in Figure 9. The conductivity type of the film was determined based on the shift observed in the MS curve [24–26]. The ZnSe thin film displays a positive shift, indicative of n-type conductivity. Furthermore, the carrier concentration (N_D) and flat band potential (E_F) of the ZnSe was determined from the linear fit of the MS curve using the following equation:

$$\frac{1}{C^2} = \frac{2}{q\varepsilon\varepsilon_0 N_D}\left[(E - E_F) - \frac{k_B T}{q}\right] \tag{5}$$

C denotes the semiconductor's free charge region, N_D represents the semiconductor's carrier concentration (representing electron donors for n-type or the concentration of hole acceptors for p-type semiconductors), E signifies the applied potential. The determination of N_D was carried out utilizing the slope of the linear fit curve and the E_F was obtained through the extrapolation of the linear fit curve ($1/C^2$=0) [27,28]. The N_D and E_F values of the ZnSe thin film were found as 4.96x10^{11} cm^{-3} and -1.27 V, respectively.

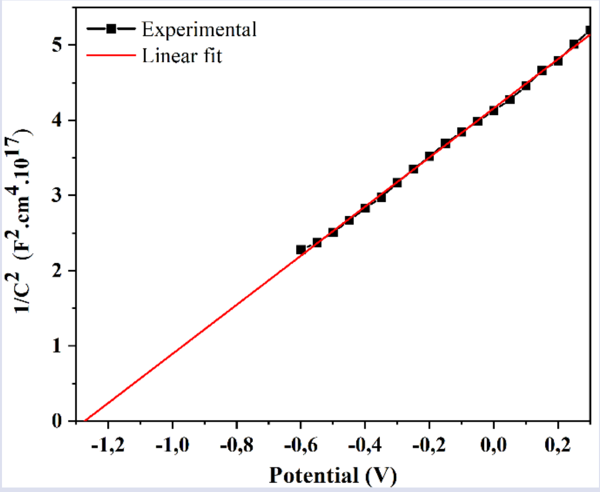

Figure 9. The Mott–Schottky experimental and linear fit curve of the ZnSe thin film.

Conclusion

The ZnSe thin film was synthesized on ITO substrate by electrodeposition technique in an aqueous solution at room temperature. The optical band gap (E_g) of ZnSe was found as 2.39 eV from the UV-Vis measurement, and the crystal structure of the ZnSe thin film matched mostly hexagonal structure by the XRD analysis. It was revealed that by the Raman analysis ZnSe thin film has a peak seen at 249 cm^{-1} associated with the LO phonon mode of the ZnSe, and by the FT-IR transmission spectrum it was seen that the stretching vibration mode and bending vibration mode of Zn-Se. SEM analysis demonstrated that the ZnSe film was made up of clusters that contain nanoparticles that range in size from 12 to 32 nm. The photoelectrochemical performance was investigated with I-t curve and it was obtained that ZnSe film exhibited a photoresponse with light illumination. Also, the value of the R$_e$, R$_2$, and W-R decreased under light illumination. The carrier type, N_D, and E_F values of the ZnSe film were determined as n-type, 4.96x10^{11} cm^{-3} and -1.27 V, respectively.

Conflicts of interest

There are no conflicts of interest in this work.

References

[1] Yudin N., Antipov O., Balabanov S., Eranov I., Getmanovskiy Y., Slyunko E., Effects of the Processing Technology of CVD-ZnSe, Cr^{2+}:ZnSe, and Fe^{2+}:ZnSe Polycrystalline Optical Elements on the Damage Threshold Induced by a Repetitively Pulsed Laser at 2.1 µm, *Ceramics*, 5 (2022) 459–471.

[2] Lal N., Chawla K., Sharma S., Chouhan R.L., Lal C., Study of electrodeposited zinc selenide (ZnSe) nanostructure thin films for solar cell applications, *Journal of the Indian Chemical Society*, 100 (2023) 101006.

[3] Prabukanthan P., Kumar T.R., Harichandran G., Influence of various complexing agents on structural, morphological, optical and electrical properties of electrochemically deposited ZnSe thin films, *Journal of Materials Science: Materials in Electronics*, 28 (2017) 14728–14737.

[4] Gromboni M.F., Mascaro L.H., Optical and structural study of electrodeposited zinc selenide thin films, *Journal of Electroanalytical Chemistry*, 780 (2016) 360–366.

[5] Dhanasekaran V., Mahalingam T., Rhee J.K., Chu J.P., Structural and optical properties of electrosynthesized ZnSe thin films, *Optik*, 124 (2013) 255–260.

[6] Yildirim E., Metin Gubur H., Alpdogan S., Ari M., Harputlu E., Ocakoglu K., The effect of annealing of ZnSe nanocrystal thin films in air atmosphere, *Indian Journal of Physics*, 90 (2016) 793–803.

[7] Khalfi R., Talantikite-Touati D., Tounsi A., Merzouk H., Effect of deposition time on structural and optical properties of ZnSe thin films grown by CBD method, *Opt. Mater*., 106 (2020) 109989.

[8] Arslan M., Maqsood A., Mahmood A., Iqbal A., Structural and optical properties of copper enriched ZnSe thin films prepared by closed space sublimation technique, *Mater. Sci. Semicond. Process*, 16 (2013) 1797–1803.

[9] Ivashchenko M.M., Buryk I.P., Opanasyuk A.S., Nam D., Cheong H., Vaziev J.G., Bibyk V. V., Influence of deposition conditions on morphological, structural, optical and electro-physical properties of ZnSe films obtained by close-spaced vacuum sublimation, *Mater. Sci. Semicond. Process*, 36 (2015) 13–19.

[10] Boo B.H., Xu N., Lee J.K., Growth of crystalline ZnSe : N thin films by pulsed laser ablation deposition, *Vacuum*, 64 (2002) 145–151.

[11] Prabukanthan P., Harichandran G., Electrochemical Deposition of n-Type ZnSe Thin Film Buffer Layer for Solar Cells, *J. Electrochem. Soc*., 161 (2014) 736–741.

[12] Xu J.L., Gong W.Y., Wang W., Meng H., Zhang X., Shi Z.N., Haarberg G.M., Electrodeposition mechanism of ZnSe thin film in aqueous solution, *Rare Metals*, 36 (2017) 816–820.

[13] Mahalingam T., Dhanasekaran V., Chandramohan R., Rhee J.K., Microstructural properties of electrochemically synthesized ZnSe thin films, *J. Mater. Sci*., 47 (2012) 1950–1957.

[14] Kowalik R., Szaciłowski K., Zabiński P., Photoelectrochemical study of ZnSe electrodeposition on Cu electrode*, Journal of Electroanalytical Chemistry*, 674 (2012) 108–112.

[15] Asil Uğurlu H., Hamurcu Y., Electrochemical growth of ZnSe thin films, characterization and heterojunction applications, *Mater. Res. Express*, 6 (2019) 116422.

[16] Lohar G.M., Thombare J. V., Shinde S.K., Han S.H., Fulari V.J., Structural, photoluminescence and photoelectrochemical properties of electrosynthesized

ZnSe spheres, *Journal of Materials Science: Materials in Electronics*, 25 (2014) 1597–1604.

[17] Lohar G.M., Shinde S.K., Rath M.C., Fulari V.J., Structural, optical, photoluminescence, electrochemical, and photoelectrochemical properties of Fe doped ZnSe hexagonal nanorods, *Mater. Sci. Semicond. Process*, 26 (2014) 548–554.

[18] Gubur Metin H., Septekin F., Alpdogan S., CdSe nanowires grown by using chemical bath deposition, *Journal of the Korean Physical Society*, 67 (2015) 1222–1227.

[19] Ildan Ozmen S., Metin Gubur H., Synthesis and characterization of CdTe/CdSe thin film on glass/ITO by electrodeposition at room temperature, *Bulletin of Materials Science*, 45(2) (2022) 77.

[20] Ildan Ozmen S., Temiz S.H., Metin Gubur H., Effects of annealing on SnS films produced by chemical bath deposition (CBD), *Phys. Scr.*, 97 (2022) 75704.

[21] Yildirim E., Ildan Ozmen S., Havare A.K., Gubur H.M., Annealing effect on CdS nanowalls grown by chemical bath deposition on glass substrate, *Phys. Scr.*, 98 (2023) 075933.

[22] Ivashchenko M.M., Opanasyuk A.S., Buryk I.P., Lutsenko V.A., Shevchenko A.V., Optical properties of pure and Eu Doped ZnSe films deposited by CSVS technique, *Journal of Nano- and Electronic Physics*, 9 (2017).

[23] Bhagavathula S.D., Kokkarachedu V., Acuna D.Q., Koduri R., Veluri S., Reddy V., Insight of electrical behavior in ferroelectric-semiconductor polymer nanocomposite films of PVDF/ZnSe and PVDF/Cu:ZnSe, *J. Appl. Polym. Sci.*, 134(25) (2017) 44983.

[24] Baran E., Yazıcı B., Preparation and characterization of poly (3-hexylthiophene) sensitized Ag doped TiO_2 nanotubes and its carrier density under solar light illumination, *Thin Solid Films*, 627 (2017) 82–93.

[25] Majumder S., Sankapal B.R., Facile fabrication of CdS/CdSe core-shell nanowire heterostructure for solar cell applications, *New Journal of Chemistry*, 41 (2017) 5808–5817.

[26] Schneider M., Langklotz U., Körsten O., Gierth U., Passive layer investigation on tin and tin solder alloys, *Materials and Corrosion*, (2023) 1-9.

[27] Baran E., Yazici B., Fabrication of TiO_2 -NTs and TiO_2 -NTs covered honeycomb lattice and investigation of carrier densities in I^-/I^{3-} electrolyte by electrochemical impedance spectroscopy, *Appl. Surf. Sci.*, 357 (2015) 2206–2216.

[28] Bayramoglu H., Peksoz A., Electronic energy levels and electrochemical properties of co-electrodeposited CdSe thin films, *Mater. Sci. Semicond. Process,* 90 (2019) 13–19.

Cumhuriyet Sci. J., 45(3) (2024) 530-536
DOI: https://doi.org/10.17776/csj.1485308

Cumhuriyet Science Journal

| csj.cumhuriyet.edu.tr | Founded: 2002 ISSN: 2587-2680 e-ISSN: 2587-246X Publisher: Sivas Cumhuriyet University

Effect of the Size of the Molecular Mass of Some Amine Groups Modified to Maleic anhydride-alt-1-Octadecene Copolymer on Thermal Stability

Hacıbayram Zengin [1,a,*]

[1] *Department of Chemistry, Faculty of Science and Arts, Cumhuriyet University, 58140 Sivas, Türkiye.*
**Corresponding author*

Research Article

History
Received: 16/05/2024
Accepted: 23/09/2024

ABSTRACT

In this study, 1-octadecene-alt-maleic anhydride (OC-MA) copolymer was synthesized by radical polymerization method. The synthesized copolymer was first time modified with ammonia, methylamine, aniline and hexamethylenediamine reagents in acetone environment. The modified amidic acid derivatives were divided into two parts as quantity. One of these amounts was dried as an amidic acid derivative, and the other was imidized in dimethylformamide environment with constant stirring at 150 °C for 5 hours. Structural characterizations of the obtained samples were determined from the FTIR spectra. Thermal stability was compared from Thermogravimetric Analysis (TGA) and Differential Scanning Calorimetry (DSC) curves. It was established that the modified copolymers were thermally more stable than that of the original OC-MA copolymer. However, it was observed that the size of the molar masses of the reagents participating in the modification reactions showed linear or parabolic increases according to thermal parameter temperature of the decomposition reaction obtained from the TGA and DSC curves.

Keywords: Copolymerization, Radical polymerization, Thermal analysis, Modification.

[a] *hbzengin@cumhuriyet.edu.tr* *https://orcid.org/0000-0003-3861-6671*

Introduction

One way to increase the thermal stability of straight chain polymers is to modify them. Polyimides (PI) have been the subject of extensive investigation since the 1960s, owing to their exceptional thermal stability, high mechanical strength, superior chemical resistance, and remarkable electrical properties [1]. Polyamide-imides are usually prepared by three methods; polycondensation of amide group containing dianhydrides or diamines; imide group containing diacids with diamines, trimellitic anhydride with diisocyanates or diamines. First method involves multi-step synthesis of dianhydride or diamine monomers and high temperature imidization [2]. Aromatic polyimides are widely acknowledged as high-performance materials renowned for their outstanding thermal and oxidative stabilities, as well as their excellent electrical and mechanical properties over prolonged periods of use. However, their rigid structure and strong intermolecular interactions render them difficult to process, presenting challenges such as poor thermoplastic flow and solubility, thereby limiting their widespread application. To address these processing issues, various strategies have been explored, including the incorporation of flexible units such as -NHCO-, -O-, and -SO_2-, some of which have been successfully commercialized [3]. Superior polymers are increasingly sought after in cutting-edge technologies such as microelectronics, semiconductors, and composites. Polyimides are frequently favored for these high-temperature applications, serving as coating materials and insulators for electronic components, thanks to their commendable thermal stability, excellent planarization, superior processability, and elevated glass transition temperature [4]. Cross-linking polymers brings about versatility to the polymer's mechanical properties and processing behavior [5]. In order to increase the heat resistance of a polymer, it is necessary to modify it. The thermal attributes of polymeric materials are widely recognized as their foremost defining features. TGA enjoys broad utilization due to its straightforward methodology and the valuable insights offered through a basic thermogram. The thermal endurance of polymer blends and alloys has undergone comprehensive examination [6-11]. Over time, driven by its relevance across diverse sectors within the polymer industries. Maleic anhydride serves as a valuable intermediary in organic synthesis, finding utility in crafting biologically potent compounds and serving as building blocks for polymerization processes [12]. Within a maleic anhydride (MA) molecule, one can find a conjugated bond alongside an electron-withdrawing carboxyl group. Hence, despite its resistance to polymerization under heat alone, maleic anhydride (MA) readily undergoes copolymerization with electron-donor monomers like 1-octadecene and vinyl acetate [13–14]. The presence of anhydride groups within the polymer chain endows this copolymer with high reactivity, facilitating its application across diverse fields. Copolymers of maleic anhydride (MA) frequently serve as compatibilizers in polymer blends [15–16]. Polyimides are synthesized through the imidization process of polyamidic acids, which are formed by the reaction of an anhydride with an amine or diamine [17]. The literature extensively documents the rapid formation of polyamidic acids at low temperatures, contrasting with the high-temperature requirement for imidization to occur. Copolymers containing maleic anhydride (MA) have been instrumental in crafting functional polymers, primarily attributed to the ring-opening reaction of the anhydride unit [18–20]. The 1-octadecene-alt-maleic anhydride (OC-MA) copolymer used in this paper has been synthesized in the authors' previous work [21-23]. The OC-MA copolymer underwent reactions with aniline (An), methylamine (MeA), ammonia (Am), and hexamethylenediamine (HMDA), yielding maleamidic acid and maleimide derivatives of OC-MA, as depicted in Fig. 1. These derivatives of the OC-MA copolymer were called as amidic acid-1-octadecene, bismaleamidic acid, maleimide and bismaleimide 1-octadecene copolymers. The polymers were characterized using Fourier transform infrared spectroscopy (FTIR), followed by comparison of their thermal degradation curves using TGA. Maleic anhydride-alt-1-octadecen (OC-MA) copolymer were sequentially modified by methylamine (MeA), ammonia (Am), aniline (An) and hexamethylenediamine (HMDA) to obtain copolymers of poly(amidic acid-1-octadecen) and poly(Bisamidic acid-1-octadecen) (BisAA-OC) by opening the maleic anhydride ring in the OC-MA copolymer.

In terms of novelty achieved, the main purpose of the present study is to obtain modified copolymers with higher thermal stability compared to the original copolymer and to expand their areas of use by synthesizing materials that are more robust and durable, especially against cracking.

Experimental

Materials

Monomers Maleic anhydride (MA, MW: 98,06) and 1-octadecene (OC, MW: 252,49) were obtained from Merck made in Germany, aniline (An, MW: 93.13), methylamine (MeA, MW: 31,06) ammonia (Am, MW: 17,03). Hexamethylenediamine (HMDA, MW: 116,21) were obtained from Aldrich Chemical Company, UK. *N,N*-dimethylformamide (DMF, MW: 73,09) was obtained from Merck Chemical Company, Germany.

Maleic anhydride- alt- 1-octadecene copolymer: OC-MA

Amidic acids:

Amidic acid-1-octadecene: AA-OC
Methylamidic acid-1-octadecene: MeAA-OC
Phenyl amidic acid-1-octadecene: PhAA-OC
Bis amidic acid-1-octadecene: BisAA-OC

Imides:

Maleimide 1-octadecene: MI-OC
Methylmaleimide 1-octadecene: MeMI-OC
Phenylmaleimide 1-octadecene: PhMI-OC
Bismaleimide 1-octadecene: BisMI-OC

Synthesis of Maleic anhydride-alt-1-octadecen copolymers

19.6 g of maleic anhydride was placed in a large dried test tube and dissolved in 30 mL of ethyl acetate. 21.6 mL 1-octadecene (1:1) and 0.8 g 2,2'-Azobis(2-methylpropionitrile) (AIBN) were added on it. It was heated from room temperature in a 70 °C water bath for two hours. Then, the mixture was placed in a beaker and precipitated by adding propanol. Following the precipitation of the maleic anhydride–alt-1-octadecene copolymer, it was filtered through a Buchner funnel under vacuum assistance. The copolymer was left in hexane solution for 24 hours, then filtered and dried again

Synthesis of Amidic acid, Bisamidic acid, Maleimide and Bismaleimide Derivatives

The poly(amidic acid-1-octadecene) copolymers were synthesized by reacting the OC-MA copolymer with An, Me, Am, and HMDA in DMF using a mixer in a large tube at room temperature. For the synthesizing amidic acid copolymers, the required amount of OC-MA copolymer is 10.0 g, one of An, MeA, Am and HMDA are 8.0 cm^3 and one of DMF used as solvent are 30 cm^3. While the reactions between OC-MA copolymer with Me, Am and HMDA rapidly are occurred when they are mixed at room temperature, those of OC-MA copolymer with An is obtained by mixing at 60 °C for 2 h. While the precipitates of amidic acid and BisAA-OC copolymers are white colored, PhAA-OC precipitate is red colored. This precipitates were dried under the vacuum at 60 °C. For the obtained maleimide-1-octadecene and BisMI-ST copolymers, 5.0 g of this precipitate are added to 50.0 cm^3 DMF and thus, they obtained a solution of amidic acid copolymers. The solutions were heated to 150°C for 5 hours and subsequently cooled to room temperature. The solid samples in the solution were filtered and dried under vacuum.

Structural Characterization and Thermal analysis of Copolymers

The copolymers were spectrophotometrically characterized using a Unicam Mark Mattson 1000 model FTIR spectrophotometer with KBr pellets. The TGA and DSC experiments were conducted utilizing a Shimadzu TA50İ model, employing a heating rate of 10°C min^{-1} under a flowing nitrogen atmosphere. The temperature range spanned from 25 to 600°C. Polymer samples weighing 10 mg each were employed for the examination. The nitrogen gas flow rate was maintained at 25 cm^3 min^{-1}.

Results and Discussion

Structural Characterization

The OC-MA copolymer (Fig. 1) exhibited anhydride units with characteristic peaks at 1804 and 1855 cm^{-1}, attributed to the symmetric and asymmetric C=O stretching vibrations, respectively [24]. The absence of these bands in the modified copolymer spectra indicates that the ring has opened and transformed into the amidic acid structure.

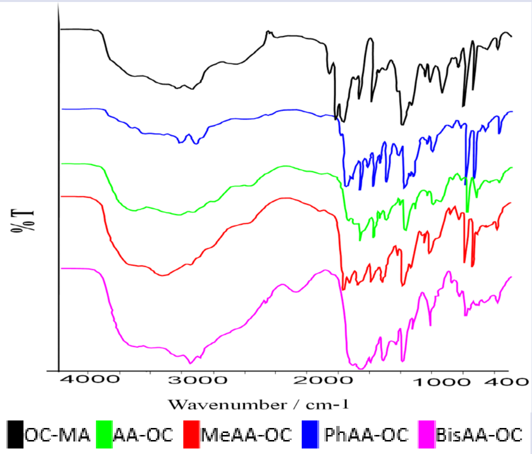

Figure 1. FTIR spectra of its amidic acid and bisamidic acid derivatives and OC-MA copolymer.

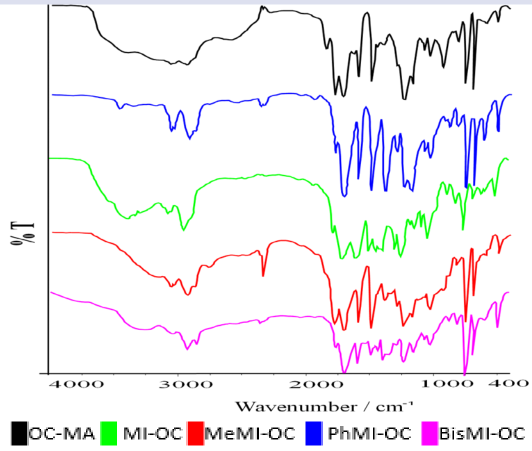

Figure 2. FTIR spectra of its maleimide and bismaleimide derivatives and OC-MA copolymer.

The C–O–C stretching vibrations stemming from the maleic anhydride (MA) ring were detected at 1025 and 935 cm^{-1}. Conversely, new peaks appeared within the range of 1778–1640 cm^{-1}, exhibiting characteristic peaks at 1640 and 1736 cm^{-1}, as well as 1727 and 1778 cm^{-1}, (Fig. 2) likely corresponding to the maleamidic acid and maleimide groups [25].

Thermal Analysis

The thermal transitions of amidic acid, BisAA-OC, MI-OC and BisMİ-OC were measured by TG technique and compared with that of OC-MA copolymers. The thermal curves are illustrated in Fig. 3 and Fig. 4, while the corresponding thermal parameters extracted from these figures are tabulated in Table 1. The thermal decomposition peaks observed at these temperatures are also reflected in the TGA thermograms, which can be observed in Fig. 3 and Fig. 4 for all the polymers. In the blue, green, red and pink colored thermograms In Figure 3, mass loss has been seen at 150 °C. This mass loss is due to loss of water arisen from the heating of amidic acid structures. Most water loss is seen in the pink colored thermogram. While 1 mol H_2O in the blue, green and red colored thermogram is removed, 2 mol H_2O in the pink colored thermogram has been removed. This structure is an indicator of bismaleimid formation.

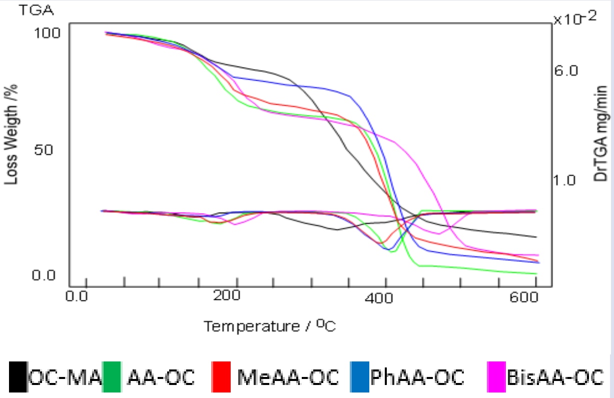

Figure 3. TGA and DrTGA curves of amidic acid and bis amidic acid copolymers.

Figure 4 by heating at 150°C for 2 hours in solution media amidic acids were heated for their imidization. their thermograms were taken and then comparatively presented. As can be shown in Figure 4, according to Figure 3 the mass loss was less than those of 150 oC. The cause of this situation may be still continuing of imidization reaction.

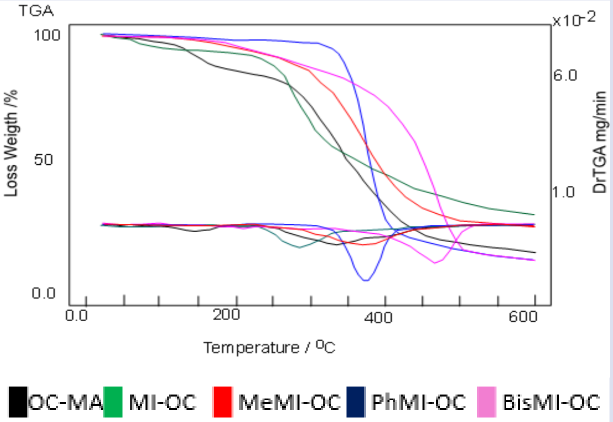

Figure 4. TGA and DrTGA curves of imides and bismaleimide copolymers.

The modification samples synthesized in Figure 4 were imitated in DMF medium at 150 °C for 5 hours. The thermograms of these modified samples were taken, which were imitated at room temperature up to 600 °C. The samples, which were both imitated outside and subjected to chemical transformation by heating the device, showed better stability against heat from the first steps compared to the starting material in this thermogram. As we mentioned in Fig. 4 and Fig. 3, there is also a regularity in thermal stability depending on the molecule size. The thermal parameters extracted from Fig. 3 and Fig. 4 indicate that the initial and final temperatures signify higher thermal stabilities for the amidic acid and MI-OC copolymers compared to the OC-MA copolymer, as depicted in Fig. 4. Based on these elucidations, the thermal stability of MI-OC surpasses that of the other copolymers due to the formation of cross-linkages via imidization, coupled with the elimination of 2 moles of water, as illustrated in Fig. 3.

T_i, initial degradation temperature, T_f final degradation temperature T_h half time temperature, T_m maximum rate temperature, T_g glass transition, R_m maximum rate and remained substance amount at maximum rate C_m given in

Table 1.The molar masses of the ammonia, methylamine, aniline and hexamethylenediamine substances added as modifications to the OC-MA copolymer are respectively (17, 31.06, 93.13 and 262.35 gmol^{-1}). Thermal parameters values plotted against molar masses Fig. 5 and Fig. 6 showed linear or parabolic increases.

Table 1. Thermal analysis parameters of copolymers

Copolymers	T_i / ^oC	T_f / ^oC	T_h / ^oC	T_m/ ^oC	T_g /^oC	R_m / mgdk^{-1}	C_m / %
OC-MA	279	434	348	328	108	0.0081	62
AA-OC	358	426	378	391	133	0.0142	41
MeAA-OC	362	428	384	403	135	0.0186	32
PhAA-OC	374	430	386	398	149	0.0172	42
BisAA-OC	420	495	426	465	160	0.0101	31
Mİ-OC	246	355	369	287	129	0.0084	63
MeMİ-OC	315	406	380	364	150	0.0096	76
PhMİ-OC	348	431	387	372	158	0.0239	61
BisMİ-OC	404	495	450	467	169	0.0169	40

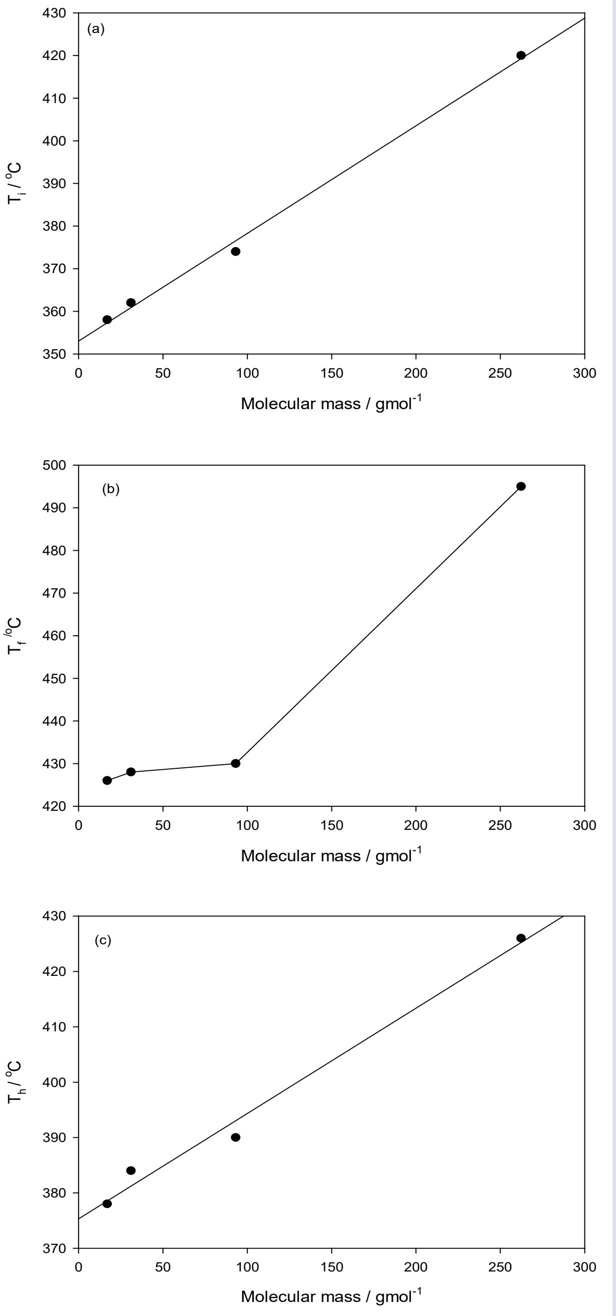

Figure 5. Variation of modified molar masses with thermal parameters (a) T_i , (b) T_f and (c) T_h of amidic acide OC-MA copolymers

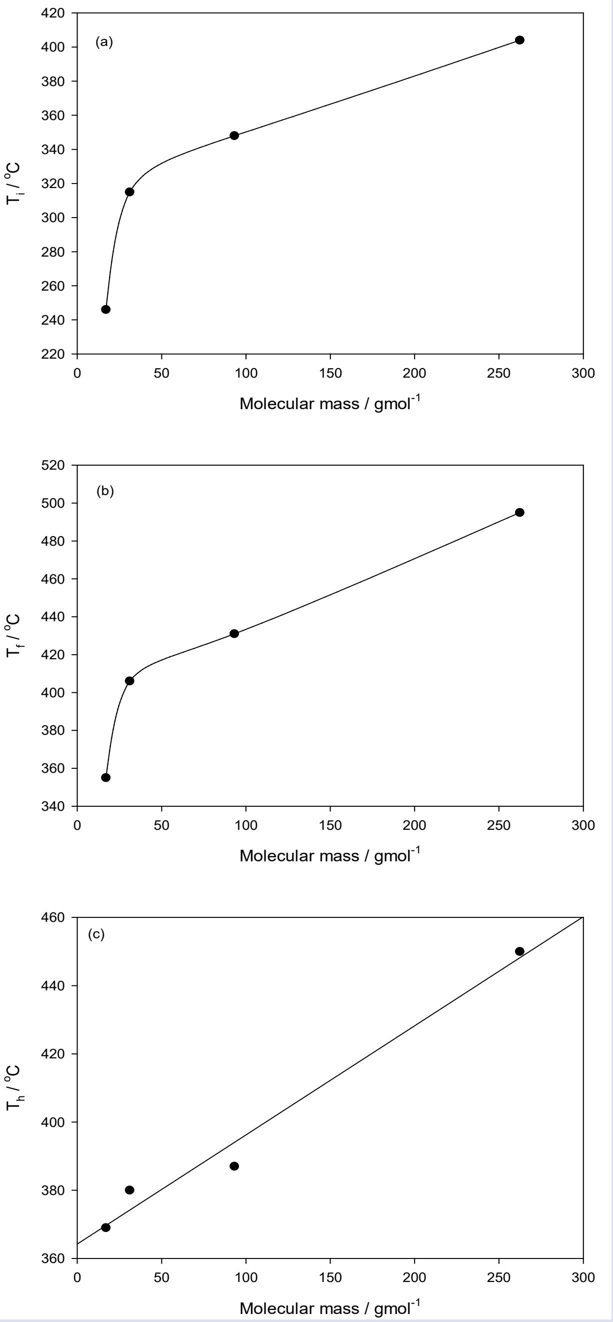

Figure 6. Variation of modified molar masses with thermal parameters (a) T_i , (b) T_f and (c) T_h of imide OC-MA copolymers

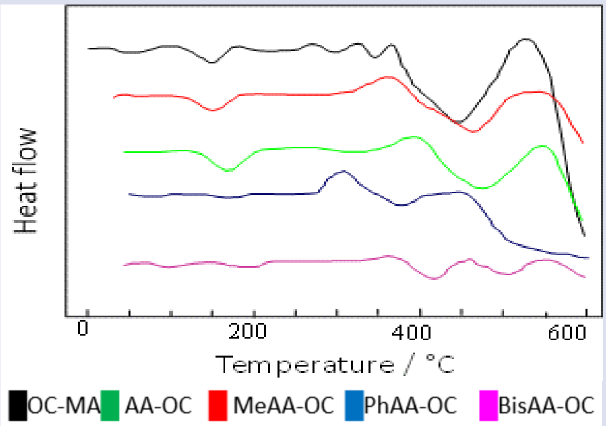

Figure 7. DSC curves of amidic acid and bis amidic acid copolymers.

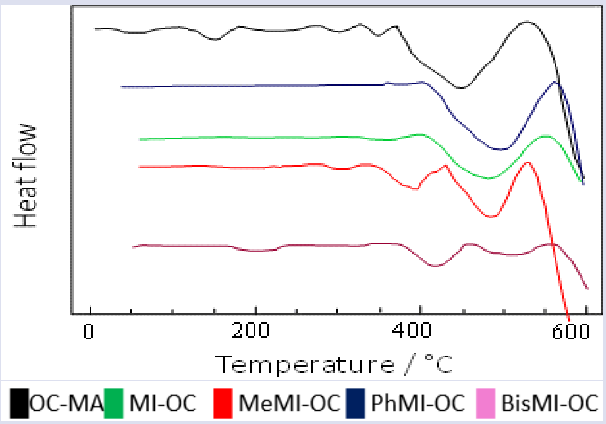

Figure 8. DSC curves of imides and bismaleimide copolymers.

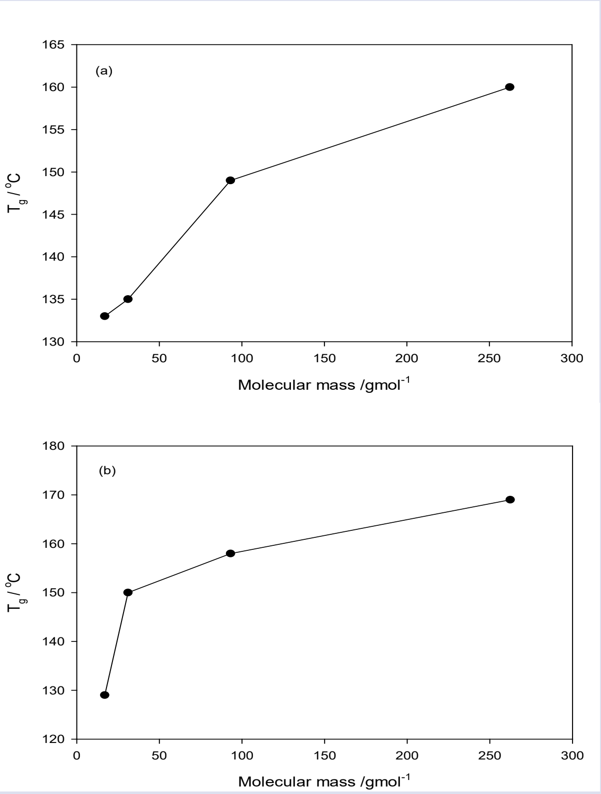

Figure 9. Variation of molecular mass size with glass transition temperature (a) T_g of amidic acid and (b) T_g imide

The glass transition temperatures obtained from DSC Fig.7 and Fig.8 thermograms showed a non-linear relationship with the size of the molecular masses of the modified amines [26].

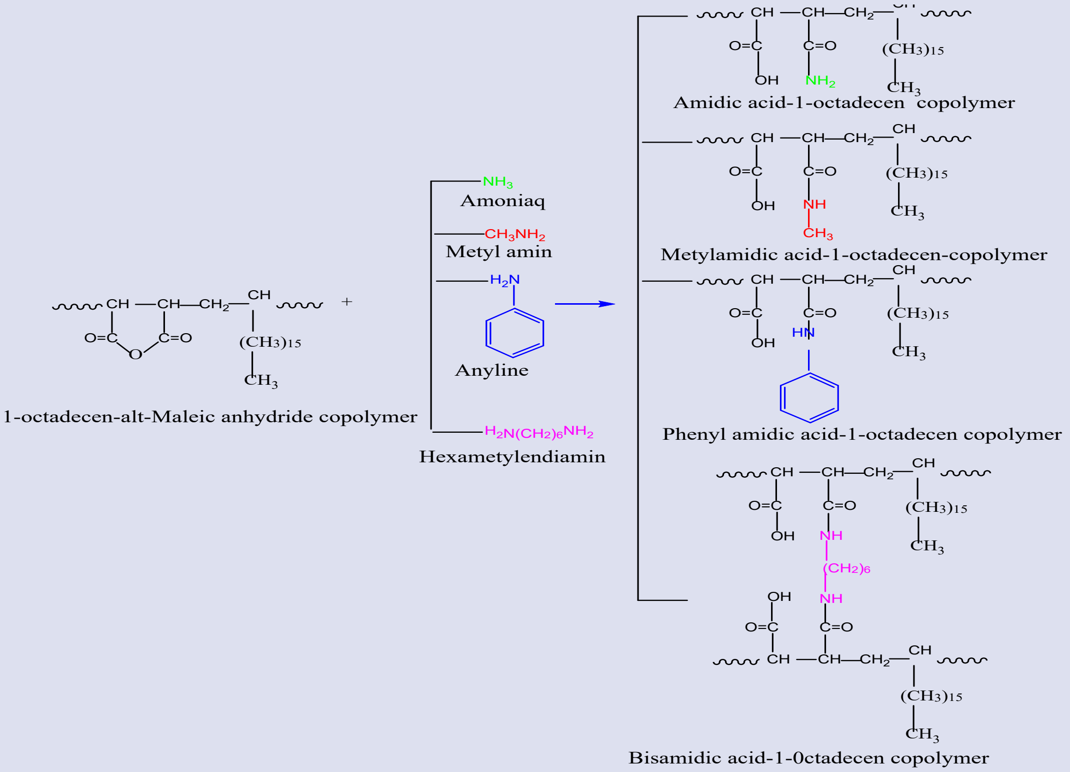

Scheme 1. Literature proposed formation mechanisms for thermal conversion of amidic acid and bisamidic acid derivatives of OC-MA copolymer.

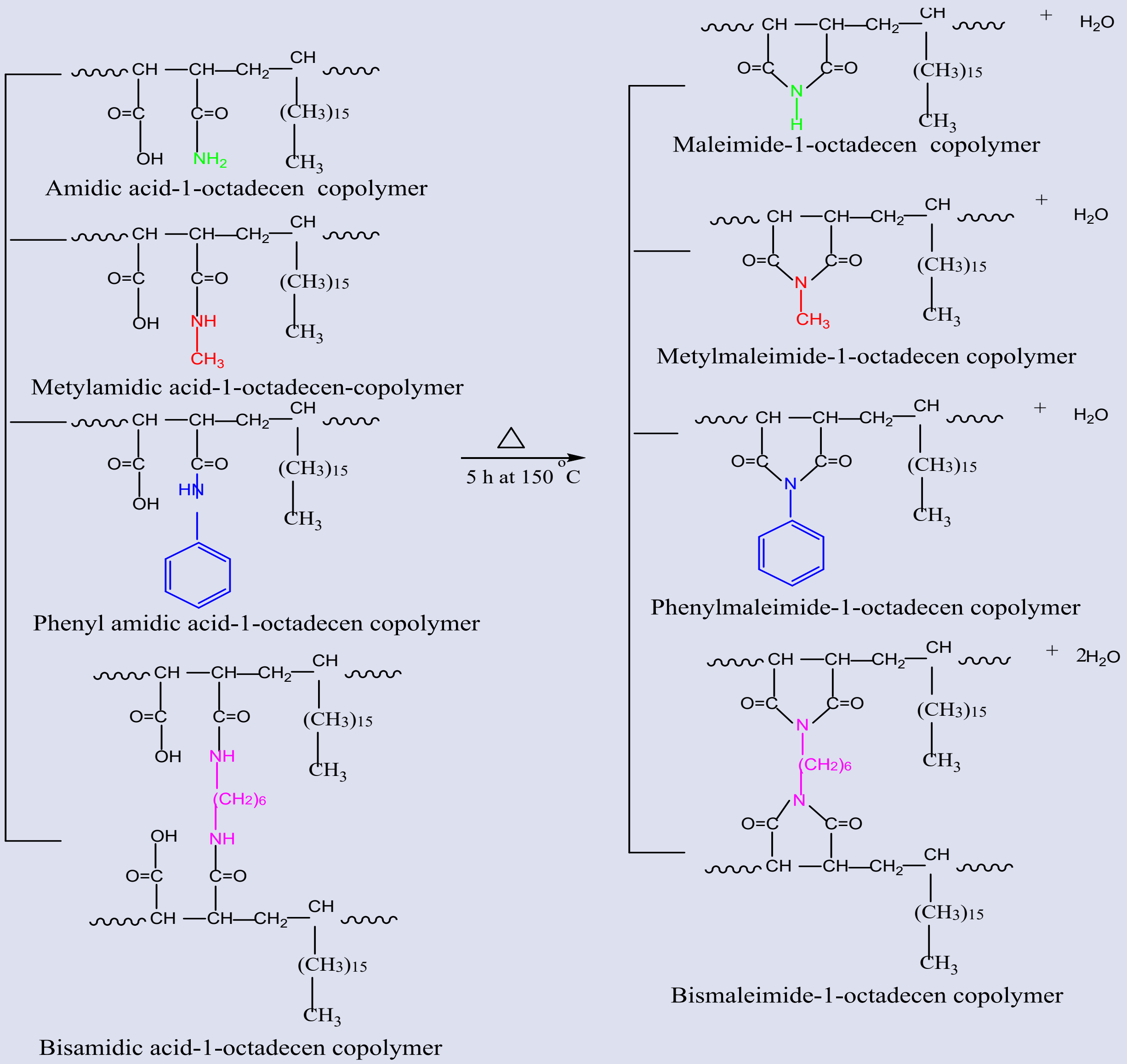

Scheme 2. Literature proposed formation mechanisms for thermal conversion of maleimide and bismaleimide derivatives of OC-MA copolymer.

Conclusions

The fact that the anhydride ring is active against amine groups enabled the reaction to occur in a short time period. The selection of modified amine groups was based on a simple structure such as ammonia, an aromatic structure such as aniline, and a hexamethylenediamine structure. The size of the molecular masses of the amines in the order of ammonia, methyl amine aniline and hexamethylenediamine (17, 31.06, 93.13 and 262.346 g mol^{-1}). The effect of the molar mass of the modified amines on thermal stability was clearly seen. The thermal stability of the newly modified copolymers obtained after modification of the OC-MA copolymer, shown in black in TGA, is higher than the OC-MA copolymer. The thermal parameters obtained in the TG curves increased linearly or parabolically with the molecular masses of the modified amine groups. This tells us that one way to increase the thermal stability of a polymer is to modify an active group in that polymer chain. Again, the glass transition temperatures obtained from the DSC curves increased either linearly or parabolically with the molar mass of the amine groups, similar to the thermal parameters in the TGA curves. Graphs were drawn between the molar mass and thermal parameters regarding the interpretation of the values obtained in the Table 1. Increases are generally seen in the graphs.

The bottom line is to modify a polymer to increase its thermal stability depending on where it will be used. The size of the molecular masses of the added modifying reactant groups causes a large effect here.

Conflicts of interest

There are no conflicts of interest in this work.

Acknowledgement

The present paper has been funded by the Research Foundation (Project number: F-105) of Cumhuriyet University in Sivas, Turkey.

References

[1] Dongdan C., Jianfeng S., Mei H., Yanhua L., Jianjun W., Lixing D., Synthesis, characterization and hydrolytic stability of poly (amic acid) ammonium salt, *Polymer Degradation and Stability*, 96 (2011) 2174-2180.

[2] Nafeesa M., Qiaodi W., Guofei C., Beenish B., Haoji L., Yuanming Z., Lala R. S., Xingzhong F., Synthesis of polyamide-imides with different monomer sequence and effect on transparency and thermal properties, *Polymer*, 190 (2020) 122218.

[3] Liaw D. J., Liaw B.Y., Synthesis and characterization of new polyamide-imides containing pendent adamantyl groups, *Polymer*, 42 (2001) 839–845.

[4] Rathanawan M., Wittaya L., Anuvat S.,. Schwank J. W., Preparation, structure, properties and thermal behavior of rigid-rod polyimide/montmorillonite nanocomposites, *Composites Science and Technology*, 61 (2001) 1253–1264.

[5] Liu. Y. L., Chen Y. W., Thermally Reversible Cross-Linked Polyamides with High Toughness and Self-Repairing Ability from Maleimide and Furan-Functionalized Aromatic Polyamides, *Macromol. Chem. Phys*, 208, (2007) 224–232.

[6] Zengin H. B.,. Boztuğ A., Basan S.¸ Synthesis and Comparative Study of Thermal Stabilities of the Imidization of Some Maleic Anhydride Copolymers, *Journal of Applied Polymer Science*, 101 (2006) 2250–2254.

[7] Jana R.N., Mukunda P. G., Nando G. B., Polym. Degrad. Stabil. “Thermogravimetric analysis of compatibilized blends of low density polyethylene and poly(dimethyl siloxane), *Rubber*, 80 (2003) 75–82.

[8] Yen H. Y., Lee F. S., and Yang M. H., Polym. Test, Thermal degradation of polysulfones. VI: evaluation of thermal pyrolysis of acrylonitrile-butadiene-styrene terpolymer 22, (2003) 31–36.

[9] Su W. Y., Wang Y., Min K., Quirk R. P., In situ copolymerization and compatibilization of polyester and polystyrene blends. I. Synthesis of functionalized polystyrenes and the reactions with polyester, *Polymer*, 42 (2001) 5107–5119.

[10] Zulfiqar S., Masud K., Stabil, Thermal degradation of blends of allyl methacrylate–methyl methacrylate copolymers with aluminum isopropoxide, *Polym. Degrad*, 78 (2002) 305–313.

[11] Yang M. H., The thermal degradation of acrylonitrile-butadiene-styrene terpolymer under various gas conditions*, Polym. Test,* 19 (2000) 105–110.

[12] Gabriele B.,. Veltri L., Salerno G., Costa M., Chiusoli G. P., Synthesis of Maleic Anhydrides and Maleic Acids by Pd-Catalyzed Oxidative Dicarbonylation of Alk-1-ynes, *Eur. J. Org. Chem*., 9 (2003) 1722–1728.

[13] Qian L., Shurong W., Yun Z., Zhongyang L., Cen K., Mechanism study of wood lignin pyrolysis by using TG–FTIR analysis*, J. Anal. Appl. Pyrolysis,* 82 (2008) 170–177.

[14] You Y. Z., Hong C. Y., Pan C. Y., Controlled alternating copolymerization of St with MAh in the presence of DBTTC, *Eur. Polym. J.*, 38 (2002) 1289–1295.

[15] Li H. M., Chen H. B., Shen Z. G., Lin S., Preparation and characterization of maleic anhydride-functionalized syndiotactic polystyrene, *Polymer*, 43 (2002) 5455–5461.

[16] Zhaohui L., Zhang X., Tasaka S., Inagaki N., The interfacial tension and morphology of reactive polymer blends, *Mater. Lett.* , 48 (2001) 81–88.

[17] Jeong J. H., Byoun Y. S., Lee Y. S., Poly(styrene-*alt*-maleic anhydride)-4-aminophenol conjugate: synthesis and antibacterial activity, *React. Funct. Polym.*, 50 (2002) 257–263.

[18] Zengin H. B., Boztuğ A., Yılmaz E., Chemical modification and thermal characterisation of poly(allylpropionate-altmaleic anhydride) copolymer modified by hexamethylenediamine, *Materials Research Innovations*,12(2) (2008),90-93.

[19] Patel H., Raval D. A., Madamwar D., Patel S. R., Polymeric prodrug: Synthesis, release study and antimicrobial property of poly(styrene-co-maleic anhydride)-bound acriflavine, *Angew. Makromol. Chem.*, , 263 (1998) 25–30.

[20] Roux M. V, Jimenez P., Angeles M., Luengo M., Davalos J. Z., Sun Z., Hosmane R. S., Liebman J. F., The Elusive Antiaromaticity of Maleimides and Maleic Anhydride: Enthalpies of Formation of *N*-Methylmaleimide, *N*-Methylsuccinimide, *N*-Methylphthalimide, and *N*-Benzoyl-*N*-methylbenzamide, *J. Org. Chem.*, 62 (1997) 2732–2737.

[21] Molaeia H., Zaaerib F., h Sharific S., Ramazania A., Safaeid S., Abdolmohammadie J., Khoobif M., Polyethylenimine-graft-poly (maleic anhydride-alt-1-octadecene) coated Fe3O4 magnetic nanoparticles: promising targeted pH-sensitive system for curcumin delivery and MR imaging, *International Journal Of Polymeric Materials And Polymeric Biomaterials*, 70(18) (2021) 1344–1353.

[22] Ute Schmidt, Stefan Zschoche, Carsten Werner, Modification of Poly(octadecene-*alt*-maleic anhydride) Films by Reaction with Functional Amines, *Journal of Applied Polymer Science*, 87 (2003) 1255–1266.

[23] Ayman M., Atta S., El-Hamouly H., AlSabagh M. A., Moataz M. G., Crosslinked Poly(octadecene-alt-maleic anhydride) Copolymers as Crude Oil Sorbers, *Journal of Applied Polymer Science*, 105 (2007) 2113–2120.

[24] Karakus G., Zengin H. B., Akin Polat Z., Yenidunya A F., Aydin Semiha., Cytotoxicity of three maleic anhydride copolymers and common solvents used for polymer solvation, *Polym. Bull*, 70 (2013) 1591–1612.

[25] Zengin H.B., Gürkan R., Novel amide- and imide-co-polymers modified with sulfathiazole as efficient chelator for selective extraction, pre-concentration and determination of trace inorganic antimony (as Sb(III)) from edible vegetable oils by ultrasound assisted-cloud point extraction coupled to micro-volume UV-spectrophotometry, *Journal of Food Composition and Analysis*, 115 (2023) 104931.

[26] Ahokas M., Wilén Carl-Eric, Synthesis of poly (styrene-co-maleimide) and poly(octadecene-co-maleimide) nanoparticles and their utilization in paper coating, *Progress in Organic Coatings,* 66 (2009) 377–381.

Cumhuriyet Sci. J., 45(3) (2024) 537-542
DOI: https://doi.org/10.17776/csj.1497258

Cumhuriyet Science Journal

| csj.cumhuriyet.edu.tr | Founded: 2002 ISSN: 2587-2680 e-ISSN: 2587-246X Publisher: Sivas Cumhuriyet University

Determination of Cytotoxic Activity of *Aronia melanocarpa* (Michx.) Elliot Fruit Extracts on Breast Cancer (MCF-7) and Cervical Cancer (HeLa) Cell Lines

Eda Sönmez Gürer[1,a,*], **Ayhan Altıntaş**[2,b]

[1] Department of Pharmacognosy, Faculty of Pharmacy, Sivas Cumhuriyet University, 58140, Sivas, Türkiye
[2] Department of Pharmacognosy, Faculty of Pharmacy, Anadolu University, 26470, Eskişehir, Türkiye
**Corresponding author*

Research Article

History
Received: 07/06/2024
Accepted: 23/09/2024

ABSTRACT

Aronia (chokeberry) fruits are consumed as fresh fruit due to their high antioxidant activity, and are also preferred among the public in the production of natural medicines. *Aronia melanocarpa* (Michx.) Elliot, a species of the Rosaceae family, contains many phytochemical compounds such as flavonoids, phenolic compounds, lignans, terpenes, tocopherols, phospholipids, organic acids and high amounts of anthocyanins. In this study, it was aimed to determine the *in vitro* anticarcinogenic activities of *A. melanocarpa* (Michx.) Elliot fruit extracts prepared with 6 different solvents. In the study, the cytotoxic effects of the fruits were investigated using breast cancer cell line (MCF-7) and cervical cancer cell line (HeLa), and their effects on healthy cells were investigated using human endothelial cells (HUVEC) and mouse fibroblast cells (L929) by the MTT method. As a result of the study; It was determined that the highest cytotoxicity on the breast cancer (MCF-7) cell line was observed in the ethanol extract (IC_{50}=111.44 µg/mL) and the lowest cytotoxicity was observed in the hexane extract (IC_{50}=661.80 µg/mL). It was determined that the highest cytotoxicity on the cervical cancer (HeLa) cell line was observed in the ethanol extract (IC_{50}=95.14 µg/mL) and the lowest cytotoxicity was observed in the ethyl acetate extract (IC_{50}=319.51 µg/mL). According to these values; It was determined that all extracts of Aronia fruit had cytotoxic effects on MCF-7 and HeLa cell lines, selectivity index values were higher in HeLa cells, and they did not have cytotoxic effects on HUVEC and L929 healthy cell lines (IC_{50}=411.25-663.27 µg/mL). Thus, it has been determined that the fruits of the *Aronia melanocarpa* species are promising in the development of new natural resources, new drugs and therapeutic agents in cancer treatment, thanks to their anticancer activities and low cytotoxicity. It is recommended that further research be conducted on the mechanisms of anticancer activity in the future.

Keywords: *Aronia melanocarpa,* Antioxidant, Anticancer, Cytotoxicity.

[a] *edagurer@cumhuriyet.edu.tr* *https://orcid.org/0000-0003-0319-6312* [b] *aaltinta@anadolu.edu.tr* *https://orcid.org/0000-0002-9413-0636*

Introduction

Of late years, the preference for native produces in the protection and therapy of illnesses has increased. *Aronia melanocarpa* grows in the form of a bush, its fruits are small, dark purple or almost black in color, and like other berry-derived fruits, it attracts the attention of researchers because it has high antioxidant potential. It is known that the most important structure that makes aronia attractive is its high phenolic compounds, most importantly anthocyanins in the form of cyanidin derivatives. Fruits contain high amounts of polyphenolic compounds, as well as many biologically active vitamins, especially vitamins C and E, various minerals, carotenoids, pectins and organic acids [1]. Aronia; Chokeberry, commonly known as Chokeberry, is a fruit belonging to the Aronia genus of the Maloideae subfamily of the Rosaceae family. There are two species of this genus consumed as fruit: *Aronia melanocarpa* (Michx.) Ell. (black currant) and *Aronia arbutifolia* (L.) Pers. (red chokeberry) [1].

Phenolic compounds, especially those commonly found in fruits, have a significant impact on human health as they prevent diabetes, allergies, vascular diseases, hypertension, thrombosis, have cardioprotective, neurological damage, and anticancer properties [2]. These secondary metabolite groups, which are important antioxidant compounds of plant origin, are the main functional compound groups that enable plants to be used for medicinal purposes and contribute to people's healthy lives and the continuity of their current state of health [3].

Berries such as blueberries, blackberries, blueberries, aronia and raspberries are food sources with high antioxidant activity [4,5]. The fact that consumption rates in the world have been increasing in recent years has significantly increased the value of these fruits in exports and imports [6]. Medicinal and aromatic plants serve humanity because they are edible and drinkable resources. Plants contain natural antioxidants, antimicrobial, antiviral and antineoplastic, etc. There are various active ingredients that act as such, and therefore they are at the center of many pharmacological activity studies. It has been shown in various studies that various functional compounds such as phenolic compounds, flavonoids and anthocyanins naturally found in plant contents provide great benefits in maintaining health in people with their antioxidant, antimicrobial, preventing Alzheimer's disease, preventing pulmonary diseases, preventing diabetes and anticarcinogenic potentials [7–9]. It has been determined that aronia, which is in the berry class, is more valuable than other berry fruits (such as blueberries, blackberries, blueberries, raspberries) due to its high content of antioxidant phytochemical compounds [10]. A study conducted with chokeberry juice, green tea and apple juice shows that; with the addition of chokeberry juice to apple juice, the content becomes richer in terms of vitamin C, phenolic acids and anthocyanins. The addition of green tea extract resulted in a much more significant enrichment of apple juice in phenolic acids and flavonoids than chokeberry juice [11].

If we look at the sources of the World Health Organization (WHO); cancer ranks second among the causes of death in the world. Mostly lung, breast, colorectal, prostate, skin and stomach cancers are seen. Lifestyles known to be related to cancer development include excessive weight, Inadequacy of consumption of fruits and vegetables, inactivity and consumption of tobacco products and alcohol [12].

The reason why Aronia species are more popular among other fruits for scientists is; It can be listed as having antiatherosclerotic, hypotensive and antiplatelet activities, primarily heart and cardiovascular diseases, protective effect on stomach ulcers, preventing liver damage, cancer diseases prevention and antiproliferative effects [1]. In this study, it was aimed to determine the *in vitro* anticarcinogenic activities of *A. melanocarpa* (Michx.) Elliot fruit extracts prepared with 6 different solvents. In the study, the cytotoxic effects of the fruits were investigated using breast cancer cell line (MCF-7) and cervical cancer cell line (HeLa), and their effects on healthy cells were investigated using human endothelial cells (HUVEC) and mouse fibroblast cells (L929) by the MTT method.

Materials and Methods

Materials

DMEM (Sigma–Aldrich), L-Glutamine Streptomycin (Sigma–Aldrich), MTT Solution (Applichem A-1080), Absolute Ethyl alcohol (Sigma), Tris-Acetic Acid-EDTA (TAE, 5x) to be used in experiments.), Dimethyl sulfoxide (DMSO), Trypsin (Applichem), Potassium chloride (KCl), phosphoric acid (H_3PO_4), sodium chloride (NaCl), sodium phosphate (NaH_2PO_4), ethyl alcohol (C_2H_5OH), FBS (Sigma–Aldrich), RPMI 1640 (Sigma–Aldrich), acetonitrile (Me-CN), Tris-Boric Acid-EDTA (TBE, 10x), Trypsin (Applichem), Sodium hydroxide (NaOH), sodium chloride (NaCl), sodium phosphate (NaH_2PO_4), thiobarbituric acid (TBA), 2,3,5-Triphenyltetrazolium chloride (TTC) (Merck, Germany) were provided.

In this study, as plant material, fruits obtained from *Aronia melanocarpa* (Michx.) Elliot type plant was purchased from the producer company named Dr. Aronia and dried in the shade.

Plant Extraction

It was added from 100 ml solvents on a 20 g of ground dry plant and kept at room temperature 24 hours a day, then drained and the same process was repeated for 3 days. The collected extracts were blown in the evaporator (40 ° C) using vacuum, the extract was combined with dark glass bottles and % yield calculation was performed for use in bioactivity studies and kept at -20 ° C.

For water extract; 100 ml of hot distilled water was added on the 20 g of ground dry plant and kept at for 10-15 minutes, then drained and the same process was repeated 3 times. Lyophilization process was applied to the collected extract, combined in dust dust dark glass bottles and % yield calculation was made and kept at -20 ° C for use in bioactivity studies.

Stock solutions were prepared from each extract at a concentration of 1 mg/mL to be used in biological activity studies. Stock solution concentrations to be used in the studies were prepared by dissolving the water extract in distilled water and the other extracts in dimethylsulfoxide (DMSO).

Determination of Antitumor Activity In vitro

Within the scope of this study, to define the *in vitro* anticancer potential of aronia plant fruit extracts; breast cancer (MCF-7) and human cervical adenocarcinoma (HeLa) cell lines were used. Cancer cell lines were incubated in DMEM in 75 flasks by placing them in a CO_2 incubator to proliferate sufficiently [13,14].

Cell lines were cultured in media containing DMEM and 10% FBS in 25 cm^2 flasks in an oven with 5% CO_2 at 37 °C. The flasks that reached the passaging state were selected and the sowing process was started in a sterile laminar Flow-cabinet. 5 mL Trypsin-EDTA solution (0.25%) and phosphate buffer (PBS) were added to the medium to remove cells adhering to the flask. 15 mL of DMEM was added onto the trypsin and the inside of the flasks were washed thoroughly by pipetting. The flasks were then transferred to the falcons, one flask to the other. In order to determine whether the cells proliferated appropriately for transplanting into 96-well cell culture plates and to count them, they were stained with Trypan blue and counted using a Thoma slide and an inverted microscope [15,16]. The falcons were centrifuged at 2000 rpm for 8 minutes, and after the centrifugation, the cells were collected at the bottom of the falcons. The upper phase was poured, the cells were removed by tapping the falcons slowly, and 20 mL DMEM and 5 mL FBS were added to the cells. 200 µL of the mixture was placed in each of 96 wells ($5x10^3$ cells in 100 µl/plate space). At the end of the process, the 96-well plates were removed to the incubator (Autoflow IR) [13,14].

Extracts at different concentrations were added to the cells planted in 96-well plates, in triplicate, and at the end of the process, the 96-well plates were placed in the incubator and the cell cultures were incubated for 24 hours. At the end of the period, 10 microliters of 12 mM MTT (Vybrant, Invitrogen) solution was added to the wells and incubated for 4 hours at 37°C in an oven with 5% CO^2 capacity. At the end of the period, the absorbance was measured in 570 nm in the microbial reader (Thermo, USA). As a result of the MTT determination, IC_{50} values were determined using the Graphpad program and graphics were drawn. components (SI) has been calculated by obtaining the IC_{50} ratio on the IC_{50}/cancer line on the healthy cell line [15].

Determination of Cytotoxic Activity In Vitro

In this study, MTT test was used on human endothelial cell (HUVEC) line and mouse fibroblast cell (L929) line for *in vitro* cytotoxicity research. In the first stage of viability tests performed with tetrazolium compounds, cells were incubated with plant extracts for 24 hours. MTT solution was prepared (5mg/ml), for which MTT chemical was dissolved in dH_2O and filtered before use. In the second stage, the media incubated in 96-well plates were emptied and 50 mL of MTT tetrazolium compound and 50 microliters of new medium were added to the cell cultures. It was incubated at 37°C for an average of 1-4 hours. For the spectrophotometer, 200 microliters of DMSO solvent was added to dissolve the formazan crystals and homogenized by gentle mixing. Finally, the amount of living and non-living cells was detected by color differences at a wavelength of 570 nm using the spectrophotometric method [16–18]. The obtained spectrophotometric data were converted to IC_{50} values in the Graphpad program and it was evaluated whether 6 different extracts made from aronia plant fruits had any lethal toxic effects on HUVEC and L929 cells.

Statistical Analysis

SPSS 23.0 (IBM Corporation, Armonk, New York, United States) program was used to analyze the data. While Independent-Samples T test is used to compare two groups, One-Way Anova test is used to compare more than two groups; LSD, Dunnett and Games Howell tests were used for post hoc analyses. The Kruskal-Wallis Test technique, one of the non-parametric conditions, was used. IC_{50} values were calculated using the Graphpad program. Quantitative data are mean ± S.D. (standard deviation) values are expressed in tables. Categorical data were expressed as n (number) and percentage (%). The results were evaluated at the 95% confidence level and considered important if the p value was less than 0.05.

Results and Discussion

In our study, firstly extractions of Aronia fruits with different solvents were prepared and biological activity analyzes were carried out according to the aim of the study. The yield calculations of the extracts prepared with different solvents were calculated as a percentage based on the dry plant. Extraction yields of the fruit vary between 68.6% g and 1.25% g. It was observed that the highest yield was in the methanol solvent and the lowest in the hexane solvent (Table 1).

Table 1. Extract yields of *Aronia melanocarpa* fruits prepared with different solvents

Extract	% Extraction efficiency
Methanol	%68,6
70% Ethanol	%36,84
Ethanol	%5,72
Ethyl acetate	%2,15
Hexane	%1,25
Water	%30,85

The extracts obtained from the fruit with 6 different solvents were applied on two separate cancer cell lines (MCF-7 and HeLa) at different concentrations between 0.1 µg/mL and 1000 µg/mL, and their cytotoxic activities were examined using the MTT test after 24 hours of incubation, all ext. It was observed that all extracts had moderate cytotoxic activities on MCF-7 and HeLa cell lines, and the highest cytotoxic activity was in the ethanol extract (Table 2). It was determined that aronia fruit extracts were more effective on the HeLa cell line than on the MCF-7 cell line, and ethanol extracts and methanol extracts had a more cell viability-reducing effect on these cells than others (Figure 1 and Figure 2).

Table 2. IC_{50} levels of *Aronia melanocarpa* fruit extracts in MCF-7 and HeLa cell lines

Extract	MCF-7 IC_{50} Values µg/mL	HeLa IC_{50} Values µg/mL
Methanol	268,42 ± 54,63	101,55 ± 24,27
70% Ethanol	237,18 ± 42,19	98,98 ± 28,31
Ethanol	111,44 ± 39,67	95,14 ± 22,87
Ethyl acetate	259,50 ± 54,43	319,51 ± 88,25
Hexane	661,80 ± 78,70	163,98 ± 73,48
Water	346,12 ± 84,56	116,12 ± 58,63

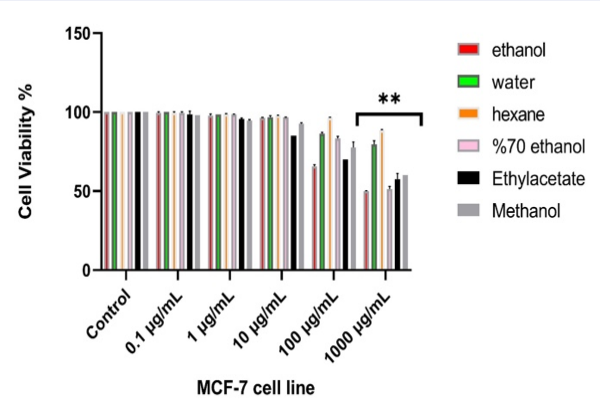

Figure 1. % Cell viability results of *Aronia melanocarpa* fruit extracts in MCF-7 cell line. Activities were evaluated after 24 hours of incubation. (**p<0.01)

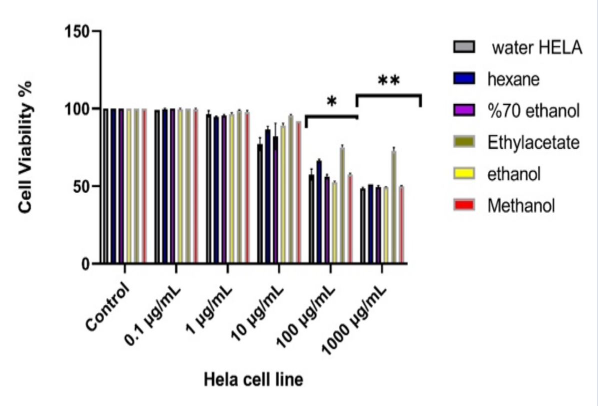

Figure 2. % Cell viability results of *Aronia melanocarpa* fruit extracts in HeLa cell line. Activities were evaluated after 24 hours of incubation. (**p<0.01)

The extracts obtained from aronia fruit with 6 different solvents were applied on two separate healthy cell lines (HUVEC and L929) at concentrations between 0.1 μg/mL and 1000 μg/mL, and after 24 hours of incubation, their cytotoxic activities were examined using the MTT test. As a result of the MTT reaction, readings were made on the Elisa device (Thermo). IC_{50} values showing the effects of extracts on different cell lines are presented in Table 2. There was no statistically important difference between the control group and the dose groups in both cell lines ($p>0.05$; Table 3.). In the light of these data, it was concluded that aronia fruit extracts did not have a cytotoxic effect on healthy cell lines HUVEC and L929.

Table 3. IC_{50} values of *Aronia melanocarpa* fruit extracts in HUVEC and L929 cell lines ($p>0,05$)

Extract	**HUVEC** **IC_{50} Values μg/mL**	**L929** **IC_{50} Values μg/mL**
Methanol	468,72± 79,11	501,22± 54,45
70% Ethanol	437,59± 51,49	497,18± 77,28
Ethanol	411,25± 49,13	459,27± 85,46
Ethyl acetate	569,47± 74,16	521,55± 96,08
Hexane	458,85± 78,27	663,27± 103,12
Water	463.27± 84,73	506,42± 114,13

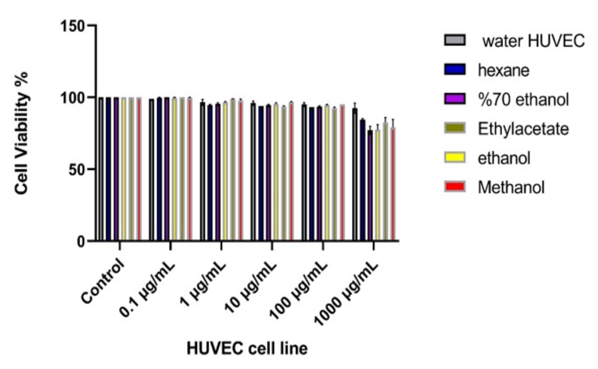

Figure 3. % cell viability results of *Aronia melanocarpa* fruit extracts in HUVEC cell line

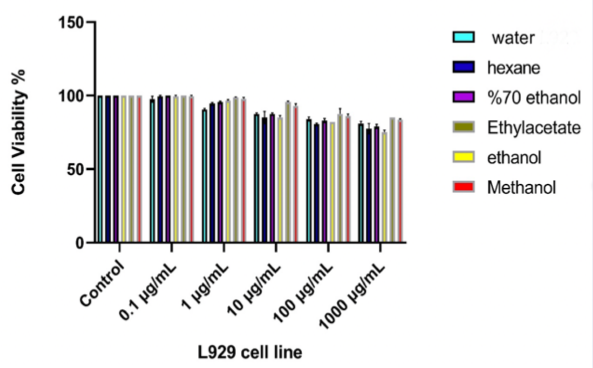

Figure 4. % cell viability results of *Aronia melanocarpa* fruit extracts in L929 cell line

By comparing the IC_{50} values of the MCF-7 and HeLa cell lines, which are cancer cell lines to which aronia fruit extracts were applied, and the healthy HUVEC cell line, comparison results were obtained regarding which cells the plant extracts are most effective on (Table 4). In this comparison, defined as the selectivity index, aronia plant ethanol extract showed the highest anticarcinogenic potential in the MCF-7 cell line with a selectivity index value of 3.69, and aronia plant methanol extract showed the highest anticarcinogenic activity in the HeLa cell line with a selectivity index value of 4.62 can be seen. In Table 4, the selectivity index values of plant extracts in the hala cells are higher.

Table 4. Selectivity Index obtained from the comparison of IC_{50} values of *Aronia melanocarpa* fruit extracts in HUVEC, MCF-7 and HeLa cell lines

	Selectivity Index	
Extract	**IC_{50} (HUVEC/MCF-7)**	**IC_{50} (HUVEC/HeLa)**
Methanol	1,75	4,62
70% Ethanol	1,84	4,42
Ethanol	3,69	4,32
Ethyl acetate	2,19	1,78
Hexane	0,69	2,80
Water	1,34	3,99

For many years; The fruits were first consumed fresh, then made into rusks, and brewed as tea for influenza infections. As fresh fruit or dried, freshly squeezed juice, jam, sherbet, sauce, cake. Conditions where it is most frequently used in treatment. *Aronia melanocarpa* is a high antioxidant capacity and rich in anthocyanins. In both *in vitro* and *in vivo* studies; Stomach ulcers have been found to have healing potentials on diseases such as many cancer and diabetes.

Sharif et al.; The effects of *Aronia melanocarpa* fruit juice on the stem cell line P19 in mouse embryonal carcinoma cells were investigated; As a result of the experiment, it was concluded that aronia fruit juice inhibited cell proliferation and caused the induction of apoptosis [19]. In a study investigating the biological effects of *Aronia melanocarpa* extracts on the human colon adenocarcinoma cell line; The anticancer activity of extracts was detected by MTT test. In conclusion; It was thought that *A. melanocarpa* leaf extract may show anticancer activity [20]. In the study conducted by Mcdougall et al.; Berry fruit extracts, rich in polyphenols, were screened for their antiproliferative activity using human cervical cancer (HeLa) cells grown in microtiter plates. Extracts of mountain ash, raspberry, blueberry, cloudberry, arctic thornbush and strawberry have shown anticancer activity[21]. In the study conducted on 5 different berry juices, the antiproliferative activity of Konic'-Ristic et al. fruit juices on HeLa cells, Fem X cells and MCF-7 cells was examined. In the results of working, it was determined that all fruit juices showed antiproliferative activity in a dose-dependent manner, with IC_{50} ranging from 10.2 to 70.5 l/ml [22].

Cyanidin glycosides, one of the major components of *Aronia melanocarpa*, have been found to inhibit HeLa human cervical tumor cell proliferation, thereby causing antiproliferative activity [23]. There are studies showing the anti-proliferative or protective effects of aronia fruit extracts on many types of cancer, especially colon cancer [10], pancreatic cancer [24], breast cancer [25], colon cancer [26]. In the study investigating the biological effects of *A. melanocarpa* leaf extracts on the human colon adenocarcinoma cell line Caco-2; extracts have been found to show anticancer activity [20].

Gao et al [27], reported that *A. melanocarpa* fruit extract showed antiproliferative activity (IC_{50} = 338.36 μg/mL) by inhibiting the growth of HepG2 human liver cancer cells.

A recent study investigated the potential effect of *Aronia melanocarpa* extract on cell viability in human colon cancer cell line (HT-29) and healthy human umbilical cord endothelial cell line (HUVEC). MTT assay showed that Aronia extract induced 50% cell death (IC_{50}) at a concentration of 186 μg/mL in HT-29 cell line 48 h after treatment. Cytotoxicity results showed a dose-dependent decrease in cell viability in HT-29 cell line. However, increasing concentrations of Aronia extract did not show a similar effect in HUVEC cell line [28]. The results obtained support our study.

Cvetanovic et al. [29], the cytotoxic activity of *A. melanocarpa* extracts on malignant cell lines (A-549, LS-174T and HeLa) and normal lung fibroblasts (MRC5) was examined. The results obtained showed that the growth of the malignant cells used was inhibited by the effect of the extracts. In addition, HeLa cells were shown to be much more sensitive to extracts than the other three cell lines. In our study, the results were found to be compatible with this study, as the extracts showed the highest anticarcinogenic activity in the HeLa cell line. Šavikinetal et al., who conducted a study similar to ours [30], reported that aronia fruit water extracts prepared in the form of infusion and decoction showed cytotoxic activity against HeLa cells and the IC_{50} values obtained were 86.99 and 11.16μg/mL, which was consistent with the IC_{50} values found in our study (116.12 ± 58.63 μg/mL) has been observed.

Conclusion

For *in vitro* anticancer activity determination, it was applied to breast cancer (MCF-7) and cervical cancer (HeLa) cell lines, and cytotoxic activities were examined using the MTT test. In conclusion; It has been determined that all extracts of aronia fruits have moderate cytotoxic activities on MCF-7 and HeLa cell lines, all extracts are more effective on the HeLa cell line, and ethanol and methanol extracts have a more cell viability-reducing effect on these cells than others.

For *in vitro* cytotoxic activity determination, application was performed on human endothelial (HUVEC) and mouse fibroblast (L929) cell lines, cytotoxic activities were examined using the MTT test and the extracts were compared in terms of effectiveness. In conclusion; It has been determined that all extracts of aronia fruits have no cytotoxic effect on healthy cell lines HUVEC and L929. The fact that any natural substance or extract obtained from plants or a single active substance does not harm healthy cells, but has a cytotoxic effect on cancerous cells, suggests that it may have potential in the development of drug substances in the future. In this context, it is promising that aronia plant fruit extracts do not have cytotoxic effects on the tested HUVEC and L929 healthy cell lines.

If we make a comparison in terms of selectivity index; It is seen that aronia plant ethanol extract shows the best anticarcinogenic activity in the MCF-7 cell line with a selectivity index value of 3.69, and aronia plant methanol extract shows the highest anticarcinogenic activity in the HeLa cell line with a selectivity index value of 4.62. It is also seen that the selectivity index values of plant extracts are higher in HeLa cells.

As a result of the data we obtained from our study; It has been shown that fruits belonging to the *Aronia melanocarpa* species can contribute to the literature in the development of new natural resources, new drugs and treatment agents in cancer treatment, thanks to their anticancer activities and low cytotoxicity. However, further research on the anticancer activity mechanisms of these extracts is recommended by the application of more advanced and comprehensive techniques, including *in vivo* experiments.

Conflicts of Interest

There are no conflicts of interest in this work.

Acknowledgment

This article is derived from Eda Sönmez Gürer's 2022 pharmacognosy doctoral thesis. The study was funded by the Anadolu University Scientific Research Project Fund (ANABAP) (Project number: 2105S218).

References

[1] Jurikova T., Mlcek J., Skrovankova S., Sumczynski D., Sochor J., Hlavacova I., Fruits of Black Chokeberry *Aronia melanocarpa* in the Prevention of Chronic Diseases, *Molecules*, 22 (2017) 944.

[2] Gorzynik-Debicka M., Przychodzen P., Cappello F., Kuban-Jankowska A., Marino Gammazza A., Knap N., Potential Health Benefits of Olive Oil and Plant Polyphenols, *Int J Mol Sci.*, 19 (2018) 686.

[3] Şekeroğlu Z.A., Şekeroğlu V., Oksidatif Mitokondrial Hasar ve Yaşlanmadaki Önemi, *Türk Bilimsel Derleme Dergisi,* 2 (2009) 69–74.

[4] Benvenuti S., Pelleti F., Melegari M., Bertelli D., Polyphenols, Anthocyanins, Ascorbic Acid and Radical Scavenging Activity of Rubus, Ribes, and Aronia, *J Food Sci.,* 69(3) (2004) 164-169.

[5] Çağlar M.Y., Demirci M., Üzümsü Meyvelerde Bulunan Fenolik Bileşikler ve Beslenmedeki Önemi, *Avrupa Bilim ve Teknoloji Dergisi*, 7 (2017) 18–26.

[6] Ağaoğlu Y.S., Türkiye'de Üzümsü Meyvelerin Dünü Bugünü ve Yarını, Ulusal Kivi ve Üzümsü Meyveler Sempozyumu Ordu, (2003) 1–14.

[7] Akalın G., Selamoglu Z., Nutrition and Foods for Skin Health, *Journal of Pharmaceutical Care*, 7(1-2) (2019) 31-33

[8] Deng H., Zhu J., Tong Y., Kong Y., Tan C., Wang M., Antibacterial Characteristics and Mechanisms of Action of *Aronia melanocarpa* Anthocyanins Against *Escherichia coli*, *LWT*, 150 (2021) 112018.

[9] Kaloudi T., Tsimogiannis D., Oreopoulou V., *Aronia melanocarpa*: Identification and Exploitation of its Phenolic Components, *Molecules,* 27 (2022) 4375.

[10] Kulling S., Rawel H., Chokeberry *(Aronia melanocarpa)* – A Review on the Characteristic Components and Potential Health Effects, *Planta Med.,* 74 (2008) 1625–1634.

[11] Średnicka-Tober D., Kazimierczak R., Rembiałkowska E., Strok T., Świąder K., Hallmann E., Bioactive Compounds in Organic Apple Juices Enriched with Chokeberry and Green Tea Extract, *Journal of Research and Applications in Agricultural Engineering,* 62 (2017) 173–177.

[12] Cancer in World Health Organization Available at: http://www.who.int/news-room/fact-sheets/detail , Retrieved January, 2024.

[13] Saraç H., Daştan T., Demirbaş A., Durna Daştan S., Karaköy T., Durukan H., Madımak (*Polygonum cognatum* Meissn.) Bitki Özütlerinin Besin Elementleri ve İn Vitro Antikanserojen Aktiviteleri Yönünden Değerlendirilmesi, *Süleyman Demirel Üniversitesi Ziraat Fakültesi Dergisi*, 1. Uluslararası Tarımsal Yapılar ve Sulama Kongresi, (2018) 340–347.

[14] Saraç H., Daştan T., Durukan H., Durna Daştan S., Demirbaş A., Karaköy T., Kırmızı Gelincik (Fam: Papaveraceae, *Glaucium grandiflorum* Boiss.&Huet *var.* grandiflorum) Bitkisinin Farklı Özütlerinin Besin Elementi İçeriğinin ve *In Vitro* Antiproliferatif Etkilerinin Değerlendirilmesi, *Ziraat Fakültesi Dergisi*, (2018) 417–428.

[15] Al-Qubaisi M., Rozita R., Yeap S.K., Omar A.R., Ali A.M., Alitheen N.B., Selective Cytotoxicity of Goniothalamin Against Hepatoblastoma HepG2 Cells, *Molecules*, 16 (2011) 2944–2959.

[16] Tokur O., Aksoy A., *In Vitro* Sitotoksisite Testleri, Harran Üniversitesi Veteriner Fakültesi Dergisi, 6 (2017) 112–118.

[17] Mosmann T., Rapid Colorimetric Assay for Cellular Growth and Survival: Application to Proliferation and Cytotoxicity Assays, *J Immunol Methods*, 65 (1983) 55–63.

[18] Riss T.L., Moravec R.A., Use of Multiple Assay Endpoints to Investigate the Effects of Incubation Time, Dose of Toxin, and Plating Density in Cell-Based Cytotoxicity Assays, *Assay Drug Dev Technol,* 2 (2004) 51–62.

[19] Sharif T., Stambouli M., Burrus B., Emhemmed F., Dandache I., Auger C., The Polyphenolic-Rich *Aronia melanocarpa* Juice Kills Teratocarcinomal Cancer Stem-Like Cells, but Not Their Differentiated Counterparts, *J Funct Foods,* 5 (2013) 1244–1252.

[20] Efenberger-Szmechtyk M., Nowak A., Nowak A., Cytotoxic and DNA-Damaging Effects of *Aronia melanocarpa*, *Cornus mas*, and *Chaenomeles superba* Leaf Extracts on the Human Colon Adenocarcinoma Cell Line Caco-2, *Antioxidants*, 9 (2020) 1030.

[21] McDougall G.J., Ross H.A., Ikeji M., Stewart D., Berry Extracts Exert Different Antiproliferative Effects against Cervical and Colon Cancer Cells Grown *In Vitro*, *J Agric Food Chem.,* 56 (2008) 3016–3023.

[22] Konić-Ristić A., Šavikin K., Zdunić G., Janković T., Juranic Z., Menković N., Biological Activity and Chemical Composition of Different Berry Juices, *Food Chem*., 125 (2011) 1412–1417.

[23] Rugină D., Sconţa Z., Leopold L., Pintea A., Bunea A., Socaciu C., Antioxidant Activities of Chokeberry Extracts and the Cytotoxic Action of Their Anthocyanin Fraction on HeLa Human Cervical Tumor Cells, *J. Med. Food*, 15 (2012) 700–706.

[24] Thani N.A.A., Keshavarz S., Lwaleed B.A., Cooper A.J., Rooprai H.K., Cytotoxicity of Gemcitabine Enhanced by Polyphenolics from *Aronia melanocarpa* in Pancreatic Cancer Cell Line AsPC-1, *J. Clin. Pathol*., 67 (2014) 949–954.

[25] Kedzierska M., Olas B., Wachowicz B., Stochmal A., Oleszek W., Jeziorski A., The Nitrative and Oxidative Stress in Blood Platelets İsolated from Breast Cancer Patients: The Protectory Action of *Aronia melanocarpa* Extract, *Platelets*, 21 (2010) 541–548.

[26] Bermudez-Soto M., Tomasbarberan F., Garciaconesa M., Stability of Polyphenols in Chokeberry (*Aronia melanocarpa*) Subjected to *In Vitro* Gastric and Pancreatic Digestion, *Food Chem*., 102 (2007) 865–874.

[27] Gao N., Wang Y., Jiao X., Chou S., Li E., Li B., Preparative Purification of Polyphenols from *Aronia melanocarpa* (Chokeberry) with Cellular Antioxidant and Antiproliferative Activity, *Molecules*, 23 (2018) 139.

[28] Caliskan Z., Yucel M.F., Celikok Y., Guler V., Duranay S. A., Preliminary Study of the Anti-Proliferative Effect of *Aronia melanocarpa* Extract on Human Colon Cancer Cells and its Relation with Human TERT Protein, *Experimental Biomedical Research*, 6(2) (2023) 88-98.

[29] Cvetanović A., Zengin G., Zeković Z., Švarc-Gajić J., Ražić S., Damjanović A., Comparative *In Vitro* Studies of the Biological Potential and Chemical Composition of Stems, Leaves and Berries *Aronia melanocarpa*'s Extracts Obtained by Subcritical Water Extraction, *Food and Chemical Toxicology*, 121 (2018) 458–466.

[30] Šavikin K., Zdunić G., Janković T., Gođevac D., Stanojković T., Pljevljakušić D., Berry Fruit Teas: Phenolic Composition and Cytotoxic Activity, *Food Research International*, 62 (2014) 677–683.

Cumhuriyet Sci. J., 45(3) (2024) 543-549
DOI: https://doi.org/10.17776/csj.1500231

Cumhuriyet Science Journal

| csj.cumhuriyet.edu.tr | Founded: 2002 ISSN: 2587-2680 e-ISSN: 2587-246X Publisher: Sivas Cumhuriyet University

Effects of Different Doses of Biochar Applications on Yield and Nutrient Element Concentrations on Wheat Grown under Salt Stress

Halil Göktan Demirbaş[1,a], Osman Sönmez[1,b], Ahmet Demirbaş[2,c], Fatma Nur Kılıç[1,d,*]

[1] *Department of Soil Science and Plant Nutrition, Faculty of Agriculture, Erciyes University, Kayseri, Türkiye*
[2] *Department of Plant and Animal Production, Sivas Cumhuriyet University, Sivas, Türkiye*
**Corresponding author*

Research Article

History
Received: 12/06/2024
Accepted: 23/09/2024

ABSTRACT

In the study, the effects of different doses of biochar applications on the yield and nutrient uptake of wheat grown under salt stress in greenhouse conditions were investigated. The study was conducted in 2 kg capacity plastic pots with three replications using a random plot design. In the study, salt doses were applied as 0 dS m^{-1}, 6 dS m^{-1} and 12 dS m^{-1} (in the form of NaCl), and biochar doses (BC) were applied as 0%, 0.5%, 1% and 2% W/W. At the end of the study, the dry matter yield of wheat plant and sodium (Na), nitrogen (N), phosphorus (P), potassium (K), calcium (Ca), zinc (Zn), manganese (Mn), iron (Fe) and copper (Cu) concentrations were determined. Study results showed that BC applications increased the dry matter production of the plant, and the highest was obtained with 2% BC application at 6 6 dS m^{-1} salt dose, 1.85 g pot^{-1}. However, due to increasing salt doses, BC applications had no effect on the phosphorus and potassium concentrations of the wheat plant, except for calcium, and decreases were determined in the average values. In the study, although all BC applications increased iron, zinc, manganese and copper concentrations compared to the control, when evaluated in terms of average values, decreases were detected in the microelement concentrations of the plant due to increasing salt doses.

Keywords: Abiotic stress, Biochar soil conditioner, Salinity mitigation, Wheat crop resilience, Enhanced nutrient availability.

[a] *tdastan@erciyes.edu.tr* *https://orcid.org/0009-0006-0195-7703*
[b] *osmansonmez@erciyes.edu.tr* *https://orcid.org/0000-0002-9134-6466*
[c] *ademirbas@cumhuriyet.edu.tr* *https://orcid.org/0000-0003-2523-7322*
[d] *fatmanur@erciyes.edu.tr* *https://orcid.org/0000-0003-3498-2455*

Introduction

The salinity problem in agricultural production areas leads to soil degradation on one hand and yield losses in plant production on the other. Saline soils are generally found predominantly in arid and semi-arid regions. The use of low quality irrigation water in agricultural areas, inappropriate irrigation methods and inadequate drainage conditions cause the salinity problem to increase day by day. It has been reported that the electrical conductivity of saline soils is higher than 4 mmhos / cm and the percentage of exchangeable sodium (Na) is less than 15 [1]. In general, it is known that the dominant salt form in soils is NaCl and that the highest crop yield losses are caused by this salt. More than 800 million hectares of land worldwide face both salinity and alkalinity problems [2]. In Türkiye, it has been reported that there is a salinity problem in an area of 1.5 million hectares [3]. There may be significant changes in the morphology of plants grown under salt stress. Accordingly, salinity retards the growth of plants, causing leaf appearance to be small and dull bluish-green, and shoot growth generally declines more than root growth [4]. It has been reported that the first symptoms of salinity-related toxicity in plants growing in saline areas are chlorosis, which starts from the tips of old leaves and progresses to the leaf blade and stem, and then turns into necrosis [5].

Biochar is produced by heating plant biomass in the absence of oxygen and is a relatively new term that has emerged in relation to issues of soil management and carbon (C) enrichment [6]. The production and application of biochar to the soil is a new process in order to limit the risk of CO_2 return in the atmosphere and reduce the CO_2 storage in the long term [6]. Carbon-rich materials obtained by heating various biomass such as wood, animal manure and leaves in a closed environment where there is little or no oxygen are called biochar. In a more technical sense, the material produced by the exchange/pyrolysis of organic materials in the presence of a limited amount of oxygen and at relatively low temperatures (<700 °C) is called biochar [7]. It is an important issue to investigate this valuable product called biochar in terms of different application areas due to its high surface area and porous structure, especially in improving soil quality and removing pollution [8]. Due to the recalcitrant nature of biochar (obtained from charcoal or biomass) in reducing greenhouse gas emissions, there has been growing interest in its use as a soil amendment [9]. Recently, studies on biochar have increasingly focused on its effectiveness in enhancing both the sustainability and productivity of agricultural systems [10-11]. In this study, the effects of different doses of biochar obtained from peanut shells on the yield and nutrient uptake of Kızıltan wheat variety grown under salt stress in greenhouse conditions were investigated.

Material and Methods

The greenhouse experiment was carried out in the greenhouses of Erciyes University, Faculty of Agriculture, Department of Soil Science and Plant Nutrition. The experiment was set up according to the random parcel design with three repetitions. The soil used in the experiment; It has a clay loam texture and slightly alkaline pH (7.98), low organic matter content (1.77%), salt-free (0.02%), medium calcareous (9.95%), low phosphorus concentration (56.8 kg P_2O_5 ha^{-1}) and low potassium concentration (987.1 kg K_2O ha^{-1}). Plastic pots were used in the experiment and 3000 g of soil was placed in each pot. In the experiment, as basic fertilization, 200 mg N kg^{-1} (in the form of $CaNO_3.4H_2O$), 100 mg P kg^{-1} and 125 mg K kg^{-1} (in the form of KH_2PO_4), 2.5 mg Zn kg^{-1} (in the form of $ZnSO_4.7H_2O$) and 2.5 mg Fe kg^{-1} (in the form of Fe-EDTA) was applied to each pot. In the experiment, salt concentrations were applied using a NaCl source at 0 dS m^{-1}, 6 dS m^{-1} and 12 dS m^{-1} levels. 1/3 of each salt dose was initially mixed into the soil, and the remaining part was completed with irrigation water along with the outlets. Pure water was used for irrigation and care was taken to avoid water loss from the bottom of the pot. The Kızıltan wheat variety was utilized as the plant material. Initially, 12 wheat seeds were sown in each pot, and after germination, the seedlings were thinned to reduce the number to 8.

In the study, biochar obtained from peanut shells by slow pyrolysis and burning at 400 ^{0}C for 2 hours was applied as 0%, 0.5%, 1% and 2% w/w. Approximately 50 days after planting, the harvested plants were brought to the laboratory and washed first with tap water, then with 0.1% N HCl, and then with pure water. The plant leaves, placed separately in a paper bag, were dried in an air circulation drying cabinet at 70 ^{0}C until they reached a constant weight. The samples, whose dry weights were determined, were ground in a plant grinding mill. 0.2 g of ground plant samples were weighed and burned in an acid mixture of H_2O_2-HNO_3 (2 ml of 35% H_2O_2 and 5 ml of 65% HNO_3) according to the wet combustion method in a microwave device, and the final volume was completed to 20 mL with pure water and filtered through blue band filter paper. From the obtained filters, phosphorus (P) concentration was measured colorimetrically in a spectrophotometer at 882 nm [12], potassium (K), calcium (Ca), sodium (Na), zinc (Zn), manganese (Mn), iron (Fe) and copper (Cu) concentrations were determined by Atomic Absorption Spectrophotometer device (Shimadzu AA-7000) [13]. Nitrogen (N) determination was made according to the Kjeldahl distillation method [14]. Research findings and all measured variables were analyzed using the SPSS 20.0 for Windows package program for statistical analysis, and the differences between the means were determined with the Tukey test at a significance level of $p < 0.05$.

Results and Discussion

In the study, the dry matter production and Na concentration of the wheat plant are given in Table 1, the N and P concentrations are given in Table 2, the K and Ca concentrations are given in Table 3, the Fe and Zn concentrations are given in Table 4, and the Mn and Cu concentrations are given in Table 5.

Table 1. Effects of the applications on the dry matter production (g pot^{-1}) and Na concentration of the wheat plant (%)

Applications		Dry Matter Production (g pot^{-1})		Na (%)	
0 dS m^{-1}	0% BC	1.23	±0.01 ef	1.68	±0.35 g
	0.5 % BC	1.61	±0.06 bc	2.28	±0.02 fg
	1% BC	1.73	±0.04 ab	2.66	±0.16 fg
	2% BC	1.73	±0.08 ab	3.55	±0.60 f
Average		1.57		2.54	
6 dS m^{-1}	0% BC	1.24	±0.20 ef	14.05	±0.70 e
	0.5 % BC	1.42	±0.02 d	16.62	±0.32 c
	1% BC	1.48	±0.01 cd	16.12	±1.19 cd
	2% BC	1.85	±0.06 a	14.50	±1.87 de
Average		1.50		15.32	
12 dS m^{-1}	0% BC	1.18	±0.04 e-g	27.56	±0.05 a
	0.5 % BC	1.14	±0.03 fg	27.09	±0.05 a
	1% BC	1.33	±0.02 de	24.67	±1.58 b
	2% BC	1.06	±0.11 g	25.86	±0.59 ab
Average		1.18		26.29	

$P<0.05$

When Table 1 is evaluated in terms of the effects of the applications on the dry matter production of the wheat plant in the research, the highest dry matter production was obtained with 1.85 g pot^{-1} in 2% BC application at 6 dS m^{-1} salt dose. This application was followed by 1% BC and 2% BC applications at 0 dS m^{-1} salt dose, production at 1.73 g pot^{-1}. The lowest dry matter production was determined at 1.06 g pot^{-1} and 2% BC application at a salt dose of 12 dS m^{-1}. Research results show that when moderate salt is applied, 2% BC application significantly increases the dry matter production of the plant compared to the control. In addition, BC applications at all three salt doses generally increased the dry matter production of wheat plants compared to the control. In a similar study, [15] conducted a study to evaluate the potential of biochar and gibberellic acid (GA3) to reduce salinity stress in wheat. In this study, two different salinity levels (2.43 dS m^{-1} and 5.11 dS m^{-1}) and eight different combinations (T1-T8) were used. The combinations applied in the trial are: T1 (control with 2.43 dS m^{-1} EC), T2 (salinity stress with 5.11 dS m^{-1} EC), T3 (10 mg kg^{-1} GA3 and 2.43 dS m^{-1} EC), T4 (10 mg kg^{-1} GA3 and 5.11 dS m^{-1} EC), T5 (0.75% biochar and 2.43 dS m^{-1} EC), T6 (0.75% biochar and 5.11 dS m^{-1} EC), T7 (2.43 dS m^{-1} EC with 10 mg kg^{-1} GA3 and 0.75% biochar) and T8 (10 mg kg^{-1} GA3 and 0.75% biochar with 5.11 dS m^{-1} EC). They reported that individual and combined applications of GA3 and biochar significantly ($P<0.05$) increased plant growth in saline conditions compared to the control. When the average dry matter production was evaluated in our research, it was determined that the dry matter production of the plant decreased as the salt doses increased. While the highest average dry matter production was determined at 0 dS m^{-1} salt dose with 1.57 g pot^{-1}, the lowest average dry matter production was determined at 12 dS m^{-1} salt dose with 1.18% g pot^{-1}.

When Na concentration was examined in the study, the highest sodium concentration was found in 0% BC application at 12 dS m^{-1} salt dose with 27.56% Na. When average Na concentrations were evaluated, it was seen that sodium concentrations increased as salt doses increased. In parallel with this increase, the dry matter production of the wheat plant also decreased. Contrary to our research results, [16] examined the effects of biochar and selenium nanoparticles (Se-NP) on the growth and biomass production of wheat irrigated with salt water in their study. In the study, biochar was used as 5% of the soil amount in 2 kg pots, 3000 ppm NaCl was applied 20 days after wheat emergence, and 30 ppm Se-NP was added 5 days after salt application. Plants were harvested after 55 days. The results showed that plants treated with the combination of NaCl, biochar and Se-NP accumulated 50% less Na in their leaves and significantly increased ($P<0.005$) growth and yield parameters. [17] reported that roots are the first organs to encounter salinity and that the decline in root growth is greater with salt stress compared to the green parts. The decline in shoot and root growth in question is due to osmotic stress in plants due to salt stress [18], ion imbalances and regressions in carbohydrate fixation [19]. Regressions in plant growth due to salt stress have been shown in different plant species, for example, wheat [20], rice [21] and corn [22].

Table 2. Effects of the applications on N and P concentration of the wheat plant (%)

Applications		N (%)		P (%)	
0 dS m^{-1}	0% BC	4.44	±0.02 ab	0.86	±0.06 ab
	0.5 % BC	4.94	±0.02 a	0.43	±0.03 d-f
	1% BC	5.04	±0.01 a	0.47	±0.02 de
	2% BC	5.10	±0.13 a	0.19	±0.01 g
	Average	4.88		0.49	
6 dS m^{-1}	0% BC	4.99	±0.15 a	0.60	±0.24 cd
	0.5 % BC	4.18	±0.00 bc	0.60	±0.00 cd
	1% BC	4.46	±0.10 ab	0.26	±0.06 fg
	2% BC	4.05	±0.19 c	0.47	±0.12 de
	Average	4.42		0.48	
12 dS m^{-1}	0% BC	3.66	±0.23 d	0.93	±0.00 a
	0.5 % BC	3.58	±0.28 de	0.69	±0.09 bc
	1% BC	3.30	±0.07 e	0.39	±0.07 ef
	2% BC	3.23	±0.25 e	0.18	±0.03 g
	Average	3.44		0.55	

$P<0.05$

The highest N concentration of wheat plant was determined in the application of 2% BC at a dose of 5.10% N and 0 dS m^{-1} (Table 2). This application was followed by 1% BC application at 0 dS m^{-1} dose, which is statistically in the same group (5.04% N). The lowest N concentration was determined in the application of 2% BC at a dose of 12 dS m^{-1} with 3.23% N. In the study, while all BC doses at 0 dS m^{-1} salt dose increased the N concentration of the plant compared to the control, BC applications at other salt doses did not have any effect and higher N concentrations were detected in the control applications. When average N concentrations were evaluated, the N concentration of the plant decreased in parallel with increasing salt doses. Similarly, BC applications had no effect on the phosphorus concentrations of the plant. The highest P concentration was determined in 0% BC application at a dose of 12 dS m^{-1} with 0.93% P. The lowest P concentration with 0.18% P was detected in 2% BC application at the same salt dose. In all three salt doses, the P concentration of wheat plants decreased compared to the control. [23] examined the effects of biochar and P-dissolving and salt-tolerant PGPRs (Bacillus thuringiensis or Bacillus tropicus) on wheat plants. For this purpose, saline soil was added to 6 kg pots and biochar and PGPR were applied at the rate of 1% of the soil amount. Research results revealed that applications increased wheat growth and yield compared to the control group. In particular, significant improvements were achieved in the K/Na ratio, available P level and microbial biomass carbon in the soil; this led to an increase in the nutrient content (N, P, K) in roots, shoots and grains. These findings indicate that the combined use of biochar and PGPR has potential benefits in wheat cultivation in saline soil conditions.

Tablo 3. Effects of the applications on K and Ca concentration of the wheat plant (%)

Applications		**K**	**Ca**
0 dS m^{-1}	0% BC	3.51 ±0.04 c	1.07 ±0.06 e-g
	0.5 % BC	3.96 ±0.05 b	0.85 ±0.06 gh
	1% BC	4.11 ±0.02 ab	0.85 ±0.11 gh
	2% BC	4.20 ±0.01 a	0.67 ±0.01 h
Average		3.94	**0.86**
6 dS m^{-1}	0% BC	3.12 ±0.10 de	1.28 ±0.27 de
	0.5 % BC	2.95 ±0.04 ef	1.37 ±0.00 d
	1% BC	3.10 ±0.01 de	1.27 ±0.01 d-f
	2% BC	3.45 ±0.03 c	1.02 ±0.12 fg
Average		3.15	**1.23**
12 dS m^{-1}	0% BC	3.22 ±0.14 d	1.85 ±0.05 c
	0.5 % BC	2.82 ±0.01 f	2.51 ±0.19 a
	1% BC	2.87 ±0.04 f	2.25 ±0.21 ab
	2% BC	3.00 ±0.25 ef	2.04 ±0.03 bc
Average		2.98	**2.16**

$P<0.05$

In the study, the K concentration of wheat plants decreased due to increasing salt doses, as did N and P concentrations (Table 3). While BC applications at 0 dS m^{-1} salt dose increased the K concentration compared to the control, BC applications at increasing salt doses were generally not effective and higher K concentrations were detected in control applications. In the study, the highest K concentration was determined in 2% BC application at 0 dS m^{-1} salt dose with 4.20% K, while the lowest was determined in 0.5% BC application at 12 dS m^{-1} salt dose with 2.82% K. When average K concentrations were evaluated, a decrease was observed due to increasing salt doses. [24] reported that excessive uptake of Na$^+$ ion in plants under salt stress led to less uptake of K$^+$ ion due to competition. Contrary to the K concentration, the calcium concentration of the plant also increased due to increasing salt doses. This situation is explained by the fact that Ca plays an important role in the selective transport of K to make the plant resistant to salinity in the presence of high Na. Consequently, under salt stress, the Ca uptake of plants increases in parallel with the sodium uptake [25-26]. Except for the 0 dS m^{-1} salt dose, all BC applications at other salt doses increased the Ca concentration of the plant compared to the control. The highest calcium concentration was determined in 0.5% BC application with 2.51% Ca and 12 dS m^{-1} salt dose, and the lowest calcium concentration was determined in 2% BC application with 0.67% Ca and 0 dS m^{-1} salt dose. [27] in their study on the use of biochar (corn stalk and rice husk) and vermicompost (VC) improves the chemical structure of the soil and the physiological and biochemical properties of plants to relieve water stress of wheat plants in saline sodic soil, VC (4% W:W), biochar (1% W:W) and VC+biochar applications were made at 50%, 75% and 100% field capacity. As a result of the study, VC-biochar combined application followed by biochar application as a single application was significantly effective on relative water content, chlorophyll content, stomatal conductance, cytotoxicity, leaf K content in relation to nutrient uptake (N, P and K), while reducing oxidative stress ($P< 0.05$) reported. Contrary to our study results, some researchers studied different plant species, such as wheat [28], sorghum [29], different pumpkin species, melon [30] and tomato [31] reported that there were decreases in Ca concentration due to salt stress. According to [32], Ca nutrition has an important role in maintaining good growth under saline conditions.

In the study, the highest Fe concentration was determined as 97.7 mg Fe kg^{-1} in 1% BC application at 0 dS m^{-1} salt dose, while the lowest was determined as 59.2 mg Fe kg^{-1} in 0% BC application at 12 dS m^{-1} salt dose (Table 4). In the study, although all BC applications at all three salt doses increased the Fe concentration of the plant compared to the control, when average Fe concentrations were examined, the Fe concentration of the plant decreased due to increasing salt doses. A similar situation applies to the Zn concentration of the plant. While Zn concentration increased with BC applications at all salt doses compared to the control, when average Zn concentrations were evaluated, decreases were detected in the Zn concentration of wheat plants due to increasing salt doses. The highest Zn concentration was detected in 2% BC application at 0 dS m^{-1} salt dose, with 147.0 mg Zn kg^{-1}. [32] investigated the determination of the effects of Zn and salt applications on the shoot parts and some element concentrations of durum wheat in a soil with Zn deficiency. In the study, 3 different Zn doses (0, 5 and 10 mg Zn kg^{-1}) were applied and 4 different salt doses (0, 0.5, 1.0 and 1.5%) were applied during the stemming period of the plants. At the end of the research, they reported that the differences in the concentration of micronutrients in the salty conditions of the durum wheat plant may be due to the decrease in water use, especially with increasing salt concentration, and the interaction resulting from the imbalance in ion uptake.

Tablo 4. Effects of the applications on Fe and Zn concentration of the wheat plant (mg kg^{-1})

Applications		Fe	Zn
0 dS m^{-1}	0% BC	69.9 ±5.37 c-e	132.3 ±0.35 b-d
	0.5 % BC	86.3 ±2.12 ab	137.2 ±3.18 a-c
	1% BC	97.7 ±2.96 a	144.1 ±9.04 ab
	2% BC	76.7 ±2.05 b-d	147.0 ±0.42 a
Average		82.6	140.1
6 dS m^{-1}	0% BC	64.7 ±2.19 e	102.7 ±8.84 fg
	0.5 % BC	66.1 ±5.16 de	115.9 ±5.44 ef
	1% BC	78.6 ±7.85 bc	129.2 ±0.07 c-e
	2% BC	76.7 ±1.98 b-d	118.4 ±3.96 de
Average		71.5	116.5
12 dS m^{-1}	0% BC	59.2 ±1.41 e	78.6 ±0.07 h
	0.5 % BC	63.2 ±2.90 e	92.0 ±1.27 gh
	1% BC	70.1 ±13.51 c-e	96.4 ±3.25 g
	2% BC	77.0 ±6.51 b-d	94.2 ±16.97 g
Average		67.4	90.3

$P<0.05$

Tablo 5. Effects of the applications on Mn and Cu concentration of the wheat plant (mg kg^{-1})

Applications		Mn	Cu
0 dS m^{-1}	0% BC	101.5 ±2.19 de	13.8 ±0.42 ab
	0.5 % BC	103.4 ±0.21 cd	13.3 ±0.07 a-d
	1% BC	143.4 ±5.23 a	14.7 ±1.63 a
	2% BC	114.6 ±1.34 b	13.1 ±0.00 b-e
Average		115.7	13.7
6 dS m^{-1}	0% BC	110.7 ±3.75 bc	12.1 ±1.06 d-g
	0.5 % BC	116.7 ±2.62 b	11.7 ±0.14 e-g
	1% BC	141.2 ±0.64 a	12.4 ±0.35 c-g
	2% BC	136.9 ±6.01 a	12.5 ±0.57 b-f
Average		126.3	12.2
12 dS m^{-1}	0% BC	81.2 ±0.78 f	11.1 ±0.35 g
	0.5 % BC	95.4 ±2.47 e	7.3 ±0.92 h
	1% BC	101.3 ±2.40 de	11.1 ±0.28 fg
	2% BC	99.05 ±7.28 de	13.7 ±0.35 a-c
Average		94.2	10.8

$P<0.05$

In terms of Mn concentration, when Table 5 is examined, the highest concentration of 143.4 mg Mn kg^{-1} was detected in the 0 dS m^{-1} salt dose with 1% BC application. This was followed by the 6 dS m^{-1}salt dose with 1% BC and 2% BC applications, which are statistically in the same group. The lowest Mn concentration was detected in 0% BC application at a salt dose of 12 dS m^{-1} (81.2 mg Mn kg^{-1}). In the study, BC applications at all salt doses increased the Mn concentration of the plant compared to the control. When the average Mn concentrations were evaluated, the highest average Mn concentration of 126.3 mg Mn kg^{-1} was determined in the 6 dS m^{-1}application, while the lowest was determined in the 12 dS m^{-1} application with 94.2 mg Mn kg^{-1}. In the study, it was seen that BC applications generally had no effect on the Cu concentration of the plant. BC applications at all salt doses did not provide a significant increase compared to the control. However, when average Cu concentrations were evaluated, it was determined that Cu concentrations decreased in parallel with increasing salt doses. In various studies, some researchers have reported that the general effect of salt stress on plants is the toxic effect of ions such as Na and Cl. This toxicity, especially in the later stages of plant development, leads to a decrease in or toxicity of nutrient uptake and transport [33-34]. As a result of this effect, the yield and quality of the plant are adversely affected [35-36].

Conclusions

In the study, which aimed to determine the effects of applying different doses of biochar obtained from peanut shells to wheat grown under salt stress in greenhouse conditions on yield and nutrient uptake, it was found that dry matter production increased with biochar applications at all salt doses, but when examined in terms of average values, dry matter production decreased with increasing salt doses. In the study, BC applications significantly increased the N concentration of the plant at the control dose of 0 dS m^{-1}, however, BC applications were not effective at increasing salt doses and control applications had higher N concentrations. BC applications had no effect on the P and K concentrations of the wheat plant, except for Ca, due to increasing salt doses, and decreases were determined in the average values. In the study, when the effects of BC applications at increasing salt doses were evaluated on the microelement concentrations of the wheat plant, although all BC applications increased Fe, Zn, Mn and Cu concentrations compared to the control, when evaluated in terms of average values, decreases were detected in the microelement concentrations of the plant due to increasing salt doses.

When the research results were evaluated as a whole, it was found that while biochar (BC) applications alone had an impact on the growth and development of the plant, the effect of BC applications on the growth and development of the wheat plant was limited when salt applications were made.

Conflict of Interest

The authors declare no conflict of interest.

References

[1] U.S. Salinity Laboratory staff. Diagnosis and improvement of salina and alkali soils. U.S. Dept. Agric. Handb., (1954) 60.

[2] FAO, FAO Land and Plant Nutr. Manag. Serv., Available at: http://www.fao.org/ag/agl/agll/spush/. Retrieved: June 14, 2024.

[3] GDRS., (2011) General Directorate of Rural Services.

[4] Greenway H., Munns R., Mechanisms of salt tolerance in nonhallophytes, *Ann. Rev. Plant Physiol.*, 31 (1980) 149-190.

[5] Mer R.K., Prajith P.K., Pandya D.H., Pandey A.N., Effect of salts on germination of seeds and growth of young plants of Hordeum vulgare, Triticum aestivum, Cicer arietinum and Brassica juncea., *J. Agron. Crop. Sci*, 185 (2000) 209-217.

[6] Lehmann J., Gaunt J., Rondon M., Bio-char sequestration in terrestrial ecosystems—A review., *Mitig. Adapt. Strateg. Glob. Change,* 11(2) (2006) 403–427.

[7] Lehmann, J., Joseph, S., Biochar for environmental management: an introduction. In Biochar for environmental management, Routledge. (2015) pp 1-13.

[8] Korkmaz H. E., Akgün M., Çelebi M. S., Korkmaz K., Fındık Zurufu ve Biyoçarından Üretilen Demir Nanopartiküllerinin (FeONP) Yaşlanmış Börülce Tohumlarında Çimlenme Üzerine Etkisi, *Akademik Ziraat Dergisi*, 12(Special Issue) (2023) 193-202.

[9] Lorenz K., Lal R., Biochar application to soil for climate change mitigation by soil organic carbon sequestration, *Journal of Plant Nut. and Soil Sci.*, 177 (2014) 651-670.

[10] Spokas K.A., Cantrell K.B., Novak J.M., Archer D.W., Ippolit, J.A., Collins H.P., Boateng A.A., Lima I.M., Lamb M.C., McAloon A.J., Lentz R.D., Nichols K.A., Biochar: a synthesis of its agronomic impact beyond carbon sequestration, *J. Environ. Qual.*, 41 (2012) 973–989.

[11] Kloss S., Zehetner F., Wimmer B., Buecker J., Rempt F., Soja G., Biochar application to temperate soils: Effects on soil fertility and crop growth under greenhouse conditions, *J. Plant Nutr. Soil Sci.*, 177 (2014) 3–15.

[12] Murphy L., Riley J.P., A modified single solution method for the determination of phosphate in natural waters, *Anal. Chem. Acta.*, 27 (1962) 31-36.

[13] Kacar B., Inal A., Plant analysis, Nobel Pres 1241 (2008) 891.

[14] Bremner J.M., Total nitrogen Methods of soil analysis: part 2 chemical and microbiological properties, *Madison*, 9 (1965) 1149-1178.

[15] Anwar T., Munwwar F., Qureshi H., Siddiqi E. H., Hanif A., Anwaar S., Kamal A., Synergistic effect of biochar-based compounds from vegetable wastes and gibberellic acid on wheat growth under salinity stress, *Scien. Rep.*, 13(1) (2023) 19024.

[16] Soliman M.H., Alnusairi G.S., Khan A.A., Alnusaire T.S., Fakhr M.A., Abdulmajeed A.M., Najeeb U., Biochar and selenium nanoparticles induce water transporter genes for sustaining carbon assimilation and grain production in salt-stressed wheat, *Journal of Plant Grow. Reg.*, 42(3) (2023) 1522-1543.

[17] Lazof D. B., Bernstein N., The NaCl induced inhibition of shoot growth: the case for disturbed nutrition with special consideration of calcium, *Adv. Bot. Res.*, 29 (1998) 113-189.

[18] Munns R., Genes and salt tolerance:bringing them together, *New Phy.*, 167 (2005) 645-663.

[19] Levitt J., Responses of plants to environmental stresses. Vol. II, 2 ed. Academic Press, New York, (1980) 607.

[20] Aşıklı S., Tuz stresinin çeşitli Triticum Spelta Buğdaylarında Antioksidatif Enzim Aktiviteleri Üzerine Etkisi, Yüksek Lisans tezi, Ç.Ü. Fen Bilimleri Enstitüsü, Toprak Bilimi ve Bitki Besleme Anabilim Dalı, (2017).

[21] Moons A., Bauw G., Prinsen E., Montagu M.V., Van der Straeten, D., Molecular and physiological responses to absisic acid and salts in roots of salt-sensitive and salt-tolerant Indica rice varieties, *Plant Phy.,* 107(1) (1995) 177-186.

[22] Eker S., Cömertpay G., Konuşkan Ö., Ülger A. C., Öztürk L., Cakmak İ., Effect of salinity on Dry Mattrer Production and Ion Accumulation in Hybrid Maize Varieties, *Turk J. Agric. For.,* 30 (2006) 365-373.

[23] Malik L., Sanaullah M., Mahmood F., Hussain S., Shahzad T., Co-application of biochar and salt tolerant PGPR to improve soil quality and wheat production in a naturally saline soil, *Rhizosphere*, 29 (2024) 100849.

[24] Davenport R.J., Reid R.J., Smith F.A., Sodium calcium interactions in two wheat spcies differing in salinity tolerance, *Phys. Pla*., 99 (1997) 323-327.

[25] Clarkson D.T., Hanson J.B., The Mineral Nutrition of Higher Plants, *Ann. Rev. Plant Physiol*., 31 (1980) 239-298.

[26] Epstein E., Genetic Engineering of Osmoregulation. Impact of Plant Productivity for Food, *Chem. and En*., (1981) 7-21

[27] Hafez E.M., Omara A.E., Alhumaydhi F.A., El-Esawi M.A., Minimizing hazard impacts of soil salinity and water stress on wheat plants by soil application of vermicompost and biochar, *Physiol. Plant*, 172 (2020) 587–602.

[28] Ali A., Ahmed I., Zaman B., Salim M., Nutritional effect of calcium on growth and ionic concentration of wheat under saline conditions, *Pak. J. Agri. Sci*., 39 (2002) 1-7.

[29] Netondo G.W., Onyango J. C., Beck E.I., Sorghum and salinity: Response of growth, water relations, and ion accumulation to NaCl salinity, *Crop. Sci*., 44 (2004) 707-710.

[30] Yetişir H., Uygur V., Plant growth and mineral element content of different gourd species and watermelon under salinity stress, *Turk J. Agric. For*., 33 (2009) 65-77.

[31] Turhan A., Seniz V., Kuşcu H., Genotypic variation in the response of tomato to salinity, *Afr. J. Biotec*., 8(6) (2009) 1062-1068.

[32] Marchner H., Mineral Nutrition of Higher Plants, Academic Press, (1995) 657-680.

[33] Torun A.A., Gülmezoğlu N., Tolay İ., Duymuş E., Aytaç Z., Cenkseven Ş., Torun B., Çinko ve NaCl Uygulamalarının Makarnalık Buğdayın (Triticum durum Desf.) Kuru Madde Verimi ve Besin Elementi Konsantrasyonları Üzerine Etkisi, *Bahri Dağ. Bit. Araş. Der.,* 8(1) (2019) 1-10.

[34] Korkmaz K., Akgün M., Kırlı A., Özcan M.M., Dede Ö., Kara Ş. M., Effects of gibberellic acid and salicylic acid applications on some physical and chemical properties of rapeseed (Brassica napus L.) grown under salt stress, *Turk. Jour. of Agr.-Food Sci. and Tech*., 8(4) (2020) 873-881.

[35] Dinler B.S., Cetinkaya H., Akgun M., Korkmaz, K., Simultaneous treatment of different gibberellic acid doses induces ion accumulation and response mechanisms to salt damage in maize roots, *Jour. of Plant Bioc. and Phy.*, 9(3) (2021) 258.

[36] Aha F. D., Özkutlu F., Tuzlu Koşullarda Bentonit Uygulamasının Makarnalık ve Ekmeklik Buğdayların Kuru Madde Verimi ve Mineral Besin Elementleri Üzerine Etkisi, *Ordu Üniversitesi Bilim ve Teknoloji Dergisi*, 13(1) (2023) 71-78.

Cumhuriyet Sci. J., 45(3) (2024) 550-556
DOI: https://doi.org/10.17776/csj.1525700

Cumhuriyet Science Journal

| csj.cumhuriyet.edu.tr | Founded: 2002 ISSN: 2587-2680 e-ISSN: 2587-246X Publisher: Sivas Cumhuriyet University

Optimized Deep Eutectic Solvent System for Liquid Phase Microextraction of Brillant Blue FCF in Diverse Analytical Food Matrices

Nebiye Kizil [1,2,a]

[1] *Department of Basic Sciences, Faculty of Engineering, Hasan Kalyoncu University, Gaziantep,Türkiye*
[2] *Environmental Application and Research Center, Hasan Kalyoncu University, Gaziantep, Türkiye*
**Corresponding author*

Research Article

History
Received: 31/07/2024
Accepted: 23/09/2024

ABSTRACT

This study introduces a novel microextraction technique for the analysis of Brilliant Blue FCF, a widely used food dye, employing a deep eutectic solvent (DES). The method aligns with green chemistry principles by favoring environmentally benign solvents, ensuring rapid and efficient extraction. Specifically, a DES composed of tetrabutylammonium bromide (TBAB) and phenol (Ph) was prepared in a cost-effective and expedient manner. To enhance extraction efficiency within the deep eutectic solvent-based dispersive liquid-liquid microextraction (DB-DLLME), critical parameters such as the volume of DES, quantity of dispersive agent, extraction time, and sample volume were systematically optimized. The accuracy of the method was conducted at pH 3 by spiking various food samples with known concentrations of the analyte. Analytical performance metrics, including recovery efficiency, limit of detection (LOD), limit of quantification (LOQ), and relative standard deviation (RSD), were determined and reported as 0.86 µg/L, 2.88 µg/L, and 0.4-1.3% respectively. Furthermore, the method has been successfully utilized for analyzing samples of confectionery, beverages, water, and chewing gum.

Keywords: Deep eutectic solvent, Spectrophotometric analysis, Brillant blue FCF, Green chemistry, Food additives..

[a] *nebiye.kizil@hku.edu.tr* *https://orcid.org/0000-0003-4994-1680*

Introduction

Food colorants often provide information about the ingredients, taste, vitamin value, and safety of the product. Food colorants are divided into two classes: synthetic such as tartrazine, patent blue V, ponceau 4R, brilliant blue, erythrosin, allura red and sunset Yellow FCF and natural such as curcumin, carmine, riboflavin, lutein, carotene, chlorophyll. Synthetic dyes, which have a very permanent and intense color, are classified according to their structure into groups such as azo dyes, chiniline, xanthan, and anthraquinone. Natural and synthetic food colors are added to foods in order to enhance their nutritional value and appearance. Synthetic colorants are utilized more than natural dyes because they are cheap and have high stability. Natural colorants are generally preferred because of their positive effects on health [1-3].

Brilliant Blue FCF (E133) is a water-soluble synthetic food color belonging to the azo dye group, also known as FD&C Blue, Acid Blue 9 or Food Blue [4-6]. It is extensively utilized to impart a blue hue to a variety of food products including chocolates, dairy items, cereals, sauces, cheese, jellies, and beverages. Despite its widespread application, Brilliant Blue FCF has been associated with potential genotoxic effects, manifesting in conditions such as skin flaking, allergic reactions, convulsions, gastrointestinal tumors, and neurotoxicity [7-9]. Conversely, the International Agency for Research on Cancer has classified Brilliant Blue FCF as having no carcinogenic effects (Mittal, 2006). The World Health Organization (WHO) and the Food and Agriculture Organization (FAO) have established the daily acceptable intake of Brilliant Blue FCF to be within the range of 0-6 mg/kg body weight [4].

Due to the essential importance of brillant blue FCF in metabolic activities, it is very important to develop sensitive and accurate methods for the determination of reliable concentration values in foods, feeds, supplements, and biological samples [10]. Therefore, many techniques such as high-performance liquid chromatography (HPLC), voltammetry, chemiluminescence, UV spectrophotometry (UV-Vis) and mass spectrometry (MS), capillary zone electrophoresis, spectroelectrochemistry are utilized for brillant blue FCF determination. However, these methods have difficulties such as trace concentration levels of brillant blue FCF in real samples and complex matrix environments. Therefore, solid and liquid phase extraction enrichment methods have been developed by researchers. Since these traditional methods are tedious, time-consuming, expensive, and not environmentally friendly, microextraction methods have drawn attention within the scope of green chemistry in recent years. Solidified floating organic drop microextraction (SFODME), hollow-fiber membrane liquid-phase microextraction (HF-LPME), fiber solid-phase microextraction (FSPME), in-tube solid-phase microextraction, headspace liquid-phase microextraction (HS-LPME), dispersive solid-phase microextraction, solvent bar microextraction (SBME), single-drop microextraction (SDME), ultrasonic assisted microextraction (UAME), dispersive liquid-liquid microextraction (DLLME) are implemented for the separation and determination of organic or inorganic species [11-16].

In 2006, for the first time reported by Rezaee et al. DLLME method, solvent systems such as switchable hydrophobicity solvent, supramolecular solvent, natural deep eutectic solvent, ionic liquid, and deep eutectic solvent are used [17-18]. In this article, a dispersive liquid phase microextraction method based on a deep eutectic solvent system (DB-DLLME) was utilized for the sensitive determination of brillant blue FCF.

DESs with low melting points are generally synthesized from the combination of a hydrogen bond acceptor (HBA) such as a quaternary ammonium salt and a hydrogen bond donor (HBD) such as carboxylic acids, alcohol, and carbohydrates by hydrogen bond interactions [19]. These solvents, which are mixed by ultrasonic, freezing, conventional heating, and microwave heating, are biodegradable. Hence, they are known as environmentally friendly and ideal solvents for microextraction studies. In addition, DESs can be used not only in high-purity extraction studies but also as auxiliary components in material synthesis [17, 20-22].

In this current paper, a DB- DLLME method for the analysis of brillant blue FCF was developed. For this purpose, DES solvent consisting of tetrabutyl ammonium bromide (TBAB and phenol (Ph) was synthesized in a very short time by heating method. It was utilized for the determination of brillant blue FCF in beverages, candies, water and chewing gum food samples.

Experimental

Instrumentation and Reagents

Brilliant Blue FCF was analyzed using UV-Vis spectrometry (Perkin-Elmer Lambda 25; Norwalk, CT, USA). pH values for optimization and analyte determination in foods were measured with a pH meter (Hanna HI 2211, USA). The ultrasound-assisted DB-DLLME method employed an ultrasonic bath (J.P. Selectra, Spain) throughout the study. To prepare the deep eutectic solvents (DES), mixtures were homogenized using a heating device ((Velp Scientifica, Italy). Distilled water utilized in the experiments was sourced from a Nuve Water Distiller ND-4.

The DB-DLLME method was also conducted using reagents of analytical grade purity. First of all, the analyte was purchased from Sigma-Aldrich (USA). The solvents TBAB and phenol, used for the formation of DES, were sourced from Carl Roth (Karlsruhe, Germany), and (Isolab Chemicals, Germany) brands, respectively. Additionally, sodium chloride (NaCl) was procured from Isolab Chemicals, Germany. Tetrahydrofuran (THF) from Sigma-Aldrich was also employed to examine the influence of the dispersing solvent on the method.

Formation of DES

DESs are obtained by combining several hydrogen bond acceptor (HBA) and hydrogen bond donor (HBD) components with distinct structures. In this study, the formation of a DES consisting of tetrabutylammonium bromide (TBAB) and phenol (Ph) for Brilliant Blue FCF microtraction was investigated. TBAB and Ph were mixed in a 1:1 molar ratio in a laboratory flask and stirred on a magnetic heating plate until the mixture became homogeneous and colorless. Meanwhile, the temperature of the heater was maintained at a constant range of 60-80°C [23]. Subsequently, the resultant solvent was cooled to room temperature for application in the separation and enrichment of Brilliant Blue FCF from real samples using the DS-DLLME method.

Des Based- Dispersive Liquid-liquid Microextraction (DB-DLLME) Method

The method was initially optimized using model solutions to achieve maximum extraction efficiency before the spectrophotometric analysis of Brilliant Blue FCF from food samples. The DB-DLLME method, with experimental parameters set at pH 3, 0.1 g NaCl, and 200 µL of DES, was applied to 10 mL volume samples containing 0.793 µg/mL of the analyte. The developed method involved ultrasonic mixing of these solutions for 5 min. Subsequently, the resulting turbid solutions were centrifuged at 4100 rpm for 3 min. to separate the organic phase from the aqueous phase. The separated phase containing Brilliant Blue FCF was then made up to 1 mL by adding approximately 0.8 mL ethanol to the extraction phase to improve the extraction process. The blue-colored solutions were analyzed using a UV-Vis spectrophotometer at 627 nm. Additionally, a schematic representation of the DB-DLLME microextraction method is provided in Fig.1.

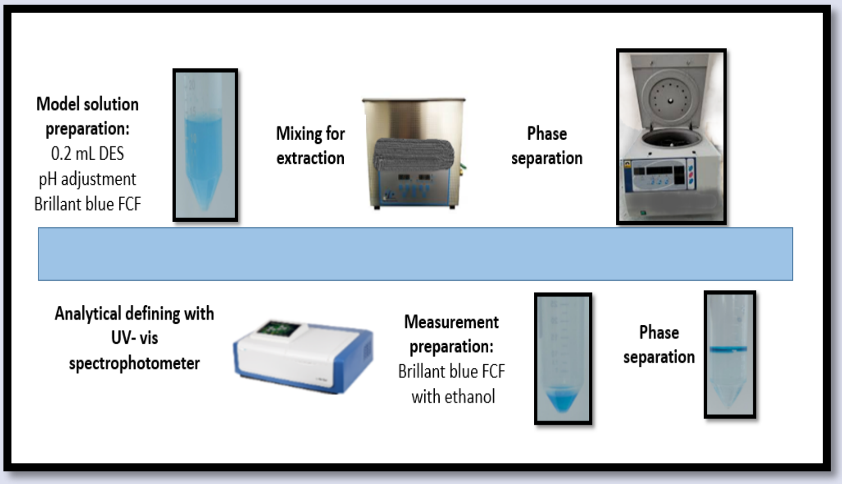

Figure 1. Schematic depiction of the DB-DLLME technique

Sample Preparation Procedures Prior to Analysis

Brilliant Blue FCF (E133) is widely used to impart a synthetic blue colour to a variety of food samples, making them readily available for analysis. Sugar confectionery, chewing gum, soft drinks were prepared for analysis using appropriate sample preparation procedures. To facilitate the dissolution of Brilliant Blue FCF, 2 grams of distilled water were added to each confectionery and chewing gum sample, which had been weighed individually. Following preparation, the samples were exposed to ultrasonic treatment for about 30 min. to aid in the extraction of the analyte. Subsequently, centrifugation was used to separate the phases and prepare them for analysis of Brilliant Blue FCF (E133). In addition, liquid samples were centrifuged prior to the application of the DB-DLLME method. Subsequently, 0.1-1 mL of the liquid phase was removed and subjected to the optimized method.

Results and Discussion

Effect of pH

pH plays a crucial role in the extraction efficiency of organic matter in the DB-DLLME method. The optimal pH, which is dependent on the structure of the analyte, facilitates a more rapid and quantitative transfer to the extraction phase. In this study, the developed method was tested on model solutions prepared at pH values of 1 and 8. The results, as depicted in Fig. 2, indicate that the interaction between brilliant blue FCF and the extraction phase is maximized at pH 3 and pH 4. However, extraction efficiency declines outside this pH range. At pH 3, the analyte's molecular form facilitates its transition from the aqueous phase to the deep eutectic solvent (DES) phase due to enhanced physical interactions. Consequently, a high extraction efficiency is achieved at this pH value. Given that the highest recovery was achieved at pH 3, this pH was selected as the optimal value. Subsequent optimization and actual sample analyses were conducted with the solvent adjusted to pH 3.

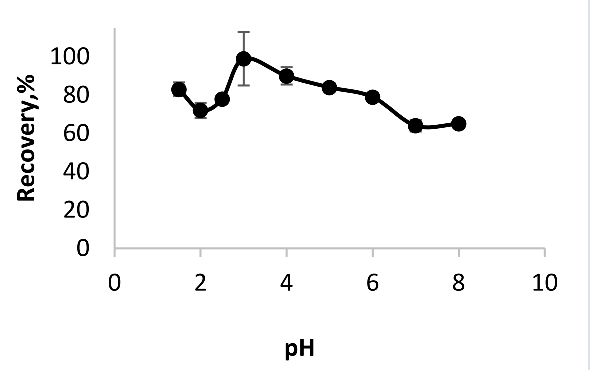

Figure 2. The optimization of pH (n: 3, eluent volume: 1 mL, DES volume: 0.2 mL, salt amount:0.1g)

DES Type Selection

In the analysis of Brillant Blue FCF, trying different types of DES is a parameter investigated to obtain the highest extraction yield. Therefore, DLLME method was applied using different molar ratio combinations of DES formed from TBAB (HBA) and phenol (HBD). According to the results given in the Fig. 3, it is seen that the best extraction value is obtained from DES4 and DES5 among DES models such as DES1 (1:2), DES2 (1:3), DES3 (1:1), DES4 (2:1), DES5 (3:1) formed from TBAB: Ph.

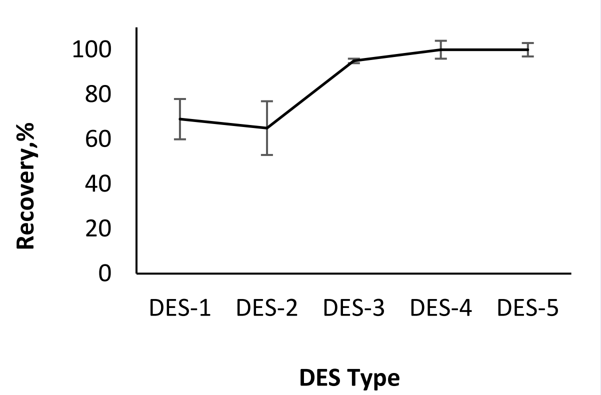

Figure 3. The impact of various DES compositions on the efficiency of Brilliant Blue FCF extraction (n: 3, eluent volume: 1 mL, DES volume: 0.2 mL, salt amount:0.1g)

DES Volume Optimization

Solvent volumes ranging from 0.05 to 0.6 mL were systematically evaluated to determine the optimum DES volume required for the microextraction of Brilliant Blue FCF. Based on the analysed data, a DES volume of 0.2 mL was found to be sufficient to obtain quantitative extraction results, as shown in Fig. 4. The recovery values started to decrease after 0.2 mL DES volume. The primary reason for the observed decrease in extraction efficiency with increasing DES volume may be attributed to the diminished interaction between the analyte and the DES, which becomes excessively diluted at higher DES volumes. In addition, the viscosity of the DES may alter at higher volumes, complicating the analyte extraction process. These factors collectively influence the distribution coefficient of the analyte, leading to a subsequent decrease in recovery rates.

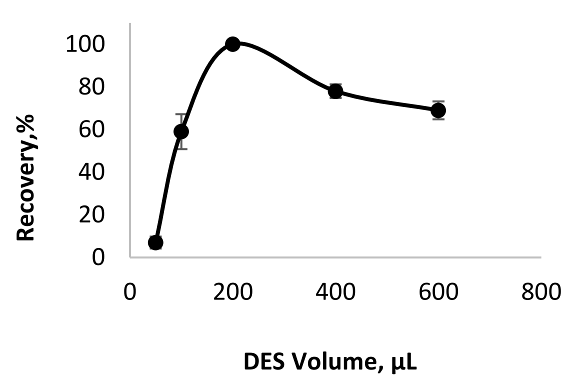

Figure 4. The impact of DES volume on the recovery of Brillant Blue FCF (n: 3, eluent volume: 1 mL, DES volume: 0.2 mL, salt amount:0.1g)

THF Volume Effects on Analytical Performance

In studies involving DLLME, aprotic solvents such as ethyl acetate, acetonitrile, diethyl ether, and tetrahydrofuran (THF) are commonly utilized. In this investigation, THF was employed as the dispersive solvent to evaluate its efficacy in the extraction process. To ascertain the necessity of THF in the extraction procedure, varying volumes of THF, ranging from 0 to 600 µL, were systematically added to the samples. The findings demonstrated that the use of tetrahydrofuran (THF) is unnecessary for this microextraction method (Fig.5). Achieving 100% extraction efficiency with reduced chemical usage highlights the study's contribution to sustainable development objectives.

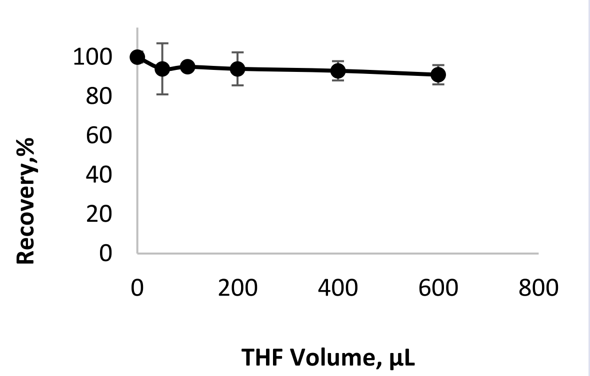

Figure 5. The impact of THF volume on the recovery of Brillant Blue FCF (n: 3, eluent volume: 1 mL, DES volume: 0.2 mL, salt amount:0.1g)

Salt Effect

In the DB-DLLME method, the addition of salt to the samples is used as one of the phase separators. Since salt affects the ionic equilibrium of the solution, it generally increases the interaction between the analyte and the organic solvent. In this way it can play a role in improving the transition of the analyte from the aqueous to the organic phase. However, too little salt can cause incomplete extraction and too much salt can cause interference. Therefore, in this study 0-3 g of salt was added to the samples to evaluate the effect of salt.

According to the results presented in Fig.6, the highest recovery values were achieved with the use of 0.1 to 0.3 grams of salt, whereas extraction efficiency began to decline when the amount of salt exceeded 0.3 grams.

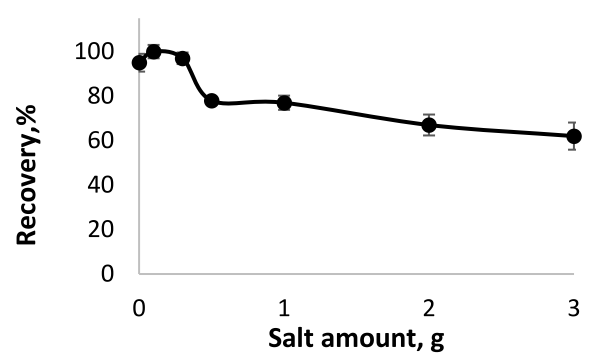

Figure 6. The impact of salt amount on the recovery of LGB (n: 3, eluent volume: 1 mL, DES volume: 0.2 mL)

Adjusting Extraction and Centrifugation Time for Optimal Performance

Determining the optimal extraction parameters for Brilliant Blue FCF is crucial for maximizing both time efficiency and extraction efficacy. In DLLME methods, either sonication or physical dispersion is typically employed. In this study, the effectiveness of the DLLME method was enhanced through sonication. To optimize the extraction process, samples were subjected to ultrasonic treatment for varying durations ranging from 1 to 10 minutes. Consistent distribution of the solute was observed across all time intervals, with high extraction efficiency achieved after 5 min. of sonication.

Additionally, model solutions undergoing the extraction process from the DES phase were subjected to rotational agitation at intervals of 1 to 10 minutes. The efficiency of the extraction process was evaluated, and the shortest duration yielding the most effective results was identified. The optimal process was determined to be a 3min. rotation period, during which recoveries exceeding 95% were consistently achieved (Fig.7).

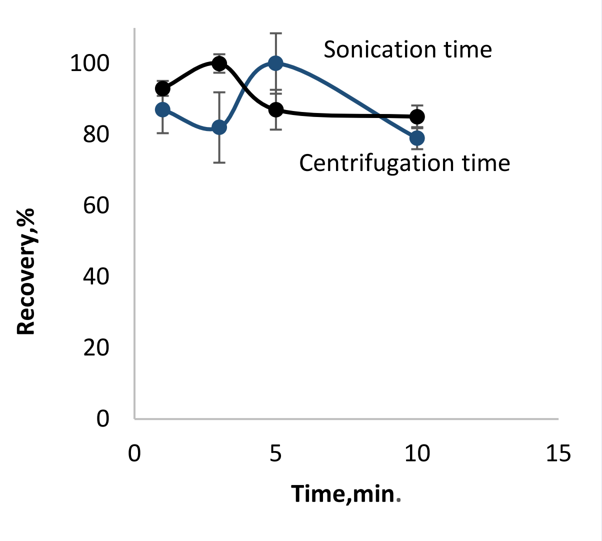

Figure 7. The effect of sonication and centrifugation time on the recovery of Brilliant Blue FCF (pH:3, n: 3, eluent volume: 1 mL, DES volume: 0.2 mL, salt amount: 0.1g)

Sample Volume

In this section, the impact of sample volume on both the enrichment factor and the method's applicability was investigated. The microextraction of Brilliant Blue FCF was conducted using the Dispersive Liquid-Liquid Microextraction (DB-DLLME) method with sample volumes ranging from 5 to 25 mL. Analysis of the results, as illustrated in the Fig.8 revealed that the method maintained quantitative extraction efficiency up to a sample volume of 22.5 mL. However, extraction efficiency declined for volumes exceeding 22.5 mL. Consequently, given that the final extract volume was 1 mL and the maximum effective sample volume was 22.5 mL, the preconcentration factor was calculated to be 22.5.

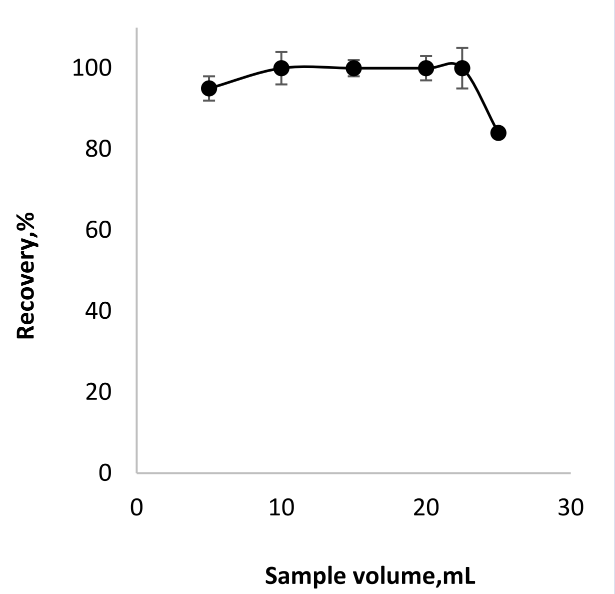

Figure 8. The effect of sample volume on the recovery of Brilliant Blue FCF (pH:3, n: 3, eluent volume: 1 mL, DES volume: 0.2 mL, salt amount: 0.1g)

Matrix Effects

To evaluate the suitability of the DB-DLLME method for quantifying Brilliant Blue FCF in diverse matrixes, we investigated the potential interference from various food additives and elemental constituents. The method was tested with synthetic dyes such as rhodamine B, curcumin, chicago sky blue, β-carotene, sudan IV. Additionally, the maximum permissible concentrations of metals, including Ag^{2+} , Cd^{2+}, Mn^{+2}, Zn^{2+}, and K^{+} that do not adversely affect the method's performance, were identified. The allowable concentration levels for these metals are detailed in Table 1. The standard deviations and recovery rates at these concentrations were computed to evaluate the method's quantitative accuracy and reliability.

Table 1. Tolerance parameters for foreign ion contaminants (pH:3, n: 3, eluent volume: 1 mL, DES volume: 0.2 mL, salt amount: 0.1g)

Foreign species	Concentration, µg L^{-1}	Recovery, %
Rhodamine B	239	98±4[a]
Curcumin	368	99±2
β carotene	2684	92±2
Riboflavin	1882	91±3
Sudan IV	380	98±4
Chicago sky blue	1986	100±4
K^{+}	120000	99±4
Ag^{2+}	500	97±2
Cd^{2+}	500	98±6
Mn^{+2}	1000	97±11
Zn^{+2}	1000	104±2

[a] Mean ± standard deviations

Real Samples Analysis

The optimized DB-DLLME method was employed for the spectrophotometric quantification of Brilliant Blue FCF in a variety of matrices, including beverages, confectioneries, chewing gum. Table 2 and Table 3 indicates that Brilliant Blue FCF was detectable in some food samples, whereas it was not found in others. Additionally, standard addition recovery experiments were conducted to verify the accuracy of the DB-DLLME method. These experiments showed that the analyte can be recovered with an efficiency in the range of 84-96%. Consequently, it can be concluded that the developed method is robust and suitable for the separation and enrichment of Brilliant Blue FCF in a wide range of food samples.

Table 2. Standard addition recovery studies on real samples (pH:3, n: 3, eluent volume: 1 mL, DES volume: 0.2 mL, salt amount: 0.1g)

Samples	Added (µg·mL-1)	Found (µg·mL-1)	Recovery (%)
Drinking water	0.0	N.D [a]	-
	0.79	0.69±0.03	87.3
	1.59	1.40±0.13	88.1
Tap water	0.00	N.D [a]	-
	0.79	0.72±0.08	91.1
	1.59	1.52±0.10	95.6
Fruit juice1	0.00	0.28±0.01	-
	0.88	1.00±0.02	86.2
	1.76	1.77±0.02	86.8
Fruit juice2	0.00	0.34±0.02	-
	0.88	1.02±0.11	83.6
	1.76	1.79±0.12	85.2

[a] N.D.: Not Dedected

Table 3. Analysis of Real Samples (pH:3, n: 3, eluent volume: 1 mL, DES volume: 0.2 mL, salt amount: 0.1g)

Samples	Found(µg·g^{-1})
Candy	N.D [a]
Chewing gam1	0.16±0.03
Chewing gam2	0.06±0.00
Fruit juice1	0.28±0.01
Fruit juice1	0.34±0.02

[a] N.D.: Not Dedected

Analytical Performance

In order to evaluate the analytical performance of the DB-DLLME method, parameters such as relative standard deviation (RSD), correlation coefficient (R^2), limit of detection (LOD), limit of quantification (LOQ), preconcentration factor (PF) were studied.

Specifically, the LOD (calculated as 3sb/m) and LOQ (calculated as 10sb/m) were determined using the standard deviation (Sb) and slope (m) parameters, yielding values of 0.86 µg/L and 2.88 µg/L, respectively. The RSD, which indicates the repeatability of the method based on five parallel measurements, was found to range from 0.4 to 1.3%. The correlation coefficient (R^2) reflecting the degree of linearity was 0.9859. The calibration curve is shown by the following equation A = 0.6963C - 0.025 (A: Absorbance and C: Concentration). Additionally, the preconcentration factor was calculated to be 22.5.

Conclusions

In this study, a DES-based liquid phase microextraction (LPME) method was developed for the determination of Brilliant Blue FCF, a commonly used food additive in food samples. The DB-DLLME method was implemented by adding only 200 µL of a DES composed of TBAB/Ph to the samples, without the need for a dispersive solvent. The molar concentrations of the DES consisting of TBAB/Ph were tested at ratios of 1:2, 1:3, 1:1, 2:1, 3:1 and extraction efficiencies above 95% were obtained at 1:1, 2:1, 3:1. This approach demonstrates that the method is highly environmentally friendly and adheres to green chemistry principles. The method was optimized by investigating and adjusting crucial parameters such as solvent usage, extraction time, and separation agent, and was validated through recovery studies in various matrixes, as detailed in Table 1. The optimized DB-DLLME microextraction technique has been effectively employed for a diverse array of food samples. Real samples were prepared very simply by ultrasonic method. The results, as presented in Table 2,3 indicate high recovery rates in the range of 83.6-95.6%. Furthermore, the DB-DLLME method was compared with other methods reported in the literature, as listed in the Table 4, and was found to exhibit very low limits of detection (LOD) and quantification (LOQ). This DB-DLLME method offers significant advantages over other techniques due to its lower observable limit, enabling effective application even at trace concentrations of analytes. A rapid and straightforward spectrophotometric method, such as UV-Vis spectroscopy, was also employed for the precise analysis of various matrix media.

Table 4. Comparative assessment of the DB-DLLME method relative to existing techniques in the literature

Method	Analytical technique	Sample	LOD^a	RSD^b %	PF^c	Recovery,%	Reference
Ultrasonic assisted ionic liquid dispersive liquid liquid microextraction (USA-IL-DLLME)	UV-vis	Energy, carbonated, fruity beverages	4.55 µg.L^{-1}	1.15	50	94.65-100.95	4
Green-ultrasound-assisted extraction technique	HPLC	Carbonated drink Fruit jelly Sugar confectionary, candy	0.42 µg·mL$^{−1}$	0.39-0.56		98.26- 102.5	7
Vortex assisted sequential-simultaneous liquid phase micro-extraction (VA-SS-LPME)	Uv-vis	Confectioneries, energy drinks, candies, jellies, pharmaceutical drugs and syrups, various teas, and cinnamon	19 µg·L^{-1}	3.2	50	96-102	24
Amine-based supramolecular solvent DLLME	*HPLC-PDA*	Spices, cotton candy, fruit-flavored candy, dried fruits, and chocolate dragee	0.07 mg.kg^{-1}	4\1-5\3	-	71-102	25
Deep eutectic solvent-based dispersive liquid-liquid microextraction (DB-DLLME)	Uv-vis	Beverage, chewing gum, candy, water samples	0.86 µg L^{-1}	0.4-1.3	22.5	84-96	This study

LOD^a: Limit of dedection, RSD^b: Relative standart deviation, PF^c: Preconcentration factor

Conflicts of interest

There are no conflicts of interest in this work.

Acknowledgment

Dr Nebiye Kizil thanks to Prof. Dr Mustafa Soylak for his contributions.

References

[1] Cetinkaya A., Kaya,S. I., Ozcelikay-Akyildiz G., Ozkan S. A., Emerging analytical techniques in the analysis of food dyes, Green Chemistry in Food Analysis*, Elsevier,* (2024) 221-258.

[2] Sigurdson G. T., Tang P., Giusti M. M., Natural colorants: Food colorants from natural sources, *Annu. Rev. Food Sci. Technol.*, 8(1) (2017) 261-280.

[3] Amchova P., Kotolova H., Ruda-Kucerova J., Health safety issues of synthetic food colorants. *Regulatory toxicology and pharmacology*, 73(3) (2015) 914-922.

[4] Erek F., Işik U., Meriç N., Synthesis and characterization of a novel ionic liquid for preconcentration of Brilliant Blue FCF (E 133) from some foods by ultrasound assisted temperature controlled ionic liquid dispersive liquid liquid microextraction method prior to spectrophotometric analysis; A comparative study, *Food Chem.*, *445* (2024) 138694.

[5] Tutunaru B., Tigae C., Spînu C., Prunaru I., Spectrophotometry and electrochemistry of Brilliant Blue FCF in aqueous solution of NaX, *Int. J. Electrochem. Sci.*, 12(1) (2017) 396-412.

[6] Gosetti F., Gianotti V., Angioi S., Polati S., Marengo E., Gennaro M. C., Oxidative degradation of food dye E133 Brilliant Blue FCF: liquid chromatography–electrospray mass spectrometry identification of the degradation pathway, *J. Chromatogr. A*, 1054(1-2) (2004) 379-387.

[7] Chakraborty A., Jayaseelan, K., Environmentally sustainable analytical quality by design aided RP-HPLC method for the estimation of brilliant blue in commercial food samples employing a green-ultrasound-assisted extraction technique, *Green Process. Synth.,* 12(1) (2023) 20230178.

[8] Ferreira L. G. B., Faria R. X., Ferreira N. C. D. S., Soares-Bezerra R. J., Brilliant Blue Dyes in daily food: How could purinergic system be affected?, *Int. J. Food Sci.*, 2016(1) (2016) 7548498.

[9] Lucarelli M. R., Shirk M. B., Julian M. W., Crouser E. D., Toxicity of Food Drug and Cosmetic Blue No. 1 dye in critically ill patients, *Chest,* 125(2) (2004) 793-795.

[10] [Guo J., Wu H., Du L., Fu Y., Determination of brilliant blue FCF in food and cosmetic samples by ionic liquid independent disperse liquid–liquid microextraction, *Anal. Methods* 5 (2013) 4021–4026.

[11] Pourali A., Abbasalizadeh A., Afshar Mogaddam M. R., Farajzadeh M. A., Tuzen M., Nemati M., Liquid Phase Microextraction of Hazardous Compounds in Dairy Products; Principal and Practical Aspects, *Crit. Rev. Anal. Chem.*, (2023) 1-17.

[12] Kizil N., Basaran E., Erbilgin D., Yola M. L., Uzcan F., Soylak M., Deep eutectic solvent (DES) based dispersive Liquid-Phase microextraction of Sunset yellow FCF in food and pharmaceutical products, *Microchem. J.*, 181 (2022) 107734.

[13] Yamini Y., Safari M., Shamsayei M., Simultaneous determination of steroid drugs in the ointment via magnetic solid phase extraction followed by HPLC-UV, *J. Pharm. Anal.*, 8(4) (2018) 250-257.

[14] Samadi F., Sarafraz-Yazdi A., Es' haghi Z., An insight into the determination of trace levels of benzodiazepines in biometric systems: Use of crab shell powder as an environmentally friendly biosorbent, *Journal of Chromatography B*, 1092 (2018) 58-64.

[15] Islas G., Ibarra I. S., Hernandez P., Miranda J. M., Cepeda A., Dispersive solid phase extraction for the analysis of veterinary drugs applied to food samples: a review, *J. Environ. Anal. Chem.*, 2017(1) (2017) 8215271.

[16] Qi L., Wang Y., Li Y., Zheng G., Li C., Su H., Microfluidic aqueous two-phase extraction of bisphenol A using ionic liquid for high-performance liquid chromatography analysis. *Anal. Bioanal. Chem.*, 407 (2015) 3617-3625.

[17] Grau J., Azorín C., Benedé J. L., Chisvert A., Salvador A., Use of green alternative solvents in dispersive liquid-liquid microextraction: A review, *J. Sep. Sci.*, 45(1) (2022) 210-222.

[18] Rezaee M., Assadi Y., Hosseini M. R. M., Aghaee E., Ahmadi F., Berijani S., Determination of organic compounds in water using dispersive liquid–liquid microextraction, *J. Chromatogr. A,* 1116 (1-2) (2006) 1-9.

[19] Abbott A. P., Capper G., Davies D. L., Rasheed R. K., Tambyrajah, V., Novel solvent properties of choline chloride/urea mixtures, *Chem. Commun.*, (1) (2003) 70-71.

[20] Vállez-Gomis V., Grau J., Benedé J. L., Giokas D. L., Chisvert A., Salvador A., Fundamentals and applications of stir bar sorptive dispersive microextraction: a tutorial review. *Anal. Chim. Acta*, 1153 (2021) 338271.

[21] Xu K., Wang Y., Huang Y., Li N., Wen Q., A green deep eutectic solvent-based aqueous two-phase system for protein extracting, *Anal. Chim. Acta*, 864 (2015) 9-20.

[22] Tang B., Zhang H., Row K. H., Application of deep eutectic solvents in the extraction and separation of target compounds from various samples, *J. Sep. Sci.*, 38(6) (2015) 1053-1064.

[23] Chen J., Li Y., Wang X., Liu W., Application of deep eutectic solvents in food analysis: A review, *Molecules*, 24(24) (2019) 4594.

[24] Bişgin A. T., Selective separation and determination strategy for monitoring E100, E127, E129 and E133 in foodstuffs: Vortex assisted sequential-simultaneous liquid phase micro-extraction, *Microchem. J., 196* (2024) 109716.

[25] Bogdanova P., Vakh C., Bulatov A., A surfactant-mediated microextraction of synthetic dyes from solid-phase food samples into the primary amine-based supramolecular solvent. *Food Chem.*, 380 (2022) 131812.

Cumhuriyet Sci. J., 45(3) (2024) 557-561
DOI: https://doi.org/10.17776/csj.1418207

Cumhuriyet Science Journal

| csj.cumhuriyet.edu.tr | Founded: 2002 ISSN: 2587-2680 e-ISSN: 2587-246X Publisher: Sivas Cumhuriyet University

Polynomial Representation of Vernam Cipher

Emin Aygün [1,a,*], **İncinur Yılmaz** [1,b]

[1] *Department of Mathematics, Faculty of Science, Erciyes University, Kayseri, Türkiye.*
[2] *Department of Mathematics, Faculty of Science, Erciyes University, Kayseri, Türkiye.*
**Corresponding author*

Research Article

History
Received: 11/01/2024
Accepted: 24/06/2024

ABSTRACT

Storing information or data has been one of the basic needs of humans for many years and these needs have led to the existence of some systems throughout the years. In this paper, soft sets represented by polynomials will be encrypted and decrypted in line with their representations. We are going to use the Rijndael Algorithm for soft sets and then encrypt and decrypt the data in accordance with its algorithm. The Rijndael algorithm is an algorithm which carries out the cyclic process according to the keys it has. At the end of each loop, the key is renewed and is applied to the data. These data are firstly shown in strings. While enumerating, it starts with zero index and ends with one less than string length.

Keywords: Soft sets, Encryption, Decryption, Vernam cipher, Stream cipher.

[a] *eaygun@erciyes.edu.tr* *https://orcid.org/0000-0003-3503-0552*
[b] *incinur.yilmaz@hotmail.com* *https://orcid.org/0000-0001-6481-8918*

Introduction

Since people need some information to send data in secret, cryptography has been a practical tool over the centuries. Thus, only the planned receiver of the data can understand it. Besides, cryptosystems have two different types: The first one is a symmetric cryptosystem which uses only one key during the encryption and decryption process while the second one is, an asymmetric cryptosystem which uses two different keys throughout the process [1,2]. A key is employed for encrypting data, while its counterparts are utilized to decrypt the encrypted information.

The symmetric cryptosystem has two different ciphers stream ciphers and block ciphers. It is not hard to distinguish. The most important difference between block and stream cipher is that while we deal with bits at a time in stream ciphers, in block ciphers, we deal with blocks all the time [3].

In this article, we examine a stream cipher known as Vernam Cipher and also application on a soft set dealing with uncertain objects to avoid some difficulties. The concept of encrypting soft set emerges from the security issues of the objects that the soft set deals with. However, we have three traditional theories dealing with uncertainties and solving complex problems in engineering, environment, economies, and others:

The first one is the theory of probability, the second is the theory of fuzzy sets [4,5] and the last one is interval mathematics [6]. Because of the assorted uncertainties of these problems, one cannot successfully use them. Additionally, each theory has its own difficulty in itself. Accordingly, these theories are not sufficient for describing a tiny change of date information and therefore they are not reliable and adequate. They also somewhat contradict aims and other difficulties.

Materials and Methods

Definition 1.

Let U be a universal set, E is the parameters' set, and $P(U)$ is the power set of U and $A \subseteq E$. Assume that there is a soft set over universal set $\left(U: f_A: E \rightarrow P(U)\right)$ such that if $e_j \notin A$ then $f_A(e_f)$ is defined F_A as $\emptyset$ so $F_A = \left\{\left(e_j, f_A(e_j)\right): e_j \in E, f_A(e_j) \in P(U)\right\}$.

Here, f_A is called the approximation function of the F_A [7].

Definition 2.

Let $U = \{u_1, u_2, u_3, \dots, u_n\}$ be a universal set, $E = \{e_1, e_2, e_3, \dots, e_m\}$ parameters' set, $A \subseteq E$ and F_A be a soft set over U.

$$R_A = \left\{(u_i, e_j): e_j \in A, u_i \in F(e_j)\right\} \subseteq U \times E$$

is called the relation form of F_A. In this case, the characteristic function of the R_A relation form is defined by

$$X_{R_A}: U \times E \rightarrow \{0,1\}, A_{R_A}(u_i, e_j) = \begin{cases} 1, & (u_i,\ e_j) \in R_A \\ 0, & (u_i, e_j) \notin R_A \end{cases}$$

R_A can be described with the following table, where $U = \{u_1, u_2, u_3, \dots, u_n\}$ is a universal set, $E = \{e_1, e_2, e_3, \dots, e_m\}$ is the set of parameters and $A \subseteq E$:

$$\begin{array}{c|cccc}
R_A & e_1 & e_2 & \cdots & e_m \\
\hline
u_1 & X_{R_A}(u_1, e_1) & X_{R_A}(u_1, e_2) & \cdots & X_{R_A}(u_1, e_m) \\
u_2 & X_{R_A}(u_2, e_1) & X_{R_A}(u_2, e_2) & \cdots & X_{R_A}(u_2, e_m) \\
\vdots & \vdots & \vdots & \ddots & \vdots \\
u_n & X_{R_A}(u_n, e_1) & X_{R_A}(u_n, e_2) & \cdots & X_{R_A}(u_n, e_m)
\end{array}$$

[8].

Definition 3.

Let $[a_{ij}], [b_{ij}] \in S_{m\times n}$. The inverse product of the soft matrices $[a_{ij}]$ and $[b_{ij}]$ are defined by $[a_{ij}] \cdot_i [b_{ij}] = [c_{ij}]$ where

$$c_{i,j} = \begin{cases} 1, & if\ a_{i,j} \neq b_{i,j} \\ 0, & if\ a_{i,j} = b_{i,j} \end{cases}$$

[9].

Definition 4.

The numerical equivalences of the letters are given in the following:

LETTERS	*A*	*B*	*C*	*D*	*E*	*F*	*G*	*H*	*I*	*J*	*K*	*L*	*M*	*N*	*O*	*P*	*Q*	*R*
NUMBERS	*0*	*1*	*2*	*3*	*4*	*5*	*6*	*7*	*8*	*9*	*10*	*11*	*12*	*13*	*14*	*15*	*16*	*17*

S	*T*	*U*	*V*	*W*	*X*	*Y*	*Z*	*Ç*	*Ğ*	*İ*	*Ö*	*Ş*	*Ü*
18	*19*	*20*	*21*	*22*	*23*	*24*	*25*	*26*	*27*	*28*	*29*	*30*	*31*

Thus, A starts from 0, and the letter Ü becomes 31. If the letters were matched with the binary system, it would be as follows:

LETTERS	*A*	*B*	*C*	*D*	*E*	*...*	*Ş*	*Ü*
BINARY SYSTEM	*00000*	*00001*	*00010*	*00011*	*00100*	*...*	*11110*	*11111*

Because we want the binary system to be 32 bits, we add six more letters such as Ç, Ğ, İ, Ö, Ş, Ü. If desired, different characters can be added to this alphabet and the number can be increased to 64 bits [9].

Definition 5.

A stream cipher which sends plaintext string $P_1, P_2, P_3, \dots,$ using the key stream $S_1, S_2, S_3, \dots,$ to a ciphertext $C_1, C_2, C_3, \dots,$ where $C_i = E_{S_i}(P_i)$. The corresponding decryption function is $D_{d_i}(C_i) = P_i$. Also, d is a decryption key corresponding to the encrypting key S_i [10].

Definition 6.

Vernam Cipher, due to Gilbert Vernam in 1917, to encrypt and decrypt telegraph messages automatically is the simplest cipher. In the Vernam Cipher, the key stream is represented by bit string $S_1, S_2, S_3, \dots, S_m,$ with the same length as the plaintext message, which is also a bit string, $P_1, P_2, P_3, \dots, P_m$ [11]. Plaintext bits are encrypted using the encryption algorithm given below:

$$\mathrm{C_i} \equiv \mathrm{E_{S_i}(P_i)} \equiv \mathrm{S_i} + \mathrm{P_i}\ (\mathrm{mod}\ 2)$$

Thus, the decryption algorithm of Vernam Cipher is,

$$\mathrm{D_{S_i(C_i)}} \equiv \mathrm{C_i} + \mathrm{S_i}(\mathrm{mod}\ 2)$$

If the similarities between encryption and decryption algorithms are wanted to be proven, it has to be proven that the decryption function produces the plaintext bit P_i again. The ciphertext bit C_i is calculated using the encryption algorithm $\mathrm{C_i} \equiv \mathrm{S_i} + \mathrm{P_i}\ (\mathrm{mod}\ 2)$ as follows:

$$\begin{aligned}
D_{S_i(C_i)} &\equiv C_i + S_i\ (mod\ 2) \\
&\equiv (x_i + S_i) + S_i\ (mod\ 2) \\
&\equiv x_i + S_i + S_i\ (mod\ 2) \\
&\equiv x_i + 2S_i\ (mod\ 2) \\
&\equiv x_i + 0\ (mod\ 2) \\
&\equiv x_i\ (mod\ 2)\ [10].
\end{aligned}$$

Polynomial Representation of Vernam Cipher

Definition 7.

A stream cipher which sends plaintext string $P_1(x), P_2(x), P_3(x), \dots,$ using the key stream $S_1(x), S_2(x), S_3(x), \dots,$ to a ciphertext $C_1(x), C_2(x), C_3(x), \dots$ where $C_i(x) = E_{S_{i(x)}}(P_i(x))$. The corresponding decryption function is

$$D_{d_{i(x)}}(C_i(x)) = P_i(x)$$

Also, $d(x)$ is a decryption key corresponding to the encrypting key $S_i(x)$ [12].

Definition 8.

In Vernam encryption, the keystream $S_1(x), S_2(x), S_3(x), \dots S_m(x)$ is a polynomial sequence $P_1(x), P_2(x), P_3(x), \dots P_m(x)$ with the same number of terms as the plaintext message. Plaintext strings are encrypted according to the following encryption algorithm:

$$C_i(x) \equiv E_{S_i(x)}(P_i(x)) \equiv P_i(x) + S_i(x)\ (mod\ 2)$$

Thus, the decryption algorithm of Vernam Cipher is,

$$D_{S_i(x)}(C_i(x)) \equiv C_i(x) + S_i(x)\ (mod\ 2)$$

For the similarities between encryption and decryption algorithms, one has to prove that the decryption function produces the plaintext bit $P_i(x)$ again. As ciphertext bit $C_i(x)$is calculated by using the encryption algorithm $C_i(x) \equiv S_i(x) + P_i(x)\ (mod\ 2)$ as following:

$$D_{S_i(x)}(C_i(x)) \equiv C_i(x) + S_i(x)\ (mod\ 2)$$

$$\equiv (X_i(x) + S_i(x)) + S_i(x)\ (mod\ 2)$$
$$\equiv X_i(x) + S_i(x) + S_i(x)\ (mod\ 2)$$
$$\equiv X_i(x) + 2S_i(x)\ (mod\ 2)$$
$$\equiv X_i(x) + 0\ (mod\ 2)$$
$$\equiv X_i(x)\ (mod\ 2)$$ [5].

Example 1.

Let's encrypt the plaintext “MATH” as a polynomial using the Vernam Encryption Algorithm with the keyword “IDEA”.

The equivalence of “MATH” in the binary system is 01100 00000 10011 00111 and the polynomial representation of the “MATH” is $P_i(x) = x^{18} + x^{17} + x^9 + x^6 + x^5 + x^2 + x + 1$,

The equivalence of “IDEA” in the binary system is 01000 00011 00100 0000. Since the polynomial representation of the “IDEA” is $S_i(x) = x^{18} + x^{11} + x^{10} + x^7$ we use the encryption algorithm $C_i(x) \equiv S_i(x) + P_i(x)(mod\ 2)$. Then,

$$C_i(x) \equiv S_i(x) + P_i(x)(mod\ 2)$$
$$C_i(x) \equiv [(x^{18} + x^{11} + x^{10} + x^7) + (x^{18} + x^{17} + x^9 + x^6 + x^5 + x^2 + x + 1)](mod 2)$$
$$C_i(x) \equiv [2x^{18} + x^{17} + x^{11} + x^{10} + x^9 + x^7 + x^6 + x^5 + x^2 + x + 1](mod 2)$$
$$C_i(x) \equiv (x^{17} + x^{11} + x^{10} + x^9 + x^7 + x^6 + x^5 + x^2 + x + 1)$$
$$C_i(x) \equiv 00100\ 00011\ 10111\ 00111$$

As a result of the above steps, the ciphertext “EDXH” is obtained. Here note that the process has been made with the coefficients of the polynomials.

Example 2.

Let's decrypt the ciphertext “EDXH” as a polynomial using the Vernam Encryption Algorithm with the keyword “IDEA”.The equivalence of “EDXH” in the binary system is 00100 00011 10111 00111 and the polynomial representation of the “EDXH” is $C_i(x) = x^{17} + x^{11} + x^{10} + x^9 + x^7 + x^6 + x^5 + x^2 + x + 1$, The equivalence of “IDEA” in the binary system is 01000 00011 00100 0000. Since the polynomial representation of the “IDEA” is $S_i(x) = x^{18} + x^{11} + x^{10} + x^7$ we use the decryption algorithm $P_i(x) \equiv C_i(x) + S_i(x)(mod\ 2)$. Then,

$$P_i(x) \equiv C_i(x) + S_i(x)(mod\ 2)$$
$$P_i(x) = [(x^{17} + x^{11} + x^{10} + x^9 + x^7 + x^6 + x^5 + x^2 + x + 1) + (x^{18} + x^{11} + x^{10} + x^7)](mod 2)$$
$$P_i(x) = (x^{18} + x^{17} + 2x^{11} + 2x^{10} + x^9 + 2x^7 + x^6 + x^5 + x^2 + x + 1)(mod 2)$$
$$P_i(x) = (x^{18} + x^{17} + x^9 + x^6 + x^5 + x^2 + x + 1)$$
$$P_i(x) = 01100\ 00000\ 10011\ 00111$$

As a result of the above steps, the plaintext “MATH” is obtained.

Suggestion For a New Cryptosystem

$[p_{ij}]_{mxm}$is the plaintext matrix, $[s_{ij}]_{mxm}$ is the key matrix and they are two square matrices. The transposes of these matrices are $[p_{ij}]^T_{mxm} and\ [s_{ij}]^T_{mxm}$;

Definition 9. Encryption procedure is obtained by

$$[p_{ij}]^T_{mxm} \cdot_c [s_{ij}]^T_{mxm} = [c_{ij}]^T_{mxm}$$

By transposing the matrix $[c_{ij}]^T_{mxm}$, the original ciphertext matrix $[c_{ij}]_{mxm}$ is obtained. The encrypted matrix given to the receiver is $[c_{ij}]_{mxm}$.

Definition 10. The decryption procedure is similar to the encryption procedure.

$$[c_{ij}]^T_{mxm} \cdot_c [s_{ij}]^T_{mxm} = [p_{ij}]^T_{mxm}$$

The transpose of the plaintext matrix $[p_{ij}]_{mxm}^T$ is obtained. By transposing the matrix $[p_{ij}]_{mxm}^T$, the original plaintext matrix $[p_{ij}]_{mxm}$ is obtained. Here, the decrypted version of the encrypted matrix given to the receiver is $[p_{ij}]_{mxm}$.

Definition 11.
The Soft Encryption Algorithm is as follows:
Step 1: An arbitrary soft set is chosen.
Step 2: A soft set quadratic matrix is created using the selected soft set.
Step 3: The message is divided into blocks and each line is converted into a binary system.
Step 4: Each row of the soft matrix is rearranged according to the received π to obtain S_π.
Step 5: The characteristic multiplication of S_π and the message is made.
Step 6: The letter equivalent of each resulting line is found and sent to the recipient.

The Soft Decryption Algorithm is as follows:
Step 1: The encrypted message reaches the recipient.
Step 2: The receiver performs the characteristic multiplication of the encrypted message and S_π.
Step 3: The soft matrix is rearranged.
Step 4: The text equivalent of the matrix is found.
Step 5: The encrypted text is decrypted.

Example 3. Encrypt and decrypt the plaintext matrix $[p_{ij}]_{3x3} = \begin{bmatrix} 1 & 0 & 1 \\ 1 & 0 & 0 \\ 0 & 1 & 0 \end{bmatrix}$ with the new encryption proposal using the key matrix $[s_{ij}]_{3x3} = \begin{bmatrix} 0 & 0 & 1 \\ 1 & 1 & 0 \\ 0 & 1 & 0 \end{bmatrix}$.

The transposes of the matrices are $[p_{ij}]_{3x3}^T = \begin{bmatrix} 1 & 1 & 0 \\ 0 & 0 & 1 \\ 1 & 0 & 0 \end{bmatrix}$ and $[s_{ij}]_{3x3}^T = \begin{bmatrix} 0 & 1 & 0 \\ 0 & 1 & 1 \\ 1 & 0 & 0 \end{bmatrix}$.

If we apply the encryption procedure then $[p_{ij}]_{mxm}^T \cdot_c [s_{ij}]_{mxm}^T = [c_{ij}]_{mxm}^T$, and therefore

$$\begin{bmatrix} 1 & 1 & 0 \\ 0 & 0 & 1 \\ 1 & 0 & 0 \end{bmatrix} \cdot_c \begin{bmatrix} 0 & 1 & 0 \\ 0 & 1 & 1 \\ 1 & 0 & 0 \end{bmatrix} = \begin{bmatrix} 0 & 1 & 1 \\ 1 & 0 & 1 \\ 1 & 1 & 1 \end{bmatrix} = [c_{ij}]_{3x3}^T$$

is obtained. If $[c_{ij}]_{mxm}^T$ is transposed, then we have $[c_{ij}]_{3x3} = \begin{bmatrix} 0 & 1 & 1 \\ 1 & 0 & 1 \\ 1 & 1 & 1 \end{bmatrix}$. (The matrix and its transpose coincided.)

If we apply the decryption procedure then $[c_{ij}]_{mxm}^T \cdot_c [s_{ij}]_{mxm}^T = [p_{ij}]_{mxm}^T$, and therefore

$$\begin{bmatrix} 0 & 1 & 1 \\ 1 & 0 & 1 \\ 1 & 1 & 1 \end{bmatrix} \cdot_c \begin{bmatrix} 0 & 1 & 0 \\ 0 & 1 & 1 \\ 1 & 0 & 0 \end{bmatrix} = \begin{bmatrix} 1 & 1 & 0 \\ 0 & 0 & 1 \\ 1 & 0 & 0 \end{bmatrix} = [p_{ij}]_{3x3}^T$$

is obtained. If the $[p_{ij}]_{mxm}^T$ is transposed, then we have $[p_{ij}]_{3x3} = \begin{bmatrix} 1 & 0 & 1 \\ 1 & 0 & 0 \\ 0 & 1 & 0 \end{bmatrix}$.

In this way, a new encryption method is discovered.

Conclusion

According to these mathematical findings, we can encrypt and decrypt a soft set using the Vernam Encryption Algorithm as well as representing it as a polynomial. Additionally, as a result of our work, we found a new cryptosystem suggestion.

Conflict of interest

There are no conflicts of interest in this work.

References

[1] Aktaş H., Çağman N., Soft Sets and Soft Groups, *Information Sciences,* 177 (2007) 2726-2735.

[2] Aktaş H., Çağman N., Erratum to “Soft Sets and Soft Groups”, Information Sciences 3 (2009), 338. *Information Sciences,* 177 (2007) 272-2735.

[3] Atagün A.O., Sezgin A., Soft Substructures Of Rings, Fields and Modules, *Computers & Mathematics With Applications,* 61 (3) (2011) 592-601.

[4] Zadeh L.A., Fuzzy Sets, *Information and Control,* 8 (1965) 338-353.

[5] Zadeh L.A., Toward A Generalized Theory Of Uncertainty (GTU)-An Outline, *Information Sciences,* 172 (2005) 1-40.

[6] Gorzalzany M.B., A Method Of Inference In Approximate Reasoning Based On Interval-Valued Fuzzy Sets, *Fuzzy Set and Systems,* 21 (1987) 1-17.

[7] Dmitry M., Soft Sets Theory – First Results, *Computers & Mathematics With Applications,* 37 (1999) 19-31.

[8] Atagün A.O., Kamacı H., Oktay O., Reduced Soft Matrices and Generalized Products With Applications In Decision Making, *Neural Computing and Applications*, 29 (2018) 445-456.

[9] Aygün E., Soft Matrix Product and Soft Cryptosystem, *Filomath,* 32 (19) (2018) 6519-6530.

[10] Hashim H.R., Husain A.M., Vernem Cipher Over A Soft Set, *Globakl Journal Of Mathematics*, 5 (2) (2015) 2395-4760.

[11] Rosen K.H., Elementary Number Theory, and Its Applications. 5th Edn., United States of America, Boston, (2005) 363.

[12] Aygün E., Yılmaz İ., Esnek Kümeler Ve Vernam Şifreleme Üzerine, 3. Başkent International Conference On Multidisciplinary Studies Full Text Book, 3. Başkent International Conference On Multidisciplinary Studies, Ankara, 2022, 1108-1115.

Cumhuriyet Sci. J., 45(3) (2024) 562-570
DOI: https://doi.org/10.17776/csj.1156101

Cumhuriyet Science Journal

| csj.cumhuriyet.edu.tr | Founded: 2002 ISSN: 2587-2680 e-ISSN: 2587-246X Publisher: Sivas Cumhuriyet University

Investigation of Solution Behavior By Sumudu Methods of Random Complex Partial Differential Equations

Mehmet Merdan [1,a,*], **Merve Merdan** [1,b], **Rıdvan Şahin** [1,c]

[1] *Department of Mathematical Engineering, Gümüşhane University, Gümüşhane, Türkiye.*
**Corresponding author*

Research Article

History
Received: 27/02/2023
Accepted: 13/08/2024

ABSTRACT

In this study, solutions of random complex partial differential equations were found using the two-dimensional Sumudu transformation method(STM). The initial conditions of a deterministic equation or the non-homogeneous part of the equation are transformed into random variables to obtain a random complex partial differential equation. With the help of the properties of two-dimensional Sumudu and inverse Sumudu transformation, an approximate analytical solution of a complex partial differential equation with random constant coefficients was obtained by selecting a random variable with an initial condition of Normal and Gamma distribution. The probability characteristics of the resulting solutions, such as expected value and variance, were obtained and graphically shown with the help of the Maple package program.

Keywords: Two-dimensional Sumudu Transform and Inverse Sumudu Transformation, Complex partial differential equation, Expected value, Variance and confidence interval.

[a] mmerdan@gumushane.edu.tr https://orcid.org/0000-0002-8509-3044
[b] mervemerdan94@hotmail.com https://orcid.org/0000-0002-6045-6531
[c] ridvansahin@gumushane.edu.tr https://orcid.org/0000-0001-7434-4269

Introduction

Complex partial differential equations first were discovered in the early 1900. D. Pompeiu is one of the important mathematicians who made substantial contributions to the field and left a name. He described the Pompeiu integral operator, which carries his name. It still serves as the foundation for the theory of complex differential equations today. Integral transforms, the Adomian decomposition approach, and the reduced differential transform were used to solve complex differential equations [1-4]. These approaches divide the equation into real and imaginer components before solving it. The Sumudu differential transformation method can be utilized in this article to resolve the problem without dividing it into real and imaginer components. Because of this, a solution can be developed with minimal effort. Watugala introduced the Sumudu transform with the article [5] in 1993. It is a transformation that is crucial in the solution of several ordinary differential equations in control engineering. The Sumudu transform's characteristics and uses are described[5-6]. The Laplace transform and its characteristics are also taken into account, and the theory that establishes the relationship between Sumudu and Laplace transformations is presented. Sumudu transformation is used in this study to solve partial differential equations more quickly. The fundamental details for integral transformations, as well as the fundamental properties of the Laplace and Sumudu transformations, are provided in the study's first sections. In the following chapters, the solution of the partial equation was obtained by applying the Sumudu transform to appropriate ordinary complex differential equations and partial differential equations.

Watugala's Sumudu transform method (STM) was used to address engineering issues [6]. Weerakoon used the technique to solve partial differential equations [7]. Subsequently, Weerakoon discovered this transformation's inverse formula [8]. The Sumudu transformation technique (STM) was employed by Demiray et al. [9] to discover precise answers to fractional differential equations. The Sumudu transform iterative method (STIM) was expanded by Kumar and Daftardar-Gejji [10] to handle various time and spatial FPDEs and FPDE systems. To solve linear fuzzy fractional differential equations (FFDEs) using Caputo fuzzy fractional derivative, Rahman and Ahmad used the fuzzy Sumudu transform (FST) [11]. Prakash et al. [12] solved nonlinear fractional Zakharov–Kuznetsov equations with the help of the Sumudu transform method, which is a new iterative technique.

Given the wealth of literature on stochastic and deterministic differential equation models, the application of random differential equations (RDE) in mathematical models is not as common. By including random effect terms in the model's parameters, deterministic models can be changed to random models. Because random parameters offer the chance to account for parameter changes, this method enables more realistic modeling of physical processes. The probability properties of the equations that are randomized in the deterministic model by choosing the coefficients on the second side of the equation or the initial conditions from continuous probability distributions will be investigated. Ordinary differential equations in mathematical modeling are not necessarily adequate for investigating natural processes. Using random and stochastic differential equations to investigate occurrences with random components yields superior findings. Using ordinary differential equations, random differential equations can be produced in three methods[13]. ii. Differential equations with random non-homogeneous sections iii. Equations using random coefficients. In this study, we considered complex partial differential equations with inhomogeneous parts and initial conditions with random values. Many physical and engineering problems can be modeled more reliably with random differential equations. In recent decades, there has been a significant amount of research in the disciplines of parameter uncertainty and randomness, as well as stochastic differential processes.

In this study, the two-dimensional Sumudu transform method is used to solve linear complex partial differential equations. The structure of the essay is as follows. Section 2 provides information on the one dimensional and two-dimensional Sumudu transformation and its attributes. Examples of the random complex differential equation are provided in Section 3. The solutions' probability features were computed and graphically displayed. Section 4 provides the conclusions.

Materials and Methods

Sumudu Transform Method

Definition 2.1. Let A be a function set defined[14] by

$$A = \{g\,(t) \mid \exists M, \tau_1, \tau_2 > 0, |g(t)| < Me^{\frac{t}{\tau_j}}, \quad (1)$$
$$if\ t \in (-1)^j x\ [0, \infty\,)\}$$

the Sumudu transform is defined over the set of functions by

$$G(u) = S[g(t)] = \int_0^\infty g(ut)e^{-t}dt,\ u \in (-\tau_1, \tau_2) \quad (2)$$

Table 1. Special Sumudu transforms[14].

	$g(t)$	$G(u) = S[g(t)]$
1	1	1
2	t	u
3	$\sin(at)$	$\frac{au}{1+(au)^2}$
4	$\cos(at)$	$\frac{1}{1+(au)^2}$
5	$t^n, n > 0$	$\Gamma(n+1)u^n$
6	e^{at}	$\frac{1}{1-au}$
7	$e^{bt}\cos(at)$	$\frac{1-bu}{(1-bu)^2+(au)^2}$
8	$e^{bt}\sin(at)$	$\frac{au}{(1-bu)^2+(au)^2}$
9	$t^n e^{at}$	$\frac{\Gamma(n+1)u^n}{(1-au)^n}$

The Double Sumudu Transform

The Sumudu transform is a simple and somewhat elegant approach to implement the double Sumudu transform, assuming the function has a power series transformation with regard to its variables. The double Laplace transform of a function defined in the positive quadrant of the xy plane is:

$$\mathcal{L}_2[g(x,y);(r,s)] = \int_0^\infty\int_0^\infty g(x,y)e^{-(rx+sy)}dxdy \qquad (3)$$

where p and q are the transformation variables of x and y, respectively.

Definition 1. [15-17] Let $g(t,x)$: $t,x \in \mathbb{R}^+$, If a function is written as a convergent infinite series, its double Sumudu transform is as follows:

$$\begin{aligned}G(u,v) &= \mathbb{S}_2[g(t,x);(u,v)] \\ &= \mathbb{S}[\mathbb{S}\{g(t,x);t \to u\};x \to v] \\ &= \frac{1}{uv}\int_0^\infty\int_0^\infty e^{-\left(\frac{t}{u}+\frac{x}{v}\right)}g(t,x)dtdx \qquad (4)\end{aligned}$$

We propose applications of the double Sumudu transform to several specific functions, which are similar to those obtained by solving population dynamics equations with age structure. However, it is a simple exercise to demonstrate that the double Sumudu and Laplace transforms are also theoretical dual. That is:

$$\begin{aligned}&uvG(u,v) \\ &= \mathcal{L}_2\left[g(x,y);\left(\frac{1}{u},\frac{1}{v}\right)\right] \qquad (5)\end{aligned}$$

The relationship between the Sumudu Transform and double Laplace Transform can be expressed as in (5).

Theorem 1. [15-17] Let $G\,(x,y)$ be a real-valued function of $x,y\ \in\ \mathbb{R}^+$.

Then,

$$\mathbb{S}_2[g(x+y);(u,v)] = \frac{1}{u-v}\{uG(u) - vG(v)\}. \ (6)$$

g represents population density, age x, and time y, or vice versa. The $(x-y)$ example is even more interesting from the point of view of biology, which is often encountered with these works in Mathematical Biology. The proof of the condition $x \geq y$ is also simple and sufficient. Thus, geometrically, although the line dividing the first quarter into two equal parts represents the η axis (represented by the lower part Q_1 and the upper part Q_2), dividing both the second and fourth quarters is the η -axis (the row facing up) and the ζ −axis (the arrow from the starting point to the fourth quarter), then the test is: Let's assume that g is a dual function, then $g\ (0)$ is odd

$$\mathbb{S}_2[g(x-y);(u,v)] = \frac{1}{uv}\int\int_{Q_1} g(x-y)e^{-\left(\frac{x}{u}+\frac{y}{v}\right)}dxdy - \frac{1}{uv}\int\int_{Q_2} g(x-y)e^{-\left(\frac{x}{u}+\frac{y}{v}\right)}\,dxdy. \tag{7}$$

$$x = \frac{1}{2}(\zeta+\eta);\, y = \frac{1}{2}(\zeta-\eta)$$

variable transformation

$$\int\int_{Q_1} g(x-y)e^{-\left(\frac{x}{u}+\frac{y}{v}\right)}dxdy = \frac{1}{2}\int_0^\infty g(\zeta)d\zeta \int_\zeta^\infty e^{-\frac{1}{2}\left(\frac{1}{u}+\frac{1}{v}\right)\zeta-\frac{1}{2}\left(\frac{1}{u}-\frac{1}{v}\right)\eta}d\eta$$

$$= \frac{uv}{u-v}\int_0^\infty e^{-\frac{\zeta}{v}}g(\zeta)d\zeta$$

$$= \frac{uv^2}{u-v}G(u).$$

similarly,

$$\int\int_{Q_1} g(x-y)e^{-\left(\frac{x}{u}+\frac{y}{v}\right)}dxdy = \frac{v^2u}{u-v}G(v).$$

Therefore, for the odd function g

$$\mathbb{S}_2[g(x-y);(u,v)]$$

$$= \frac{uG(u)-vG(v)}{u+v} \tag{8}$$

and if g is a even function

$$\mathbb{S}_2[g(x-y);(u,v)] = \frac{uG(u)+vG(v)}{u-v} \tag{9}$$

$G(u) = \mathbb{S}[g(t)] = \int_0^\infty g(ut)e^{-t}dt,\ \ u\epsilon(-\tau_1,\tau_2)$ Sumudu conversion

From the equations $G\ (u)$ and (8), if g is an even function, then it is obvious that

$$(u+v)\mathbb{S}_2[g(x-y)] = (u-v)\mathbb{S}_2[g(x+y)] \tag{10}$$

are obtained. If STM is applied to partial derivatives as follows: $g(0,a) = \ G_0(a)$,

$$\mathbb{S}_2\left[\frac{\partial g(t,a)}{\partial t};(u,v)\right] = \frac{1}{uv}\int_0^\infty\int_0^\infty e^{-\left(\frac{t}{u}+\frac{s}{v}\right)}\frac{\partial}{\partial t}g(t,a)dtda = \frac{1}{v}\int_0^\infty e^{-\frac{s}{v}}\left\{\frac{1}{u}\int_0^\infty e^{-\frac{t}{u}}\frac{\partial}{\partial t}g(t,a)dt\right\}da.$$

The inner integral given in the equation (5),

$$\frac{G(u,a)-g(0,a)}{u} \tag{11}$$

$$\mathbb{S}_2\left[\frac{\partial g(t,a)}{\partial t};(u,v)\right] = \frac{1}{u}\left\{\frac{1}{v}\int_0^\infty e^{-\frac{a}{v}}G(u,a)da - \frac{1}{v}\int_0^\infty e^{-\frac{a}{v}}g_0(a)da\ \right\}$$

$$= \frac{1}{u}\{G(u,v)-G_0(v)\} \tag{12}$$

Also,

$$\mathbb{S}_2\left[\frac{\partial g(t,a)}{\partial a};(u,v)\right] = \frac{1}{v}\int_0^\infty e^{-\frac{a}{v}}\left\{\frac{1}{u}\int_0^\infty e^{-\frac{t}{u}}\frac{\partial}{\partial a}g(t,a)dt\right\}da$$

$$= \frac{1}{v}\int_0^\infty e^{-\frac{a}{v}}\frac{\partial}{\partial a}G(u,a)da$$

$$= G_u(u,v). \tag{13}$$

Alternatively,

$$\mathbb{S}_2\left[\frac{\partial g(t,a)}{\partial t};(u,v)\right]=\frac{1}{u}\int_0^\infty e^{-\frac{a}{v}}\left\{\frac{1}{v}\int_0^\infty e^{-\frac{a}{u}}\frac{\partial g}{\partial a}da\right\}dt$$

$$=\frac{1}{u}\int_0^\infty e^{-\frac{t}{u}}\frac{1}{v}[G(t,v)-g(t,0)]dt$$

$$=\frac{1}{v}(G(u,v)-G_0(u)) \tag{14}$$

Where $G\ (u,0)=G_0(u)$ and $G(0,v)=G_0(v)$. From the equations (12) and (13)

$$G_v(u,v)=\frac{G(u,v)-G_0}{v}$$

it is expressed as.

Definition 2.[15-17]: Let $G(t,X)$ and $H(T,X)$ functions have a two-dimensional Sumudu transformation. Then the two-dimensional Sumudu transformation of $g(t,x)$ and $h(t,x)$ of two-dimensional convolution,

$$(g**h)(t,x)=\int_0^x\int_0^t g(\zeta,\eta)h(t-\zeta,x-\eta)d\zeta d\eta$$

$$\mathbb{S}_2[(g**h)(t,x);u,v]=uvG(u,v)H(u,v)$$

Also, the two-dimensional Sumudu transformation of the partial derivative of the two-dimensional convolution with respect to x e was obtained below,

$$\mathbb{S}_2\left[\frac{\partial}{\partial x}(g**h)(t,x);u,v\right]=uv\mathbb{S}_2\left[\frac{\partial}{\partial x}(t,x);u,v\right]=\mathbb{S}_2[h(t,x);u,v]$$

or

$$uv\mathbb{S}_2[f(t,x);u,v]\mathbb{S}_2\left[\frac{\partial}{\partial x}h(t,x);u,v\right].$$

Thus, the relationship between the Sumudu and Laplace Transform of the two-dimensional function,

$$\mathbb{S}_2[(g**h)(t,x);u,v]=\frac{1}{uv}\mathcal{L}_t\mathcal{L}_x[g**h)(t,x)]$$

to solve PDEs using the Sumudu transformation, partial derivatives of this transformation are needed. Thus, by applying the two-dimensional Sumudu transformation to its second-order partial derivatives with respect to x

$$\mathbb{S}_2\left[\frac{\partial^2}{\partial x^2}g(t,x);u,v\right]=\frac{1}{v^2}G(u,v)-\frac{1}{v^2}G(u,0)-\frac{1}{v}\frac{\partial}{\partial x}G(u,0)$$

expression is obtained. Similarly, given in the second-order partial derivative with respect to t;

$$\mathbb{S}_2\left[\frac{\partial^2}{\partial t^2}g(t,x);u,v\right]=\frac{1}{u^2}G(u,v)-\frac{1}{u^2}G(0,v)-\frac{1}{u}\frac{\partial}{\partial t}G(0,v).$$

Numerical Examples

Sumudu transformation method (STM) is used in this section to solve random complex partial differential equations. Examples of variances, confidence intervals, and estimated values for various probability distributions of these solutions are also provided. Complex differential equations with random effect terms and various probability distributions are included in each case. Mean-square computation has been used in the past to solve a few first-order random differential models and equations [18–23]. A stochastic differential equation (SDE) is a differential equation in which one or more elements are stochastic processes[24], and the solution is also stochastic. SDEs have numerous applications in pure mathematics, including modeling the behaviors of stochastic models such as stock markets [25], random growth models [26], and physical systems exposed to thermal fluctuations.

SDEs have a random differential, which in the most basic example is random white noise computed as the derivative of a Brownian motion, or more broadly, a semimartingale. Other sorts of random behavior are possible, such as hopping processes like Lévy processes[27] or hopping semimartingales. Random differential equations are equivalent to stochastic differential equations. Stochastic differential equations can also be expanded to differential manifolds[28-30].

Example 3.1.

$$\frac{\partial w}{\partial z}-\frac{\partial w}{\partial \bar{z}}-5w=0, \qquad w(x,0)=Be^{3x} \tag{15}$$

obtain the probability characteristics by solving the approximate analytical solution of the given partial differential equation $B\sim N(\mu,\sigma^2)$, independent random variables with a normal distribution, using the Sumudu method.
In equation (15)

$$\frac{\partial w}{\partial z}=\frac{1}{2}\left(\frac{\partial w}{\partial x}-i\frac{\partial w}{\partial y}\right)$$
$$\frac{\partial w}{\partial \bar{z}}=\frac{1}{2}\left(\frac{\partial w}{\partial x}+i\frac{\partial w}{\partial y}\right)$$

if their equality is written instead

$$\frac{1}{2}\left(\frac{\partial w}{\partial x}-i\frac{\partial w}{\partial y}\right)-\frac{1}{2}\left(\frac{\partial w}{\partial x}+i\frac{\partial w}{\partial y}\right)-5w=0$$

are obtained. If $w=u+iv$ is written in the given equation,

$$\frac{1}{2}\left[\frac{\partial u}{\partial x}+i\frac{\partial v}{\partial x}-i\left(\frac{\partial u}{\partial y}+i\frac{\partial v}{\partial y}\right)\right]-\frac{1}{2}\left[\frac{\partial u}{\partial x}+i\frac{\partial v}{\partial x}+i\left(\frac{\partial u}{\partial y}+i\frac{\partial v}{\partial y}\right)\right]-5(u+iv)=0$$
$$\frac{\partial v}{\partial y}-5u=0$$
$$-\frac{\partial u}{\partial y}-5v=0$$

if Sumudu transformation is applied to its equations, $S[u(x,y)]=R_1(x,s)$
$S[v(x,y)]=R_2(x,s)$
when,

$$\frac{1}{s}[R_2(x,s)-v(x,0)]-5R_1(x,s)=0$$
$$-\frac{1}{s}[R_1(x,s)-u(x,0)]-5R_2(x,s)=0$$

if the Cramer rule applies to the resulting Sumudu transformations,

$$-5R_1(x,s)+\frac{1}{s}R_2(x,s)=\frac{v(x,0)}{s}$$
$$-\frac{1}{s}R_1(x,s)-5R_2(x,s)=-\frac{u(x,0)}{s}.$$
$$\begin{vmatrix}-5 & \frac{1}{s}\\ \frac{-1}{s} & -5\end{vmatrix}=25+\frac{1}{s^2}=\Delta$$
$$R_1(x,y)=\frac{\begin{vmatrix}\frac{v(x,0)}{s} & \frac{1}{s}\\ -\frac{u(x,0)}{s} & -5\end{vmatrix}}{\Delta}=\frac{Be^{3x}}{1+(5s)^2}$$
$$R_2(x,y)=\frac{\begin{vmatrix}-5 & \frac{v(x,0)}{s}\\ \frac{-1}{s} & -\frac{u(x,0)}{s}\end{vmatrix}}{\Delta}=\frac{Be^{3x}5s}{(5s)^2+1}$$

taking the inverse Sumudu transformation into his equations,$u(x,y)=S^{-1}[R_1(x,s)]$

$=S^{-1}\left[\frac{Be^{3x}}{1+(5s)^2}\right]$, $\quad\left\{S[cos(ay)]=\frac{1}{1+(as)^2}, S^{-1}\left[\frac{1}{1+(as)^2}\right]=cos(ay)\ \right\}$
$=Be^{3x}\cos(5y)$

$$
\begin{aligned}
v(x,y) &= S^{-1}[R_2(x,y)] \\
&= S^{-1}\left[\frac{Be^{3x}5s}{(5s)^2+1}\right], \left\{S[sin(ay)] = \frac{as}{1+(as)^2}, S^{-1}\left[\frac{as}{1+(as)^2}\right] = sin(ay)\right\} \\
&= Be^{3x}\sin(5y)
\end{aligned}
$$

are obtained. Then

$$
\begin{aligned}
w(z) &= Be^{3x}[cos(5y) + isin(5y)] \\
&= Be^{4z-\bar{z}}
\end{aligned}
$$

can be found. Let's try to find the probability characteristics of the solution we found. A random variable X is normally distributed $(X \sim N(\mu,\sigma^2))$ if its probability distribution function is $f(x) = \frac{1}{\sigma\sqrt{2\pi}}exp\left(-\frac{1}{2}\left(\frac{x-\mu}{\sigma}\right)^2\right)$.

Let $B \sim N(\mu,\sigma^2)$ be a random variable with a Normal distribution[32]. Moment generating function of Normal distribution,

$$M_x(t) = E[e^{tx}] = e^{\mu t+\frac{1}{2}\sigma^2 t^2}.$$

Expected value and variance of the first, second moments of the random variable $x \sim N(\mu,\sigma^2)$

$E[x] = \mu, E[x^2] = \mu^2 + \sigma^2 \quad ve\ Var[x] = \sigma^2.$

Using these moments and if x and y are random arguments $E[xy] = E[x]E[y]$ since, approximate formulas of expected value and variance

$$E[w(k,h)] = \sum_{k=0}^{n}\sum_{h=0}^{n} E[w(k,h)]x^k y^h$$

The expected value and variance of the solution we found above are, respectively,

$$
\begin{aligned}
E[w(z)] &= E[B]e^{4z-\bar{z}} \\
&= \mu e^{4z-\bar{z}}.
\end{aligned}
$$

Variance

$$
\begin{aligned}
Var[w(z)] &= Var[B]e^{8z-2\bar{z}} \\
&= \sigma^2 e^{8z-2\bar{z}}.
\end{aligned}
$$

Specifically, the expected value if $\mu = 2, \sigma^2 = 1$ is selected,

$E[w(z)] = 2e^{4z-\bar{z}}$

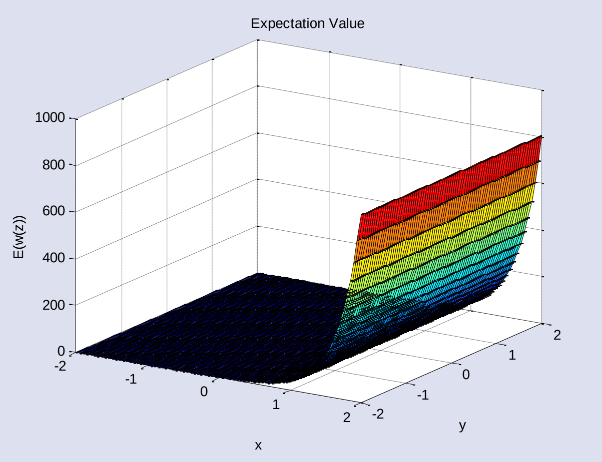

Figure 1 Expected value of equation (15) for values $\mu = 2, \sigma^2 = 1$

The expectations can be given in a single graph for a comparison with the deterministic results of equation (1) as above (Figure 1). Maximum and minimum values of expected values of the random variables are obtained as follows: $w(z)$ takes its maximum value 806,8576 and its minimum value 0,0050.

Variance

$Var[w(z)] = e^{8z-2\bar{z}}.$

If the variance found for the selected parameter values is plotted with MATLAB (2013a), the graph in Figure 2. is obtained.

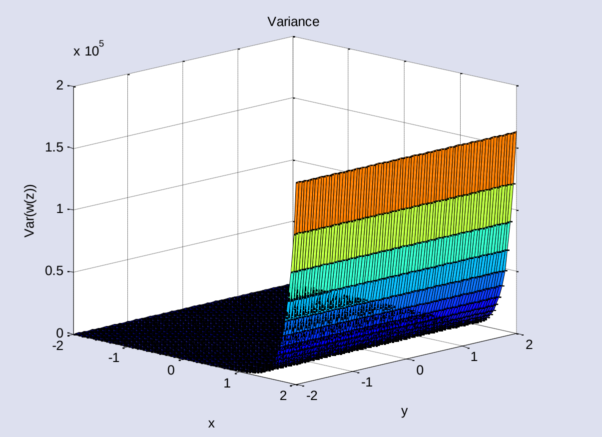

Figure 2 Variance of equation (13) for values $\mu = 2, \sigma^2 = 1$

These are the results for the confidence intervals for the expectations (Figure 3). The dashed line indicates the upper end of the confidence range while the dashed-dot lines show the lower ends of the interval in this case. Three standard deviations were utilized to produce the confidence intervals.

The variance of $w(z)$ is given above (Figure 2). Extremum values of the variances of the random variables are obtained as follows: $min[Var(w(z))] = 6.1442x10^{-6}$ and $max[Var(w(z))] = 1.6275x10^5$.

Confidence intervals for expected values of random variables,

$(E[w(z)] - K.std(w(z)), E(w(z)) + K.std(w(z))$

is equal to and this can be obtained through standard deviations. For $K = 3$, this formula gives approximately 99% confidence interval for the approximate expected value of the normally distributed random variable [21]. If the 99% confidence interval is plotted with MATLAB (2013a), the graph in Figure 3. is obtained. Known as the three-sigma rule, this popular rule indicates that about 99.73% of values for a normally distributed variable are within about three standard deviations of the mean. Therefore, using appropriate parameters, we will compare the variations of the results for two continuous distributions with limited and unlimited support, respectively. Appropriate parameters will ensure that almost all possible values for random effects are drawn from the same range for both distributions.

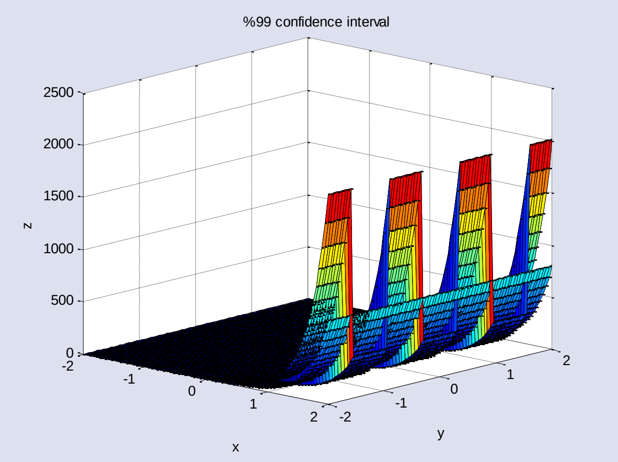

Figure 3. Confidence interval(%99) of equation (15) for values $\mu = 2, \sigma^2 = 1$

The confidence intervals of $w(z)$ are given in Figure 3. The extremum values of the confidence intervals are as follows: $min\big(E(w(z)) - 3std(w(z))\big)$ =0.0025 and $max(E(w(z)) + 3std(w(z)))$ = 2017.1 . Here, $K = 3$ gives an approximate 99% confidence interval.

Example 3.2.

$$w_z - w_{\bar{z}} = A - B,\ w(x,0) = (A+B)x \qquad (16)$$

obtain the probability characteristics by solving the approximate analytical solution of the given partial differential equation with $A, B \sim G(\alpha,\beta)$ gamma distribution, independent random variables with Sumudu method. In equation (16).

$$\frac{\partial w}{\partial z} = w_z = \frac{1}{2}\left[w_x - iw_y\right]$$
$$\frac{\partial w}{\partial \bar{z}} = w_{\bar{z}} = \frac{1}{2}\left[w_x + iw_y\right]$$

if $w = u + iv$ is written instead of equations,

$$\frac{1}{2}\left[\frac{\partial u}{\partial x} + i\frac{\partial v}{\partial x} - i\left(\frac{\partial u}{\partial y} + i\frac{\partial v}{\partial y}\right)\right] - \frac{1}{2}\left[\frac{\partial u}{\partial x} + i\frac{\partial v}{\partial x} + i\left(\frac{\partial u}{\partial y} + i\frac{\partial v}{\partial y}\right)\right] = A - B$$

are obtained. After the necessary procedures are carried out,

$$\frac{\partial v}{\partial y} = A - B$$
$$-\frac{\partial u}{\partial y} i = 0$$

if Sumudu transformation is applied to its equations,

$$S[u(x,y)] = R_1(x,s)$$
$$S[v(x,y)] = R_2(x,s)$$

when,

$$\frac{1}{s}[R_2(x,s) - v(x,0)] = A - B$$
$$-\frac{1}{s}[R_1(x,s) - u(x,0)] = 0.$$

if the Cramer rule applies to the resulting Sumudu transformations,

$$R_1(x,s) = u(x,0) = (A+B)x,$$
$$R_2(x,s) = v(x,0) + s(A-B) = s(A-B)$$

taking the inverse Sumudu transformation into his equations,

$$u(x,y) = S^{-1}[(A+B)x]$$
$$= (A+B)x$$
$$v(x,y) = S^{-1}[s(A-B)]$$
$$= (A-B)y$$

are obtained. Then $w(z) = u(x,y) + iv(x,y) = (A+B)x + i(A-B)y = Az + B\bar{z}$ can be found. A random variable X is gamma distributed $(X \sim G(\alpha,\beta))$ if its probability distribution function is $f(x;\alpha,\beta) = \frac{x^{\alpha-1}e^{-\beta x}\beta^{\alpha}}{\Gamma(\alpha)}$. When $z \sim G(\alpha,\beta)$, the expected value and its variance are given below, respectively [32].

$$E[z] = \alpha\beta\,, E[z^2] = (\alpha + \alpha^2)\beta^2\,,\ Var[z] = \alpha\beta^2,$$

The expected value and variance of the solution we found above are, respectively,

$$E[w(z)] = E[Az + B\bar{z}]$$
$$= E[A]z + E[B]\bar{z}$$
$$= \alpha\beta(z + \bar{z}).$$
$$Var[w(z)] = Var[Az + B\bar{z}]$$
$$= Var[A]z^2 + Var[B]\bar{z}^2$$
$$= \alpha\beta^2(z^2 + \bar{z}^2).$$

Expected value if $\alpha = 1\,, \beta = 2$ are selected specifically,
$E[w(z)] = 2(z + \bar{z})$

.

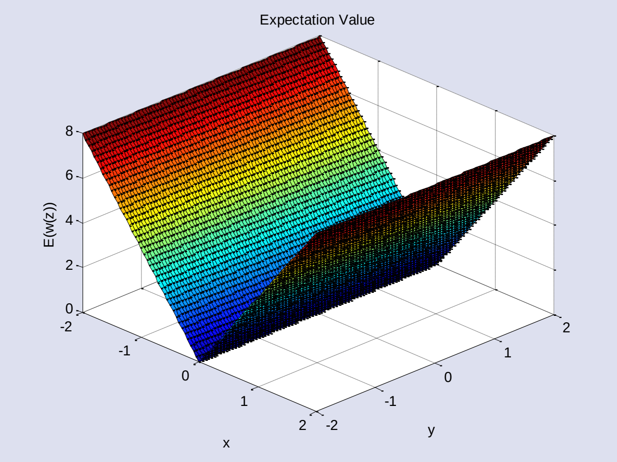

Figure 4. The expected value of equation (16) for values $\alpha = 1\,, \beta = 2$

The expectations can be given in a single graph for a comparison with the deterministic results of equation (1) as above (Figure 4). Maximum and minimum values of expected values of the random variables are obtained as follows: $w(z)$ takes its maximum value 8 and its minimum value 0. Variance,

$$Var[w(z)] = 4(z^2 + \bar{z}^2)$$

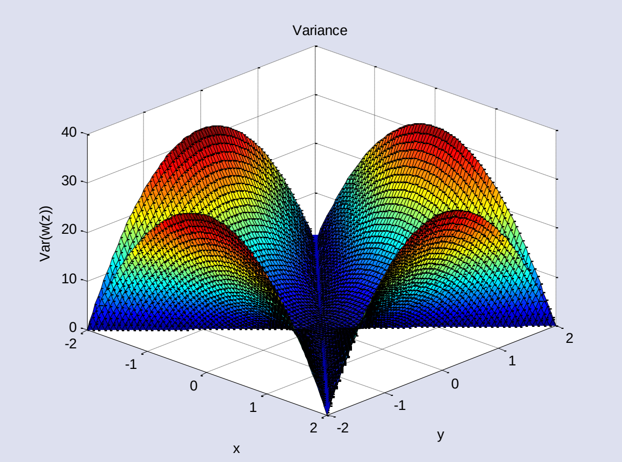

Figure 5. Variance of equation (16) for values $\alpha = 1$, $\beta = 2$

The variance of $w(z)$ is given above (Figure 5). Extremum values of the variances of the random variables are obtained as follows: $min[Var(w(z))] = 0$ and $max[Var(w(z))] = 32$

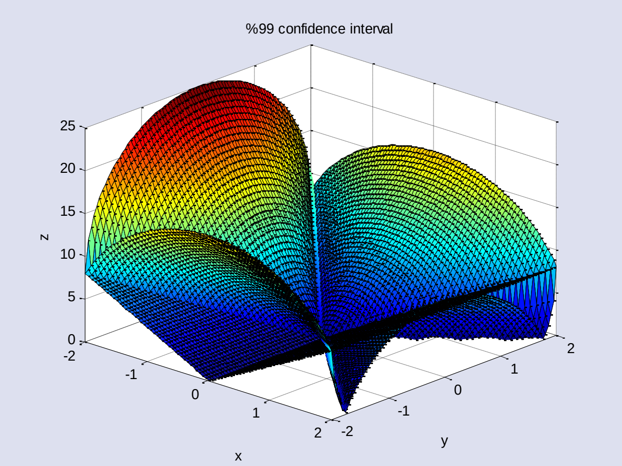

Figure 6. Confidence interval(%99) of equation (14) for values $\alpha = 1$, $\beta = 2$

The confidence intervals of $w(z)$ are given in Figure 3. The extremum values of the confidence intervals are as follows: $min\big(E(w(z)) - 3std(w(z))\big) = 0$ and $max(E(w(z)) + 3std(w(z))) = 24.9706$. Here, $K = 3$ gives an approximate 99% confidence interval.

Conclusion

With the aid of random variables chosen from the initial conditions, a random complex differential equation was used in this work. With the aid of transformations, a system of random partial differential equations was created from a normal and gamma distribution. The two-dimensional Sumudu and inverse Sumudu transformations have been used to analytically solve the resulting system of equations. Several examples demonstrate approximations to the solution stochastic process's mean and standard deviation functions. Calculated and graphically displayed are the found solution's probability characteristics.

Conflict of interest

The author declares no conflicts of interest

References

[1] Düz M., Solution of complex differential equations with variable coefficients by using reduced differential transform, Mis. Math. Not., 21(1) (2020) 161–170.

[2] Düz M., Application of Elzaki Transform to first order constant coefficients complex equations, *Bul. Int. math. Virt. inst*., 7 (2017) 387–393.

[3] Düz M., On an application of Laplace transforms, *NTMSCI*., 5(2) (2017) 193–198.

[4] Düz M., Solution of complex equations with Adomian Decomposition method, *TWMS J. App. Eng. Math*.,7(1) (2017) 66–73.

[5] Watugala G. K., Sumudu transform: a new integral transform to solve differential equations and control engineering problems, *Int. J. Math. Educ. Sci. Technol.,* 24(1) (1993) 35–43.

[6] Anac H., Merdan M., Kesemen T., Solving for the random component time-fractional partial differential equations with the new Sumudu transform iterative method, *SN App. Sci.,* 2 (2020) 1112 .

[7] Weerakoon S., Application of Sumudu transform to partial differential equations*, Int. J. Math. Educ. Sci. Technol.,* 25(2) (1994) 277–283.

[8] Weerakoon S., Complex inversion formula for Sumudu transform, *Int. J. Math. Educ. Sci. Technol.* 29(4) (1998) 618–621.

[9] Demiray S.T., Bulut H., Belgacem F.B.M., Sumudu transform method for analytical solutions of fractional type ordinary differential equations, *Math Prob Eng*., (2015) https ://doi.org/10.1155/2015/13169 0

[10] Kumar M., Daftardar-Gejji V., Exact solutions of fractional partial differential equations by Sumudu transform iterative method., (2018) arXiv :1806.03057 v1

[11] Rahman N.A.A., Ahmad M.Z., Solving fuzzy fractional differential equations using fuzzy Sumudu transform, *J. Nonl. Sci. Appl.,* 10(5) (2017) 2620–2632

[12] Prakash A., Kumar M., Baleanu D., A new iterative technique for a fractional model of nonlinear Zakharov–Kuznetsov equations via Sumudu transform, *Appl. Math. Comput.,* 334 (2018) 30–40.

[13] Soong, T.T., Random Differential Equations in Science and Engineering, *Academic Press*, 327, (1973).

[14] Belgacem F.B.M, Karaballi A.A, Sumudu Transform Fundamental Properties Investigations and Applications, *J. Appl. Math. Stoch. Analy.,* (2006) Article ID 91083 1–23

[15] Eltayeb H., Kılıçman A., A Note on the Sumudu Transforms and Differential Equations, *Applied Math. Sci.*, 4(22) (2010) 1089 –1098.

[16] Watugala, G.K. The Sumudu transform for functions of two variables, *Mathematical Engin. in Indus.*, 8(4)(2002) 293–302.

[17] Kılıçman A., Eltayeb H.,Agarwal R.P., On Sumudu Transform and System of Differential Equations*, Abstract Appl. Analy.*, (2010), Article ID 598702, 11 pages.

[18] Merdan M., Anac H., Bekiryazici Z., Kesemen, T., Solving of Some Random Partial Differential Equations by Using Differential Transformation Method and Laplace-Padé Method*, J. Gumushane Univ. Inst. Sci. Tech.*, 9(1) (2019) 108-118.

[19] Merdan M., Atasoy N., On Solutions Of Random Partial Differential Equations With Laplace Adomian Decomposition, *Cumhuriyet Sci. J.*, 44(1) (2023) 160-169.

[20] Merdan M., Şişman Ş., Analysıs of Random Discrete Tıme Logistic Model, *Sigma J. Eng. Nat. Sci.,* 38(3) (2020) 1269-1298.

[21] Merdan M., Altay Ö., Bekiryazici Z., Investigation of the Behaviour of Volterra Integral Equations with Random Effects, *J. Gumushane Univ. Inst. Sci. Tech.*, 10(1) (2020) 205-216.

[22] Merdan M., Ordinary and partial complex differential equations with random effects. Master's Thesis, Gumushane University, Institute of Science, (2020).

[23] Merdan, M., Merdan, M., ve Şahin, R., Investigation of Behavior on Solutions of Lane–Emden Complex Differential Equations by a Random Differential Transformation Method, *Compl*., (2023) 3713454.

[24] Rogers, L.C.G., Williams, David., Diffusions, Markov Processes and Martingales, Vol 2: Ito Calculus (2nd ed., Cambridge Mathematical Library ed.). *Cambridge University Press*.(2000).

[25] Musiela, M., Rutkowski, M., Martingale Methods in Financial Modelling, 2nd Edition, *Springer Verlag*, Berlin, (2004).

[26] Øksendal, Bernt K., Stochastic Differential Equations: An Introduction with Applications. Berlin: *Springer,* (2003).

[27] Kunita, H., Stochastic Differential Equations Based on Lévy Processes and Stochastic Flows of Diffeomorphisms. In: Rao, M.M. (eds) Real and Stochastic Analysis. Trends in Mathematics. *Birkhäuser,* (2004).

[28] Imkeller P., Schmalfuss B., The Conjugacy of Stochastic and Random Differential Equations and the Existence of Global Attractors. *J. Dyn. Diff. Equ*., 13 (2) (2001) 215–249.

[29] Michel E., Stochastic calculus in manifolds. Springer Berlin, *Heidelberg*, (1989).

[30] Brzeźniak Z., Elworthy K.D., Stochastic differential equations on Banach manifolds*, Methods Funct. Anal. Top.* 6(1) (2000) 43-84.

[31] Feller W., An Introduction to Probability Theory and Its Applications, volume 1, 3rd edition. New York: *John Wiley & Sons*. (1968)

[32] Khaniyev, T., Ünver, İ., Küçük, Z., ve Kesemen T. (2017). Olasılık Kuramında Çözümlü Problemler, Nobel Akademik Yayıncılık.

Cumhuriyet Sci. J., 45(3) (2024) 571-577
DOI: https://doi.org/10.17776/csj.1444015

Cumhuriyet Science Journal

| csj.cumhuriyet.edu.tr | Founded: 2002 ISSN: 2587-2680 e-ISSN: 2587-246X Publisher: Sivas Cumhuriyet University

Darboux Frame of Pancake Curve in Euclidean 3-Space

Emre Öztürk [1,a,*]

[1] *Management Information Systems, Faculty of Economics and Administrative Sciences, Hatay Mustafa Kemal University, Hatay, Türkiye.*
**Corresponding author*

Research Article

History
Received: 28/02/2024
Accepted: 12/09/2024

ABSTRACT

In this paper, we focus on a rare curve, “The pancake curve” which was named by Robert Ferréol. We investigate the Darboux frame of the curve, and we calculate the curvatures: geodesic curvature, normal curvature, and geodesic torsion. We discuss two cases, for instance, pancake curve as an intersection of Plücker’s conoid and unit cylinder, and the intersection of a hyperbolic paraboloid and unit cylinder. Moreover, we give the relations between the Frenet and Darboux curvatures. Finally, we give some examples related to the Frenet and Darboux frame and curvatures.

Keywords: Plücker’s conoid, Hyperbolic paraboloid, Darboux frame, Unit cylinder, Pancake curve

[a] *emre.ozturk@mku.edu.tr* *https://orcid.org/0000-0001-6638-3233*

Introduction

The curve theory has continued to extend for centuries. There are many well-known planar and space curves in Euclidean space, and in other spaces. Today, especially in geometry and related branches, the focus is on space curves in 3-dimension and in higher dimensions. While most of the curves in space look well-known, some of them are encountered in the literature rarely. For example, one of them is the “pancake curve” which takes place at the intersection of such two surfaces: (a) Plücker’s conoid and unit cylinder, (b) hyperbolic paraboloid and unit cylinder, and (c) parabolic cylinder and unit cylinder. Here, we mean by “unit cylinder” that it is a circular cylinder with a unit radius. We note that this curve was first named the “pancake curve” by Robert Ferréol [1]. A quotation from [1] can be given as follows: “As far as I know, this curve doesn't have any name of its own. However, it is closely related to a famous item of 19th-century mathematics, the cylindroid surface, discovered by William Kingdon Clifford during his research into the theory of screws. The equation of the cylindroid in 3D Cartesian coordinates commonly reads $z=\frac{x^2-y^2}{x^2+y^2}$. Turning the whole thing thru 90 deg about the z axis yields $z=\frac{2xy}{x^2+y^2}$, and there you are: your curve is the intersection of this cylindroid and the unit cylinder about the z axis. This is generic: cylindroid and cylinder with common axis always intersect in this kind of space curve”. In fact, the author mentions Plücker’s conoid by saying “cylindroid”.

On the other hand, pancake curve has many interesting properties and applications. The pancake curve is a special case of cylindrical sine wave; therefore if we make it roll on a plane, the contact point describes a sinusoid. The projection on $x\circ y$ plane is a circle; the projections on $x\circ z$ and $y\circ z$ planes are isometric lemniscates of Gerono [1]. The projections on the planes passing by Oz are the besaces. The projections on the planes passing by Oz give a portion of parabola and an ovoid quartic. The projections on the planes containing Oy give a circle and the piriform quartic [1]. In real life, pancake curve has a lot of applications in several areas. For example, in the food industry, the edges of potato chips (pringles) form a pancake curve. Furthermore, in architecture and design, it has many applications for various aims like constructing decorative lightings and buildings.

In this study, we consider the pancake curve as an intersection of two surfaces such as: (a) Plücker’s conoid and unit cylinder, and (b) hyperbolic paraboloid and unit cylinder. We investigate the Darboux frame, and the curve-surface curvatures. Moreover, in Theorem 3.8, the relation between Frenet and Darboux frame of pancake curve is given. In the last section, some examples are given, and the Frenet and Darboux frame of the pancake curve are illustrated.

Preliminaries

It is well known that Euclidean space is furnished by the following metric:

$$d(x,y)=\left(\sum_{i=1}^{n}(x_i-y_i)^2\right)^{1/2},$$

where $x=(x_1,x_2,\dots,x_n)$, and $y=(y_1,y_2,\dots,y_n)$. The dot product of two vectors in $n-$dimensional Euclidean space is given by

$$x \bullet y = \sum_{i=1}^{n} x_i y_i.$$

Let $\psi: I \to \mathbb{R}^3$ be a regular curve in $\mathbb{R}^3$ Euclidean space (i.e. $\|\psi'\|$ is nowhere zero), where I is an interval in $\mathbb{R}$. The curve ψ is called a Frenet curve of rank three if $\psi'(s), \psi''(s), \psi^{(3)}(s)$ are linear independent and $\psi'(s), \psi''(s), \psi^{(3)}(s), \psi^{(4)}(s)$ are no longer linear independent for all s in I. In this case, ψ lies in $3-$dimensional Euclidean subspace of $\mathbb{R}^3$. For each unit speed Frenet curve of rank three, there occur an associated orthonormal $3-$frame field $\{T, N, B\}$ along ψ, the Frenet $3-$frame, and functions $\kappa, \tau: I \to \mathbb{R}$, the Frenet curvatures such that

$$\begin{pmatrix} T' \\ N' \\ B' \end{pmatrix} = \begin{pmatrix} 0 & \kappa & 0 \\ -\kappa & 0 & \tau \\ 0 & -\tau & 0 \end{pmatrix} \begin{pmatrix} T \\ N \\ B \end{pmatrix}.$$

where $T' = dT/ds, \kappa$ and τ is called the curvature and the torsion of the curve. The principal normal vector of the curve $N(s) = T'(s)/\|T'(s)\|$, and the binormal vector is cross product of unit tangent and unit normal vector, $B = T \times N$. Let us consider the ψ lies on surface M in $\mathbb{R}^3$. Then, instead of the Frenet frame field, we can consider the Darboux frame field $\{\mathbb{T}_\psi = T, \mathbb{V}_\psi, \mathbb{N}_\psi\}$ where $\mathbb{T}_\psi$ is the unit tangent vector field of ψ, $\mathbb{N}_\psi$ is surface normal which restricted to ψ, and $\mathbb{V}_\psi = \mathbb{N}_\psi \times \mathbb{T}_\psi$. Here we note that ψ is a unit-speed curve. The derivative formulas of the Darboux frame field are given by

$$\begin{pmatrix} \mathbb{T}'_\psi \\ \mathbb{V}'_\psi \\ \mathbb{N}'_\psi \end{pmatrix} = \begin{pmatrix} 0 & \kappa_g & \kappa_n \\ -\kappa_g & 0 & \tau_g \\ -\kappa_n & -\tau_g & 0 \end{pmatrix} \begin{pmatrix} \mathbb{T}_\psi \\ \mathbb{V}_\psi \\ \mathbb{N}_\psi \end{pmatrix}, \qquad (1)$$

where κ_n, κ_g and τ_g are the normal curvature of the surface in the direction of $\mathbb{T}_\psi$, the geodesic curvature and the geodesic torsion of the curve ψ, respectively [2].

From Eq. (1) we have,

$$\kappa_g = \mathbb{T}'_\psi \bullet \mathbb{V}_\psi, \quad \kappa_n = \mathbb{T}'_\psi \bullet \mathbb{N}_\psi, \quad \tau_g = \mathbb{V}'_\psi \bullet \mathbb{N}_\psi.$$

On the other hand, for the non-unit speed ψ curve, it is written by [3], such that

$$\kappa_g = \frac{1}{|\psi'|} \mathbb{T}'_\psi \bullet \mathbb{V}_\psi, \ \kappa_n = \frac{1}{|\psi'|} \mathbb{T}'_\psi \bullet \mathbb{N}_\psi,$$
$$\tau_g = \frac{1}{|\psi'|} \mathbb{V}'_\psi \bullet \mathbb{N}_\psi. \qquad (2)$$

Here, ψ is geodesic, asymptotic or principal curve if and only if either κ_g, τ_g or κ_n vanishes everywhere respectively [4]. For some of the studies on the Frenet and Darboux frames in various spaces, see [5-10].

The Intersection of Plücker's Conoid and Unit Cylinder

In this section, we consider the pancake curve as an intersection of such two surfaces: Plücker's conoid and unit cylinder (see Figure 1).

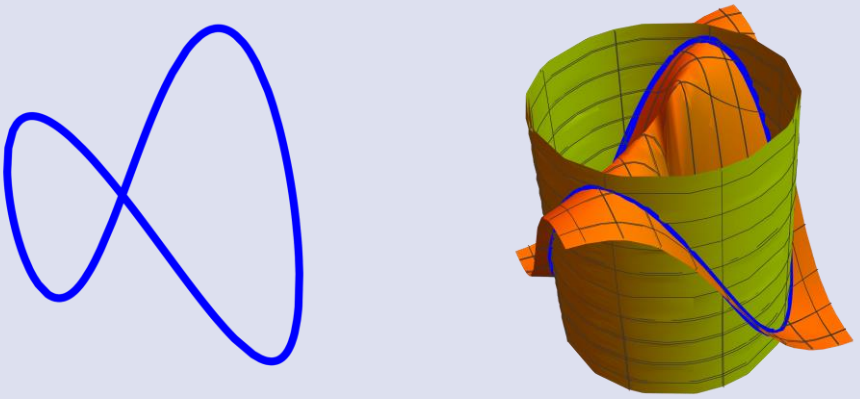

Figure 1 Pancake curve as an intersection of Plücker's conoid and unit cylinder.

In our calculations and illustrations, we utilized *Mathematica*. Here, note that we investigate the Darboux frame of the pancake curve on Plücker's conoid. According to [11], we can give the Plücker's conoid surface by

$$\Upsilon(u, v) = \left(u, v, \frac{2uv}{u^2 + v^2}\right). \qquad (3)$$

The unit normal $\vec{n}$ on the surface $\Upsilon(u, v)$ is given by

$$(\vec{n} \circ \Upsilon)(u, v) = \frac{\Upsilon_u \times \Upsilon_v}{|\Upsilon_u \times \Upsilon_v|} = \frac{1}{\sqrt{\mu^2 + \frac{4\lambda^2}{\mu}}} \left(\frac{2\lambda v}{\mu}, -\frac{2\lambda u}{\mu}, \mu\right),$$

where $\lambda = u^2 - v^2$ and $\mu = u^2 + v^2$.

Since the curve is the intersection of Plücker's conoid and the unit cylinder, we can consider first and second components of the intersection curve as $u = coss$ and $v = sins$, respectively. Then, the third component must be $\frac{2uv}{u^2+v^2} = \frac{2sinscoss}{sin^2s+cos^2s} = sin(2s)$. Hence, we calculate the equation of the intersection curve as follows:

$$\alpha(s) = (coss, sins, sin(2s)). \qquad (4)$$

Obviously, α satisfies the equations of both Plücker's conoid and unit cylinder. Now, we can give our calculations with the help of Eq. (4). First of all, $|\alpha'(s)| = \sqrt{1 + 4cos^2(2s)}$, and α is not unit-speed curve. By Eq. (4) we have the unit tangent vector,

$$\mathbb{T}_\alpha\,(s) = \frac{\alpha\prime(s)}{|\alpha\prime(s)|}\frac{1}{\sqrt{3+2cos(4s)}}(-sins, coss, 2cos(2s)). \quad (5)$$

Since $\mathbb{N}_\alpha$ is the surface normal restricted to α,

$$\mathbb{N}_\alpha(s) = (\vec{n} \circ \alpha)(s) = \vec{n}\big(\Upsilon(coss, sins)\big)$$
$$= \frac{1}{\sqrt{3+2cos(4s)}}(2\,cos(2s)\,sins, -coss - cos(3s)\,, 1). \quad (6)$$

By Eqs. (5) and (6), we calculate the binormal vector as follows:

$$\mathbb{V}_\alpha(s) = \mathbb{N}_\alpha(s) \times \mathbb{T}_\alpha(s) = (-coss, -sins, 0). \qquad (7)$$

Hence, we have the Darboux frame $\{\mathbb{T}_\alpha, \mathbb{V}_\alpha, \mathbb{N}_\alpha\}$ the pancake curve on Plücker's conoid. Now we can give our results about the curvatures.

Theorem 3.1 The geodesic curvature of the pancake curve on Plücker's conoid is

$$\kappa_g(s) = \frac{1}{3 + 2\,cos(4s)}.$$

Proof. Since α(s) is a non-unit speed curve, from Eqs. (2), (5) and (7) we obtain,

$$\mathbb{T}'_\alpha(s) = \left(\frac{-3(coss + cos(3s)) + cos(5s)}{(3 + 2cos(4s))^{3/2}}, \frac{-3sins + 3sin(3s) + sin(5s)}{(3 + 2cos(4s))^{3/2}}, -\frac{4sin(2s)}{(3 + 2cos(4s))^{3/2}}\right)$$

and

$$\kappa_g(s) = \mathbb{T}'_\alpha(s) \bullet \mathbb{V}_\alpha(s) = \frac{1}{3 + 2\,cos(4s)},$$

which completes the proof.

Theorem 3.2 The geodesic torsion of the pancake curve on Plücker's conoid is

$$\tau_g(s) = \frac{2cos(2s)}{3 + 2\,cos(4s)}.$$

Proof. Since α(s) is non-unit speed curve, from Eqs. (2), (6) and (7) we obtain

$$\mathbb{V}'_\alpha(s) = (sins, -coss, 0),$$

and

$$\tau_g(s) = \frac{1}{|\alpha'(s)|}\mathbb{V}'_\alpha(s) \bullet \mathbb{N}_\alpha(s) = \frac{2\,cos(2s)}{3 + 2\,cos(4s)},$$

which is intended.

Theorem 3.3 The normal curvature of the Plücker's conoid in the direction of $\mathbb{T}_\alpha$ is given by

$$\kappa_n(s) = -\frac{4(2\,sin(2s) + sin(6s))}{(3 + 2\,cos(4s))^{5/2}}.$$

Proof. Since α(s) is non-unit speed curve, from Eqs. (2), (5) and (6) we obtain

$$\kappa_n(s) = \frac{1}{|\alpha'(s)|}\mathbb{T}'_\alpha(s) \bullet \mathbb{N}_\alpha(s)$$
$$= -\frac{4(2\,sin(2s) + sin(6s))}{(3 + 2\,cos(4s))^{5/2}},$$

which completes our proof.

Corollary 3.4 The pancake curve is a non-geodesic curve on Plücker's conoid.

Proof. It follows from Theorem 3.1 that $\kappa_g(s)$ never vanishes, and obviously α is non-geodesic.

Corollary 3.5 The piece of pancake curve is an asymptotic curve on Plücker's conoid if and only if

$$s = \frac{\pi n}{2} - \frac{\pi}{4}, n \in \mathbb{Z}.$$

Corollary 3.6 The piece of pancake curve is a principal curve on Plücker's conoid if and only if

$$s = \frac{\pi n}{2}, n \in \mathbb{Z}.$$

Corollary 3.7 The trace of binormal vector $\mathbb{V}_\alpha$ represents a circle.

Theorem 3.8 There is the following equation between the curvatures of Frenet and Darboux frames of the pancake curve on Plücker's conoid:

$$\kappa^2\tau + 3\tau_g{\kappa_g}^2 = 0,$$

where κ_g is the geodesic curvature and τ_g is the geodesic torsion of the pancake curve on Plücker's conoid.

Proof. By Frenet derivative formulas we calculate the Frenet curvature and torsion as follows:

$$\kappa(s) = T'(s) \bullet N(s) = \frac{\sqrt{11 - 6\cos(4s)}}{(3 + 2\,cos(4s))^{3/2}},$$

and

$$\tau(s) = N'(s) \bullet B(s) = \frac{6cos2s}{-11 + 6\cos(4s)}.$$

By straightforward calculations, we obtain the equation.

The Hyperbolic Paraboloid and Unit Cylinder

In this section, we consider the pancake curve as an intersection of such two surfaces: hyperbolic paraboloid, and unit cylinder (see Figure 2).

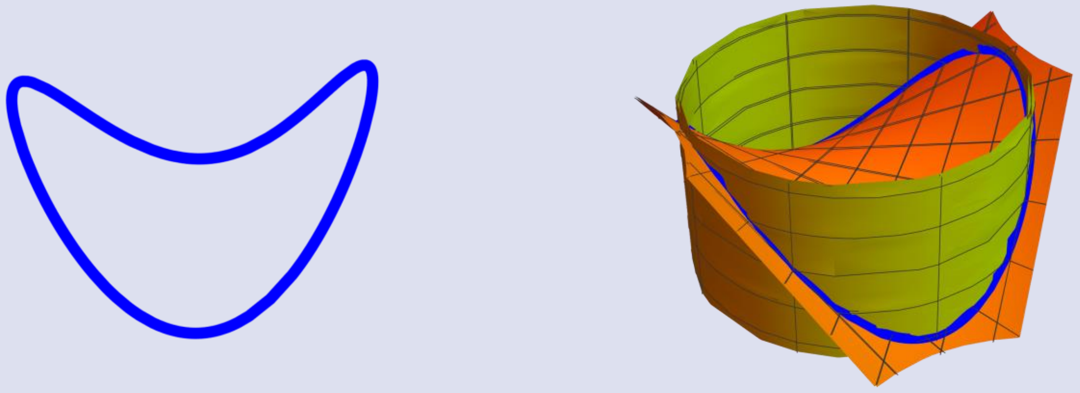

Figüre 2. Pancake curve as an intersection of hyperbolic paraboloid and unit cylinder.

Here, note that we investigate the Darboux frame of the pancake curve on hyperbolic paraboloid. According to [1], we can give the hyperbolic paraboloid surface by

$$\Psi(u, v) = (u, v, uv). \tag{8}$$

The unit normal $\vec{n}$ on the surface $\Psi(u, v)$ is given by

$$(\vec{n} \circ \Psi)(u, v) = \frac{\Psi_u \times \Psi_v}{|\Psi_u \times \Psi_v|} = \frac{1}{\sqrt{1 + u^2 + v^2}}(-v, -u, 1).$$

Since the curve is intersection of hyperbolic paraboloid, and unit cylinder, we can consider first and second components of the curve as $u = coss$ and $v = sins$, respectively. Then, third component of the intersection curve must be $uv = coss\ sins = \frac{sin(2s)}{2}$. Hence, we calculate the equation of the intersection curve as follows:

$$\beta(s) = \left(coss, sins, \frac{sin(2s)}{2}\right). \tag{9}$$

Now, we can give our calculations with the help of Eq. (9). First of all, $|\beta'(s)| = \sqrt{1 + cos^2(2s)}$, and β is not unit-speed curve. By Eq. (9) we have the unit tangent vector,

$$\mathbb{T}_\beta(s) = \frac{\beta'(s)}{|\beta'(s)|}$$
$$= \frac{1}{\sqrt{1 + cos^2(2s)}}(-sins, coss, cos(2s)). \tag{10}$$

Since $\mathbb{N}_\beta$ is the surface normal restricted to β,

$$\begin{aligned}\mathbb{N}_\beta(s) &= (\vec{n} \circ \beta)(s)\\ &= \vec{n}\big(\Psi(coss, sins)\big)\\ &= \left(\frac{-sins}{\sqrt{2}}, \frac{-coss}{\sqrt{2}}, \frac{1}{\sqrt{2}}\right).\end{aligned} \tag{11}$$

By Eqs. (10) and (11), we calculate the binormal vector as follows:

$$\mathbb{V}_\beta(s) = \mathbb{N}_\beta(s) \times \mathbb{T}_\beta(s)$$
$$= \frac{1}{\sqrt{3 + cos(4s)}}(-2cos^3 s, -2sin^3 s, -sin(2s)). \tag{12}$$

Hence, we have the Darboux frame of β as $\{\mathbb{T}_\beta, \mathbb{V}_\beta, \mathbb{N}_\beta\}$. Now we can give our results about the curvatures.

Theorem 4.1 The geodesic curvature of the pancake curve on hyperbolic paraboloid is

$$\kappa_g(s) = \frac{5 - cos(4s)}{(3 + cos(4s))^{3/2}}.$$

Proof. Since β(s) is non-unit speed curve, from Eqs. (2), (10) and (12) we obtain

$$\mathbb{T}'_\beta(s) = \left(\frac{-6coss - 3cos(3s) + cos(5s)}{\sqrt{2}(3 + cos(4s))^{3/2}}, \frac{-6sins + 3sins(3s) + sin(5s)}{\sqrt{2}(3 + cos(4s))^{3/2}}, -\frac{2sin(2s)}{(1 + cos^2(2s))^{3/2}}\right),$$

and,

$$\kappa_g(s) = \frac{1}{|\beta'(s)|}\mathbb{T}'_\beta(s) \bullet \mathbb{V}_\beta(s) = \frac{5 - cos(4s)}{(3 + cos(4s))^{3/2}},$$

which completes the proof.

Theorem 4.2 The geodesic torsion of the pancake curve on hyperbolic paraboloid is

$$\tau_g(s) = -\frac{2cos(2s)}{3 + cos(4s)}.$$

Proof. Since β(s) is non-unit speed curve, from Eqs. (2), (11) and (12) we obtain

$$\mathbb{V}'_\beta(s) = \left(\frac{cos^2 s(18\, sins - 5\sin(3s) + \sin(5s))}{(3 + \cos(4s))^{3/2}}, -\frac{(18\, coss + 5\cos(3s) + \cos(5s))sin^2 s}{(3 + \cos(4s))^{3/2}}, -\frac{8\cos(2s)}{(3 + \cos(4s))^{3/2}}\right),$$

and

$$\tau_g(s) = \frac{1}{|\beta'(s)|}\mathbb{V}'_\beta(s) \bullet \mathbb{N}_\beta(s) = -\frac{2cos(2s)}{3 + cos(4s)},$$

which is intended.

Theorem 4.3 The normal curvature of the hyperbolic paraboloid in the direction of $\mathbb{T}_\beta$ is given by

$$\kappa_n(s) = -\frac{\sqrt{2}sin(2s)}{3 + cos(4s)}.$$

Proof. Since β(s) is non-unit speed curve, from Eqs. (2), (10) and (11) we obtain

$$\kappa_n(s) = \frac{1}{|\beta'(s)|}\mathbb{T}'_\beta(s) \bullet \mathbb{N}_\beta(s) = -\frac{\sqrt{2}sin(2s)}{3 + cos(4s)},$$

which completes our proof.

Corollary 4.4 Pancake curve is a non-geodesic curve on hyperbolic paraboloid.

Proof. By definition of cosine function $-1 \leq cos(4s) \leq 1$. It follows from Theorem 4.1 that $\kappa_g(s) = 5 - cos(4s)$ never vanishes, and obviously β is non-geodesic.

Other results are similar to *Corollary 3.5* and *Corollary 3.6*.

Corollary 4.5 The trace of normal vector restricted to β represents a circle in space.

Examples

Example 5.1 Let us consider the Darboux frame of the curve which is given by Eqs. (4)-(7) and lies on Plücker's conoid. Let us take the point P as $P = \alpha(\pi/3) = \left(\frac{1}{2}, \frac{\sqrt{3}}{2}, \frac{\sqrt{3}}{2}\right)$ on the curve. Then, the Darboux frame of the curve at point P is given as follows:

$$\mathbb{T}_\alpha\left(\frac{\pi}{3}\right) = \left(-\frac{\sqrt{6}}{4}, \frac{\sqrt{2}}{4}, -\frac{\sqrt{2}}{2}\right),$$

$$\mathbb{V}_\alpha\left(\frac{\pi}{3}\right) = \left(-\frac{1}{2}, -\frac{\sqrt{3}}{2}, 0\right),$$

$$\mathbb{N}_\alpha(\pi/3) = \left(-\frac{\sqrt{6}}{4}, \frac{\sqrt{2}}{4}, \frac{\sqrt{2}}{2}\right).$$

On the other hand, the curvatures at point P are calculated as

$$\kappa_g(\pi/3) = \frac{1}{2}, \quad \tau_g(\pi/3) = -\frac{1}{2}, \quad \kappa_n(\pi/3) = -\frac{\sqrt{6}}{2}.$$

The illustration of Darboux frame of this curve is given by Figure 3.

.

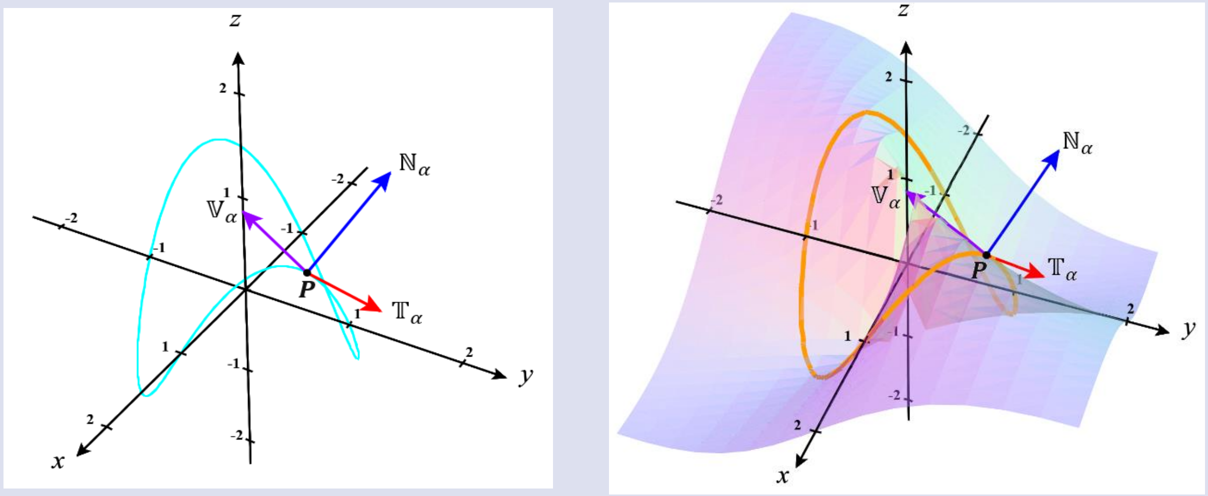

Figüre 3. Darboux frame of α at point $P\left(\frac{1}{2}, \frac{\sqrt{3}}{2}, \frac{\sqrt{3}}{2}\right)$.

Example 5.2 Let us consider the Darboux frame of the curve which is given by Eqs. (9)-(12) and lies on hyperbolic paraboloid. Let us take the point Q as $Q=\beta(\pi/6)=\left(\frac{\sqrt{3}}{2},\frac{1}{2},\frac{\sqrt{3}}{4}\right)$ on the curve. Then, the Darboux frame of the curve at point Q is given as follows:

$$\mathbb{T}_\beta\left(\frac{\pi}{6}\right)=\left(-\frac{\sqrt{5}}{5},\frac{\sqrt{15}}{5},\frac{\sqrt{5}}{5}\right),$$

$$\mathbb{V}_\beta\left(\frac{\pi}{6}\right)=\left(-\frac{3\sqrt{30}}{20},-\frac{\sqrt{10}}{20},-\frac{\sqrt{30}}{10}\right),$$

$$\mathbb{N}_\beta(\pi/6)=\left(-\frac{\sqrt{2}}{4},-\frac{\sqrt{6}}{4},\frac{\sqrt{2}}{2}\right).$$

On the other hand, the curvatures at point Q are calculated as

$$\kappa_g(\pi/6)=\frac{11\sqrt{10}}{25},\quad \tau_g(\pi/6)=-\frac{2}{5},\quad \kappa_n(\pi/6)=-\frac{\sqrt{6}}{5}.$$

The illustration of Darboux frame of this curve is given by Figure 4.

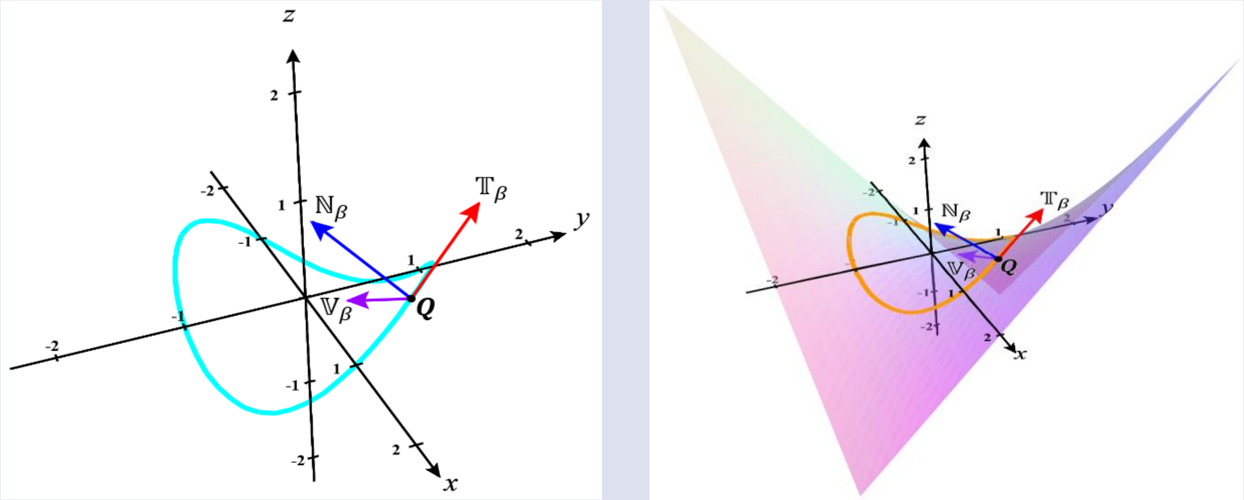

Figüre 4. Darboux frame of β at point $Q\left(\frac{\sqrt{3}}{2},\frac{1}{2},\frac{\sqrt{3}}{4}\right)$.

Example 5.3 Let the space curve is given by Eq. (4), $\alpha(s)=(coss,sins,sin(2s))$. At point $R=\alpha(\pi/4)=\left(\frac{\sqrt{2}}{2},\frac{\sqrt{2}}{2},1\right)$, the Frenet and Darboux frame of this curve is given by

$$T\left(\frac{\pi}{4}\right)=\left(-\frac{\sqrt{2}}{2},\frac{\sqrt{2}}{2},0\right),$$
$$N\left(\frac{\pi}{4}\right)=\left(-\frac{\sqrt{2}}{2\sqrt{17}},-\frac{\sqrt{2}}{2\sqrt{17}},-\frac{4}{\sqrt{17}}\right),$$
$$B(\pi/4)=\left(-\frac{2\sqrt{2}}{\sqrt{17}},-\frac{2\sqrt{2}}{\sqrt{17}},\frac{1}{\sqrt{17}}\right),$$

and,

$$\mathbb{T}_\alpha\left(\frac{\pi}{4}\right)=\left(-\frac{\sqrt{2}}{2},\frac{\sqrt{2}}{2},0\right),$$
$$\mathbb{V}_\alpha(\pi/4)=\left(-\frac{\sqrt{2}}{2},-\frac{\sqrt{2}}{2},0\right),\quad \mathbb{N}_\alpha(\pi/4)=(0,0,1).$$

The picture of these frames at point R is given by Figure 5.

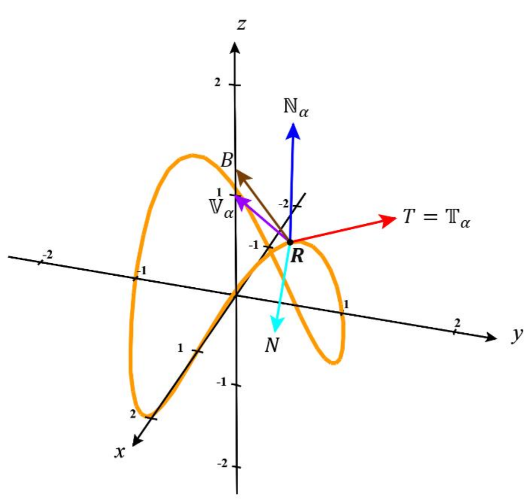

Figüre 5. Frenet and Darboux frame of the curve α at point $R\left(\frac{\sqrt{2}}{2},\frac{\sqrt{2}}{2},1\right)$.

Conclusion and Recommendations

This study initiates a new curve and its Darboux frame on Plücker's conoid and hyperbolic paraboloid surfaces. With the help of Darboux frame, the curvatures of pancake curves on surfaces are calculated. Moreover, a relation between the Frenet and Darboux curvatures of the pancake curve is obtained. While our focus was Plücker's conoid and hyperbolic paraboloid surfaces, one can examine the Darboux frame of pancake curves on a parabolic cylinder. Moreover, the relation between the pancake curve and the other curves (cylindrical sine wave, lemniscates of Gerono, besaces, ovoid quartic, etc.) can be investigated. According to current knowledge, there is not enough paper related to the curve except on the website of Robert Ferréol. Therefore, this paper will be instructive for further studies about the curve.

Acknowledgement

The author would like to thank the referees for carefully reading which helped to improve the manuscript.

Conflict of interest

There are no conflicts of interest in this work.

References

[1] Encyclopédie des formes mathématiques remarquables. Available at: https://mathcurve.com/courbes3d.gb/crepe/crepe.shtml. Retrieved: December 20, 2023.

[2] O'Neill B. Elementary Differential Geometry Revised Second Edition. USA: Academic Press Elsevier, (2006) p. 248.

[3] Sabuncuoğlu, A. Diferensiyel Geometri. 5. Basım. Ankara: Nobel Yayınevi, (2014) p. 306.

[4] Kühnel, W. "Differential Geometry Curves-Surfaces-Manifolds". USA: American Mathematical Society, (2006).

[5] Li, Y., Gür Mazlum, S., Şenyurt, S., The Darboux trihedrons of timelike surfaces in the Lorentzian 3-space, International *Journal of Geometric Methods in Modern Physics*, 20 (2) (2023).

[6] Ouarab, S., Smarandache Ruled Surfaces according to Darboux Frame in E^3, *Journal of Mathematics*, Article ID 9912624, (1) (2021) 1-10.

[7] Aksan, B., Gür Mazlum, S., On Darboux Frames of Indicatrices of Spacelike Salkowski Curve with Spacelike Binormal in E_1^3, Black Sea, *Journal of Engineering and Science*, 6 (4) (2023) 401-413.

[8] Ünlütürk, Y., Cimdiker, M., Ekici, C., Characteristic properties of the parallel ruled surfaces with Darboux frame in Euclidean 3- space., *Communication in Mathematical Modeling and Applications,* 1 (1) (2016) 26-43.

[9] Gür Mazlum, S., Geometric properties of timelike surfaces in Lorentz-Minkowski 3-space, Filomat, 37 (17) (2023) 5735–5749.

[10] Altın, M., Kazan, A., Tubular Hypersurfaces According to Extended Darboux Frame Field of First Kind in E^4, *Turkish Journal of Science*, 7 (2) (2022) 75-84.

[11] Gray, A., Abbena, E., Salamon, S. Differential Geometry of Curves and Surfaces with Mathematica. 3rd edition. USA: Chapman & Hall/CRC, (2006).

Cumhuriyet Science Journal

Cumhuriyet Sci. J., 45(3) (2024) 578-584
DOI: https://doi.org/10.17776/csj.1453508

| csj.cumhuriyet.edu.tr | Founded: 2002 ISSN: 2587-2680 e-ISSN: 2587-246X Publisher: Sivas Cumhuriyet University

Static Magnetic Field Focusing with Neodymium Magnets for Wound Healing: A Numerical Study

Elif Feyza Aydın [1,a], Reyhan Zengin [1,b,*]

[1] *Department of Biomedical Engineering, Faculty of Engineering, İnönü University, Malatya, Türkiye.*
**Corresponding author*

Research Article

History
Received: 15/03/2024
Accepted: 16/09/2024

ABSTRACT

Static magnetic fields (SMFs) find widespread applications in diverse scientific, technological, and medical domains. This study explores the potential of neodymium permanent magnets in focusing and controlling SMFs, specifically emphasizing wound healing applications. Numerical simulations using COMSOL Multiphysics create a uniform static magnetic field for wound healing. The study systematically increases the number of neodymium magnets, demonstrating enhanced magnetic flux density and a focused magnetic field. The results affirm the efficacy of neodymium magnets in generating a uniform static magnetic field between 190-620 m Tesla. This research proposes neodymium permanent magnets as a promising tool for wound healing applications, offering a non-invasive and focused therapeutic approach. While the study provides valuable insights, further experimental and clinical validations are necessary to establish the real-world efficacy of this method. The work contributes to the evolving understanding of static magnetic fields as a viable therapeutic modality for various medical conditions, particularly in the context of wound healing.

Keywords: Static magnetic fields, Wound healing, Neodymium permanent magnets.

a *elifeyza97@hotmail.com* *https://orcid.org/0009-0008-3743-6672* b *reyhan.zengin@inonu.edu.tr* *https://orcid.org/0000-0001-8631-3339*

Introduction

Static magnetic fields (SMFs) have extensive applications in contemporary science and technology, as well as in industrial, agricultural, medical, and healthcare sectors, among other fields [1]. Static magnetic fields are essential in numerous fields, including but not limited to applications like magnetic resonance imaging (MRI) [2], transcranial magnetic stimulation [3], control of magnetic nanoparticles for gene and drug delivery [4,5], and the development of magnetic sensors [6]. Higher static magnetic fields facilitate the advancement of these applications. There are two distinct approaches to enhancing static magnetic fields: one aims to amplify them over a wide free space, potentially enhancing spatial resolution in MRI applications. The other concentrates on intensifying static magnetic fields within a confined space, enhancing sensitivity in magnetic sensors, and advancing the application of magnetic nanoparticles in gene and drug delivery [1]. Magnetic fields are increasingly utilized in diverse bioengineering and biomedical applications, offering significant advantages in lower patient invasiveness, especially regarding non-ionizing radiations. The non-magnetic nature of human tissues allows magnetic fields to penetrate without attenuation, distinguishing them from electric fields. This property is harnessed in various diagnostic and therapeutic methods, including Magnetic Resonance Imaging (MRI), Magnetic Fluid Hyperthermia (MFH) for hyperthermia and thermoablation with magnetic nanoparticles, and Transcranial Magnetic Stimulation (TMS). In MRI, a homogeneous magnetic field is crucial for imaging various pathologies across different anatomical regions, requiring a larger field of view (FOV). Conversely, in Magnetic Fluid Hyperthermia (MFH), the focused magnetic field induces localized heating for cancer therapy, aiming to preserve surrounding tissue. Similarly, in Transcranial Magnetic Stimulation (TMS), focusing the induced electric field within the brain enhances procedure effectiveness and accuracy and reduces patient invasiveness. The challenge lies in generating the desired magnetic distribution due to diffraction and attenuation phenomena, especially at lower frequencies, prompting research into technologies for optimizing and controlling this aspect [7]. The literature has documented various radiation configurations capable of manipulating diverse magnetic fields, representing significant advancements in this field. Volume, Helmholtz, and Birdcage Coils generate and focus magnetic fields for various applications. Volume Coils offer advantages such as medium homogeneity, scalability in terms of geometry, and high efficiency. However, a notable drawback is that their length must be greater than the solenoid section [8, 12-15, 16, 17]. On the other hand, Helmholtz coils provide a very homogeneous field but come with the disadvantage of poor efficiency [9,10,11]. Birdcage coils are characterized by their ability to generate circular or linear homogeneous fields, but their design complexity is a notable drawback [18,19].

In contemporary research, there is significant interest in utilizing neodymium permanent magnets to focus and control static magnetic fields. Their capacity to concentrate magnetic fields presents potential advantages across diverse fields, from medical imaging systems to industrial applications. General Motors and

Hitachi collaborated in the 1980s to create neodymium-iron-boron magnets. Due to their ability to generate substantial magnetic force with minimal material, these magnets have gained significance in producing robust permanent magnets composed of rare earth elements. In information technology, neodymium magnets find specific applications in hard disc drives, mobile phones, and television audio and video systems [20]. Neodymium magnets find application in the health sector, integrated into medical devices like magnetic resonance imaging (MRI) machines used for diagnosing and treating various conditions such as chronic pain syndrome, arthritis, wound healing, insomnia, headaches, and other diseases, owing to their capacity to generate a static magnetic field. Over the past decade, there has been a notable rise in their utilization [21].

The static magnetic field (SMF) emerges as a viable and non-invasive therapeutic approach with potential advantages [22-24]. Despite having less robust support in scientific literature, magnets have been utilized in alternative medicine to expedite the healing process and alleviate pain. Limited data indicates three potential mechanisms underlying the effectiveness of static magnetic fields (SMF): 1) an anti-inflammatory impact; 2) assistance in endothelial cell proliferation; 3) stimulation of collagen formation [25]. SMFs are recognized as powerful promoters of cell proliferation, migration, and differentiation, hastening the differentiation of osteoblast-like cells in laboratory settings [23].

Recent studies suggest that exposure to static magnetic fields (SMF) can affect the release of inflammatory cytokines by macrophages and lymphocytes [26]. The US FDA has approved SMF for the treatment of pain and edema, confirming its impact on cell metabolism and proliferation [27]. Prolonged exposure to SMF has shown potential in controlling hypertension [28] and has produced positive results in the treatment of osteoarthritis and nonunion fractures [27, 29, 30].

Research findings indicate that a static magnetic field of 220 mT enhanced the recovery rate in normal rats [25]. More recent investigations have delved into the effects of a 230 mT static magnetic field generated by a permanent NeFeB magnet on cutaneous wound healing in diabetic rats [24]. Additionally, a study conducted in 2016 demonstrated accelerated wound healing in rats by applying a pulsed electromagnetic field (PEMF) signal using a Helmholtz coil at a frequency of 75 Hz and a magnetic field intensity of 1 mT. This effect was observed when combined with pulsed radiofrequency energy (PRFE) at a carrier frequency of 27.12 MHz [31].

Furthermore, current studies have noted that a moderate-intensity static magnetic field (0.6 T) notably enhances the healing of wounds in a mouse model of type 2 diabetes. Even field strengths below 180-230 mT have demonstrated positive effects on healing streptozotocin-induced diabetic wounds in mice [32].

In this research, we examined the focusing of static magnetic fields using permanent neodymium magnets for applications in wound healing. Numerical simulations were employed to generate a uniform static magnetic field, specifically between neodymium magnets positioned at defined distances, to achieve optimal focus.

Materials and Methods

Static magnetic field theory

Static magnetic fields occur from either permanent magnets or direct current (DC) flow in conductive materials. The Biot-Savart law defines the contribution of a magnetic field (d**B**) created by a small wire segment of length **(dL)** carrying a current (**I**) as follows [33]:

$$d\boldsymbol{B} = \frac{\mu I \, d\boldsymbol{L} \times \boldsymbol{r}}{4\mu r^2} \tag{1}$$

Here, **r** is the vector from the current element to the point where the field is being calculated, and µ represents the permeability of the medium. Equation (1) illustrates that the magnetic field is a vector circulating around the current element and decreases with the square of the distance from it. Integrating this law (Equation 1) enables the assessment of magnetic fields around structures carrying current, such as coils or electrical distribution networks.

Magnetic fields are identified by the force they exert on moving charges, such as those composing electric currents. The force (**F**) in newtons is proportional to the charge (q) in coulombs and velocity (**v**) in meters per second, and it is perpendicular to both the motion and the field direction. Mathematically, this relationship is expressed as:

$$\boldsymbol{F} = q(\boldsymbol{v} \times \boldsymbol{B}) \tag{2}$$

The magnetic flux densities (**B**) are measured in tesla (T). The actual magnetic field strength (**H**) is quantified in amperes per meter (A m^{-1}) and is linked to magnetic flux density through

$$\boldsymbol{B} = \mu \boldsymbol{H} \tag{3}$$

In materials without magnetic properties, such as air, permeability is equivalent to the permeability of free space (μ_0), defined as $4\pi\times10^{-7}$H m^{-1}**.**

Numerical Studies

Numerical analysis is often used to solve problems that may have complex or impossible analytical solutions. This study utilizes the numerical analysis program COMSOL Multiphysics based on the finite element method. This study aims to develop a uniform static magnetic field environment for wound healing techniques. Static magnetic fields have been produced in various ways in the past, but this study aims to concentrate a homogeneous static magnetic field on a specific region and create a setting that can be used in animal experiments with permanent magnets. Four neodymium magnets were positioned in Figure 1 to generate a uniform magnetic field. The dimensions of the magnets were chosen as 10 cm x 10 cm x 5 cm. The distance between the two magnets is 16 cm. In COMSOL, Magnetic Fields, No Currents module was selected as the Physics Module. The air environment that would contain the magnets was also modeled. Figure 2 (a) shows two selected domains subjected to magnetization in the y direction, and Figure 2 (b) shows two selected domains subjected to magnetization in the x direction. The mesh image for four magnets is shown in Figure 3.

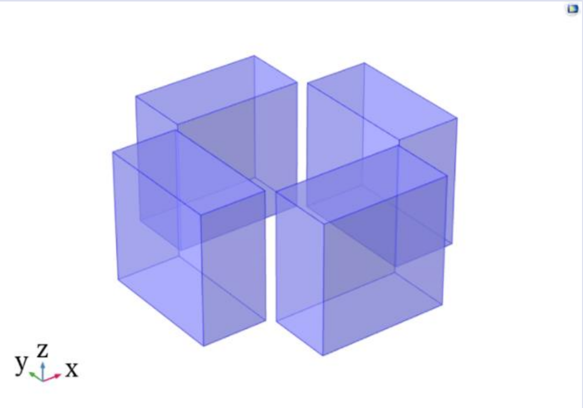

Figure 1. 3D geometry of neodymium magnets is arranged in a mutually facing configuration with four magnets focused. The dimensions of the magnets are 5 cm x 10 cm x 10 cm along the x, y, and z axes, respectively.

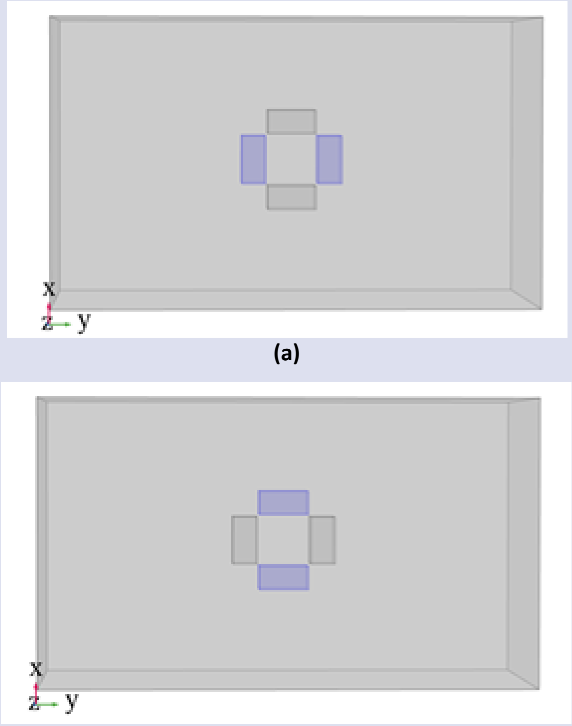

(a)

(b)

Figure 2. Selected areas for magnetization applied in the (a) y direction and (b) x direction.

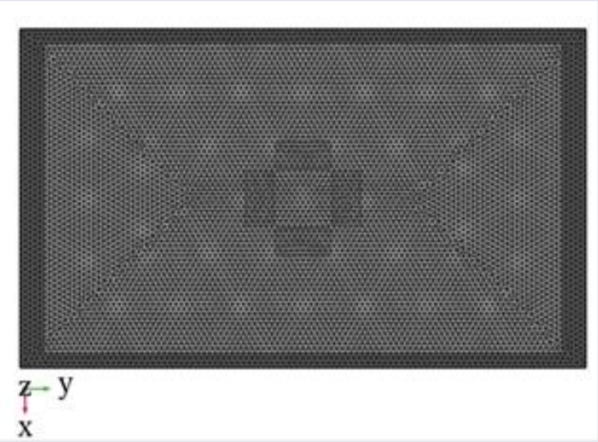

Figure 3. Mesh image of four magnets placed opposite each other.

The mesh consists of 6289137 domain elements, 77580 boundary elements, and 1326 edge elements. Each model takes approximately 148 seconds to run. We used a Free Tetrahedral element size with an extremely fine mesh structure. The mesh was highly detailed to achieve results as close to the actual outcome.

First, the edges of the rectangular structure surrounding the magnet, defined as air in Figure 2 and other figures, were set as boundary conditions. These boundary conditions were defined as Magnetic Insulation.

In Figure 4 (a), eight electrodes are modeled by adding one magnet behind each of the four magnets. The number of magnets was increased to increase the magnetic flux density value in the area between the magnets. Figure 4 (b) shows four selected domains that were subjected to magnetization in the y direction. Figure 4 (c) shows four selected domains that were subjected to magnetization in the x direction.

In Figure 5 (a), twelve electrodes are modeled by adding two magnets behind each of the four magnets. The number of magnets was increased to increase the magnetic flux density value in the area between the magnets. Figure 5 (b) shows six selected domains that were subjected to magnetization in the y direction. Figure 5 (c) shows six selected domains that were subjected to magnetization in the x direction.

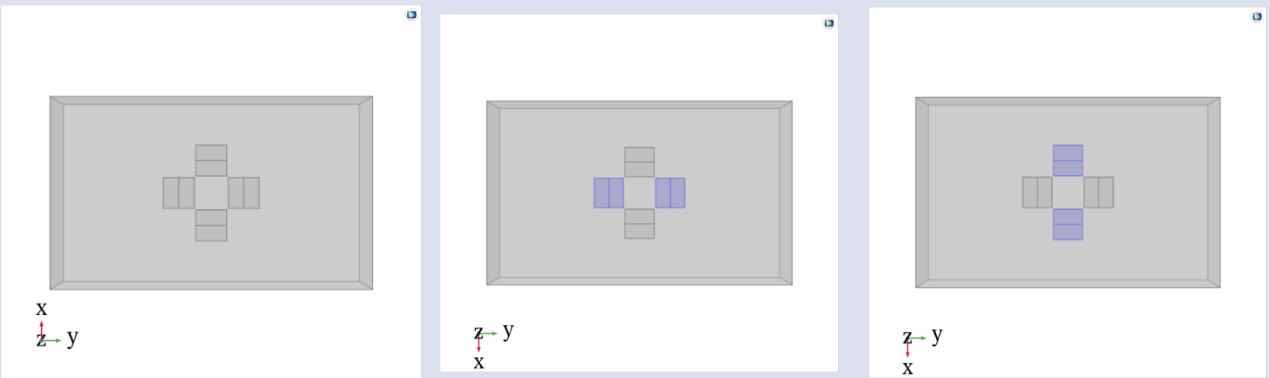

(a) **(b)** **(c)**

Figure 4. (a) Two pairs of Neodymium magnets arranged in a mutually facing configuration with eight magnets focused, (b) Selected areas for magnetization applied in the y direction, (c) Selected areas for magnetization applied in the x direction.

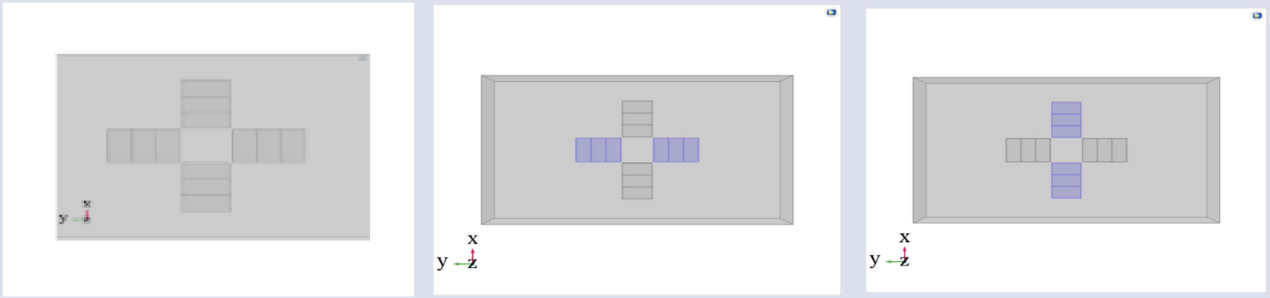

(a) **b)** **(c)**

Figure 5. (a) Triple pairs of Neodymium magnets are arranged with twelve magnets focused in a mutually facing configuration, (b) Selected areas for magnetization applied in the y direction, (c) Selected areas for magnetization applied in the x direction.

Results

Single, double, and triple permanent magnet groups were utilized to obtain static magnetic flux distributions focused on a wide area within the region between the magnets. These distributions are given in Figures 6 (a-c) for single, dual, and triple magnet configurations, respectively. Magnetic field changes were graphed as a 1D plot on a line passing through the center of opposing magnets. To compare these three configurations, a line graph showing the change in magnetic flux density value depending on distance is shown in Figure 6 (d-f). Figure 7 shows a line graph showing the change of magnetic flux density value depending on distance for comparison of all magnets.

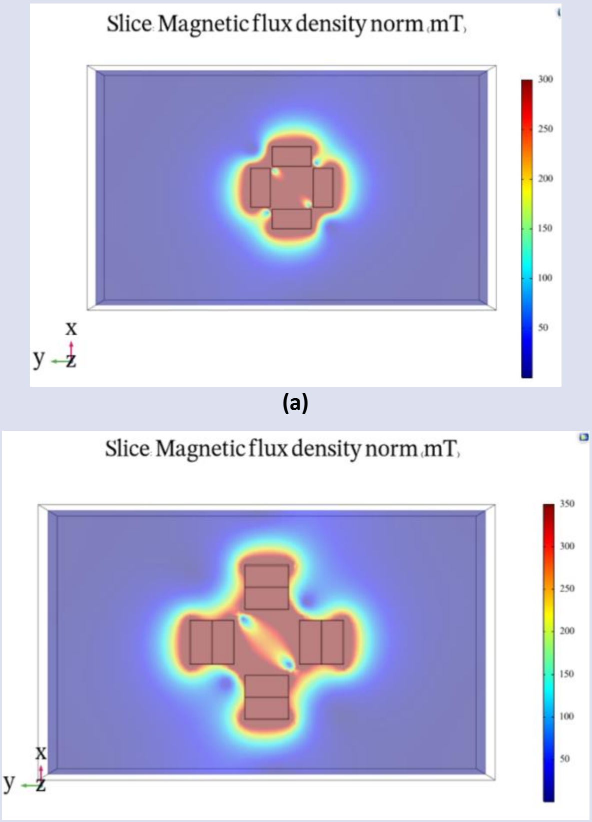

(a)

(b)

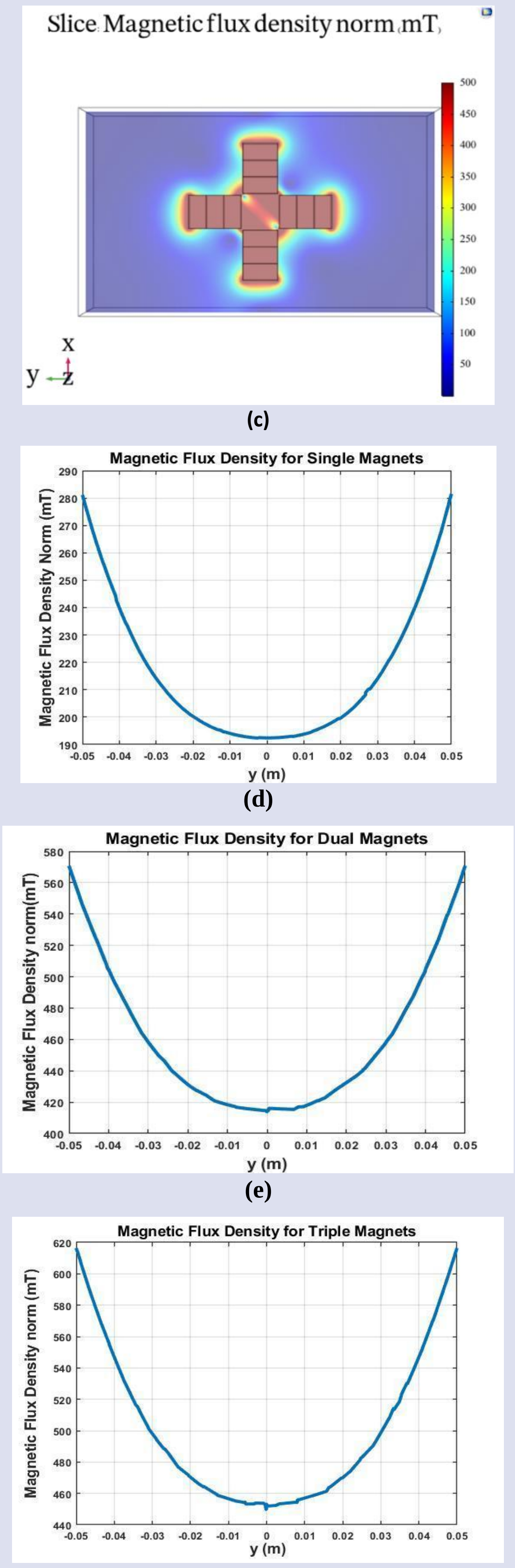

(c)

(d)

(e)

(f)

Figure 6. Magnetic flux density distribution of (a) single magnets, (b) dual magnets, and (c) triple magnets. Line graph showing the change of magnetic flux density value depending on distance for single (d), dual (e), and triple (f) magnets.

.

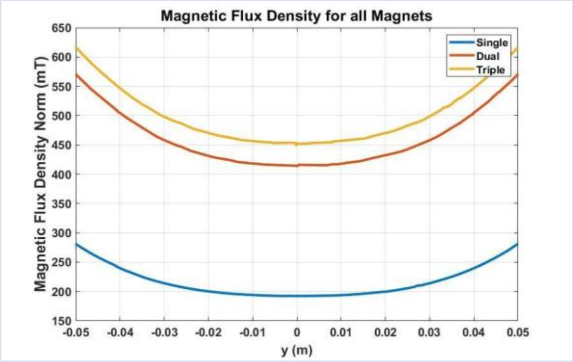

Figure 7. Line graph showing the change of magnetic flux density value depending on distance for comparison of all magnets.

Figure 6 and Figure 7 demonstrate that the SMF distribution ranges from 190-290 mTesla with a single magnet group in an area of approximately 10 cm^2 between the magnets. The SMF distribution with the dual magnet group is within the 400-580 mT range. With the triple magnet group, the SMF distribution is within the 440-620 mT range in a higher and wider area. As a result, increasing the number of magnets increased the magnetic flux density values.

Conclusions and Discussion

Static magnetic fields (SMFs) play a pivotal role in various scientific, technological, and medical applications, including magnetic resonance imaging (MRI), transcranial magnetic stimulation, and magnetic nanoparticle-based therapies. The ability to enhance and control static magnetic fields is crucial for advancing these applications. This study explored the utilization of neodymium permanent magnets to focus and control static magnetic fields, with a specific focus on wound healing applications.

The literature review highlighted the diverse applications of SMFs in bioengineering and biomedical fields, emphasizing their non-invasive nature and penetrative capability through human tissues. The study delved into the potential therapeutic benefits of SMFs, including anti-inflammatory effects, cell proliferation assistance, and collagen formation stimulation.

Numerical simulations using COMSOL Multiphysics were conducted to generate a uniform static magnetic field for wound healing. The study systematically increased the number of neodymium magnets to enhance magnetic flux density, resulting in a focused and homogeneous magnetic field. The numerical results demonstrated that increasing the number of magnets led to higher magnetic flux density values, emphasizing the effectiveness of the neodymium magnets in creating a uniform static magnetic field.

Overall, the findings suggest that neodymium permanent magnets hold promise for applications in wound healing, offering a non-invasive and focused approach to harnessing the therapeutic benefits of static magnetic fields. Further experimental validations and clinical studies are warranted to validate the efficacy of this approach in real-world medical scenarios. The study contributes to the ongoing exploration of static magnetic fields as a viable therapeutic modality with potential benefits for various medical conditions, including wound healing.

Conflict of interest

There are no conflicts of interest in this work.

Acknowledgement

The Scientific and Technological Research Council of Turkey (TÜBİTAK), project number 122E150, supports this study.

References

[1] Wang S., Zheng M., Lou C., Chen S., Guo H., Gao Y., Lv H., Yuan X., Zhang X., Shang P. , Evaluating the biological safety on mice at 16 T static magnetic field with 700 MHz radio-frequency electromagnetic field, *Ecotoxicology and Environmental Safety*, 230 113125 (2021).

[2] Brown M. A., Semelka R. C. , MRI: Basic Principles and Applications, *Wiley-Blackwell*, (2010).

[3] Kobayashi M., Pascual-Leone A., Transcranial magnetic stimulation in neurology, *Lancet Neurology*, 2(3) (2003) 145–156.

[4] Veiseh O., Gunn J. W., Zhang M., Design and fabrication of magnetic nanoparticles for targeted drug delivery and imaging, *Advanced Drug Delivery Reviews*, 62(3) (2010) 284–304.

[5] Dobson J., Magnetic micro- and nano-particle-based targeting for drug and gene delivery, *Nanomedicine*, 1(1) (2006) 31–37.

[6] Ripka P., Janosek M. , Advances in magnetic field sensors, *IEEE Sensors Journal*, 10(6) (2010) 1108–1116.

[7] Rotundo S., Brizi D., Flori A., Giovannetti G., Menichetti L., Monorchio A., Shaping and Focusing Magnetic Field in the Human Body: State-of-the-Art and Promising Technologies, *Sensors*, 22(14) (2022) 5132.

[8] Stauffer P. R., Sneed P. K., Hashemi H., Phillips T. L. , Practical induction heating coil designs for clinical hyperthermia with ferromagnetic implants, *IEEE Transactions on Biomedical Engineering*, 41 (1994) 17–28.

[9] Nemkov V., Ruffini R., Goldstein R., Jackowski J., DeWeese T. L., Ivkov R. , Magnetic field generating inductor for cancer hyperthermia research, *COMPEL - The International Journal for Computation and Mathematics in Electrical and Electronic Engineering*, 30(5) (2011).

[10] Nieskoski M. D., Trembly B. S., Comparison of a single optimized coil and a Helmholtz pair for magnetic nanoparticle hyperthermia, *IEEE Transactions on Biomedical Engineering*, 61 (2014) 1642–1650.

[11] Hadadian Y., Azimbagirad M., Navas E. A., Pavan T. Z., A versatile induction heating system for magnetic hyperthermia studies under different experimental conditions, *Review of Scientific Instruments*, 90 (2019) 074701.

[12] Cano M. E., Barrera A., Estrada J. C., Hernandez A., Cordova T., An induction heater device for studies of magnetic hyperthermia and specific absorption ratio measurements, *Review of Scientific Instruments*, 82 (2011) 114904.

[13] Mazon E. E., Sámano A. H., Calleja H., Quintero L. H., Paz J. A., Cano M. E., A frequency tuner for resonant inverters suitable for magnetic hyperthermia applications, *Measurement Science and Technology*, 28 (2017) 095901.

[14] Brizi D., Fontana N., Giovannetti G., Flori A., Menichetti L., Doumett S., Baldi G., Monorchio A., A novel approach for determining the electromagnetic properties of a colloidal fluid with magnetic nanoparticles for hyperthermia applications, *IEEE Journal of Electromagnetics, RF and Microwaves in Medicine and Biology*, 2 (2018) 70–77.

[15] Di Barba P., Dughiero F., Sieni E. , Magnetic field synthesis in the design of inductors for magnetic fluid hyperthermia, *IEEE Transactions on Magnetics*, 46, (2010) 2931–2934.

[16] Frijia F., Flori A., Giovannetti G., Design, simulation, and test of surface and volume radio frequency coils for 13C magnetic resonance imaging and spectroscopy, *Review of Scientific Instruments*, 92 (2021) 081402.

[17] Bordelon D. E., Goldstein R. C., Nemkov V. S., Kumar A., Jackowski J. K., DeWeese T. L., Ivkov R., Modified solenoid coil that efficiently produces high amplitude AC magnetic fields with enhanced uniformity for biomedical applications, *IEEE Transactions on Magnetics*, 48 (2011) 47–52.

[18] Gresits I., Thuróczy G., Sági O., Gyüre-Garami B., Márkus B. G., Simon F., Non-calorimetric determination of absorbed power during magnetic nanoparticle based hyperthermia, *Scientific Reports*, 8, (2018) 1–9.

[19] Giovannetti G., Landini L., Santarelli M. F., Positano V., A fast and accurate simulator for the design of birdcage coils in MRI, *Magnetic Resonance Materials in Physics, Biology and Medicine*, 15 (2002) 36–44.

[20] Du X., Graedel T. E., Global rare earth in-use stocks in NdFeB permanent magnets, *Journal of Industrial Ecology*, 15 (2011) 836–843.

[21] Colbert A. P., Wahbeh H., Harling N., Connelly E., Schiffke H. C., Forsten C., William L. G., Marko S. M., James J. S., Patricia E., Valerie K., Static magnetic field therapy: a critical review of treatment parameters, *Evidence-Based Complementary and Alternative Medicine*, 6 (2009) 133–139.

[22] Lim K. T., Cho C. S., Choung Y. H., Influence of static magnetic field stimulation on cells for tissue engineering, *Tissue Engineering and Regenerative Medicine*, 6(1–3) (2009) 250–258.

[23] Yun H. M., Ahn S. J., Park K. R., Magnetic nanocomposite scaffolds combined with static magnetic field in the stimulation of osteoblastic differentiation and bone formation, *Biomaterials*, 85 (2016) 88–98.

[24] Zhao J., Li Y., Deng K., Yun P., Gong Y., Therapeutic Effects of Static Magnetic Field on Wound Healing in Diabetic Rats, *Journal of Diabetes Research*, (1-3) (2017) 1–5.

[25] Henry S. L., Concannon M. J., Yee G. J., The Effect of Magnetic Fields on Wound Healing Experimental Study and Review of the Literature, *Eplasty*, 8, (2008) e40.

[26] Vergallo C., Dini L., Szamosvölgyi Z., Tenuzzo B. A., Carata E., Panzarini E., László J., In Vitro Analysis of the Anti-Inflammatory Effect of Inhomogeneous Static Magnetic Field-Exposure on Human Macrophages and Lymphocytes, *PLoS One*, 8(8) (2013).

[27] Zhang L., Wang J., Wang H., Wang W., Li Z., Liu J., Zhang X., Moderate and strong static magnetic fields directly affect EGFR kinase domain orientation to inhibit cancer cell proliferation, *Oncotarget*, 7(27) (2016) 41527–41539.

[28] Tasić T., Djordjević D., De Luka S., Trbovich A., Japundžić-Žigon N., Static magnetic field reduces blood pressure short-term variability and enhances baroreceptor reflex sensitivity in spontaneously hypertensive rats, *International Journal of Radiation Biology*, 93(5) (2017) 527–534.

[29] Brown C. S., Ling F. W., Wan J. Y., Pilla A. A., Efficacy of static magnetic field therapy in chronic pelvic pain: a double-blind pilot study, *American Journal of Obstetrics and Gynecology*, 187(6) (2002) 1581–1587.

[30] Darendeliler M. A., Darendeliler A., Sinclair P. M., Effects of static magnetic and pulsed electromagnetic fields on bone healing, *The International Journal of Adult Orthodontics and Orthognathic Surgery*, 12(1) (1997) 43–53.

[31] Gümüşay M., Gülbağça F., Aydemir I., Sayğılı S., Kaya A., Tuğlu M. İ., Sıçan Derisinde Oluşturulan Yara Modeli Üzerinde İyileşme Sağlanması için Elektromanyetik Alan Sistemi Geliştirilmesi ve Sensör Uygulaması, *EMO Dergisi*, (2016) 678-681.

[32] Shang W., Chen G., Li Y., Zhuo Y., Wang Y., Fang Z., Ren H., Static Magnetic Field Accelerates Diabetic Wound Healing by Facilitating Resolution of Inflammation, *J Diabetes Res*. (2019).

[33] Health Protection Agency., *Static Magnetic Fields*, (2008).

Cumhuriyet Sci. J., 45(3) (2024) 585-590
DOI: https://doi.org/10.17776/csj.1387124

Cumhuriyet Science Journal

| csj.cumhuriyet.edu.tr | Founded: 2002 ISSN: 2587-2680 e-ISSN: 2587-246X Publisher: Sivas Cumhuriyet University

Investigation of the Annealing and Cu Doping Effect on Structural and Optical Properties of CdZnS Nanomaterial Deposited by Ultrasonic Spray Pyrolysis

Ahmed Abdulhasan Zarkooshi [1,2,a,*], Murat Kaleli [3,4,b]

[1] Department of Medical Instrumentation Techniques Engineering, Dijlah University, Baghdad, Iraq.
[2] The National Nuclear Radiological Chemical and Biological Commission, Baghdad, Iraq.
[3] Department of Physics, Faculty of Arts and Sciences, Süleyman Demirel University, Isparta, Türkiye
[4] Innovative Technologies Application and Research Center (YETEM), Süleyman Demirel University, Isparta, Türkiye
*Corresponding author

Research Article

History
Received: 06/11/2023
Accepted: 18/07/2024

ABSTRACT

This study investigates doped CdZnS thin films synthesized through the ultrasonic spray pyrolysis technique, followed by annealing at temperatures of 400 and 500 °C. X-ray diffraction analysis demonstrated that both undoped CdZnS and Cu-doped CdZnS thin films exhibit cubic crystal structures, with a preferred orientation along the (111) plane. Scanning electron microscopy (SEM) measurements indicated that the CdZnS thin film has a smooth surface, whereas the Cu-doped CdZnS film shows clustered particles, attributed to the effect of copper doping acting as an activator metal ion. Electron dispersive scanning (EDS) analysis confirmed that the Cd, Zn, and S elements are present in acceptable chemical stoichiometry (Cd + Zn/S = 1:1), with a ratio of 3:1, consistent with the molar amounts used in the precursor solutions. The band gap of the CdZnS thin film decreased from 3.12 to 2.56 eV after annealing at 500 °C, attributed to an increase in crystal size. In contrast, the band gap of the Cu-doped CdZnS thin film decreased from 2.51 to 2.22 eV, lower than that of pure CdZnS, due to the formation of additional phases such as zinc oxide and copper oxide within the CdZnS host structure during annealing.

Keywords: Ultrasonic spray pyrolysis, CdZnS thin film, Annealing, Band gap energy.

[a] ahmedeliraqi77@yahoo.com https://orcid.org/0000-0001-6715-1709 [b] muratkaleli@sdu.edu.tr https://orcid.org/0000-0002-3290-2020

Introduction

The II-VI compound group holds significant importance in the field of material science due to their specific bandgap spanning from UV to IR light wavelengths. These compounds are composed of elements from group II (like zinc, cadmium, and mercury) and group VI (including oxygen, sulfur, selenium, and tellurium). Their appeal to scientists lies in their direct bandgap energy, typically falling between 1.5 to 3.7 eV, which makes them highly suitable for optical applications. They exhibit exceptional optical absorption characteristics, capable of absorbing 99% of incident light with just a 1µm thickness, making them a focus of extensive research [1, 2].

There are many methods to produce CdZnS thin film like chemical bath deposition (CBD) [3,4], thermal vacuum evaporation technique (PVD) [5], electrodeposition technique [7,8], and ultrasonic spray pyrolysis (USP) [9, 10]. Among these techniques, USP technique is the most preferred one, it is easy, and many layers can be deposited.

Previous studies reported that CdZnS thin film could be doped with cationic metals such as Cu, Zn, Ag, and Al or anionic metals such as B, Cl, and Fe, etc. In our study doping by copper ions has been used to improve the electro-optical properties and to increase the efficiency of photocatalytic activity by enhancing the electron transition [11], [12, 13, 14, 15, 16, 17].

In this study, first, pure CdZnS ternary and Cu-doped CdZnS quaternary thin film samples were fabricated by the USP technique and then annealed at 400 and 500 °C, to investigate of annealing effect on the crystal structures, surface morphology, chemical composition, and optical properties of the fabricated samples.

Materials and Methods

To fabricate the CdZnS thin films, zinc chloride (ZnCl2), cadmium chloride (CdCl2), and thiourea (CH_4N_2S) salts were used as precursor materials. First, 0.3 M of ZnCl2 was dissolved in 20 ml of distilled water, and after 10 minutes, two drops of hydrochloric acid (HCl) was added to this solution to prevent oxychloride formation. Then, 0.6 M of thiourea was dissolved in a separate beaker with 10 ml of distilled water and mixed with the ZnCl2 solution. Subsequently, 0.1 M of CdCl2 was dissolved in 20 ml of distilled water in another beaker. This solution was then poured into the first prepared solution, and the mixture was stirred with a magnetic stirrer for two hours until it became completely homogeneous. This solution was divided into two separate beakers: one for the preparation of pure CdZnS thin films and the other for the preparation of Cu-doped CdZnS thin film samples, to which 2 mg of copper sulfate (CuSO4.5H2O) was added.

The glass substrate cleaning process involved using ethanol, acetone, and ethanol sequentially. The Sono-Tek Flexi Coat, equipped with a nitrogen gas generator, was utilized in an ultrasonic spray pyrolysis (USP) deposition system. Other optimization parameters were set as follows: nitrogen pressure at 2.5 kg/cm^2, substrate-to-nozzle distance at 12 cm, and solution flow rate at 0.5 ml/minute. Doped and undoped CdZnS thin films were produced on substrates with a 10×10 cm^2 deposition area at a substrate temperature of 275 °C in an ambiance containing 3% oxygen. Both thin films were annealed at 400 °C and 500 °C, respectively, using an oven supplied with nitrogen gas and excess sulfur (sulfurization) to improve crystallinity【18,19】.

The structural properties of CdZnS and CdZnS: Cu thin films were studied by using Bruker D8 Advanced Twin-twin XRD system with the Cu-Kα radiation with a wavelength of 1.5406 Å and 2θ ranging from 20° to 80°. Morphology and elemental analyses of the films were examined by FEI Quanta FEG 250 Scanning Electron Microscope (SEM) which attached an EDAX EDS system. Optical characterization was also held by using Perkin Elmer Lambda 950 UV/Vis spectrophotometer in between 300 – 1000 nm wavelength.

Glutathione (GSH) is a tripeptide found within cells. It plays a critical role in neutralizing free radicals and reactive oxygen species (ROS), thereby preventing oxidative stress and maintaining cellular homeostasis. It is a central component in preserving redox homeostasis (the oxidative state within cells) [11]. The balance between oxidized glutathione (GSSG) and reduced glutathione (GSH) determines a cell's capacity to cope with oxidative stress. This ensures that cells function healthily and prevent the onset of pathological conditions. Therefore, GSH and its metabolism are considered potential therapeutic targets in many diseases associated with oxidative stress [12, 13].

Malondialdehyde (MDA), a by-product of lipid peroxidation, is also considered an indicator of oxidative damage. It is used to assess the extent and effects of oxidative damage to membrane lipids [14, 15].

In particular, in research and clinical studies, the examination of GSH and MDA aids in understanding oxidative damage and elucidating cellular mechanisms at the cellular level. In this study, the effects of toluene exposure-induced oxidative stress in rats were investigated. Additionally, it was assessed whether resveratrol plays a protective role against these adverse effects. Levels of MDA, an indicator of lipid peroxidation, and GSH, which plays a significant role in cellular antioxidant defense, were analyzed.

Results and Discussion

X-Ray Diffraction Measurements

The XRD patterns recorded for CdZnS and CdZnS: Cu thin films deposited on glass substrates for as-grown and annealed samples at 400 °C and 500 °C are given in Figures 1. a) and b), respectively. It can be seen, all the planes displayed in cubic structure and polycrystalline in nature. The major peak of cubic structure for both films CdZnS and CdZnS: Cu were found at 2θ values of 28.62° and 28.39°, respectively, which are attributed (111) directional plane as a preferred plane orientation. Scherer's equation [19](Eq.1) has been applied to calculate the average crystal size.

$$D=0.92\lambda/B\cos\theta \qquad (1)$$

Where λ =1.5406 Å for CuKα , B is full width at half maximum (FWHM) and θ is Bragg's angle. Crystal size was Calculated of CdZnS and Cu-doped thin films are listed in Table 1 and 2, respectively.

Table 1. Crystal size for CdZnS and CdZnS : Cu doping thin films.

Sample	peak position for (111) indices	FWHM (deg)	Average of crystal size A°
Undoped sample as grown	28.62°	0.784	116.2
Undoped sample annealed 400 °C	28.72°	0.735	124.0
Undoped sample annealed 500 °C	28.28	0.692	131.5
Doped sample as grown	28.39°	3.515	26.0
Doped sample annealed 400 °C	28.21°	3.084	29.5
Doped sample annealed 500 °C	27.92°	3.352	27.2

Table 1 shows that the crystal size of CdZnS and CdZnS: Cu doping thin films increases with annealing temperature due to the reduction of structural defects within the lattice by applying extra thermal energy［19, 21, 22］, but this trend is disrupted after annealing at 500 °C for copper doping thin film. This is due to the substitution of Cu^{2+} ions, which have a smaller ionic radius (0.73 Å) compared to Cd^{2+} ions (0.97 Å). Cu^{2+} ions can easily enter the CdZnS lattice, causing distortion in the CdZnS lattice structure, which aligns with previous reports in the literature［22,23］.

Figure 1.a) shows that the improvement of the main diffraction peak intensity of CdZnS thin film depended on the increase of the annealing temperature, this improvement might be attributed by the high thermal energy helps the atoms to move to the correct position in the lattice. As a result the defects will be reduced that leads to re re-crystallization in the lattice [19, 21 ,22]. Whereas Figure 1.b) shows that after annealing the samples up to 500 °C, it is clear there is a disruption of the main diffraction peak for CdZnS: Cu thin film, and a slight shifting for the major peak (111). This reason is argued by

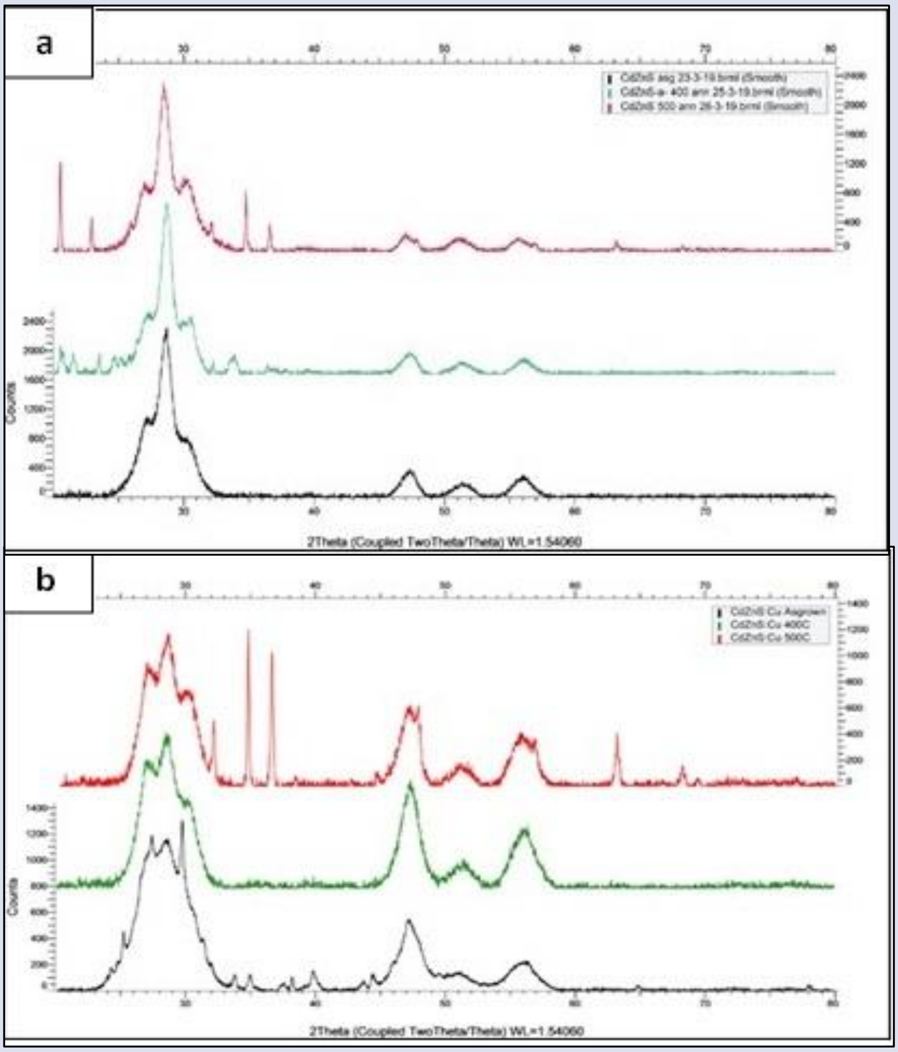

Figure 1. (A) GSH levels in rat lung. (B) GSH levels in rat serum

the oxidization and with copper oxide crystal structure has been generated to take its poison inside the hostel crystal, however all the peaks matching with CdZnS structure PDF 01-079-7040 library, it is in consistent with the literatures reported [23, 24, 25].

Surface Morphology Analysis

Figure 2. a) and b) represents images of scanning electron microscopy (SEM) for the surface of CdZnS and CdZnS:Cu thin films, respectively.

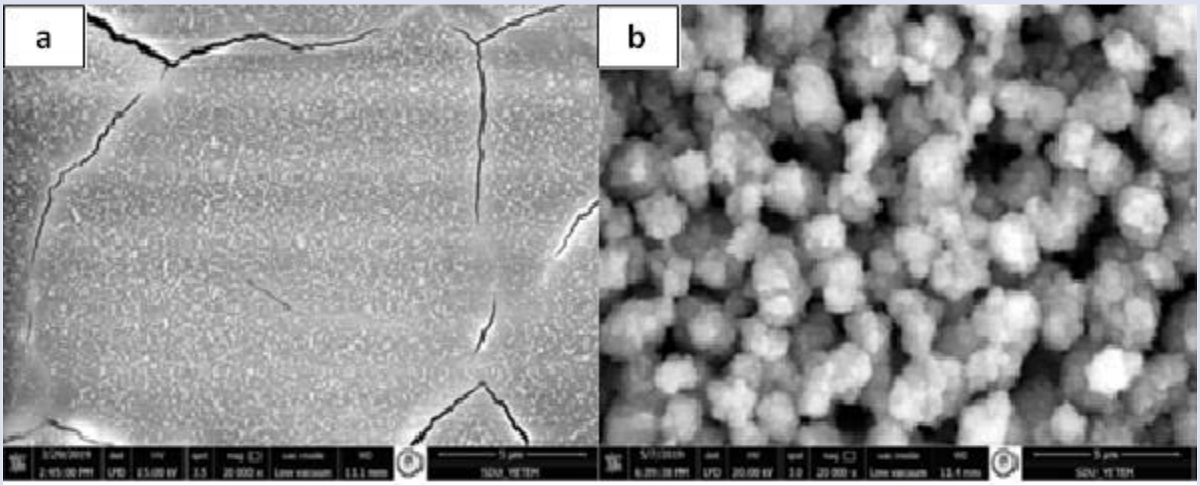

Figure 2. As grown SEM images of a) CdZnS and, b) CdZnS: Cu thin films

SEM images shows that the surface of CdZnS thin film has smooth and a few cracks, whereas the surface of CdZnS: Cu thin film has clusters, due to the effect of doped copper metal which was added to the precursor solution and generated agglomerated particles.

The energy dispersive spectroscopy (EDS) system is followed by SEM measurements, and the elemental composition analysis of the CdZnS and CdZnS: Cu thin films for as grown, annealed at 400 °C and 500 °C, respectively, are given in Table 3. and 4. It was observed that Cd, Zn, and S elemental compositions are approximately the same for CdZnS and CdZnS: Cu thin films. Although there were slight differences in their concentrations due to the deposition process was not homogeneous. However, all the elements in both films are closed to be aimed composition with the acceptable chemical stoichiometry (Cd+Zn/S =1:1), and the ratio of Zn: Cd = 3:1, according to the amount of molarity which has been used. After annealing under sulfur resulted in an excess number of sulfur elements in the thin film structure as expected. It is also clear that the crystallographic results gained from XRD and elemental composition results obtained from EDS measurements are in good agreement with each other.

Table 3. EDS measurements as atomic percentage(A%) of CdZnS and Cu doping thin film as grown, and annealed at 400 °C and 500 °C.

Samples	S	Cd	Zn	Cu	Zn/Cd	Zn+Cd/S
undoped sample as grown	39.07	8.36	33.3	--	3.98	1.06
undoped sample annealed 400 °C	40.05	9.09	38.13	--	4.19	1.17
undoped sample annealed 500 °C	36.62	8.07	39.5	--	4.89	1.29
doped sample as grown	33.55	7.78	30.6	0.36	3.933	1.14
doped sample annealed 400 °C	30.98	7.97	36.3	0.45	4.55	1.42
doped sample annealed 500 °C	33.32	8.1	39.06	0.37	4.82	1.41

Optical Properties

Figure 3.a) and b) showed the Absorption spectra for both CdZnS and Cu doped respectively. The absorption spectra for both films were recorded by using UV-vis system at room temperature in the wavelength ranging from 300 -1000 nm, the result showed that the absorption spectrum is shifted to the blue region which exhibited lower absorption in the longer wavelength. The band gap energy was estimated with help of absorption spectra and by using Tauc relation [25] (Eq. 2)

$$\alpha hv = A (hv - E_g)^n \qquad \textbf{(2)}$$

Where α; is an absorption coefficient, hv; photon energy, E_g; band gap, A; constant and n = 1/2 for allowed direct band gap transition of CdZnS. By plotting the graph of $(\alpha hv)^2$ versus and applying the extrapolation method, the band gap energy values of the samples shown in the figure3

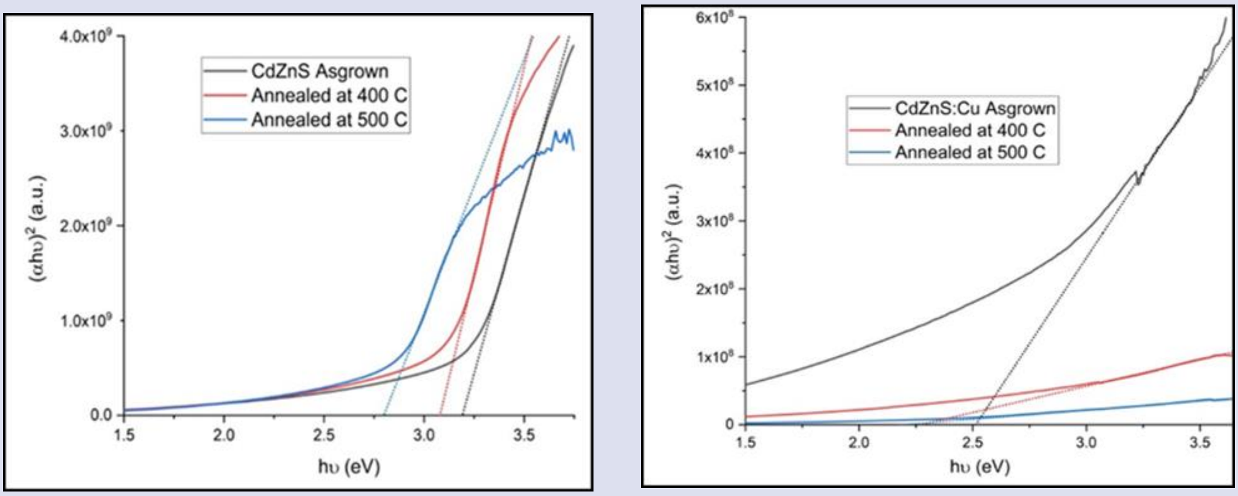

(a) (b)

Figure 3. Band gap energy of a) CdZnS and b) CdZnS: Cu doped thin films.

Figure 3.a) shows that an absorption edge is shifted to the blue region, which exhibited lower absorption in the longer wavelength, and optical band gap value decreased from 3.12, 3.01 to 2.56 eV for as grown, annealed sample at 400 °C and annealed sample at 500 °C, respectively. The decrease in the bandgap values arises from increasing of crystal size as is shown in Table 3. And quantum confinement which taking a place in the crystal structure [26, 27].

Figure 3.b) indicates that the energy band gap value of CdZnS: Cu thin film decreases with increasing annealing temperature. The bandgap energy values decrease from 2.51, 2.30, and 2.22 eV which is associated with an extra phase of zinc oxide and copper oxide, generated inside the host structure of CdZnS due to the effect of thermal metal oxidization. That will cause to shift toward lower energies. However, this is in agreement with the previous literatures reported related to metal doping to CdZnS thin films [28, 29].

Conclusion

CdZnS and Cu-doped thin films were fabricated by ultrasonic spray pyrolysis method and annealed at 400 and 500 °C to investigate the annealing effect on the crystal structures, surface morphology, chemical composition, and the optical properties of the fabricated samples, XRD, SEM, EDS, and UV-VIS measurements were conducted. XRD analysis showed that the CdZnS and Cu-doped CdZnS thin film samples have cubic crystal phase and polycrystalline structure. SEM measurements indicated that CdZnS thin film has a smooth surface, whereas CdZnS: Cu has cluster particles due to the effect of copper doping which presents as an activator metal ion. EDS analysis exhibited that all the components Cd, Zn, and S are composed in chemical stoichiometry (Cd+Zn/S =1:1), and the ratio of Zn: Cd = 3:1. After annealing at 500 °C, it was observed that the bandgap energy value of CdZnS thin film decreased from 3.12 to 2.56 eV due to an increase in crystal size , and at the same time bandgap energy of the CdZnS: Cu thin film was lower than pure CdZnS decreasing from 2.51 to 2.22 eV resulting from the associated to extra phases of zinc oxide and copper oxide, generated inside the host structure of CdZnS by annealing effect. This is evidence that doping by copper ions is playing a major strategic role in the enhancement of photocatalytic activity.

In addition, some studies can be carried out on the application of the USP deposited CdZnS thin films as a window layer for solar cells since their suitable band gap energy values can be changed by applying annealing and copper doping as required

Conflict of interest

There is no conflict of interest among the authors.

References

[1] Shadia I J., Introduction to II-VI Compounds. AlIsra University, Faculty of Information Technology, Department of Basic Sciences-Physics, Jordan, (2015) 1-16.

[2] Jia G., Wang N., Gong L., Fei X., Growth characterization of CdZnS thin films prepared by chemical bath deposition, *Chalcogenide Lett.*, 6(9) (2009) 463–467.

[3] Ma L., Ai X., Wu X., Effect of substrate and Zn doping on the structural, optical and electrical properties of CdS thin films prepared by CBD method, *J. Alloys Compd.*, 691(1) (2017) 399–406.

[4] Zellagui R., Dehdouh H., Boughelout A., Sahraoui T., Chaumont D., Adnane M., Effect of zinc / cadmium proportion in CdS layers deposited by CBD method, *Int. Multidiscip. Res. J.*, 9(2019) 8–12.

[5] Lee J. H., Song W. C., Yi J. S., Yoo Y. S., Characteristics of the CdZnS thin film doped by thermal diffusion of vacuum evaporated indium films, *Sol. Energy Mater. Sol. Cells*, 75 (2003) 227–234.

[6] Rajendran S. K. S A., Structural and optical analysis of electrodeposition CdZnS thin films for solar cell applications, *MOJ Sol. photoenergy Syst.*, 3(1) (2019) 30–32.

[7] Mahanama G. D. K., Madarasinghe D. A., Dharmaratna W. G. D., Jayasundara D., Optical and structural properties of CdS thin films prepared using electro-deposition technique, *Ruhuna J. Sci.*, 9(1) (2018) 1- 57.

[8] Hamedani H. A., Investigation of Deposition Parameters in Ultrasonic Spray Pyrolysis for Fabrication of Solid Oxide Fuel Cell,Master thesis, George W. Woodruff School of Mechanical Engineering , Georgia Institute of Technology, 2008.

[9] Baykul M. C., Orhan N., Band alignment of $Cd_{1-x}Zn_xS$ produced by spray pyrolysis method, *Thin Solid Films*,518(8) (2010) 1925–1928.

[10] Sethi R., Kumar L., Sharma P. K., Pandey A. C., Tunable Visible Emission of Ag-Doped CdZnS Alloy Quantum Dots, *Nanoscale Res. Lett.*,5(1) (2010) 96–102.

[11] Selvan G., Abubacker M. P., Balu A. R., Structural, optical and electrical properties of Cl-doped ternary CdZnS thin films towards optoelectronic applications, *Optik (Stuttg).*, 127(12) (2016) 4943–4947.

[12] Noor H., Ali S., Mohammad D., Abbas Abdzaid D., Study the structural and optical properties of pure and Aluminum doped CdS thin films prepared by chemical bath deposition method, *J. Kufa Phys.*, 10 (1) (2018) 1–7.

[13] Assadi M H N., Hanaor D A H., The effects of copper doping on photocatalytic activity at (101) planes of anatase TiO 2 : A theoretical study, *Appl. Surf. Sci.*, 387 (November)(2018) 682–689.

[14] Yongvanich N., Thongkaew K., Yuanlae N., Sae-Ung S., Suwanchawalit C., nfluence of Copper Doping in Nanostructured ZnO Thin Films by Spin Coating, *IEEE Trans. Nanotechnol.*, 17(6) (2018) 1125–1128.

[15] Oeba D. A., Optical and electrical properties of CdS: B thin film deposited by chemical bath deposition for photovoltaic application, Int. J. Thin.Fil. Sci. Tec., 8 (3) (2019) 93-99.

[16] Saleh K. M., Study Influence of Substrate Temperature on Optical Properties of CdS Thin Films Prepared by Chemical Spray pyrolysis, *Ibn AL-Haitham J. Pure Appl. Sci.*, 32(1) (2019) 7–16.

[17] Fidha G., Bitri El N., Mahjoubi S., Abaab M., Ly I., Effect of the spraying temperatures and the sulfurization on the properties of the absorber Cu_2FeSnS_4 thin films in a solar cell, *Mater. Lett.*, 215(2018) 62–64.

[18] Monshi A., Foroughi M R., Monshi M R., Modified Scherrer Equation to Estimate More Accurately Nano-Crystallite Size Using XRD, *World J. Nano Sci. Eng.*, 2(3) (2012) 154–160.

[19] Goswami M., Adhikary N C. Bhattacharjee S., Effect of annealing temperatures on the structural and optical properties of zinc oxide nanoparticles prepared by chemical precipitation method, *Optik (Stuttg).*,158(2018)1006–1015.

[20] Hossain M S., Effect of annealing on the properties of $Zn_xCd_{1-x}S$ thin film growth by RF magnetron co-sputtering, *Energy Procedia*, 33(2013) 214–222.

[21] Figueiredo V., Effect of post-annealing on the properties of copper oxide thin films obtained from the oxidation of evaporated metallic copper, *Appl. Surf. Sci.*, 254 (13) (2008) 3949–3954.

[22] Muthusamy M., Muthukumaran S., Effect of Cu-doping on structural, optical and photoluminescence properties of CdS thin films, *Optik (Stuttg).*, 126 (24) (2015) 5200–5206.

[23] Ann L C., Mahmud S., Khadijah S., Bakhori M., Applied Surface Science Electron spectroscopy imaging and surface defect configuration of zinc oxide nanostructures under different annealing ambient, *Appl. Surf. Sci.*, 265(2013) 137–144.

[24] Parameshwari P M., Spray Deposition and Characterization of Nanocrystalline Cd 1-x Zn x S thin films, International Journal of Nanotechnology and Applications, 11(1) (2017) 45–58.

[25] Lui T Y., Photoluminescence and photoconductivity properties of copper-doped $Cd_{1-x}Zn_xS$ nanoribbons, *Nanotechnology*,17(24) (2006) 5935–5940.

[26] Azizi S., Investigating Annealing Effect On Optical properties of $Cd_{0.8}Zn_{0.2}S$ Thin Film, *World Sci. Publ. Co.*,21(5) (2014) 1–7.

[27] Ajeel H M., The Effect of Annealing on the Structural and Optical Properties of Copper Oxide Thin Films Prepared by SILAR Method. J. Baghdad for Sci. 11(2) (2014) 1–12.

[28] Serin N., Serin T., Horzum Ş., Çelik Y., Annealing effects on the properties of copper oxide thin films prepared by chemical deposition, *Semicond. Sci. Technol.*, 20(5) (2005) 398–401.

Cumhuriyet Sci. J., 45(4) (2024) 591-597
DOI: https://doi.org/10.17776/csj.1483156

Cumhuriyet Science Journal

| csj.cumhuriyet.edu.tr | Founded: 2002 ISSN: 2587-2680 e-ISSN: 2587-246X Publisher: Sivas Cumhuriyet University

Geometry Optimization, Molecular Docking and ADMET Studies of Echimidine Molecule

Bilge Bıçak [1,a,*]

[1] *Physics Department, Science Faculty, Istanbul University, 34134, Istanbul, Türkiye.*
**Corresponding author*

Research Article

History
Received: 13/05/2024
Accepted: 12/08/2024

ABSTRACT

Plants are an important food group that has been used as a source of nutrition and healing from past to present. Plants contain secondary metabolites that are still under investigation in drug development studies. Alkaloids, which are secondary metabolites, have antioxidant and antibacterial properties as well as therapeutic potential in various diseases such as Alzheimer's disease. Acetylcholinesterase (AChE) inhibitors come to the fore in the treatment strategy of Alzheimer's disease. Echimidine, a pyrrolizidine alkaloid, is an important compound known to be active in AChE inhibition. Molecular docking method has an important place in elucidating biochemical processes by examining the interactions of drugs or drug candidates with the receptors targeted for the disease. Additionally, information on the absorption, distribution, metabolism, excretion, and toxicity (ADMET) of drug candidate molecules is important in drug development studies. In this study, echimidine molecule was optimized, the molecular docking study was carried out with AChE and the interaction types, binding profile, and binding affinity of echimidine was determined. ADMET analysis of echimidine was also realized to estimate its drug potential. With this study, geometry optimization of the molecule, elucidation of its interactions with AChE, and prediction of its pharmacokinetic properties were achieved for the first time.

Keywords: Echimidine, Acetylcholinesterase, Molecular Docking, ADMET.

[a] *bbicak@istanbul.edu.tr* *https://orcid.org/0000-0003-1147-006X*

Introduction

Plants are known to contain various secondary metabolites such as alkaloids, phenols, steroids, glycosides, tannins, terpenoids and phytoalexins to survive and reproduce. Alkaloids are structures that have an important place among secondary metabolites [1]. Alkaloids are secondary metabolites that come to the fore in treatment studies that show various effects such as AChE inhibitor, butyrylcholinesterase inhibitor, muscarinic and adenosine receptor agonists [2]. Moreover, alkaloids are compounds that show antioxidant, anti-inflammatory, antibacterial effects and have therapeutic potential in various diseases such as Alzheimer's disease [3-5]. Pyrrolizidine alkaloids are secondary metabolites found in plants used for medicinal purposes but are known for their hepatotoxic, genotoxic and neurological effects [6]. It has been reported that these compounds, which are the subject of controversy due to their toxic effects, can be used temporarily, considering that the exposure will be low, when found in trace amounts in herbal medicinal products [7]. Echimidine, a pyrrolizidine alkaloid, is an important compound known to be active in AChE inhibition [8]. As it is known, Cholinesterase inhibitors are an important enzyme that stands out in studies on the treatment of diseases such as Alzheimer's disease [8, 9]. Echimidine also shows binding activity to Muscarinergic receptors and 5-HT2 [10]. Echimidine has been reported to have comprehensive pharmacological effects due to its various activations [1].

The three-dimensional structures of molecules are related to molecular interactions and affect biological processes. Considering that the three-dimensional structures of molecules are important, the optimization of these structures is also very important. With geometry optimization, information is obtained about the optimum three-dimensional arrangement of the atoms that make up the molecules. The molecular docking method is a computer-aided method that plays a key role in elucidating biochemical processes by theoretically examining the interactions of small molecules called ligands and the receptors that these ligands have the potential to interact with. ADMET analysis, a predictive tool to evaluate a molecule's drug potential, provides information regarding absorption, distribution, metabolism, excretion, and toxicity.

In this study, firstly, the optimized geometry of the echimidine molecule was obtained using the DFT/B3LYP/6-311++G(d,p) method. Then, in order to elucidate the AChE inhibitor activity of the echimidine molecule, its binding affinity and binding profile were obtained by molecular docking method. Finally, the pharmacokinetic properties and toxicity profile of the echimidine molecule were evaluated by the ADMET study.

Methods

Molecular Optimization

The three-dimensional molecular structure of echimidine was downloaded from Pubchem (https://pubchem.ncbi.nlm.nih.gov/, CID: 5281729). The optimization of echimidine was realized with DFT method, B3LYP theory level, 6-311++G(d,p) basis set using Gaussian09 software program [11].

Molecular Docking

Echimidine molecule was prepared as a ligand for molecular docking study with AutoDock Tools 1.5.6. The structure of AChE given with 2ACE PDB Code was downloaded from PDB DataBank (https://www.rcsb.org/) [12]. AChE was prepared for molecular docking study by deleting water and other ligands and adding polar hydrogens. After the ligand and receptor were prepared, the grid box was prepared and all the necessary input information for the molecular docking study was obtained. Then, molecular docking study was successfully carried out by AutoDock Vina [13]. The Echimidine-AChE complex structure and the binding profile of echimidine obtained as a result of the molecular docking study were visualized with the Discovery Studio Visualizer 2019 [14].

ADMET Analysis

ADME and toxicity properties of echimidine molecule were determined by SwissADME and pkCSM online servers [15, 16].

Results and Discussion

Optimization

Echimidine molecule was optimized using Gaussian09 package program at DFT/B3LYP/6-311++G(d,p) basis set. The optimized parameters of the molecule were listed in Table 1,2,3. The energy value of optimized molecule was calculated as -1362.4795376 a.u.

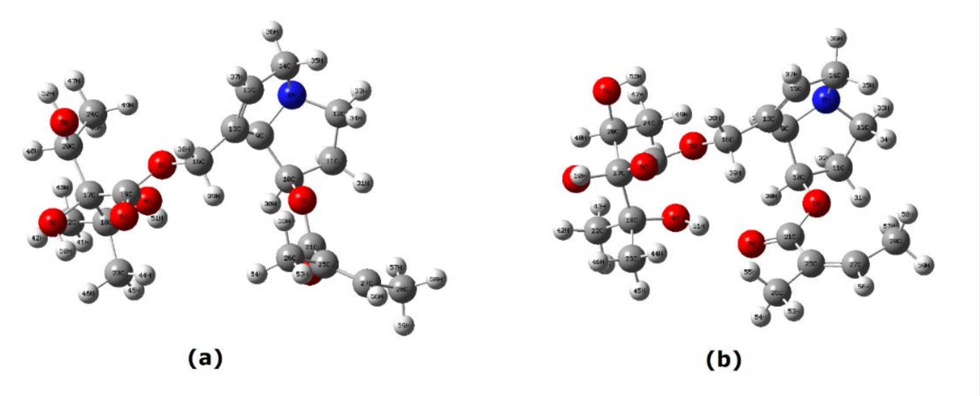

Figure 1 The input and output structures of Echimidine

Table 1. The bond lengths of optimized echimidine molecule.

Bond	Length (Å)	Bond	Length (Å)	Bond	Length (Å)
R(1,10)	1,4579	R(11,12)	1,534	R(22,41)	1,0922
R(1,21)	1,347	R(11,31)	1,0908	R(22,42)	1,0905
R(2,16)	1,4535	R(11,32)	1,0936	R(22,43)	1,0907
R(2,19)	1,3418	R(12,33)	1,0939	R(23,44)	1,093
R(3,17)	1,4237	R(12,34)	1,1022	R(23,45)	1,0925
R(3,50)	0,9676	R(13,15)	1,3332	R(23,46)	1,0897
R(4,18)	1,4296	R(13,16)	1,4953	R(24,47)	1,0936
R(4,51)	0,9684	R(14,15)	1,5031	R(24,48)	1,088
R(5,20)	1,4364	R(14,35)	1,1023	R(24,49)	1,0917
R(5,52)	0,9633	R(14,36)	1,0983	R(25,26)	1,5122
R(6,19)	1,2105	R(15,37)	1,0841	R(25,27)	1,3458
R(7,21)	1,219	R(16,38)	1,0908	R(26,53)	1,0909
R(7,51)	2,0136	R(16,39)	1,0926	R(26,54)	1,0928
R(8,9)	1,4878	R(17,18)	1,5939	R(26,55)	1,0937
R(8,12)	1,4665	R(17,19)	1,5361	R(27,28)	1,497
R(8,14)	1,4681	R(17,20)	1,5661	R(27,56)	1,0892
R(9,10)	1,5467	R(18,22)	1,5329	R(28,57)	1,0851
R(9,13)	1,5144	R(18,23)	1,5357	R(28,58)	1,0971
R(9,29)	1,0979	R(20,24)	1,5252	R(28,59)	1,0946
R(10,11)	1,5295	R(20,40)	1,0915		
R(10,30)	1,0859	R(21,25)	1,4906		

Table 2. The angle values of optimized echimidine molecule.

Angle	Degree(º)	Angle	Degree(º)	Angle	Degree(º)
A(10,1,21)	118,2036	A(8,14,35)	111,4463	A(18,22,41)	108,8119
A(16,2,19)	115,9465	A(8,14,36)	111,7616	A(18,22,42)	110,6741
A(17,3,50)	107,5038	A(15,14,35)	111,5863	A(18,22,43)	111,6055
A(18,4,51)	109,6462	A(15,14,36)	111,5232	A(41,22,42)	109,0885
A(20,5,52)	107,9582	A(35,14,36)	106,5445	A(41,22,43)	107,6632
A(9,8,12)	109,5407	A(13,15,14)	111,9899	A(42,22,43)	108,9201
A(9,8,14)	109,6123	A(13,15,37)	125,2854	A(18,23,44)	111,8142
A(12,8,14)	117,4101	A(14,15,37)	122,7219	A(18,23,45)	108,5819
A(8,9,10)	105,9679	A(2,16,13)	108,7554	A(18,23,46)	111,1434
A(8,9,13)	104,1709	A(2,16,38)	109,5147	A(44,23,45)	107,8425
A(8,9,29)	110,372	A(13,16,38)	111,4775	A(44,23,46)	108,4926
A(10,9,13)	120,9332	A(13,16,39)	112,0527	A(45,23,46)	108,8723
A(10,9,29)	105,7523	A(38,16,39)	107,7218	A(20,24,47)	108,1866
A(13,9,29)	109,4268	A(3,17,18)	106,7093	A(20,24,48)	112,3584
A(1,10,9)	112,1335	A(3,17,19)	106,8099	A(20,24,49)	111,1192
A(1,10,11)	107,4348	A(3,17,20)	105,4648	A(47,24,48)	109,1928
A(1,10,30)	108,6231	A(18,17,19)	110,6013	A(47,24,49)	108,7286
A(9,10,11)	101,9672	A(18,17,20)	115,6273	A(48,24,49)	107,1896
A(9,10,30)	112,4717	A(19,17,20)	111,0296	A(21,25,26)	113,1742
A(11,10,30)	114,058	A(4,18,17)	111,327	A(21,25,27)	125,9756
A(10,11,12)	103,5985	A(4,18,22)	106,6775	A(26,25,27)	120,8259
A(10,11,31)	112,4104	A(4,18,23)	109,6945	A(25,26,53)	110,5886
A(10,11,32)	108,4265	A(17,18,22)	109,3928	A(25,26,54)	110,9602
A(12,11,31)	113,7485	A(17,18,23)	110,25	A(25,26,55)	111,4338
A(12,11,32)	110,3041	A(22,18,23)	109,4199	A(53,26,54)	108,7161
A(31,11,32)	108,2129	A(2,19,6)	123,2313	A(53,26,55)	108,4597
A(8,12,11)	103,9	A(2,19,17)	114,0812	A(54,26,55)	106,5436
A(8,12,33)	111,52	A(6,19,17)	122,6872	A(25,27,28)	131,8754
A(8,12,34)	111,3774	A(5,20,17)	108,5073	A(25,27,56)	114,6884
A(11,12,33)	112,1565	A(5,20,24)	110,2124	A(28,27,56)	113,4323
A(11,12,34)	110,3313	A(5,20,40)	104,4908	A(27,28,57)	113,5444
A(33,12,34)	107,5975	A(17,20,24)	119,3883	A(27,28,58)	109,7989
A(9,13,15)	110,0286	A(17,20,40)	103,8546	A(27,28,59)	109,4414
A(9,13,16)	124,7614	A(24,20,40)	109,2385	A(57,28,58)	108,0134
A(15,13,16)	125,2042	A(1,21,7)	122,917	A(57,28,59)	109,4586
A(8,14,15)	104,0933	A(1,21,25)	115,3681	A(58,28,59)	106,325
A(2,16,39)	107,2087	A(7,21,25)	121,6946		

Table 3. The dihedral values of optimized echimidine molecule.

Dihedral	Degree(º)	Dihedral	Degree(º)	Dihedral	Degree(º)
D(21,1,10,9)	106,6397	D(1,10,11,31)	42,7373	D(18,17,20,40)	75,141
D(21,1,10,11)	-142,1149	D(1,10,11,32)	162,3243	D(19,17,20,5)	-47,0553
D(21,1,10,30)	-18,285	D(9,10,11,12)	37,5617	D(19,17,20,24)	80,2945
D(10,1,21,7)	-4,0904	D(9,10,11,31)	160,7876	D(19,17,20,40)	-157,808
D(10,1,21,25)	177,5263	D(9,10,11,32)	-79,6253	D(4,18,22,41)	64,4626
D(19,2,16,13)	-175,9019	D(30,10,11,12)	159,0629	D(4,18,22,42)	-175,6821
D(19,2,16,38)	-53,8575	D(30,10,11,31)	-77,7113	D(4,18,22,43)	-54,202
D(19,2,16,39)	62,7482	D(30,10,11,32)	41,8758	D(17,18,22,41)	-175,0097
D(16,2,19,6)	5,978	D(10,11,12,8)	-36,3639	D(17,18,22,42)	-55,1544
D(16,2,19,17)	-173,8507	D(10,11,12,33)	-156,9475	D(17,18,22,43)	66,3257

D(50,3,17,18)	116,1846	D(10,11,12,34)	83,1183	D(23,18,22,41)	-54,1343
D(50,3,17,19)	-2,1398	D(31,11,12,8)	-158,7044	D(23,18,22,42)	65,721
D(50,3,17,20)	-120,3387	D(31,11,12,33)	80,712	D(23,18,22,43)	-172,7989
D(51,4,18,17)	87,5893	D(31,11,12,34)	-39,2223	D(4,18,23,44)	60,4099
D(51,4,18,22)	-153,1311	D(32,11,12,8)	79,5011	D(4,18,23,45)	-58,455
D(51,4,18,23)	-34,7139	D(32,11,12,33)	-41,0825	D(4,18,23,46)	-178,1839
D(52,5,20,17)	95,3723	D(32,11,12,34)	-161,0168	D(17,18,23,44)	-62,5319
D(52,5,20,24)	-37,0578	D(9,13,15,14)	-2,4788	D(17,18,23,45)	178,6031
D(52,5,20,40)	-154,3039	D(9,13,15,37)	176,9338	D(17,18,23,46)	58,8742
D(12,8,9,10)	3,1538	D(16,13,15,14)	178,3584	D(22,18,23,44)	177,1148
D(12,8,9,13)	131,7405	D(16,13,15,37)	-2,229	D(22,18,23,45)	58,2499
D(12,8,9,29)	-110,8922	D(9,13,16,2)	-34,3118	D(22,18,23,46)	-61,479
D(14,8,9,10)	-127,0152	D(9,13,16,38)	-155,1561	D(5,20,24,47)	-57,559
D(14,8,9,13)	1,5716	D(9,13,16,39)	84,0255	D(5,20,24,48)	-178,1757
D(14,8,9,29)	118,9389	D(15,13,16,2)	144,7308	D(5,20,24,49)	61,7288
D(9,8,12,11)	20,4841	D(15,13,16,38)	23,8864	D(17,20,24,47)	175,8877
D(9,8,12,33)	141,4956	D(15,13,16,39)	-96,932	D(17,20,24,48)	55,2711
D(9,8,12,34)	-98,2828	D(8,14,15,13)	3,3593	D(17,20,24,49)	-64,8245
D(14,8,12,11)	146,3056	D(8,14,15,37)	-176,0708	D(40,20,24,47)	56,7027
D(14,8,12,33)	-92,6829	D(35,14,15,13)	-116,9549	D(40,20,24,48)	-63,914
D(14,8,12,34)	27,5387	D(35,14,15,37)	63,615	D(40,20,24,49)	175,9905
D(9,8,14,15)	-2,8785	D(36,14,15,13)	124,0176	D(1,21,25,26)	166,4001
D(9,8,14,35)	117,5299	D(36,14,15,37)	-55,4126	D(1,21,25,27)	-15,391
D(9,8,14,36)	-123,3767	D(3,17,18,4)	-178,7229	D(7,21,25,26)	-12,0049
D(12,8,14,15)	-128,6647	D(3,17,18,22)	63,6284	D(7,21,25,27)	166,204
D(12,8,14,35)	-8,2563	D(3,17,18,23)	-56,7411	D(21,25,26,53)	-179,287
D(12,8,14,36)	110,8371	D(19,17,18,4)	-62,911	D(21,25,26,54)	59,9852
D(8,9,10,1)	89,2652	D(19,17,18,22)	179,4403	D(21,25,26,55)	-58,567
D(8,9,10,11)	-25,3709	D(19,17,18,23)	59,0708	D(27,25,26,53)	2,4009
D(8,9,10,30)	-147,9615	D(20,17,18,4)	64,3549	D(27,25,26,54)	-118,3269
D(13,9,10,1)	-28,6614	D(20,17,18,22)	-53,2938	D(27,25,26,55)	123,1209
D(13,9,10,11)	-143,2975	D(20,17,18,23)	-173,6633	D(21,25,27,28)	-0,4908
D(13,9,10,30)	94,1119	D(3,17,19,2)	-167,1485	D(21,25,27,56)	-179,7178
D(29,9,10,1)	-153,5459	D(3,17,19,6)	13,0218	D(26,25,27,28)	177,5918
D(29,9,10,11)	91,818	D(18,17,19,2)	77,1024	D(26,25,27,56)	-1,6353
D(29,9,10,30)	-30,7726	D(18,17,19,6)	-102,7273	D(25,27,28,57)	-13,4654
D(8,9,13,15)	0,567	D(20,17,19,2)	-52,6561	D(25,27,28,58)	107,5574
D(8,9,13,16)	179,7343	D(20,17,19,6)	127,5142	D(25,27,28,59)	-136,0911
D(10,9,13,15)	119,3895	D(3,17,20,5)	68,2752	D(56,27,28,57)	165,7692
D(10,9,13,16)	-61,4432	D(3,17,20,24)	-164,3751	D(56,27,28,58)	-73,208
D(29,9,13,15)	-117,4522	D(3,17,20,40)	-42,4775	D(56,27,28,59)	43,1435
D(29,9,13,16)	61,7151	D(18,17,20,5)	-174,1063		
D(1,10,11,12)	-80,4886	D(18,17,20,24)	-46,7566		

Molecular Docking

Molecular docking study of echimidine molecule was realized with AChE using Autodock Vina program. The binding profile and binding affinities of echimidine were determined. The best binding affinity was calculated as -8.5 kcal/mol and the binding interactions was provided by hydrogen bond, pi interactions, and van der Waals interactions (see Figure 2). Echimidine made weak hydrogen bonds (3.05 Å and 3.14 Å) and pi-alkyl interactions with Tyr-121 residue in the PAS region of AChE. Echimidine made a pi-sigma interaction with Tyr-279, another important residue in the PAS region. Trp-84, Phe-330 and Phe-331 residues on the anionic site are other residues that make pi-alkyl interactions with echimidine. Echimidine had a van der Waals interaction with the His-440 residue from the CAS region. As a result of molecular docking, van der Waals interactions were observed with Gly-118 and Gly-119, which are important residues in the oxyanion hole. In the binding profile where van der Waals interactions were dominant, other residues participating in the van der Waals interaction was Gly-335, Ile-287, Arg-289, Ser-122, Asn-85, Ser-81, Asp-72, Tyr-70, Phe-290 and Tyr-334. Additionally, echimidine made unfavorable donor-donor interaction with Phe-288 residue of AChE. The echimidine molecule interacted with most of the residues that Galantamine, used in Alzheimer's disease, interacts with in the active site of AChE [17]. Considering that the binding affinity value of Rivastigmine, a cholinesterase inhibitor, in the molecular docking study performed with AChE using Autodock Vina was -7.7 kcal/mol [18], the binding affinity obtained as a result of the molecular docking study of the Echimidine molecule with AChE had a lower value, and it was predicted that it could provide a strong binding profile. Additionally, considering that the AChE structure used is important for the docking result, a docking study was performed again for Rivastigmine with the prepared protein structure in this study. As a result of the study, it was determined that the binding affinity was again lower than echimidine.

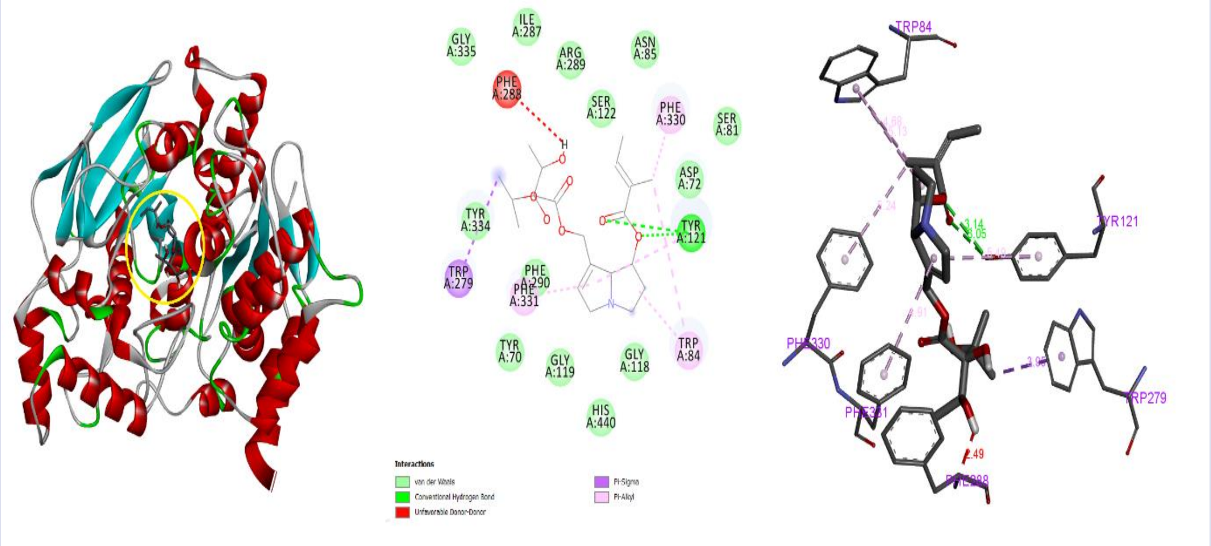

Figure 2. The molecular docking profile of echimidine at AChE active site

ADMET Analysis

Pharmacokinetic properties of echimidine were obtained by ADMET (absorption, distribution, metabolism, excretion, toxicity) analysis by using SwissADME and pkCSM servers, and tabulated in Table 4. It is stated that drug candidates that can be taken orally may violate at most 1 of the 4 criteria specified according to Lipinski's rules [19]. These 4 criteria are called the Lipinski's rule of five and consist of the principles that the molecular weight (MW) should not exceed 500 Daltons, the hydrogen bond donors (HBD) should not be greater than 5, the hydrogen bond acceptors (HBA) should not be greater than 10, and the octanol-water partition coefficient (logP) should not exceed 5. Apart from the Lipinski rule, other rules such as Ghose and Veber, which contain different rules, can also be evaluated for drug candidates. The Ghose filter indicates that the absorption rate will be high if the molecular weight, logP, molar refractivity and total number of atoms are within certain ranges [20, 21]. Veber's rule for oral bioavailability states that a drug should have fewer than 10 rotatable bonds and its polar surface area should not exceed 140 Å2 [22, 23]. Egan's rule states that polar surface area (PSA) and logP values must be within a certain range [24, 25]. The Muegge's rule selects even more specific ranges. The ranges of MW, LogP, PSA, number of rings, number of carbons, number of heteroatoms, rotatable bonds, HBD and HBA was stated by this rule [26]. According to SwissADME server results, it was determined that echimidine complies with all the rules. The results of echimidine showed poor BBB penetration and did not inhibit CYP450 enzymes according to the SwissADME server results. On the other hand, the molecule displayed optimum bioavailability scores and showed high GI absorption. P-glycoprotein, another prominent parameter in ADME estimation, is an important protein in the elimination of toxins and the absorption and disposition of the drug [27]. These substances that use the P-glycoprotein transporter for such activities are called p-glycoprotein substrates. In the prediction made according to the SwissADME server, echmidine was evaluated to be a P-gp substrate. When the skin permeability parameter was evaluated, it was predicted that echimidine had low skin permeability. When the echimidine molecule was evaluated using pkCSM server, it was determined that it was not mutagenic according to the AMES toxicity estimate, had no skin sensitization, and had no potential as a hERG I-II inhibitor in this study. However, it was evaluated in the toxicity prediction study that it should not be ignored that the molecule may have a hepatotoxic effect. It was observed that the prediction that echimidine, a pyrrolizidine alkaloid, may have a hepatotoxic effect is supported by literature studies [6, 28].

Table 4. Predicted ADMET properties of Echimidine.

Physicochemical Properties		**Lipophilicity**	
MW	397.46 g/mol	LogP$_{O/W}$(iLOGP)	3.43
No. of heavy atoms	28	LogP$_{O/W}$(XLOGP3)	0.74
No. rotatable bonds	9	LogP$_{O/W}$(WLOGP)	-0.08
No. of HBA	8	LogP$_{O/W}$(MLOGP)	0.30
No. of HBD	3	LogP$_{O/W}$(SILICOS-IT)	1.00
Polar surface area	116.53 Å²	Consensus LogPO/W	1.08
Water Solubility		**Pharmacokinetics**	
Log S (ESOL)	-2.18	GI absorption	High
Solubility	2.65e+00 mg/ml; 6.66e-03 mol/l	BBB permeant	No
Class	Soluble	P-gp substrate	Yes
Log S (Ali)	-2.77	CYP1A2 inhibitor	No
Solubility	6.81e-01 mg/ml; 1.71e-03 mol/l	CYP2C19 inhibitor	No
Class	Soluble	CYP2C9 inhibitor	No
Log S (SILICOS-IT)	-0.60	CYP2D6 inhibitor	No
Solubility	9.98e+01 mg/ml; 2.51e-01 mol/l	CYP3A4 inhibitor	No
Class	Soluble	Log K$_P$ (skin permeation)	-8.20 cm/s
Druglikeness		**Toxicity**	
Lipinski	Yes, 0 violation	AMES toxicity	No
Ghose	Yes	Max. tolerated dose (human)	0.37 (log mg/kg/day)
Veber	Yes	hERG I inhibitor	No
Egan	Yes	hERG II inhibitor	No
Muegge	Yes	Hepatotoxicity	Yes
Bioavailability Score	0.55	Skin Sensitisation	No

Conclusion

In this study, the structure of the echimidine molecule was elucidated for the first time, its interactions with AChE were examined in detail, and predictions regarding its pharmacokinetic properties and toxicity were provided. The three-dimensional structure of the echimidine molecule, which plays a role in AChE inhibition, was optimized, and the interaction profile of the optimized structure with AChE was elucidated by molecular docking study. The binding profile and binding affinity of echimidine with molecules with proven interactions with AChE, such as galantamine and rivastigmine, were compared. As a result of the studies, it was evaluated that Echimidine has similar binding points to Galantamine used in Alzheimer's disease and can provide a stronger binding than the binding affinity of rivastigmine, a cholinesterase inhibitor. Additionally, the ADMET profile of echimidine was examined and it was determined that it complied with Lipinski's rules and other druglikeness rules, but its hepatotoxicity should not be ignored. This study is a molecular modeling study on echimidine, and it is anticipated that the different properties of this molecule can be further elucidated through experimental studies.

.

Conflict of interest

There are no conflicts of interest in this work.

Acknowledgement

I would like to thank the editor and referees for their contributions to the review and evaluation of the manuscript.

References

[1] Debnath, B., Singh, W.S., Das, M., Goswami, S., Singh, M.K., Maiti, D., Manna, K., Role of plant alkaloids on human health: A review of biological activities, *Mater. Today Chem.*, 9 (2018) 56-72.

[2] Hussain, G., Rasul, A., Anwar, H., Aziz, N., Razzaq, A., Wei, W., Ali, M., Li, J., Li, X., Role of plant derived alkaloids and their mechanism in neurodegenerative disorders, *Int. J. Biol. Sci*., 14(3) (2018) 341.

[3] Ng, Y.P., T.C.T. Or, N.Y. Ip, Plant alkaloids as drug leads for Alzheimer's disease, *Neurochem. Int*., 89 (2015) 260-270.

[4] Račková, L., Májeková, M., Košťálová, D., Štefek, M., Antiradical and antioxidant activities of alkaloids isolated from Mahonia aquifolium. Structural aspects, *Bioorg. Med. Chem*., 12(17) (2004) 4709-4715.

[5] Rehman, S., Khan H., Advances in antioxidant potential of natural alkaloids, *Curr. Bioact. Compd*., 13(2) (2017) 101-108.

[6] Tamariz, J., Burgueño-Tapia, E., Vázquez, M. A., & Delgado, F., Pyrrolizidine alkaloids. *The alkaloids: chemistry and biology*, 80 (2018) 1-314.

[7] Allgaier, C., Franz S., Risk assessment on the use of herbal medicinal products containing pyrrolizidine alkaloids, Regul. Toxicol. *Pharmacol.,* 73(2) (2015) 494-500.

[8] Wang, W., Jin, J., Xu, H., Shi, Y., Boersch, M., Yin, Y., Comparative analysis of the main medicinal substances and applications of Echium vulgare L. and Echium plantagineum L.: A review, *J. Ethnopharmacol*., 285 (2022) 114894.

[9] Wei, X., Ruan W., Vrieling K., Current knowledge and perspectives of pyrrolizidine alkaloids in pharmacological applications: A mini-review, *Mol*., 26(7) (2021) 1970.

[10] Schmeller, T., El-Shazly A., Wink M., Allelochemical activities of pyrrolizidine alkaloids: interactions with neuroreceptors and acetylcholine related enzymes, *J. Chem. Ecol*., 23 (1997) 399-416.

[11] Frisch, M., et al., Gaussian 09, Revision A. 1. Gaussian Inc., Wallingford. CT., (2009).

[12] Raves, M.L., Harel, M., Pang, Y. P., Silman, I., Kozikowski, A.P., & Sussman, J.L., Structure of acetylcholinesterase complexed with the nootropic alkaloid,(–)-huperzine *A, Nat. Struct. Mol. Biol.,* 4(1) (1997) 57-63.

[13] Trott, O., Olson A.J., AutoDock Vina: improving the speed and accuracy of docking with a new scoring function, efficient optimization, and multithreading, *J. Comput. Chem.*, 31(2) (2010) 455-461.

[14] Biovia, D.S., Discovery studio. Dassault Systèmes BIOVIA, (2016).

[15] Daina, A., Michielin O., Zoete V., SwissADME: a free web tool to evaluate pharmacokinetics, drug-likeness and medicinal chemistry friendliness of small molecules, *Sci. Rep.*, 7(1) (2017) 42717.

[16] Pires, D.E., Blundell T.L., Ascher D.B., pkCSM: predicting small-molecule pharmacokinetic and toxicity properties using graph-based signatures, *J. Med. Chem*., 58(9) (2015) 4066-4072.

[17] Haroon, M., Khalid, M., Shahzadi, K., Akhtar, T., Saba, S., Rafique, J., ... & Imran, M., Alkyl 2-(2-(arylidene) alkylhydrazinyl) thiazole-4-carboxylates: Synthesis, acetyl cholinesterase inhibition and docking studies, *J. Mol. Struct*., 1245 (2021) 131063.

[18] Ali, M.R., Sadoqi, M., Møller, S.G., Boutajangout, A., Mezei, M., Assessing the binding of cholinesterase inhibitors by docking and molecular dynamics studies, *J. Mol. Graph. Model*., 76 (2017) 36-42.

[19] Lipinski, C.A., Lead-and drug-like compounds: the rule-of-five revolution, Drug Discov. *Today Technol*., 1(4) (2004) 337-341.

[20] Ghose, A.K., Viswanadhan V.N., Wendoloski J.J., A knowledge-based approach in designing combinatorial or medicinal chemistry libraries for drug discovery. 1. A qualitative and quantitative characterization of known drug databases, *J. Comb. Chem*., 1(1) (1999) 55-68.

[21] Vélez, L.A., Delgado, Y., Ferrer-Acosta, Y., Suárez-Arroyo, I.J., Rodríguez, P., & Pérez, D., Theoretical Calculations and Analysis Method of the Physicochemical Properties of Phytochemicals to Predict Gastrointestinal Absorption, (2022).

[22] Abouzied, A.S., Break, M., Huwaimel, B., Hussein, W., Alafnan, A., Younes, K., ... & Abouzied, A., Discovery of a novel synthetic thiazole-benzimidazole conjugate that acts as a potent pancreatic lipase inhibitor using in silico and in vitro approaches, *Indian J. Pharm. Educ. Res*, 57(1) (2023) 218-227.

[23] Vlad, I.M., Nuta, D.C., Chirita, C., Caproiu, M.T., Draghici, C., Dumitrascu, F., ... & Limban, C., In Silico and In Vitro Experimental Studies of New Dibenz [b, e] oxepin-11 (6 H) one O-(arylcarbamoyl)-oximes Designed as Potential Antimicrobial Agents, *Mol.,* 25(2) (2020) 321.

[24] Craciun, D., Modra D., Isvoran A., ADME-Tox profiles of some food additives and pesticides, in AIP Conference Proceedings. (2015).

[25] Egan, W.J., Merz K.M., Baldwin J.J., Prediction of drug absorption using multivariate statistics, *J. Med. Chem*., 43(21) (2000) 3867-3877.

[26] Muegge, I., Heald S.L., Brittelli D., Simple selection criteria for drug-like chemical matter, *J. Med. Chem*., 44(12) (2001) 1841-1846.

[27] Lin, J.H., Yamazaki M., Role of P-glycoprotein in pharmacokinetics: clinical implications, *Clin. Pharmacokinet*., 42 (2003) 59-98.

[28] Smith, L., Culvenor C., Plant sources of hepatotoxic pyrrolizidine alkaloids, *J. Nat. Prod*., 44(2) (1981) 129-152.

Cumhuriyet Sci. J., 45(4) (2024) 598-603
DOI: https://doi.org/10.17776/csj.1482632

Cumhuriyet Science Journal

| csj.cumhuriyet.edu.tr | Founded: 2002 ISSN: 2587-2680 e-ISSN: 2587-246X Publisher: Sivas Cumhuriyet University

Production of GeOx Films at Different Oxygen Flow Rates and Different Annealing Temperatures and Examination of Energy Band Gaps using Kubelka Munk Method

Ayfer Özdemir[1,a], Şahide Gülizar Kızıl[1,b], Ebru Şenadım Tüzemen[1,2,c*]

[1] *Department of Physics, Faculty of Science, Sivas Cumhuriyet University, Sivas, Türkiye.*
[2] *Nanophotonics Research and Application Center, Sivas Cumhuriyet University, Sivas, Türkiye.*
**Corresponding author*

Research Article

History
Received: 12/05/2024
Accepted: 21/08/2024

ABSTRACT

In this study, GeO_x films were grown on silicon substrates using the Radio Frequency (RF) Magnetron Sputtering method at different oxygen flow rates and annealing temperatures. The films were produced at a substrate temperature of 250°C and a working pressure of 13 mTorr. Subsequently, the films were annealed at temperatures of 300°C, 500°C, 600°C, 700°C, 900°C, and 1000°C. Total and diffuse reflection measurements were performed to investigate the optical properties of the films. Energy band gaps were determined using diffuse reflection measurements and they were calculated using the Kubelka-Munk method. It was observed that the energy band gap increased with increasing oxygen ratio. Additionally, annealing temperatures were found to cause changes in the energy band gaps.

Keywords: GeO_2, Reflectance, RF Magnetron.

[a] *ayferozdmrr1@gmail.com* *https://orcid.org/0009-0007-4573-5587*
[b] *sahidegulizarkizil@gmail.com* *https://orcid.org/0009-0003-1910-3659*
[a] *esenadim@cumhuriyet.edu.tr* *https://orcid.org/0000-0001-9166-7422*

Introduction

Due to its small difference between indirect and direct bandgap, high carrier mobility, and strong photon absorption, Germanium's optical properties are highly attractive compared to other semiconductors [1]. Furthermore, its large exciton Bohr radius, lower bandgap, and smaller effective carrier mass [2], along with its unique energy bandgap structure, make it appealing for scientific research and open up new possibilities for next-generation applications [3]. However, electronic devices based on narrow bandgap materials suffer from being unsuitable for operating at high temperatures and having high power consumption during processing [4]. The high processing cost and chemical instability of pure semiconductors also limit their application areas [5].

Therefore, in recent years, the production and engineering of semiconductor oxide materials at the nano scale have gained significant importance due to their exceptional physical and chemical properties and have attracted great interest due to their potential applications in modern nano-scale electronic and optical devices. Among various semiconductor oxides, Germanium oxide (GeO_2) is a promising material exhibiting interesting properties such as high transparency, wide energy bandgap (> 5 eV), good mechanical strength, high dielectric constant, high thermal stability, high carrier concentration, and refractive index [6,9]. The unique properties of crystalline GeO_2 make it suitable for optoelectronic and memory applications [8, 10-12]. Additionally, GeO_2 finds various uses in optical applications such as infrared lenses, prisms, spectroscopy devices, electronic memory devices [13], fiber optics [14], piezoelectric material [15,16], and potential anode materials for high-energy Li-ion batteries [17,18]. Apart from these, GeO_2 is used as the main material in devices emitting photoluminescence emission in the visible region [10]. However, the technological importance of films in optical fields strongly depends on quality and structural properties that can be adjusted with varying growth conditions and growth parameters [19,20].

In recent years, various techniques have been developed for the growth of GeO_2 thin films, including the sol-gel technique [21], hydrothermal technique at different synthesis pressures and temperatures [22], electron beam evaporation [23], RF and DC magnetron sputtering [24,25], and pulsed laser deposition (PLD) technique [26]. Yin and Garside [27] produced GeO_2 thin films through radio frequency (RF) sputtering and reactive direct current (DC) sputtering. In both techniques, high deposition rates were achieved. Valligatla et al. prepared GeO_2 planar waveguides on v-SiO_2 substrates using an RF magnetron sputtering system with GeO_2 target, applying 80 W rf power at a pressure of 5.4×10^{-3} mbar with Ar gas, and then annealed with a pulsed CO2 laser. They examined the effects of this annealing on the optical and structural properties of the produced material using m-line and micro-Raman spectroscopy and AFM measurements. When they looked at the Raman spectroscopy and AFM results after pulsed CO2 laser annealing [28], they found that the materials produced showed a crystalline environment that changed with the varying irradiation time. Xie et al. [29] grew GeO_2 with a thickness of 300 nm on n-type Ge (100) using radio frequency magnetron sputtering method with a GeO_2

target in Ar/O_2 at a base pressure of 6×10^{-6} Pa at room temperature. Chiasera et al. [30] grew GeO_2 planar waveguides on a silica substrate of size 7.5 × 2.5 cm under an Ar atmosphere at a pressure of 5.4×10^{-3} mbar using the Radio Frequency Sputtering (RFS) technique with 80 W RF power and then annealed with a pulsed CO2 laser.

The aim of this study is to optimize the performance of germanium dioxide (GeO_2) annealed at different temperatures and produced at different oxygen flow rates by examining its optical properties. Understanding the effects of annealing temperature and oxygen flow rates on the energy band gap of GeO_2 in detail is critical to increase the efficiency of the material in various high-tech applications. Our motivation for this study is the increasing importance of GeO_2, especially in optoelectronic and sensor technologies. However, studies on the properties of GeO_2 produced by RF magnetron sputtering at different annealing temperatures and different oxygen flow rates are limited in the current literature. This research was carried out to address this deficiency and to maximize the potential of GeO_2 in applications. In our study, the effects of changes in the optical properties resulting from the annealing of GeO_2 at different temperatures and different oxygen flow rates were comprehensively analyzed. In addition, this study provides valuable information for future research and applications by revealing the effects of different annealing temperatures and different oxygen flow rates on the performance of GeO_2 in detail.

Materials and Methods

In this study, GeO_x films were produced on silicon using the RF magnetron sputtering method. The NANOVAK NVTS-400 Thermal and Sputter combined system was utilized to fabricate the films. Germanium with a purity of 99.999% was used as the target material, and GeO_x thin films with different oxygen ratios of 7%, 8%, and 9% were obtained. The films were produced at a substrate temperature of 250°C, with a rotation speed of 10 rpm, a power of 100 W, a growth rate of 0.4-0.6 Å/s, and a working pressure of 13 mTorr.

Subsequently, the films were annealed at temperatures of 300°C, 500°C, 600°C, 700°C, 900°C, and 1000°C. Reflection measurements for the optical study of the GeO_x semiconductor films, produced under different growth conditions on silicon substrates, were performed using a Cary 5000 UV-VIS-NIR Optical spectrophotometer. Total and diffuse reflection measurements were taken in the wavelength range of 250-800 nm using the spectrophotometer. The diffuse reflection measurements allowed us to determine the energy band gap.

Result and Discussion

Figure 1 (a, b, c) shows the total reflection measurements of the films produced at three different oxygen ratios and annealed at different temperatures.

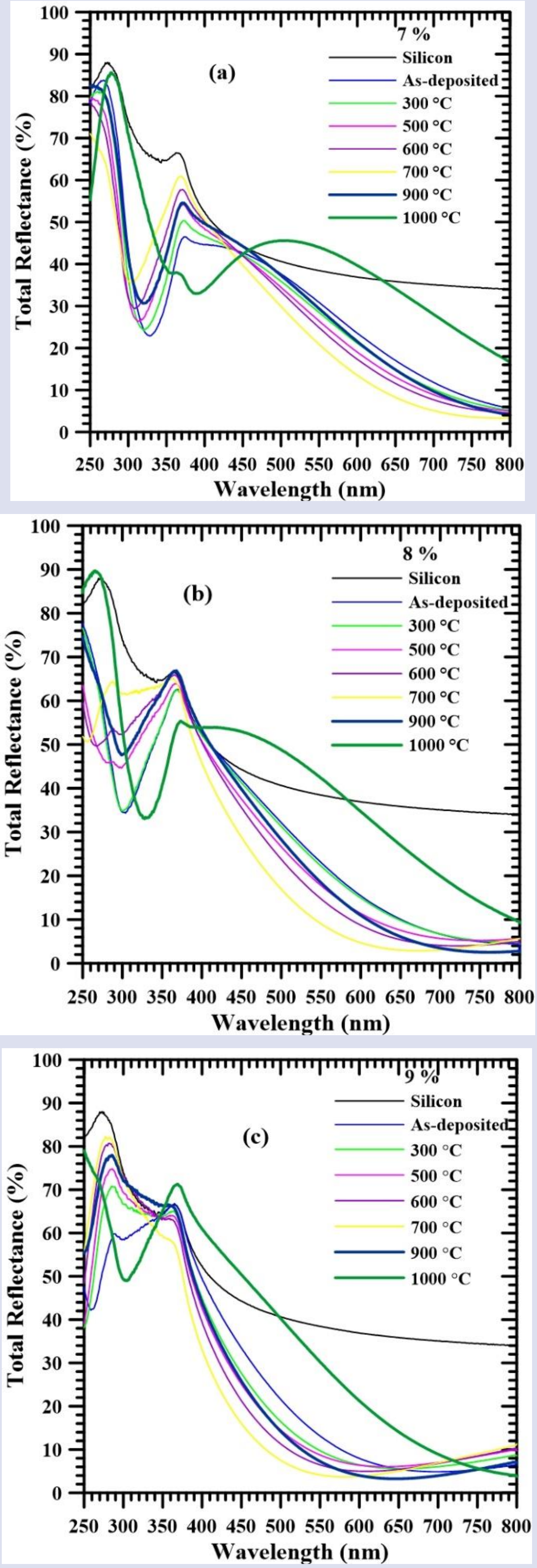

Figure 1. Variation of total reflectance as a function of wavelength **(a)** 7% oxygen flow **(b)** 8% oxygen flow **(c)** 9% oxygen flow.

It has been observed that there is a shift towards shorter wavelengths in thin films with oxygen ratios of 7% and 8% up to 700°C, followed by an increase again. In the case of the thin film with a 9% oxygen ratio, there is a shift towards shorter wavelengths up to 600°C, followed by an increase. After 600°C, it can be said that the surface properties of the film have changed. Films produced with different oxygen percentages were annealed at different annealing temperatures and as annealing increased, total reflection first increased and then decreased. The decrease in reflection with annealing is thought to be related to the removal of defects. Accordingly, the energy band gap first increased and then decreased. It was observed that the energy band gap first increased and then decreased with the increase in annealing temperature. The shift in the energy band gap is generally related to oxygen deficiencies in the crystal phase.

The graphs of diffuse reflection measurements are provided in Figure 2. When examining the graphs, it is observed that as the temperature increases in the ultraviolet region, the diffuse reflection also increases. Although there is a gradual decrease in diffuse reflection after 700°C for thin films with oxygen ratios of 7% and 8%, a decrease is observed after 600°C for the film with a 9% oxygen ratio. The energy band gap of the produced thin films was determined using diffuse reflection measurements. For this purpose, the Kubelka-Munk method was employed [31]. The diffuse reflection of the film is related to the Kubelka-Munk function denoted as F(R). Calculation of the reflection data is performed using the Kubelka-Munk method as follows:

$$F(R)=\frac{(1-R)^2}{2R} \qquad (1)$$

This equation relates the film's diffuse reflection (R) to the Kubelka-Munk function (F(R)). From here, graphs of $(F(R)\times E)^2$ are plotted against energy to determine the energy band gap. In the Cary 5000 device, there is a transition from the Deuterium lamp to the halogen lamp at a wavelength of 350 nm. Therefore, the fluctuations seen in Figure 3 (b) have occurred.

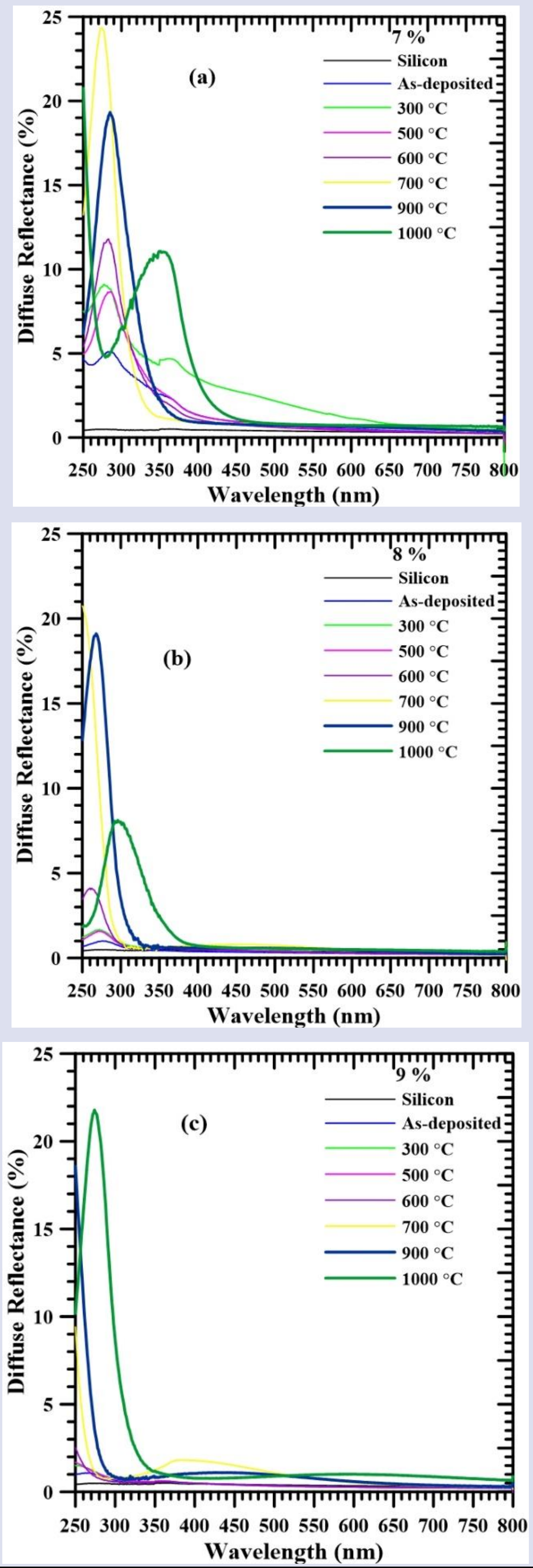

Figure 2. Variation of diffuse reflectance as a function of wavelength **(a)** 7% oxygen flow **(b)** 8% oxygen flow **(c)** 9% oxygen flow

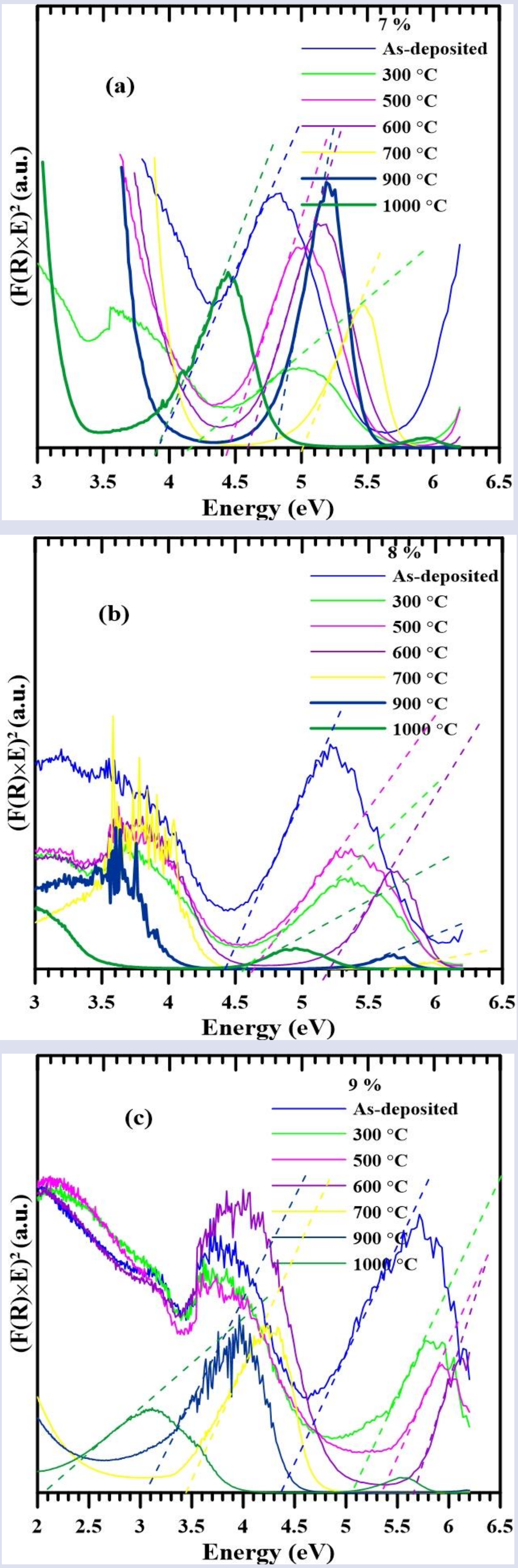

Figure 3. Variation of $(F(R)\times E)^2$ of the film with 7% oxygen content according to energy **(b)** Variation of $(F(R)\times E)^2$ of the film with 8% oxygen content according to energy **(c)** Variation of $(F(R)\times E)^2$ of the film with 9% oxygen content according to energy

In Figure 3 (a), tangents are drawn at the absorption edges based on the first peaks (absorption edge). The points where these tangents intersect the x-axis provide the energy band gap. It is observed that the energy band gap increases up to 600°C. The highest increase in the energy band gap is also observed at 700°C. After this temperature, a decrease in the energy band gap is observed. It has been visually observed that the color of the films changes after 700°C. As seen in Figure 4, the energy band gap of the as-annealed samples with a substrate temperature of 250°C varied with increasing oxygen flow. Up to annealing temperatures of 300°C, 500°C, and 600°C, the energy band gap of all three samples increased. However, at higher temperatures the energy band gap decreased. When comparing films produced at 7% and 8% oxygen ratios, there was no decrease in the energy band gaps. However, for the film produced at a 9% oxygen ratio, a decrease was observed after 600°C.

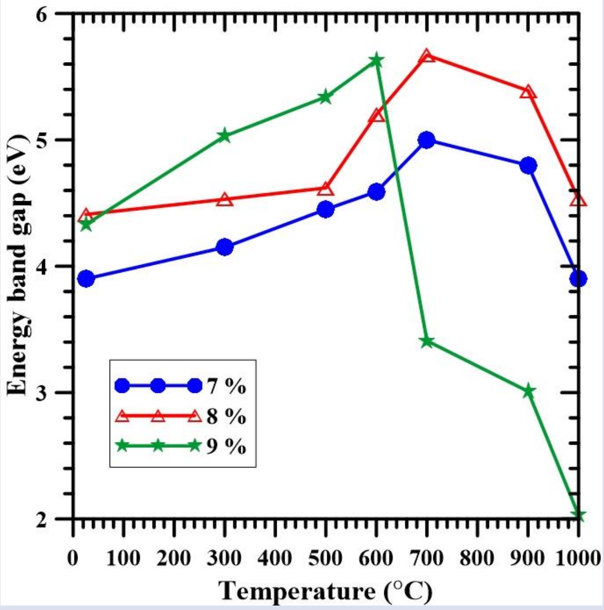

Figüre 4. Energy Band Gaps of Thin Films Produced at 7%, 8%, and 9% Oxygen Ratios

This is because the produced film maintains its structure up to a certain temperature. After a certain value of the annealing temperature, there may be a decrease in the band gap values, a decrease in the number of oxygen vacancies and/or defects that may be grain boundaries. This leads to a decrease in the carrier concentration in the conduction band of the material. At the same time, the annealing process improves crystallinity and increases the average grain size. Ultimately, this results in the reduction of defects. It reduces the tension in films. As a result, high-temperature annealing improves the crystal structure of the material and increases the ordering at the atomic level. This can cause a narrowing of the energy band gap. This change is related to the crystallization and defect correction that occurs during the annealing process [32,33,34].

Conclusion

GeO_x films produced on silicon substrates with different oxygen percentages were successfully produced by the RF magnetron sputtering method at different annealing temperatures. It has been observed that there is a shift towards shorter wavelengths in thin films with oxygen ratios of 7% and 8% up to 700°C, followed by an increase again. In the case of the thin film with a 9% oxygen ratio, there is a shift towards shorter wavelengths up to 600°C, followed by an increase. It is observed that the energy band gap increases up to 600°C. The highest increase in the energy band gap with a 7% oxygen ratio is also observed at 700°C. After this temperature, a decrease in the energy band gap is observed. For the film produced at a 9% oxygen ratio, a decrease was observed after 600°C. This is because the produced film maintains its structure up to a certain temperature.

Acknowledgement

This study is supported by TÜBİTAK 2209-A University Students Research Projects, No. 2209-A Tübitak-1919B012108759.

Conflicts of interest

There are no conflicts of interest in this work.

References

[1] Manna S., Katiyar A., Aluguri R., Ray S. K., Temperature dependent photoluminescence and electroluminescence characteristics of core-shell Ge–GeO_2 nanowires, *Journal of Physics D: Applied Physics*, 48 (2015) 215103.

[2] Rao N. S., Pathak A. P., Sathish N., Devaraju G., Saikiran V., Kulriya P. K., Agarwal D. C., Synthesis of Ge nanocrystals by atom beam sputtering and subsequent rapid thermal annealing, *Solid State Communications*, 150 (2010) 2122-2126.

[3] Bruno E., Scapellato G. G., Napolitani E., Mirabella S., Boninelli S., LaMagna A., Mastromatteo M., Salvador D. D., Fortunato G., Privitera V., Priolo F., Challenges and Opportunities for Doping Control in Ge for Micro and Optoelectronics Applications, *ECS Transactions*, 50 (5) (2013) 89.

[4] Rivera M., Velázquez R., Aldalbahi A., Zhou A. F., Feng P., High Operating Temperature and Low Power Consumption Boron Nitride Nanosheets Based Broadband UV Photodetector, *Scientific Reports*, 7 (2017) 42973.

[5] Hwang J., Jo C., Kim M. G., Chun J., Lim E., Kim S., Jeong S., Kim Y., Lee J., Mesoporous Ge/GeO_2/Carbon Lithium-Ion Battery Anodes with High Capacity and High Reversibility, *ACS Nano*, 9 (2015) 5299–5309.

[6] Murphy N. R., Grant J. T., Sun L., Jones J. G., Jakubiak R., Shutthanandan V., Ramana C. V., Correlation between optical properties and chemical composition of sputter-deposited germanium oxide (GeO_x) films, *Opt. Mater.*, 36 (2014) 1177-1182.

[7] Ramana C. V., Troitskaia I. B., Gromilov S. A., Atuchin V. V., Electrical properties of germanium oxide with α-quartz structure prepared by chemical precipitation, *Ceram. Int.*, 38 (2012) 5251-5255.

[8] Chiasera A., Macchi C., Mariazzi S., Valligatla S., Lunelli L., Pederzolli C., Rao D. N., Somoza A., Brusa R. S., Ferrari M., CO_2 Laser irradiation of GeO_2 planar waveguide fabricated by rf-sputtering, *Opt. Mater. Express*, 3 (2013) 1561-1570.

[9] Miller J. W., Chesaux M., Deligiannis D., Mascher P., Bradley J. D. B., Low-loss GeO_2thin films deposited by ion-assisted alternating current reactive sputtering for waveguide applications, *Thin Solid Films*, 709 (2020) 138165.

[10] Peng M., Li Y., Gao J., Zhang D., Jiang Z., Sun X., Electronic Structure and Photoluminescence Origin of Single-Crystalline Germanium Oxide Nanowires with Green Light Emission, *J. Phys. Chem. C*, 115 (2011) 11420-11426.

[11] Kim H. W., Shim S. H., Lee J. W., Cone-shaped structures of GeO_2 fabricated by a thermal evaporation process, *Appl. Surf. Sci.*, 253 (2007) 7207-7210.

[12] Hernández A. G., Escobosa-Echavarría A. E., Kudriavtsev Y., White luminescence emission from silicon implanted germanium, *Appl. Surf. Sci.*, 428 (2018) 1098-1105.

[13] Feng J., Hu W., Zeng F., Lin H., Li L., Yang B., Peng Y., Wu D., Huo B., Tang X., Investigation of physically transient resistive switching memory based on GeO_2 thin films, *Appl. Phys. Lett.*, 117 (2020) 192102.

[14] Sakaguchi S., Todoroki S., Optical properties of GeO_2 glass and optical fibers, *Applied Optics*, 36(27) (1997) 6809-6814.

[15] Armand P., Lignie A., Beaurain M., Papet P., Flux-Grown Piezoelectric Materials: Application to α-Quartz Analogues, *Crystals*, 4 (2014) 168-189.

[16] Balitskii D. B., Sil O. Y., Balitskii V. S., Pisarevskii Y. V, Pushcharovskii D. Y., Philippot E., Elastic, Piezoelectric, and Dielectric Properties of a-GeO2 Single Crystals, *Crystallography Reports*, 45(1) (2000) 145-147.

[17] Lin Y. M., Klavetter K. C., Heller A., Mullins C. B., Storage of Lithium in Hydrothermally Synthesized GeO_2 Nanoparticles, *J. Phys. Chem. Lett.*, 4 (2013) 999-1004.

[18] Wang X. L., Han W. Q., Chen H., Bai J., Tyson T. A., Yu X. Q., Wang X.J., Yang X. Q., Amorphous Hierarchical Porous GeO_x as High-Capacity Anodes for Li Ion Batteries with Very Long Cycling Life, *Journal of American Chemical Society*, 133 (2011) 20692-20695.

[19] Ramana C. V., Carbajal-Franco G., Vemuri R. S., Troitskaia I. B., Gromilov S. A., Atuchin V. V., Optical properties and thermal stability of germanium oxide (GeO_2) nanocrystals with α-quartz structure, *Mater. Sci. Eng. B Solid-State Mater. Adv. Technol.*, 174 (2010) 279-284.

[20] Afonso C. N., Gonzalo J., Pulsed laser deposition of thin films for optical applications, *Nucl. Instruments Methods Phys. Res. B.*, 116 (1996) 404-409.

[21] Jang J. H., Koo J., Bae B., Fabrication and Ultraviolet Absorption of Sol–Gel-Derived Germanium Oxide Glass Thin Films, *J. Am. Ceram. Soc.*, 83 (2000) 1356-1360.

[22] Bose N., Basu M., Mukherjee S., Study of optical properties of GeO_2 nanocrystals as synthesized by hydrothermal technique, *Mater. Res. Bull.*, 47 (2012) 1368-1373.

[23] Ardyanian M., Rinnert H., Devaux X., Vergnat M., Structure and photoluminescence properties of evaporated $GeOx$ thin films, *Appl. Phys. Lett.*, 89 (2006) 011902.

[24] Lange T., Njoroge W., Weis H., Beckers M., Wuttig M., Physical properties of thin GeO_2 films produced by reactive DC magnetron sputtering, *Thin Solid Films*, 365 (2000) 82-89.

[25] Yin Z.Y., Garside B. K., Low-loss GeO_2 optical waveguide fabrication using low deposition rate rf sputtering, *Appl. Opt.*, 21 (1982) 4324–4328.

[26] Wolf P.J., Christensen T.M., Coit N. G., Swinford R. W., Seiler F. J., Thin film properties of germanium oxide synthesized by pulsed laser sputtering in vacuum and oxygen environments, *J. Vac. Sci. Technol. A.*, 11 (1993) 2725-2732.

[27] Yin Z., Garside B. K., Low-loss GeO_2 optical waveguide fabrication using low deposition rate rf sputtering, *Appl. Opt.*, 21 (1982) 4324-4328.

[28] Chiasera A., Macchi C., Mariazzi S., Valligatla S., Lunelli L., Pederzolli C., Rao D.N., Somoza A., Brusa R. S., Ferrari M., CO2 Laser irraation of GeO 2 planar waveguide fabricated by rf-sputtering, *Optical Materials Express*, 3(9) (2013) 1561-1570.

[29] Xie M., Nishimura T., Yajima T., Toriumi A., Reaction of GeO_2 with Ge and crystallization of GeO_2 on Ge, *J. Appl. Phys.*, 127 (2020) 024101.

[30] Chiasera A., Macchi C., Mariazzi S., Valligatla S., Varas S., Mazzola M., Bazzanella N., Lunelli L., Pederzolli C., Rao D.N., Righini G.C., Somoza A., Brusa R. S., Ferrari M., Proceedings Volume 8982, *Optical Components and Materials XI*; 89820D (2014).

[31] Baghdedi D., Hopoğlu H., Sarıtaş S., Demir İ., Altuntaş İ., Abdelmoula N., Gür E., Şenadım Tüzemen E., Comprehensive growth and characterization study of GeO_x/Si, *Journal of Molecular Structure*, 1274 (2023) 134398.

[32] Sahu D. R., Parija S., Biswas S. K., Influence of annealing temperature on the structural and optical properties of ZnO thin films prepared by sol–gel method, *Cryst. Res. Technol.*, 44 (2009) 186–192.

[33] Oba E., Sartori S. A., Zaghete M. A., Effects of annealing on the structural and optical properties of TiO_2 thin films, *Materials Letters*, 65 (2011) 588-590.

[34] El-Nahass M. M., Zeyada H. M., Farag A. A. M., Optical constants and dispersion parameters of thermally evaporated cadmium sulfide thin films: Effects of annealing, *Physica B: Condensed Matter*, 405 (2010) 1339-1347.

Cumhuriyet Sci. J., 45(4) (2024) 604-608
DOI: https://doi.org/10.17776/csj.1510611

Cumhuriyet Science Journal

| csj.cumhuriyet.edu.tr | Founded: 2002 ISSN: 2587-2680 e-ISSN: 2587-246X Publisher: Sivas Cumhuriyet University

Employing Virial Coefficients for Optimal Solutions in Variational Calculations

Mahmut Özgür Sezer [1,a,*]

[1] *Department of Physics, Science Faculty, Selcuk University, Konya, Türkiye.*
**Corresponding author*

Research Article

History
Received: 04/07/2024
Accepted: 03/09/2024

ABSTRACT

In this study, virial coefficients for one and two-electron hydrogen and helium-like quantum dot structures confined in an infinite potential well were calculated. The virial coefficients were determined based on the dot radius using the Quantum Genetic Algorithm (QGA) method. Calculations were performed using Fernandez's expression; however, due to calculation errors in confined systems, this equivalent expression was found unsuitable as a direct stopping criterion. Instead, virial coefficients were calculated using the ⟨T⟩/⟨V⟩ relationship, and the results were plotted. The fitting function obtained for the virial coefficients is proposed as an effective cutoff criterion for electronic structure calculations of quantum dot systems.

Keywords: Quantum Genetic Algorithm (QGA)**,** Variational calculations, Virial coefficients, Quantum dots.

[a] *msezer@selcuk.edu.tr* *https://orcid.org/0000-0002-8415-8440*

Introduction

There are many studies on quantum structures confined to various confining potentials for a long time [1-3]. Specifically, it is possible to calculate a various physical parameters including the optical properties of the dot structures, the states both with and without the influence of external electric and magnetic fields , and the transitions between these states [4-5]. Most of the calculations made have been used methods based on energy minimization and the calculations involve many iterations [6]. However, in order to ensure that precise and reliable results are obtained in iterative calculations, a termination criterion is needed to know where to stop the iteration. It is possible to reach the solution of such problems with the help of the virial Theorem, which was first formulated in classical mechanics and later found applications in quantum mechanics. The virial coefficient obtained from the virial theorem can be used as a cut off parameter in calculations based on the minimization of energy for any quantum system in a bound state.

The virial theorem, a fundamental concept in theoretical physics and astrophysics, plays a crucial role in understanding the dynamics of many-particle systems. Lord Rayleigh, a prominent physicist, published a generalized version of the virial theorem concerning gas pressure [7]. This theorem establishes an equality between the average total kinetic and potential energies of systems with many particles, providing insight into the energy transformations and formation processes of complex systems [8-11].

Cottrell and Paterson derived a version of the virial theorem in quantum mechanics, specifically for a particle system confined within a box. [12].

$$2\bar{T} - \overline{\sum_j \boldsymbol{r}_j . \nabla_j V} + \alpha \frac{\partial E}{\partial \alpha} = 0$$

Parker's formulation of the tensor form of the virial theorem [13] is regarded as a pioneering application of this theorem. Moreover, the virial theorem facilitates intricate calculations in statistical mechanics, such as those involving the proportionality theorem and temperature calculations based on average total kinetic energy. In astrophysics, it assists in determining the internal temperature, mass, radius, and stability of stars. Additionally, it provides insights into systems that exhibit temperature independence and are not in thermal equilibrium.

In 1964, William G. Hoover and Francis H. Ree presented a comprehensive combinatorial approach to star integrals, enabling the precise calculation of the first five virial coefficients for gases composed of rigid parallel squares and cubes with attractive forces [14].

A trial wave function uniformly expands all its coordinate vectors from a specific origin by a certain scale factor, aiming to better align with the actual spatial domain occupied by the system. By treating the scale factor as a variable parameter, the variational principle can be used to derive the virial theorem. In equilibrium or with fixed nuclei, the virial theorem has demonstrated its applicability for any normalized trial function through an appropriate choice of the scale factor. Therefore, satisfying the virial theorem is necessary but not sufficient to confirm that a wave function is an exact solution to the Schrödinger equation. By considering the first derivative of energy with respect to any parameter, a general form of the Hellmann-Feynman theorem is obtained. Using Ritz's variational method to solve the Schrödinger equation allows one to derive not only the energy for each state but also its derivative with respect to the scale factor. While scale factors can be independently varied for states with different symmetry types, scaling becomes more complex for states sharing the same symmetry.

Fernandez et al. [15,16] conducted research on applying the virial theorem to confined systems. These studies propose modifications to the formulation of the virial theorem, taking into account its relationship with boundary conditions. Mukhopadhyay and Bhattacharya [17] derived the accurate modified form of the virial theorem for bounded systems. Demir and colleagues [18] computed the virial coefficients for He and Li atoms confined within infinite spherical potentials, as defined for free atoms.

In this study, virial coefficients were calculated for H and He type quantum dot structures with one and two electrons confined to infinite potential. It has been suggested that virial coefficients can be used as a cut-off criterion to stop the iteration in electronic structure calculations of quantum dots performed with variational methods.

Theory

Where H is the time-independent Hamiltonian and ψ is state function of the system, the Schrödinder equation of the system is as follows,

$$\hat{H}\psi = E\psi. \tag{1}$$

If the operatör $\hat{A}$ is a linear and time-independent operator as below,

$$\hat{A} = \sum_i \hat{q}_i\hat{p}_i = -i\hbar\sum_i q_i\frac{\partial}{\partial q_i}, \tag{2}$$

Where the sum is over on 3n coordinates of n particles and then

$$\int \psi[\hat{H},\hat{A}]\psi d\tau = 0 \qquad (3)$$

can be written and, is known as hypervirial theorem [19]. The commutation of $\hat{A}$ ve $\hat{H}$ is,

$$\left[\hat{H},\sum_i \hat{q}_i\hat{p}_i\right] = i\hbar\sum_i q_i\frac{\partial\hat{V}}{\partial q_i} - 2i\hbar\hat{T} = 0. \tag{4}$$

Here, $\hat{T}$ and $\hat{V}$ are kinetic and potential energy operators, respectiveliy and,

$$\left\langle \sum_i q_i\frac{\partial\hat{V}}{dq_i}\right\rangle = 2\langle T\rangle \tag{5}$$

is written. Where bra-ket represents to quantum mechanical averages.This equation is known as the quantum mechanical virial theorem for bound states. If there is a confining potential surrounding system and R is the dot Radius then Eq. 5 is written as follows [20].

$$\left\langle \sum_i q_i\frac{\partial\hat{V}}{dq_i}\right\rangle = 2\langle T\rangle + r\frac{\partial E}{\partial r_0} \tag{6}$$

Materials and Methods

For one electron system with an impurity confined infinite potential, Hamiltonian in given Eq.1 can be written as follow,

$$\hat{H} = -\frac{\hbar^2}{2m^*}\nabla^2 - \frac{Ze^2}{\varepsilon r} + V_c(\vec{r}) \tag{7}$$

where Z is the impurity charge, m^* is the effective mass and ε is the dielectric constant of the medium. The confining potential V_c is,

$$V_c(\vec{r}) = \begin{cases} 0, & r < R \\ \infty, & r \geq R \end{cases} \tag{8}$$

If Hamiltonien in Eq.7 is submitted in Eq.1 the energy and state function of the system can be computed from Schrödinger equations. In this case, state function of the system is one-electron wave fuction $\emptyset_{nlm}$. where nlm is the quantum numbers of the state function, this function can be written as linear combination of Slater-type orbital as follows,

$$\phi_p = \sum_{k=1}^{\sigma} c_{pk}\chi_k(\zeta_k,\vec{r}) \tag{9}$$

Where $k \to nlm$, σ is size of the basis set, c_{pk} is the expansion coefficients and ζ_k is screening constant. Unnormalized complex STOs $\chi_k(\zeta_k,\vec{r})$ are as follows

$$\chi_k(\zeta_k,\vec{r}) = r^{n-1}e^{-\zeta r}Y_{\ell m}(\theta,\varphi) \tag{10}$$

Hamiltonian of the two-electron system confined to infinite spherical potential (V_c) can be written as,

$$\hat{H} = -\sum_{i=1}^{2}\left(\frac{\hbar^2}{2m^*}\nabla_i^2 - \frac{Ze^2}{\varepsilon r_i}\right) + \frac{Ze^2}{\varepsilon|\vec{r}_1-\vec{r}_2|} + V_c(\vec{r}_1,\vec{r}_2)\,. \tag{11}$$

where,

$$V_c(\vec{r}_1,\vec{r}_2) = \begin{cases} 0, & \vec{r}_1,\vec{r}_2 < R \\ \infty, & \vec{r}_1,\vec{r}_2 \geq R \end{cases}.$$

The additional term is the coulomb interaction between electrons. ψ is the state function of the system and is constructed from the Slater determinant (ground state) or the appropriate combination of these determinants (excited states) and it can be given for ground states as follows,

$$\psi(\vec{r}_1,\vec{r}_2) = \frac{1}{\sqrt{2}}\left(\emptyset_{1s}(\vec{r}_1)\emptyset_{1s}(\vec{r}_2)\right)[\alpha(1)\beta(2) - \alpha(2)\beta(1)] \tag{12}$$

Where $\emptyset_{1s}(\vec{r}_1)$ is one electron orbital and is given Eq. 9, $\alpha(i)\ ve\ \beta(i)$ are electron spin up and down functions. For the system confined to the infinite spherical potential considered, with the approach of Fermandez [16], virial coefficients were calculated using the expression

$$2E - < V \geq -r_0\frac{\partial E}{\partial r_o} = \frac{r_0}{2}\left|\frac{d\psi(\vec{r}_1,\vec{r}_2)}{dr}\right|^2 \tag{13}$$

The wave function of the system is constructed from Slater determinants, which are generated from single-electron spin orbitals. Since single-electron spin orbitals are constructed as linear combinations of Slater-type orbitals in determining the electronic structure of atomic systems, the same approach can be applied to confined systems, often referred to as artificial atoms. In this study, a linear combination of STOs with different screening parameters for s (or p, d) type atomic orbitals was selected to construct one-electron atomic orbitals. To preserve the orthogonality of the orbitals, the same set of screening parameters was used for all spatial orbitals with the same angular momentum. To accurately calculate the expected energy value, five basis sets (σ = 5) were used, and the QGA procedure was combined with the HFR methods to minimize the total energy over the STOs. This approach allowed for both the accurate representation of wave function behavior and the optimization of energy calculations.

The Genetic Algorithm (GA) can be defined as a search and numerical optimization technique in which individuals that adapt well to the environment survive, while those that do not adapt are eliminated [21-24]. The Quantum Genetic Algorithm (QGA) consists of three main processes: reproduction (or copying), crossover, and mutation. In the reproduction process, the survival probabilities of individuals are calculated. Individuals with a high probability of survival are passed on to the next generation, while those with a lower probability are eliminated. The crossover process is similar to the natural crossover mechanism in biology and is carried out on individuals obtained during the reproduction stage. The genetic information of two randomly selected individuals is exchanged by cutting at a specific point. The information on the left of the cut in one individual is swapped with the information on the right of the cut in the other, and vice versa. This allows both individuals to carry each other's genetic information. The mutation process is applied to escape local minima and is performed on a randomly selected individual. In the application of crossover and mutation processes, a probability of execution is determined. The crossover probability is chosen to be high in order to increase diversity within the population, while the mutation probability is kept low to avoid incorrect solutions. If the probability is set too high, convergence becomes difficult, and randomness increases. The initial population was composed of 100 randomly selected individuals who were solutions of the Schrödinger equation. Each individual in the initial population was evaluated, and then the QGA method was executed based on these energy values.

Achieving the desired precision in calculating physical quantities using the variational method often requires extensive iterations. However, to effectively manage computation time, establishing a stopping criterion is essential. Although its application in atomic and molecular systems differs, the virial coefficient can serve as a viable stopping parameter for determining the electronic structure of bonded systems, even considering their distinct states compared to free atoms and molecules. Virial ratio can be written as

$$\frac{\langle T\rangle}{\langle V\rangle} = -\frac{1}{2} \tag{14}$$

When determining the electronic structure of confined systems, the ratio approaches a certain value at large dot radii, but significantly different values can be obtained due to the confinement effect at small dot radii.

Results and Discussion

The virial coefficients for one and two-electron confined systems were calculated using Equation 13 derived by Fernandez. Virial coefficients were determined using the system energy and wave functions calculated with the quantum genetic algorithm. Since the errors that occur in calculations in confined systems depend on the dot radius, it was not appropriate to use Fernandez's equivalent expression as a direct stopping criterion. Considering that in finite systems errors in calculations depend on the dot radius, it was not considered appropriate to use Fernandez's equivalent expression as a direct stopping criterion. Virial coefficients in the system were calculated from ⟨T⟩/⟨V⟩. The graph of the values found is drawn depending on the dot radius and can be seen in Fig.1.

In this study, virial coefficients of unconfined Hydrogen and Helium atoms were used as a stopping criterion in the electronic structure calculations of Hydrogen and Helium-like quantum dot structures confined by an infinite potential well. The graph of the obtained virial coefficients as a function of dot radius was plotted, and a fitting function was defined for this purpose, as shown in Figure 1

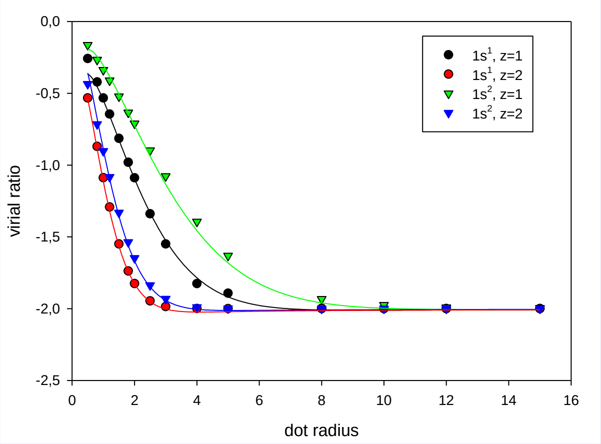

Figure 1. The curves of the virial coefficients calculated for one and two electron systems were drawn according to the dot radius. The continuous lines show the fit functions.

The best fit function representing data shown in Figure 1 was found as follows.

$$V_{fit} = -2 + a.exp(-b.R^{3/2}) + c/R. \tag{15}$$

Here V_{fit} refers to virial ratios and R represents of dot radius. a, b and c are parameters and also absolute error values were found by fit programme of each parameter are given in Table 1.

Table 1. Parameters of fit function given in Eq. (15)

Level, impurity	a	b	c	∆a	∆b	∆c	r^2
1s1, z=1	2.0396	0.2661	-0.1112	0.0937	0.0097	0.0511	0.99
1s1, z=2	2.2283	0.8045	-0.1090	0.0647	0.0143	0.0265	0.99
1s2, z=1	2.0992	0.1639	-0.0876	0.0698	0.0060	0.0431	0.99
1s2, z=2	2.2358	0.6374	-0.0714	0.1080	0.0168	0.0470	0.99
1s1, z=1	2.0396	0.2661	-0.1112	0.0937	0.0097	0.0511	0.99
1s1, z=2	2.2283	0.8045	-0.1090	0.0647	0.0143	0.0265	0.99

Using absolute error of parameters a, b and c absolute error of V_{fit} given in Eq.15 is given as follows,

$$\Delta V_{fit} = \sqrt{\left(\left(\frac{\partial(V_{fit})}{\partial a}\Delta a\right)^2 + \left(\frac{\partial(V_{fit})}{\partial b}\Delta b\right)^2 + \left(\frac{\partial(V_{fit})}{\partial c}\Delta c\right)^2\right)} \tag{16}$$

Table 2. As an example, the table of virial coefficients calculated with the help of the Fernandez equation and the curve fitting method for the case of $1s^1$, z=2.

R	V_{cal}	V_{fit}	$\lvert V_{cal}-V_{fit}\rvert$	ΔV
1s1, z=1	2.0396	0.2661	-0.1112	0.0937
1s1, z=2	2.2283	0.8045	-0.1090	0.0647
1s2, z=1	2.0992	0.1639	-0.0876	0.0698
1s2, z=2	2.2358	0.6374	-0.0714	0.1080
1s1, z=1	2.0396	0.2661	-0.1112	0.0937
1s1, z=2	2.2283	0.8045	-0.1090	0.0647

The iteration process was stopped when the difference between the virial coefficient calculated from the iteration and the one obtained from the fit function was smaller than ΔVfit. Values for several different dot radii are presented in Table 2. As can be seen in Table 2, when the 4th and 5th columns are compared, it is observed that Vcal - Vfit consistently remains smaller than ΔVfit. This indicates that while the absolute error is relatively large for small dot radii, it significantly decreases for larger dot radii. Therefore, it was concluded that these results provide a robust and reliable criterion for stopping the iteration process, ensuring the accuracy and precision of the calculations. In summary, this approach not only enhances the reliability of the method but also contributes to the overall efficiency and accuracy of the computational process. Therefore, it is deemed appropriate to consider the use of virial coefficients as a stopping criterion in iterative calculations performed with variational methods as a strategic approach that can both enhance the speed and ensure the accuracy of the computations.

Conflict of interest

There is no conflict of interest among the authors.

References

[1] Özmen, A., Yakar, Y., Çakır, B., Atav, Ü., Computation of the oscillator strength and absorption coefficients for the intersubband transitions of the spherical quantum dot, *Opt. Commun*., (2009) 282, 3999.

[2] Çakır, B., Yakar, Y., Özmen, A., Sezer, M.Ö., Şahin, M., Linear and nonlinear optical absorption coefficients and binding energy of a spherical quantum dot, *Superlattices Microstruct*., (2010) 47, 556.

[3] Çakır, B., Yakar, Y., Özmen, A., Linear and nonlinear optical absorption coefficients of spherical quantum dot inside external magnetic field. *Physica B*, (2017) 510, 86-91.

[4] Rahimi, F., Ghaffary, T., Naimi, Y., Khajehazad, H., Effect of magnetic field on energy states and optical properties of quantum dots and quantum antidots, *Optical and Quantum Electronics*, (2021) 53 (47).

[5] Çakır, B., Yakar, Y., Özmen, A., Refractive index changes and absorption coefficients in a spherical quantum dot with parabolic potential, *Journal of luminescence*, (2012) 132, 10, 2659.

[6] Çakır, B., Özmen, A., Atav, Ü., Yüksel, H., Yakar, Y., Investigation of electronic structure of a quantum dot using Slater-type orbitals and Quantum Genetic Algorithm, *Int. J. Mod. Phys. C*, (2007)18, 61-72.

[7] Rayleigh, Lord, Scientific Papers (1905), Vol. 5: 1902-1910. Cambridge: University Press.

[8] Poincaré, H., *Lectures on Cosmological Theories*, (1911) Paris: Hermann.

[9] Zwicky, F. "Die Rotverschiebung von extragalaktischen Nebeln", Helvetica Physica Acta (1933) 6: 110–127.

[10] Ledoux, P., On the radial pulsation of gaseous stars, *Astrophysical Journal*, (1945) 102, 143–153.

[11] Kohn, W., Two applications of the variational method to quantum mechanics, *Physical Review*, (1947), 71(10), 635-636.

[12] Cottrell, T. L., & Paterson, S., The virial theorem in quantum mechanics, The London, Edinburgh, and Dublin *Philosophical Magazine and Journal of Science*, (1951) 42(327), 391-395.

[13] Parker, E. N., Tensor Virial Equations. *Physical Review*, (1954) 96(6), 1686–1689.

[14] Hoover, W. G., & Ree, F. H., Calculation of Virial Coefficients., *J. Chem. Phys.*, (1965) 43(2), 375-392.

[15] Fernandez F. M., Castro, E., Hypervirial theorems and enclosed quantum-mechanical systems, *Phy. Rev. A*, (1981) 24(5), 2344.

[16] Fernandez F. M., Castro, E., Virial theorem and boundary conditions for approximate wave functions, *Int. J. Quantum. Chem*., (1982) 11, 741.

[17] Mukhopadhyay, S., Bhattacharyya, K., Confined systems and the modified virial theorem from semiclassical considerations, *Int. J. Quantum Chem*., (2005) 101, 27.

[18] Demir, C., Yakar, Y., Çakır, B., Özmen, A., Excited state energies, orbital energies and virial coefficients in confined multi-electron systems*, J. Lumin*., 251, 119185, 2022.

[19] Hirschfelder, J. O., Classical and Quantum Mechanical Hypervirial Theorems, *J. Chem. Phys*., (1960) 33 (5), 1462-1466.

[20] Fernandez, F. M., Castro, E., The virial theorem for systems subjected to sectionally defined potentials, *J. Chem. Phys*., 75 (6), 2908, 1981.

[21] J. H. Holland, *Adaptation in Natural and Artificial Systems* (1975) University of Michigan Press, Ann Arbor, MI.

[22] Çakir, B., Özmen, A., & Yakar, Y., Investigation of electronic structure of a Quantum Dot using Slater-Type Orbitals and Quantum Genetic Algorithm*, Int. J. of Modern Physics C*, (2007) 8(1), 61-72.

[23] Çakır, B., Özmen, A., Atav, Ü., Yakar, Y., Yüksel, H., Calculation of electronic structure of a spherical quantum dot using a combination of quantum genetic algorithm and Hartree Fock Roothaan method, *Int. J. of Modern Physics C*, (2008) 19(4), 599-609.

[24] Demir, C., Yakar, Y., Çakır, B., Özmen, A., Energies of the ground and excited states of confined two-electron atom in finite potential well, *Physica B*, (2023) 662, 414967.

Cumhuriyet Sci. J., 45(4) (2024) 609-613
DOI: https://doi.org/10.17776/csj.1511216

Cumhuriyet Science Journal

| csj.cumhuriyet.edu.tr | Founded: 2002 ISSN: 2587-2680 e-ISSN: 2587-246X Publisher: Sivas Cumhuriyet University

The Investigation of Bunching and No Bunching Regions of Sinusoidal Mounds

Ahmet Türker Tüzemen [1,a,*]

[1] *Department of Mathematics and Science Education, Faculty of Education, Sivas Cumhuriyet University, Sivas, Türkiye..*
**Corresponding author*

Research Article

History
Received: 05/07/2024
Accepted: 12/09/2024

ABSTRACT

We studied the evolution of an initial surface which was sinusoidal mound shaped for Diffusion Limited (DL) regime. We supposed that there were two dimensional concentric circular steps on initial surface and attractive/repulsive interactions between these monoatomic steps. While following the surface's evolution, the equation of motion related to each step radius's change and diffusion equation have been solved. We obtained bunching and no bunching regions of studied initial surfaces in a parameter space with their scaling characteristics. Our results in this examination can be summarized as; bunching (no bunching) region expands (shrinks) with increasing of wavelength or amplitude of the initial surface. The curves separating bunching/no bunching regions scale with each other. In the case of the amplitude (wavelength) is changed, the scaling factor is $(A_0/A_0')^{1/6}$ $((\lambda/\lambda')^{1/2})$. When both the wavelength and amplitude of the surface are changed at the same time, the scaling factor is equal to $(A_0/A_0')^{1/6} \times (\lambda/\lambda')^{1/2}$.

Keywords: Diffusion, Surface structure, Semiconducting Materials, Step Bunching.

a *atuzemen@cumhuriyet.edu.tr* *https://orcid.org/0000-0002-6120-6008*

Introduction

Studies on crystal morphology, which provides information about the structural properties and growth mechanisms of various materials, have long been an interesting field in material science. Crystal morphology is also important for understanding the complex dynamics of mass transfer, surface structure and surface processes. Vicinal surfaces are characterized by a conscious deviation from the crystallographic orientation and they play an important role in understanding surface dynamics with growth kinetics [1-7]. This deviation causes the formation of step bunches that affects the surface roughness and morphology. Vicinal surfaces consist of steps and terraces under their roughening temperature. We have to know the interaction type between these steps to understand surface dynamics. There are repulsive and attractive interactions between steps on the surface [8-12]. The repulsive interaction which arises from the elastic [13-15] or entropic [16] interactions varies inversely with the square of the average step separation. It has been demonstrated through experimental studies that the attractive interaction is inversely proportional to the step separation [17-21]. This type of interaction appears from dipole–dipole interactions [22,23] or indirect electronic interactions [24,25]. Step bunching that occurs in semiconductor materials is significant because of its effects on device performance and fabrication [4,26-30]. Discovering the dynamics of step bunching and mound formation finds out the interplays between surface diffusion and adatom kinetics. The crystals can growth under different regimes like Diffusion-Limited (DL) and Attachment-Detachment-Limited (ADL) regimes. In DL regime, the growth rate is determined by the mass transport rate. On the other hand, atoms' attachment/detachment at/from the surface direct the growth kinetics in the ADL regime. Particularly, DL regime governs the evolutions of step bunches and the semiconductor mounds. A lot of works have been done on the step bunching phenomenon from past to present. Some of the studies carried out in recent years are as follows; Siewierska and Tonchev [31] studied on the scaling of the minimum distance between consecutive two steps in the bunch. Sato [32] examined that how the surface diffusion field affects the growth law of the bunch size in the step bunching induced by immobile impurities. In the model they created Popova et al. [33] investigated step bunches on the surface of growing and sublimating crystals and showed that the overall picture of the bunching process changes entirely when steps cannot overlap, thus forming macrosteps. In another study Popova [34] studied the effect of step–step exclusion on growing vicinal surfaces destabilized by a step-up (SU) or step-down (SD) driving force in Diffusion-Limited (DL) and Kinetics Limited (KL) growth regimes. In the presence of repulsive and attractive interactions between steps, Tüzemen et al. [35] searched a surface which consists of two dimensional concentric circular monoatomic steps in DL regime. They obtained a phase diagram separating the step bunching and no step bunching regions for the surface they examined. In addition, Tüzemen [36] investigated the bunching - no bunching regions for different initial surfaces consist of concentric circular monoatomic steps in a parameter space. He found out the scaling characteristics of these bunching/no bunching regions under the effects of attractive and repulsive interactions between steps.

In this investigation, we studied a sinusoidal mound shaped initial surface in two dimensions for Diffusion Limited (DL) regime. We assumed that this surface had concentric circular steps with attractive and repulsive interactions between them. We determined bunching and no bunching regions of examined initial surfaces in a parameter space with their scaling features. To achieve our goals, we solved the diffusion equation and obtained an equation of motion regarding the change of radius of each circular step. After that we achieved the solution of these coupled equations numerically

Theory

We investigate that how an initial surface whose edge structure coincide with a sinusoidal function in the form of $A_0 \sin(2\pi x/\lambda)$ reaches to equilibrium situation in course of time in this study. The wavelength and amplitude variables that define sinusoidal surface structure are identified by λ and A_0 respectively. The working surface has monoatomic and concentric circular steps in two dimensions. There are flat terraces between consecutive two steps. Figure 1 shows the general structure and side view of the initial surface. The radii of the each circular steps are defined as r_1, r_2, r_3.... etc. in Figure 1. The movements of steps on the surface under roughening temperature provide the surface evolving. The mechanism that controls these movements is by the attachment and/or detachment of particles to/from step edges. In the absence of bulk diffusion or evaporation/condensation processes, local mass transfer takes place with surface diffusion. The borders belonging to i^{th} terrace are specified by i (from above) and $i+1$ (from below). In the case where we assume that there is no flux to the surface, we can write the general diffusion and steady state diffusion equations for i^{th} terrace atom concentration in polar coordinates as follows respectively [37],

$$D_s \nabla^2 C_i(\vec{r}) = \frac{\partial C_i(\vec{r})}{\partial t} \tag{1}$$

and

$$\frac{\partial^2 C_i(\vec{r})}{\partial r^2} + \frac{1}{r}\frac{C_i(\vec{r})}{\partial r} = 0 \tag{2}$$

D_s is the surface diffusion constant. The solution of Eqn. (2) is given by $C_i(\vec{r}) = A_i \ln r + B_i$. We calculate the constant A_i in expression by doing mathematical solution details of which are given in Ref. [35].

$$A_i = \frac{C_i^{eq} - C_{i+1}^{eq}}{ln\frac{r_i}{r_{i+1}} - \frac{D_s}{k}\left(\frac{1}{r_i} + \frac{1}{r_{i+1}}\right)} \tag{3}$$

C_i^{eq} defines the equilibrium concentration of atoms on the adjacent terrace to the i^{th} step. The value of C_i^{eq} (according to the Gibbs-Thompson relation) is given as,

$$C_i^{eq} = \bar{C}^{eq} exp\left(\frac{\mu_i}{T}\right) \approx \bar{C}^{eq}\left(1 + \frac{\mu_i}{T}\right) \tag{4}$$

The value of Boltzman's constant is taken as 1 due to the used units in the calculations. μ_i indicates the step chemical potential written depending on the line tension, repulsive and attractive interactions between the nearest neighbor steps.

For ease of mathematical calculation we can write the equations of motion related with the change of radiis of circular steps in dimensionless form. To do this we make the following definitions respectively [21,35,37]

$$\dot{\sigma_i} = \frac{d\sigma_i}{d\tau} = \frac{A_i' - A_{i-1}'}{\sigma_i} \tag{5}$$

Here σ and τ are the dimensionless radius and time. A_i' corresponds the dimensionless form of arbitrary constant A_i given in Eqn. (3). The expressions of σ, τ and A_i' can be written as,

$$\sigma_i = \frac{T}{\Omega\Gamma} r_i \tag{6}$$

$$\tau = D_s \bar{C}^{eq} \Omega \left(\frac{T}{\Omega\Gamma}\right)^2 \left(1 + \frac{D_s T}{k\Omega\Gamma}\right)^{-1} t \tag{7}$$

$$A_i' = \frac{\mu_i' - \mu_{i+1}'}{(1-q)ln\frac{\sigma_i}{\sigma_{i+1}} - q\left(\frac{1}{\sigma_i} + \frac{1}{\sigma_{i+1}}\right)} \tag{8}$$

where T, Ω, and Γ express the absolute temperature value, the area owned of a diffusing particle and the steps' line tension respectively. The equilibrium value of particle concentration at the step edge is shown by $\bar{C}^{eq}$. k charactizes the step attachment/detachment coefficient. The q parameter in Eqn. (8) identifies in which regime the surface will evolve. When $q = 0$, the surface evolves in the DL regime. If $q = 1$, surface evolution regime is ADL. The value of chemical potential μ_i' obtained with dimensionless radii can be written as

$$\begin{aligned}\mu_i' = \frac{1}{\sigma_i} + \gamma\Bigg[\Bigg(&\frac{2\sigma_{i+1}}{(\sigma_{i+1}+\sigma_i)}\frac{1}{(\sigma_{i+1}-\sigma_i)^3} \\ &- \frac{2\sigma_{i-1}}{(\sigma_i+\sigma_{i-1})}\frac{1}{(\sigma_i-\sigma_{i-1})^3}\Bigg) \\ -\beta\Bigg(&\frac{\sigma_{i+1}}{(\sigma_{i+1}+\sigma_i)}\frac{1}{(\sigma_{i+1}-\sigma_i)^2} - \frac{\sigma_{i-1}}{(\sigma_i+\sigma_{i-1})}\frac{1}{(\sigma_i-\sigma_{i-1})^2}\Bigg)\Bigg]\end{aligned} \tag{9}$$

The first term is the line tension, the second and the third terms are repulsive and attractive interactions between the nearest neighbor steps respectively. Dimensionless coefficients are $\gamma = (T^2\gamma'/\Omega^2\,\Gamma^3)$ and $\beta = (\Omega\Gamma/T)(\beta'/\gamma')$. γ' and β' indicates the repulsive and attractive interaction strengths respectively.

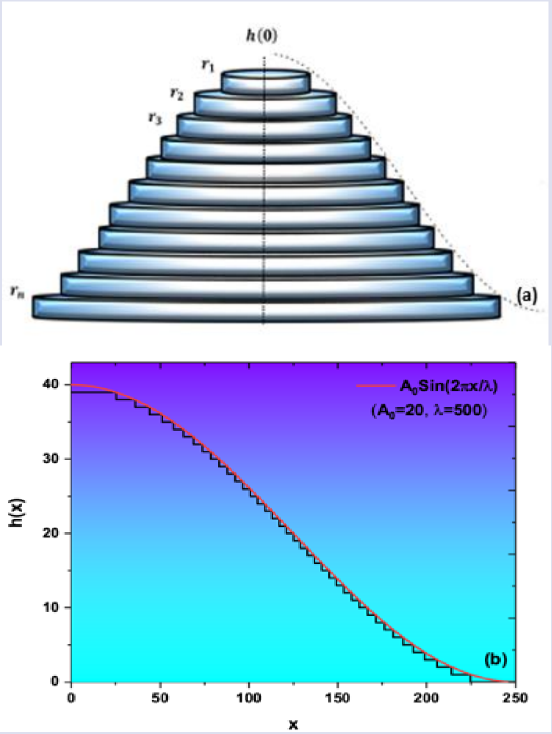

Figure 1. (a) The initial surface with monoatomic circular steps with radii $r_1, r_2, r_3, \dots \dots r_n$. The extrapolated height of initial surface is given by $h(0)$. The sinusoidal function coincided with the edge structure is shown with dashed lines, (b) side view of the initial surface.

Results and Discussion

For Diffusion Limited (DL) regime, we discussed initial surfaces which have sinusoidal shaped and its edge structures fit $A_0 \sin(2\pi x/\lambda)$ function in two dimensions. Initial surfaces have circular and concentric monoatomic steps. Surface evolution takes place by disappearing some top steps on the surface because of transfering particles on it to other terraces and steps. We investigated bunching/no bunching regions of different initial surface structures as a function of the repulsive and attractive interaction parameters γ and β by following the step bunchings formed throughout the surface evolution. We changed the values of the repulsive interaction parameter γ from 5×10^{-7} to 1×10^{-3} in all examinations.

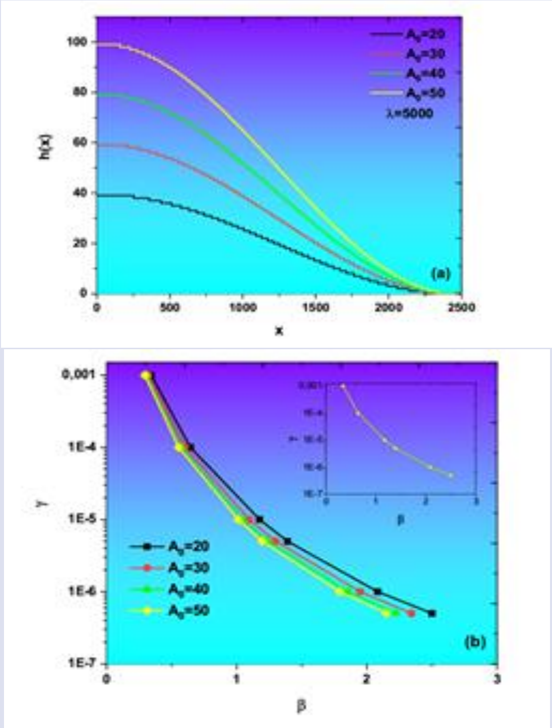

Figure 2. (a)The initial surfaces with different values of amplitudes $(A_0 = 20, 30, 40, 50)$ and the same wavelength $(\lambda = 5000)$, (b) the bunching/no bunching regions of the surfaces given in Fig. 2a as a function of β and γ. The inset shows the scaling behavior of obtained curves.

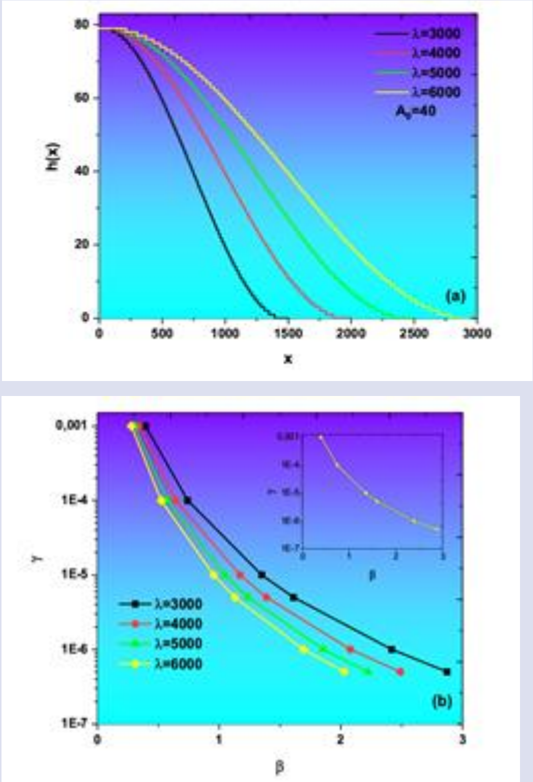

Figure 3. (a) The initial surfaces which have different wavelengths $(\lambda = 3000, 4000, 5000, 6000)$ and the same amplitude value $(A_0 = 40)$, (b) the bunching/no bunching regions of the surfaces given in Fig. 3a as a function of β and γ. The inset gives the scaling behavior of obtained curves.

We studied the initial surfaces with the same wavelength for the first part of our work (Figure 2a). While we took the wavelength's value as 5000, we altered the amplitudes of the surfaces by increasing by 10 from 20 to 50. In other words, we kept fixed the point where the rightmost parts of the initial surfaces intersect the x-axis and changed the steps' numbers owned by these surfaces. We numerically obtained the bunching/no bunching regions of the step interaction parameters γ and β by revealing the β value corresponding to each γ value mentioned above [35,36]. The results are given in Figure 2b. The regions above and below obtained curves indicate the bunching and no bunching regions, respectively. The relations between the line tension of a step and repulsive/attractive interactions between nearest neighbor circular steps ensure the determining these two regions. If Figure 2b is analyzed carefully, it can be seen that the bunching region of the surface expands with increasing the surface's amplitude (number of the steps on initial surface). Besides we found that the bunching/no bunching regions were scaled as $(A_0/A_0')^{1/6}$ for initial surfaces which had different amplitudes as A_0 and A_0' respectively. The inset in Figure 2b shows the scaled case of the curves. All curves have been scaled according to the curve with $A_0 = 20$. The scaling factors are $(5/2)^{1/6}$, $(4/2)^{1/6}$, $(3/2)^{1/6}$ and 1 for the amplitude's value of the initial surfaces $A_0 = 50, 40, 30$ and 20.

In the second part of the study, we examined the effect of altering the wavelength belonging to the initial surface on the surface's evolution in time and the areas of the bunching/no bunching regions. While doing this, we assumed the value of amplitude as constant while changing the wavelength values. Figure 3a indicates the initial surfaces with the same amplitude $(A_0 = 40)$ and different wavelengths $(\lambda = 3000, 4000, 5000, 6000)$.

In these conditions, the behaviors of obtained bunching/no bunching regions relating to given surfaces in Fig. 3a are presented in Figure 3b. We found that when we increase the surface's wavelength, the bunching region expands. In addition to this result, we identified that the curves (which separates the bunching/no bunching regions) scaled as $(\lambda/\lambda')^{1/2}$ for initial surfaces which have different wavelength values as λ and λ' respectively. The inset gives the scaled behavior of the curves. The curves have been scaled according to the curve with $\lambda = 3000$. The scaling factors are $(6/3)^{1/2}$, $(5/3)^{1/2}$, $(4/3)^{1/2}$, 1 for $\lambda = 6000, 5000, 4000, 3000$ respectively.

As last part, we changed both of the amplitudes and the wavelengths of the all initial surfaces. While we took the values of amplitudes as $20, 30, 40$ and 50, we used the values from 3000 to 6000 in increments of 1000 for the wavelength respectively. The initial surfaces studied here are given in Figure 4a. When we analyzed the curves obtained as a function of β and γ in Figure 4b, we found that when both the amplitude and wavelength were increased, the bunching region expanded and these curves were scaled among themselves. The scaling coefficient here was appeared as the product of the scaling coefficients we found before $((A_0/A_0')^{1/6}\,(\lambda/\lambda')^{1/2})$. All curves have been scaled according to the curve with $A_0 = 20$ and $\lambda = 3000$. The scaling factors are $(5/2)^{1/6}\,(6/3)^{1/2}$, $(4/2)^{1/6}\,(5/3)^{1/2}$, $(3/2)^{1/6}\,(4/3)^{1/2}$ and 1

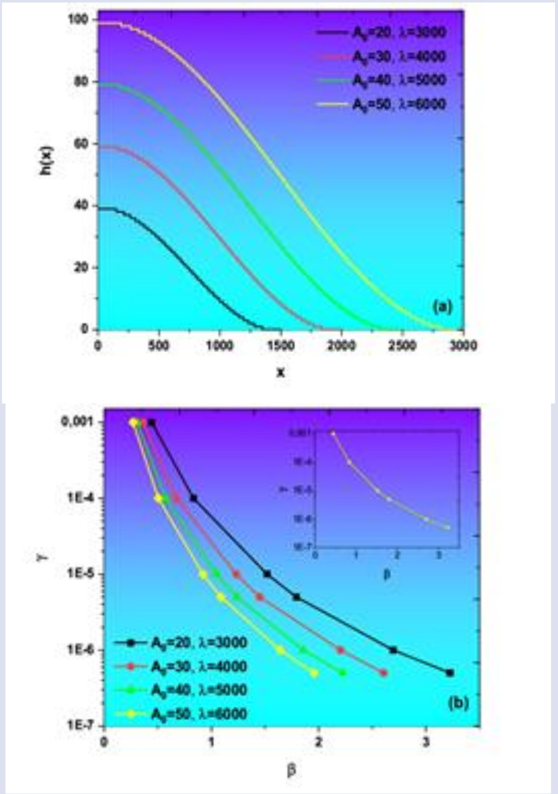

Figure 4. (a) The initial surfaces which have different amplitudes $(A_0 = 20, 30, 40, 50)$ and the wavelengths $(\lambda = 3000, 4000, 5000, 6000)$, (b) the bunching/no bunching regions of the given surfaces as a function of β and γ. The scaling behavior of obtained curves is given in inset.

.

Conclusions

In this study, we investigated the evolution of a two dimensional initial surface which is sinusoidal mound shaped for Diffusion Limited (DL) regime. We supposed that there were concentric circular steps on initial surface and attractive/repulsive interactions between steps. We obtained the equation of motion regarding the change of radius of each circular step together with the solution of the diffusion equation to follow surface's evolution. We examined bunching and no bunching regions of studied initial surfaces in a parameter space with their scaling properties. We can summarize our results as follows: while the wavelength λ (amplitude A_0) of the initial surface under consideration is constant, increasing its amplitude (wavelength) causes the bunching area of the surface to grow. In both cases, the resulting curves scale with each other. In case where the amplitude (wavelength) is changed and the wavelength (amplitude) is constant, the scaling factor is $(A_0/A_0')^{1/6}$ $((\lambda/\lambda')^{1/2})$. In the condition that both the wavelength and amplitude of the surface are changed, the scaling factor is equal to the product of the expressions obtained above $((A_0/A_0')^{1/6}$ $(\lambda/\lambda')^{1/2})$.

Conflict of interest

The author declares no conflicts of interest.

Acknowledgement

This research did not receive any specific grant from funding agencies in the public, commercial, or not-for-profit sectors

References

[1] Guin L., Jabbour M.E., Shaabani-Ardali L., Benoit-Mar´echal L., Triantafyllidis N., Stability of Vicinal Surfaces: Beyond the Quasistatic Approximation, *Phys. Rev. Letts.*, 124 (2020) 036101.

[2] Krzyżewski F., Załuska-Kotur M., Krasteva A., Popova H., Tonchev V., Scaling and Dynamic Stability of Model Vicinal Surfaces, *Cryst. Growth Des.,* 19 (2019) 821−831.

[3] Misbah C., Pierre-Louis O., Saito Y., Crystal surfaces in and out of equilibrium: A modern view, *Rev. Mod. Phys.*, 82 (2010) 981.

[4] Toktarbaiuly O., Usov V., Ó Coileáin C., Siewierska K., Krasnikov S., Norton E., Bozhko S.I., Semenov V.N., Chaika A.N., Murphy B.E., Lübben O., Krzyżewski F., Załuska-Kotur M.A., Krasteva A., Popova H., Tonchev V., Shvets I.V., Step bunching with both directions of the current: Vicinal W(110) surfaces versus atomistic-scale model, *Phys. Rev. B*, 97 (2018) 035436.

[5] Pérez León C., Drees H., Wippermann S.M., Marz M., Hoffmann-Vogel R., Atomically resolved scanning force studies of vicinal Si(111), *Phys. Rev. B*, 95 (2017) 245412.

[6] Hecquet P., Stability of vicinal surfaces and role of the surface stress, *Surface Science*, 604 (2010) 834–852.

[7] Mugarza A., Schiller F., Kuntze J., Cord´on J., Ruiz-Os´es M., Ortega J.E., Modelling nanostructures with vicinal surfaces, *J. Phys. Condens. Matter*, 18 (2006) 27–49.

[8] Ciobanu C.V., Tambe D.T., Shenoy V.B., Wang C.Z., Ho K.M., Atomic-scale perspective on the origin of attractive step interactions on Si(113), *Phys. Rev. B*, 68 (2003) 201302.

[9] Persichetti L., Sgarlata A., Fanfoni M., Bernardi M., Balzarotti A., Step-step interaction on vicinal Si(001) surfaces studied by scanning tunneling microscopy, *Phys. Rev. B*, 80 (2009) 075315.

[10]Magri R., Gupta S.K., Rosini M., Step energy and step interactions on the reconstructed GaAs(001) surface, *Phys. Rev. B*, 90 (2014) 115314.

[11] Sawada K., Iwata J.I., Oshiyama A., Origin of repulsive interactions between bunched steps on vicinal solid surfaces, *e-J, Surf. Sci. Nanotechnol.*, 13 (2015) 231–234.

[12] Righi G., Franchini A., Magri R., Attractive interactions between like-oriented surface steps from an ab initio perspective: role of the elastic and electrostatic contributions, *Phys. Rev. B*, 99 (2019) 075311.

[13] Andreev A.F., Kosevich A.Y., *Sov. Phys. JETP*, 54 (1981) 761.

[14] Pearson E.M., Halicioglu T., Tiller W.A., Long-range ledge-ledge interactions on Si(111) surfaces: I. No kinks or surface point defects, *Surf. Sci.*, 184 (1987) 401-424.

[15] Andreev A.F., *Sov. Phys. JETP*, 53 (1981) 1063.

[16] Gruber E.E., Mullins W.W., On the theory of anisotropy of crystalline surface tension, *J. Phys. Chem. Solids*, 28 (1967) 875–887.

[17] Saenz J.J., Garcia N., Classical critical behaviour in crystal surfaces near smooth and sharp edges, *Surf. Sci.*, 155 (1985) 24–30.

[18] Metois J.J., Heyraud J.C., Analysis of the critical behaviour of curved regions in equilibrium shapes of in crystals, *Surf. Sci.*, 180 (1987) 647–653.

[19] Sudoh K., Iwasaki H., Williams E.D., Facet growth due to attractive step step interactions on vicinal Si(113), *Surf. Sci.*, 452 (2000) 287–292.

[20] Shenoy V.B., Zhang S., Saam W.F., Step-bunching transitions on vicinal surfaces with attractive step interactions, *Surf. Sci.*, 467 (2000) 58–84.

[21] Jeong H.C., Williams E.D., Steps on surfaces: experiment and theory, *Surf. Sci.*, Rep. 34 (1999) 171–294.

[22] Jayaprakash C., Rottman C., Saam W.F., Simple model for crystal shapes: step-step interactions and facet edges, *Phys. Rev. B*, 30 (1984) 6549.

[23] Wolf D.E., Villain J., Shape fluctuations of crystal bars, *Phys. Rev. B*, 41 (1990) 2434.

[24] Frohn J., Giesen M., Poensgen M., Wolf J.F., Ibach H., Attractive interaction between steps, *Phys. Rev. Lett.*, 67 (1991) 3543.

[25] Redfield A.C., Zangwill A., Attractive interactions between steps, *Phys. Rev. B*, 46 (1992) 4289.

[26] Fujita K., Ichikawa M., Stoyanov S.S., Size-scaling exponents of current-induced step bunching on silicon surfaces, *Phys. Rev. B*, 60(23) (1999) 16006.

[27] Fok P.-W., Rosales R.R., Margetis D., Unification of step bunching phenomena on vicinal surfaces, *Phys. Rev. B*, 76 (2007) 033408.

[28] Borovikov V., Zangwill A., Step bunching of vicinal 6H-SiC{0001} surfaces, *Phys. Rev. B*, 79(24) (2009) 245413.

[29] Załuska-Kotur M.A., Krzyz˙ewski F., Step bunching process induced by the flow of steps at the sublimated crystal surface, *J. App. Phys.*, 111 (2012) 114311.

[30] Tonchev V., Classification of step bunching phenomena, Bulgarian *Chemical Communications*, 44 (2012) 1-8.

[31] Siewierska K., Tonchev V., Scaling of the minimal step-step distance with the step-bunch size: Theoretical predictions and experimental findings, *Crystal Growth*, 43(4) (2016) 204.

[32] Sato M., Step Bunching Induced by Immobile Impurities in a Surface Diffusion Field, *Journal of the Physical Society of Japan*, 86 (2017) 114603.

[33] Popova H., Krzyżewski F., Załuska-Kotur M.A., Tonchev V., Quantifying the Effect of Step−Step Exclusion on Dynamically Unstable Vicinal Surfaces: Step Bunching without Macrostep Formation, *Cryst. Growth Des.*, 20 (2020) 7246−7259.

[34] Popova H., Analyzing the Pattern Formation on Vicinal Surfaces in Diffusion-Limited and Kinetics-Limited Growth Regimes: The Effect of Step−Step Exclusion, *Cryst. Growth Des.*, 23 (2023) 8875−8888.

[35] Tüzemen A.T., Esen M., Ozdemir M., The investigation of the morphology of a decaying conic mound in the presence of repulsive and attractive step interactions, *Journal of Crystal Growth*, 501 (2018) 1-6.

[36] Tüzemen A.T., Scaling characteristics of bunching and no bunching regions of semiconductor mounds, *Journal of Crystal Growth*, 546 (2020) 125788.

[37] Israeli N., Kandel D., Profile of a decaying crystalline cone, *Phys. Rev. B,* 60 (1999) 5

Cumhuriyet Sci. J., 45(3) (2024) 614-617
DOI: https://doi.org/10.17776/csj.1212015

Cumhuriyet Science Journal

| csj.cumhuriyet.edu.tr | Founded: 2002 ISSN: 2587-2680 e-ISSN: 2587-246X Publisher: Sivas Cumhuriyet University

Modeling of Growth in Turkeys by Nonlinear Regression Models

Esin Köksal Babacan [1,a,*], **Umut Demir** [2,b]

[1] *Statistics Department, Science Faculty, Ankara University, Ankara, Türkiye.*
[2] *Tokat-Erzincan Avenue, Kemal Paşa Street, Suşehri District Police Department, Suşehri, Sivas, Türkiye.*
**Corresponding author*

Research Article

History
Received: 02/12/2022
Accepted: 20/08/2024

ABSTRACT

Nonlinear regression models are commonly used in many areas, such as physics, chemistry, biology, and engineering. In these models, the solution of normal equations is more difficult than normal equations of linear regression models. Iterative algorithms are used to solve these equations. It is highly important to choose an appropriate initial value while using these algorithms. The values obtained during the study or from previous studies can be used as an initial value. With an inappropriately chosen initial value, the number of iterations will increase, and convergence may also not occur. In this study, the nonlinear Gompertz, Richards, and Weibull models of turkey growth were considered by taking the data on female turkey weight, and it was investigated which of these models was the most appropriate model for turkey growth using the R program.

Keywords: Nonlinear regression, Growth models, Convergence.

[a] *ekoksal@science.ankara.edu.tr* *https://orcid.org/0000-0002-9649-5276*
[b] *umut.1991.demir@gmail.com* *https://orcid.org/0000-0002-6196-0713*

Introduction

Nonlinear regression models are commonly used in many areas, such as physics, chemistry, biology, and engineering. The model's nonlinearity originates from its geometry or the parameters in the model. Linearity refers to the linearity of the variables or parameters in the model. The linearity mentioned here is whether the parameters in the model are linear or not. In the model, if the value obtained when the first-degree derivative is taken according to the parameters is independent of the parameter, in other words, if it is a constant value, the model is called linear. Estimates in linear models are unbiased least squares estimates with minimum variance. However, estimates in nonlinear models are usually biased and may not have minimum variance. When a large sample is taken, the parameter estimation results will best fit the linear case approximation.

In nonlinear regression models, the solution of normal equations is more difficult than normal equations of linear regression models. Algorithms, such as Gauss-Newton, Newton-Raphson, and steepest descent, are used to solve these equations. It is highly important to choose an appropriate initial value while using these algorithms. The values obtained during the study or from previous studies can be used as an initial value. With an inappropriately chosen initial value, the number of iterations will increase, and convergence may also not occur.

In the literature, there are also some heuristic methods that are not affected much by the starting point and do not require derivatives. Nelder-Mead (1964) developed the Nelder-Mead simplex method, which allows finding the local minimum of a multivariate function [1]. In 1964 and 1973, Huber conducted studies on robust estimators and developed M-estimators [2,3].

In their study, Bates and Watts (1988) included nonlinear regression models and applications [4]. In the study by Çağlar (1995), the likelihood function was maximized by the Gauss-Newton method in nonlinear regression models, and the model parameters were estimated [5]. In the study by Aksoy (1996), after the nonlinear regression model was established, autocorrelations between model residuals were also included in the model, and nonlinear parameters were estimated by the linearization method [6].

Şengül and Kiraz (2003) used nonlinear regression models to obtain growth models for male and female turkeys [7]. In their study, they considered the Gompertz, Logistic, Morgan-Mercer-Flodin (MMF), and Richards nonlinear models, and at the end of the study, the researchers concluded that the Gompertz, Logistic, and Richards models were mathematically appropriate.

In their study, Çelik et al. (2022) expressed growth for male and female turkeys with a multiphasic model [8].

In the second section of the study, the Gompertz, Richards, and Weibull nonlinear models, which are the most used growth models in the literature, were given, and it was explained how the initial values to be used for parameter estimation in these models could be obtained by transforming the models. In the third section, namely the application section, the data on female turkey weight in the study by Çelik et al. (2022) were taken into account, and the suitability of these data to the Gompertz, Richards, and Weibull models was examined [9]. The conclusion and discussion were included in the final section.

Materials and Methods

The models most commonly used as growth models in living things in the literature are the Gompertz model, the Richards model, and the Weibull model. The formats of the models are given in Table 1, where x represents the time and y represents the body weight.

Table 1. Growth Models

Gompertz model	$y = \beta_1 e^{-\beta_2 e^{-\beta_3 x}} + \varepsilon$
Richards model	$y = \dfrac{\beta_1}{(1+\beta_2 e^{-\beta_3 x})^{\frac{1}{\beta_4}}} + \varepsilon$
Weibull model	$y = \beta_1 - \beta_2 e^{-\beta_3 x^{\beta_4}} + \varepsilon$

where $x = 1,2,\dots,n$, β_1 represents the maximum value that y will take in case of $n \to \infty$, β_2 represents the scale parameter, β_3 refers to the location parameter, β_4 denotes the inflection parameter that determines the shape of the function, and ε represents the Normally distributed random error term with a mean of 0 and a variance of σ^2.

As is seen, these models are nonlinear models according to their parameters. Accordingly, the model's parameters can be estimated using parameter estimation methods in nonlinear regression models. The most important thing for the parameter estimation of the models is to determine the appropriate initial values. When the appropriate initial value is not given, the parameter estimation results cannot be achieved, and an error occurs. Therefore, it is crucial to determine the initial values of the parameters appropriately. In this study, transformations to the models were used to determine the initial values of the models' parameters [10]. How the initial values for each model are obtained is explained in detail in the following section.

Let us consider the Gompertz model first. A logarithmic transformation can be applied to the model to determine the initial values where the model is

$$y = \beta_1 e^{-\beta_2 e^{-\beta_3 x}} + \varepsilon_x \tag{1}$$

when the natural logarithm of both sides is taken, where

$$ln(y) = ln(\beta_1) - \beta_2 e^{\beta_3 x} + ln(\varepsilon_x)$$

and, if necessary arrangements are made, it is obtained as follows:

$$ln\left(ln\left(\frac{\beta_1}{y}\right)\right) = ln(\beta_2) - \beta_3 x$$

In this equation obtained, if

$$y^* = ln\left(ln\left(\frac{\beta_1}{y}\right)\right), \beta_2^* = ln(\beta_2), \beta_3^* = -\beta_3$$

is taken,

$$y^* = \beta_2^* + \beta_3^* x \tag{2}$$

linear regression model is obtained. The initial value can be taken as $\hat{\beta}_1^{(0)} > max(y)$ for β_1. Accordingly, the parameters of the linear regression model (2) obtained by applying the mentioned transformations are estimated to be able to determine the initial values for other parameters. Thus, by substituting the estimates for β_2^* and β_3^*, the initial values for the parameters are obtained with the inverse transformation:

$$\hat{\beta}_2^{(0)} = e^{\hat{\beta}_2^*}, \hat{\beta}_3^{(0)} = -\hat{\beta}_3^*.$$

Second, let us consider the Richards model. A logarithmic transformation can be applied to the model to determine the initial values where the model is

$$y = \frac{\beta_1}{(1+\beta_2 e^{-\beta_3 x})^{1/\beta_4}} + \varepsilon_x \tag{3}$$

when the natural logarithm of both sides is taken, where

$$ln(y) + \frac{1}{\beta_4} ln\left(1+\beta_2 e^{-\beta_3 x}\right) = \ln(\beta_1)$$

and, if necessary arrangements are made, it is obtained as follows:

$$\left(\frac{\beta_1}{y}\right)^{\beta_4} - 1 = \beta_2 e^{-\beta_3 x}$$

$$ln\left(\left(\frac{\beta_1}{y}\right)^{\beta_4} - 1\right) = ln\beta_2 - \beta_3 x$$

where, if

$$y^* = ln\left(\left(\frac{\beta_1}{y}\right)^{\beta_4} - 1\right), \beta_2^* = ln\beta_2 \text{ and } \beta_3^* = -\beta_3 \tag{4}$$

is taken,

$$y^* = \beta_2^* + \beta_3^* x$$

linear regression model is obtained. The initial value can be taken as $\hat{\beta}_1^{(0)} > max(y)$ for β_1, and the initial value can be taken as $\hat{\beta}_4^{(0)} = 1$ for β_4. Accordingly, the parameters of the linear regression model (4) obtained by applying the mentioned transformations are estimated to be able to determine the initial values for other parameters. Then, by substituting these parameter values, the initial values for the parameters are obtained with the inverse transformation:

$$\hat{\beta}_2^{(0)} = e^{\hat{\beta}_2^*}, \hat{\beta}_3^{(0)} = -\hat{\beta}_3^*.$$

Finally, let us consider the Weibull model. If two logarithmic transformations are applied to the model to determine the initial values where the model is

$$y = \beta_1 - \beta_2 e^{-\beta_3 e^{\beta_3 x^{\beta_4}}} + \varepsilon_x \tag{5}$$

and necessary arrangements are made,

$$\beta_1 - y = \beta_2 e^{-\beta_3 e^{\beta_3 x^{\beta_4}}}$$

$$ln\left(-ln\left(\frac{\beta_1 - y}{\beta_2}\right)\right) = \ln(\beta_3) + \beta_4 . ln(x)$$

is obtained. In this equation obtained,

$$y^* = ln\left(-ln\left(\frac{\beta_1 - y}{\beta_2}\right)\right), \beta_3^* = \ln(\beta_3),\ \beta_4^* = \beta_4 \text{ and}$$
$$x^* = \ln(x)$$

where, if

$$y^* = \beta_3^* + \beta_4^* x^* \tag{6}$$

linear regression model is obtained. Since the initial value is $\hat{\beta}_1^{(0)} > max(y)$ for β_1 and it is $y_0 = \beta_1 - \beta_2$, it is $\beta_1 = \beta_2$ and the initial value is taken as $\hat{\beta}_2^{(0)} = \hat{\beta}_1^{(0)} > max(y)$ for β_2. Accordingly, the parameters of the linear regression model (6) obtained by applying the mentioned transformations are estimated to be able to determine the initial values for other parameters. Then, by substituting the obtained parameter estimates, the initial values for the parameters are obtained with the inverse transformation in the following way:

$$\hat{\beta}_3^{(0)} = e^{\hat{\beta}_3^*},\ \hat{\beta}_4^{(0)} = \hat{\beta}_4^*.$$

Application Study

In this study, weekly body living weight values of female turkeys between 4-60 weeks, which were obtained from Kahramanmaraş Sütçü İmam University, Faculty of Agriculture, Department of Zootechnics, Livestock Research and Application Center (Haymer) and used in the master's thesis entitled "Multiphasic Growth Functions and Some Applications," were taken into account, and it was attempted to obtain the most appropriate growth model for the growth of female turkeys. The data are presented in Table 2.

It was aimed to determine the appropriate growth model using weekly weight values of female turkeys. Therefore, three widely used nonlinear growth models given in Table 1 were considered, and it was attempted to determine which model was the most appropriate for the data by making parameter estimations regarding the models. In these three models taken for comparison, the weeks and female turkey weights are expressed by x and y, respectively.

Table2. Weights of female turkeys

week	weight	week	weight	week	weight
4	439	23	5250	42	11250
5	614.5	24	5432	43	11680
6	835	25	5578	44	11680
7	1183	26	5838.5	45	11685
8	1483	27	5807	46	11908
9	1845	28	6075.5	47	12110
10	2165	29	6283.5	48	12345
11	2520	30	6445.5	49	12460
12	2652	31	6432	50	12578
13	2935.5	32	6783	51	12614
14	3207	33	7245	52	12723
15	3505	34	7936	53	12715
16	3784	35	8746	54	12812
17	3994.5	36	9102	55	12894
18	4049.5	37	9457	56	12889
19	4342.5	38	9364	57	12892
20	4577	39	9809	58	13053
21	4823.5	40	10182	59	13046
22	5007.5	41	10895	60	13055

In the linear regression models obtained by applying the transformations described, parameter estimations were made using the R program, and the initial values of the parameters were obtained for each model with the necessary transformations. The initial values of the parameters for each model are presented in Table 3.

Table 3. Parameter initial values of the Gompertz, Richards, and Weibull models

Model	β_1	β_2	β_3	β_4
Gompertz	13056	12.2509	0.1215	-
Richaards	13056	44.7727	0.14	1
Weibull	13056	13056	0.0020	1.844

With these initial values obtained, parameter estimates of the three growth models were obtained using the "nls" command, which performs analysis with the nonlinear least squares method in the R program. This command calculates the parameter estimates using the Gauss-Newton algorithm [11]. According to the parameter estimates obtained, the graphs of the curves fitted with the data are shown in Figure 1.

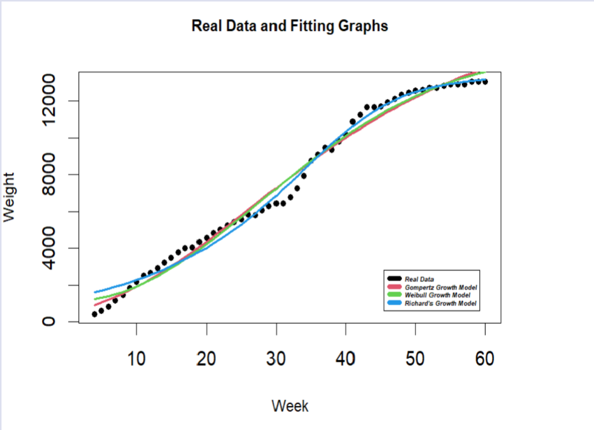

Figure 1. Graph of the estimate and actual values of the real data application

It was seen that the nonlinear regression models obtained were quite compatible with the data. When we are fitting several models to certain sample data and the aim is to select the preferable model among these models, we use *F*-test such that, where p is the number of parameters and n is the number of observations,

$$F = \frac{MSR}{MSE} = \frac{SS_{Reg}/p}{SS_e/n-p-1} \tag{7}$$

when the sum of squared residuals (errors) is denoted by SS_e and the sum of squared regression is represented by SS_{Reg}, so that:

$$SS_{Reg} = \sum_{i=1}^{n}(y_i - \bar{y})^2 - \sum_{i=1}^{n}(y_i - \hat{y}_i)^2 \tag{8}$$

$$SS_e = \sum_{i=1}^{n} {e_i}^2 = \sum_{i=1}^{n}(y_i - \hat{y}_i)^2 \tag{9}$$

It is better to use a model with a considerable and higher F value. The models can be compared using the information theory-based Akaike information criterion (AIC) in order to provide a more thorough assessment of their performance. The AIC value is calculated as follows,

$$AIC = n ln\left({SS_e}/{n}\right) + 2p$$

A smaller value of AIC criteria indicate a preferable model [12].

In Table 4, the parameter estimate values, standard errors, number of iterations, and AIC values required for model comparison are given for each model.

Table 4. The models' results of turkey growth

Model	Parameter Estimate	AIC	Number of Iterations	SE
Gompertz	$\beta_1 = 16867$ $\beta_2 = 3.5083$ $\beta_3 = 0.0476$	874.0791	9	495.4
Richards	$\beta_1 = 13305$ $\beta_2 = 970.3538$ $\beta_3 = 0.1694$ $\beta_4 = 2.9424$	861.8387	42	441.3
Weibull	$\beta_1 = 14669$ $\beta_2 = 13573$ $\beta_3 = 0.00053$ $\beta_4 = 2.0627$	874.0259	13	491.1

According to the results in Table 4, the model with the smallest AIC value was the second model, the Richards model. Furthermore, the model with the smallest standard error was the Richards model. Therefore, it can be said that the most appropriate model for turkey growth based on the available data was the Richards model.

Conclusion and Discussion

In the study, the Gompertz model, Richards model, and Weibull model, which are nonlinear growth models, were fitted to the 60-week living weight growth data of turkeys, and the models' parameter estimations were made. One of the most important problems in parameter estimation in nonlinear models is to determine the initial values of parameters. In this study, linear regression models were obtained by applying transformations to the models in order to determine the initial values of the parameters, and the initial values of the original model parameters were determined by the inverse transformation method by making parameter estimations in these linear regression models. In conclusion, it was seen that all three models fitted the data quite well. The AIC values of the models were calculated to determine the best model, and it was observed that the model with the smallest AIC value was the Richards model. This result was consistent with the results of previous studies in the literature.

Conflicts of interest

There are no conflicts of interest in this work.

References

[1] Nelder J. A. , Mead R. A., Simplex Method for Function Minimization, *The Computer Journal*, 7(4) (1965) 308–313.

[2] Huber P.J., Robust Estimation of a Location Parameter, *Ann. Math. Statist*., 35(1) (1964) 73-101.

[3] Huber P.J., Robust Regression: Asymptotics, Conjectures and Monte Carlo, *Annals of Statistics*, 1 (1973) 799-821.

[4] Bates D.M., Watts D.G., Nonlinear Regression Analysis and Its Applications, Wiley, New York (1988).

[5] Çağlar A., Forming Confidence Regions for Parameter Estimation in Nonlinear Models and a Comparison, MSc Thesis, Gazi University, Ankara, Turkey (1995).

[6] Aksoy S., Otokorelasyonlu Hata Terimli Doğrusal Olmayan Regresyon Modellerinde Parametre Tahmini, PhD Thesis, Gazi University, Ankara, Turkey (1996).

[7] Şengül T. ,Kiraz S., Non-Linear Models for Growth Curves in Large White Turkeys, *Turk J. Vet. Anim. Sci*., 29 (2005) 331-337.

[8] Çelik A., Aslan Y., Efe E., Investigation of Growth in Turkeys Using a Multiphasic Model, *Black Sea Journal Of Engineering And Science*, 5(1) (2022) 18-25.

[9] Çelik A., Multiphasic Growth Functions and Some Applications, MSc Thesis, Kahramanmaras Sutcu Imam University, Kahramanmaras, Turkey (2013).

[10] Ghanim Al-Ani Ban., Statistical modeling of the novel COVID-19 epidemic in Iraq, *Epidemiol. Methods*, 10(1) (2021) 20200025.

[11] Ritz C., Streibig J. C., Nonlinear Regression with R, Use R!, Springer Verlag (2008).

[12] Teleken J. T., A. C. Galvão, Robazza W. S., ‘‘Comparing Non-linear Mathematical Models to Describe Growth of Different Animals.’’ Acta Scientiarum, *Animal Sciences,* 39(1) (2017) 73–81.

Cumhuriyet Sci. J., 45(3) (2024) 618-628
DOI: https://doi.org/10.17776/csj.1467360

Cumhuriyet Science Journal

| csj.cumhuriyet.edu.tr | Founded: 2002 ISSN: 2587-2680 e-ISSN: 2587-246X Publisher: Sivas Cumhuriyet University

Modeling Long Memory Volatilities of Nigeria Selected Macro Economic Variables with Arfima and Arfima Figarch

Adewole Ayoade [1,a,*]

[1]*Department of Mathematics, Tai Solarin University of Education Ijagun Ogun State, Nigeria.*
**Corresponding author*

Research Article

History
Received: 10/04/2024
Accepted: 20/08/2024

ABSTRACT

The research delved into analysing the stochastic characteristics of Nigeria's Real GDP, the exchange rate of the Naira to US Dollar, and the inflation rate employing Autoregressive fractionally integrated moving average (ARFIMA) and the Autoregressive Fractionally Integrated Moving Average Fractionally Integrated Generalized Autoregressive Conditional Heteroskedasticity (FIGARCH) modelling approach. The ability of the hybrid formation of ARFIMA-FIGARCH model with Nigeria macroeconomic variables in modeling the periodicity of long memory volatilities was examined. ARIMA GARCH method of modeling was also employed in analyzing the volatilities of Nigeria selected macroeconomic variables to enrich the study. The efficiency of ARFIMA, ARFIMA FIGARCH and ARIMA GARCH models were evaluated with the forecast evaluation measurements. Results revealed that ARFIMA FIGARCH and ARIMA GARCH models are more adequate in modeling the Inflation rate and the exchange rate while ARFIMA present more adequacies in modeling the RGDP. This result revealed evidence of high volatilities in Nigeria Inflation and the exchange rate of Naira to US dollar.

Keywords: Volatilities, Long Memory, Macroeconomic variables, Arfima Figarch.

[a] *hayorhade2005@gmail.com - adewoleai@tasued.edu.ng* *https://orcid.org/0000-0002-5416-9202*

Introduction

Improvements in econometrics methods have fetched different tools of exploring the theoretical features of economic variables over time. Analyzing and modelling applied times series from diverse area of application in econometric study is very essential due to their salient features. Recently, there is evolution of phenomenon of modelling and forecasting series with long memory behavior with time varying conditional variance,[1-3] introduced a widely adopted method for analyzing long memory time series data through the utilization of autoregressive fractionally integrated moving average (ARFIMA) processes. The perception of long memory characteristics relates to the interdependence among data points gathered over a period of time. In the study of [4,5], long-term memory descriptions were described as the gradual decrease occurring in the autocorrelation function's graphical representation within a dataset. This phenomenon led to suggestion of applying fractional differencing in mean models when long memory is being identified in the time series data.

Researchers have extensively worked on analyzing significant inferences of long memory returns of modelling financial economic series. Modern researches delved into modelling of long memory in econometrics model, prediction of prices of agricultural products and numerous financial series [3,6,1,7] among others.

However, ARFIMA model is based on the assumptions of linearity, stationarity and homoscedasticity of error variance, ARFIMA model is incompetent in handling dataset that exhibits presence of high volatility, most financial time series portrays features involving high volatilities in unstable phase succeeding stability periods. Autoregressive conditional heteroscedastic (ARCH) model was proposed by [8] to handle cases of volatility in Times series.

Nevertheless, ARCH model has the features of rapid decay in squared residuals of unconditional autocorrelation function when compared to a usual observed values unless there is large extreme lag. The generalized autoregressive conditional heteroskedasticity (GARCH) model was developed by [9,10] with the purpose of handling the evolving pattern of conditional variance, thus addressing the limitations of the ARCH model. The square volatility modelling was assumed to relate to its past values and errors in estimating the parameters involved, GARCH model are independent of one another. Several theoretical and empirical works has been established relating GARCH and its kind.[11,12]. Long memory procedure allows the integration of conditional heteroscedasticity which revealed the presence non-periodic cycles. [13-15] Employed a seasonal ARFIMA model with GARCH errors in analyzing PM concentration. [16,17] explored nonlinear time series with GARCH models and nonetheless, neither the Generalized Autoregressive Conditional Heteroscedasticity nor ARCH process can effectively capture the handling of the presence of long memory in model volatility. Addressing long-term memory effects in variations, incorporating fractional differencing into variance models.

Developed a new notable model named FIGARCH in the realm of long-term memory variance from Exponential Generalized Autoregressive Conditional Heteroscedasticity (EGARCH), a generalized family of GARCH that allows persistency in conditional variance. Fractionally Integrated Generalized Autoregressive Conditional Heteroscedasticity (FIGARCH) model is mostly used for modeling long memory in time series with volatility. [18] FIGARCH model was introduced mainly to create a more flexible process of estimating and summarizing conditional variance that has dependencies in financial market volatility, the FIGARCH model permits gradual hyperbolic rate of decay for the lagged squared in the conditional variance function. Several studies had been conducted on modelling and forecasting times series model applying concept and relevance of FIGARCH model. FIGARCH model was employed by [2,19] in modeling and predicting the effect of long-range relationship long memory patterns in conditional variance. Applicability of FIGARCH in other field were well spelt out by researchers, [20,21] introduced a FIGARCH model with seasonality, the work gives room for examining both periodic patterns and long memory comportments in conditional variance.[22] ascertained that FIGARCH model operates in the opposite direction as that of ARFIMA in persistency, as the fractional parameters parameter approaches zero, the memory of the process rises. ARFIMA-FIGARCH model is a connection between ARFIMA model and FIGRACH model [23]. Several studies show the significant evidences of long memory model in series that exhibits volatilities through the use of ARFIMA-FIGARCH [24,25] among others.

A number of recent studies suggest that most macroeconomic variables exhibit long-range dependence followed by the periods of instability in volatility and should be modelled as a fractionally integrated process [26-28] among others. Although long-memory models have gained popularity in modeling and forecasting future series but there are limited studies explored the possibility of long-period dependence and volatilities of macro-economic variables in Nigeria. Modeling time series volatility aids in improving parameter estimation efficiency and forecast accuracy [29].

However, this study aims to leverage the combination of ARFIMA-FIGARCH models to capture both the mean and long memory aspects of volatility within combined data samples. The research endeavors to explore the empirical stochastic properties of the inflation rate, exchange rate, and Nigeria's Real GDP using both the autoregressive fractionally integrated moving average (ARFIMA) and the Autoregressive Fractionally Integrated Moving Average Fractionally Integrated Generalized Autoregressive Conditional Heteroskedasticity (FIGARCH) modeling approaches.

Moreover, this work investigates the capability of the ARFIMA-FIGARCH model using Nigeria macroeconomic variables to estimate the long memory volatilities. The model efficiency is then evaluated with the forecast evaluation measurements.

Material and Method

ARFIMA Model Process

The Autoregressive Fractionally Integrated Moving Average (ARFIMA) process is stated as:

$$\gamma(U)\,(1-U)^d X_t = \vartheta(U)\varepsilon_t \tag{1}$$

U is defined as the lag operator such that

$$UX_t = UX_{t-1} \tag{2}$$

and the $(1U)^d$ fractional difference operator replaced the usual standard difference operator $(1-U)$ of a short memory ARIMA process, d is a non-integer parameter that represent the level of the fractional difference. ε_t is independently and identically distributed with mean 0 and variance σ^2, $\gamma(U)$ and $\vartheta(U)$ signify AR and MA components respectively. The method is covariance stationary for the interval of d lying between - 0.5 and 0.5; which involve mean reversion when d is less than 1. [29],[4] and [5]) generalized process of ARFIMA as the fractional white-noise process Where $\gamma(U)$ is established to equal to unity to further analyze the features of the method. Following the fact that many time series steadily exhibits slow decay autocorrelations process, the possibility virtue of exploiting ARFIMA process with decay hyperbolic autocorrelation patterns in financial time series modeling are numerous compared to modelling the process of ARMA model that have either geometric exponential decay.

$$\begin{aligned}(1-U)^d &= \sum_{k=0}^{\infty}(-1)^k\binom{d}{k}(U)^k\\ &= 1-dU\\ &+\frac{d(d-1)}{2!}U^2\frac{d(d-1)(d-2)}{3!}U^3+,\ldots,+\sum_{k=0}^{\infty}C_k(d)\end{aligned} \tag{3}$$

for any d>-1. When $d = 0$, equation (3) above reduces to the classical ARMA(p,q) model, following the expression in equation (3), obvious significance of the hyperbolic features is shown.

Long Memory Test

Testing whether the observed data series exhibits long memory behavior is a prior process to method of estimating ARFIMA models. The techniques of Hurst Exponent will be employed in checking whether the data conforms to long memory structures.

Hurst Exponent

The Hurst exponent is one of the time series long-memory family. The long memory structure happens when the values of H fall in the interval 0.5 < H < 1. The Hurst exponent estimation process uses the formula;

$$H = \frac{\log\left(\frac{R}{S}\right)}{\log(N)} \qquad (4)$$

N signifies length of the sample data, R is the range, S is the standard deviation and $\frac{R}{S}$ is the matching value of the rescaled evaluation.

ARFIMA process estimation

The estimations of d are usually done in frequency domain. ARFIMA estimators of d are generally categorized into semi parametric and parametric forms.

This research employed the approaches of the Hurst exponent and semi-parametric approaches of Geweke and Porter–Hudak (GPH) methods to test and estimate long memory parameters, using the following regression,

$$\ln(w_k) = U - dln[4sin^2(w_k/2)] + n_k \qquad (5)$$

where $w_k = \frac{2nk}{T}, k = 1,2, \ldots, n,\ n_k$ is the white noise term and w_k represent the Fourier frequencies.

The periodogram of a time series a_1 is $I(w_k)$ defined as;

$$I(w_k) = \frac{1}{2\pi T} \left| \sum_{t=1}^{T} a_1 e^{-w_k t} \right|^2 \qquad (6)$$

GARCH Model

The variance equation of GARCH(u,v) model can expressed as;

$$\sigma_t^2 = \ \omega + \sum_{t=1}^{u} \alpha_i \varepsilon_{t-1}^2 + \sum_{t=1}^{v} \beta_j \sigma_{t-j}^2 \qquad (7)$$

The σ_t^2 are the model parameter to be estimated according to GARCH(u,v) models where $\omega > 0$, for i= 1…,u and $\beta_j \geq 0$, for j = 1,…,v.

α_i represent the parameter determining the effect of previous residual ε_{t-1}^2while βj measures the effect of change in its lagged value σ_{t-j}^2..

From equation (7), conditional variance $\sigma_{t.}^2, \varepsilon_t$ at time t dependent on the occurrence of the lagged squared errors in the preceding past periods and also on the conditional variance over the past periods.

In general, [7] has established that the stationarity of GARCH (*u, v*) if there is satisfactory of the following conditions,

$$E(\varepsilon_t) = 0 \qquad (8)$$

$$Var(\varepsilon_t) = \frac{\omega}{(1-\alpha(1)-\beta(1))} \qquad (9)$$

$Cov(\varepsilon_t, \varepsilon_s), t \neq s,\ provided\ \alpha(1) + \beta(1)$ is less than 1

The Fractionally Integrated Generalized Autoregressive Conditional Heteroscedasticity (FIGARCH).

The FIGARCH (*u,D,v*); model was introduced by [2]) in depicting long memory in volatility. The effect of shocks on the volatility is not finite. This infinite idea leads to the process of fractional integration in volatility. Fractional difference parameter (*D*) is used to model the persistent behavior of volatility in the FIGARCH model, whereas short term volatility is being considered by usual ARCH and GARCH parameters.

Considering, the typical (GARCH) model defined as;

$$\sigma_t^2 = \ \omega + \alpha(U)\varepsilon_t^2 + \beta(U)\sigma_t^2 \qquad (10)$$

where σ_t^2 and ε_t^2 are conditional and unconditional variances of ε_t respectively. U is the backshift operator and

$$\alpha(U) = \ \alpha_1 u + \ \alpha_2 u^2 +, \ldots, \alpha_v u^v$$

$$\beta(U) = \ \beta_1 u + \ \beta_2 u^2 +, \ldots, \beta_u u^u$$

To ascertain the stability and covariance stability of the ε_t process, all the roots of 1- $\alpha(U) - \ \beta(U)$and 1- $\beta(U)$ lies outside the unit circle.

From GARCH (*u,v*) model, the conditional variance of $\sigma_t^2,\ \varepsilon_t^2$ depends on the squared innovations in the previous *u* periods, and the conditional variance in the previous *v* periods. Equation (10) can be expressed as;

$$\sigma_t^2 = \ \omega + \sum_{t=1}^{p} \alpha_i \varepsilon_{t-1}^2 + \sum_{t=1}^{q} \beta_j \sigma_{t-j}^2 \qquad (11)$$

where $\sigma_{t-j}^2$is the volatility at day $t - j$, ω > 0, αi ≥ 0 for i = 1, … , p, and βj ≥ 0 for j = 1, … , q, are parameters of the model to be estimated.

The GARCH (*u, v*) process in equation [10] can be simplified as an ARMA (r,s) process in ε_t^2 as follows;

$$1 - \alpha(U) - \ \beta(U)\varepsilon_t^2 = \omega + \ \beta(U)v_t \qquad (12)$$

where r is equivalent to maximum of {u, v} and

$$v_t = \varepsilon_t^2 - \sigma_t^2 = (\epsilon_t^2 - 1)\ \sigma_t^2 \qquad (13)$$

The$\{v_t\}$ is known to be the innovations for the conditional variance. $\epsilon_t{}'s$ are uncorrelated with E(ϵ_t)= 0 and var (ϵ_t) *is* one.

From the integrated GARCH (IGARCH) models of [30] whose unconditional variance does not occur represented in equation (14) below

$$\text{(IGARCH) (p,q)} = \emptyset(U)(1 - U)\varepsilon_t^2 = \ \omega + [1 - \beta(U)v_t] \qquad (14)$$

where

$$(\emptyset(U) = \text{ 1-}\ \alpha(U) - \ \beta(U)(1 - U)^{-1} \qquad (15)$$

is of order r-1.

The Fractionally Integrated Generalized Autoregressive Conditional Heteroscedasticity (FIGARCH) is achieved by substituting first difference in equation (15) above with fractional difference operator $(1-U)^d$ such that;

$$\emptyset(U)(1-U)^d\varepsilon_t^2 = \omega + [1-\beta(U)]v_t \tag{16}$$

If d=0, the FIGARCH (u, D, v) process reduces to a GARCH (u, v) process and if d=1, the FIGARCH process becomes an integrated GARCH process. Rearranging the terms in Eq.(16), the FIGARCH model can be simplified as;

$$1-\beta(U)\sigma_t^2 = \omega + [1-\beta(U)]\,(1-U)^d\varepsilon_t^2 \tag{17}$$

ARFIMA- FIGARCH Model

The ARFIMA-FIGARCH model is employed to simultaneously investigate the long memory and volatility characteristics of a time series. The ARFIMA (*u,d,v*)-FIGARCH (*U,D.V*) model is a conditional time-dependent variance of the process σ_t^2 specified by the FIGARCH model defined in equation (16). The FIGARCH model propose enhanced flexibility in modeling volatility by enforcing an ARFIMA structure on ε_t^2 yielding a hybrid of ARFIMA FIGARCH model. In this hybrid forms, the two fractional integration parameters *d* and *D* will account for the long-term dynamics of the volatility of the series.

The ARFIMA (*u,d,v*)-FIGARCH (*U,D.V*) model follow this polynomial form

$$\emptyset(1-U)^d\,(r_{t-}\mu) = \theta(U)\varepsilon_t \tag{18}$$

$$1-\beta(U)(1-U)^D\varepsilon_t^2 = \omega + [1-\alpha(U)v_t] \tag{19}$$

$$\varepsilon_t = z_t\sigma_t\; z_t \sim N(0.1)$$

μ is an unconditional mean, u and v representing the AR and MA lag orders addressing the short memory, $d\epsilon(0,1)$ represents the long memory in the series; ε_t is a white noise process;

$$\emptyset(U) = 1-\emptyset_1U - \emptyset_2U^2 -, \dots, \emptyset_pU^u \tag{20}$$

And

$$\theta(U) = 1+\theta_1U + \theta_2U^2 +, \dots, \theta_qU^v \tag{21}$$

are the AR and MA polynomials, $D\epsilon(0,1)$ measures the degree of volatility persistence; where $\omega$is a constant,

$$\alpha(U) = \alpha_1U+\alpha_2U^2 +, \dots, \alpha_qU^v \tag{22}$$

$$\beta(U) = \beta_1U+\beta_2U^2 +, \dots, \beta_pU^u \tag{23}$$

are the ARCH and GARCH polynomials; v_t represents serially uncorrelated, zero-mean residuals, measured by

$$v_t = \varepsilon_t^2 - \sigma_t^2 \tag{24}$$

The methodology involved in the work involved the iterative steps of [31] which include identification of the adequate model, parameter estimations of the parameters involved, model diagnostic and forecasting.

THE ARIMA-GARCH Model

The ARIMA-GARCH model is employed to examine trend and volatility of a time series concurrently. ARIMA (p,d,q) and GARCH(u,v) is generally defined as

$$\emptyset(B)(1-U)^dY_t = \emptyset(U)\varepsilon_t \tag{25}$$

$$\varepsilon_t\,\left|Y_{t-1} \sim N(\mu,\sigma_t^2)\right. \tag{26}$$

The ARIMA-GARCH method has been established to handle the serial correlated residuals encountered in ARIMA models. ARIMA-GARCH model permits concurrent modeling of both the conditional means and the volatility of the series. Moreover, this method of modeling times series yields more precise estimate values and higher forecast performance compared to ARIMA models.

Test Statistics

Model Identification: stationarity and fractional integration modelling of the data involved were evaluated with the Autocorrelation function, partial autocorrelation function, ADF and KPSS at 0.05 level of significant level.

Augmented Dickey Fuller Test of Stationarity: ADF test model is expressed as;

$$\begin{aligned}\Delta X_t = \alpha X_{t-p} + Y_t\varphi + \beta_1\Delta X_{t-1}\\ + \beta_2\Delta X_{t-2}+, \dots, \beta_p\Delta X_{t-p}\end{aligned} \tag{27}$$

where,

ΔX_t denotes the differenced series

ΔX_{t-p} denotes the immediate past observations.

Y_t signifies the optional exogenous regressor which can be constant or be represented as constant trend

α and φ are parameters needed to be estimated.

$\beta_1, \dots, \beta_p$ signifies the coefficients of the lagged terms.

The ADF test statistic is denoted by

$$t_\alpha = \frac{\overbrace{\alpha}}{S_e(\overbrace{\alpha})} \tag{28}$$

The test of hypothesis involves;

H_0:$\alpha = 0$, it implies that the series contains unit roots

H_1:$\alpha < 0$, it implies that the series contains no unit roots.

Decision rule: Reject H_0: if t_α is less than asymptotic critical value

Kwiatkowski-Philips-Schmidt-Shin(KPSS)Test

Considering the following DGP with no linear trend that assumes the null hypothesis of stationarity;

$$y_t = x_t + z_t \tag{29}$$

where

$$x_t = \alpha_1 x_{t-1} + \alpha_2 x_{t-2} +, \dots, \alpha_p x_{t-p} + u_t \tag{30}$$

$u_t \sim iid(0.\sigma^2)$ and z_t is assume to follow a stationary process.

KPSS test statistic is expressed as;

$$KPSS = \frac{1}{N^2}\sum_{n=1}^{N}\frac{s_t^2}{\sigma^2\infty} \tag{31}$$

Where $s_t = \sum_{j=1}^{t}\widehat{m}_j$ with $\widehat{m}_t = x_t - x$ and $\hat{\sigma}_\infty{}^2$ is a long run variance estimator of the
stationary Process z_t.

Model selection

The model selection was accomplished implementing the optimum selection criteria by choosing the model with minimum Akaike Information Criteria (AIC), Schwarz Information Criterion (SIC) and Hannan-Quinn Information Criteria (HQIC).

Model estimation

After identification of the best tentative model, Quasi Maximum Likelihood (QMLE) method of estimation will be adopted to estimate the ARFIMA-FIGARCH model that is normally distributed based with the following log-likelihood function:

$$Log\ (\varepsilon_t\ \theta) = -\frac{1}{2}\log N(2\pi) - \frac{1}{2}\sum_{n=1}^{N}\left[\log\sigma_t^2 + \frac{\varepsilon_t^2}{\sigma_t^2}\right] \tag{32}$$

where $\theta' = (\alpha_0, d, \beta_1, \dots, \beta_p, \emptyset_1, \dots, \emptyset_q)$

Model Diagnostics

The white noise, serial correlation and the heteroscedasticity test was examined applying the residual normality test, the Portmanteau test and Autoregressive Conditional Heteroscedasticity Lagrange Multiplier (ARCH-LM) test respectively to validate the adequacy of the selected ARFIMA models. It is actualized by examining the test of the hypothesis of white noise residuals that assumed to be independently distributed.

Employing the methods of [29] the variance of autocorrelation is defined as

$\text{Var}(\rho_k(\varepsilon)) = \frac{1}{N(N-2)}$ (N-K), k= 1,2,…, K

And

$$\left(\sqrt{\frac{N-K}{N(N+2)}}\right)^{-1} \qquad \rho_k(\varepsilon) \approx N(0,1)$$

$$Q_{LB} = \left(\left(\sqrt{\frac{N-K}{N(N+2)}}\right)^{-1} \quad \rho_k(\varepsilon)\right)^2 \tag{33}$$

$$= N(N+2)\sum_{k=1}^{K}\frac{[\rho_k(\varepsilon)]^2}{N-K} \quad \approx \chi^2\ (K-1) \tag{34}$$

where K-1 = k-p-q and there is no inclusion of constant term in p+q, N is the sample size and ρ symbolize the autocorrelation coefficient.

Autoregressive Conditional Heteroscedastic-Lagrange Multiplier (ARCH –LM) Test

[8] proposed ARCH-LM test that allows issues of conditional heteroscedasticity in squared residuals, it has the null hypothesis that there is no heteroscedasticity in the model residuals. The test statistic is given by;

$$Q = B(B+2)\sum_{i=1}^{M}\frac{\rho_i}{(M-1)'} \tag{35}$$

the Q statistic is an asymptotic χ^2distribution that has n degrees of freedom with uncorrelated squared residuals, B is the number of observation and the sample correlation coefficient between squared residuals $\hat{\varepsilon}_t^2$ *and* $\hat{\varepsilon}_{t-1}^2$is denoted by ρ_i.

Model Forecasting and Performance Evaluation

Validation criterion such as; Akaike Information criteria (AIC), Schwarz Information Criterion (SIC) and Hannan-Quinn Information Criteria (HQIC) were employed for examining and comparing the predicting performances of the selected models

$$AIC = 2T - m \tag{36}$$

$$SIC = 2Tlogn - logm \tag{37}$$

$$HQIC = -2logm + 2Tlogn \tag{38}$$

where T symbolizes the total of estimable parameters, m denotes the maximum likelihood and n is the digits of samples. Moreover, the forecasts accuracy of fitted ARFIMA and ARFIMA FIGARCH model are evaluated in terms of Root Mean Square Error (RMSE), the Mean Absolute Error (MAE) and the Relative Mean Absolute Percentage Error (MAPE) respectively.

MAE is the absolute value of the difference between the forecasted value and the actual value. It calculates the average absolute deviation of predicted values from real values. MAE is estimated as follow:

$$HQIC = -2logm + 2Tlogn \tag{38}$$

$$MAE = \frac{1}{n}\sum_{t=1}^{n}\left|\hat{y}_f - y_t\right| \tag{39}$$

RMAPE is projected as the mean absolute percent error for each time period minus real values divided by real values. It computes the percentage of mean absolute error occurred in the model formation. It is stated as follows;

$$RMAPE = \frac{1}{n}\sum_{t=1}^{n}\left|\frac{\hat{y}_f - y_t}{y_t}\right| \times 100\% \quad (40)$$

RMSE illustrate the absolute fit of the model to the observed data, it is computed as follows:

$$RMSE = \sqrt{\frac{1}{n}\sum_{t=1}^{n}\left(\hat{y}_f - y_t\right)^2} \quad (41)$$

Where: $\hat{y}_f$ and y_t are the estimated and the real values respectively; n is the sample size. Model with lesser value is likely to have the best precision power of forecast.

Data Collection and Description

The data for this study is a secondary monthly data set from 1970 to 2023 obtained from Nigeria CBN bulletin, it comprised figures of Real Gross Domestic Product (RGDP) per capital, Inflation rate and Exchange rate of Naira-US Dollar.

Results and Discussion

Table 1. Summary Statistics

	RGDP	Inflation Rate	Exchange rate
Mean	173.8996	0.181853	91.78458
Median	73.48	0.1301	21.89526
Maximum	574.18	0.7284	425.9792
Minimum	9.18	0.0346	0.546781
Std. Dev.	175.9127	0.151777	115.8329
Skewness	0.893138	2.010273	1.302508
Kurtosis	2.190781	6.343058	3.872064
Jarque-Bera	8.492408	6.3776556	16.66542
P- value	0.014318	0.0000000	0.000241
Sum Sq. Dev.	1609155	1.197882	697698
Observations	648	648	648

NB: RGDP is Real Gross Domestic Product per capital.

Table 1. gives the summary statistics of monthly average macro-economic data for this study, the series ranges from 1970 to 2023.The total observation is 648, which is large enough for modelling Autoregressive Fractionally Integrated Moving Average models. The series are normally distributed as revealed by the high p-value and low Jarque-Bera test values.

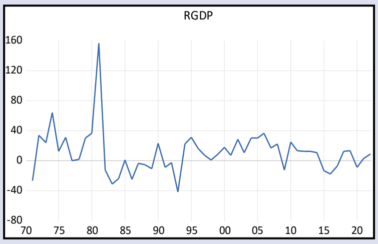

Figure 1. Times series plot of RGDP

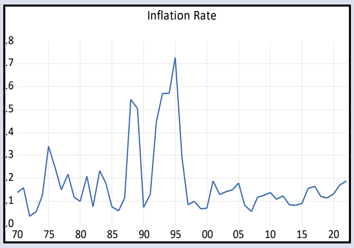

Figure 2. Times series plot of INF. RT

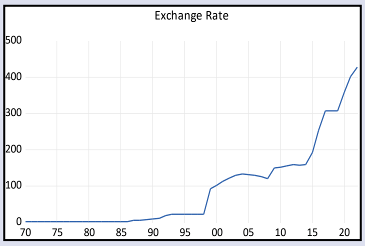

Figure 3. Times series plot of EXC. RT.

Fig 1, 2 and 3 displays times series plots of the average annual series of Nigeria Real Gross Domestic Product (RGDP) per capital, Inflation rate and exchange rate of Naira-US dollar respectively. The plot shows the direction of the series over time.

Table 2. Stationarity test results at level.

	ADF		KPPS	
Variables	ADF Test Stat	Prob.	KPSS Test Stat	Prob.
RGDP	-4.2670	0.0278	0.5196	0.0341
INFLATION RATE	0.1953	0.1374	0.3301	0.0922
EXCHANGE RATE	-2.3203	0.0732	0.6282	0.0638

Table 3. Stationarity test results at First Difference.

	ADF		KPPS	
Variables	ADF Test Stat	Prob.	KPSS Test Stat	Prob.
RGDP	-2.1023	0.008	0.6318	0.000
INFLATION RATE	0.2310	0.002	0.6027	0.036
EXCHANGE RATE	-4.1203	0.000	0.8924	0.091

Table 2 and 3 shows the result of ADF and KPSS test for unit root of Nigeria Real Gross Domestic Product (RGDP) per capital, Inflation rate and exchange rate of Nigeria Naira to US Dollar using the lag length of 12. The outcome of the unit root test for ADF-test of RGDP shows that the variable is stationary at level of 5% level of significant, which implies that RGDP is integrated of order zero i.e., 1(0) while the results of ADF of the inflation and exchange rate indicate that the time series data integrated at I (1). The KPSS tests at both level and first difference are greater than 5% critical values which shows that the series is neither I(0) nor I(1), this warrant needs to carry out fractional difference on the data.

Table 4: Long Memory tests of the ARFIMA models.

	Macroeconomics Variables		
	RGDP	INFLATION RATE	EXCHANGE RATE
HURST.E/RS	0.6302 (0.002)	0.7210 (0.000)	0.6664 (0.008)

Hurst. E/ RS is the Hurst Exponent Rescaled Range.

Table 4. above shows the Hurst exponent values of Nigeria RGDP per capital, Inflation and Exchange rate of Nigeria Naira to US Dollar data using the rescaled Range, Table 4 confirmed the existence of long memory of the series under study. Also, the Hurst exponent test gives values in the range of $0 < d < 1$.

Fig 4,5 and 6 above displayed the correlogram of Nigeria RGDP per capital, Inflation and Exchange rate of Nigeria Naira to US Dollar respectively. From the correlogram of the series presented in fig 4,5 and 6 above, several speculative ARFIMA models for the variables were fitted to the series.

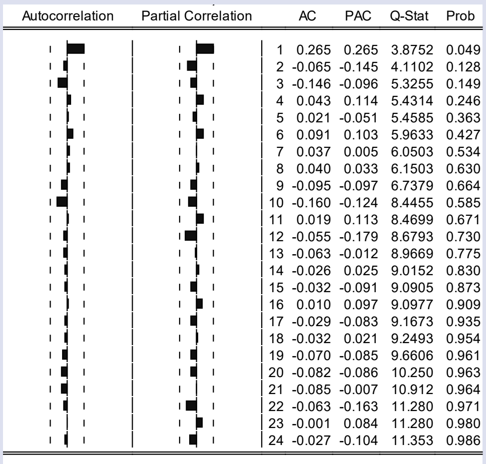

```
Autocorrelation   Partial Correlation      AC     PAC   Q-Stat   Prob

                                       1  0.265  0.265  3.8752  0.049
                                       2 -0.065 -0.145  4.1102  0.128
                                       3 -0.146 -0.096  5.3255  0.149
                                       4  0.043  0.114  5.4314  0.246
                                       5  0.021 -0.051  5.4585  0.363
                                       6  0.091  0.103  5.9633  0.427
                                       7  0.037  0.005  6.0503  0.534
                                       8  0.040  0.033  6.1503  0.630
                                       9 -0.095 -0.097  6.7379  0.664
                                      10 -0.160 -0.124  8.4455  0.585
                                      11  0.019  0.113  8.4699  0.671
                                      12 -0.055 -0.179  8.6793  0.730
                                      13 -0.063 -0.012  8.9669  0.775
                                      14 -0.026  0.025  9.0152  0.830
                                      15 -0.032 -0.091  9.0905  0.873
                                      16  0.010  0.097  9.0977  0.909
                                      17 -0.029 -0.083  9.1673  0.935
                                      18 -0.032  0.021  9.2493  0.954
                                      19 -0.070 -0.085  9.6606  0.961
                                      20 -0.082 -0.086  10.250  0.963
                                      21 -0.085 -0.007  10.912  0.964
                                      22 -0.063 -0.163  11.280  0.971
                                      23 -0.001  0.084  11.280  0.980
                                      24 -0.027 -0.104  11.353  0.986
```

Figure 4. Correlogram of RGDP

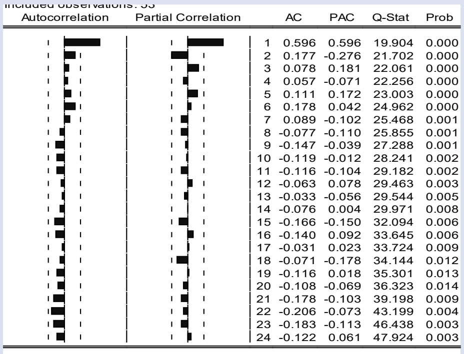

```
Autocorrelation   Partial Correlation      AC     PAC   Q-Stat   Prob

                                       1  0.596  0.596  19.904  0.000
                                       2  0.177 -0.276  21.702  0.000
                                       3  0.078  0.181  22.061  0.000
                                       4  0.057 -0.071  22.256  0.000
                                       5  0.111  0.172  23.003  0.000
                                       6  0.178  0.042  24.962  0.000
                                       7  0.089 -0.102  25.468  0.001
                                       8 -0.077 -0.110  25.855  0.001
                                       9 -0.147 -0.039  27.288  0.001
                                      10 -0.119 -0.012  28.241  0.002
                                      11 -0.116 -0.104  29.182  0.002
                                      12 -0.063  0.078  29.463  0.003
                                      13 -0.033 -0.056  29.544  0.005
                                      14 -0.076  0.004  29.971  0.008
                                      15 -0.166 -0.150  32.094  0.006
                                      16 -0.140  0.092  33.645  0.006
                                      17 -0.031  0.023  33.724  0.009
                                      18 -0.071 -0.178  34.144  0.012
                                      19 -0.116  0.018  35.301  0.013
                                      20 -0.108 -0.069  36.323  0.014
                                      21 -0.178 -0.103  39.198  0.009
                                      22 -0.206 -0.073  43.199  0.004
                                      23 -0.183 -0.113  46.438  0.003
                                      24 -0.122  0.061  47.924  0.003
```

Figure 5. Correlogram of INF.RT

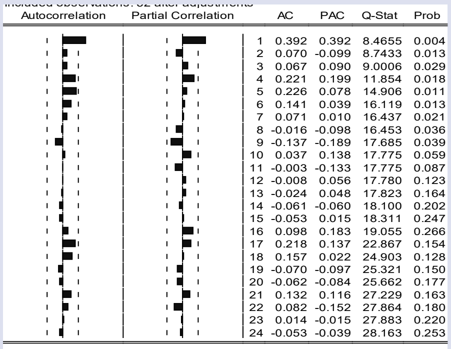

```
Autocorrelation   Partial Correlation      AC     PAC   Q-Stat   Prob

                                       1  0.392  0.392  8.4655  0.004
                                       2  0.070 -0.099  8.7433  0.013
                                       3  0.067  0.090  9.0006  0.029
                                       4  0.221  0.199  11.854  0.018
                                       5  0.226  0.078  14.906  0.011
                                       6  0.141  0.039  16.119  0.013
                                       7  0.071  0.010  16.437  0.021
                                       8 -0.016 -0.098  16.453  0.036
                                       9 -0.137 -0.189  17.685  0.039
                                      10  0.037  0.138  17.775  0.059
                                      11 -0.003 -0.133  17.775  0.087
                                      12 -0.008  0.056  17.780  0.123
                                      13 -0.024  0.048  17.823  0.164
                                      14 -0.061 -0.060  18.100  0.202
                                      15 -0.053  0.015  18.311  0.247
                                      16  0.098  0.183  19.055  0.266
                                      17  0.218  0.137  22.867  0.154
                                      18  0.157  0.022  24.903  0.128
                                      19 -0.070 -0.097  25.321  0.150
                                      20 -0.062 -0.084  25.662  0.177
                                      21  0.132  0.116  27.229  0.163
                                      22  0.082 -0.152  27.864  0.180
                                      23  0.014 -0.015  27.883  0.220
                                      24 -0.053 -0.039  28.163  0.253
```

Figure 6. Correlogram of EXC

(RGDP) per capital, INF. RATE and EXCH. RATE is the inflation rate and exchange rate of Nigeria Naira to US Dollar respectively.

Table 5 report the estimates of the fractional difference of Nigeria RGDP per capital, inflation and exchange rate series employing an automatic commencement of integration employing approaches of Geweke and Porter-Hundlak log-periodogram. The competitive estimated models of each series and their respective values for the selection criteria are as tabulated in Table 5. The optimum model for each series is in bold print and asterisk mark for easier identification.

Table 5. ARFIMA Model Identification

MODEL	ARFIMA (p,d,q)	D	AIC	SIC	HQIC
		RGDP			
MODEL 1	ARFIMA 1, d, 1	0.5117	6.393*	6.937*	6.842*
MODEL 2	ARFIMA 1, d, 2	0.1956	7.220	7.479	6.926
MODEL 3	ARFIMA 2, d, 1	0.8945	6.451	6.952	6.970
		INF. RATE			
MODEL 1	ARFIMA 1, d, 1	0.5339	12.002	10.573	10.208
MODEL 2	ARFIMA 1, d, 2	0.7167	13.342	9.175	9.944
MODEL 3	ARFIMA 2, d, 2	0.6802	9.035*	8.884*	9.240*
		EXCH. RATE			
MODEL 1	ARFIMA 1, d, 1	0.6930	4.720*	4.717*	4.509*
MODEL 2	ARFIMA 2, d, 2	0.7760	4.939	4.958	4.820

NB: RGDP is the of Nigeria Real Gross Domestic Product

Table 6: Parameter Estimates of the ARFIMA fitted model.

Parameter	Coefficient	Standard Error	Prob.
	RGDP		
D	0.5117	0.0324	0.0001
γ_1	0.1972	0.0208	0.0000
ϑ_1	0.8287	0.0450	0.0009
	Inflation Rate		
D	0.6802	0.5810	0.0057
γ_1	-0.9567	0.3981	0.0002
γ_2	0.8326	0.3106	0.0028
ϑ_1	0.2798	0.2851	0.0000
ϑ_2	0.2089	0.0495	0.0005
	Exchange Rate		
D	0.6930	0.8314	0.0049
γ_1	1.0038	0.0348	0.0000
ϑ_1	-0.9822	0.3119	0.0000

Diagnostics checking of ARFIMA Models.

Table 7: Statistical tests of the residuals of selected ARFIMA models.

Times series	**ARFIMA(p,fd,q)**	**Autocorrelation Test**		**Heteroskedacity Test**		**Normality test**	
	Model	**Lung Box Q**	**Portmanteau**	**Breusch Pagan**	**White**	**Jarque Test**	**Bera Shapiro Wiki**
		p- value	**p- value**	**p-value**	**p. value**	**p-value**	**p-value**
RGDP	ARFIMA(1,0.5117,1)	0.1923	0.1011	0.1422	0.1721	0.2431	0.2142
Inflation RT	ARFIMA(2, 0.6802,2)	0.2831	0.1829	0.2160	0.3230	0.2206	0.3339
Exchange RT	ARFIMA(1, 0.6930,1)	0.2925	0.2026	0.2542	0.4951	0.3534	0.1474
α		0.05	0.05	0.05	0.05	0.05	0.05

Table 7 gives the outcome of the autocorrelation, Heteroskedacity and the normality check and the respective p values for each selected ARFIMA models for the variables. The normality tests revealed that the residuals generated from the selected ARFIMA models are normally distributed, the Ljung-Box and the Portmanteau value for all the variables are greater than the significant level which inferred that there is no autocorrelation among the residual of the model's forecast errors, moreso, the results of heteroscedasticity tests of residuals for the variables revealed homoscedasticity nature of the residuals.

FIGARCH Model Estimation.

Heteroscedasticity Test

Table 8: Results of test for ARCH effect on the series.

	RGDP		**Inflation Rate**		**Exchange Rate**	
	Test statistic value	**Prob.**	**Test statistic value**	**Prob.**	**Test statistic value**	**Prob.**
F Statistic	134.4516	0.0000^{**}	89.3780	0.0001^{**}	158.2819	0.0000^{**}
Observed R^2	140.1827	0.0000^{**}	94.2268	0.000**	147.2072	0.0000^{**}

**1% level

To model the volatility of a time series variable, it is mandatory to test for the presence of ARCH Effect in the residuals of the series.

The result of the ARCH-LM test in Table 8 revealed the presence heteroscedasticity in the series. The macro-economic variables reveal presence of conditional volatility from the result which can well be captured by fitting a FIGARCH model to the series.

Table 9: FIGARCH 1, D,1 Models

	RGDP	**Inflatıon**	**Exchange**
ω	1.3269 (1.7219)	1.4649 (1.0172)	1.2895 (1.0170)
α_1	0.0496 (0.1206)	-0.0427(0.192)	-0.3102(0.282)
β_1	0.3314(0.225)	0.3509 (0.422)	0.5819 (0.014)
D	0.3842(0.162)	0.4682(0.332)	0.3936(0.171)
In (L)	1928.816	1048.619	2734.307
AIC	8.3694	6.2791	4.9164
SIC	8.2001	6.2640	.49387
Q(5)	7.8854	12.1552	5.3458
ARCH 5	0.6852 (0.773)	0.5293 (0.1193)	0.2204 (0.7898)
Skewness	-0.0295	0.0074	0.00367
Jarque Bera	43.39	68.06	92.18
Kurtosis	1.4438	1.3941	1.4140

Table 9 above presented the estimates of FIGARCH models, the standard errors are reported in parenthesis, the model selection is based on the selecting model that has the lowest selection criteria and passes Q-test simultaneously using AIC, SIC and Ljung-Box Q-statistics.

The model fitting specifications are given in Table 9, Estimate of long memory parameter 'D' from the FIGARCH model above is shown to be significantly different from zero and falls within theoretical range. the revealing that the volatility exhibits a long memory process in the macro-economic variables under study. This justifies the significance of modeling persistence behavior in volatility and hence there is need for the dual long memory test. This justification brings about the examination of blended ARFIMA- FIGARCH model in investigating the structure of long memory and volatility simultaneously in the series.

Table 10: Estimates of ARFIMA FIGARCH Model.

Series	**RGDP**	**Inflation**	**Exchange Rate**
Mean Equation			
Constant (μ)	0.024^{**} (0.020)	0.037^{**} (0.016)	0.042^{**} (0.028)
AR 1	-0.168^{**} (0.221)	-0.721 (0.217)	-0.150 (0.4 20)
AR 2		0.135^{**}(0.024)	
MA 1	-0.354^{**} (0.095)	-0.779^{**} (0.010)	0.241 (0.193)
MA 2		-0.372^{**}(0.005)	
D	0.257^{**} (0.040)	0.450^{**} (0.000)	0.665^{**} (0.012)
Variance Equation			
Constant (ω)	0.025^{**} (0.001)	0.016^{**} (0.062)	0.033^{**} (0.031)
α_1	0.326^{**} (0.000)	0.064^{**} (0.000)	0.283^{**} (0.000)
β_1	0.532^{**} (0.005)	0.715^{**}(0.021)	0.867^{**} (0.041)
D	0.696^{**} (0.019)	0.305^{**} (0.001)	0.518^{**} (0.02)
In (L)	-6403.186	-3949.247	-7351.233
AIC	8.278	6.125	9.223
SIC	8.279	6.532	.9246
Q(5)	7.304	4.365	2.294
ARCH(5)	3.680	1.526	3.389

Notes: Table 10 gives the estimates of the quasi-maximum likelihood estimation of the hybrid of ARFIMA-FIGARCH model for the monthly data of Nigeria macroeconomic variables.

ARFIMA FIGARCH model combines the ARFIMA model that considered the mean behavior of the time series and the FIGARCH model which is employed to model the variance behavior (ARCH effect).

Table 11: Estimate of ARIMA GARCH.

	Coefficient	Std. Error	t- value	Prob.
		RGDP		
θ	0.3203	0.2936	-1.3144	0.0144
ω	0.0016	0.0026	2.0270	0.0039
α	0.1231	0.0182	2.2033	0.0000
β	0.2849	0.0315	4.3184	0.0007
		INFLATION RATE		
θ	0.2701	0.0631	0.3164	-2.284
ω	0.0019	0.0000	1.2012	0.0022
α	0.3861	0.0742	2.5433	0.0000
β	0.3849	0.0201	5.2934	0.0001
		EXCHANGE RATE		
θ	0.3031	0.1333	-1.8344	0.0038
ω	0.0029	0.0018	0.3712	0.0000
α	0.2171	0.0182	0.3733	0.0050
β	0.3749	0.0171	2.1634	0.0000

Applying the residual series obtained from the fitted ARFIMA models, suitable FIGARCH models were built. Table 10 above present results of the combined ARFIMA-FIGARCH model fitted to the macro-economic variables series and parameter estimates with their respective standard error in bracket, the best model is selected on the basis of the selection criteria. From Table 10, the fractional parameters for all the variables at 5% level of significance revealed significances.

ARIMA-GARCH model combines the ARIMA model that considered the mean behavior of the time series and the GARCH model which is employed to model the variance behavior (ARCH effect).

Table 12: Diagnostics check for the ARIMA GARCH Model.

Times series	Model	Portmanteau Test	ARCH LM Test
RGDP	ARIMA(1,1,1) GARCH(1,1)	(1623.258) 0.0122	(11.6128) 0.4721
INF RATE	ARIMA(1,1,1) GARCH(1,1)	(2102.1671) 0.3190	(9.336) 0.2775
EXCH RATE	ARIMA(1,1,1) GARCH(1,1)	(1918.2052) 0.1884	(11.3688) 0.0326

Applying the residual series obtained from the fitted ARIMA models, suitable GARCH models were built. The results of the combined models are presented in Table 11 above while Table 12 presents the serial correlation and heteroscedascity diagnostics for the ARIMA-GARCH models.

Table 13: Evaluation of selected ARFIMA, ARFIMA FIGARCH and ARIMA GARCH Models forecast Accuracy.

	ARFIMA			ARFIMA FIGARCH			ARIMA GARCH		
	RGDP	INF RATE	EXCH RATE	RGDP	INF RATE	EXCH RATE	RGDP	INF RATE	EXCH RATE
RMSE	0.0312	0.5051	0.3347	0.5147	0.0212	0.0112	0.0172	0.2934	0.0311
MAE	0.0235	0.4637	0.2619	0.1196	0.0257	0.0214	0.0219	0.4826	0.0292
MAPE	0.1947	0.6853	0.4417	0.2226	0.0051	0.0092	0.0039	0.5044	0.0018
R^2	0.9274	0.8155	0.8771	0.9742	0.9602	0.8899	0.9912	0.9187	0.8938

Table 13 displayed the ARFIMA, ARFIMA FIGARCH and ARIMA GARCH selected models for Nigeria macro-economic variables forecast accuracy measures respectively. From the Results comparison of ARFIMA, ARFIMA FIGARCH and ARIMA GARCH modeling from Table 13, low estimates of the validation statistics such as RMSE, MAE and MAPE from ARFIMA FIGARCH and ARIMA GARCH models revealed the adequacy of the models in modeling the Inflation Rate and the exchange rate while estimates of validation statistics from ARFIMA model shows more adequacy in modeling the RGDP. This result revealed evidence of high volatilities in Nigeria Inflation and the exchange rate of Naira to US dollar. The low values of an unbiased statistic MAPE of ARFIMA FIGARCH models in Table 13 revealed the adequacy of the selected ARFIMA FIGARCH models. Moreover, the general error measures showed evidence of better forecast performance with ARFIMA FIGARCH models in forecasting the inflation and exchange values of Naira to US dollar.

Conclusion

The study investigated the relevance of two iterative methods of long memory dependency in modeling and forecasting the rate and volatilities of selected major macro-economic variables of Nigeria, these variables were chosen based on the crucial roles they played in influencing the overall economic performance of Nigeria economy; the selected predictors are some of the powerful instruments for upgrading developing nations from their current economic status. Hybrid of ARFIMA-FIGARCH and ARFIMA model were employed in modeling the series. FIGARCH techniques of modeling were applied to model the residuals sequence from the fitted ARFIMA model. ARIMA GARCH methods of modeling were also employed in analyzing the volatilities of Nigeria selected macroeconomic variables to enrich the study. Results comparison of ARFIMA, ARFIMA-FIGARCH and ARIMA

GARCH modeling revealed that ARFIMA-FIGARCH and ARIMA GARCH models are more adequate in modeling the Inflation Rate and the exchange rate while ARFIMA present more adequacies in modeling the RGDP. The selection of the best model is based on the minimum selection criteria. The result from the research revealed evidence of high volatilities in Nigeria inflation and the exchange rate of Naira to US dollar. Certainty of the fitted models was established by the evidence of minimal values of MAPE. Both conditional mean and conditional variance parameters of the long memory were statistically significant, this revealed the prevalence of the dual long memory property in the series and volatility.

Conflict of Interest

Author declares no conflict of interest.

References

[1] Adewole A.I., Statistical Modelling and Forecasting of Temperature and Rainfall in Ijebu Ode Nigeria Using SARIMA, *FNAS Journal of Scientific Innovations*, 5(2) (2023) 55-68.

[2] Baillie R.T., Bollerslev T., and Mikkelsen H.O., Fractionally integrated generalized autoregressive conditional Heteroskedasticity, *Journal of Econometrics,* 74 (1996) 3–30.

[3] Beran J., Statistics for Long-Memory Processes*,* Chapman and Hall Publishing Inc., New York, (1995).

[4] Granger C.W.J., Joyeux R., an Introduction to Long-Memory Time Series Models and Fractional Differencing, *Journal of Time Series Analysis*, 1 (1980) 15-29.

[5] Hosking J.R.M., Fractional Differencing, *Biometrika*, 68 (1981) 165-176.

[6] Robinson P.M., Log-periodogram regression of time-series with long-range dependence, *The Annals of Statistics*, 23 (1995) 1048–1072.

[7] Paul R.K., Gurung B., Paul A.K., Modelling and Forecasting of Retail Price of Arhar Dal in Karnal, Haryana, *Indian Journal of Agricultural Science*, 85(1) (2015a) 69-72.

[8] Engle R.F. Autoregressive conditional heteroscedasticity with estimates of the Variance of U.K. inflation, Econometrica**,** 50 (1982) 987-1008.

[9] Bollerslev T., Generalized autoregressive conditional heteroskedasticity, Journal of Econometrics**,** 31 (1986) 307-327.

[10] Taylor S. J., Modeling Financial Time Series, New York, Wiley, (1986).

[11] Fung, H.G., Lo W.C., Peterson J.E., Examining the Dependence in Intra-Day Stock Index Futures, the Journal of Futures Markets, 14 (1994) 405-419.

[12] Adewole A.I., On the Hybrid of ARIMA and GARCH Model in Modeling Volatilities in Nigeria Stock Exchange. Bima Journal of Science and Technology, 8(1A) (2024) 169-180.

[13] Reisen V.A., Sarnaglia A.J.Q., Reis J., L'Evy-Leduc N.C., Santos J.M., Modeling and Forecasting Daily Average PM10 Concentrations by a Seasonal Long-Memory Model with Volatility, Environmental Modeling and Software, 51 (2014) 286-295.

[14] Adewole A.I. The Performance of ARIMA and ARFIMA in Modeling the Exchange Rate of Nigeria Currency to other Currencies**.** Al- Bahir Journal for Engineering and Pure Sciences, 4 (2) (2024)142-155.

[15] Tong H., Nonlinear Time Series Analysis, International Encyclopedia of Statistical Science, Springer, Berlin, Heidelberg, (2011) 955-958.

[16] Narayan P.K., Liu R., Westerlund J. A., Garch Model for Testing Market Efficiency. Journal of International Financial Markets, Institutions and Money, 41 (2016) 121-138.

[17] Bollerslev T., Mikkelsen H.O., Modeling and pricing long memory in stock market volatility, Journal of Econometrics, 73 (1) (1996) 151-184.

[18] Bordignon S., Caporin M., Lisi F. A., seasonal fractionally integrated GARCH model*,* working paper*,* University of Padova, Italy (2004).

[19] Paul R.K., Forecasting Wholesale Price of Pigeon Pea Using Long Memory Time-Series Models, Agricultural Economics Research Review, 27 (2) (2014) 167-176.

[20] Paul R.K., Samanta S., Gurung B., Monte Carlo simulation for comparison of different estimators of Long Memory parameter: An application of ARFIMA model for forecasting price, Model Assisted Statistics and Application, 10 (2) (2015b) 116-127.

[21] Davidson J., Moment and memory properties of linear conditional heteroscedasticity models, and a new model. Journal of Business and Economic Statistics, 22 (2004) 16-29.

[22] Kang S. H., Yoon S. M., Dual Long Memory Properties with Skewed and Fat-Tail Distribution, International Journal of Business and Information, 7 (2) (2012) 225-249.

[23] Slaveya Z., ARFIMA-FIGARCH, HYGARCH and FIAPARCH Models of Exchange Rates, Journal of the Union of Scientists, 7 (2) (2018) 142-153.

[24] Umar A. G., Dikko H. G, Garba J., Tasi'u M. A., Study of Nigeria Monthly Stock Price Index using ARTFIMA-FIGARCH Hybrid Model**,** UMYU Scientifica, 2 (4) (2023) 114 – 121.

[25] Skare M., Stjepanović S., A Fractionally Integrated Model for the Croatian Aggregate Output (Gdp) Series, Ekonomska Istraživanja, 26 (2) (2013) 1–34.

[26] Caporale, Guglielmo M., Škare, M., Long memory in UK real GDP, 1851- 2013: An ARFIMA-FIGARCH Analysis, *DIW Discussion Paper*s, Deutsches Institut für Wirtschaftsforschung (DIW), Berlin 1395 (2014).

[27] Aliyu M. A., Dikko H. G., Danbaba U. A., Statistical modeling for forecasting volatility in Naira per Dollar Exchange rate using ARFIMA-GARCH and ARFIMA FIGARCH models, World scientific Journal, *176* (2022) 27–42.

[28] Tayafi M., Ramanathan T.V., An overview of FIGARCH and related time-series models, Australian Journal of Statistics, 141 (2012) 175-196.

[29] Granger, C.W.J., Long memory relationships and the aggregation of dynamic models, Journal of Econometrics, 14 (1980) 227-238.

[30] Engle R.F., Bollerslev T., Modelling the persistence of conditional variances, *Econometric Reviews,* 5(1) (1986) 1-50.

[31] Box, G.E.P and Jenkins, M, Time Series analysis forecasting and control. Holden –Day Inc (1976).

Cumhuriyet Sci. J., 45(3) (2024) 629-635
DOI: https://doi.org/10.17776/csj.1294596

Cumhuriyet Science Journal

| csj.cumhuriyet.edu.tr | Founded: 2002 ISSN: 2587-2680 e-ISSN: 2587-246X Publisher: Sivas Cumhuriyet University

Parameter Estimation of the Inverted Kumaraswamy Distribution by Using L-Moments Method: An Application on Precipitation Data

Kübra Bağcı Genel [1,a,*]

[1] *Econometrics Department, Faculty of Economics and Administrative Sciences, Van Yüzüncü Yıl University, Van, Türkiye.*
**Corresponding author*

Research Article

History
Received: 09/05/2023
Accepted: 10/09/2024

ABSTRACT

Modeling precipitation data plays a critical role in water resource and flood management. Statistical distributions are frequently used in describing hydrological variables. Different distributions and estimation methods have been presented in previous studies for modeling precipitation data. In this study, the inverted Kumaraswamy distribution is considered for its advantageous properties, and the L-moments and maximum likelihood methods are employed in estimating the parameters of the inverted Kumaraswamy distribution. In the application part, the annual maximum monthly precipitations recorded in the Rize, Türkiye are modeled with the inverted Kumaraswamy distribution. To the best of the author's knowledge, the L-moment method is considered for the first time to estimate the parameters of the inverted Kumaraswamy distribution. In addition, the efficiencies of the estimation methods are compared with a Monte-Carlo simulation study. For evaluating the performances of the estimation methods, the goodness of fit criteria including root mean square error, Kolmogorov Smirnov test, and coefficient of determination (R^2) are used in the application part of the study. The results show that for the data considered, the L-moments method yields more accurate results than the maximum likelihood method in estimating the parameters when the sample size is small. Accordingly, the corresponding distribution with L-moments estimations provides a better fit to precipitation data obtained from the Rize station.

Keywords: L-moments, Parameter estimation, Inverted kumaraswamy, Precipitation.

[a] *kubrabagci@yyu.edu.tr* *https://orcid.org/0000-0002-6679-9738*

Introduction

According to European Environment Agency [1] increased flooding is likely to be one of the most serious effects of climate change in Europe over the coming decades. In connection with flood management planning, modeling precipitation data has been one of the highlights in the field of hydrology. In recent years, there has been a growing interest in using probability distribution models to analyze precipitation data. The accurate prediction of precipitation is essential for effective flood management, water management, and hydrological modeling. Accordingly, the primary concerns of the studies using probability distribution models are to fit the most suitable probability density function (pdf) to data and estimate its parameters accurately.

In parameter estimation, several methods are available in the literature, such as maximum likelihood (ML), least squares, L-moment methods, and so on. The L-moment estimation is one of the methods for estimating the parameters of a probability distribution based on order statistics presented by Hosking [2]. The L-moment method is generally known for its applications in the hydrology field. It has some advantageous features that make it attractive for application to precipitation data where extreme rainfall events are possible. The use of L-moments has been shown to provide robust estimates of the parameters of distributions, especially when dealing with small sample sizes or skewed data [3]. As mentioned, another concern of using probability models is, fitting the most suitable distribution to data. Since every region has its own characteristics, the selection of the pdf mainly depends on the available precipitation data at a particular site [4]. Different pdf's are employed in modeling various natural phenomena including precipitation previously. The Kumaraswamy distribution is one of the distributions generally known for its applications in the hydrology field. A transformation of the Kumaraswamy distribution introduced by Abd Al-Fattah et al. [5] called the inverted Kumaraswamy (IKum) distribution presents some advantageous features such as having a longer right tail that increases the modeling ability of the distribution. The use of the IKum distribution in modeling ecological (precipitation and wind speeds) variables has been studied previously, see [6] and [7] respectively. Bagci et al. [7] have shown that the Ikum distribution can provide a better fit to given data compared to other well-known distributions, such as the Weibull, in some cases.

Consequently, the IKum distribution is employed in this study for modeling the precipitation data obtained from Rize province since it has some tractable properties. Rize is a province located in the eastern Black Sea region of Türkiye, which is a flood-prone area due to its geographical and climatic features. Unfortunately, Rize has been the subject of devastating flooding and landslides most recently. In addition, Rize is the rainiest province in Türkiye, having a total annual precipitation of over 2300 mm [8]. As a result, many studies are addressing the issue using different approaches. However, the studies in the region mostly concentrated on time series analysis. Such as Yozgatlıgil and Türkeş [9], modeled monthly maximum precipitation amounts for 60 year period using a pdf and time series analysis approach for several stations in the Black Sea region. They employed the generalized extreme value distribution in the analysis and the time series analysis. Cengiz et al. [10] analyzed historical precipitation changes at 16 stations during 1960–2015 in the Black Sea region of Türkiye. They emphasized the limitations in time series analysis such as normality, and independence of series, and used a combination of graphical and statistical methods to relax some of these restrictive assumptions. Aksu et al. [11] employed a comprehensive set of statistical methods to provide a detailed analysis of precipitation patterns in the Black Sea region mostly focused on trend analysis.

Numerous studies have been presented to compare different parameter estimation methods in the literature additionally. Upon analysis of these studies, it becomes apparent that the most effective probability distribution and estimation method may differ based on the unique precipitation characteristics of the region being studied. For example, Lee et al. [12] investigated the estimation of rainfall data using L-moments. The authors tested their method using daily rainfall data from several stations in Korea and conducted a simulation study to test the effectiveness of the method for different sample sizes. Shabri et al. [13] proposed a new method called LQ-moment for estimating the parameters of the kappa distribution. This method relies on the concept of L-moment and is an extension of the L-moment method for estimating parameters of other distributions. The LQ-moment method is compared with the L-moment estimation. The results showed that the LQ-moment and L-moment methods performed similarly. Wan Zin et al. [14] modeled the maximum daily rainfall data obtained from several rain gauge stations in Malaysia. Ngongondo et al. [15] conducted a regional frequency analysis of rainfall extremes in Southern Malawi using the index rainfall and L-moment approaches. They found that the generalized extreme value distribution is the most suitable model for precipitation data analysis. Galorie et al. [16] conducted a study using rainfall data recorded for 66 years in Austria and estimated parameters of several well-known distributions using methods including the L-moment and ML. Rahman et al. [17] conducted a study to investigate appropriate probability distribution and associated parameter estimation procedures in at-site flood frequency analysis. They employed the ML, L-moment, and method of moments estimation for fitting annual maximum floods from Australia. According to their study different estimation methods and pdfs performed better for each station. Similarly, [18] used the L-moments approach to analyze daily rainfall extremes in Iran. They found that the generalized extreme value and three-parameter log-normal distributions are the best fit for their data. According to their study, the best-fitting distribution depends on the method of estimation and the data mostly follow the generalized logistic distribution, and the L-moment method performed better than the LQ-moment. Li et al. [19] conducted a study on the frequency analysis of extreme precipitation in the Heihe River basin in China, using daily precipitation observations between 1960-2010 years. They showed that theoretical return levels with the ML estimation show better approximations to the empirical ones for the precipitation data of the Heihe River. Zhou et al. [20] utilized Pearson type 3 and generalized extreme value distribution to forecast the annual maximum precipitation at the Changxi Station, located in the Taihu Basin. They employed different parameter estimation techniques, including the ML, L-moment, and conventional moment, and concluded that the generalized extreme value distribution with parameters estimated through the L-moment method yielded the best fit for the observed data at the Changxi Station. Khan et al. [21] investigated the effectiveness of different estimation methods including the L-moment, ML, and maximum product of spacing methods for modeling extreme precipitations. Their study found that the L-moment method performed the best in terms of accuracy and efficiency in estimating extreme values of precipitation data. It is also emphasized that the L-moment method can be preferred in case of small sample sizes.

In Türkiye, several studies have been carried out on modeling precipitation data. Some of them have already been discussed in the previous section. More studies using L-moment estimation are reviewed additionally. Although these studies employ the L-moment method in estimation, they generally focused more on fitting the most suitable pdf to data, a study [22] conducted a regional frequency analysis of rainfall data recorded in Trabzon province using L-moment estimation. The authors aimed to determine the most suitable pdf for the data and estimate the return periods of extreme rainfall events. Their study provides insights into extreme rainfall patterns and can contribute to the development of effective flood management strategies in the region. Seçkin et al. [23] conducted a flood frequency analysis employing the L-moment method. They analyzed flood events in six regions of Türkiye and found that the 3-parameter log-normal and Pearson type III distributions were the most suitable models for the precipitation data. [24] conducted a regional flood frequency analysis of the Çoruh Basin considering the L-moment method. Topcu et al. [25] analyzed the drought conditions of the Seyhan Basin by utilizing the L-moment method. Their findings highlighted the potential of these tools for drought analysis and management in the region. Also, Ghaei et al. [26] used the L-moment approach to conduct a regional intensity–duration–frequency analysis in the Eastern Black Sea region in Türkiye. They found that the generalized extreme value distribution provided the best fit for precipitation data.

Considering all of the reasons mentioned above, this paper investigates the efficiency of L-moment estimation with a particular focus on the application of the Inverted Kumaraswamy (IKum) distribution in modeling precipitation data from Rize, Türkiye. It should be noted that to the best of the author's knowledge L-moment estimation for parameters of the IKum distribution are obtained for the first time in this study. Moreover, with the L-moment estimation, the maximum likelihood (ML) method is considered in estimating parameters for comparison. In addition, a Monte-Carlo simulation study is conducted to examine these methods' efficiencies. Although, the L-moment method has the advantages of being robust and computationally simpler as emphasized in the study of [2] as is known the ML method is the most efficient estimation method under regularity conditions. It also stated that the L-moment estimates can even be more accurate than the ML estimates in small sample sizes. The comparison is done by using several well-known criteria including the root mean square error (RMSE), coefficient of determination (R^2), Kolmogorov Smirnov (KS) test and KS p-value.

Contributions of the study to related literature are given as follows. First, the L-moment estimates of unknown parameters of the IKum distribution are obtained and compared with ML estimates; second, a critical region in terms of flood risk is selected for analysis and the precipitation data of Rize is modeled for the first time using the IKum distribution.

The study is structured as follows: In Section 2 the methods used in the analysis along with L-moments of the IKum distribution described. Afterward, the presentation of precipitation data and modeling results are given. Finally, Section 4 discusses the findings of the study, which concludes with some final remarks.

Materials and Methods

In this section, primarily the data set is described. Then, the pdf of the IKum distribution is given and the L-moment estimations of its parameters are provided. Afterward, the results of the Monte-Carlo simulation are presented.

Data Set

In this study, the precipitation records obtained from the Rize gauge station are considered in the application. The data comprises monthly maximum precipitations between the dates of January 2021 and March 2023. The data are obtained from the Turkish State Meteorological Service. The data may be shared by the author upon request. As mentioned previously, Rize province experienced a devastating flood last year. For this reason, the data of this region is considered in this study and it is believed that it is important to obtain accurate predictions of the precipitations in the region.

The geographic location of Rize is given in Table 1.

Table 1. Geographical information of the Rize province

Latitude	Longitude
41.026089	40.518929

Descriptive statistics for precipitation data of Rize are provided in Table 2.

Table 2. Descriptive statistics

Descriptive Statistics	Values
Mean	45.6630
Skewness	1.723
Kurtosis	2.100
Variance	1196.713

The IKum Distribution

The IKum distribution is presented by Abd AL-Fattah et al. [5]. Due to its advantageous features, the IKum distribution has attracted attention. Consequently, many applications and extensions of it are presented in the literature, see [6] and [27].

Let X be a random variable following the IKum distribution with shape parameters α and θ, then its pdf is

$$f(x;\alpha,\theta)=\alpha\theta(1+x)^{-(\alpha-1)}(1-(1+x)^{-\alpha})^{\theta-1};$$
$$x>0,\alpha,\theta>0.$$

The Theoretical Background of the L-Moment Method

The L-moment theory proposed by Hosking [2] is based on order statistics. The method is generally adopted by the hydrology field. Hosking [2] showed that L-moments can be expressed by using linear combinations of probability-weighted moments PWMs (β_r) as well.

The first four theoretical L-moments are defined as

$$\lambda_1=\mathrm{E}[\mathrm{X}_{1:1}]=\int_0^1\mathrm{x(F)dF},$$
$$\lambda_2=\frac{1}{2}\mathrm{E}[\mathrm{X}_{2:2}-\mathrm{X}_{1:2}]=\int_0^1\mathrm{x(F)(2F-1)dF},$$
$$\lambda_3=\frac{1}{3}\mathrm{E}[\mathrm{X}_{3:3}-2\mathrm{X}_{2:3}+\mathrm{X}_{1:3}]=\int_0^1\mathrm{x(F)(6F^2-6F+1)dF},$$

and

$$\lambda_3=\frac{1}{4}\mathrm{E}[\mathrm{X}_{4:4}-3\mathrm{X}_{3:4}+3\mathrm{X}_{2:4}-\mathrm{X}_{1:4}]=\int_0^1\mathrm{x(F)(20F^3-30F^2+12F-1)dF}.$$

Here, X a real-valued random variable with cumulative distribution function $F(x)$ and quantile function $x(F)$ and $\mathrm{X}_{1:1}\leq\mathrm{X}_{2:n}\ldots\leq\mathrm{X}_{n:n}$ are the order statistics of a random sample of size n drawn from the distribution of X. Let n be the sample size, the *r*-th sample L-moment is

$$l_r=\Sigma\Sigma\ldots\Sigma r^{-1}\sum_{k=0}^{r-1}-1^k\binom{r-1}{k}x_{i_{r-k:n}}.$$
$$1\leq i_1<i_2\ldots<i_r\leq n,$$

L-moments can be obtained using the PWMs [28] given as follows,

$$\beta_r = \int_0^1 x(F)F^r dF$$

Here, F is non-exceedance probability.

$\lambda_1 = \beta_0,$
$\lambda_2 = 2\beta_1 - \beta_0,$
$\lambda_3 = 6\beta_2 - 6\beta_1 + \beta_0,$
$\lambda_4 = 20\beta_3 - 30\beta_2 + 12\beta_1 - \beta_0$ and sample L-moments are $l_1 = b_0, l_2 = 2b_1 - b_0, l_3 = 6b_2 - 6b_1 + b_0$ and $l_4 = 20b_3 - 30b_2 + 12b_1 - b_0$ when b_0, b_1, b_2 and b_3 are

$$b_0 = \frac{1}{n}\sum_{i=1}^{n} x_{i:n},\ b_1 = \frac{1}{n}\sum_{i=1}^{n} \frac{(i-1)}{(n-1)} x_{i:n},$$
$$b_2 = \frac{1}{n}\sum_{i=1}^{n} \frac{(i-1)(i-2)}{(n-1)(n-2)} x_{i:n},$$
$$b_3 = \frac{1}{n}\sum_{i=1}^{n} \frac{(i-1)(i-2)(i-3)}{(n-1)(n-2)(n-3)} x_{i:n}.$$

L-moment Estimation

The first four theoretical L-moments of the IKum distribution are

$$\lambda_1 = \theta\,\beta\left(\theta, 1-\frac{1}{a}\right) - 1,$$
$$\lambda_2 = 2\,\theta\beta\left(1-\frac{1}{a}, 2\,\theta\right) - \theta\,\beta\left(\theta, 1-\frac{1}{a}\right),$$
$$\lambda_3 = \theta\,\beta\left(\theta, 1-\frac{1}{a}\right) - 6\,\theta\,\beta\left(1-\frac{1}{a}, 2\,\theta\right) + 6\,\theta\,\beta\left(1-\frac{1}{a}, 3\,\theta\right)$$

and

$$\lambda_4 = 12\,\theta\,\beta\left(1-\frac{1}{a}, 2\,\theta\right) - \theta\,\beta\left(\theta, 1-\frac{1}{a}\right) - 30\,\theta\,\beta\left(1-\frac{1}{a}, 3\,\theta\right) + 20\theta\,\beta\left(1-\frac{1}{a}, 4\,\theta\right)$$

where $\alpha > 1$ and $\theta > 0$.

The L-moments estimations of the parameters of the IKum distribution are obtained by equating the first two theoretical L-moments to the corresponding sample moments, i.e., l_1 and l_2, respectively. Since these equations can not be solved explicitly, iterative techniques are employed in obtaining L-moment estimates of the parameters of the IKum distribution.

ML Estimation

The ML methodology aims to obtain the parameters maximizing the likelihood function. The ML estimators of the IKum distribution are not provided here for brevity since they were obtained previously in [5]. See [5] for more information on the ML estimators of the IKum distribution.

Simulation Study

As mentioned previously a Monte-Carlo simulation is conducted for comparing efficiencies of the ML and L-moment estimation methods. For the simulation study $n = 25, 50, 100, 500,$ and 1000 sample sizes are utilized. Performances of these methods are compared using Mean Squared Error (MSE) values for the cases considered. The simulations are implemented using the optimization toolbox in MatlabR2021 software and results are provided in Tables 3, 4 and 5. The formulas for the MSE criterion are,

$$MSE(\hat{a}) = E(\hat{a} - a)^2 \text{ and } MSE(\hat{\theta}) = E(\hat{\theta} - \theta)^2.$$

Table 3. Simulation results for a=3 and θ=1

	a=3			θ=1		
	Mean	**Var**	**MSE**	**Mean**	**Var**	**MSE**
n=25						
ML	3.3658	0.8573	0.9911	1.1266	0.1089	0.1249
L-Moment	3.3192	0.8465	0.9484	1.1319	0.1027	0.1201
n=50						
ML	3.1469	0.3863	0.4079	1.061	0.043	0.0467
L-Moment	3.1904	0.4346	0.4709	1.0719	0.0756	0.0808
n=100						
ML	3.0826	0.1689	0.1757	1.029	0.0197	0.0205
L-Moment	3.1338	0.2585	0.2764	1.0495	0.0424	0.0449
n=500						
ML	3.0156	0.0345	0.0348	1.005	0.0036	0.0036
L-Moment	3.0205	0.0634	0.0639	1.0068	0.0091	0.0092
n=1000						
ML	3.0131	0.0168	0.017	1.0045	0.0018	0.0018
L-Moment	3.0165	0.0332	0.0334	1.0059	0.0049	0.0049

Table 4. Simulation results for a=2 and θ=2

	a=2			θ=2		
	Mean	**Var**	**MSE**	**Mean**	**Var**	**MSE**
n=25						
ML	2.165	0.2676	0.2948	2.3199	0.7615	0.8638
L-Moment	2.3101	0.341	0.4372	2.5948	1.4917	1.8455
n=50						
ML	2.0922	0.1108	0.1193	2.1524	0.2503	0.2735
L-Moment	2.1858	0.1661	0.2006	2.3179	0.5267	0.6277
n=100						
ML	2.0518	0.0523	0.055	2.0867	0.1105	0.118
L-Moment	2.1181	0.0976	0.1115	2.2123	0.3014	0.3465
n=500						
ML	2.0084	0.0096	0.0097	2.0205	0.018	0.0184
L-Moment	2.0436	0.0265	0.0284	2.0836	0.0684	0.0754
n=1000						
ML	2.0033	0.0052	0.0052	2.0081	0.0089	0.009
L-Moment	2.022	0.0172	0.0177	2.0414	0.04	0.0417

Table 5. Simulation results for a=5 and θ=0.5

	a=5			θ=0.5		
	Mean	**Var**	**MSE**	**Mean**	**Var**	**MSE**
n=25						
ML	5.8202	4.1115	4.7842	0.552	0.0198	0.0225
L-Moment	5.7911	4.9961	5.622	0.5378	0.0424	0.0439
n=50						
ML	5.3649	1.5977	1.7309	0.5212	0.0086	0.0091
L-Moment	5.3999	2.0187	2.1786	0.5239	0.0188	0.0194
n=100						
ML	5.1719	0.6874	0.717	0.5084	0.0036	0.0036
L-Moment	5.1828	0.9579	0.9913	0.508	0.008	0.0081
n=500						
ML	5.0287	0.1265	0.1273	0.503	0.0007	0.0007
L-Moment	5.0301	0.1843	0.1852	0.5027	0.0016	0.0016
n=1000						
ML	5.0112	0.0619	0.062	0.5008	0.0003	0.0003
L-Moment	5.0069	0.0958	0.0958	0.5	0.0008	0.0008

According to Table 3, for both of the parameters, when sample size n= 25, the L-moment estimation performed better and for the other sample sizes the ML estimation provided more effective estimations. When both of the parameters are set to 2, for all sample sizes ML estimation performed better as presented in Table 4. Similarly, for the parameter settings, α=5 and θ=0.5 ML estimations are superior for all sample sizes. Overall, it can be said that although ML estimations are superior in general, for larger samples MSE values are close between the rivals. For the small samples, although ML estimations provided good performance in one scenario the L-moment method is better. Consequently, the L-moment estimation has shown a performance worth examining especially for small sample sizes.

Return Period

The return period is the average time between the occurrence of a specific event, such as a natural disaster or weather event, of a certain magnitude or greater. If an event of magnitude x_T occurs once in T years, where x represents the precipitations, the probability (P) of the variable exceeding or equaling x in any given year is expressed as follows

$$P(x \geq x_T) = 1/T$$

Application

In this section, the data are modeled using the IKum distribution. In estimating the parameters, the ML and L-moments methods are used and estimates of the parameters are given in Table 6, in addition, precipitations for the 10, 25, 50, and 100-year return periods are provided.

Table 6. Estimates of the parameters of the IKum distribution

Parameters	$\hat{\alpha}$	$\hat{\theta}$
L-Moment	2.22678	1793.4614
ML	1.6121	210.1573

Values of evaluating criteria for the L-moment and ML methods are provided in Table 7. As is known lower values of the KS and RMSE, higher values of KS (p-value) and R^2 criteria indicate a better fit.

Table 7. Fitting performance for the IKum distribution using estimation methods

Criteria	R^2	RMSE	KS (*p*-value)
L-Moment	0.9758	0.0451	0.1016 (0.9169)
ML	0.9438	0.0594	0.1582 (0.4616)

It can be seen from Table 7 that the L-moment provided the smallest values for the KS and RMSE and the largest values for the R^2. Thus, the L-moments method performed better in all criteria and provided more accurate estimates than ML in modeling the precipitation records of Rize province. It should be noted that the sample size in this study can be regarded as small (n=27). Furthermore, fitted density plots for the ML and L-moment methods are provided in Figure 1.

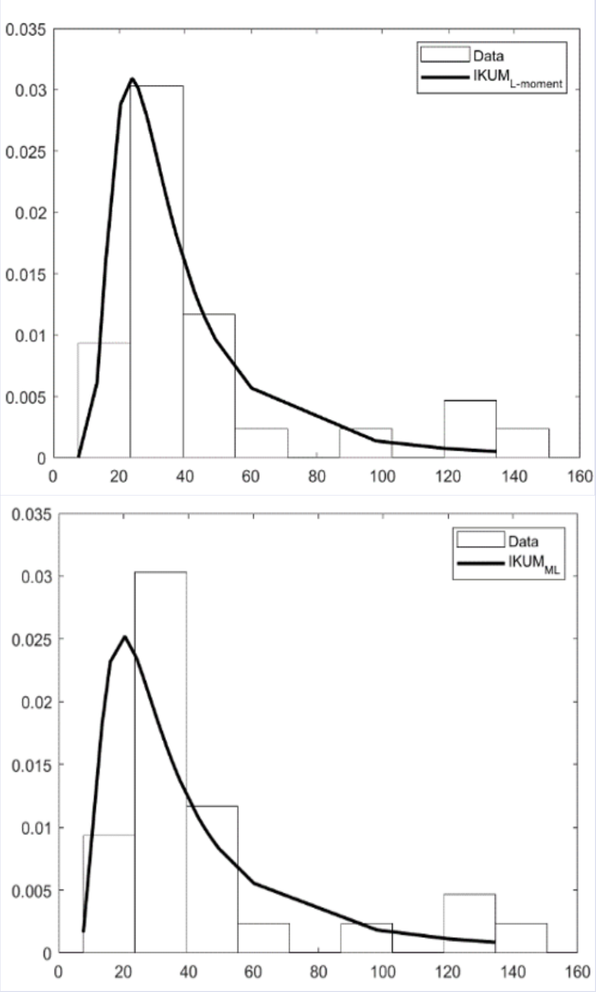

Figure 1. Fitted density plots of the IKum distribution using the L-moments and ML methods.

Figure 1 shows that the ML performed poorly than the L-moment at the peak of the distribution, although it fitted quite satisfactorily for the remaining part of the distribution. It can also be seen that the IKum distribution presents the advantages of having a longer right tail and the precipitation data in the right tail of the distribution are modeled quite well. Consequently, the results pointed out in Table 7 are also supported by the plots.

Return period information is a valuable tool for policymakers and planners, enabling them to make informed decisions within defined timeframes. The return periods are obtained for the precipitations of the Rize station for the ML and L-moment estimations. When the ML method is utilized, the precipitations equivalent to 10, 25, 50, and 100-year return periods are 110.4272, 199.6232, 309.3570, and 477.5745, respectively. However when the L-moment estimation is considered the precipitations are calculated as 78.4441, 120.6133, 165.7886, and 227.2125 for the given return periods. For instance, the precipitation value of 78.4441 can be considered as the average occurrence expected once every 10 years when the L-moment method is used. Thus, one can see how much the estimation method can differentiate the results. This situation may pose risks in terms of planning and emphasizes the importance of the accurate prediction of precipitation is essential for effective hydrological modeling.

Conclusion

Modeling precipitations using probability distributions generally paired with the L-moment method in parameter estimation. In this study, the estimations of the L-moment method and the ML are compared. In this context, the L-moment estimations of parameters for the IKum distribution are obtained for the first time. It has been noted that, although the simulation study favored the MLE method, the L-moments method was more effective in one scenario, when the sample size was small. In the application part, the annual maximum monthly precipitations recorded in Rize are modeled and results show that the L-moment method allows for estimating parameters more accurately. While simulation results often favor the MLE, real data applications may not always align with these results as in this case. Overall, the prediction of precipitation amounts is an important issue for the planning and design of flood protection systems. It is hoped that this study will contribute to the management of risks arising from floods.

Conflicts of interest

There are no conflicts of interest in this work.

References

[1] European Environmental Agency, EEA, (2023) Available at: https://www.eea.europa.eu/tr.

[2] Hosking J.R.M., L-Moments: Analysis and Estimation of Distributions Using Linear Combinations of Order Statistics, *Journal of the Royal Statistical Society: Series B (Methodological),* 52(1) (1990) 105–124.

[3] Hosking J. R. M., Wallis J.R., *Regional Frequency Analysis*, (1997).

[4] Amin M.T., Rizwan M., Alazba A.A., A best-fit probability distribution for the estimation of rainfall in northern regions of Pakistan, *Open Life Sciences*, 11(1) (2016) 432–440.

[5] Abd AL-Fattah A.M., El-Helbawy A.A., Al-Dayian G.R., Inverted Kumaraswamy Distribution: Properties and Estimation, *Pakistan Journal of Statistics,* 33 (1) (2017).

[6] Usman R.M., Ahsan ul Haq M., The Marshall-Olkin extended inverted Kumaraswamy distribution: Theory and applications, *J. King Saud Univ. Sci.,* 32(1) (2020) 356–365.

[7] Bagci K., Arslan T., Celik H.E., Inverted Kumarswamy distribution for modeling the wind speed data: Lake Van, Turkey, *Renewable and Sustainable Energy Reviews,* 135 (2021) 110110.

[8] Şen O., Kahya E., Impacts of climate change on intensity–duration–frequency curves in the rainiest city (Rize) of Turkey, *Theor Appl Climatol,* 144(3) (2021) 1017–1030.

[9] Yozgatlıgil C., Türkeş M., Extreme value analysis and forecasting of maximum precipitation amounts in the western Black Sea subregion of Turkey, *International Journal of Climatology,* 38(15) (2018) 5447–5458.

[10] Cengiz T.M. et al., Combined Use of Graphical and Statistical Approaches for Analyzing Historical Precipitation Changes in the Black Sea Region of Turkey, *Water (Basel),* 12(3) (2020).

[11] Aksu H. et al., Spatial and temporal characterization of standard duration-maximum precipitation over Black Sea Region in Turkey, *Natural Hazards,* 111(3) (2022) 2379–2405.

[12] Lee S.H. and Maeng S.J., Estimation of drought rainfall using L-moments, *Irrigation and Drainage,* 54(3) (2005) 279–294.

[13] Shabri A. and Jemain A.A., LQ-moments: Parameter estimation for kappa distribution, *Sains Malays,* 39(5) (2010) 845–850.

[14] Wan Zin W.Z., Jemain A.A., and Ibrahim K., The best fitting distribution of annual maximum rainfall in Peninsular Malaysia based on methods of L-moment and LQ-moment, *Theor Appl Climatol,* 96(3) (2009) 337–344.

[15] Ngongondo C.S. et al., Regional frequency analysis of rainfall extremes in Southern Malawi using the index rainfall and L-moments approaches, *Stochastic Environmental Research and Risk Assessment,* 25(7) (2011) 939–955.

[16] Galoie M., Zenz G., Eslamian S., Application of L-moments for IDF determination in an Austrian basin, *International Journal of Hydrology Science and Technology,* 3(1) (2013) 30–48.

[17] Rahman A.S. et al., A study on selection of probability distributions for at-site flood frequency analysis in Australia, *Natural Hazards,* 69(3) (2013) 1803–1813.

[18] Malekinezhad H., Zare-Garizi A., Regional frequency analysis of daily rainfall extremes using L-moments approach, *Atmósfera,* 27(4) (2014) 411–427.

[19] Li Z. et al., Frequency analysis of precipitation extremes in Heihe River basin based on generalized Pareto distribution, *Stochastic Environmental Research and Risk Assessment,* 28(7) (2014) 1709–1721.

[20] Zhou Z. et al., Frequency Analysis for Predicting Extreme Precipitation in Changxing Station of Taihu Basin, China, *J Coast Res,*(68(10068)) (2014) 144–151.

[21] ul R. Khan M.S., Hussain Z., and Ahmad I., Effects of L-Moments, Maximum Likelihood and Maximum Product of Spacing Estimation Methods in Using Pearson Type-3 Distribution for Modeling Extreme Values, *Water Resources Management,* 35(5) (2021) 1415–1431.

[22] Anli A.S., Apaydin H., and Öztürk F., Regional frequency analysis of the annual maximum precipitation observed in Trabzon Province, *Tarim Bilimleri Dergisi,* 15(3) (2009) 240–248.

[23] Seckin N., Haktanir T., Yurtal R., Flood frequency analysis of Turkey using L-moments method, *Hydrol Process,* 25(22) (2011) 3499–3505.

[24] Aydoğan D., Kankal M., Önsoy H., Regional flood frequency analysis for Çoruh Basin of Turkey with L-moments approach, *J Flood Risk Manag,* 9(1) (2016) 69–86.

[25] Topcu E., Seckin N., Drought analysis of the Seyhan Basin by using standardized precipitation index SPI and L-moments, *J Agric Sci,(Belihuloya)* 22(2) (2016) 196–215.

[26] Ghiaei F. et al., Regional intensity–duration–frequency analysis in the Eastern Black Sea Basin, Turkey, by using L-moments and regression analysis, *Theor Appl Climatol,* 131(1) (2018) 245–257.

[27] Bagci K. et al., Alpha power inverted Kumaraswamy distribution: Definition, different estimation methods, and application, *Pakistan Journal of Statistics and Operation Research,*(2022) 13–25.

[28] Greenwood J.A. et al., Probability weighted moments: Definition and relation to parameters of several distributions expressable in inverse form, *Water Resour Res,* 15(5) (1979) 1049–1054.

AUTHOR GUIDELINES

Thank you for choosing to submit your paper to Cumhuriyet Science Journal. The following instructions will ensure we have everything required so your paper can move through pre-evaluating, peer review, production and publication smoothly. Please take the time to read and follow them as closely as possible, as doing so will ensure your paper matches the journal's requirements.

Submission

Cumhuriyet Science Journal is an international, peer-reviewed, free of charge journal covering the full scope of both natural and engineering sciences. Manuscripts should be submitted by one of the authors of the manuscript as online submission after registration to the Cumhuriyet Sciences Journal. Microsoft Word (.doc, .docx, .rtf), files can be submitted. There is no page limit. If there is a problem while uploading the files of manuscript, please try to reduce their file size, especially manuscripts including embedded figures. Submissions by anyone other than one of the authors will not be accepted. The submitting author takes responsibility for the paper during submission and peer review. If for some technical reason submission through the online submission systme is not possible, the author can contact csj@cumhuriyet.edu.tr for support.

Submission or processing charges

Cumhuriyet Science Journal does not charge any article submission, processing charges, and printing charge from the authors.

Terms of Submission

Papers must be submitted on the understanding that they have not been published elsewhere (except in the form of an abstract or as part of a published lecture, review, or thesis) and are not currently under consideration by another journal. The submitting author is responsible for ensuring that the article's publication has been approved by all the other coauthors. It is also the authors' responsibility to ensure that the articles emanating from a particular institution are submitted with the approval of the necessary institution. Only an acknowledgment from the editorial office officially establishes the date of receipt. Further correspondence and proofs will be sent to the author(s) before publication unless otherwise indicated. It is a condition of submission of a paper that the corresponding author permit editing of the paper for readability. All enquiries concerning the publication of accepted papers should be addressed to csj@cumhuriyet.edu.tr. Please note that Cumhuriyet Science Journal uses iThenticate software to screen papers for unoriginal material. By submitting your paper to Cumhuriyet Science Journal are agreeing to any necessary originality checks your paper may have to undergo during the peer review and production processes. Upon receiving a new manuscript, the Editorial office conducts initial pre-refereeing checks to ensure the article is legible, complete, correctly formatted, original, within the scope of the journal in question, in the style of a scientific article and written in clear English. Any article that has problems with any of the journal criteria may be rejected at this stage.

Peer Review

This journal operates a single blind review process. All contributions will be initially assessed by the editor for suitability for the journal. Papers deemed suitable are then typically sent to a minimum of two independent expert reviewer to assess the scientific quality of the paper. The author is required to upload the revised article to the system within 15 days by making the corrections suggested by the referee. The article will be rejected if there are no fixes in it. The Editor is responsible for the final decision regarding acceptance or rejection of articles. The Editor's decision is final

Title and Authorship Information

The following information should be included

Paper title

Full author names

Full institutional mailing addresses

Corresponding address

Email address

Abstract

The manuscript should contain an abstract. The researchers who are native speakers of Turkish have to add Turkish title and abstract as well. The abstract should be self-contained and citation-free and should be 250-300 words.

Keywords

Keywords of the scientific articles should be selected from the web address of www.bilimadresleri.com

Introduction

This section should be succinct, with no subheadings.

Materials and Methods

This part should contain sufficient detail so that all procedures can be repeated. It can be divided into subsections if required.

Conflicts of interest

Sample sentence if there is no conflict of interest: The authors stated that did not have conflict of interests.

Acknowledgements

Sample sentences for acknowledgements: The work was supported by grants from CUBAP (T-11111). We would like to acknowledge Prof. Mehmet Sözer, MD, for his precious technical and editorial assistance. We would like to thank

References

References to cited literature should be identified by number in the text in square brackets and grouped at the end of the paper in numerical order of appearance. Each reference must be cited in the text. Always give inclusive page numbers for references to journal articles and a page range or chapter number for books. References should be styled and punctuated according to the following examples

[1] Karaca E., Ulusoy S., Morgül Ü., Ulusoy H.I., Development of Analytical Method for Sensitive Determination of Streptozotocin based on Solid Phase Extraction, Cumhuriyet Sci. J., 41 (4) (2020) 826-831. (sample reference for journals)

[2] Keskin B., Ozkan A.S., Inverse Spectral Problems for Dirac Operator with Eigenvalue Dependent Boundary and Jump Conditions, Acta Math. Hungar., 130 (2011) 150-159(sample reference for journals)

[3] Mazur M.T., Kurman R.J., Dysfunctional Uterine Bleeding. In: Mazur M.T., Kurman R.J., (Eds). Diagnosis of endometrial biopsies and curettings, A practical approach. 2nd ed. Berlin: Springer, (2005) 100-120. (sample reference for book chapters)

[4] Mazur M.T., Kurman R.J.,Diagnosis of endometrial biopsies and curettings, A practical approach. 2nd ed. Berlin, (2005) 100-120. (sample reference for book)

[5] National Cancer Institute, Surveillance Epidemiology and End Results. Cancer of the Corpus and Uterus, NOS. Available at: http://seer.cancer.gov/statfacts/html/corp.html?statfacts_page=corp. Retrieved March 2, 2008. (sample reference for websites)

[6] Surname N., Title of thesis, PD or master thesis, Name of university, name of institue, year. (sample reference for thesis)

[7] Surname N., Title of fulltext conference paper, name of conference, city, year, pages. (sample reference for Abstratcs in conferences are not accepted as a valid reference except full text)

Preparation of Figures

Each figure can be integrated in the paper body or separately uploaded and should be cited in a consecutive order. Figure widths can be 4-6 inch as 300 dpi. The labels of the figures should be clear and informative. The name and the subtitles of the figures must be 9-point font.

Preparation of Tables

Tables should be cited consecutively in the text. Every table must have a descriptive title and if numerical measurements are given, the units should be included in the column heading. Tables should be simple with simple borders and text written as left text. The name and the subtitle of the tables must be 9-point font

Proofs

Corrected proofs must be returned to the publisher within 2 weeks of receipt. The publisher will do everything possible to ensure prompt publication. It will therefore be appreciated if the manuscripts and figures conform from the outset to the style of the journal.

Copyright

Open Access authors retain the copyrights of their papers, and all open access articles are distributed under the terms of the Creative Commons Attribution license, which permits unrestricted use, distribution and reproduction in any medium, provided that the original work is properly cited.

The use of general descriptive names, trade names, trademarks, and so forth in this publication, even if not specifically identified, does not imply that these names are not protected by the relevant laws and regulations.

While the advice and information in this journal are believed to be true and accurate on the date of its going to press, neither the authors, the editors, nor the publisher can accept any legal responsibility for any errors or omissions that may be made. The publisher makes no warranty, express or implied, with respect to the material contained herein.

Ethical Guidelines

New methods and ethically relevant aspects must be described in detail, bearing in mind the following:

Human Experiments. All work must be conducted in accordance with the Declaration of Helsinki (1964). Papers describing experimental work on human subjects who carry a risk of harm must include:

A statement that the experiment was conducted with the understanding and the consent of the human subject.

A statement that the responsible Ethical Committee has approved the experiments.

Animal Experiments. Papers describing experiments on living animals should provide:

A full description of any anaesthetic and surgical procedure used.

Evidence that all possible steps were taken to avoid animal suffering at each stage of the experiment. Papers describing experiments on isolated tissues must indicate precisely how the donor tissues were obtained.

Submission Preparation Checklist

As part of the submission process, authors are required to check off their submission's compliance with all of the following items, and submissions may be rejected that do not adhere to these guidelines.

The submission has not been previously published, nor is it before another journal for consideration (or an explanation has been provided in Comments to the Editor).

The submission file is in Microsoft Word document file (Times New Roman) format.

Where available, URLs for the references have been provided.

The text is single-spaced; uses a 11-point font; employs italics, rather than underlining (except with URL addresses); and all illustrations, figures, and tables are placed within the text at the appropriate points, rather than at the end.

The text adheres to the stylistic and bibliographic requirements outlined in the Author Guidelines, which is found in About the Journal.

If submitting to a peer-reviewed section of the journal, the instructions in Ensuring a Double-Blind Review have been followed.